VOLCANIC ISLANDS - A CHALLENGE FOR VOLCANOLOGY

EDITED BY: Alessandro Bonforte, Joan Marti, Antonio Paonita and Michel Pichavant

PUBLISHED IN: Frontiers in Earth Science



frontiers Research Topics

Frontiers eBook Copyright Statement

The copyright in the text of individual articles in this eBook is the property of their respective authors or their respective institutions or funders. The copyright in graphics and images within each article may be subject to copyright of other parties. In both cases this is subject to a license granted to Frontiers.

The compilation of articles constituting this eBook is the property of Frontiers.

Each article within this eBook, and the eBook itself, are published under the most recent version of the Creative Commons CC-BY licence. The version current at the date of publication of this eBook is CC-BY 4.0. If the CC-BY licence is updated, the licence granted by Frontiers is automatically updated to the new version.

When exercising any right under the CC-BY licence, Frontiers must be attributed as the original publisher of the article or eBook, as applicable.

Authors have the responsibility of ensuring that any graphics or other materials which are the property of others may be included in the CC-BY licence, but this should be checked before relying on the CC-BY licence to reproduce those materials. Any copyright notices relating to those materials must be complied with.

Copyright and source acknowledgement notices may not be removed and must be displayed in any copy, derivative work or partial copy which includes the elements in question.

All copyright, and all rights therein, are protected by national and international copyright laws. The above represents a summary only. For further information please read Frontiers' Conditions for Website Use and Copyright Statement, and the applicable CC-BY licence.

ISSN 1664-8714
ISBN 978-2-88976-579-9
DOI 10.3389/978-2-88976-579-9

About Frontiers

Frontiers is more than just an open-access publisher of scholarly articles: it is a pioneering approach to the world of academia, radically improving the way scholarly research is managed. The grand vision of Frontiers is a world where all people have an equal opportunity to seek, share and generate knowledge. Frontiers provides immediate and permanent online open access to all its publications, but this alone is not enough to realize our grand goals.

Frontiers Journal Series

The Frontiers Journal Series is a multi-tier and interdisciplinary set of open-access, online journals, promising a paradigm shift from the current review, selection and dissemination processes in academic publishing. All Frontiers journals are driven by researchers for researchers; therefore, they constitute a service to the scholarly community. At the same time, the Frontiers Journal Series operates on a revolutionary invention, the tiered publishing system, initially addressing specific communities of scholars, and gradually climbing up to broader public understanding, thus serving the interests of the lay society, too.

Dedication to Quality

Each Frontiers article is a landmark of the highest quality, thanks to genuinely collaborative interactions between authors and review editors, who include some of the world's best academicians. Research must be certified by peers before entering a stream of knowledge that may eventually reach the public - and shape society; therefore, Frontiers only applies the most rigorous and unbiased reviews.
Frontiers revolutionizes research publishing by freely delivering the most outstanding research, evaluated with no bias from both the academic and social point of view. By applying the most advanced information technologies, Frontiers is catapulting scholarly publishing into a new generation.

What are Frontiers Research Topics?

Frontiers Research Topics are very popular trademarks of the Frontiers Journals Series: they are collections of at least ten articles, all centered on a particular subject. With their unique mix of varied contributions from Original Research to Review Articles, Frontiers Research Topics unify the most influential researchers, the latest key findings and historical advances in a hot research area! Find out more on how to host your own Frontiers Research Topic or contribute to one as an author by contacting the Frontiers Editorial Office: frontiersin.org/about/contact

VOLCANIC ISLANDS - A CHALLENGE FOR VOLCANOLOGY

Topic Editors:
Alessandro Bonforte, Istituto Nazionale di Geofisica e Vulcanologia (INGV), Italy
Joan Marti, Spanish National Research Council (CSIC), Spain
Antonio Paonita, Istituto Nazionale di Geofisica e Vulcanologia (INGV), Italy
Michel Pichavant, CNRS Orléans, France

Citation: Bonforte, A., Marti, J., Paonita, A., Pichavant, M., eds. (2022). Volcanic Islands - A Challenge for Volcanology. Lausanne: Frontiers Media SA. doi: 10.3389/978-2-88976-579-9

Table of Contents

04 ***Editorial: Volcanic Islands—A Challenge for Volcanology***
Alessandro Bonforte, Joan Martí, Antonio Paonita and Michel Pichavant

06 ***Eruption Style, Emplacement Dynamics and Geometry of Peralkaline Ignimbrites: Insights From the Lajes-Angra Ignimbrite Formation, Terceira Island, Azores***
Adriano Pimentel, Stephen Self, José M. Pacheco, Adam J. Jeffery and Ralf Gertisser

29 ***Unraveling the Holocene Eruptive History of Flores Island (Azores) Through the Analysis of Lacustrine Sedimentary Records***
Mariana Andrade, Ricardo S. Ramalho, Adriano Pimentel, Armand Hernández, Steffen Kutterolf, Alberto Sáez, Mario Benavente, Pedro M. Raposeiro and Santiago Giralt

47 ***Eruption Sequences and Characteristics of Weizhou Island Volcano, Guangxi Province, South of China***
Hongmei Yu, Wenjian Yang, Bo Zhao, Zhengquan Chen, Bin Zhou, Guanjun Nie and Hao Luo

63 ***Gas Emissions From the Western Aleutians Volcanic Arc***
Tobias P. Fischer, Taryn M. Lopez, Alessandro Aiuppa, Andrea L. Rizzo, Tehnuka Ilanko, Katherine A. Kelley and Elizabeth Cottrell

80 ***Intermittent Growth of a Newly-Born Volcanic Island and Its Feeding System Revealed by Geological and Geochemical Monitoring 2013–2020, Nishinoshima, Ogasawara, Japan***
Fukashi Maeno, Atsushi Yasuda, Natsumi Hokanishi, Takayuki Kaneko, Yoshihiko Tamura, Mitsuhiro Yoshimoto, Shun Nakano, Akimichi Takagi, Minoru Takeo and Setsuya Nakada

103 ***The Submarine Boundaries of Mount Etna's Unstable Southeastern Flank***
Morelia Urlaub, Jacob Geersen, Florian Petersen, Felix Gross, Alessandro Bonforte, Sebastian Krastel and Heidrun Kopp

120 ***The Volcanic Hazards of Jan Mayen Island (North-Atlantic)***
Eirik Gjerløw, Ármann Höskuldsson, Stefania Bartolini, Sebastien Biass, Sophie Mossoux, Jennie Gilbert, Rolf Birger Pedersen and Joan Martí

139 ***A 1.5 Ma Marine Record of Volcanic Activity and Associated Landslides Offshore Martinique (Lesser Antilles): Sites U1397 and U1399 of IODP 340 Expedition***
Benoît Villemant, Anne Le Friant, Benoît Caron, Giulia Del Manzo, Sara Lafuerza, Laurent Emmanuel, Osamu Ishizuka, Hervé Guyard, Nathalie Labourdette, Agnès Michel and Samia Hidalgo

165 ***Mantle and Crustal Xenoliths in a Tephriphonolite From La Palma (Canary Islands): Implications for Phonolite Formation at Oceanic Island Volcanoes***
Andreas Klügel, Elmar Albers and Thor H. Hansteen

191 ***The Geochemical Evolution of Santa Cruz Island, Galápagos Archipelago***
E. L. Wilson, K. S. Harpp, D. M. Schwartz and R. Van Kirk

frontiers | Frontiers in Earth Science

EDITORIAL
published: 22 June 2022
doi: 10.3389/feart.2022.954902

Editorial: Volcanic Islands—A Challenge for Volcanology

Alessandro Bonforte[1]*, *Joan Martí*[2], *Antonio Paonita*[3] and *Michel Pichavant*[4]

[1]Istituto Nazionale di Geofisica e Vulcanologia (INGV), Sezione di Catania - Osservatorio Etneo, Catania, Italy, [2]Geosciences Barcelona, CSIC, Barcelona, Spain, [3]Istituto Nazionale di Geofisica e Vulcanologia (INGV), Sezione di Palermo - Osservatorio Etneo, Palermo, Italy, [4]Institut des Sciences de la Terre d'Orléans, CNRS, Orléans, France

Keywords: eruption, magma-water interaction, seafloor, submarine volcanic edifice, eruptive stratigraphy, eruptive scenarios, hazard and risk

Editorial on the Research Topic

Volcanic Islands - A Challenge for Volcanology

Most volcanoes on the Earth rise from the bottom of seas and oceans. Most of them do not reach the surface of sea and remain hidden to all conventional observations from surface and space. Only some of them rise above the sea level, forming islands and passing from submarine to subaerial volcanism. Volcanic islands develop in virtually all the geodynamic contexts on Earth, from mid-ocean ridges (Iceland), to intraplate (Hawaii), to volcanic arcs (Aeolian Islands). All the liquid-descent evolutive degrees of magma are finally represented, from primitive compositions up to strongly evolved rhyolite, trachyte and phonolite lavas. So, the eruptive styles of these volcanoes range consequently from mild effusions to plinian eruptions.

The interface with the sea poses some particular conditions due to the interaction with seawater, both at surface and below. Large hydrothermal activity easily develops due to the circulation of seawater at depth, and consequent interaction with magmatic gases and hot country rocks. The presence of the water and sea erosion also triggers particular instability conditions of the slopes of these volcanic edifices, so that the effects by seismicity and ground deformations can become disastrous. Volcanic island are by far the most vulnerable environments on Earth, not only because of their high exposure to the impact of multi-hazards, where several hazardous phenomena may interact in a simultaneous or consecutive way, but also due to their isolation from the main land, which makes external supply chains and help during a crisis difficult. A large number of volcanic islands are in fact intensively inhabited, despite the limited available lands, thus the common volcanic phenomenologies pose severe hazardous scenarios and submarine eruptions and landslides triggering catastrophic tsunami waves have to be considered.

One of the most important Research Topics to be considered when investigating and monitoring island volcanoes, is that most of the edifice is submerged and the emerging part only constitutes the summit of the volcano. This poses enormous difficulties to scientists, both from a scientific and technological point of view, because the development of monitoring systems at seafloor is still in its infancy. On this ground, such edifices represent one of the most important and interesting challenges for volcanologists and Earth scientists in general.

This Research Topic collected 10 contributions, covering a very wide range of disciplines, from petrology to submarine geophysics, all aimed at understanding and characterizing the activity, dynamics and hazards of volcanoes developing at the interface between land and sea, not only forming islands but also raising above the sea along a continental coastline. This latter is the case of Mt. Etna, whose submerged eastern flank has been investigated in one of the contributions (Urlaub et al.), describing and analyzing a wide series of geophysical imaging and seafloor geodetic surveys

OPEN ACCESS

Edited and reviewed by:
Valerio Acocella,
Roma Tre University, Italy

***Correspondence:**
Alessandro Bonforte
alessandro.bonforte@ingv.it

Specialty section:
This article was submitted to Volcanology, a section of the journal Frontiers in Earth Science

Received: *27 May 2022*
Accepted: *07 June 2022*
Published: *22 June 2022*

Citation:
Bonforte A, Martí J, Paonita A and Pichavant M (2022) Editorial: Volcanic Islands—A Challenge for Volcanology. Front. Earth Sci. 10:954902. doi: 10.3389/feart.2022.954902

that unveil some volcano-tectonic structures probably representing the link between flank dynamics and tectonic triggering of the instability.

Arc volcanic islands have also been investigated in this Research Topic, that is the case of the Aleutian Arc segment (Fischer et al.). Geochemical data show that all these volcanoes host high-temperature magmatic-hydrothermal systems and have gas discharges typical of volcanoes in oceanic arcs. Volcanic CO_2 fluxes from this arc segment are small, probably due to the lower sediment flux delivered to the trench in this part of the arc.

In volcanic islands, stratigraphy and sedimentary records can be particularly useful to reconstruct past volcanic activity. One of the contributions (Andrade et al.) focused on Flores island (Azores) shows in fact that the volcano experienced vigorous volcanic activity during the Late Holocene; therefore, contrary to what is assumed, the possibility of future eruptions should be properly considered, and the volcanic hazard here should not be underestimated.

The Hazard aspects have been investigated also for remote islands, in a contribution (Gjerløw et al.) focused on Jan Mayen Island, in the North-Atlantic. The eruptive history of this island, showing variable activity styles, has been exploited for evaluating the different vent opening probabilities, exposure to different volcanic phenomena and recurrence times for depicting different scenarios and qualitative hazard maps.

A similar hazard evaluation come from tha PDCs deposits on Terceira island (Pimentel et al.). Studies on the geometry and structure of two ignimbrite deposits on the island reveal interesting details on the eruptions that produced them. Even if ignimbrite-forming eruptions are not frequent on that volcano, this kind of hazard is significant, since its effect can be dramatic for the population.

Geochronological and isotopes analyses, as well as field surveys and petrological analysis were used for reconstructing the eruptive history of Weizhou island in the Guangxi Province (China), for evaluating the risk to inhabitants (Yu et al.). A very variable eruptive style has been found on the four volcanoes discovered, spanning from explosive, PDC-forming eruptions to effusive ones, also with some evidences of magma-water interaction.

The Canary Islands are a classical site locality for alkaline, SiO_2-undersaturated intraplate magmas (Klügel et al.). Products from one eruption of the now active Cumbre Vieja volcano of La Palma contain abundant inclusions from different levels of the plumbing system, mantle rocks, oceanic gabbros and cumulates. Phonolites form beneath oceanic island volcanoes by combined differentiation and periodic recharge by mantle magmas. They require a balance between rates and volumes of magma recharge pulses and of eruptive events.

In small islands such as Martinique (Lesser Antilles), the history of the volcanic activity is generally better preserved in submarine deposits than on-land (Villemant et al.). Cores of marine sediments reconstitute the chronostratigraphy of tephra, volcaniclastic turbidites, and mass-wasting events over 1.5 Ma. Results provide a framework for further petrological studies of Mt Pelée and Pitons du Carbet and for the timing of flank collapses and submarine landslides.

The very recent eruptive history of a newborn and growing island has been analyzed and correlated with the variations of the chemical composition of erupted magma (Maeno et al.). Results of this analysis have been used to infer the minimum eruption rates and durations required for forming volcanic islands able to survive to the erosion.

Volcanism on ocean island can also serve as windows into the composition and behavior of mantle plumes (Wilson et al.). Santa Cruz volcano (Galapagos) followed a distinct geochemical evolution from the present-day western shields, having been constructed under the influence of the Galápagos Spreading Center. Ocean island evolution can change dramatically depending on the plume's tectonic setting.

AUTHOR CONTRIBUTIONS

All authors listed have made a substantial, direct, and intellectual contribution to the work and approved it for publication.

Conflict of Interest: The authors declare that the research was conducted in the absence of any commercial or financial relationships that could be construed as a potential conflict of interest.

Publisher's Note: All claims expressed in this article are solely those of the authors and do not necessarily represent those of their affiliated organizations, or those of the publisher, the editors and the reviewers. Any product that may be evaluated in this article, or claim that may be made by its manufacturer, is not guaranteed or endorsed by the publisher.

Copyright © 2022 Bonforte, Martí, Paonita and Pichavant. This is an open-access article distributed under the terms of the Creative Commons Attribution License (CC BY). The use, distribution or reproduction in other forums is permitted, provided the original author(s) and the copyright owner(s) are credited and that the original publication in this journal is cited, in accordance with accepted academic practice. No use, distribution or reproduction is permitted which does not comply with these terms.

frontiers in Earth Science

ORIGINAL RESEARCH
published: 25 June 2021
doi: 10.3389/feart.2021.673686

Eruption Style, Emplacement Dynamics and Geometry of Peralkaline Ignimbrites: Insights From the Lajes-Angra Ignimbrite Formation, Terceira Island, Azores

Adriano Pimentel[1,2]*, *Stephen Self*[3], *José M. Pacheco*[2], *Adam J. Jeffery*[4] and *Ralf Gertisser*[4]

[1]Centro de Informação e Vigilância Sismovulcânica dos Açores (CIVISA), Ponta Delgada, Portugal, [2]Instituto de Investigação em Vulcanologia e Avaliação de Riscos (IVAR), Universidade dos Açores, Ponta Delgada, Portugal, [3]Department of Earth and Planetary Science, University of California, Berkeley, CA, United States, [4]School of Geography, Geology and the Environment, Keele University, Keele, United Kingdom

Ignimbrites are relatively uncommon on ocean island volcanoes and yet they constitute a significant portion of the stratigraphy of Terceira Island (Azores). The Lajes-Angra Ignimbrite Formation (ca. 25 cal ka BP) contains the youngest ignimbrites on Terceira and records two ignimbrite-forming eruptions of Pico Alto volcano that occurred closely spaced in time. Here, we present the first detailed lithofacies analysis and architecture of the Angra and Lajes ignimbrites, complemented by petrographic, mineral chemical, whole rock and groundmass glass geochemical data. The two ignimbrites have the same comenditic trachyte composition, but show considerable variability in trace element and groundmass glass compositions, revealing complex petrogenetic processes in the Pico Alto magma reservoir prior to eruption. The Angra Ignimbrite has a high-aspect ratio and is massive throughout its thickness. It was formed by a small-volume but sustained pyroclastic density current (PDC) fed by a short-lived, low pyroclastic fountain. Overall, the PDC had high particle concentration, granular fluid-based flow conditions and was mostly channelled into a valley on the south part of Terceira. By contrast, the Lajes Ignimbrite has a low-aspect ratio and shows vertical and lateral lithofacies variations. It was formed by a sustained quasi-steady PDC generated from vigorous and prolonged pyroclastic fountaining. The ignimbrite architecture reveals that depositional conditions of the parent PDC evolved as the eruption waxed. The dilute front of the current rapidly changed to a high particle concentration, granular fluid-based PDC that extended to the north and south coasts, with limited capacity to surmount topographic highs. Contrary to what is commonly assumed, the low-aspect ratio of the Lajes Ignimbrite is interpreted to result from deposition of a relatively low velocity PDC over a generally flat topography. This work highlights that the geometry (aspect ratio) of ignimbrites does not necessarily reflect the kinetic energy of PDCs and thus should not be used as a proxy for PDC emplacement dynamics. Although the probability of an ignimbrite-forming eruption on Terceira is relatively low, such a scenario should not be underestimated, as a future event would have devastating consequences for the island's 55,000 inhabitants.

Keywords: explosive volcanism, oceanic island, pyroclastic fountaining, pyroclastic density current, ignimbrite aspect ratio, comenditic trachyte, volcanic hazard

OPEN ACCESS

Edited by:
Joan Marti,
Consejo Superior de Investigaciones Científicas (CSIC), Spain

Reviewed by:
Claudio Scarpati,
University of Naples Federico II, Italy
Dario Pedrazzi,
Instituto de Ciencias de la Tierra Jaume Almera (ICTJA), Spain

***Correspondence:**
Adriano Pimentel
adriano.hg.pimentel@azores.gov.pt

Specialty section:
This article was submitted to Volcanology, a section of the journal Frontiers in Earth Science

Received: *28 February 2021*
Accepted: *07 June 2021*
Published: *25 June 2021*

Citation:
Pimentel A, Self S, Pacheco JM, Jeffery AJ and Gertisser R (2021) Eruption Style, Emplacement Dynamics and Geometry of Peralkaline Ignimbrites: Insights From the Lajes-Angra Ignimbrite Formation, Terceira Island, Azores. Front. Earth Sci. 9:673686. doi: 10.3389/feart.2021.673686

INTRODUCTION

Ignimbrites are formed by sedimentation of hot mixtures of ash and vesiculated juvenile (pumiceous) clasts from pyroclastic density currents (PDCs) generated during explosive volcanic eruptions (Sparks et al., 1973; Cas and Wright, 1987; Branney and Kokelaar, 2002). Ignimbrite-forming events can result from a wide range of eruption styles, from caldera-forming eruptions to short-lived explosions, and occur in different geodynamic settings (e.g., Freundt and Schmincke, 1986; Lipman, 1997; Giordano, 1998; Giordano et al., 2002; Sulpizio et al., 2007; Sulpizio et al., 2010; Cas et al., 2011; Pensa et al., 2015; Pimentel et al., 2015; Scarpati et al., 2020).

Although relatively uncommon on ocean island volcanoes, ignimbrites are known to occur in Iceland (Jørgensen, 1980), the Canary Islands (Gran Canaria and Tenerife; Bogaard and Schmincke, 1998; Brown et al., 2003), Cape Verde (Santo Antão Island; Eisele et al., 2015), and have also been reported on the island of Hawaii (Shea and Owen, 2016). In the Azores archipelago, ignimbrites are found on at least four islands: São Miguel, Terceira, Graciosa, and Faial (Self, 1976; Gaspar, 1996; Duncan et al., 1999; Gertisser et al., 2010; Pensa et al., 2015; Pimentel et al., 2015). Ignimbrites on Terceira constitute a significant portion of the island's geological record, including at least seven major formations containing peralkaline ignimbrites dated between ca. 86 ka and ca. 25 cal ka BP (Self, 1974; Gertisser et al., 2010; Jeffery et al., 2017).

The reconstruction of ignimbrite-forming eruptions on islands is challenging, as the deposits are often incompletely preserved on account of the small area of deposition, the typical rough topography, and the high erosion rates on volcanic islands. Small oceanic islands are particularly vulnerable to explosive eruptions and the risk is potentially aggravated by their geographical isolation and the weak socio-economic conditions of local communities. Therefore, detailed studies are needed to widen our understanding of ignimbrite-forming eruptions on oceanic islands and their potential impacts. Here, we focus on the youngest ignimbrite formation from Terceira, the Lajes-Angra Ignimbrite Formation (ca. 25 cal ka BP), hereafter abbreviated as LAI following Gertisser et al. (2010). The LAI is composed of two closely related ignimbrites (Lajes and Angra members) originating from Pico Alto volcano that together extend over nearly two-thirds of the island (Self, 1974; Self, 1976; Gertisser et al., 2010). Although closely related, the two ignimbrites contrast strongly in their spatial distribution, thickness and architecture.

In this paper, we use lithofacies analysis and ignimbrite architecture coupled with petrography, mineral chemistry, and whole rock and glass compositions to provide insights into the pre-eruptive magmatic system, and to infer the eruption style, transport and depositional processes of the parent PDCs of Angra and Lajes ignimbrites. We also reassess the use of aspect ratio as a proxy for emplacement dynamics of PDCs. The insights gained from this study are fundamental in improving our knowledge of the future eruptive behaviour of Pico Alto volcano and have significant implications for the assessment of volcanic hazard on Terceira and on other small islands prone to this type of volcanic activity.

Ignimbrite Geometry and Pyroclastic Density Current Emplacement Dynamics

Ignimbrite geometry, or aspect ratio (Walker et al., 1980; Walker, 1983), is one of the most common criteria used to classify ignimbrites. The aspect ratio is determined as the ratio of the average thickness of the deposit (H) to the diameter of a circle with an equal area to that covered by the ignimbrite (L). Accordingly, ignimbrites are subdivided into two endmembers: high-aspect ratio ignimbrites (HARIs) and low-aspect ratio ignimbrites (LARIs). The aspect ratio of ignimbrites has also been widely used as a proxy for PDC emplacement dynamics (i.e., as an estimate of kinetic energy, and hence velocity and competence).

HARIs are characteristically thick when compared to their horizontal extent (H/L 10^{-2}–10^{-3}) and are usually confined to valleys or topographic depressions. Well known examples include the 0.76 Ma Bishop Tuff Ignimbrite, California (Wilson and Hildreth, 1997), the AD 1912 Valley of Ten Thousand Smokes Ignimbrite, Alaska (Hildreth and Fierstein, 2012), and the ignimbrite of the AD 1991 eruption of Mt. Pinatubo, Philippines (Scott et al., 1996). HARIs are thought to result from deposition of low energy PDCs (e.g., Walker, 1983; Druitt, 1998; Cas et al., 2011).

By contrast, LARIs are relatively thin and widespread deposits (H/L 10^{-4}–10^{-5}) that mantle the landscape with a rather uniform thickness, including veneers on topographic highs. Well studied examples include the 2.08 Ma Cerro Galán Ignimbrite, Argentina (Cas et al., 2011), the 45 ka Green Tuff Ignimbrite, Pantelleria (Williams et al., 2014), and the AD 186 Taupo Ignimbrite, New Zealand (Wilson, 1985). LARIs are often interpreted to result from deposition by highly energetic PDCs that are able to surmount topographic barriers by momentum rather than mere inundation (e.g., Walker et al., 1980; Walker, 1983; Druitt, 1998; Dade, 2003; Cas et al., 2011).

However, the aspect ratio as a simple geometric relationship does not correlate with lithofacies variations observed in ignimbrites (Giordano and Doronzo, 2017), which mainly reflect flow-boundary zone conditions in PDCs (Branney and Kokelaar, 2002). Therefore, it can be misleading to directly derive fundamental differences in emplacement dynamics of PDCs from the geometry of the deposits. Study of ignimbrite lithofacies and architecture is thus of paramount importance for better understanding of the temporal and spatial evolution of PDCs.

GEOLOGICAL SETTING AND EVOLUTION OF TERCEIRA ISLAND

The Azores archipelago consists of nine volcanic islands spread over 600 km in the Atlantic Ocean that sit astride the triple junction of the North American, Eurasian and Nubian

lithospheric plates (**Figure 1** inset). Terceira Island comprises four overlapping central volcanoes: Cinco Picos, Guilherme Moniz, Pico Alto, and Santa Bárbara; as well as a fissure zone (**Figure 1A**; Self, 1974; Self, 1976; Madeira, 2005).

Cinco Picos volcano forms the eastern third of Terceira (**Figure 1A)** and is dominated by a 7 km-wide caldera that is strongly eroded and buried by products of neighbouring volcanoes. The caldera floor is covered by basaltic lavas and scoria cones of the fissure zone. The products of the Cinco Picos Volcanic Complex are mostly hawaiitic to mugearitic lavas, with minor exposures of comenditic trachyte lavas and pyroclastic deposits (Self, 1974; Self, 1976; Self and Gunn, 1976; Madeira, 2005; Gertisser et al., 2010). The history of this extinct volcano is as poorly known as it is exposed; Cinco Picos is the oldest edifice of the island (dated at 401 ± 6 ka; Hildenbrand et al., 2014), its eruptive activity started in the Pleistocene and the caldera was formed less than 280 ka ago (Féraud et al., 1980). The NE flank of Cinco Picos is deeply dissected by the NW-SE-trending fault scarps of the Lajes Graben (**Figure 1A**).

Guilherme Moniz volcano, in the centre of the island, is characterized by an elliptical caldera with a general NW-SE elongation (**Figure 1A**), marked by near-vertical walls in the south, while the northern sector is almost entirely buried by recent lava domes and coulées from Pico Alto (Self, 1974; Self, 1976; Madeira, 2005; Gertisser et al., 2010). The floor of the caldera is filled by basaltic lavas of the fissure zone. Guilherme Moniz Volcanic Complex shows a wide range of products from hawaiitic lavas to comenditic coulées and ignimbrites (Self, 1974; Self, 1976; Self and Gunn, 1976; Gertisser et al., 2010). The eruptive activity of this extinct volcano started more than 270 ka and ceased sometime after 111 ka (Calvert et al., 2006).

Pico Alto volcano, located north of Guilherme Moniz, is characterized by a cluster of lava domes and coulées that completely fill and overflow a caldera (**Figure 1A**). The Pico Alto Volcanic Complex comprises thick pyroclastic formations, including comenditic trachyte ignimbrites, comenditic-pantelleritic trachyte lavas and pumice fall deposits (Self, 1974; Self, 1976; Self and Gunn, 1976; Mungall and Martin, 1995; Pimentel, 2006; Gertisser et al., 2010). The eruptive history of Pico Alto started more than 141 ka ago (Gertisser et al., 2010) and shows evidence of several violent eruptions. The last major ignimbrite-forming period is dated at ca. 25 cal ka BP and is recorded by the LAI. Since then, the volcano has produced many domes and coulées, often preceded by pumice fall deposits (Self, 1974; Self, 1976; Calvert et al., 2006; Pimentel, 2006).

Santa Bárbara volcano occupies the western third of the island (**Figure 1A**) and is a conical-shape edifice truncated by two small overlapping calderas. The 2 km-wide inner caldera is filled by lava domes and is nested within an older caldera. The slopes of the volcano show several alignments of lava domes and coulées (Self, 1974; Self, 1976; Madeira, 2005; Pimentel, 2006). The Santa Bárbara Volcanic Complex includes a broad range of products, from basaltic-hawaiitic lavas and pyroclastic deposits to comenditic lava domes and coulees with associated pumice fall deposits (Self, 1974; Self, 1976; Self and Gunn, 1976; Mungall and Martin, 1995; Pimentel, 2006). Santa Bárbara is the youngest central volcano on Terceira (dated at 65 ± 13 ka; Hildenbrand et al., 2014); its eruptive activity started during the Late Pleistocene and has continued until the present (Self, 1974; Self, 1976; Calvert et al., 2006).

The fissure zone intersects Terceira along a general WNW-ESE to NW-SE orientation (**Figure 1A**). This volcanic system is characterized by a 2 km-wide diffuse alignment of vents (scoria cones, spatter cones and eruptive fissures) best seen in the central part of the island, which has produced basaltic-hawaiitic lava flows (Self, 1974; Self, 1976; Self and Gunn, 1976; Mungall and Martin, 1995; Zanon and Pimentel, 2015; Pimentel et al., 2016). Fissure volcanism extends offshore for several kilometres forming submarine ridges along the flanks of the island (Chiocci et al., 2013; Casalbore et al., 2015). The age of the fissure zone is poorly constrained to more than 43 ka (Calvert et al., 2006) in the SE segment but it is probably as old as the island itself, spanning from the Pleistocene to present. Three historical eruptions are known to have occurred: one paired subaerial eruption in the centre of the island in 1761 (Pimentel et al., 2016) and two submarine eruptions along the Serreta Ridge in 1867 and 1998–2001 (Weston, 1964; Gaspar et al., 2003; Casas et al., 2018).

The stratigraphy of Terceira is divided into two main groups (**Figure 1B**), according to the scheme of Self (1974): the Lower Terceira Group (LTG) and the Upper Terceira Group (UTG). These are separated by the LAI which forms a widespread lithostratigraphic horizon across much of the island. The UTG is formed by the products of at least 116 intercalated eruptions of Pico Alto, Santa Bárbara, and the fissure zone (Self, 1974; Self, 1976).

OVERVIEW OF THE LAJES-ANGRA IGNIMBRITE FORMATION

The LAI is the youngest of at least seven ignimbrite-bearing formations that fall into a relatively narrow period of activity between ca. 86 ka and ca. 25 cal ka BP ago (**Figure 2**). It is thought that most of the ignimbrite-forming events were associated with caldera-forming (or caldera-enlarging) phases of Pico Alto and, possibly, Guilherme Moniz volcanoes (Gertisser et al., 2010).

All ignimbrite-bearing formations pre-dating the LAI are part of the LTG. Most are named according to the type locations of the members found on the north and south coasts of the island (**Figure 2**). These formations are bounded by major unconformities and have been interpreted to result from single eruptions or, more often, from a few events closely spaced in time (Gertisser et al., 2010). Most of the older ignimbrites on Terceira share similarities with the LAI, including mildly peralkaline compositions, lithofacies, and internal architecture, suggesting that the magmatic and eruptive processes involved in ignimbrite-forming eruptions have been recurrent over the last ca. 100 kyr (Gertisser et al., 2010; Jeffery et al., 2017).

The LAI presently crops out along the north and south coasts, and in a few localities in the interior of the island, but originally may have covered nearly two-thirds of Terceira (Self, 1974; Self, 1976; Gertisser et al., 2010). The LAI consists of two members: the Angra Ignimbrite is named after the city of Angra do Heroísmo

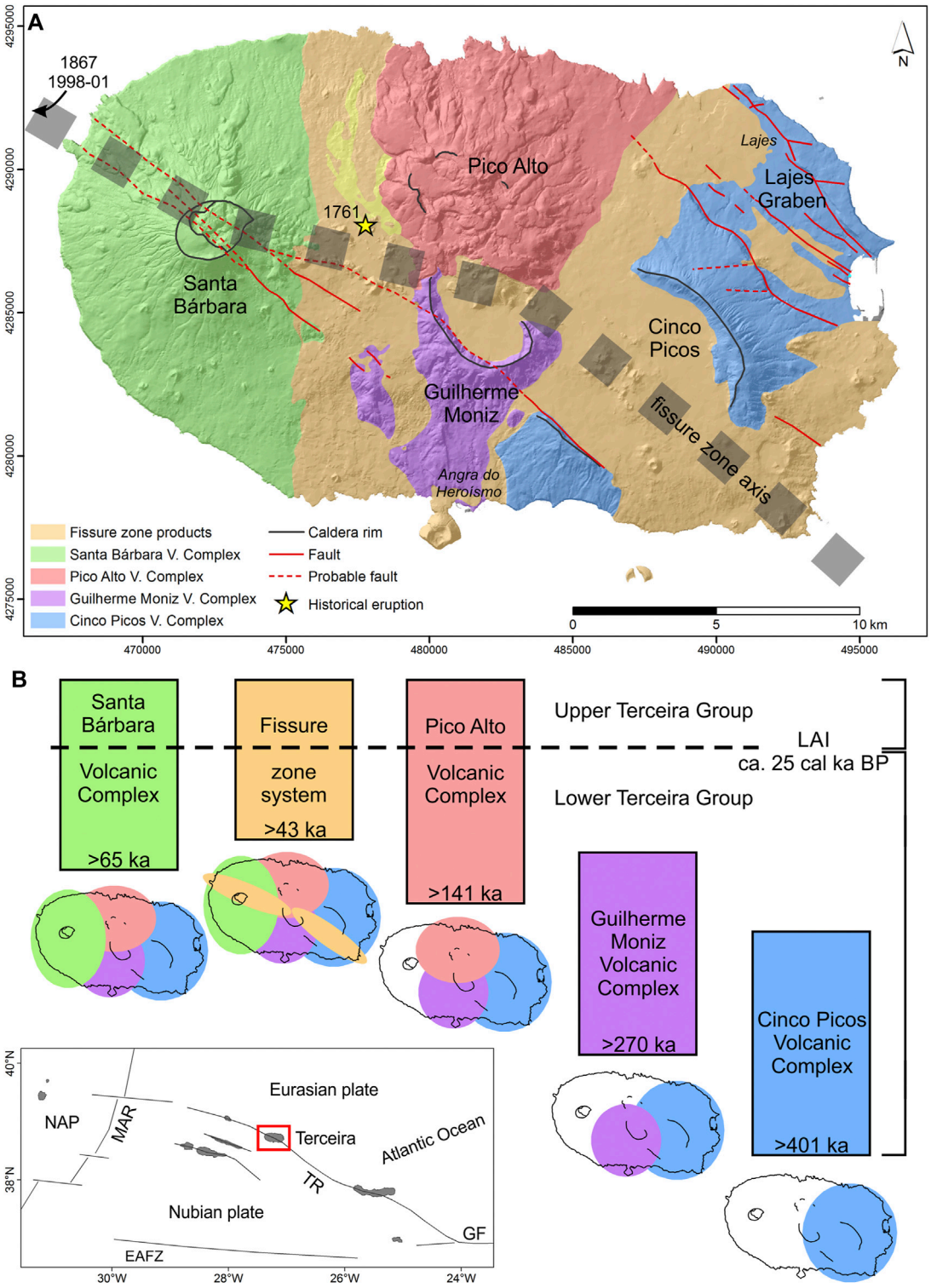


FIGURE 1 | (A) Simplified geological map of Terceira Island (modified from Madeira, 2005); UTM coordinates, zone 26S. **(B)** Stratigraphic scheme and reconstruction of the different phases of evolution of Terceira Island (ages from Calvert et al., 2006; Gertisser et al., 2010; Hildenbrand et al., 2014); LAI—Lajes-Angra Ignimbrite Formation. Inset shows the geodynamic setting of the Azores archipelago and main structural features of the region (NAP—North American plate; MAR—Mid-Atlantic Ridge; TR—Terceira Rift; EAFZ—East Azores Fracture Zone; GF—Gloria Fault).

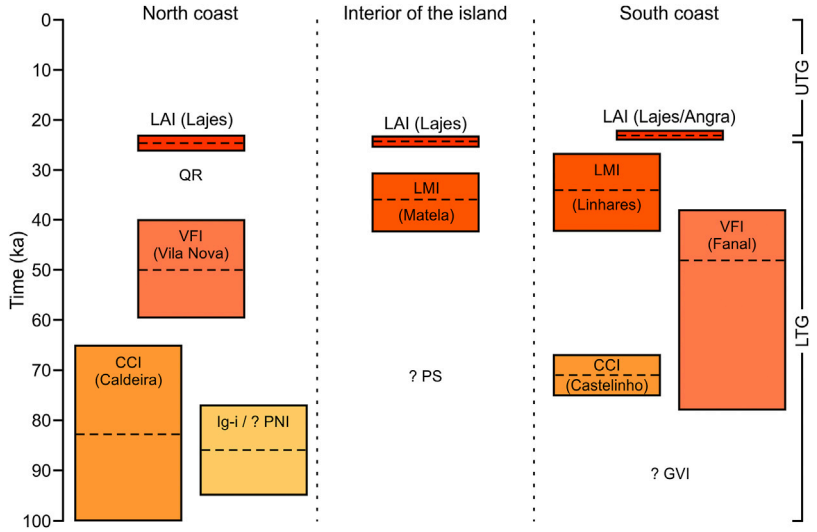


FIGURE 2 | Correlation of ignimbrite formations on Terceira, showing average ages and maximum errors for formations found on the north and south coasts and in the interior of the island. Ignimbrite members are given in parenthesis. Abbreviations: LAI—Lajes-Angra Ignimbrite; LMI—Linhares- Matela Ignimbrite; VFI—Vila Nova-Fanal Ignimbrite; CCI—Caldeira-Castelinho Ignimbrite; GVI—Grota do Vale Ignimbrite; PS—Posto Santo spatter-flow deposit; QR—Quatro Ribeiras pyroclastic flow deposit; Ig-i—Ignimbrite i; PNI—Pedras Negras Ignimbrite (adapted from Gertisser et al., 2010).

(in the south of the island, see **Figure 1** for location) where thick ignimbrite exposures are found; the Lajes Ignimbrite is named after the village of Lajes (in the NE sector of the island, see **Figure 1** for location) where it is best represented and was initially described. The Lajes Ignimbrite was one of the first examples of low-aspect ratio ignimbrites described in the literature (Self, 1971, followed by Walker et al., 1980).

The two ignimbrites were initially interpreted by Self (1974), Self (1976) as resulting from two eruptions of Pico Alto volcano that occurred approximately 4 kyr apart. This interpretation was based on three radiocarbon ages (Shotton and Williams, 1973; Shotton et al., 1974) and a quarry outcrop in the centre of the island, where the Lajes Ignimbrite was interpreted possibly overlying the Angra Ignimbrite (Self, 1971). However, in the light of present-day knowledge of Terceira ignimbrite stratigraphy we now think that the lower unit of this outcrop was not the Angra Ignimbrite but an older ignimbrite (possibly the Linhares-Matela Ignimbrite; Gertisser et al., 2010). Unfortunately, this key exposure has been removed by subsequent quarrying.

Radiocarbon dates from recent studies (Calvert et al., 2006; Gertisser et al., 2010), calibrated with the IntCal20 calibration curve (Reimer et al., 2020), closed the age gap between the Angra and Lajes ignimbrites: Angra Ignimbrite ages range from 25.3–25.8 cal ka BP (2σ) to 24.9–28.1 cal ka BP (2σ) (Gertisser et al., 2010); Lajes Ignimbrite ages range from 23.0–25.3 cal ka BP (2σ) to 26.0–28.8 cal ka BP (2σ) (Gertisser et al., 2010). High precision dating provided ages of 25.2–25.7 cal ka BP (2σ) and 25.5–25.9 cal ka BP (2σ) for the Lajes Ignimbrite (Calvert et al., 2006). As these ages overlap within uncertainty, we infer that both ignimbrites were erupted approximately at the same time ca. 25 cal ka BP ago. Available age data for the Angra and Lajes ignimbrites are provided in **Supplementary Material S1**.

FIELD AND LABORATORY METHODS

The LAI was studied in detail during field surveys, which combined geological mapping and lithofacies analysis. In total 83 stratigraphic sections were reconstructed throughout the island; each stratigraphic section was thoroughly described, measured and photographed. Maximum clast size (juveniles and lithics) was determined by averaging the length of the longest axis of the three largest clasts. The presence of major unconformities, including palaeosols and erosion surfaces, was used to delimit the deposits.

Lithofacies were described by non-genetic terms, based upon the lithological characteristics of the deposits (e.g., internal structures, grain size, sorting, component variations and intensity of welding). Nomenclature and abbreviations of lithofacies (**Table 1**) followed the schemes of Branney and

TABLE 1 | Lithofacies nomenclature and abbreviation (modified from Branney and Kokelaar 2002; Sulpizio et al., 2007).

Name	Abbreviation
Massive lapilli-ash	mLA
Eutaxitic massive lapilli-ash	emLA
Diffuse-stratified lapilli-ash	dsLA
Diffuse-bedded lapilli-ash	dbLA
Massive lithic breccia	mlBr
Massive ash	mA
Crystal-rich ash	crA
Lithic-rich ash	lA
Pumice-rich lapilli-blocks lens	pLBlens
Lithic-rich lapilli-blocks lens	lLBlens
Fines-poor lithic-rich pipe	lpip

Kokelaar (2002) and Sulpizio et al. (2007). Terminology used for the description of bed thickness, grain size, and sorting was adopted from Sohn and Chough (1989).

Fifteen samples of fresh juvenile clasts were collected for petrographic, whole rock, glass and mineral chemistry analyses. Petrographic descriptions were performed by thin-section observation under an Olympus BX51 binocular microscope. Modal counting was carried out with a CPX-Solutions MicroStepper ID818 point-counter stage, counting at least 1,000 points on each thin-section.

Whole rock major and trace element analyses were undertaken at Actlabs (Activation Laboratories Ltd, Canada), using inductively coupled plasma optical emission spectroscopy (ICP-OES) and inductively coupled plasma mass spectrometry (ICP-MS). Major element compositions of groundmass glass and mineral phases were determined at the Dipartimento di Scienze della Terra "Ardito Desio", Università degli Studi di Milano (Italy) using a JEOL JXA 8200 Superprobe equipped with five wavelength-dispersive spectrometers, an energy-dispersive detector and cathodoluminescence system. Further details on analytical methods are presented in **Supplementary Material S2**. Full whole rock and groundmass glass data are given in **Supplementary Material S3**.

IGNIMBRITE DISTRIBUTION

The spatial distribution of the Angra and Lajes ignimbrites was reconstructed combining direct field measurements with geological interpretation, accounting for the inferred palaeotopography and distance from source (following the method of Wilson, 1991). The Angra Ignimbrite crops out only in the southern part of the island, north of Angra do Heroísmo, where it reaches up to 14 m thickness, and along the coastal cliffs east of the city. Its distribution is constrained to one valley on the southern flank of Guilherme Moniz volcano (**Figure 3**) and the reconstructed extent occupies an area of approximately 10 km^2.

The Lajes Ignimbrite crops out on the northern part of the island, between Biscoitos and Lajes villages, and on the southern part at São Mateus and Porto Judeu villages (**Figure 4**). It is best exposed on low-lying areas between Agualva and Lajes villages, where thick ignimbrite (up to

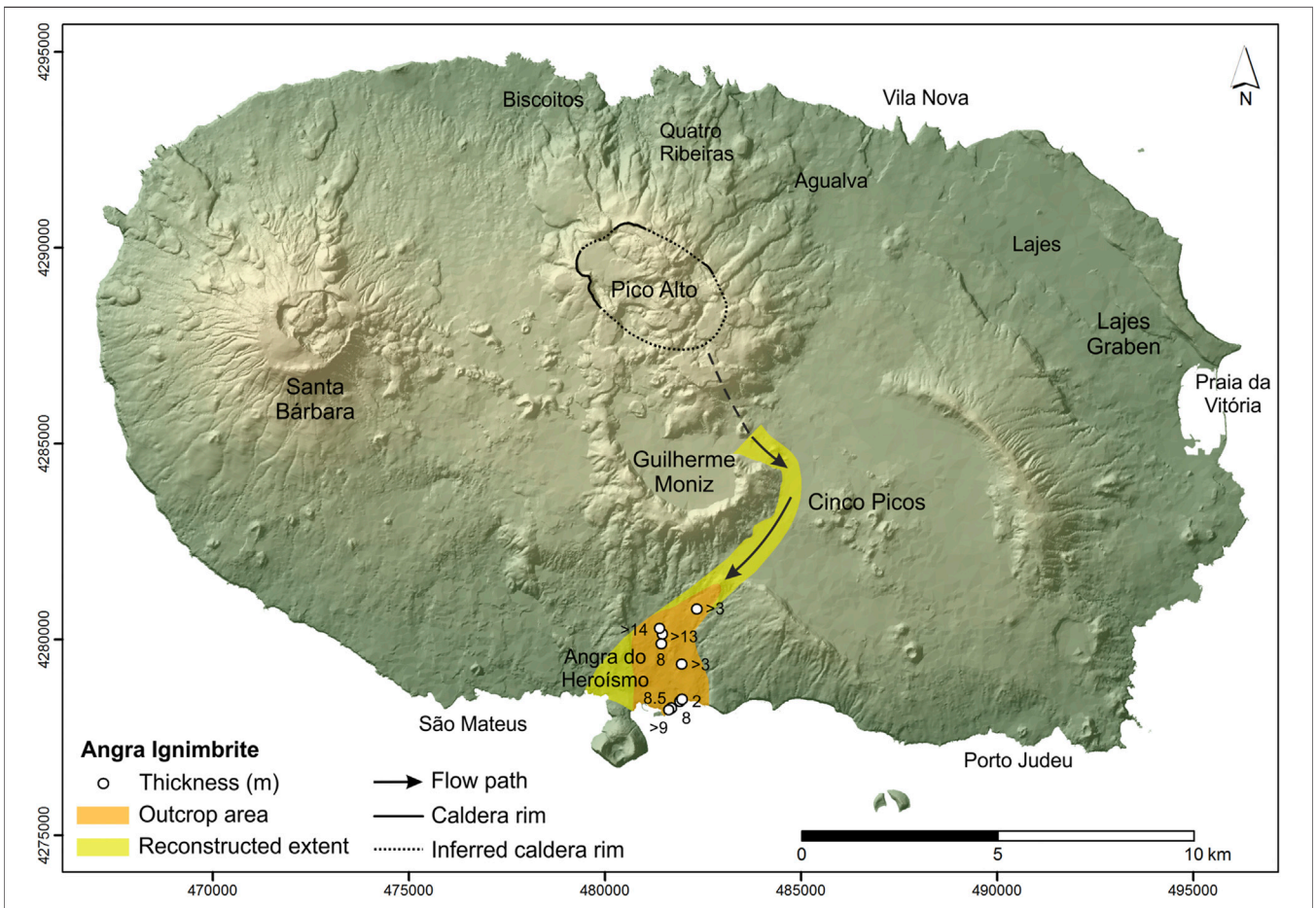


FIGURE 3 | Distribution map of the Angra Ignimbrite, including documented stratigraphic sections (white circles). Arrows indicate main flow paths; Locality names referred throughout the text are shown; UTM coordinates, zone 26S.

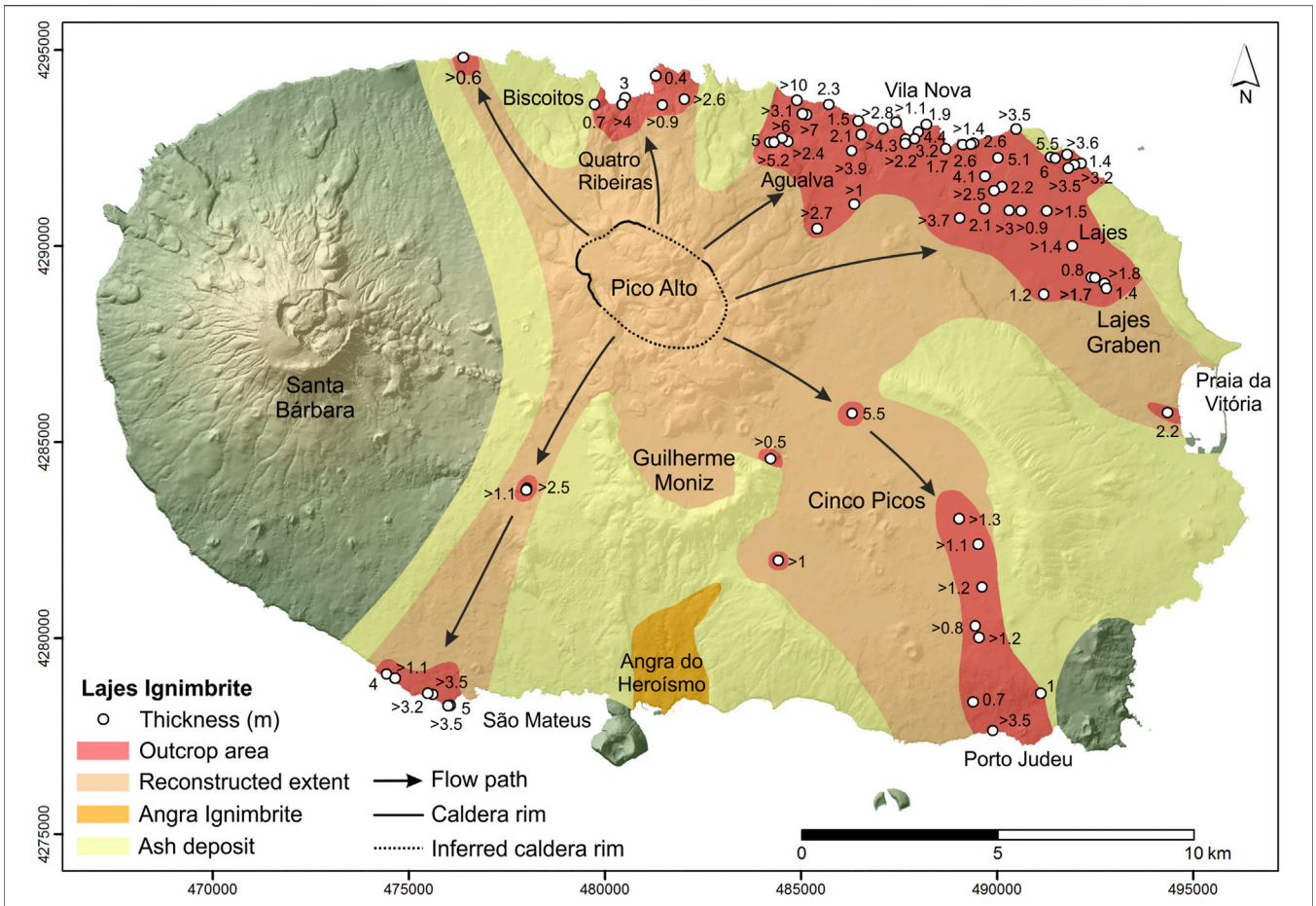


FIGURE 4 | Distribution map of the Lajes Ignimbrite, including documented stratigraphic sections (white circles). Arrows indicate the main flow paths; Locality names referred throughout the text are shown; UTM coordinates, zone 26S.

10 m in thickness) is ubiquitously found along the coastal cliffs. In the NE sector of the island, the floor of the Lajes Graben is largely filled by the Lajes Ignimbrite. North of Porto Judeu the outcrops extend into Cinco Picos caldera following a stream valley. Other minor patches of the ignimbrite crop out in the middle of the island in active or abandoned quarries. The reconstructed extent of the Lajes Ignimbrite occupies an area of at least 168 km^2.

Remnants of a fine ash deposit, commonly weathered into orange-brown soil, crop out over large areas of Terceira (**Figure 4**) at the same stratigraphic position of the Angra and Lajes ignimbrites. In places, the top of the ignimbrites can be traced to this ash deposit. The ash deposit occupies a much wider area than that of the ignimbrites and can be found covering topographic highs with a relatively uniform thickness (<50 cm). Where the ignimbrites are not present, this ash deposit forms a valuable lithostratigraphic marker horizon.

Overall, the LAI, including the associated ash deposit, extends radially outward from Pico Alto caldera over most of the island, except for the western third (**Figure 4**). It is estimated that the deposits of this ignimbrite formation occupy a minimum area on land of 284 km^2 (i.e., >70% of the surface area of Terceira).

IGNIMBRITE LITHOFACIES

Massive Lapilli-Ash

Description: Massive lapilli-ash (mLA) is the most common lithofacies and typically constitutes the main part of the Angra and Lajes ignimbrites. It is matrix-supported, ranging from well sorted to very poorly sorted (Angra 1.5 < σϕ < 4.1 vs. Lajes 2.7 < σϕ < 5.0; Self, 1974), with variable proportions of juvenile and lithic clasts in a light grey to dark grey matrix of vitric ash and abundant feldspar crystals (up to 3 mm in length) (**Figures 5A**,**B**). Juvenile clasts are rounded to subrounded, ranging from light grey pumice to dark grey/black scoria; black dense clasts are only found in the Lajes Ignimbrite. The juvenile clasts are usually coarsely porphyritic with feldspar crystals up to 5 mm in length (see detailed description of juvenile clasts in section "Petrography and mineral chemistry"). Lapilli-sized clasts are predominant but maximum clast sizes of 20–25 cm are common and locally blocks

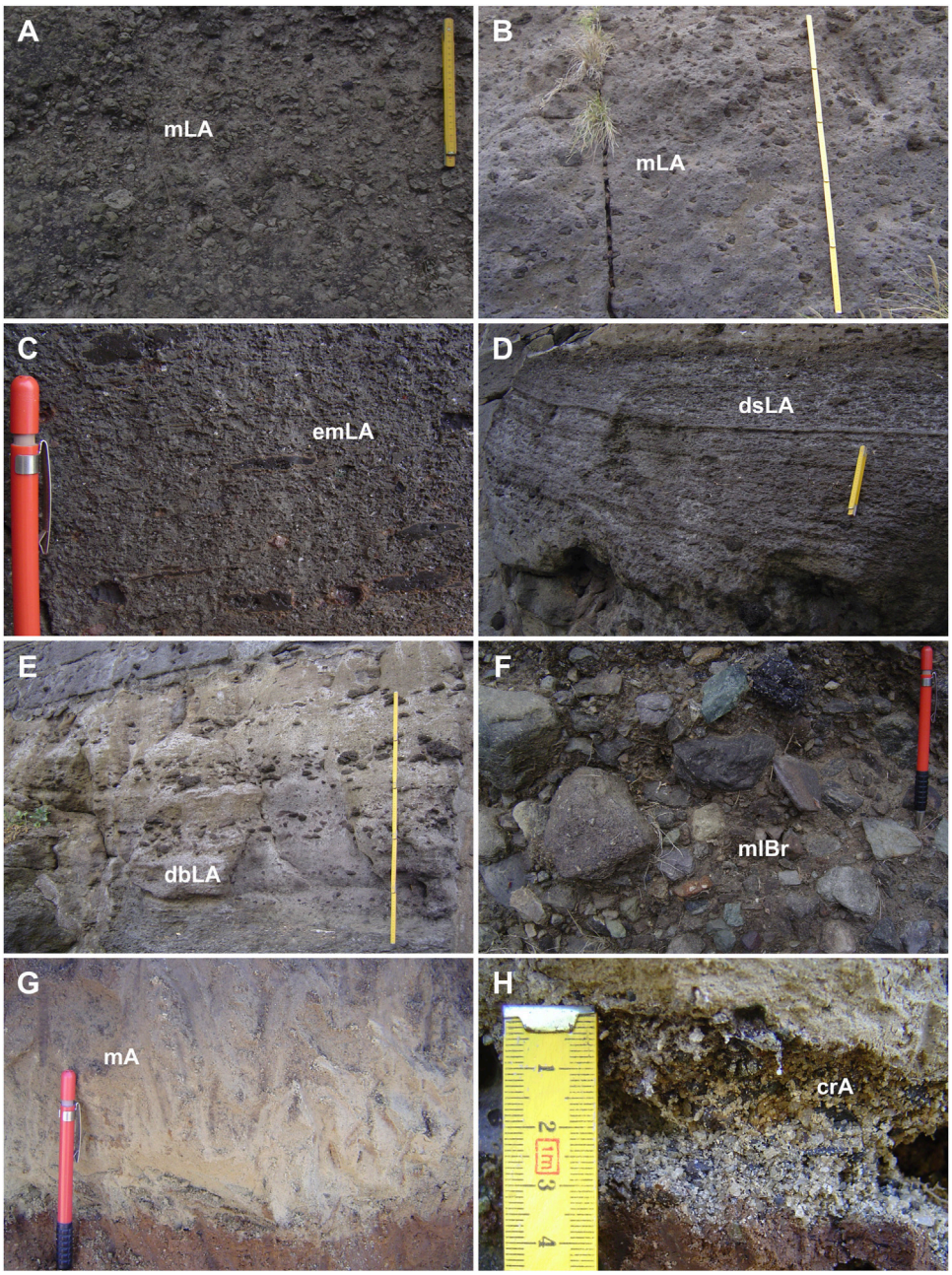


FIGURE 5 | Lithofacies of the LAI. **(A)** Massive lapilli-ash (mLA) from the Angra Ignimbrite (TERL63 in **Figure 7**; 20 cm scale). **(B)** Lithified massive lapilli-ash (mLA) from the Lajes Ignimbrite (TERL2 in **Figure 8**; 1 m scale). **(C)** Eutaxitic massive lapilli-ash (emLA) from the Lajes Ignimbrite (TERL61 in **Figure 7**; pen for scale). **(D)** Diffuse-stratified lapilli-ash (dsLA) and **(E)** diffuse-bedded lapilli-ash (dbLA) from the Lajes Ignimbrite (both from TERL59 in **Figure 7**; D scale is 20 cm; E scale is 1 m); **(F)** Massive lithic breccia (mlBr) from the Lajes Ignimbrite (TERL39 in **Figure 8**; pen for scale); **(G)** Massive ash (mA) from the Lajes Ignimbrite (TERL20 in **Figure 8**; pen for scale). **(H)** Crystal-rich ash (crA) from the Lajes Ignimbrite (TERL18 in **Figure 8**; scale in cm).

can reach up to 80 cm. Lithic clasts are subordinate, angular to subrounded and comprise basaltic and trachytic lavas, hydrothermally altered clasts, and syenite xenoliths, in decreasing order of abundance. The lithics are typically <10 cm in size but in places blocks reach up 65 cm. Massive lapilli-ash deposits lack internal stratification, although locally framework-supported pumice-rich or lithic-rich lapilli-blocks lenses (pLBlens, lLBlens) are recognized; fines-poor lithic-rich pipes (lpip) are rare. This lithofacies is non-welded, but is commonly lithified, and contains abundant carbonized wood fragments.

Interpretation: The massive nature, poor sorting and absence of stratification suggest rapid progressive aggradation from a sustained high particle concentration, granular fluid-based PDC

with a fluid escape-dominated flow-boundary zone, although the presence of clast lenses suggests the development of a granular flow-dominated flow-boundary zone (Druitt, 1998; Branney and Kokelaar, 2002; Scarpati et al., 2020). In a fluid escape-dominated flow-boundary zone clasts are supported by the upward flux of interstitial fluid escaping the matrix as a result of hindered settling, while in a granular flow-dominated flow-boundary zone clast interaction is the main support mechanism due to the high particle concentration and granular shear (Branney and Kokelaar, 2002; Sulpizio and Dellino, 2008).

Eutaxitic Massive Lapilli-Ash

Description: Eutaxitic massive lapilli-ash (emLA) is commonly seen in the lower part of the Lajes Ignimbrite but in places can represent more than half of its thickness. In the Angra Ignimbrite, this lithofacies is only found at one location on the costal cliff. The eutaxitic massive lapilli-ash lithofacies is welded and matrix-supported with juvenile and lithic clasts in varying proportions. The matrix is typically dark grey and crystal-rich, with feldspar crystals up to 3 mm in length. The welding intensity varies from poorly to densely welded with well-developed eutaxitic texture (**Figure 5C**). Where densely welded, juvenile clasts are strongly flattened dense clasts, which form fiamme up to 30 cm in length. In poorly welded examples, juvenile clasts range from slightly flattened (oblate shapes) to subrounded clasts with scoriaceous texture. Lithic clasts have identical lithologies to those described in the non-welded massive lapilli-ash but are finer-grained (up to 3 cm in size) and less abundant. This lithofacies typically lacks internal stratification but diffuse juvenile-rich or lithic-rich horizons are recognized locally.

Interpretation: The massive nature of this lithofacies suggests that particles were predominately deposited from a current with fluid escape-dominated to granular flow-dominated flow-boundary zones (Branney and Kokelaar, 2002; Scarpati et al., 2020), similarly to the non-welded lithofacies. The welding of the deposits, together with the coexistence of fiamme and oblate scoriaceous clasts, suggest rapid progressive aggradation from a high temperature PDC, where syn-depositional agglutination of pyroclasts occurred at temperatures exceeding the glass transition, rather than by load compaction (Russell and Quane, 2005; Dávila-Harris et al., 2013; Scarpati et al., 2020).

Diffuse-Stratified Lapilli-Ash

Description: Diffuse-stratified lapilli-ash (dsLA) is found locally in the Angra and Lajes ignimbrites. It consists of matrix-supported, poorly sorted deposits, with variable proportions of juvenile and lithic clasts in a light grey to dark grey ash matrix rich in feldspar crystals (up to 3 mm in length). This lithofacies is commonly lithified. The juvenile clasts are rounded to subrounded and comprise the same lithologies of those described in the massive lapilli-ash lithofacies. Lapilli-sized clasts are predominant, with maximum clast sizes up to 6 cm. Lithic clasts are angular to subrounded and have the same lithologies of those described in massive lithofacies but are finer-grained (up to 5 cm in size). The internal structure is marked by very thin layers (<1 cm thick) with diffuse parallel to sub-parallel stratification (**Figure 5D**). Individual layers are composed of juvenile and/or lithic fine lapilli clasts that alternate with ash layers. In places, the fine lapilli layers show normal or inverse grading, defined by subtle grain size variations. The layers often show small thickness variations and are lateral discontinuous over a few meters.

Interpretation: Diffuse stratification and laterally discontinuous layering are indicative of subtle unsteadiness during deposition from a sustained high particle concentration PDC with transitional flow-boundary zones between fluid escape-dominated and granular flow-dominated, with short periods of traction-dominated conditions (Branney and Kokelaar, 2002; Brown and Branney, 2004; Brand et al., 2014). The unsteadiness within the flow-boundary zone likely arises from one or more mechanisms: 1) successive surges or waves in a fluctuating sustained PDC, 2) periodic impingement into the flow-boundary zone of turbulent eddies, 3) intrinsic frictional effects within the thickening granular flow-dominated flow-boundary zone (Branney and Kokelaar, 2002), and 4) flow-boundary zone perturbations travelling up-current in response to interaction with topography (Brand et al., 2014; Báez et al., 2020a).

Diffuse-Bedded Lapilli-Ash

Description: Diffuse-bedded lapilli-ash (dbLA) is only found in the upper part of the Lajes Ignimbrite, along the south coast. It is matrix-supported, poorly sorted, with juvenile and lithic clasts in varying proportions in a dark grey ash matrix with feldspar crystals (up to 3 mm in length). This lithofacies is commonly lithified. The juvenile clasts (rounded to subrounded) and lithic clasts (angular to subrounded) have the same lithologies of those described in the massive lapilli-ash lithofacies. Lapilli-sized clasts are predominant but maximum clast sizes of juveniles and lithics can reach up to 20 and 7 cm, respectively. The internal structure is defined by parallel to sub-parallel beds of juvenile clasts and few lithic clasts (**Figure 5E**). Individual beds are centimetre to decimetre thick (typically <25 cm) and laterally discontinuous over a few metres; local thickness variations are common. Most beds are internally massive but some show inverse grading of juvenile clasts and/or normal grading of lithic clasts. The tops and bases of individual beds show diffuse boundaries.

Interpretation: Diffuse bedding suggests local current unsteadiness during deposition from a sustained high particle concentration PDC with granular flow-dominated to fluid escape-dominated flow-boundary zones (Branney and Kokelaar, 2002; Brown and Branney, 2004). The mechanisms that generate the unsteadiness within the flow-boundary zone are the same as described for the diffuse-stratified lithofacies. The occurrence of normal or inverse grading patterns within beds record marked current unsteadiness, possibly with brief periods of tractional deposition. The lateral discontinuous nature and thickness variations of the beds may result from current non-uniformity (Brown et al., 2007; Kokelaar et al., 2007).

Massive Lithic Breccia

Description: Massive lithic breccia (mlBr) is only found in the Lajes Ignimbrite, on the northern part of the island. It consists of matrix-supported, poorly sorted, lithic-rich deposits with a dark grey lapilli-ash matrix rich in feldspar crystals (up to 3 mm in length). Lithic clasts are angular to subrounded, with variable lithologies including basaltic and

trachytic lavas, hydrothermally altered clasts (orange to reddish colour), syenite xenoliths, obsidian chips and basaltic scoria clasts, in decreasing order of abundance (**Figure 5F**). Lapilli-sized lithic clasts are predominant but larger clasts with maximum clast sizes of 30–35 cm are common. Juvenile clasts are subordinate, rounded to subrounded and comprise scoria and dense clasts. The juvenile clasts reach up to 6 cm in size. The lithofacies is massive, without recognizable internal structures.

Interpretation: The massive nature and poor sorting suggest progressive aggradation from a sustained granular fluid-based lithic-rich PDC with transitional flow-boundary zones between fluid escape-dominated and granular flow-dominated (Branney and Kokelaar, 2002; Brown and Branney, 2004; Dávila-Harris et al., 2013; Báez et al., 2020a), where the high lithic clast concentration was enough to suppress basal turbulence and traction. It reflects a greater competence of the current with respect to the massive lapilli-ash lithofacies. The abundance of lithic clasts in these deposits may indicate significant conduit wall erosion or partial edifice (caldera) collapse (Branney and Kokelaar, 2002; Báez et al., 2020a).

Massive Ash

Description: Massive ash (mA) is only found in the lower part of the Lajes Ignimbrite. It consists of well sorted to poorly sorted ($1.5 < \sigma\phi < 3.0$; Self, 1974) light grey vitric ash, that locally grades upward to dark grey, abundant feldspar crystals (up to 3 mm in length) and rare juvenile and lithic fine lapilli clasts (**Figure 5G**). Juvenile clasts are rounded to subrounded and comprise pumice and scoria (up to 1 cm in size). Lithic clasts are angular to subrounded and have the same lithologies of other lithofacies (up to 0.6 cm in size). The massive ash deposits are structureless, locally lithified, and contain abundant carbonized wood fragments.

Interpretation: The massive nature, absence of internal structures, clast lenses and alignments, and fine grain size suggest steady progressive aggradation from a sustained high particle concentration, fine-grained granular fluid-based PDC with a fluid escape-dominated flow-boundary zone and a minimal granular flow-dominated component (Branney and Kokelaar, 2002; Brown et al., 2007; Kokelaar et al., 2007).

Crystal-Rich (Lithic-Rich) Ash

Description: Crystal-rich ash (crA) is commonly found at the base of Lajes Ignimbrite and locally at the base of the Angra Ignimbrite. It is clast-supported, well sorted, although rare poorly sorted examples exist (Angra $1.0 < \sigma\phi < 2.2$ vs. Lajes $1.1 < \sigma\phi < 2.8$; Self, 1974), and fines-depleted, mostly composed of feldspar crystals up to 3 mm in length (**Figure 5H**). In places, it is rich in ash-sized to fine lapilli lithics (lA). Lithic clasts are angular to subangular and comprise basaltic and trachytic lavas, hydrothermally altered clasts, and syenite xenoliths, in decreasing order of abundance. Juvenile clasts are subordinate, rounded to subrounded, ash-sized to fine lapilli pumice clasts; rare dense clasts are only found in the Lajes Ignimbrite. Small, carbonized wood fragments are common. This lithofacies is typically massive (structureless) but plane-parallel bedding and imbrication of the denser clasts (crystals or lithics) are observed locally.

Interpretation: The typically good sorting, crystal-rich (lithic-rich) nature and depletion of fine ash suggest rapid deposition of material from a dilute PDC or dilute part of a PDC (Branney and Kokelaar, 2002; Cas et al., 2011; Scarpati et al., 2015). The depletion of fine vitric ash and enrichment in crystals and lithic clasts implies density segregation during turbulent flow transport, where fine juvenile ash is elutriated. The ingestion and heating of cold air at the front of a PDC generates vigorous turbulence and consequently segregation of the denser clasts (crystals or lithics). The present of carbonized wood fragments reveals the current was hot enough to burn vegetation, which may have also enhanced elutriation of fine ash (Branney and Kokelaar, 2002; Scarpati et al., 2015). The crystal-rich (lithic-rich) ash bed at the base of the ignimbrites is interpreted as a ground layer (Sparks, 1976; Walker et al., 1981; Wilson, 1985; Scarpati et al., 2015).

IGNIMBRITE ARCHITECTURE

Vertical Variations

The Angra Ignimbrite typically starts with a light grey, fine-grained massive lapilli-ash base, although locally diffuse-stratified lapilli-ash is observed (**Figure 6A**). In a few places a thin fines-poor, crystal-rich bed is present at the base. At one outcrop on the costal cliff (TERL72, see **Figure 7** for location), the lowermost part of the ignimbrite is incipiently welded, showing weak eutaxitic texture. Upwards it grades diffusely into non-welded light grey, coarse-grained massive lapilli-ash. Pumice-rich lenses are present within the massive lapilli-ash. The topmost portion of the ignimbrite is typically finer grained.

The Lajes Ignimbrite typically starts with a thin basal fines-poor, crystal-rich, locally lithic-rich bed (<4 cm thick on average). This basal crystal-rich bed is locally absent, for example along the south coast. The upper contact of this thin bed is usually sharp but in places can be diffuse. It is conformably overlain by light grey massive ash. It diffusely grades up into dark grey, fine-grained massive lapilli-ash, which is commonly welded showing well-developed eutaxitic texture. Upwards it gradually passes through incipiently welded to non-welded dark grey, coarse-grained massive lapilli-ash (**Figure 6B**). Pumice-rich or lithic-rich lenses are locally present in the massive lapilli-ash. Locally it can grade from diffuse-stratified to diffuse-bedded lapilli-ash. In a few places in the north part of the island it includes a massive lithic breccia. The topmost portion of the ignimbrite is typically finer grained. The vertical contacts between the different lapilli-ash lithofacies are diffuse.

There is no evidence of unconformities (e.g., major erosion surfaces, reworked horizons, pumice/ash fall layers) in the ignimbrites. Neither the Lajes nor Angra ignimbrites have pumice fall deposits at the base or the top.

Lateral Variations

No significant lateral variations of lithofacies were observed in the Angra Ignimbrite as it has a very restricted outcropping area, which is topographically constrained to one valley (**Figure 7**).

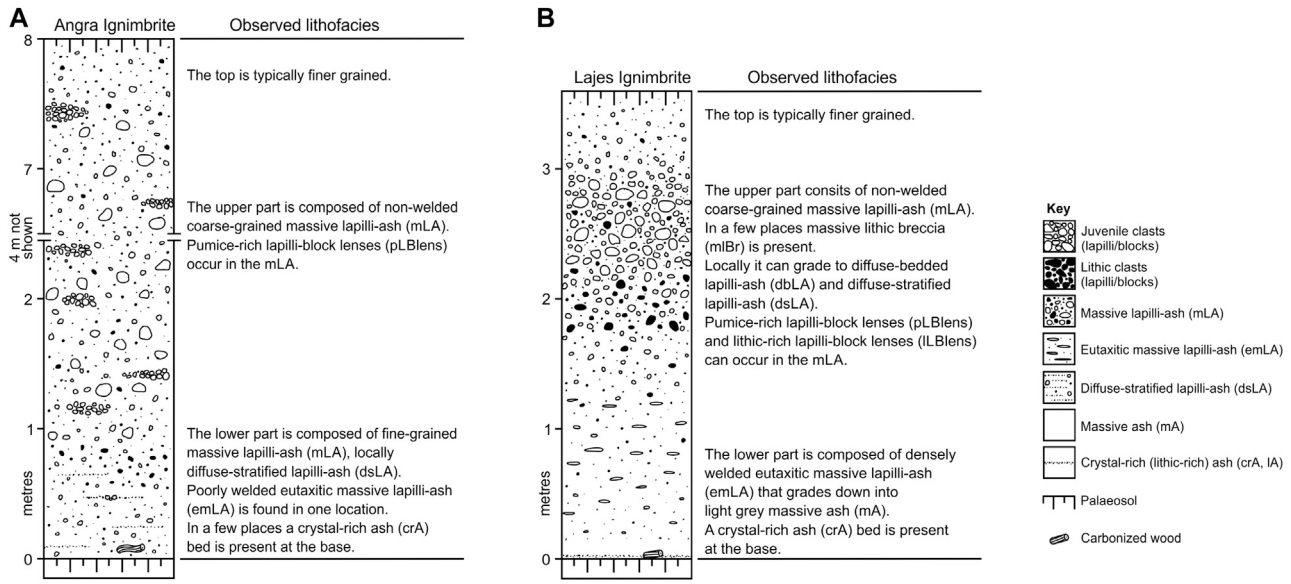


FIGURE 6 | Generalized stratigraphic sections of the Angra Ignimbrite **(A)** and the Lajes Ignimbrite **(B)**, with description of the observed lithofacies.

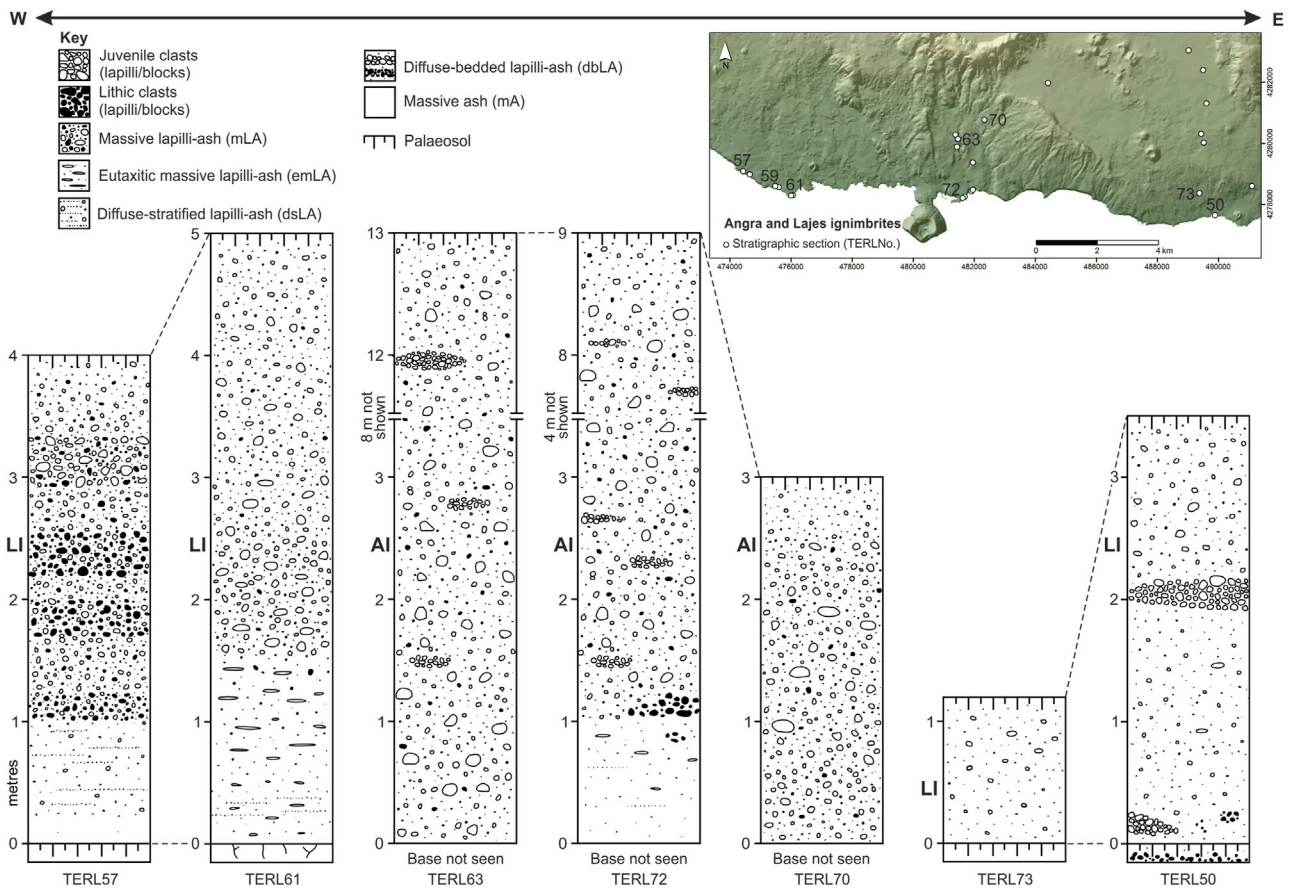


FIGURE 7 | Representative stratigraphic sections of the Angra and Lajes ignimbrites along the south coast of Terceira. AI—Angra Ignimbrite.; LI—Lajes Ignimbrite.

The Lajes Ignimbrite shows lateral lithofacies variations along the north and south coastal areas (**Figures 7**, **8**). On the north coast, where the Lajes Ignimbrite is best exposed, it is possible to observe lateral variations closely related to the underlying topography. Along the coastal cliffs, the deposit has a rather uniform thickness (3.5 m on average) and shows the same vertical lithofacies sequence (described previously) over several hundreds of metres (**Figure 9**). However, thicker deposits (up to 10 m thick) are found in palaeovalleys and tend to be coarser-grained. Where thick, coarse-grained ignimbrite gradually thins against a topographic feature, it can be traced uphill to thin (typically <1 m) fine-grained massive lapilli-ash or massive ash deposit with crystal-rich base. This lateral transition is gradational and generally marked by the thinning and fining of the sequence.

PETROGRAPHY AND GEOCHEMISTRY

Petrography and Mineral Chemistry

The juvenile clasts of the LAI include light grey pumices (**Figure 10A**), which may be porphyritic, dark grey/black coarsely porphyritic scoriae (**Figure 10C**), and black coarsely porphyritic dense clasts (**Figure 10E**) that are exclusive to the Lajes Ignimbrite. Pumices are highly vesicular (53–81 vol. %) with low phenocryst contents (typically <10 vol. % but up to 20 vol. % in some instances). Phenocrysts are set in a whitish glassy groundmass with few to no microlites. Vesicles range from several millimetres to a few micrometres in size and have subcircular to slightly elongated shapes (**Figure 10B**). Some examples show extreme vesicle elongation (i.e., tube pumice). Glomerophyric aggregates of phenocrysts are found sporadically.

Scoriae have lower vesicularity (30–47 vol. %) and higher phenocryst content (14–23 vol. %) than pumices. Coarsely porphyritic scoriae show large phenocrysts (4–5 mm) set in brown glassy, or more rarely microcrystalline, groundmass. Glomerophyric aggregates are more common than in pumices. Scoriae are typically microvesicular, with vesicles reaching up to a few millimetres in size (**Figure 10D**), and subcircular to irregularly shaped (separated by thicker walls). Vesicles are frequently coalescent and in some cases are strongly stretched. Cryptocrystalline bands of devitrified glass are occasionally found alternating with microlite-free brown glass.

Dense clasts are characterized by low vesicularity (16–27 vol. %) and high phenocryst content (15–22 vol. %). They are coarsely porphyritic and characterized by brown glassy microlite-free or microlite-poor groundmasses. Glomerophyric aggregates of phenocrysts are common. The vesicles are small (not more than a few tens of micrometres in size), ranging from irregularly shaped, elongated to strongly stretched. In the most extreme cases,

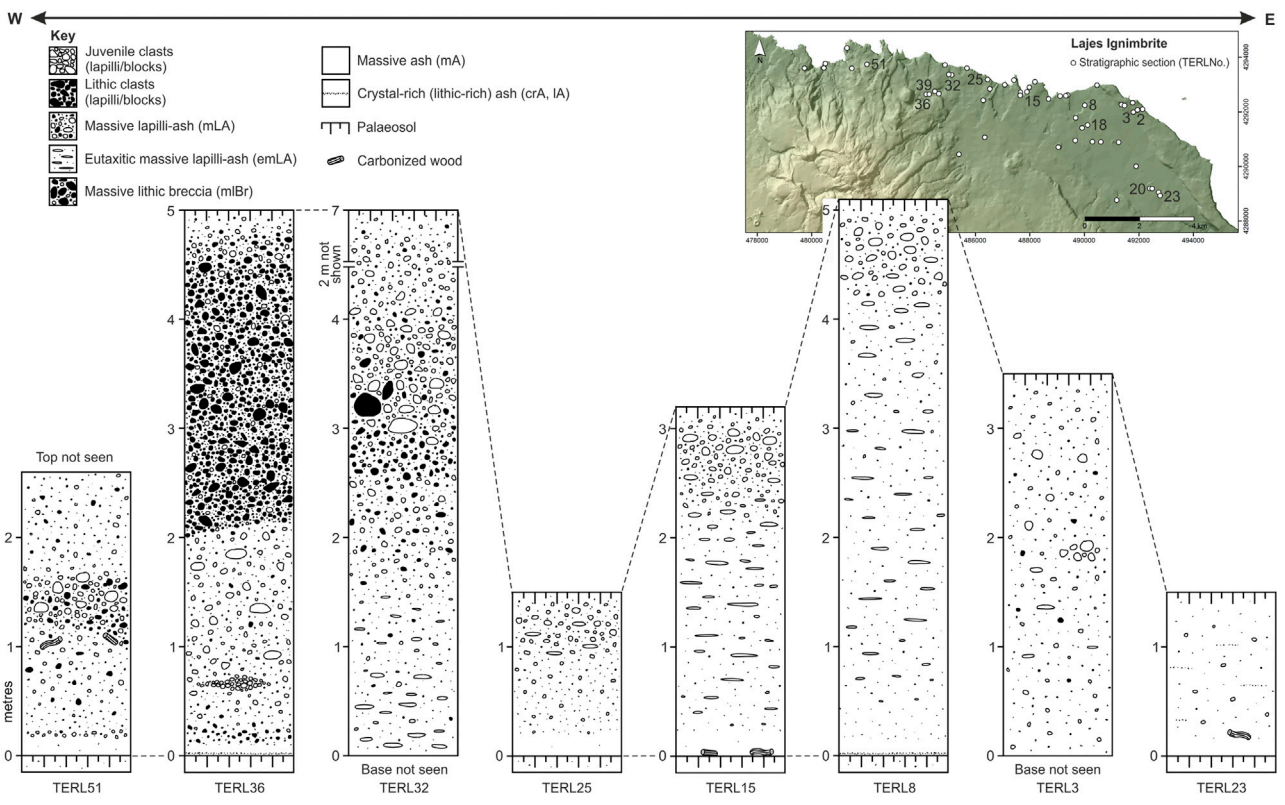


FIGURE 8 | Representative stratigraphic sections of Lajes Ignimbrite along the north coast of Terceira.

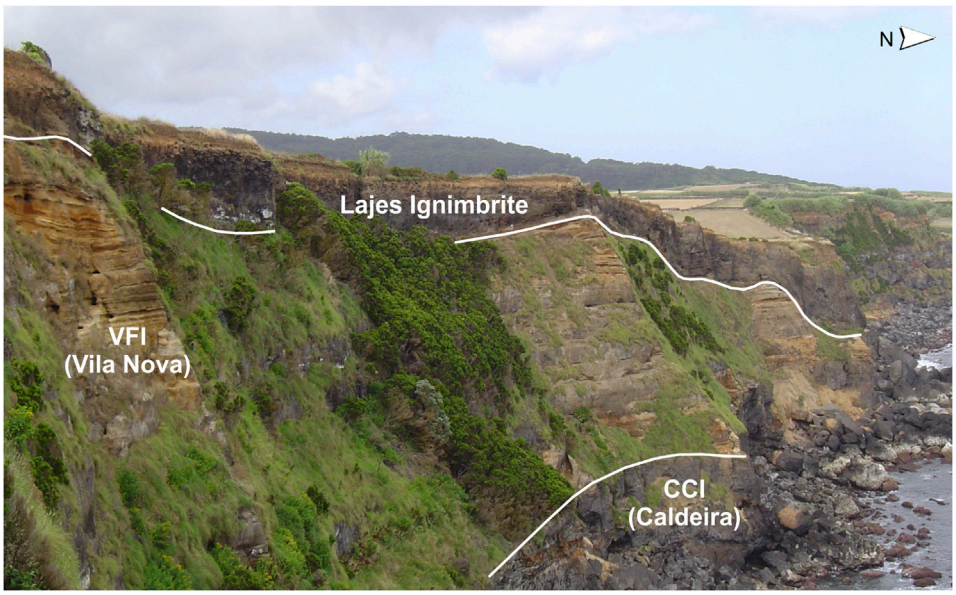


FIGURE 9 | View of cliffs along the north coast of Terceira showing the Lajes Ignimbrite overlying a sequence of older pyroclastic formations containing ignimbrites (VFI and CCI) separated by major erosion surfaces. Abbreviations are as given in **Figure 2**; members are given in parenthesis. Cliff is 30 m high in the foreground (left side of the picture).

vesicles are completely collapsed (**Figure 10F**). Alternating bands of dark brown and light brown glass are distinguishable and, in many cases, deformed, clearly draping around phenocrysts (i.e., flow structures). Isolated or clustered spherulites are present occasionally.

The mineral contents, proportions, and compositions of the Angra and Lajes ignimbrites are similar. Anorthoclase (An_{0-4}, Ab_{64-71}, Or_{25-35}) phenocrysts represent the predominant mineral phase in the juvenile clasts of both ignimbrites (≤22 vol. %), reaching sizes of up to 5 mm in length, and exhibiting variable morphologies, including euhedral crystals (**Figure 11A**), subhedral crystals with rounded edges, crystals with embayments, and large crystals with resorbed cores filled by glassy pockets (which are frequently vesicular; **Figure 11B**). Small microphenocrysts, and microlites when present, are euhedral and do not show disequilibrium features. Glomerocrysts comprising predominantly anorthoclase are common. Euhedral to subhedral augite (En_{24-38}, Fs_{20-34}, Wo_{39-43}) phenocrysts are less common (≤1.2 vol. %), reaching up to 3 mm in length. Large phenocrysts are frequently fractured and show disequilibrium features with the host rock (e.g., reaction rims and rounded edges). Microphenocrysts of clinopyroxene can also be found partially or fully included within alkali feldspars. Clinopyroxene phenocrysts are commonly associated with smaller Fe-Ti oxides (**Figure 11C**) and acicular apatite. Olivine is rare (<1 vol. %) and occurs as phenocrysts (up to 800 μm), but more frequently as microphenocrysts. Phenocrysts of olivine commonly show disequilibrium features, such as anhedral morphologies, or partially resorbed crystals with reaction rims (**Figure 11D**). Microphenocrysts tend to be subhedral. Olivine occurs as either isolated crystals or in glomerophyric aggregates with other mineral phases. Compositionally, they cover a narrow range of chemical compositions of Fo_{30-41}. Fe-Ti oxides (≤0.6 vol. %) are euhedral to anhedral and range from phenocryst (up to 400 μm) to microlites. They are frequently found in association with, or as inclusions in, clinopyroxene and olivine (**Figures 11C,D**). Apatite is an accessory mineral phase and is found as isolated microphenocrysts (<300 μm) or as acicular inclusions within clinopyroxene and olivine (**Figure 11D**). In compositional terms it can be classified as fluorapatite (3.2 wt. % F). In addition to mineral phases, LAI juvenile material contains rare, medium-grained syenitic xenoliths comprised predominantly of alkali feldspar (Gertisser et al., 2010; Jeffery et al., 2017).

Whole Rock and Glass Composition

Whole rock major element geochemical data indicate that both the Angra and Lajes ignimbrites are classified as peralkaline trachyte, with SiO_2 contents that range from 65 to 66 wt. %, total alkali contents of 11–12 wt. % (**Figure 12A**), and peralkalinity indices (PI = molar $Na_2O + K_2O/Al_2O_3$) between 1.00 and 1.12. Groundmass glass analyses for both ignimbrites show slightly more chemical diversity and some minor differences between the two (e.g., Angra total alkalis = 9.6 to 11.4 vs. Lajes total alkalis = 10.1 to 13.1 wt. %; Angra PI = 0.88 to 0.99 vs. Lajes PI = 0.91 to 1.29; **Figure 12B**). In the Al_2O_3 vs. FeO_T classification scheme of Macdonald (1974), all the peralkaline samples of this study (whole rock and groundmass glass) are comenditic trachyte, excluding a small number of glass analyses from the Lajes Ignimbrite which plot as comendite (**Figure 12C**).

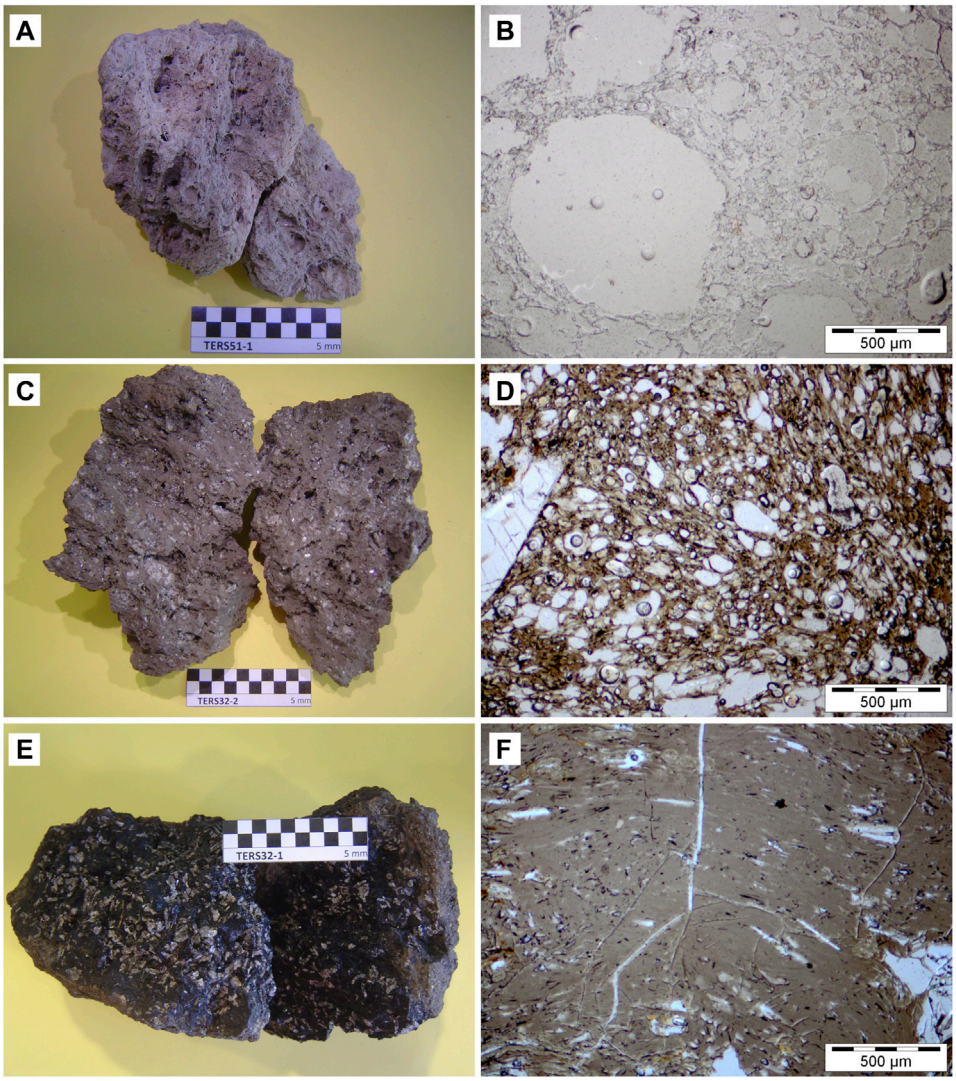


FIGURE 10 | Representative juvenile clasts of the LAI and photomicrographs showing their textures. **(A)** Light grey pumice clasts. **(B)** Highly vesicular pumice with millimetre-sized subcircular vesicles. **(C)** Dark grey coarsely porphyritic scoria clats. **(D)** Microvesicular scoria with subcircular to slightly elongated vesicles and an alkali feldspar phenocryst. **(E)** Black coarsely porphyritic dense clasts. **(F)** Dense clast with brown glassy groundmass, collapsed vesicles, and dispersed alkali feldspar microphenocrysts.

On the basis of major element chemistry alone, the two ignimbrites are difficult to distinguish from each other. However, trace element compositions yield further information. Zirconium concentrations, which are used here as a differentiation index, show a considerable range between 435 and 963 ppm. Plotted against Zr, FeO_T concentrations increase with differentiation, whilst MgO and CaO contents decrease (**Figure 13**). When plotted against other incompatible elements such as Nb and Rb, the LAI is defined by a positive, linear trend (**Figures 13D,E**). Groundmass glass compositions from the Lajes Ignimbrite extend across the full length of this range, whereas whole rock analyses are limited to <760 ppm. The whole rock data for the Angra Ignimbrite are similar to those of the Lajes Ignimbrite; however, the groundmass glass compositions are bimodal, with the majority of data clustering around 790 ppm, and a smaller cluster around 520 ppm. Strontium concentrations are characteristically low for peralkaline magmas (<20 ppm) and exhibit a scattered but broadly negative correlation with Zr (**Figure 13F**). Barium exhibits a similar relationship with Zr but also shows considerable scatter and range (55–737 ppm; **Figure 13G**). Chrondrite-normalised REE patterns are typically LREE enriched relative to the HREE, with both ignimbrites having average La_N/Yb_N ratios of 9.7 (**Figure 14**). Variably negative Eu anomalies occur in both the Angra and Lajes ignimbrites, with average Eu/Eu* of 0.61 and 0.51, respectively. Furthermore, Eu/Eu* values show a negative correlation with Zr concentrations (**Figure 13H**).

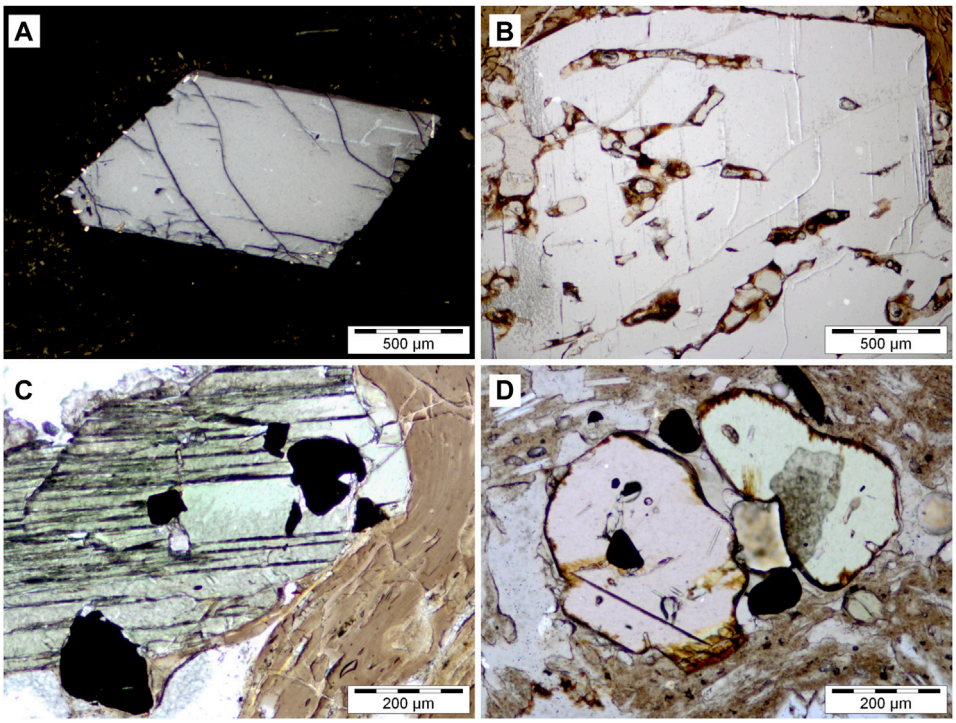


FIGURE 11 | Representative photomicrographs of mineral phases from the Angra and Lajes ignimbrites. **(A)** Euhedral alkali feldspar phenocryst. **(B)** Alkali feldspar phenocryst with partially resorbed core filled by vesicular glassy pockets. **(C)** Subhedral clinopyroxene phenocryst with Fe-Ti oxide inclusions. **(D)** Olivine phenocrysts with reaction rims and inclusions of Fe-Ti oxides and small acicular apatite.

DISCUSSION

Ignimbrite Aspect Ratio and Volume

The aspect ratio of the Angra Ignimbrite was estimated based on an average thickness of 8 m and the diameter of a circle with an equal area to that reconstructed for the ignimbrite (10 km^2; **Figure 3**). This yields an aspect ratio of 1:500 ($H/L = 2 \times 10^{-3}$) which is in the range of typical values considered for HARIs (Walker et al., 1980; Giordano and Doronzo, 2017). The aspect ratio of the Lajes Ignimbrite was estimated assuming an average thickness of 3.5 m and the diameter of a circle with the same area as that reconstructed for the ignimbrite (168 km^2; **Figure 4**). This corresponds to an aspect ratio of 1:4200 ($H/L = 2.4 \times 10^{-4}$). Alternatively, if the maximum run-out distance of the Lajes Ignimbrite is considered, from Pico Alto caldera to Porto Judeu coastal cliffs (15 km; **Figure 4**), then the aspect ratio of the Lajes Ignimbrite is in the order of 1:8600 ($H/L = 1.2 \times 10^{-4}$). Both these values are within the typical range considered for LARIs (Walker et al., 1980; Dade, 2003; Giordano and Doronzo, 2017).

Volumes of the Angra and Lajes ignimbrites were conservatively estimated by multiplying the average thickness of the deposits by the area of the reconstructed extents (**Figures 3**, **4**). The bulk on-land volume estimated for the Angra Ignimbrite is 0.08 km^3. This converts to a dense rock equivalent (DRE) on-land volume of 0.04–0.06 km^3, based on ignimbrite densities of 1,300–1800 kg/m^3 and a trachytic magma density of 2,500 kg/m^3 (Self, 1974). The Lajes Ignimbrite yields a bulk on-land volume of 0.59 km^3. This corresponds to a DRE on-land volume of 0.31–0.42 km^3 using the same range of ignimbrite densities and trachytic magma density as for the Angra Ignimbrite.

Estimating physical parameters of old pyroclastic deposits on islands such as Terceira is challenging due to various factors, including the small size of the island, the thick cover of younger UTG products, the luxuriant vegetation and the absence of deeply dissecting streams, which limit the number of exposures. Taking into account the thickness of the outcrops along the north and south coastal cliffs it is reasonable to assume that a significant (unknown) amount of erupted material was deposited at sea, as commonly reported for other islands such as Montserrat (Lesser Antilles), Stromboli (Aeolian Islands), Faial and São Miguel (Azores archipelago) (e.g., Trofimovs et al., 2006; Andronico and Pistolesi, 2010; Pimentel et al., 2015; Porreca et al., 2018). Therefore, the values obtained for the Lajes and Angra ignimbrites are minimal.

Nevertheless, the volume of erupted magma estimated for the Lajes Ignimbrite (0.31–0.42 km^3 DRE) is within the same order of magnitude of other major explosive eruptions recorded in the Azores, such as the 4.6 ka Fogo A Plinian eruption (Fogo volcano, São Miguel) with 0.64 km^3 DRE (Booth et al., 1978) and the 16 ka Santa Bárbara caldera-forming eruption (Sete Cidades volcano, São Miguel) with 0.25–0.54 km^3 DRE (Kueppers et al., 2019). However, these differ from the Lajes Ignimbrite-forming eruption as they produced thick pumice fall deposits in addition to ignimbrites (Pensa et al., 2015; Queiroz et al., 2015).

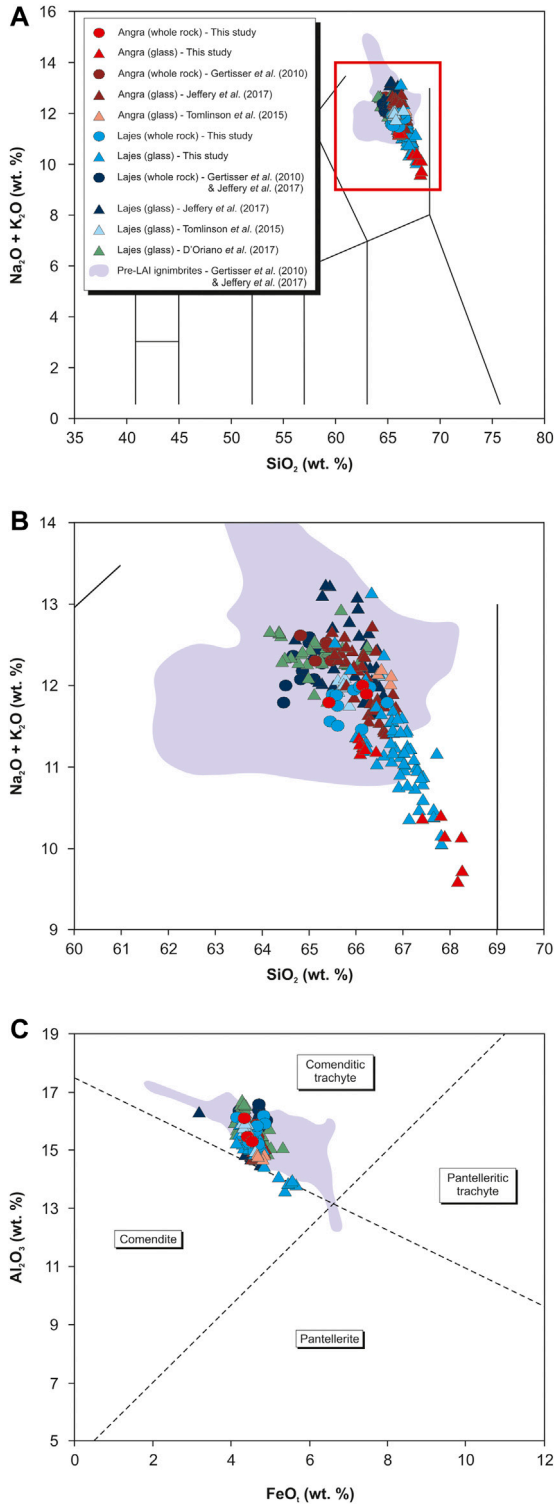


FIGURE 12 | Major element classification plots for the Angra and Lajes ignimbrites. Whole rock and groundmass glass analyses are distinguished for clarity. Ignimbrites that pre-date the LAI are also shown for reference. **(A)** Chemical compositions of the Angra and Lajes ignimbrites plotted in the total alkali vs. silica diagram (Le Maitre et al., 2002). **(B)** Enlargement of panel 12A, highlighting the chemical variation within the LAI. **(C)** Peralkaline compositions for the Angra and Lajes ignimbrites plotted on the Al_2O_3 vs. FeO_T classification scheme for oversaturated peralkaline rocks (Macdonald, 1974).

Magmatic System and Eruption Style

The Angra and Lajes ignimbrites share the same comenditic trachyte whole rock major element composition (**Figure 12**) and mineral assemblage dominated by anorthoclase. However, their whole rock trace element and groundmass glass compositions vary considerably (**Figure 13**). Such variability is also observed in trace element composition of groundmass glasses and in textures and compositions of anorthoclase crystals of the Lajes Ignimbrite (D'Oriano et al., 2017). The data presented in this study are consistent with the presence of a zoned magma reservoir which fed the Angra and Lajes ignimbrite-forming eruptions. This is a recurrent theme for the magma system of Pico Alto volcano (and potentially Guilherme Moniz), where the interplay of complex petrogenetic processes acting in the magma reservoir has been identified (D'Oriano et al., 2017; Jeffery et al., 2017). These include the derivation of the ignimbrite-forming comenditic trachyte from a zoned magma reservoir, with thermometric and hygrometric gradients, dominated by extended fractional crystallization and important contributions from *in-situ* crystallization, remobilization of cumulate material (crystal mush) and magma mixing processes. All these processes are, to some extent, masked by the seemingly homogeneous trachytic major element compositions of the eruptive products.

Chemically zoned magma reservoirs are common in other peralkaline volcanic systems, such as Furnas volcano on São Miguel (Jeffery et al., 2016), and are recorded by peralkaline ignimbrites such as the 13.9 Ma Ignimbrite "TL" (Sumner and Branney, 2002), the 13.6 Ma Ignimbrite "A" (Troll and Schmincke, 2002), and the 11.8 Ma Ayagaures ignimbrite (Jutzeler et al., 2010), on Gran Canaria, and the 45 ka Green Tuff Ignimbrite, Pantelleria (Williams, 2010), as well as a range of other ocean island systems (Jeffery and Gertisser, 2018 and references therein). Despite this, the data presented in this study cannot be accounted for adequately by a traditional zoned magma reservoir model featuring a single magma body with an upward gradational transition from less to more evolved magma, and may instead highlight a more complex magmatic plumbing system, potentially comprising multiple magma bodies.

Although the eruption triggering mechanism is uncertain, D'Oriano et al. (2017) proposed that the magmatic system of Pico Alto was disturbed by a heat source, most probably induced by the arrival of a hotter magma from depth, but without mixing with the resident comenditic trachyte magma reservoir. The thermal destabilization at the base of the reservoir and the onset of eruption caused syn-eruptive mixing between different portions of the zoned magma reservoir, which contributed to the homogenization of the resident magma. We speculate that the first eruptive event tapped the uppermost part of the reservoir, which is recorded by the Angra Ignimbrite. Some (unknown) time after the initial event, a second eruptive event took place involving the withdrawal of a larger volume of magma and probably reaching the lower parts of the reservoir. The latter is recorded by the Lajes Ignimbrite.

The Angra Ignimbrite-forming eruption was characterized by short-lived low pyroclastic fountaining, most probably located in the

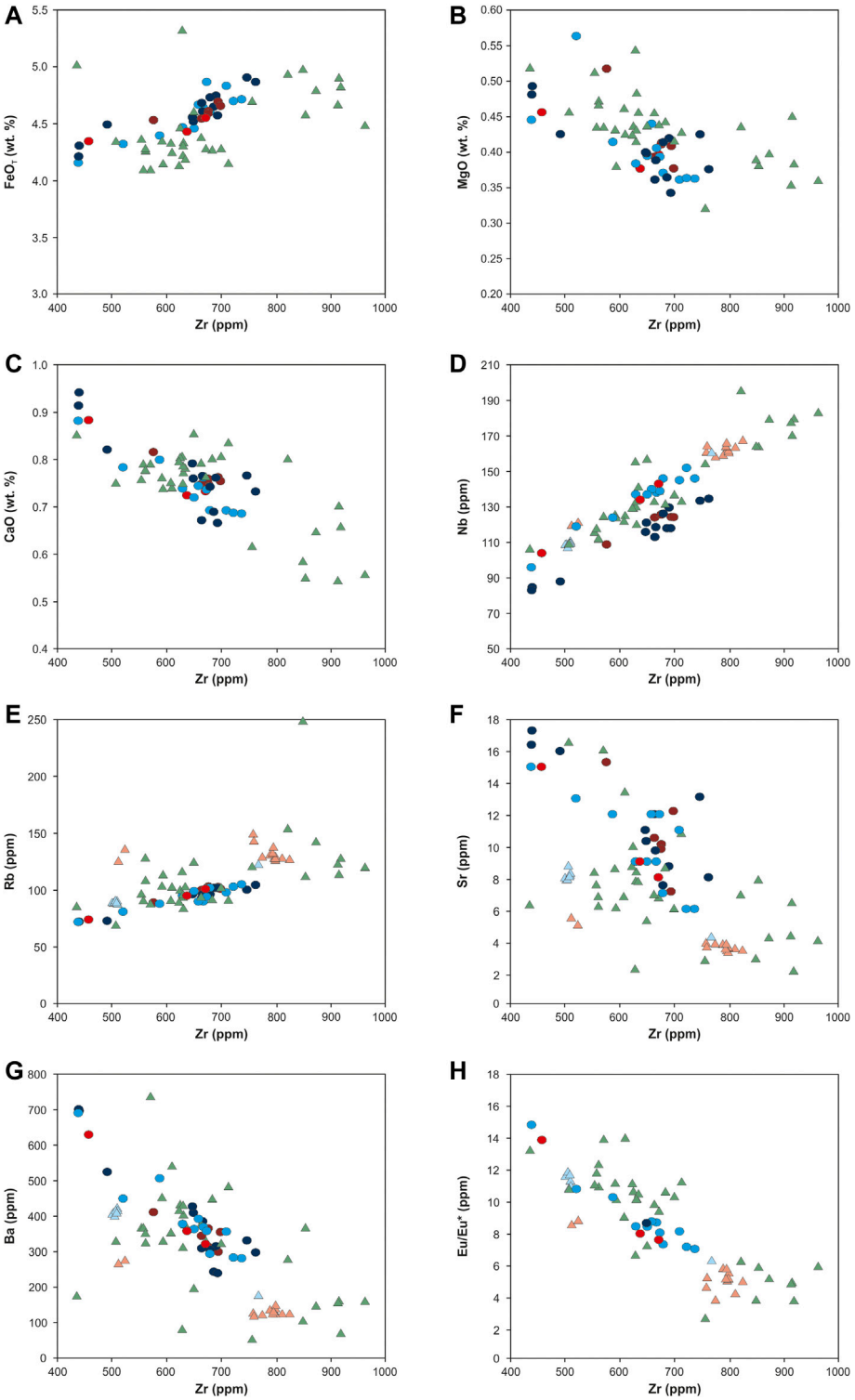


FIGURE 13 | Selected major and trace element data plotted vs. Zr, which is applied as an index of differentiation. Major element data are reported in wt. %, trace elements as ppm. All symbols and data sources are as given in **Figure 12**.

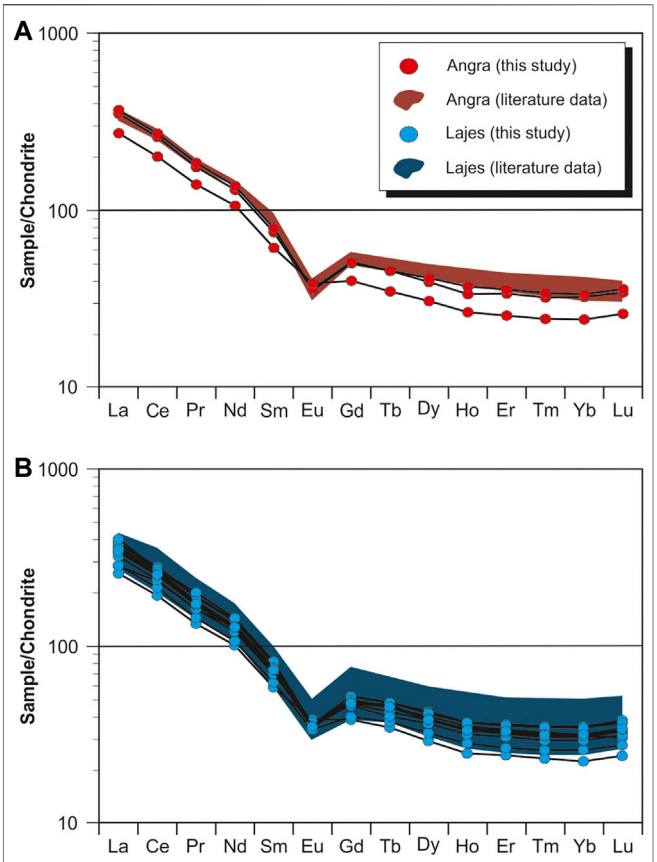


FIGURE 14 | Chondrite-normalised REE patterns for the Angra **(A)** and the Lajes **(B)** ignimbrites. Coloured fields denote the total range of literature data derived from Tomlinson et al. (2015), D'Oriano et al. (2017), and Jeffery et al. (2017). Chondrite values taken from Sun and McDonough (1989).

southern part of Pico Alto caldera. The event did not form a convective eruptive column, as no pumice fall deposit was found in the ignimbrite sequence. The pyroclastic fountain generated a small but sustained PDC that seems to have been mostly channelled along a valley on the southern part of Terceira (**Figure 3**). The eruption of the Lajes Ignimbrite was dominated by vigorous and prolonged low pyroclastic fountaining (or boiling-over) from Pico Alto caldera generating a sustained PDC, which spread radially towards both the north and south coasts of the island (**Figure 4**). Other ignimbrites worldwide have also been interpreted to result from boiling-over eruptions (e.g., Cas et al., 2011; Willcock et al., 2013; Pacheco-Hoyos et al., 2018). Like the Angra Ignimbrite, the Lajes Ignimbrite-forming eruption was neither preceded nor followed by the formation of a convective eruptive column, as there are no pumice fall deposits associated with this ignimbrite sequence.

Pyroclastic Density Current Emplacement Dynamics

The vertical and lateral lithofacies variations observed in the Angra and Lajes ignimbrites reflect different conditions of the parent PDCs during deposition. Vertical lithofacies variations (**Figure 6**) record changes in PDC deposition through time (i.e., current unsteadiness), while lateral lithofacies variations (**Figures 7**, **8**) record spatial variability of the PDC during deposition and its interaction with the topography (i.e., current non-uniformity) (Branney and Kokelaar, 2002).

The Angra Ignimbrite is composed of non-welded massive lapilli-ash throughout most of its thickness (**Figure 6A**). The massive nature and small volume of this ignimbrite indicate that it was deposited from a small but sustained high particle concentration granular fluid-based PDC. The dilute front of the current, which left in places a thin, fines-poor and crystal-rich bed, rapidly changed to high particle concentration, granular fluid-based flow conditions, overall dominated by steady deposition from fluid escape-dominated to granular flow-dominated flow-boundary zones (Branney and Kokelaar, 2002). Locally, subtle unsteadiness developed within the flow-boundary zone, leading to deposition of diffuse-stratified lapilli-ash. No unconformities were observed within the ignimbrite, which implies that the emplacement was continuous without significant time breaks, representing a single depositional unit. The Angra Ignimbrite has a high-aspect ratio geometry and limited areal extent, cropping out in only one valley south of Guilherme Moniz caldera, suggesting that the parent PDC may have been mostly channelled along this valley (**Figure 3**). However, it cannot be excluded that the Angra Ignimbrite is buried under younger deposits in the middle of the island, particularly on the floor of Guilherme Moniz and Cinco Picos calderas. The features of the Angra Ignimbrite are typical of HARIs deposited from relatively low velocity PDCs confined to topographic depressions (e.g., Walker, 1983; Cas and Wright, 1987; Cas et al., 2011; Martí et al., 2019).

The vertical lithofacies variations observed in the Lajes Ignimbrite reveal an overall inverse grading pattern, starting as a finer-grained base and grading to a coarser-grained upper part. However, the topmost portion of the ignimbrite is typically finer grained (**Figure 6B**). From its characteristics, we can infer that the ignimbrite was mostly deposited from a sustained, quasi-steady, high particle concentration granular fluid-based PDC that progressively waxed in competence during emplacement and then rapidly waned at the end (Kneller and Branney, 1995; Branney and Kokelaar, 2002). This reveals that the PDC dynamics changed as the eruption intensified. The initial dilute front of the PDC deposited a basal, fines-poor and crystal-rich bed (similar to the ground layer of other ignimbrites; Sparks, 1976; Scarpati et al., 2015), but it rapidly evolved to a high particle-concentration, granular fluid-based current dominated by steady deposition from fluid escape-dominated to granular flow-dominated flow-boundary zones. The high temperature of the PDC promoted the syn-depositional agglutination of pyroclasts and thus welding of the deposit, which is recorded by the eutaxitic massive lapilli-ash. As the PDC progressively waxed in competence, it deposited non-welded, coarse-grained massive lapilli-ash. The increase in the concentration and size of lithic clasts had a cooling effect on the current (Eichelberger and Koch, 1979; Martí et al., 1991), sufficient to inhibit welding of the upper part of the deposit. Local current unsteadiness, with transitional flow-boundary zones between fluid escape-dominated and granular flow-dominated, with brief periods of traction-

dominated conditions (Branney and Kokelaar, 2002), led to deposition of diffuse-stratified and diffuse-bedded lapilli-ash.

Overall, the vertical sequence of the Lajes Ignimbrite indicates that this thin ignimbrite sheet (3.5 m average thickness) corresponds to a single depositional unit from a sustained quasi-steady PDC. This contrasts with previous studies (Self, 1974; Self, 1976; Gertisser et al., 2010) that interpreted the presence of two depositional layers based on strong pumice concentration zones and sharp boundaries between welded and non-welded lithofacies. However, these pumice concentrations are not ubiquitous; they are found in a few places in the northern part of the island, and the sharp welded/non-welded boundaries are only seen locally at São Mateus (south coast). Several lines of evidence support the single depositional unit, including the gradual transitions of lithofacies (i.e., diffuse boundaries), the gradual variation of welding intensity, and the absence of unconformities such as intra-ignimbrite pumice or ash fall layers and erosion surfaces.

The lateral variations of lithofacies observed in the Lajes Ignimbrite (**Figures 7**, **8**) cannot be interpreted as typical valley-pond ignimbrite to veneer deposit transitions commonly seen in LARIs. The thin fine-grained massive lapilli-ash or massive ash deposit with crystal-rich base observed where the ignimbrite thins against topography differs from the stratified veneer lithofacies described for intermediate to small volume ignimbrites (e.g., Walker et al., 1980; Walker et al., 1981; Wilson and Walker, 1982; Wilson, 1985; Giordano et al., 2002). In the present case, the lateral transition corresponds to a condensed sequence of the Lajes Ignimbrite, including the lateral extent of the ground layer. The absence of stratified lithofacies suggests that the upper part of the current was not as turbulent as in other more dynamic PDCs. This sequence clearly differs from the fine ash deposit (commonly weathered into soil) that displays mantle bedding and is widespread across the island, including on topographic highs (**Figure 4**), which we interpret to correspond to the co-ignimbrite ash fall deposit.

Thus, the lateral lithofacies variations can be interpreted as recording non-uniformity within the flow-boundary zone (Branney and Kokelaar, 2002). The simultaneous deposition of coarse-grained massive lapilli-ash in a certain location and massive ash in another location may result from current instabilities and relatively non-uniform deposition. This is evident where the Lajes Ignimbrite parent PDC interacted with more irregular topography, such as stream valleys, fault scarps or caldera walls, which led to marked lateral variations of lithofacies in the space of just a few metres distance.

Although the Lajes Ignimbrite has a low-aspect ratio geometry, the parent PDC generally flowed along areas of low-lying ground with limited capacity to overcome topographic highs, such as the faults scarps of the Lajes Graben (10–70 m high) and the caldera walls of Cinco Picos and Guilherme Moniz volcanoes (up to 200 m high). In the western part of the island, the PDC was limited by the slopes of Santa Bárbara volcano (**Figure 4**). This contrasts with the typical flow behaviour of PDCs that generate LARIs, which are interpreted as highly energetic currents capable of surmounting significant topographic barriers (Walker et al., 1980; Cas and Wright, 1987; Wilson et al., 1995; Cas et al., 2011).

Therefore, the low-aspect ratio of the Lajes Ignimbrite may simply result from deposition over a generally flat topography such as the coastal areas and the floor of the Lajes Graben, rather than from a highly energetic PDC. We propose that the ignimbrite was emplaced from a sustained high particle concentration, granular-fluid-based PDC with relatively low velocity and low heat loss. The low energy, placid style of emplacement helped conserve heat and promote welding in the Lajes Ignimbrite. Similar emplacement dynamics have been proposed for large volume ignimbrites such as the 4.3 Ma Kizilkaya ignimbrite, Turkey (Schumacher and Mues-Schumacher, 1996), the 2.08 Ma Cerro Galán Ignimbrite, Argentina (Cas et al., 2011), and the <73 ka Campo de la Piedra Pómez ignimbrite, Argentina (Báez et al., 2020b), but this mechanism apparently also holds for smaller volume ignimbrites.

The different flow paths from Pico Alto caldera towards the north and south coasts of the island (**Figure 4**) mostly reflect the interaction of the PDC with palaeotopography, in particular with the caldera walls of Guilherme Moniz and Cinco Picos volcanoes, and the fault scarps of the Lajes Graben. The parent PDC seems to have been deflected by the fault scarps of the graben to reach the eastern end of the island at Praia da Vitória. The detailed geochemical reconstruction of the Lajes Ignimbrite indicates that the PDC was not simultaneously emplaced radially but rather different flow paths were emplaced at different times (D'Oriano et al., 2017). Similar flow behaviour has been recognized for the 45 ka Green Tuff Ignimbrite, Pantelleria (Williams et al., 2014) and for the 39 ka Campanian Ignimbrite, Italy (Fedele et al., 2016) through detailed chemical stratigraphy of the deposit.

Implications for Hazard Assessment

The geological record of Terceira shows that several ignimbrite-forming eruptions coming from Pico Alto and, possibly, Guilherme Moniz volcanoes have occurred in the last ca. 100 kyr (Gertisser et al., 2010). Although the frequency of ignimbrite-forming eruptions is relatively low and the last events occurred ca. 25 cal ka BP ago (recorded by the LAI), Pico Alto is an active central volcano and the possibility of other similar eruptions in the future should not be underestimated. The probability of an ignimbrite-forming eruption occurring from Santa Bárbara volcano is low, as its stratigraphy does not include ignimbrites, although a lithic-rich PDC deposit has been reported (Calvert et al., 2006). However, Santa Bárbara volcano has the potential to produce explosive and, therefore, ignimbrite-forming eruptions, thus a future event cannot be ruled out.

A future ignimbrite-forming eruption of Pico Alto volcano could strongly impact the island, with devastating and long-term socio-economic consequences for its 55,000 inhabitants (PORDATA, 2020) and for the entire Azores archipelago (Medeiros et al., 2021). An eruption with similar characteristics to the Lajes Ignimbrite-forming event would be a worst-case scenario in terms of hazard assessment for a small island such as Terceira (400 km^2). If a future event behaved similarly to the Lajes Ignimbrite parent PDC, it would affect

all of the central part of island and flow towards the sea on the north and south coasts (**Figure 4**). The relatively low velocity of the PDC might mean it would have limited ability to surmount topographic barriers, such as the fault scarps of the Lajes Graben or the caldera walls of Cinco Picos and Guilherme Moniz volcanoes, but it could be channelled to more distal areas maintaining high temperatures.

The well-populated villages along the north coast of the island between Biscoitos and Lajes would be strongly impacted due to their proximity to Pico Alto caldera (**Figure 4**). However, other densely populated areas on the eastern part of the island between Lajes and Praia da Vitória, and several villages on the south coast between São Mateus and Porto Judeu, including the city of Angra do Heroísmo could also be affected by channelled PDCs. In this scenario the western part of the island would not be affected and could possibly serve as a retreat area in case of evacuation of the affected villages. Moreover, the hazard would be especially compounded by the lack of an opening Plinian fallout phase that could give warning of impending PDCs and during which evacuations or other mitigation operations could be prepared.

Apart from dwellings, all critical infrastructure of the island might be expected to be damaged or destroyed. The geothermal power plant located on the southwest flank of Pico Alto caldera would most likely also be destroyed. All of the island's communication hubs, including the only airport and NATO Air Base on the floor of Lajes Graben and the main harbour located on Praia da Vitória could suffer significant damage (see **Figure 4** for location). This would make Terceira difficult to be reached by air or maritime transport, with major implications for evacuations and emergency response. The only hospital and the headquarters of the Azores Regional Civil Protection and Fire Services, both located in the city of Angra do Heroísmo (see **Figure 4** for location), could also be severely affected.

In the light of this and despite the relatively low probability of such an event, this worst-case scenario should be considered by regional and national authorities in risk management plans. The potential risk is aggravated by the small size, remote location, high population density and weak economy of Terceira, as is commonly the case of volcanic islands (Pelling and Uitto, 2001; Wilkinson et al., 2016; Pimentel et al., 2020), such as demonstrated recently by the 2021 explosive eruption of La Soufrière volcano, St. Vincent (Lesser Antilles).

CONCLUSIONS

The Lajes-Angra Ignimbrite Formation (LAI) is the youngest (ca. 25 cal ka BP) of at least seven major formations containing peralkaline ignimbrites on Terceira Island (Azores). Most of the older ignimbrites share physical and geochemical similarities with the LAI, suggesting that the processes involved in ignimbrite-forming eruptions have been recurrent in the last ca. 100 kyr, with significant implications for volcanic hazard assessment. In this paper we combined lithofacies analysis and ignimbrite architecture with petrographic and geochemical data to provide insights into the pre-eruptive magmatic system of Pico Alto volcano and infer the eruption style and emplacement dynamics of the parent PDCs of the Angra and Lajes ignimbrites.

The two ignimbrites are difficult to distinguish based on whole rock major element chemistry alone, as both have comenditic trachyte compositions. However, whole rock trace element and groundmass glass compositions show considerable variability, which together with disequilibrium textures and compositions of anorthoclase crystals, reveal the occurrence of complex petrogenetic processes in the Pico Alto magma reservoir prior to eruption. Although the two ignimbrite-forming events were closely spaced in time (unresolvable by radiocarbon dating), their PDCs had dissimilar eruptive and depositional processes. The Angra Ignimbrite was formed by a small-volume sustained PDC that was fed by a short-lived, low pyroclastic fountain, which generated a high particle concentration, granular fluid-based PDC. This current seems to have been mostly channelled along a single valley on the south part of the island, forming a high-aspect ratio ignimbrite. On the other hand, the Lajes Ignimbrite resulted from a sustained quasi-steady PDC that was fed by vigorous and prolonged pyroclastic fountaining. Ignimbrite architecture suggests evolving depositional conditions of the parent PDC through time and space. The dilute front of the current rapidly evolved to a high particle concentration, granular fluid-based PDC as the eruption waxed. The PDC spread radially from Pico Alto caldera to both the north and south coasts with limited capacity to overcome topographic highs. The low-aspect ratio of the Lajes Ignimbrite most probably resulted from deposition of a relatively low velocity PDC over a generally flat topography, rather than from a highly energetic current. This placid style of emplacement allowed the PDC to conserve heat, which in turn, prompted welding in this thin ignimbrite sheet. We highlight that ignimbrite geometry (aspect ratio) does not directly reflect the kinetic energy of a PDC and therefore should not be used to infer on PDC emplacement dynamics.

A future ignimbrite-forming eruption of Pico Alto volcano would have devastating consequences for Terceira. In this worst-case scenario, the central part of the island and the villages located along the north and south coasts would be affected by PDCs, including all critical infrastructure and communication hubs. Despite the relatively low probability, such an event presents a considerable challenge for civil protection authorities. The findings of this study can provide a framework to better understand ignimbrite-forming eruptions on other active volcanic islands, as well as their potential impacts in case of future volcanic unrest.

DATA AVAILABILITY STATEMENT

The original contributions presented in the study are included in the article/**Supplementary Material**, further inquiries can be directed to the corresponding author.

AUTHOR CONTRIBUTIONS

AP was responsible for the formulation of this study as part of his PhD project, collection of field data, data analysis, and preparing the manuscript. SS took part in the fieldwork (including during the 1970s) and assisted with data analysis. JP contributed to the formulation of the study and data analysis. AJ and RG took part in fieldwork, compilation of geochemical data, provided figures, and assisted with data analysis. All authors contributed to writing and reviewing the paper.

FUNDING

This study was funded by a PhD scholarship of Fundo Regional da Ciência e Tecnologia to AP (M3.1.2/F/022/2007) and partially supported by Fundação para a Ciência e Tecnologia through MARES project (PTDC/GEO-FIQ/1088/2014). SS and RG thank The Open University, United Kingdom, for supporting field trips to Terceira in the period 2005–2010. Publication made possible in part by support from the Berkeley Research Impact Initiative (BRII) sponsored by the UC Berkeley Library.

ACKNOWLEDGMENTS

We thank Claudio Scarpati, Dario Pedrazzi and Chief Editor Valerio Acocella for their constructive comments that significantly improved this paper. We also thank Guest Associate Editor Joan Martí for the editorial handling. Vittorio Zanon of the Instituto de Investigação em Vulcanologia e Avaliação de Riscos (IVAR), Universidade dos Açores, Andrea Risplendente and Stefano Poli of the Dipartimento di Scienze della Terra "Ardito Desio", Università degli Studi di Milano are acknowledged for the help with microprobe analyses.

SUPPLEMENTARY MATERIAL

The Supplementary Material for this article can be found online at: https://www.frontiersin.org/articles/10.3389/feart.2021.673686/full#supplementary-material

REFERENCES

Andronico, D., and Pistolesi, M. (2010). The November 2009 Paroxysmal Explosions at Stromboli. *J. Volcanology Geothermal Res.* 196, 120–125. doi:10.1016/j.jvolgeores.2010.06.005

Báez, W., Bustos, E., Chiodi, A., Reckziegel, F., Arnosio, M., de Silva, S., et al. (2020a). Eruptive Style and Flow Dynamics of the Pyroclastic Density Currents Related to the Holocene Cerro Blanco Eruption (Southern Puna Plateau, Argentina). *J. South Am. Earth Sci.* 98, 102482. doi:10.1016/j.jsames.2019.102482

Báez, W., de Silva, S., Chiodi, A., Bustos, E., Giordano, G., Arnosio, M., et al. (2020b). Pulsating flow dynamics of sustained, forced pyroclastic density currents: insights from a facies analysis of the Campo de la Piedra Pómez ignimbrite, southern Puna, Argentina. *Bull. Volcanol.* 82, 53. doi:10.1007/s00445-020-01385-5

Bogaard, P. v. d., and Schmincke, H.-U. (1998). "Chronostratigraphy of Gran Canaria," in Proc. ODP, Sci. Res. *157*. Editors P.P.E. Weaver, H.-U. Schmincke, J.V. Firth, and W. Duffield (College Station, TX: Ocean Drilling Program), 127–140. doi:10.2973/odp.proc.sr.157.116.1998

Booth, B., Croasdale, R., and Walker, G. (1978). A Quantitative Study of Five Thousand Years of Volcanism on Sao Miguel, Azores. *Phil. Trans. Roy. Soc. London, Ser. A, Math. Phys. Sci.* 288, 271–319. doi:10.1098/rsta.1978.0018

Brand, B. D., Mackaman-Lofland, C., Pollock, N. M., Bendaña, S., Dawson, B., and Wichgers, P. (2014). Dynamics of Pyroclastic Density Currents: Conditions that Promote Substrate Erosion and Self-Channelization - Mount St Helens, Washington (USA). *J. Volcanology Geothermal Res.* 276, 189–214. doi:10.1016/j.jvolgeores.2014.01.007

Branney, M. J., and Kokelaar, P. (2002). Pyroclastic Density Currents and the Sedimentation of Ignimbrites. *Geol. Soc. London, Mems* 27, 152. doi:10.1144/GSL.MEM.2003.027

Brown, R. J., Barry, T. L., Branney, M. J., Pringle, M. S., and Bryan, S. E. (2003). The Quaternary Pyroclastic Succession of Southeast Tenerife, Canary Islands: Explosive Eruptions, Related Caldera Subsidence, and Sector Collapse. *Geol. Mag.* 140, 265–288. doi:10.1017/S0016756802007252

Brown, R. J., and Branney, M. J. (2004). Event-stratigraphy of a Caldera-Forming Ignimbrite Eruption on Tenerife: the 273 ka Poris Formation. *Bull. Volcanol.* 66, 392–416. doi:10.1007/s00445-003-0321-y

Brown, R. J., Kokelaar, B. P., and Branney, M. J. (2007). Widespread Transport of Pyroclastic Density Currents from a Large Silicic Tuff Ring: the Glaramara Tuff, Scafell Caldera, English Lake District, UK. *Sedimentology* 54, 1163–1190. doi:10.1111/j.1365-3091.2007.00877.x

Calvert, A. T., Moore, R. B., McGeehin, J. P., and Rodrigues da Silva, A. M. (2006). Volcanic History and 40Ar/39Ar and 14C Geochronology of Terceira Island, Azores, Portugal. *J. Volcanology Geothermal Res.* 156, 103–115. doi:10.1016/j.jvolgeores.2006.03.016

Cas, R. A. F., Wright, H. M. N., Folkes, C. B., Lesti, C., Porreca, M., Giordano, G., et al. (2011). The Flow Dynamics of an Extremely Large Volume Pyroclastic Flow, the 2.08-Ma Cerro Galán Ignimbrite, NW Argentina, and Comparison with Other Flow Types. *Bull. Volcanol.* 73, 1583–1609. doi:10.1007/s00445-011-0564-y

Cas, R. A. F., and Wright, J. V. (1987). Volcanic Successions. *Modern and Ancient*. London: Allen & Unwin, 528.

Casalbore, D., Romagnoli, C., Pimentel, A., Quartau, R., Casas, D., Ercilla, G., et al. (2015). Volcanic, Tectonic and Mass-Wasting Processes Offshore Terceira Island (Azores) Revealed by High-Resolution Seafloor Mapping. *Bull. Volcanol.* 77, 24. doi:10.1007/s00445-015-0905-3

Casas, D., Pimentel, A., Pacheco, J., Martorelli, E., Sposato, A., Ercilla, G., et al. (2018). Serreta 1998-2001 Submarine Volcanic Eruption, Offshore Terceira (Azores): Characterization of the Vent and Inferences about the Eruptive Dynamics. *J. Volcanology Geothermal Res.* 356, 127–140. doi:10.1016/j.jvolgeores.2018.02.017

Chiocci, F. L., Romagnoli, C., Casalbore, D., Sposato, A., Martorelli, E., Alonso, B., et al. (2013). Bathy-morphological Setting of Terceira Island (Azores) after the FAIVI Cruise. *J. Maps* 9, 590–595. doi:10.1080/17445647.2013.831381

D'Oriano, C., Landi, P., Pimentel, A., and Zanon, V. (2017). Magmatic Processes Revealed by Anorthoclase Textures and Trace Element Modeling: The Case of the Lajes Ignimbrite Eruption (Terceira Island, Azores). *J. Volcanology Geothermal Res.* 347, 44–63. doi:10.1016/j.jvolgeores.2017.08.012

Dade, W. B. (2003). The Emplacement of Low-Aspect Ratio Ignimbrites by Turbulent Parent Flows. *J. Geophys. Res.* 108, 2211–2220. doi:10.1029/2001JB001010

Dávila-Harris, P., Ellis, B. S., Branney, M. J., and Carrasco-Núñez, G. (2013). Lithostratigraphic Analysis and Geochemistry of a Vitric Spatter-Bearing Ignimbrite: the Quaternary Adeje Formation, Cañadas Volcano, Tenerife. *Bull. Volcanol.* 75, 722. doi:10.1007/s00445-013-0722-5

Druitt, T. H. (1998). "Pyroclastic Density Currents,". *The Physics of Explosive Volcanic Eruptions*. Editors J.S. Gilbert and R.S.J. Sparks (London, UK: Geol. Soc., London, Special Publications), 145, 145–182. doi:10.1144/GSL.SP.1996.145.01.08

Duncan, A. M., Queiroz, G., Guest, J. E., Cole, P. D., Wallenstein, N., and Pacheco, J. M. (1999). The Povoação Ignimbrite, Furnas Volcano, São Miguel, Azores. *J. Volcanology Geothermal Res.* 92, 55–65. doi:10.1016/S0377-0273(99)00067-0

Eichelberger, J. C., and Koch, F. G. (1979). Lithic Fragments in the Bandelier Tuff, Jemez Mountains, New Mexico. *J. Volcanology Geothermal Res.* 5, 115–134. doi:10.1016/0377-0273(79)90036-2

Eisele, S., Freundt, A., Kutterolf, S., Ramalho, R. S., Kwasnitschka, T., Wang, K.-L., et al. (2015). Stratigraphy of the Pleistocene, Phonolitic Cão Grande Formation on Santo Antão, Cape Verde. *J. Volcanology Geothermal Res.* 301, 204–220. doi:10.1016/j.jvolgeores.2015.03.012

Fedele, L., Scarpati, C., Sparice, D., Perrotta, A., and Laiena, F. (2016). A Chemostratigraphic Study of the Campanian Ignimbrite Eruption (Campi Flegrei, Italy): Insights on Magma Chamber Withdrawal and deposit Accumulation as Revealed by Compositionally Zoned Stratigraphic and Facies Framework. *J. Volcanology Geothermal Res.* 324, 105–117. doi:10.1016/j.jvolgeores.2016.05.019

Féraud, G., Kaneoka, I., and Allègre, C. (1980). K/Ar Ages and Stress Pattern in the Azores: Geodynamic Implications. *Earth Planet. Sci. Lett.* 46, 275–286. doi:10.1016/0012-821X(80)90013-8

Freundt, A., and Schmincke, H.-U. (1986). Emplacement of Small-Volume Pyroclastic Flows at Laacher See (East-Eifel, Germany). *Bull. Volcanol.* 48, 39–59. doi:10.1007/BF01073512

Gaspar, J. L. (1996). Ilha Graciosa (Açores). História vulcanológica e avaliação do hazard. PhD thesis, Ponta Delgada: Universidade dos Açores, 361.

Gaspar, J. L., Queiroz, G., Pacheco, J. M., Ferreira, T., Wallenstein, N., Almeida, M. H., et al. (2003). "Basaltic Lava Balloons Produced during the 1998-2001 Serreta Submarine Ridge Eruption (Azores), *Explosive Subaqueous Volcanism*. Editors J. D. L. White, J. L. Smellie, and D. A. Clague (Washington DC, USA: AGU Geophysical Monograph), 140, 205–212. doi:10.1029/140gm13

Gertisser, R., Self, S., Gaspar, J. L., Kelley, S. P., Pimentel, A., Eikenberg, J., et al. (2010). "Ignimbrite Stratigraphy and Chronology on Terceira Island, Azores,"*Stratigraphy and Geology of Volcanic Areas*. Editors G. Groppelli and L. Viereck-Goette (Boulder, USA: Geol. Soc. Amer., Spec. Pap.), 464, 133–154. doi:10.1130/2010.2464(07)

Giordano, G., De Rita, D., Cas, R., and Rodani, S. (2002). Valley Pond and Ignimbrite Veneer Deposits in the Small-Volume Phreatomagmatic 'Peperino Albano' Basic Ignimbrite, Lago Albano Maar, Colli Albani Volcano, Italy: Influence of Topography. *J. Volcanology Geothermal Res.* 118, 131–144. doi:10.1016/S0377-0273(02)00253-6

Giordano, G., and Doronzo, D. M. (2017). Sedimentation and Mobility of PDCs: a Reappraisal of Ignimbrites' Aspect Ratio. *Sci. Rep.* 7, 4444. doi:10.1038/s41598-017-04880-6

Giordano, G. (1998). The Effect of Paleotopography on Lithic Distribution and Facies Associations of Small Volume Ignimbrites: the WTT Cupa (Roccamonfina Volcano, Italy). *J. Volcanology Geothermal Res.* 87, 255–273. doi:10.1016/S0377-0273(98)00096-1

Hildenbrand, A., Weis, D., Madureira, P., and Marques, F. O. (2014). Recent Plate Re-organization at the Azores Triple Junction: Evidence from Combined Geochemical and Geochronological Data on Faial, S. Jorge and Terceira Volcanic Islands. *Lithos* 210-211, 27–39. doi:10.1016/j.Lithos.2014.09.009

Hildreth, W., and Fierstein, J. (2012). The Novarupta-Katmai Eruption of 1912 - Largest Eruption of the Twentieth century: Centennial Perspectives. *U.S. Geol. Surv. Prof. Pap.* 1791, 259.

Jeffery, A. J., Gertisser, R., O'Driscoll, B., Pacheco, J. M., Whitley, S., Pimentel, A., et al. (2016). Temporal Evolution of a post-caldera, Mildly Peralkaline Magmatic System: Furnas Volcano, São Miguel, Azores. *Contrib. Mineral. Petrol.* 171, 42. doi:10.1007/s00410-016-1235-y

Jeffery, A. J., and Gertisser, R. (2018). Peralkaline Felsic Magmatism of the Atlantic Islands. *Front. Earth Sci.* 6, 145. doi:10.3389/feart.2018.00145

Jeffery, A. J., Gertisser, R., Self, S., Pimentel, A., O'Driscoll, B., and Pacheco, J. M. (2017). Petrogenesis of the Peralkaline Ignimbrites of Terceira, Azores. *J. Pet.* 58, 2365–2402. doi:10.1093/petrology/egy012

Jørgensen, K. A. (1980). The Thorsmörk Ignimbrite: An Unusual Comenditic Pyroclastic Flow in Southern Iceland. *J. Volcanol. Geotherm. Res.* 8, 7–22. doi:10.1016/0377-0273(80)90004-9

Jutzeler, M., Schmincke, H.-U., and Sumita, M. (2010). The Incrementally Zoned Miocene Ayagaures Ignimbrite (Gran Canaria, Canary Islands). *J. Volcanology Geothermal Res.* 196, 1–19. doi:10.1016/j.jvolgeores.2010.07.002

Kneller, B. C., and Branney, M. J. (1995). Sustained High-Density Turbidity Currents and the Deposition of Thick Massive Sands. *Sedimentology* 42, 607–616. doi:10.1111/j.1365-3091.1995.tb00395.x

Kokelaar, P., Raine, P., and Branney, M. J. (2007). Incursion of a Large-Volume, Spatter-Bearing Pyroclastic Density Current into a Caldera lake: Pavey Ark Ignimbrite, Scafell Caldera, England. *Bull. Volcanol.* 70, 23–54. doi:10.1007/s00445-007-0118-5

Kueppers, U., Pimentel, A., Ellis, B., Forni, F., Neukampf, J., Pacheco, J., et al. (2019). Biased Volcanic Hazard Assessment Due to Incomplete Eruption Records on Ocean Islands: An Example of Sete Cidades Volcano, Azores. *Front. Earth Sci.* 7, 122. doi:10.3389/feart.2019.00122

Lipman, P. W. (1997). Subsidence of Ash-Flow Calderas: Relation to Caldera Size and Magma-Chamber Geometry. *Bull. Volcanology* 59, 198–218. doi:10.1007/s004450050186

Macdonald, R. (1974). Nomenclature and Petrochemistry of the Peralkaline Oversaturated Extrusive Rocks. *Bull. Volcanol.* 38, 498–516. doi:10.1007/BF02596896

Madeira, J. (2005). The Volcanoes of Azores Islands: A World-Class Heritage. Examples from Terceira, Pico and Faial Islands. *IV International Symposium ProGEO on the Conservation of the Geological Heritage - Field Trip Guidebook*. Braga: Universidade do Minho, 104.

Martí, J., Diez-Gil, J. L., and Ortiz, R. (1991). Conduction Model for the Thermal Influence of Lithic Clasts in Mixtures of Hot Gases and Ejecta. *J. Geophys. Res.* 96 (B13), 21879–21885. doi:10.1029/91JB02149

Martí, J., Doronzo, D. M., Pedrazzi, D., and Colombo, F. (2019). Topographical Controls on Small-volume Pyroclastic Flows. *Sedimentology* 66, 2297–2317. doi:10.1111/sed.12600

Medeiros, J., Carmo, R., Pimentel, A., Vieira, J. C., and Queiroz, G. (2021). Assessing the Impact of Explosive Eruptions of Fogo Volcano (São Miguel, Azores) on the Tourism Economy. *Nat. Hazards Earth Syst. Sci.* 21, 417–437. doi:10.5194/nhess-21-439-202110.5194/nhess-21-417-2021

Mungall, J. E., and Martin, R. F. (1995). Petrogenesis of Basalt-comendite and Basalt-pantellerite Suites, Terceira, Azores, and Some Implications for the Origin of Ocean-Island Rhyolites. *Contr. Mineral. Petrol.* 119, 43–55. doi:10.1007/BF00310716

Pacheco-Hoyos, J. G., Aguirre-Díaz, G. J., and Dávila-Harris, P. (2018). Boiling-over Dense Pyroclastic Density Currents during the Formation of the ~ 100 km^3 Huichapan Ignimbrite in Central Mexico: Stratigraphic and Lithofacies Analysis. *J. Volcanology Geothermal Res.* 349, 268–282. doi:10.1016/j.jvolgeores.2017.11.007

Pelling, M., and Uitto, J. I. (2001). Small Island Developing States: Natural Disaster Vulnerability and Global Change. *Glob. Environ. Change B: Environ. Hazards* 3, 4962. doi:10.1016/S1464-2867(01)00018-3

Pensa, A., Cas, R., Giordano, G., Porreca, M., and Wallenstein, N. (2015). Transition from Steady to Unsteady Plinian Eruption Column: the VEI 5, 4.6 ka Fogo A Plinian Eruption, São Miguel, Azores. *J. Volcanology Geothermal Res.* 305, 1–18. doi:10.1016/j.jvolgeores.2015.09.012

Pimentel, A. (2006). *Domos e coulées da Ilha Terceira (Açores): Contribuição para o estudo dos mecanismos de instalação*. Ponta Delgada: MSc thesis, Universidade dos Açores, 143.

Pimentel, A., Pacheco, J., and Self, S. (2015). The ~1000-years BP Explosive Eruption of Caldeira Volcano (Faial, Azores): the First Stage of Incremental Caldera Formation. *Bull. Volcanol.* 77, 42. doi:10.1007/s00445-015-0930-2

Pimentel, A., Ramalho, R. S., Becerril, L., Larrea, P., and Brown, R. J. (2020). Editorial: Ocean Island Volcanoes: Genesis, Evolution and Impact. *Front. Earth Sci.* 8, 82. doi:10.3389/feart.2020.00082

Pimentel, A., Zanon, V., de Groot, L. V., Hipólito, A., Di Chiara, A., and Self, S. (2016). Stress-induced Comenditic Trachyte Effusion Triggered by Trachybasalt Intrusion: Multidisciplinary Study of the AD 1761 Eruption at Terceira Island (Azores). *Bull. Volcanol.* 78, 22. doi:10.1007/s00445-016-1015-6

PORDATA (2020). *Retrato Dos Açores PORDATA, Edição 2020*. Lisboa: Fundação Francisco Manuel dos Santos, 76.

Porreca, M., Pimentel, A., Kueppers, U., Izquierdo, T., Pacheco, J., and Queiroz, G. (2018). Event Stratigraphy and Emplacement Mechanisms of the Last Major Caldera Eruption on Sete Cidades Volcano (São Miguel, Azores): the 16 ka Santa Bárbara Formation. *Bull. Volcanol.* 80, 76. doi:10.1007/s00445-018-1250-0

Queiroz, G., Gaspar, J. L., Guest, J. E., Gomes, A., and Almeida, M. H. (2015). "Eruptive History and Evolution of Sete Cidades Volcano, São Miguel Island, Azores,". *Volcanic Geology of São Miguel Island (Azores Archipelago)*. Editors J. L. Gaspar, J. E. Guest, A. M. Duncan, F. J. A. S. Barriga, and D. K. Chester (London, Mems: Geol. Soc.), 44, 87–104. doi:10.1144/M44.7

Reimer, P. J., Austin, W. E. N., Bard, E., Bayliss, A., Blackwell, P. G., Bronk Ramsey, C., et al. (2020). The IntCal20 Northern Hemisphere Radiocarbon Age Calibration Curve (0-55 cal kBP). *Radiocarbon* 62, 725–757. doi:10.1017/RDC.2020.41

Le Maitre, R., Streckeisen, A., Zanettin, B., Le Bas, M., Bonin, B., and Bateman, P. (2002). *Igneous Rocks: A Classification and Glossary of Terms: Recommendations of the International Union of Geological Sciences Subcommission on the Systematics of Igneous Rocks*. 2nd Ed. (Cambridge University Press. Cambridge, United Kingdom), doi:10.1017/CBO9780511535581

Russell, J. K., and Quane, S. L. (2005). Rheology of Welding: Inversion of Field Constraints. *J. Volcanology Geothermal Res.* 142, 173–191. doi:10.1016/j.jvolgeores.2004.10.017

Scarpati, C., Sparice, D., and Perrotta, A. (2020). Dynamics of Large Pyroclastic Currents Inferred by the Internal Architecture of the Campanian Ignimbrite. *Sci. Rep.* 10, 22230. doi:10.1038/s41598-020-79164-7

Scarpati, C., Sparice, D., and Perrotta, A. (2015). The Ground Layer of the Campanian Ignimbrite: an Example of Deposition from a Dilute Pyroclastic Density Current. *Bull. Volcanol.* 77, 97. doi:10.1007/s00445-015-0985-0

Schumacher, R., and Mues-Schumacher, U. (1996). The Kizilkaya Ignimbrite - an Unusual Low-Aspect-Ratio Ignimbrite from Cappadocia, central Turkey. *J. Volcanology Geothermal Res.* 70, 107–121. doi:10.1016/0377-0273(95)00046-1

Scott, W. E., Hoblitt, R. P., Torres, R. C., Self, S., Martinez, M. M. L., and Nillos, T. (1996). "Pyroclastic Flows of the June 15, 1991, Climactic Eruption of Mount Pinatubo," in *Fire and Mud: Eruptions and Lahars of Mount Pinatubo, Philippines*. Editors C. G. Newhall and R. S. Punongbayan (Seattle: PHIVOLCS, Quezon City and University of Washington Press), 545–570.

Self, S., and Gunn, B. M. (1976). Petrology, Volume and Age Relations of Alkaline and Saturated Peralkaline Volcanics from Terceira, Azores. *Contrib. Mineral. Petrol.* 54, 293–313. doi:10.1007/BF00389409

Self, S. (1974). *Recent Volcanism on Terceira, Azores. PhD Thesis*. London: Imperial College, 236.

Self, S. (1971). The Lajes Ignimbrite, Ilha Terceira, Açores. *Comun. Serv. Geól. Portugal* 55, 165–184.

Self, S. (1976). The Recent Volcanology of Terceira, Azores. *J. Geol. Soc.* 132, 645–666. doi:10.1144/gsjgs.132.6.0645

Shea, T., and Owen, J. (2016). Discovery of a Trachyte Ignimbrite Sequence at Hualālai, Hawaii. *Bull. Volcanol* 78, 34. doi:10.1007/s00445-016-1027-2

Shotton, F. W., and Williams, R. E. G. (1973). Birmingham University Radiocarbon Dates VII. *Radiocarbon* 15, 451–468. doi:10.1017/S0033822200008924

Shotton, F. W., Williams, R. E. G., and Johnson, A. S. (1974). Birmingham University Radiocarbon Dates VIII. *Radiocarbon* 16, 285–303. doi:10.1017/S0033822200059610

Sohn, Y. K., and Chough, S. K. (1989). Depositional Processes of the Suwolbong Tuff Ring, Cheju Island (Korea). *Sedimentology* 36, 837–855. doi:10.1111/j.1365-3091.1989.tb01749.x

Sparks, R. S. J. (1976). Grain Size Variations in Ignimbrites and Implications for the Transport of Pyroclastic Flows. *Sedimentology* 23, 147–188. doi:10.1111/j.1365-3091.1976.tb00045.x

Sparks, R. S. J., Self, S., and Walker, G. P. L. (1973). Products of Ignimbrite Eruptions. *Geology* 1, 115–118. doi:10.1130/0091-7613(1973)1<115:POIE>2.0.CO;2

Sulpizio, R., Bonasia, R., Dellino, P., Mele, D., Di Vito, M. A., and La Volpe, L. (2010). The Pomici di Avellino eruption of Somma-Vesuvius (3.9 ka BP). Part II: sedimentology and physical volcanology of pyroclastic density current deposits. *Bull. Volcanol.* 72, 559–577. doi:10.1007/s00445-009-0340-4

Sulpizio, R., and Dellino, P. (2008). "Chapter 2 Sedimentology, Depositional Mechanisms and Pulsating Behaviour of Pyroclastic Density Currents," in *Caldera Volcanism: Analysis, Modelling, and Response. Developments in Volcanology 10*. Editors J. Gottsman and J. Marti (Amsterdam: Elsevier), 57–96. doi:10.1016/s1871-644x(07)00002-2

Sulpizio, R., Mele, D., Dellino, P., and La Volpe, L. (2007). Deposits and Physical Properties of Pyroclastic Density Currents during Complex Subplinian Eruptions: the AD 472 (Pollena) Eruption of Somma-Vesuvius, Italy. *Sedimentology* 54, 607–635. doi:10.1111/j.1365-3091.2006.00852.x

Sumner, J. M., and Branney, M. J. (2002). The Emplacement History of a Remarkable Heterogeneous, Chemically Zoned, Rheomorphic and Locally Lava-like Ignimbrite: 'TL' on Gran Canaria. *J. Volcanology Geothermal Res.* 115, 109–138. doi:10.1016/S0377-0273(01)00311-0

Sun, S.-s., and McDonough, W. F. (1989). "Chemical and Isotopic Systematics of Oceanic Basalts: Implications for Mantle Composition and Processes,". *Magmatism in the Ocean Basins*. Editors A. D. Saunders and M. J. Norry (London: Geol. Society.), 42, 313–345. doi:10.1144/gsl.sp.1989.042.01.19

Tomlinson, E. L., Smith, V. C., Albert, P. G., Aydar, E., Civetta, L., Cioni, R., et al. (2015). The Major and Trace Element Glass Compositions of the Productive Mediterranean Volcanic Sources: Tools for Correlating Distal Tephra Layers in and Around Europe. *Quat. Sci. Rev.* 118, 48–66. doi:10.1016/j.quascirev.2014.10.028

Trofimovs, J., Amy, L., Boudon, G., Deplus, C., Doyle, E., Fournier, N., et al. (2006). Submarine Pyroclastic Deposits Formed at the Soufrière Hills Volcano, Montserrat (1995-2003): What Happens when Pyroclastic Flows Enter the Ocean? *Geol.* 34, 549–552. doi:10.1130/G22424.1

Troll, V. R., and Schmincke, H.-U. (2002). Magma Mixing and Crustal Recycling Recorded in Ternary Feldspar from Compositionally Zoned Peralkaline Ignimbrite A', Gran Canaria, Canary Islands. *J. Pet.* 43, 243–270. doi:10.1093/petrology/43.2.243

Walker, G. P. L., Heming, R. F., and Wilson, C. J. N. (1980). Low-aspect Ratio Ignimbrites. *Nature* 283, 286–287. doi:10.1038/283286a0

Walker, G. P. L. (1983). Ignimbrite Types and Ignimbrite Problems. *J. Volcanology Geothermal Res.* 17, 65–88. doi:10.1016/0377-0273(83)90062-8

Walker, G. P. L., Self, S., and Froggatt, P. C. (1981). The Ground Layer of the Taupo Ignimbrite: a Striking Example of Sedimentation from a Pyroclastic Flow. *J. Volcanology Geothermal Res.* 10, 1–11. doi:10.1016/0377-0273(81)90051-2

Weston, F. S. (1964). List of Recorded Volcanic Eruptions in the Azores with Brief Reports. *Boletim do Museu e Laboratório Mineralógico e Geológico da Faculdade de Ciências de Lisboa* 10, 3–18.

Wilkinson, E., Lovell, E., Carby, B., Barclay, J., and Robertson, R. (2016). The Dilemmas of Risk-Sensitive Development on a Small Volcanic Island. *Resources* 5, 21. doi:10.3390/resources5020021

Willcock, M. A. W., Cas, R. A. F., Giordano, G., and Morelli, C. (2013). The Eruption, Pyroclastic Flow Behaviour, and Caldera In-Filling Processes of the Extremely Large Volume (>1290 km^3), Intra- to Extra-caldera, Permian Ora (Ignimbrite) Formation, Southern Alps, Italy. *J. Volcanology Geothermal Res.* 265, 102–126. doi:10.1016/j.jvolgeores.2013.08.012

Williams, R., Branney, M. J., and Barry, T. L. (2014). Temporal and Spatial Evolution of a Waxing Then Waning Catastrophic Density Current Revealed by Chemical Mapping. *Geology* 42, 107–110. doi:10.1130/G34830.1

Williams, R. (2010). *Emplacement of Radial Pyroclastic Density Currents over Irregular Topography: The Chemically Zoned, Low Aspect-Ratio Green Tuff Ignimbrite, Pantelleria, Italy. PhD Thesis*. Leicester: University of Leicester, 224.

Wilson, C. (1991). Ignimbrite Morphology and the Effects of Erosion: a New Zealand Case Study. *Bull. Volcanol.* 53, 635–644. doi:10.1007/BF00493690

Wilson, C. J. N., and Hildreth, W. (1997). The Bishop Tuff: New Insights from Eruptive Stratigraphy. *J. Geology* 105, 407–440. doi:10.1086/515937

Wilson, C. J. N., Houghton, B. F., Kampt, P. J. J., and McWilliamst, M. O. (1995). An Exceptionally Widespread Ignimbrite with Implications for Pyroclastic Flow Emplacement. *Nature* 378, 605–607. doi:10.1038/378605a0

Wilson, C. J. N. (1985). The Taupo Eruption, New Zealand II. The Taupo Ignimbrite. *Phil. Trans. Roy. Soc.* A314, 229–310. doi:10.1098/rsta.1985.0020

Wilson, C. J. N., and Walker, G. P. L. (1982). Ignimbrite Depositional Facies: the Anatomy of a Pyroclastic Flow. *J. Geol. Soc.* 139, 581–592. doi:10.1144/gsjgs.139.5.0581

Zanon, V., and Pimentel, A. (2015). Spatio-temporal Constraints on Magma Storage and Ascent Conditions in a Transtensional Tectonic Setting: The Case of the Terceira Island (Azores). *Am. Mineral.* 100, 795–805. doi:10.2138/am-2015-4936

Conflict of Interest: The authors declare that the research was conducted in the absence of any commercial or financial relationships that could be construed as a potential conflict of interest.

Copyright © 2021 Pimentel, Self, Pacheco, Jeffery and Gertisser. This is an open-access article distributed under the terms of the Creative Commons Attribution License (CC BY). The use, distribution or reproduction in other forums is permitted, provided the original author(s) and the copyright owner(s) are credited and that the original publication in this journal is cited, in accordance with accepted academic practice. No use, distribution or reproduction is permitted which does not comply with these terms.

frontiers in Earth Science

ORIGINAL RESEARCH
published: 29 September 2021
doi: 10.3389/feart.2021.738178

Unraveling the Holocene Eruptive History of Flores Island (Azores) Through the Analysis of Lacustrine Sedimentary Records

Mariana Andrade[1,2,3], Ricardo S. Ramalho[1,2,4,5,6], Adriano Pimentel[7,8], Armand Hernández[1], Steffen Kutterolf[9], Alberto Sáez[10], Mario Benavente[3], Pedro M. Raposeiro[11,12] and Santiago Giralt[3]*

[1]Instituto Dom Luiz (IDL), Faculdade De Ciências, Universidade De Lisboa, Campo Grande, Portugal, [2]Departamento De Geologia, Faculdade De Ciências, Universidade De Lisboa, Campo Grande, Portugal, [3]Geosciences Barcelona (Geo3BCN-CSIC), Barcelona, Spain, [4]School of Earth and Environmental Sciences, Cardiff University, Cardiff, United Kingdom, [5]School of Earth Sciences, University of Bristol, Bristol, United Kingdom, [6]Lamont-Doherty Earth Observatory of Columbia University, Palisades, NY, United States, [7]Centro de Informação e Vigilância Sismovulcânica Dos Açores (CIVISA), Ponta Delgada, Portugal, [8]Instituto de Investigação Em Vulcanologia e Avaliação de Riscos (IVAR), Universidade Dos Açores, Ponta Delgada, Portugal, [9]GEOMAR Helmholtz Centre for Ocean Research, Kiel, Germany, [10]Department of Earth and Ocean Dynamics, Universitat de Barcelona, Barcelona, Spain, [11]CIBIO, Centro de Investigação Em Biodiversidade e Recursos Genéticos, InBio Laboratório Associado, Azores, Portugal, [12]Departamento de Biologia, Faculdade de Ciências e Tecnologias, Universidade Dos Açores, Ponta Delgada, Portugal

OPEN ACCESS

Edited by:
Antonio Paonita, Istituto Nazionale di Geofisica e Vulcanologia (INGV), Italy

Reviewed by:
Dmitri Rouwet, Istituto Nazionale di Geofisica e Vulcanologia, Italy
Dario Pedrazzi, Instituto de Ciencias de la Tierra Jaume Almera (ICTJA), Spain

***Correspondence:**
Mariana Andrade
mdandrade@fc.ul.pt

Specialty section:
This article was submitted to Volcanology, a section of the journal Frontiers in Earth Science

Received: *08 July 2021*
Accepted: *15 September 2021*
Published: *29 September 2021*

Citation:
Andrade M, Ramalho RS, Pimentel A, Hernández A, Kutterolf S, Sáez A, Benavente M, Raposeiro PM and Giralt S (2021) Unraveling the Holocene Eruptive History of Flores Island (Azores) Through the Analysis of Lacustrine Sedimentary Records. Front. Earth Sci. 9:738178. doi: 10.3389/feart.2021.738178

Lacustrine sequences from active volcanic settings usually hold a rich and continuous record of tephra layers, providing a critical source of information to reconstruct a most complete eruptive history of a region. Lake sedimentary records on volcanic islands are particularly useful as the typical small size of these islands and their steep subaerial and submarine slopes lead to a lower preservation of potential erodible pyroclastic deposits. Here we explore the lacustrine sedimentary record of Lagoa da Lomba, a crater lake in the central upland area of Flores Island (Azores), to gain insight into the recent eruptive history of this island. The strategic location of Lagoa da Lomba, half distance between the two clusters of recent volcanic activity of the island, together with its long-lasting record, back to 23.52 cal kyr BP, makes this lake a privileged site to investigate the Holocene volcanic history of Flores. Based on a detailed stratigraphic characterization of sediments from a lake transect of three cores, supported by glass shard geochemistry and radiocarbon dating, we recognized four Holocene eruptive events taking place between 6.28 and 2.36 cal kyr BP, demonstrating that the Holocene volcanic activity at Flores Island may have lasted longer than previously reported. Glass shard geochemistry from the different tephra layers suggests three populations, basaltic to trachybasaltic in composition, where the last eruption is the least evolved endmember. Two of the four eruptive events correlate with subaerially-exposed pyroclastic sequences, in terms of stratigraphy and geochemistry. The most recent event recorded at Lagoa da Lomba was constrained to 3.66 – 2.36 cal kyr BP and linked to an eruption sourced from Lagoa Comprida Volcanic System. The second most recent eruptive event was sourced from Lagoa Funda Volcanic System and dated at 3.66 cal kyr BP. Our observations show that Flores experienced vigorous volcanic activity during the Late Holocene. Therefore, contrary to what is

assumed, the possibility of future eruptions should be properly considered, and the volcanic hazard here should not be underestimated. Moreover, we highlight the importance of tephrostratigraphy in recent lake sediments to reconstruct past volcanic activity, especially at small volcanic islands, such as Flores, where exposure is poor due to erosion within the limited subaerial area and the dense vegetation.

Keywords: ocean island volcanoes, lake tephrostratigraphy, glass geochemistry, holocene volcanism, lagoa da lomba, Flores Island, azores archipelago

INTRODUCTION

Lakes are natural traps in drainage basins, and their sedimentary records are potentially continuous on time scales of several millennia. Depending on the age of the lake basin and the sediments, as well as on sedimentation rates, lakes may host crucial information to reconstruct climatic, ecological, and tectonic histories of volcanic regions (e.g., Björck et al., 2006; Sáez et al., 2007; Giralt et al., 2008; Stockhecke et al., 2014; Hernández et al., 2017; Vázquez-Loureiro et al., 2019). In these regions, lacustrine sequences are usually rich in tephra layers, which constitute one of the best means to investigate the frequency, size, and style of eruptions affecting that region, often with a detail that cannot be achieved using terrestrial deposits alone (e.g., Wulf et al., 2004; Stern 2008; Van Daele et al., 2014; Kutterolf et al., 2016; McNamara et al., 2018).

Lake records on volcanic islands may be particularly important, providing information that otherwise would not be accessible, due to the typical small size and irregular topography of these islands, which make the preservation of erodible pyroclastic deposits difficult on land, particularly in areas with high rainfall such as the Azores Archipelago. Moreover, in densely vegetated areas, access to outcrops is frequently limited (Kueppers et al., 2019). There is also a much smaller potential of preservation of pyroclastic deposits in the energetic shallow coastal waters or along the steep, unstable submarine flanks of the islands (Mitchell, 2003), and since deep-sea drilling is technically very challenging and expensive, we rarely have access to offshore records. As such, lake sedimentary records are key to improve our scientific knowledge of the recent eruptive history of many volcanic archipelagos, particularly those where crater and caldera lakes are very abundant and perennial, as it happens in the Azores Archipelago (**Figure 1A**). The potential of Azorean lacustrine sequences to reconstruct the volcanic activity of the islands is, to date, still unexplored. This study employs lacustrine sediment records from one of the Azores islands – Flores (**Figure 1B**) – to investigate its recent eruptive history and volcanic hazard potential.

Despite being a young oceanic volcanic island, Flores did not experience any eruption since the Portuguese settlement in the 15th century and therefore its volcanic hazard is usually considered as low (Chester et al., 2017). Moreover, hydrogeochemical and diffuse CO_2 degassing studies of Flores lakes show that, presently, there is no volcanic/hydrothermal signature (Cruz et al., 2006; Andrade et al., 2019), suggesting that volcanism is either dormant or extinct. However, the geological record of the island shows that a brief, but intense period of monogenetic volcanism occurred 2.9–3 kyr ago (Morisseau and Traineau, 1985; Azevedo and Portugal Ferreira, 2006). This volcanism is thought to be responsible for the formation of numerous scoria cones, and several maars and tuff rings. The latter are grouped in two clusters (**Figure 1B**): Lagoa Funda Volcanic System and Lagoa Comprida Volcanic System, hereafter abbreviated as FVS and CVS, respectively. Given this context, it is crucial to improve our knowledge about the recent volcanism of Flores to better evaluate the possibility of future eruptions and associated hazards. In 2017, a coring survey visited several lakes in Flores and Corvo islands to investigate the spatial and temporal climatic evolution of the western Azores Atlantic region. Using the existence of these cores, we conduct a detailed tephrostratigraphic, geochemical, and chronological characterization of the lacustrine sediment record of Lagoa da Lomba (Lomba Lake), an old crater lake in the upland central area of Flores Island. Lagoa da Lomba is located half distance between the two clusters of recent activity of the island (**Figure 1B**) and, as our study shows, its sedimentary record extends beyond the Holocene. Lagoa da Lomba thus presents the potential to host primary Holocene tephra deposits, being an ideal site to investigate the last volcanic eruptions on Flores.

GEOLOGICAL SETTING

Flores Island, located in the North Atlantic Ocean, is part of the Azores Archipelago, which is a volcanic archipelago that straddles the triple junction of the North American, Eurasian and Nubian lithospheric plates (**Figure 1A**). The archipelago results from volcanic processes associated with the interaction of the lithospheric plates and eventually to the upwelling of unusually hot or volatile-enriched mantle (Métrich et al., 2014; Genske et al., 2016). Flores lies approximately 100 km west of the axis of the Mid-Atlantic Ridge, in the more stable North American plate. Together with the neighboring Corvo Island, it forms the western group of the Azores Archipelago. The islands of Flores and Corvo are the emergent portions of a NNE-SSW-trending volcanic ridge that is subparallel to the Mid-Atlantic Ridge (MAR) (**Figure 1A**).

Flores is a small island (142 km^2) built by overlapping volcanic complexes that reach a maximum altitude of 911 m at Morro Alto (**Figure 1B**). Current constrains from K/Ar dating indicate that the island edifice formed during the late Pliocene, 2.15 Ma ago (Azevedo et al., 1991), on a 9 Ma old oceanic crust (Freire Luis et al., 1994). Flores Island is the result of a complex geological history with vertical movements and recurrent episodes of mass

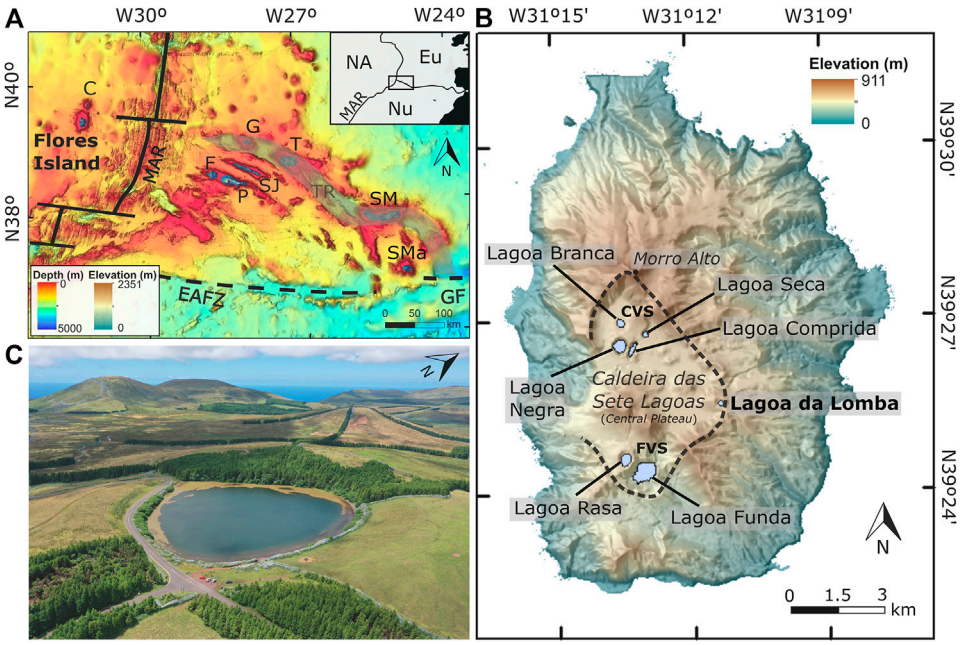


FIGURE 1 | (A) Bathymetric map of the North Atlantic at the Azores triple junction, showing the geotectonic setting of Flores Island, located west of the Mid-Atlantic Ridge (MAR), as well as the main tectonic structures of the region: East Azores Fracture Zone (EAFZ), Gloria Fault (GF), and Terceira Rift (TR). The location of the other islands of the archipelago is also indicated: Corvo (C), Pico (P), Faial (F), São Jorge (SJ), Terceira (T), Graciosa (G), São Miguel (SM) and Santa Maria (SMa). Bathymetry from EMODnet Bathymetry Consortium (2018); subaerial topography was generated from a 1:5000 scale digital altimetric database from Secretaria Regional do Turismo e Transportes of the Azores Government. Upper right inset depicts the regional setting of the Azores Archipelago within the triple junction of the North American (NA), Eurasian (Eu) and Nubian (Nu) lithospheric plates **(B)** Digital elevation model of Flores Island showing the location of the seven lakes in the upland central area of the island (Caldeira das Sete Lagoas, outlined by the dashed line). Lagoa da Lomba is highlighted in the DEM **(C)** Aerial image of Lagoa da Lomba obtained during a fieldwork campaign in August 2020.

wasting (Azevedo et al., 1991; Hildenbrand et al., 2018). The island's topography is characterized by a central upland area, the *Central Plateau* (500 m above sea level), surrounded by steep slopes and notched valleys. Two main stratigraphic groups characterize the island (Azevedo et al., 1991): the Base Complex, which corresponds to rocks formed during the proto-island stage; and the Upper Complex, which comprises the record of subaerial volcanism. The subaerial volcanic history of the island was dominated by three stages of volcanic activity separated by long periods of quiescence (Azevedo and Portugal Ferreira, 2006):

1) The first stage (700 – 500 ka) includes the most voluminous volcanism, which was characterized by effusive and explosive events;
2) The intermediate stage (400 – 200 ka) involved a larger number of small-scale feeder centers, with predominant effusive eruptions;
3) The final stage (3 – 2.9 ka) was short-lived and marked by Strombolian and subsequent phreatomagmatic activity.

The products of the Holocene volcanic activity crop out mainly in the middle of the *Central Plateau*, in an area locally known as *Caldeira das Sete Lagoas* (**Figure 1B**). According to Azevedo and Portugal Ferreira (2006), the Holocene Strombolian activity was centered at about 30 scoria cones, with gentle flanks and smooth craters, that produced widespread scoria lapilli and ash fall deposits. The most recent volcanic activity on the island is thought to have formed maars and tuff rings that are currently occupied by lakes. These volcanic vents are grouped into two clusters, one in the north part of Caldeira das Sete Lagoas and one in the south sector. The four main northern vents (Lagoa Comprida, Lagoa Negra, Lagoa Seca, and Lagoa Branca) are inferred to be associated with N25°E and N-S fractures, while the southern vents (Lagoa Funda and Lagoa Rasa) are possibly related to N40°W and N20°-25°E fractures. The maars (Lagoa Comprida, Lagoa Negra, Lagoa Seca, and Lagoa Funda) show great depths, steep slopes and diameters ranging from 280 m to ~1 km, while the tuff rings (Lagoa Branca and Lagoa Rasa) have low crater rims, smooth slopes, and diameters in the order of 300–400 m (**Figure 1B**). The associated phreatomagmatic deposits are lithic-rich, showing lateral continuity for several hundreds of meters. From the seven crater lakes found in Caldeira das Sete Lagoas, only Lagoa da Lomba (N39°25′31″ W31°11′19″; **Figure 1C**) was formed in an early stage, prior to the Holocene, and therefore it has the potential to hold the longest lacustrine record on the island. This older topographic depression, located in the upland area of Flores Island (650 m high), has a surface area of 37,885 m^2, a perimeter of 716 m and a volume of 143,000 m^3. The average lake depth is relatively shallow (7.4 m), but Lagoa da Lomba has steep slopes (~30° in some areas), reaching a maximum interior crater depth of 16 m (**Figure 2**; Direção Regional do Ambiente, 2001).

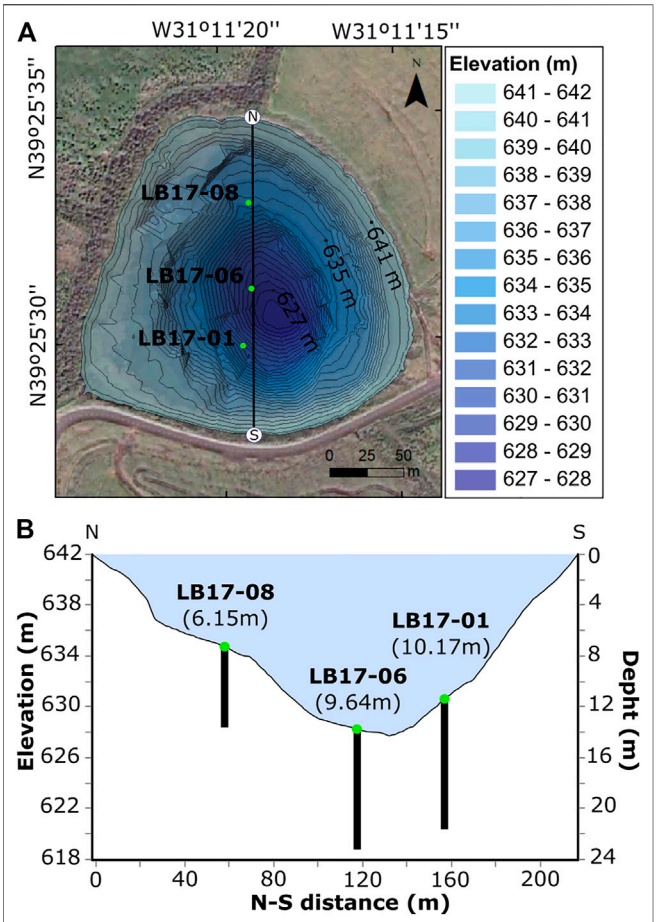


FIGURE 2 | (A) Orthophotomap with the bathymetry of Lagoa da Lomba showing as green dots the location of cores LB17-01 (N39°25′29.92″ W31°11′19.55″), LB17-06 (N39°25′31.18″ W31°11′19.28″), and LB17-08 (N39°25′33.06″ W31°11′19.32″). Bathymetry from Direção Regional do Ambiente (2001). Light blue colors represent the shallowest areas and dark blue the deepest parts. Contour lines are spaced at every 50 cm **(B)** N-S profile of Lagoa da Lomba indicating the site where each core was collected, as well as the lengths (in brackets) of each recovered sequence. The left axis is the elevation relative to sea level, and the right axis the depth of Lagoa da Lomba. The horizontal axis represents the distance between north and south margins [N and S points of the panel **(A)**]. All values are in meters.

METHODS

Coring Survey and Petrographic Analysis

Lagoa da Lomba sediments were drilled in 2017 using a UWITEC® piston corer installed on a platform raft. We performed a transect of three cores, from south to north, LB17-01 (N39°25′29.92″ W31°11′19.55″), LB17-06 (N39°25′31.18″ W31°11′19.28″), and LB17-08 (N39°25′33.06″ W31°11′19.32″) that were collected at lake depths of 10.1, 13.5, and 7.1 m, and whose total lengths are 10.17, 9.64, and 6.15 m, respectively (**Figure 2**).

Following the methodology employed by Hernández et al. (2017) and Vázquez-Loureiro et al. (2019), a detailed characterization of lacustrine volcanic and non-volcanic facies was conducted through visual core description, supported by smear slides observation under a petrographic microscope at GEO3BCN-CSIC, Barcelona, Spain. Variations in grain size, texture and components were carefully documented next to observed sedimentation features (lamination, boundary conditions, structures). Juvenile clasts (scoria lapilli) from tephra layers were sampled for subsequent geochemical microanalyses.

Field Observations

Two field campaigns taking place in the summer of 2019 and 2020 were conducted to test possible correlations between tephra layers found in cores of Lagoa da Lomba and subaerially-exposed volcanic sequences around the lake, as well as to identify potential sources for the inferred volcanic events. Given that the most recent eruptions at Flores are thought to have been centered at FVS and CVS (Morisseau and Traineau, 1985; Azevedo and Portugal Ferreira, 2006), we investigated the volcanic stratigraphy in the proximal areas of these vents for comparison with the lacustrine record. Accordingly, a detailed field survey was conducted in the *Central Plateau* area, and a small number of key exposures was selected for logging and sampling. Exposed sequences from field sites (named as FLxxMA) were described in detail regarding their stratigraphical, depositional, and textural characteristics (grain size, components, and thickness). Samples of juvenile scoria lapilli were selectively collected at different horizons for geochemical microanalyses.

Electron Microprobe Analysis

Juvenile scoria lapilli samples were crushed, and together with the lake sediment washed and sieved into 63–125 μm (4-3Φ) fraction. The resulting fragments and glass shards were embedded with epoxy resin into acrylic tablets and then polished. Glass shards (318 in total) were analyzed for major and minor elements on 18 epoxy embedded samples using a JEOL JXA 8200 wavelength dispersive EMP at GEOMAR Helmholtz Centre for Ocean Research, Kiel (Germany), utilizing the methods of Kutterolf et al. (2011). A calibrated measuring program was used based on international standards with a 10 μm electron beam to minimize sodium loss. Oxide concentrations were determined using the ZAF correction method. Accuracy was monitored by Lipari obsidian (Hunt and Hill, 2001) and Smithsonian basaltic standard VGA99 (Jarosewich et al., 1980) having two measurements on each standard after every sixty single glass shard measurements (~15 per sample). Standard deviations are <0.5% for major and <10% for minor elements (except for MnO_2 in samples >55 wt% SiO_2). All analyses with totals >97 wt% were normalized to 100% to eliminate the effects of variable post-depositional hydration and minor deviations in focusing of the electron beam. The acceptable analyses of each sample were then averaged in order to characterize the elemental compositions of each tephra. Layers with heterogenous compositions but internal differentiation trends were included with their intra-sample deviation in the data base whereas widely heterogenous compositions outside any possible differentiation trend were

excluded. All the resulting major element data and their respective errors are listed in **Supplementary Tables S1 and S2**.

Lake Chronology

A detailed chronological study was conducted for LB17-01 master core (the longest and most complete sequence recovered at Lagoa da Lomba), which was complemented with a few chronological analyses of LB17-06 and LB17-08 cores. Sediment samples were collected at different levels, particularly at the base of tephra layers to constrain the ages of the volcanic events. Accelerated mass spectrometer (AMS) radiocarbon ages were obtained from pollen enrichment extracts prepared by acid digestion (Rull et al., 2010). Pollen concentrates were prepared at the Laboratory of Sedimentology of the University of Barcelona (Spain) and sent to the Radiochronology Laboratory of the Centre d'Études Nordiques, University of Laval (Canada) for AMS ^{14}C dating. The radiocarbon ages were calibrated with the CALIB 8.2 software, using the IntCal20 calibration curve (Stuiver et al., 2021).

The age-depth model for LB17-01 core was calculated with the R rbacon library v2.5.1 (Blaauw et al., 2021), using the AMS ^{14}C dates as anchor points. This R script calibrated radiocarbon ages using the newest IntCal20 calibration curve (Stuiver et al., 2021). Layers of tephra and terrigenous gravel, as well as eventual reworked horizons, were considered as deposited instantaneously/flash events to avoid errors in the estimation of accumulation rates. The deposition of large amounts of tephra in both the lake and the catchment area can strongly modify the available amount of sediment that might be deposited in the lake. Therefore, we used a low value for the memory of the system. The reddish muddy sediments present between 640 and 623 cm of core depth together with the significant sediment age difference just before (14.12 cal kyr BP) and just afterwards (10.7 cal kyr BP) have been interpreted as temporal lake dry-up and incipient soil formation. Therefore, the top of these reddish sediments was considered as indicative of the existence of a hiatus. Due to model dating uncertainties, ages were rounded to whole numbers, i.e., to tens of years.

RESULTS

Core Analysis and Facies Description

Three sedimentary facies were defined for the sequences of Lagoa da Lomba based on textural, lithological, and biological features (**Figure 3A**):

1) Organic-rich fine grained lacustrine facies (F1): This facies is composed of a dark-brown organic-rich mud, with high contents of organic matter (ca. 65%) and abundant bioclasts (ca. 30%, e.g., diatoms, sponge spicules and chironomids remains) with a small (ca. 5%) amount of dispersed lithoclasts and minerals, ranging in grain size from silts to very fine sands (~20–100 μm).
2) Terrigenous/volcaniclastic fine to coarse grained facies (F2): This facies is mainly made up of clayey-silts to fine sandy-silts and well-sorted, sub-rounded gravel layers, with variable amounts of organic matter and varying degrees of oxidation. The lithoclastic and mineral fraction (ca. 60–80%) consists of volcanic lithics (lava fragments and weathered scoria clasts), as well as loose plagioclase, olivine, and pyroxene crystals. The organic component (ca. 20–40%) is essentially made up of amorphous organic matter with almost no bioclasts and particulate organic matter (both not exceeding 1%). Gravel levels are in most cases supported by a dark-brown muddy matrix, in some cases with dispersed plant macro-remains. Occasionally, the distinction between gravel and tephra layers was only possible using backscatter electron images (BSE), which helped to identify (or not) the presence of glass shards (e.g., LB17-06 gravel layers, **Figures 3B–D**).
3) Volcanic facies (F3): This facies corresponds to layers of tephra, which were labeled according to the core number and the sequential number of occurrence in the core (e.g. LBx-Tx), from base to top (**Figure 3A**). Thicknesses of tephra layers vary from 7.9 to 58.5 cm, and all consist of clast-supported scoria, fine to medium lapilli, with variable amounts of olivine (Ol) and plagioclase (Pl) crystals. Tephra layers are relatively homogeneous in terms of grain size, excepting LB1-T3 and LB8-T1 layers, which exhibit a very similar textural pattern, with grain size showing slightly normal to reverse symmetric grading from medium-to-fine lapilli and again back to medium lapilli, i.e., both tephra layers display a tenuous distinctive horizon (~5 cm thick) of fine lapilli in the middle or in the upper third of the layer. Although some tephra layers are almost exclusively composed of juvenile clasts with pristine morphologies (i.e., very angular, lunate, bubble-wall and highly vesicular shapes, **Figure 3B**), others contain blocky, dense, poor vesiculated juveniles and occasional to frequent lithic clasts, sometimes reaching up to 50 vol% (e.g., **Figure 3C**). It is worth noting that of the ten individual tephra layers recognized, only two layers (LB1-T1 and LB1-T2) are exclusively composed of juvenile material (scoria lapilli), with all other layers exhibiting variable amounts of lithics. Except for tephra layers from LB17-08 core, which show a significant degree of oxidation, tephras from the other cores are well preserved. A detailed description of the textural features and components of the tephra layers identified on each core is summarized in **Table 1**.

Sedimentological and stratigraphical analyses of the three studied cores reveal that lake sediment deposition was in general continuous, except for the hiatus considered at 623 cm of LB17-01 sequence, and some intervals that exhibit reworking features (**Figure 4**):

1) Between LB1-T3 and LB1-T4, where we found reworked deposits (small mass movement deposits) composed of volcaniclastic clayey silts intercalated with thin beds of dispersed volcaniclastic sand and a few lenses of a light brown volcaniclastic clay. Bioclasts and organic matter are absent in this interval.

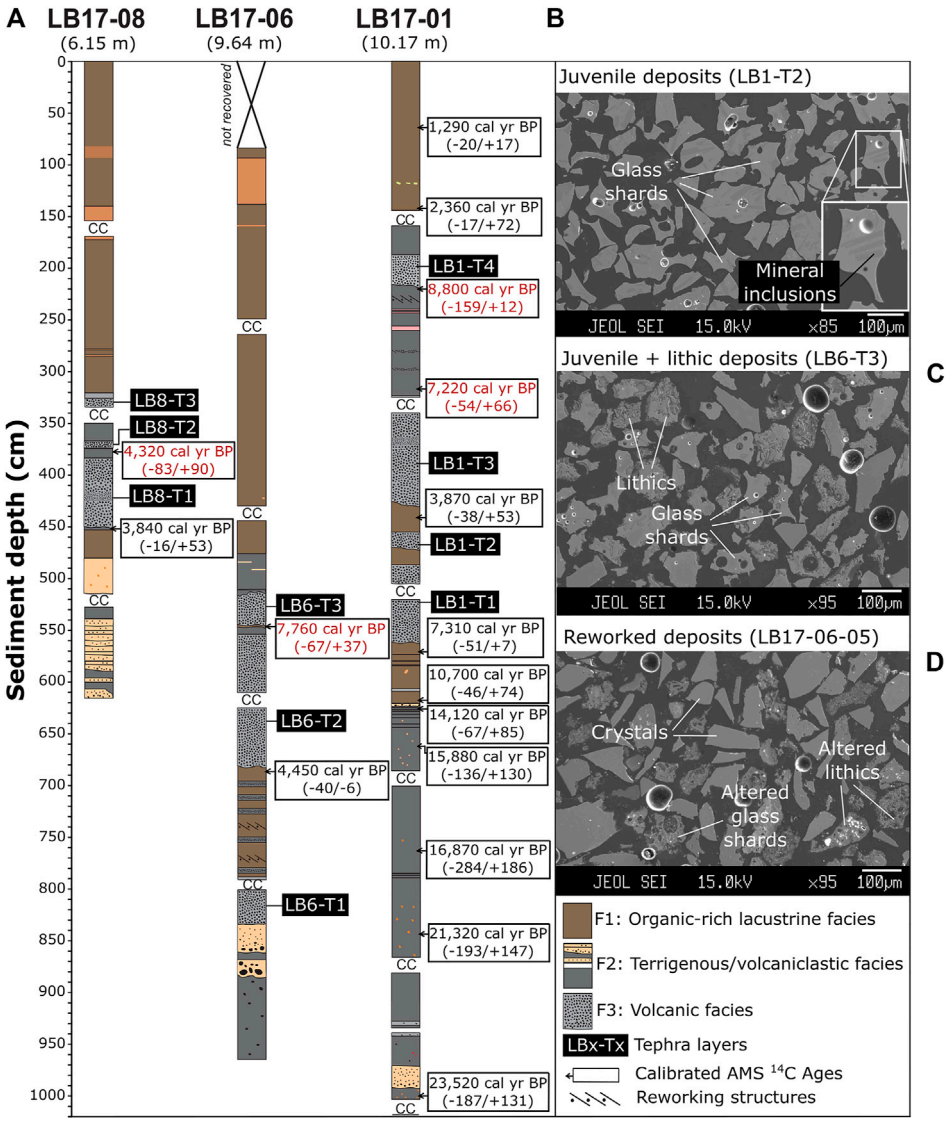


FIGURE 3 | (A) Sediment logs of the core sequences collected at Lagoa da Lomba. Three facies are differentiated using texture, components, and volcanic origin. CC represents the potential length of the sediments retained by the core catcher. White boxes show the position of the obtained radiocarbon ages. Reversal AMS ^{14}C ages are highlighted in red. Dark squares identify each tephra layer. BSE images showing **(B)** purely juvenile clasts with typical angular, lunate, bubble-walled and highly vesicular shapes (e.g., LB1-T2) **(C)** juvenile and lithic clasts (e.g., LB6-T3), and **(D)** altered lithic clasts and crystals (e.g., gravel, LB17-06).

2) Between LB6-T1 and LB6-T2 some reworking structures are present, accompanied by thin mass movement deposits of volcaniclastic sand intercalated with biogenic clays. Between LB6-T2 and LB6-T3 there is a thin lens (5 cm) of volcaniclastic clayey-silts. This lens seems to be a sediment blob incorporated in the tephra deposit. The uppermost 2 cm of the lens consist of a biogenic clay, composed almost exclusively of diatoms and plant remains. Volcaniclastic material at the top of LB6-T3 seems to be resedimented material from the tephra layer itself, including transported sediments from the lake slopes.
3) The LB8-T1 and LB8-T2 tephra layers are separated by a thin sediment lens (7 cm-thick) of volcaniclastic material. It exhibits rounded edges suggesting this could be a sediment blob interbedded in the tephras.

Chronology

Radiocarbon geochronology shows that the sedimentary record of Lagoa da Lomba extends back to the late Pleistocene, as attested by the 23,520 (−187/+131) cal yr BP age obtained at the base of core LB17-01 (**Figure 3A**). The twelve AMS ^{14}C dates from LB17-01 core (**Table 2**) are for the most part stratigraphically coherent, with only two reversals dated as 8,800 (−159/+12) and 7,220 (−54/+66) cal yr BP (**Figure 3**). It is assumed that such ages were imprinted by local reworking processes, which is supported by the presence of small mass

TABLE 1 | Description of tephra layers from lacustrine sequences recovered at Lagoa da Lomba. M = major (>80%), D = dominant (50–80%), A = abundant (20–50%), C = common (5–20%), P = present (1–5%) and R = rare (0.1–1%). Pl = plagioclase, Ol = olivine.

Layer	Thickness (cm)	Grain size (Juv max. grain size)	Mineralogy	Description
LB6-T3	17	medium to fine lapilli	Pl (P)	Juvenile (D) + lithics (A). Scoriaceous textures are not very evident, particles are blocky, dense, poor vesiculated and sometimes sub-rounded. The top of the lapilli layer is covered by 3 cm of volcanic ash
LB6-T2	58.5	medium to coarse lapilli (2.3 cm)	Pl (P)	Juvenile particles (M) with well-preserved scoriaceous textures. Grain size increases to the top
LB6-T1	34.7	medium lapilli (1.77 cm)	Pl (P)	Juveniles (M) + lithics (P) with well-preserved scoriaceous textures. The layer contains oxidized particles, suggesting alteration and/or reworking processes
LB8-T3	5.2	fine lapilli	Pl, Ol (P)	Juveniles (D) + lithics (A). Some particles are blocky, dense, poor vesiculated and sub-rounded. The layer is covered by 3.5 cm of volcaniclastic ash
LB8-T2	7.9	fine lapilli to coarse ash	—	Juvenile (D) + lithics (C). Grain size gets finer towards the top. The layer contains oxidized particles, suggesting alteration and/or reworking processes
LB8-T1	47	medium to fine lapilli	Pl (P)	Juvenile (D) + lithics (C). Very well-preserved scoriaceous textures. Internal grain size transition (medium-fine-medium lapilli). The top and the bottom of the tephra layer are slightly altered showing brownish to orange colors
LB1-T4	20	fine to medium (1.6 cm)	Ol (P)	Juveniles (D) + lithics (A). Well-sorted, particles are blocky, dense, poor vesiculated and sub-angular to sub-rounded
LB1-T3	47.5	fine to medium lapilli (1.5 cm)	Pl (P)	Juveniles (D) + syenitic xenoliths (R) + pumice clasts (R) + lithics (C). Very well-preserved scoriaceous textures. Grain size transition (medium-fine-medium lapilli). Below the grain size transition the layer is exclusively made up of juveniles. Well-sorted at the base to moderately sorted at the top
LB1-T2	8	medium to fine lapilli (1 cm)	Pl (P)	Juveniles (M) with well-preserved scoriaceous textures. Well-sorted, particles are angular to sub-angular
LB1-T1	38.6	medium lapilli (1.63 cm)	Pl, Ol (P)	Juveniles (M) with very well preserved scoriaceous textures. Wel- sorted, particles are angular to subangular

movement deposits described in *Core analysis and facies description*. Moreover, since these two dates correspond to sediments trapped between tephra layers, punctual contributions of volcanic CO_2 might have apparently aged the radiocarbon dated material. The same could be for overturned ages at LB17-06 and LB17-08 cores, where reversed radiocarbon ages also seem to be imprinted by reworking processes and related to older sediment ages in sediment blobs between tephra layers (**Figure 3A**). Since there are no signs of reworking at the base of LB8-T1 tephra layer, the reliability of the 3,840 (−16/+53) cal yr BP age is considerably high. Moreover, this age is compatible with the age obtained at a similar layer of LB17-01 (LB1-T3), that is dated to 3,870 (−38/+53) cal yr BP, suggesting a presumable correlation between these two tephra layers.

Except for the two reversals at 8.8 and 7.22 cal kyr BP, all the other AMS ^{14}C ages obtained for LB17-01 were used to construct the Lagoa da Lomba age-depth model (**Table 2**). The age model curve is staircase-shaped between 0 and 6,280 (−578/+626) cal yr BP due to several tephra layers and reworked sediments, showing that sedimentation rates were much higher during periods of volcanic activity. In fact, ~40% of the sedimentary sequence was deposited over the 3 kyr during which volcanic eruptions occurred at Flores, while the remaining 60% was deposited over 20 kyr (**Figure 5**). Based on the age-depth model, we estimate a precise age for the three oldest tephra layers, LB1-T1, LB1-T2 and LB1-T3, which have been deposited at 6,280 (−578/+626), 4,990 (−773/+685) and 3,660 (−210/+194) cal yr BP, respectively (**Figure 5**). Due to the reworked character of the sediments below LB1-T4, we cannot assign a precise age to this tephra layer. However, since LB1-T4 is conformably overlain by lacustrine sediments dated at 2,360 (−17/+72) cal yr BP (see **Figure 3**), we can constrain its age to the 3,660 (−220/+174) – 2,360 (−17/+72) cal yr BP interval (**Figure 5**).

Geochemistry of Lacustrine Tephra Layers

Glass shards of scoriae from the tephra layers defined at *Core analysis and facies description* are characterized by abundant mineral micro-inclusions (**Figure 3B**). Glass compositions are quite homogeneous, with 45–50 wt% of SiO_2 and 4–8 wt% of Na_2O + K_2O, mainly lying on the boundary between the trachybasalt and the tephrite/basanite fields. A group of three slightly more primitive compositions, namely samples from LB1-T4, LB6-T3, and LB8-T3 layers, which correspond to the uppermost tephra layer at each core, lay close to the triple junction of the basalt – trachybasalt – tephrite/basanite fields (**Figure 6**).

Variation diagrams for the major elements vs CaO show three main geochemical populations, demonstrating that some tephra layers are geochemically distinct from others (**Figure 7**). These populations follow a general geochemical trend, with more primitive compositions towards the top of the sedimentary sequences, demonstrated by the increase in MgO and decrease in SiO_2 contents. LB1-T3 and LB8-T1 are the only layers showing an internal geochemical variation, which coincides with a granulometric transition mentioned in the volcanic facies description (*Core analysis and facies description*).

Geochemical Group 1 includes LB1-T1, LB1-T2, LB1-T3a, and LB8-T1a tephra layers, and consistently has the lower CaO contents, varying between 9 and 9.8 wt%. Geochemical Group 2 has intermediate CaO contents, from 9.8 to 11 wt%, and includes LB1-T3b, LB8-T1b, LB8-T2, LB6-T1, and LB6-T2

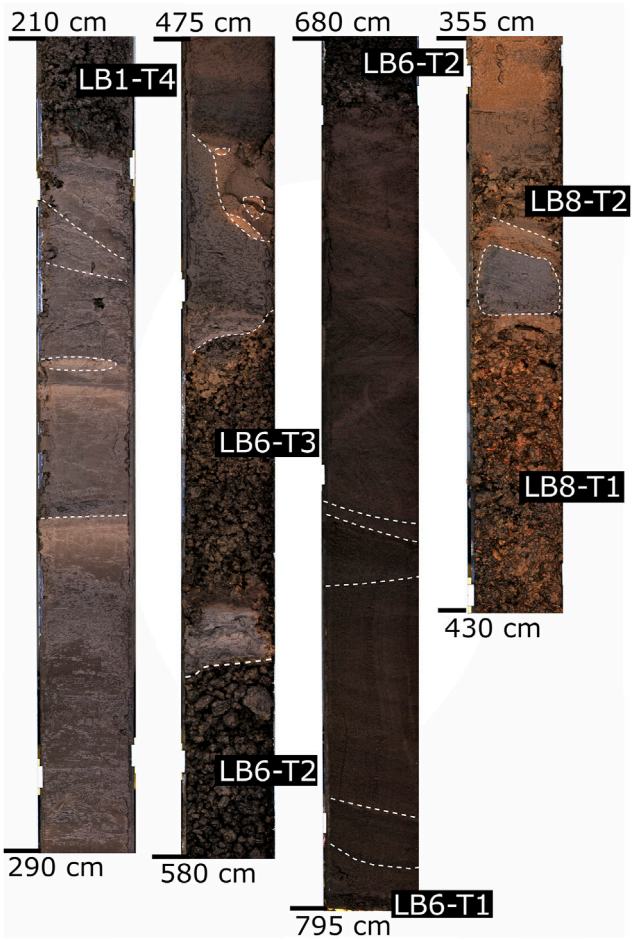


FIGURE 4 | Photographs of selected core sections showing reworking structures (erosional surfaces, variation of the horizontality of the layers, small mass movement deposits and sediment pods). Sediment depth is specified at the top and at the bottom of each section. Dark rectangles indicate the nomenclature of each tephra layer.

layers. Finally, geochemical Group 3 has the higher CaO contents, from 11 to 12.5 wt%, and comprises the uppermost tephra layer of each core, which includes LB1-T4, LB6-T3 and LB8-T3 layers (**Figure 7**).

Characterization of Subaerially-Exposed Pyroclastic Sequences

Four field sites deemed the most representative of the recent volcanic stratigraphy of the study area were established (see **Figure 8A**) and studied in detail.

FL20MA field site (N39°23′53.74″ W31°12′57.17″) corresponds to a quarry located on the southern flank of FVS, just below the rim of the southernmost crater, where a very proximal volcanic sequence crops out (**Figure 8A**). This quarry constitutes one of the best tephrostratigraphic exposures on the island and is a crucial site to reconstruct the stratigraphy of this volcanic system. In this exposure (**Figure 8B**), the basal unit consists of welded spatter accumulation that is >1.70 m thick. Large bombs with well-preserved fluidal shapes are observed in this unit, most of them containing large crystals of plagioclase. The spatter is overlapped by a unit of remobilized material, with variable thickness up to 80 cm (**Figure 8B**). The remobilized material is followed by a thick (>2.5 m) unit of scoriaceous coarse lapilli, also with well-preserved fluidal shapes and common olivine and plagioclase crystals. Overlapping these scoriae, there is a very thick (~15 m), well-bedded sequence, heterogeneous in composition, made up of very fine ash layers, in places with accretionary lapilli, intercalated with ash layers rich in lithic clasts, up to coarse lapilli and blocks (**Figure 8B**). Juveniles are rare along these sequences and when present are usually dense, sub-rounded and blocky. Bomb sag structures are frequent and deform the underlying layers, wavy and cross-stratification is often present within and between fine-grained subunits. These features yield for a phreatomagmatic nature of the sequence. Glass compositions of the scoriaceous lapilli overlap with geochemical Group 1 of Lagoa da Lomba sedimentary record (**Figure 9**).

The FL17MA field site (N39°26′14.89″ W31°13′10.99″) corresponds to an abandoned quarry located on the southeast flank of Comprida scoria cone (**Figures 8A,C**). The outcropping sequence (~4 m-thick) consists of welded spatter accumulation showing a normal grading pattern, ranging from block-sized clasts at the base to lapilli-sized scoria and coarse scoriaceous ash towards the top. Although it is essentially made up of juvenile material, it contains occasional lithic blocks (up to 20 cm across), as well as syenitic xenoliths within the spatter. The upward decrease in the grain size of juvenile clasts is accompanied by a gradual increase of the lithic clast content. The Comprida sequence ends with a 1.70 m-thick, well-bedded, succession of fine ash layers intercalated with ash layers rich in lithic clasts, up to coarse lapilli and blocks (phreatomagmatic nature; **Figure 8D**). The sequence contains parallel to subparallel stratification, sometimes with wavy and cross-stratification (**Figure 8D**) and the ash layers frequently contain accretionary lapilli. Variable amounts of olivine and plagioclase crystals are present along the sequence. Glass compositions of scoria lapilli overlap with geochemical Group 3 of Lagoa da Lomba sedimentary record (**Figure 9**).

Outcrop FL154MA (N39°25′34.86″ W31°11′8.12″), located on the NE flank of Lagoa da Lomba (**Figure 8A**), consists of a subaerial stratigraphic sequence identical to that observed in core LB17-01. It contains two tephra deposits (Tephra 1, with 25 cm of thickness; and Tephra 2, with 93 cm of maximum thickness) separated by a thin (10 cm thick), weathered, very fine ash bed; **Figure 8E**). Tephra 1 exhibits a sharp grain size variation of scoria clasts from medium-to-fine lapilli, and back to medium lapilli towards the top. This grain size transition is accompanied by a thin oxidation crust where the fine lapilli are present. The glass compositions of the medium lapilli-sized scoriae below the oxidation crust (FL154MAa) overlap with Lagoa da Lomba geochemical Group 1, and the compositions of the scoria lapilli above the oxidation crust (FL154MAb) overlap with geochemical Group 2 of Lagoa da Lomba (**Figure 9**). Unfortunately, the intense weathering of tephra

TABLE 2 | Radiocarbon dates and calibrated ages for Lagoa da Lomba sediment cores. Shaded entries represent the ages not included in the construction of the depth-age model.

Core	Sample depth (cm)	Lab ID	$F^{14}C$	±	$D^{14}C$ (‰)	±	^{14}C age (BP)	±	Median probability (cal yr BP)	2σ (cal yr BP)
LB17-01	63.5	ULA-7642	0.846	0.002	−154.3	1.8	1,345	20	1,290	−20/+17
LB17-01	142.5	ULA-7643	0.745	0.001	−254.6	1.4	2,360	20	2,360	−17/+72
LB17-01	225	ULA-8361	0.372	0.001	−628.0	1.0	7,945	25	8,800	−159/+16
LB17-01	320	ULA-8366	0.456	0.001	−544.4	1.5	6,315	30	7,220	−54/+66
LB17-01	436	ULA-8353	0.641	0.001	−358.8	1.1	3,570	15	3,870	−38/+53
LB17-01	573.5	ULA-7644	0.451	0.001	−548.8	0.9	6,395	20	7,310	−51/+7
LB17-01	618.6	ULA-8355	0.308	0.001	−691.9	0.8	9,460	20	10,700	−46/+74
LB17-01	626	ULA-8365	0.218	0.001	−781.8	0.6	12,230	25	14,120	−67/+85
LB17-01	663	ULA-8367	0.193	0.001	−807.2	0.6	13,225	30	15,880	−136/+130
LB17-01	762	ULA-7735	0.178	0.001	−822.2	0.7	13,870	35	16,870	−284/+156
LB17-01	843	ULA-8362	0.111	0.001	−888.8	0.5	17,640	40	21,320	−193/+147
LB17-01	998.5	ULA-7736	0.088	0.001	−912.3	0.6	19,550	60	23,520	−187/+131
LB17-06	690	ULA-9491	0.610	0.001	−390.2	1.0	3,975	15	4,450	−40/−6
LB17-06	557	ULA-9497	0.422	0.001	−578.4	0.8	6,940	15	7,760	−67/+37
LB17-08	455	ULA-9498	0.643	0.001	−356.7	1.1	3,545	15	3,840	−16/+53
LB17-08	382	ULA-9499	0.618	0.001	−382.5	1.3	3,875	20	4,320	−83/+90

2 scoriae precluded the geochemical analysis of the glass shards.

The same pattern is observed on FL31MA field site (N39°24′54.04″ W31°11′35.02"; **Figure 8A**) located ~1 km SSW of Lagoa da Lomba. In this field site, the outcropping tephra 1 (104 cm-thick) shows a very similar grain size variation to that of tephra 1 at FL154MA, with the fine lapilli scoria and a thin oxidation crust in the middle of the deposit (**Figure 8F**). Moreover, scoria lapilli above the crust (FL31MAb) yielded glass compositions that overlap with that of geochemical Group 2 of Lagoa da Lomba, whereas the scoriae below this horizon (FL31MAa) fit well with geochemical Group 1 (**Figure 9**). As well as in site FL154MA, the scoriae of tephra 1 from site FL31MA are overlapped by a 10 cm-thick fine ash bed, in turn covered by another scoriaceous tephra layer, tephra 2, which is 15 cm-thick (**Figure 8F**). As well as in site FL154MA, these scoriae are intensively weathered, making impractical the geochemical analysis of glass shards.

DISCUSSION

Interpretation of Lagoa da Lomba Facies and Correlation Between Tephra Layers

Based on the distinctive features of the facies identified in Lagoa da Lomba, we propose different interpretations for their origin:

1) The muddy organic lacustrine facies (F1) was deposited during periods of volcanic quiescence, incorporating significant amounts of organic matter, mainly from lake biogenic production as well as fine clastic sediments from runoff on catchment during regular rains.
2) The terrigenous/volcaniclastic facies (F2) was deposited during periods of intense clastic inputs in the lake due to an increase of flood frequency and/or to an increase in the availability of materials in the basin catchment (either by intense soil weathering or deposition of pyroclastic fall deposits in the surroundings of Lagoa da Lomba).
3) The volcanic facies (F3), which includes all the tephra layers, are interpreted as pyroclastic fall deposits, thus representing periods of volcanic activity on the island. This interpretation is based on the clast-supported nature of the tephra layers and on the pristine morphologies of the juvenile clasts (scoria lapilli). The high content of lithic clasts of some tephra layers suggests the occurrence of phreatomagmatic activity and/or the enlargement and erosion of the conduit walls (Barberi et al., 1989; Sulpizio et al., 2005; Pimentel et al., 2015). The higher degree of oxidation observed in the tephra layers of LB17-08 may be related to its lake shallow conditions of deposition.

Separation of predominantly basaltic (*sensu latu*) eruptive events based on major element geochemistry alone is often problematic, on account of the generally similar geochemistry of basaltic magmas derived from the same source, i.e., same island and same volcanic system (e.g., Zanon and Pimentel, 2015; Zanon et al., 2020). However, our results clearly allowed to discriminate different geochemical populations that proved to be crucial to identifying volcanic events. The distinct glass compositions of juvenile material (scoria lapilli), together with lake core stratigraphy and radiocarbon ages, allowed the establishment of consistent correlations between the tephra layers (**Figure 10**), as detailed below, from the most recent to the oldest.

We correlated the LB1-T4, LB6-T3, and LB8-T3 tephra layers (**Figure 10**) as corresponding to the same volcanic event based on their stratigraphic position (all constitute the uppermost tephra layer of each sequence and all lie on the top of a reworked section), but especially on their distinctive geochemical signature, which is

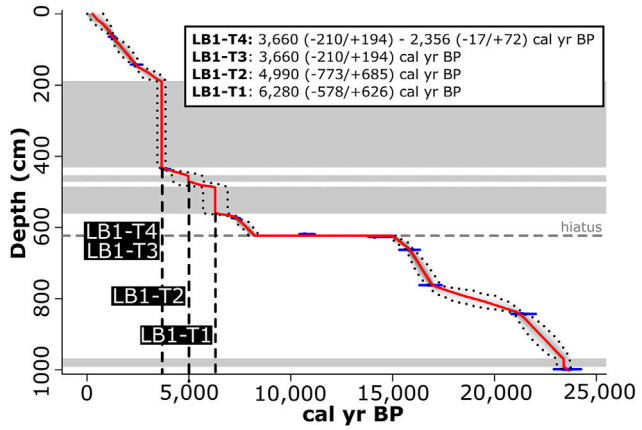


FIGURE 5 | Age depth model for Lagoa da Lomba constructed with the R rbacon function (Blaauw et al., 2021), using the AMS ^{14}C radiocarbon dates. The red line represents the age-depth function and dark doted lines correspond to the error of the model. The small blue traces indicate the AMS ^{14}C radiocarbon dates used as anchor points and their uncertainties. Light grey bands represent abrupt events of sedimentation (tephra accumulation), which were not used to calculate the age model. A hiatus was considered at 623 cm depth. Vertical dashed lines are projecting the age obtained at the base of LB1-T1, LB1-T2, and LB1-T3, and LB1-T4 tephra layers, which are indicated on the top right box.

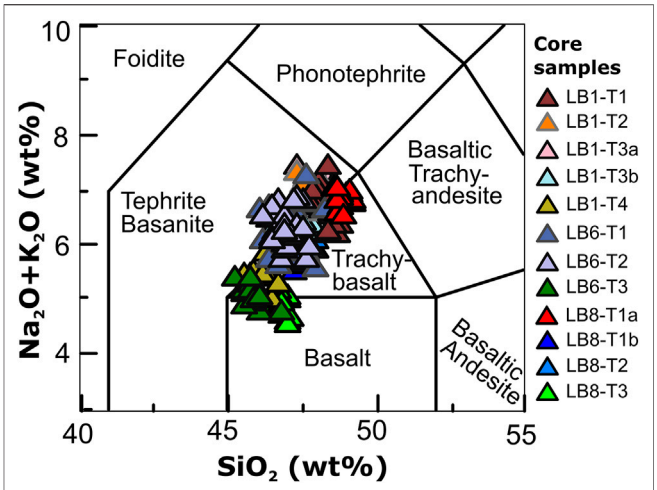


FIGURE 6 | Total alkalis vs silica (TAS) diagram (Le Bas et al., 1986) for the classification of glasses of Lagoa da Lomba tephra layers. Glasses are normalized to 100% volatile free. Compositions cluster around the transition of the basalt, trachybasalt and tephrite/basanite fields.

exclusive of those tephras (the more primitive geochemical Group 3). Important to highlight is a very thin lens of organic-rich clay (F1) almost exclusively made up of diatoms and plant remains, just below LB6-T3. This suggests a period of high in-lake productivity, and therefore a short-time break in the volcanic activity immediately before the deposition of LB6-T3 tephra layer, during which lacustrine sediments were deposited in the deepest area of Lagoa da Lomba. Accordingly, LB1-T4, LB6-T3, and LB8-T3 tephra layers record the youngest volcanic eruption preserved at Lagoa da Lomba, and its distinct geochemistry may potentially be used to discriminate subaerially exposed tephras in the study area, as we demonstrate. Since all the material between LB1-T3 and LB1-T4 tephra layers is interpreted as reworked (F2), it is not possible to obtain a precise age for the most recent eruption. However, the absence of muddy and organic lacustrine deposits between these horizons suggests that the transport and sedimentation of volcaniclastic material was rapid, taking place at a much shorter time scale than regular lacustrine sediments. This rapid transport of material may have been initiated during the emplacement of LB1-T3 tephra layer either by lateral flow, creeping or just the pressure posed by the deposition of the lapilli on the water-saturated sediment. Therefore, it is assumed that the time interval between the deposition of LB1-T3 and LB1-T4 layers was considerably short. Given these considerations, and taking into account that tephra layer LB1-T4 is conformably overlain by lacustrine sediments dated at 2,360 (−17/+72) cal yr BP (see **Figure 3**), our data suggest that the eruption took place sometime in between 3,660 (−210/+194) cal yr BP and 2,360 (−17/+72) cal yr BP.

The subjacent volcanic event is recorded by both the LB1-T3 and LB8-T1 tephra layers, given the fact that the correlation between them is consistent. A thin sediment lens separates LB8-T1 and LB8-T2 tephra layers, which may have been emplaced by a syn-eruptive mass flow that ripped-up sediments from the lake slopes. In this case, instead of two tephra deposits, LB8-T1 and LB8-T2 would comprise a single deposit. Another possibility is that both the volcaniclastic lens and the LB8-T2 tephra layer are reworked material. Despite this, LB1-T3 and LB8-T1 tephra layers show a distinctive internal grain size variation that was not observed at any other lacustrine-hosted tephras and they are both overlain by reworked sediments (**Figure 4**). More importantly, they are similar in terms of glass compositions, as both show a more primitive composition at the upper part (geochemical Group 2) and a slightly more evolved composition (geochemical Group 1) at the base. Additionally, radiocarbon ages of the sediments at the base of LB1-T3 and LB8-T1 tephra layers (3,840 (−38/+53) cal yr BP and 3,870 (−16/+53) cal yr BP, respectively) are very similar, indicating that these tephras were deposited at the same time. Our age model suggests an approximate age of 3,660 (−210/+194) cal yr BP for this eruption(s).

Except for the LB6-T3 tephra layer, there is no other solid option for a correlation of the tephras from LB17-06 sequence with the LB17-01 and LB17-08 cores, as there is no characteristic grain size or geochemical transition in the tephra layers. The LB6-T2 tephra layer may not be a primary deposit, i.e., a fall deposit, but a volcaniclastic deposit that results from in-lake and/or near lake redeposition processes. This is supported by the small mass movement deposits occurring below LB6-T2, as well as by the repetition of the geochemical Group 2 on the older LB6-T1 tephra. Such repetition does not occur on LB17-01 sequence, which we assume to be continuous. Therefore, we do not expect to find a repetition of the geochemical Group 2 in the lake stratigraphy. Eventually, the top of LB6-T1 tephra layer could be correlated with the top of layers LB8-T1 and LB1-T3 given the fact that it constitutes the older deposit whose tephras lie on

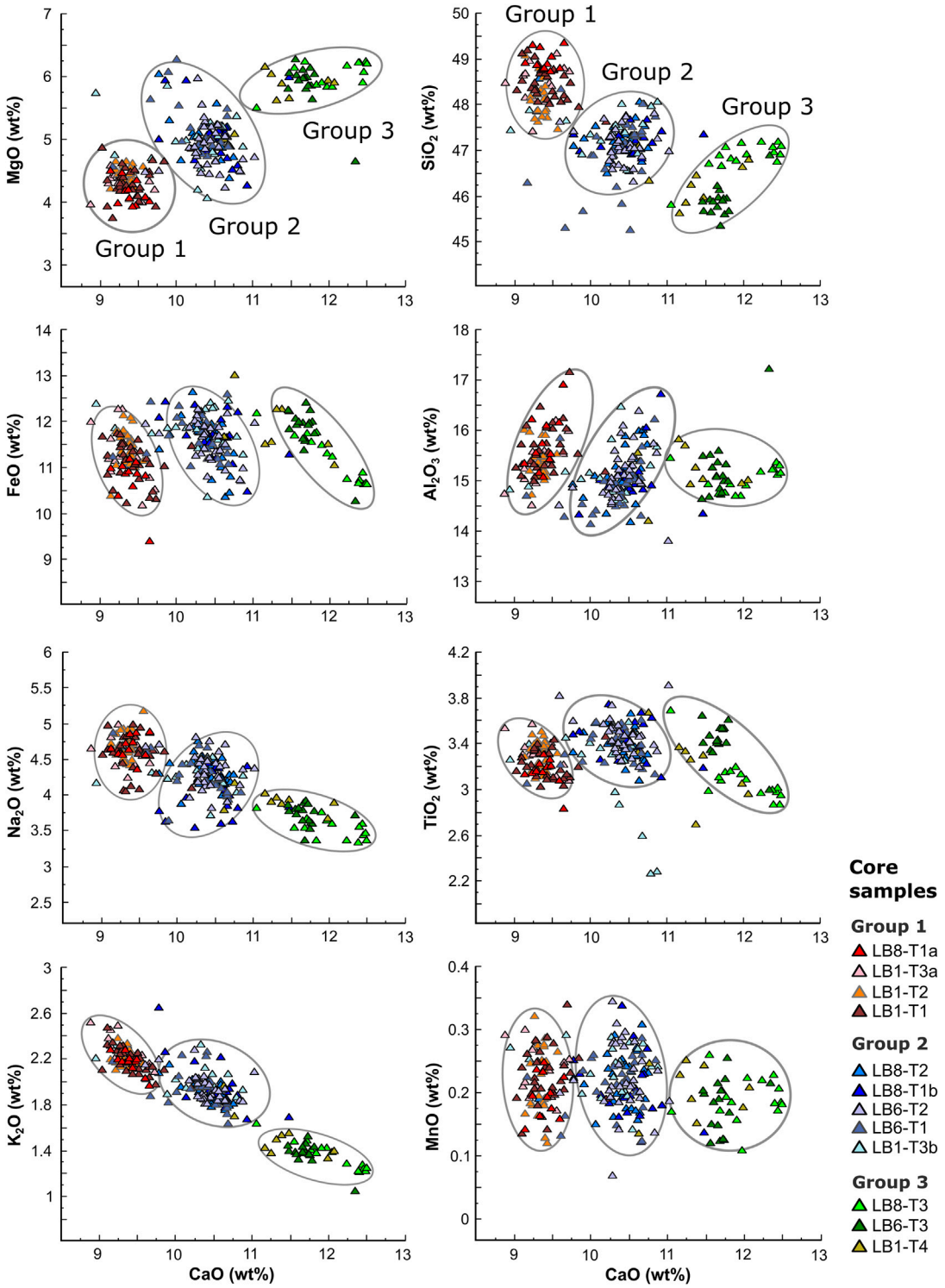


FIGURE 7 | Variation diagrams of major elements (wt%) vs CaO (wt%) for the glasses of Lagoa da Lomba tephra layers. Glasses are normalized to 100% volatile free. Glass compositions plot in three different geochemical populations, with decreasing degree of evolution towards the most recent tephra layers.

geochemical Group 2. However, due to its location on the central and deepest part of Lagoa da Lomba where the accumulation of sediments is higher and possibly more vulnerable to the deposition of reworked/slumped material, the Holocene period may not be completely recorded on LB17-06 sequence as it is on LB17-01. Thus, since it is not possible to establish any solid



FIGURE 8 | (A) Elevation map of Flores Island showing the location of Lagoa Funda and Lagoa Comprida Volcanic Systems (FVS and CVS, respectively) in relation to Lagoa da Lomba, as well as the location of four subaerially-exposed pyroclastic sequences used to investigate the origin of the tephra layers of Lagoa da Lomba lacustrine record **(B)** Photo of a proximal volcanic sequence on the SE rim of Lagoa Funda (FL20MA: N39°23′53.74″ W31°12′57.17″). Volcanic succession consists, from the base to the top, on spatter accumulation, remobilized material (RM), scoriaceous lapilli and lithic-rich sequence of ash intercalated with lapilli, bombs, and blocks (phreatomagmatic) **(C)** Photo of an outcrop of spatter and scoria produced during CVS eruptions. The volcanic sequence is located on the SE flank of Lagoa Comprida cone (FL17MA: N39°26′14.89″ W31°13′10.99″) **(D)** Photo of the upper part of the scoria cone produced during CVS eruptions showing that it is overlapped by a sequence of intercalated very fine ash layers and lithic lapilli and blocks layers (phreatomagmatic). Scale is 7 cm **(E)** Photo of the sequence located ~200 m NE of Lagoa da Lomba (FL154MA: N39°25′34.86″ W31°11′8.12″). Shows an internal grain size transition on Tephra 1 deposit, which is similar to the one found at LB1-T3 tephra layer. On FL154MA sequence, this transition is accompanied by a thin oxidation crust. Scale is 1 m **(F)** Photo of the sequence located half-way between Lagoa da Lomba and FVS (FL31MA: N39°.24′54.04″ W31°11′35.02″). Shows a lapilli tephra deposit with the grain size transition and oxidation crust that characterizes tephra 1 deposit from FL154MA site and LB1-T3 layer. Scale is 7 cm.

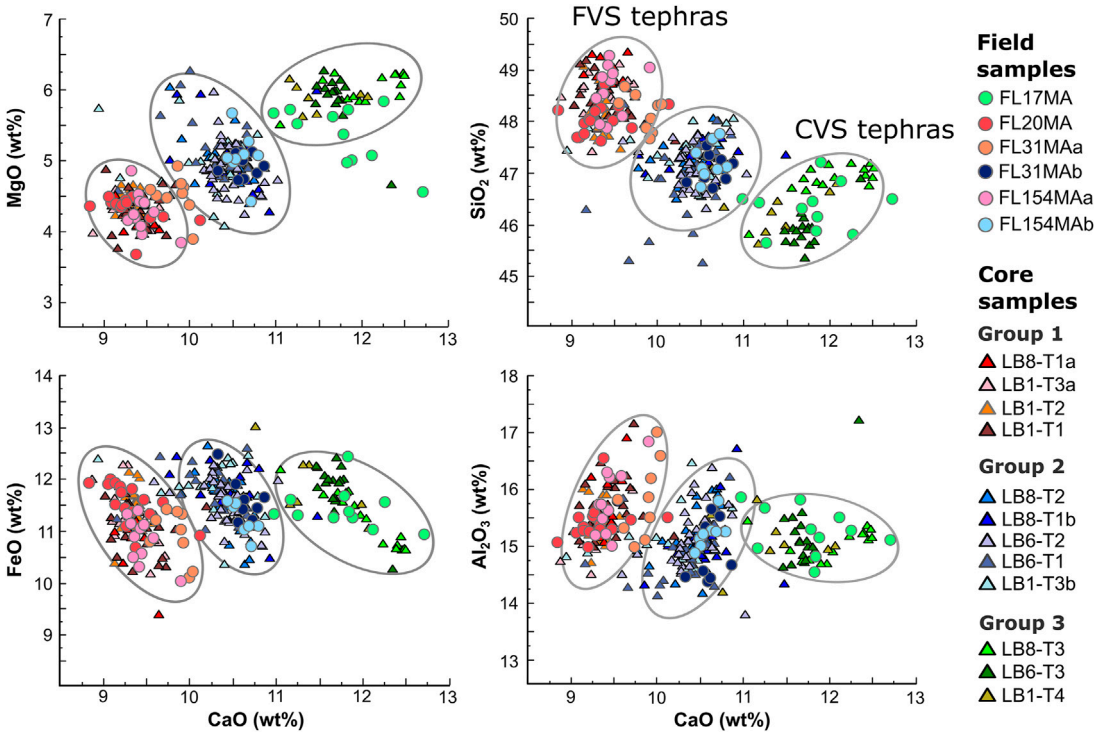


FIGURE 9 | Variation diagrams of major elements (wt%) vs CaO (wt%) for the glasses of Lagoa da Lomba tephra layers and subaerial tephra deposits on **Figure 8**. Glasses are normalized to 100% volatile free. Glass compositions of subaerial deposits fit well in the three geochemical groups defined for Lagoa da Lomba lacustrine record. Geochemical Group 1 correlates with Lagoa Funda Volcanic System (FVS) deposits and Group 3 with Lagoa Comprida Volcanic System (CVS) deposits. The internal geochemical variation described for LB1-T3 and LB8-T1 tephra layers is also found on FL154MA and FL31MA deposits, with samples below the oxidation crust (FL31MAa and FL154MAa) lying on geochemical Group 1 and samples collected above the oxidation crust (FL31MAb and FL154MAb) fitting in geochemical Group 2.

stratigraphic or geochemical correlation, we consider that LB6-T1 tephra layer most likely corresponds to remobilized tephras, which slumped downslope from a higher position. The great thickness of reworked sediment at LB17-06 core sequence may be explained by the steep subaqueous slopes of Lagoa da Lomba, which are close to 30° in some areas. This steepness promotes the flow of sediments along the slopes and consequently favors its deposition in the deepest area of the lake (see LB17-06 location in **Figure 2**).

In core LB17-01, two other tephra layers (LB1-T2 and LB1-T1) are interpreted as primary volcanic deposits and consequently are thought to be representative of two older eruptions, which – according to our age model – occurred approximately at 4,990 (−773/+685) and 6,280 (−578/+626) cal yr BP. These two tephra layers are very similar in composition, given that they both fall in geochemical Group 1, similarly to LB1-T3a.

In summary, the lacustrine record of Lagoa da Lomba attest to the occurrence of at least four different volcanic eruptions that took place at Flores during the Holocene (**Figure 5**). Furthermore, this record confirms that all four eruptions occurred within a time interval between 6,280 (−578/+626) and 2,360 (−17/+72) cal yr BP. Finally, it is worth mentioning that the 23,520 (−187/+131) cal yr BP age for the base of LB17-01 places an upper boundary for the eruption that formed the crater of Lagoa da Lomba itself, confirming it was formed during the late Pleistocene.

Correlation Between Lake and Subaerially-Exposed Sequences and Possible Sources

Considering the results and interpretations of the previous chapters, we confirm that the volcanic succession preserved at Lagoa da Lomba – and particularly that of the longest and most complete core LB17-01 – is generally consistent with the subaerially-exposed record. Moreover, the evidence presented above allows the identification of possible sources for the described eruptions, as we demonstrate below.

The youngest eruptive event – represented by LB1-T4, LB6-T3, LB8-T3 tephra layers – is recorded by the sequence of CVS (outcrop FL17MA; **Figure 10**), given that its geochemical signature lie within the more primitive geochemical Group 3. Despite the absence of geochemical analyses, based on their stratigraphic position we assume that this event is also recorded by tephra 2 from outcrops FL31MA and FL154MA (**Figure 10**). The age interval [3,660 (−210/+194) – 2,360 (−17/

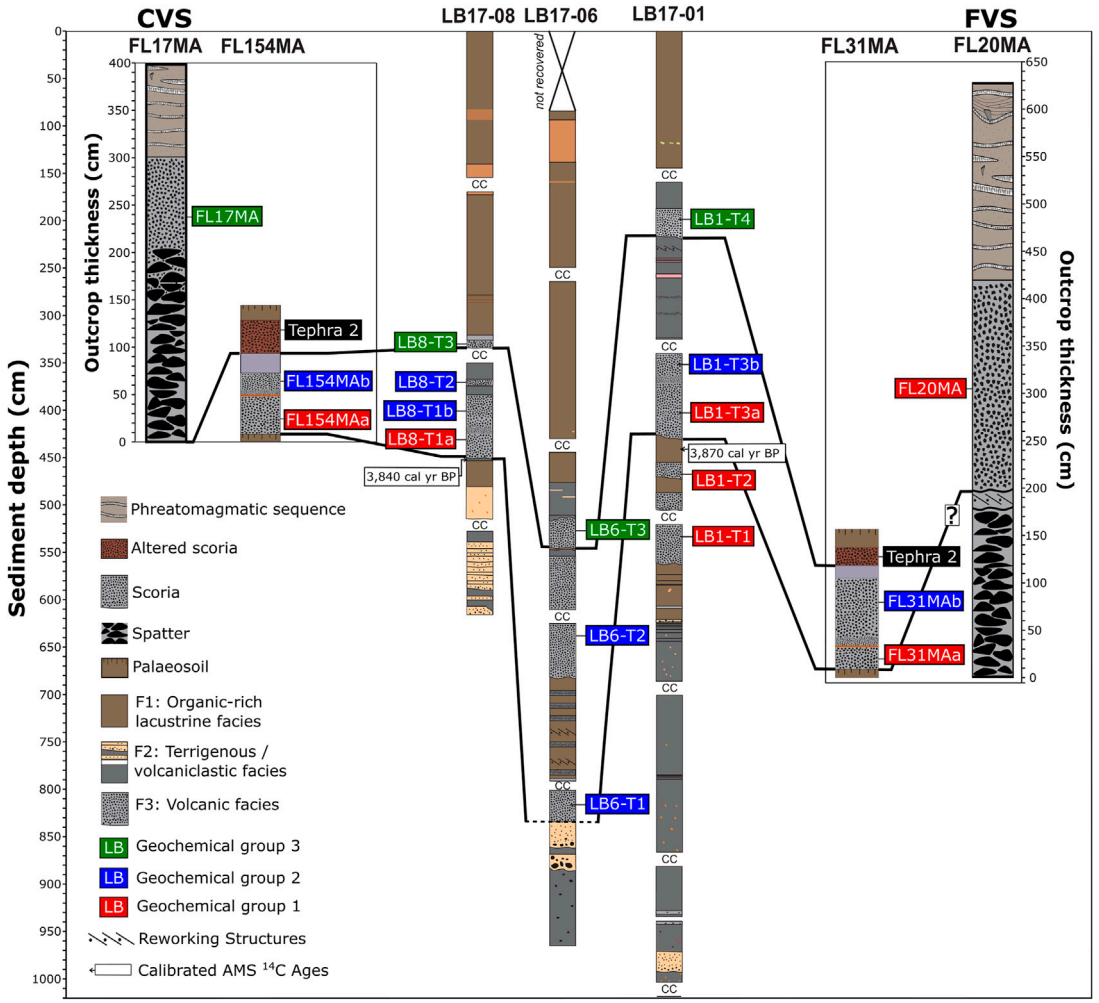


FIGURE 10 | Correlation panel of the sedimentary sequences collected at Lagoa da Lomba and subaerial volcanic sequences. Red, blue and green colors indicate the geochemical Group to which each tephra layer belongs. The dashed line on the bottom of LB6-T1 tephra layer indicates a possible correlation that is uncertain. We named the tephras below and above the granulometric transition of LB8-T1 and LB1-T3 as *a* and as *b*, respectively.

+76) cal yr BP] we infer for this event agrees well with the 3,050 (−206/+217) cal yr BP (2,900 ± 100 uncalibrated ^{14}C yr BP) age proposed by Morisseau and Traineau (1985). We, therefore, confirm that the youngest volcanic eruption that took place at Flores Island was initiated from vents located in the northern volcanic cluster that includes the maars of Lagoa Comprida, Lagoa Negra, and Lagoa Seca, the Lagoa Branca tuff ring, and a few other smaller unnamed craters (**Figure 1B**). The sequences exposed on the flanks of Lagoa Comprida (FL17MA), suggest that this event started with a vigorous magmatic phase (Hawaiian/Strombolian style) and subsequently, transitioned (rather rapidly/instantaneously) to highly explosive phreatomagmatic activity that ultimately led to the formation of the maars and tuff rings. Such shifts of eruption style from Strombolian to phreatomagmatic were described at different volcanic islands, e.g., Fuencaliente and Tinguaton Tao volcanoes, Canary Islands (Clarke et al., 2009), Miyakejima volcano, Japan (Geshi et al., 2019), as well as in other volcanic regions, e.g., Garrinada and Montsacopa volcanoes (Martí et al., 2010), Pinacate volcanic field (Gutmann, 2002). The early magmatic phase of this eruption involved the extrusion of magma with a composition that lies at the junction of the basalt, trachybasalt and tephrite/basanite fields, being the less evolved of all magmas that fed the Holocene eruptions of Flores.

The second oldest eruptive event, in turn, is well-recorded by lake tephra layers LB1-T3 and LB8-T1, and tephra 1 of outcrops FL31MA and FL154MA (**Figure 10**). All these units exhibit a very distinctive petrographic and geochemical pattern characterized by a peculiar grain size variation and a composition that changed from a more evolved endmember (represented by geochemical Group 1) towards a less evolved endmember (represented by geochemical Group 2), with higher MgO contents and lower SiO_2, CaO, and Na_2O. This characteristic pattern provides a valuable tool to discriminate this event in the field, facilitating

the identification of its source. Effectively, a preliminary field survey showed that the spatial distribution, thickness variation, and the size of the larger clasts of this deposit found within a large area between Lagoa Funda and Lagoa da Lomba, as well as to the east of Lagoa da Lomba, suggest that its source is located at FVS.

A comparison of glass compositions between lake-hosted tephra layers and scoriaceous lapilli at outcrop FL20MA (located in the southern flank of FVS) confirms that these overlap with LB1-T3a and LB8-T1a within geochemical Group 1 (**Figure 9**), with geochemical Group 2 being absent from this field sequence. The presence of remobilized material below the lapilli unit (**Figure 8B**), may suggest a time break in the eruption characterized by geochemical Group 1 (or probably two eruptions in close succession). Regardless of its absence, Group 2 is interpreted as an internal compositional variation of the deposit rather than a deposit from a different, individual eruption (or eruption phase). The grain size variations may either result from changes in the wind direction and/or velocity or from a decrease in the eruption rate, resulting in the deposition of finer material closer to the vent location (Carey and Sparks, 1986). In turn, the geochemical variation may result from the initial eruption of a more differentiated magma, stored at the upper part of the magmatic reservoir, followed by less evolved composition, which may have suffered (or not) an injection of new magma. Additionally, such internal changes in the deposit coincide with an increase in the lithic content, which may indicate an enlargement of the crater and erosion of the conduit walls (Sulpizio et al., 2005) and/or the initiation of a phreatomagmatic pulse (Barberi et al., 1989; Pimentel et al., 2015). This transition between contrasting eruptive styles, i.e., "dry" magmatic to "wet" phreatomagmatic, is dominantly controlled by variations in degassing patterns, magma ascent rates and degrees of interaction with external water (Houghton et al., 1999; Gutmann, 2002; Geshi et al., 2019). In an early stage, high rates of magma ascent may have inhibited groundwater from entering the conduit. Later, groundwater may have entered the system as a response of a widening of the conduit and/or a decrease in the eruption rate. This, would increase the explosivity of the eruption, resulting in the optimization of magma fragmentation, highlighted by the rapid decrease in grain size that characterize LB1-T3 and LB8-T1 deposits, as well as tephra 1 from FL154MA and FL31MA sites.

We infer that the second oldest eruptive event recorded at Lagoa da Lomba was sourced at FVS (**Figure 10**), and the absence of geochemical Group 2 in the proximal deposits is possibly due to an incomplete record at FL20MA. According to our age model, we estimate that this eruption was initiated at ca. 3,660 (−210/+194) cal yr BP, similar to the 3,360 (−283/+219) cal yr BP (3,150 ± 100 uncalibrated ^{14}C yr BP) age suggested by Morisseau and Traineau (1985). Moreover, the sequence at FL20MA also suggests that this eruption experienced a rapid transition from an initial magmatic phase (Hawaiian/Strombolian style) to phreatomagmatic activity, ultimately leading to the formation of the maar of Lagoa Funda and the tuff ring of Lagoa Rasa and other adjacent unnamed craters (**Figure 1B**). The occurrence of phreatomagmatism is supported by the internal structure of the deposits, with parallel to subparallel stratification, in places gently undulated, the presence of very fine-grained ash layers, occasionally containing accretionary lapilli, and the high lithic content of some layers, which often show bomb sag features (Barberi et al., 1989; De Rita et al., 2002; Pimentel et al., 2015).

Due to limitations on the outcrop exposure, including high erosion rates of subaerial pyroclastic deposits on volcanic islands, the products of the two older eruptions (recorded by LB1-T1 and LB1-T2 tephra deposits) were not observed on land. For this reason, we were not able to assign the source of those eruptions. Based on the age-depth model, the eruptions occurred with an interruption of approximately 1,000 years, occurring between 6,280 (−578/+626) cal yr BP and 4,990 (−773/+685) cal yr BP. It is, however, important to highlight the difference in the products between these two older eruptions and the two most recent ones. While CVS and FVS tephras have a high lithic component, the deposits of the older eruptions are exclusively made up of scoria lapilli and ash (glass shards), and a few loose crystals. This may attest to the later phreatomagmatic behaviour of CVS and FVS eruptions, which contrasts with the older eruptions, which probably were exclusively magmatic. This is supported by the thick phreatomagmatic deposits that cap the sequences at both volcanic systems, which are directly associated with the formation of the visible maars/tuff rings that host the lakes. Based on this, we suggest that such deposits could have resulted from the eruption of monogenetic scoria cones described by Azevedo and Portugal Ferreira (2006), e.g., Pico do Touro or Marcela cones, which are the two closest volcanic sources to Lagoa da Lomba (**Figure 8A**). Another possibility would be that these events have been sourced from older vents at FVS, given that the sequence at FL20MA site suggests the occurrence of earlier magmatic, largely effusive events, such as the one that emitted the young lava flows that flowed down the adjacent Lajes valley (see **Figure 8A** for location) – a hypothesis to be confirmed in future studies.

The Holocene Volcanism of Flores and Hazard Implications

Compared to other islands of the Azores Archipelago, Flores Island lies on a more stable tectonic environment and did not experience historical eruptions but hitherto its volcanic history is still poorly studied. Until now, available ages for the Holocene eruptions at Flores are constrained to the 2.9 – 3.0 ka interval (Morisseau and Traineau, 1985). However, the lacustrine tephrostratigraphy described here shows that this period was considerably longer, extending at least up to ca. 6.7 ka ago.

During the Holocene period, at least four eruptions were recorded in Lagoa da Lomba lacustrine sequence. The most recent eruption was related to CVS and the second most recent related to FVS, with two earlier events from yet unknown sources. In terms of composition, there is no great variability amongst the Holocene eruptions, all being basaltic to trachybasaltic in composition. However, glass geochemistry of the erupted products shows a trend towards a more primitive basaltic composition as we move up in the stratigraphy. This

suggests the gradual activation of a different magma feeding system over time.

Although the eruptive frequency was relatively low during the Holocene, Flores is an active volcanic island, and the possibility of future eruptions should not be ruled out. Given the small size of the island, remote geography and lack of adequate monitoring networks, the reconstruction of its volcanic history, including the size and style of the eruptions, assumes paramount importance for the development of long-term hazard assessment strategies. Our dataset demonstrates that different eruptive styles have occurred throughout the Holocene, with evidence of magmatic and phreatomagmatic activity. Phreatomagmatic eruptions may be highly hazardous phenomena, especially in basaltic systems where a sudden and unexpected shift of eruption style can transform a mild effusive eruption into a violent explosive event (Geshi et al., 2019). A future eruption on Flores with similar characteristic to the last two events (CVS and FVS) could have a devastating impact on the island and its 3,600 inhabitants. If a future eruptive event would occur, tephra fallout would probably affect all the central part of the island and could reach the inhabited coastal areas depending on the wind direction. In proximal areas, associated volcanic hazards would likely include ballistic projectiles (bombs), pyroclastic density currents, lahars and gas emissions. Ongoing studies are currently being undertaken to carefully access the long-term volcanic hazard at Flores Island.

CONCLUSION

Core sequences collected at Lagoa da Lomba (Flores Island) provide valuable insights to reconstruct the recent volcanic history of Flores Island. Based on tephrostratigraphy supported by glass geochemistry and radiocarbon ages, we correlated lacustrine-hosted tephras with subaerially-exposed sequences from key outcrops, resulting in a robust reconstruction of the eruptive events that took place in central part of Flores Island during the Holocene. Our reconstructions confirm that at least four eruptive events occurred at Flores, within a period comprising 2.36 and 6.28 cal kyr BP. The youngest volcanic event was sourced from the Lagoa Comprida Volcanic System (sometime between 2.36 and 3.66 cal kyr BP), and the second most recent was sourced at the Lagoa Funda Volcanic System, approximately at 3.66 cal kyr BP. Both events seem to have started with vigorous magmatic activity, of Hawaiian/Strombolian style, but rapidly changed to highly explosive phreatomagmatic activity. Two older eruptive events (6.28 and 4.99 cal kyr BP), exclusively magmatic in nature, are evident by deposits preserved on the Lagoa da Lomba sedimentary record but are not exposed onland. Our observations reinforce the importance of tephrostratigraphy in lake records to reconstruct past volcanic activity of volcanic islands, especially on small and highly vegetated islands like those of the Azores Archipelago. Moreover, the use of geochemical tools (glass compositions) proved to be very useful to confirm and establish stratigraphical correlations, opening a pathway for more detailed field studies. We also demonstrate that Flores experienced an intense period of volcanic activity during the Holocene, that extended longer than previously known. Therefore, additional work is needed to better understand the past volcanism of the island and ultimately assess the possibility of future eruptions and the associated hazards. Finally, these new insights into the Holocene history of Flores show that the island went through a vigorous volcanic activity during the Late Holocene, and therefore, contrary to what is typically assumed, the possibility of future eruptions and associated hazards should be properly considered.

DATA AVAILABILITY STATEMENT

The original contributions presented in the study are included in the article/**Supplementary Material**, further inquiries can be directed to the corresponding author.

AUTHOR CONTRIBUTIONS

MA, RSR, AP, and AH undertook the field work; AH, AS, PMR, and SG collected the sediment cores within the remit of the project PALEOMODES; MA, AH, AS, MB, and SG performed all core description and analyses; MA and SK performed all glass shard geochemical analyses and subsequent data processing; and MA led the writing of the manuscript with contributions from all authors.

FUNDING

MA acknowledges the financial support given through her doctoral grant funded by Fundação para a Ciência e Tecnologia (SFRH/BD/138261/2018). The acquisition of sediment cores was funded by the Spanish Ministry of Economy and Competitiveness through the research project PaleoModes (CGL 2016-75281-C2). The radiocarbon dating was partially funded by FCT through the research project DISCOVERAZORES (PTDC/CTA-AMB/28511/2017), PaleoModes and RapidNAO (CGL 2013-40608-R). RSR and PMR acknowledge their IF/01641/2015 and DL57/2016/ICETA/EEC 2018/25 fellowship funded by FCT, respectively. This work was also supported by projects FCT/UID/GEO/50019/2019 and FCT/UIDB/50019/2020 - IDL funded by FCT.

ACKNOWLEDGMENTS

We would like to acknowledge the GEO3BCN-CSIC and the University of Barcelona as well as the GEOMAR Helmholtz Centre for providing the facilities and technical support during the study of the lacustrine records and geochemical analyses, respectively. We thank M. Antunes at Secretaria Regional do Turismo e Transportes for providing the digital altimetric database used in this study. We also acknowledge Serviços Florestais das Flores e Corvo as well as Câmara Municipal das

Lajes das Flores, for their support in field logistics and access to outcrops. We also acknowledge J. Madeira and J. Cabral for their informal review of the manuscript, prior to submission, and DR and DP, for their constructive reviews that helped to improve the overall quality of the manuscript.

SUPPLEMENTARY MATERIAL

The Supplementary Material for this article can be found online at: https://www.frontiersin.org/articles/10.3389/feart.2021.738178/full#supplementary-material

REFERENCES

Andrade, C., Cruz, J., Viveiros, F., and Coutinho, R. (2019). CO2 Flux from Volcanic Lakes in the Western Group of the Azores Archipelago (Portugal). *Water* 11 (3), 599. doi:10.3390/w11030599

Azevedo, J. M. M., Ferreira, M. R., and Martins, J. Á. (1991). The Emergent Volcanism of Flores Islands, Azores (Portugal). *Arquipélago-Life Earth Sci.* 9, 37–46.

Azevedo, J. M. M., and Portugal Ferreira, M. R. (2006). The Volcanotectonic Evolution of Flores Island, Azores (Portugal). *J. Volcanology Geothermal Res.* 156 (1–2), 90–102. doi:10.1016/j.jvolgeores.2006.03.011

Barberi, F., Cioni, R., Rosi, M., Santacroce, R., Sbrana, A., and Vecci, R. (1989). Magmatic and Phreatomagmatic Phases in Explosive Eruptions of Vesuvius as Deduced by Grain-Size and Component Analysis of the Pyroclastic Deposits. *J. Volcanology Geothermal Res.* 38 (3-4), 287–307. doi:10.1016/0377-0273(89)90044-9

Bas, M. J. L., Maitre, R. W. L., Streckeisen, A., and Zanettin, B. (1986). A Chemical Classification of Volcanic Rocks Based on the Total Alkali-Silica Diagram. *J. Petrol.* 27, 745–750. doi:10.1093/petrology/27.3.745

Björck, S., Rittenour, T., Rosén, P., França, Z., Möller, P., Snowball, I., et al. (2006). A Holocene Lacustrine Record in the central North Atlantic: Proxies for Volcanic Activity, Short-Term NAO Mode Variability, and Long-Term Precipitation Changes. *Quat. Sci. Rev.* 25 (1-2), 9–32. doi:10.1016/j.quascirev.2005.08.008

Blaauw, M., Christen, J. A., and Aquino Lopez, M. A. (2021). Rbacon: Age-Depth Modelling Using Bayesian Statistics. R package version 2.5.5. Available at: https://CRAN.R-project.org/package=rbacon (Accessed June 17, 2021).

Carey, S., and Sparks, R. S. J. (1986). Quantitative Models of the Fallout and Dispersal of Tephra from Volcanic Eruption Columns. *Bull. Volcanol* 48 (2), 109–125. doi:10.1007/BF01046546

Chester, D., Duncan, A., Coutinho, R., Wallenstein, N., and Branca, S. (2017). "Communicating Information on Eruptions and Their Impacts from the Earliest Times until the Late Twentieth century," in *Observing the Volcano World* (Cham: Springer), 419–443. doi:10.1007/11157_2016_30

Clarke, H., Troll, V. R., and Carracedo, J. C. (2009). Phreatomagmatic to Strombolian Eruptive Activity of Basaltic Cinder Cones: Montaña Los Erales, Tenerife, Canary Islands. *J. Volcanology Geothermal Res.* 180 (2-4), 225–245. doi:10.1016/j.jvolgeores.2008.11.014

Cruz, J. V., Antunes, P., Amaral, C., França, Z., and Nunes, J. C. (2006). Volcanic Lakes of the Azores Archipelago (Portugal): Geological Setting and Geochemical Characterization. *J. Volcanology Geothermal Res.* 156 (1-2), 135–157. doi:10.1016/j.jvolgeores.2006.03.008

De Rita, D., Giordano, G., Esposito, A., Fabbri, M., and Rodani, S. (2002). Large Volume Phreatomagmatic Ignimbrites from the Colli Albani Volcano (Middle Pleistocene, Italy). *J. Volcanology Geothermal Res.* 118 (1-2), 77–98. doi:10.1016/S0377-0273(02)00251-2

Direção Regional do Ambiente (2001). Plano Regional da água. Relatório técnico. Available at: http://sig-sraa.azores.gov.pt/SIG/(S(t3wmy4450zukatyelzq1p2v5))/MapViewer/SectionsViewer.aspx?id=34 (Accessed March 3, 2021).

EMODnet Bathymetry Consortium (2018). *EMODnet Digital Bathymetry (DTM 2018)*. France: Hydrographic and oceanographic service of the navy (SHOM). doi:10.12770/18ff0d48-b203-4a65-94a9-5fd8b0ec35f6

Freire Luis, J., Miranda, J. M., Galdeano, A., Patriat, P., Rossignol, J. C., and Mendes Victor, L. A. (1994). The Azores Triple junction Evolution since 10 Ma from an Aeromagnetic Survey of the Mid-Atlantic Ridge. *Earth Planet. Sci. Lett.* 125 (1–4), 439–459. doi:10.1016/0012-821X(94)90231-3

Genske, F. S., Beier, C., Stracke, A., Turner, S. P., Pearson, N. J., Hauff, F., et al. (2016). Comparing the Nature of the Western and Eastern Azores Mantle. *Geochimica et Cosmochimica Acta* 172, 76–92. doi:10.1016/j.gca.2015.08.019

Geshi, N., Németh, K., Noguchi, R., and Oikawa, T. (2019). Shift from Magmatic to Phreatomagmatic Explosions Controlled by the Lateral Evolution of a Feeder dike in the Suoana-Kazahaya Eruption, Miyakejima Volcano, Japan. *Earth Planet. Sci. Lett.* 511, 177–189. doi:10.1016/j.epsl.2019.01.038

Giralt, S., Moreno, A., Bao, R., Sáez, A., Prego, R., Valero-Garcés, B. L., et al. (2008). A Statistical Approach to Disentangle Environmental Forcings in a Lacustrine Record: the Lago Chungará Case (Chilean Altiplano). *J. Paleolimnol* 40 (1), 195–215. doi:10.1007/s10933-007-9151-9

Gutmann, J. T. (2002). Strombolian and Effusive Activity as Precursors to Phreatomagmatism: Eruptive Sequence at Maars of the Pinacate Volcanic Field, Sonora, Mexico. *J. Volcanology Geothermal Res.* 113 (1-2), 345–356. doi:10.1016/S0377-0273(01)00265-7

Hernández, A., Sáez, A., Bao, R., Raposeiro, P. M., Trigo, R. M., Doolittle, S., et al. (2017). The Influences of the AMO and NAO on the Sedimentary Infill in an Azores Archipelago lake since Ca. 1350 CE. *Glob. Planet. Change* 154, 61–74. doi:10.1016/j.gloplacha.2017.05.007

Hildenbrand, A., Marques, F. O., and Catalão, J. (2018). Large-scale Mass Wasting on Small Volcanic Islands Revealed by the Study of Flores Island (Azores). *Sci. Rep.* 8 (1), 1–11. doi:10.1038/s41598-018-32253-0

Houghton, B. F., Wilson, C. J. N., and Smith, I. E. M. (1999). Shallow-seated Controls on Styles of Explosive Basaltic Volcanism: a Case Study from New Zealand. *J. volcanology geothermal Res.* 91 (1), 97–120. doi:10.1016/S0377-0273(99)00058-X

Hunt, J. B., and Hill, P. G. (2001). Tephrological Implications of Beam Size-Sample-Size Effects in Electron Microprobe Analysis of Glass Shards. *J. Quat. Sci.* 16 (2), 105–117. doi:10.1002/jqs.571

Jarosewich, E., Nelen, J. A., and Norberg, J. A. (1980). Reference Samples for Electron Microprobe Analysis*. *Geostandards Newsl.* 4 (1), 43–47. doi:10.1111/j.1751-908X.1980.tb00273.x

Kueppers, U., Pimentel, A., Ellis, B., Forni, F., Neukampf, J., Pacheco, J., et al. (2019). Biased Volcanic hazard Assessment Due to Incomplete Eruption Records on Ocean Islands: an Example of Sete Cidades Volcano, Azores. *Front. Earth Sci.* 7, 122. doi:10.3389/feart.2019.00122

Kutterolf, S., Freundt, A., and Burkert, C. (2011). Eruptive History and Magmatic Evolution of the 1.9 Kyr Plinian Dacitic Chiltepe Tephra from Apoyeque Volcano in West-central Nicaragua. *Bull. Volcanol* 73, 811–831. doi:10.1007/s00445-011-0457-0

Kutterolf, S., Schindlbeck, J. C., Anselmetti, F. S., Ariztegui, D., Brenner, M., Curtis, J., et al. (2016). A 400-ka Tephrochronological Framework for Central America from Lake Petén Itzá (Guatemala) Sediments. *Quat. Sci. Rev.* 150, 200–220. doi:10.1016/j.quascirev.2016.08.023

Martí, J., Planagumà, L., Geyer, A., Canal, E., and Pedrazzi, D. (2011). Complex Interaction between Strombolian and Phreatomagmatic Eruptions in the Quaternary Monogenetic Volcanism of the Catalan Volcanic Zone (NE of Spain). *J. Volcanology Geothermal Res.* 201 (1-4), 178–193. doi:10.1016/j.jvolgeores.2010.12.009

McNamara, K., Cashman, K. V., Rust, A. C., Fontijn, K., Chalié, F., Tomlinson, E. L., et al. (2018). Using lake Sediment Cores to Improve Records of Volcanism at Aluto Volcano in the Main Ethiopian Rift. *Geochem. Geophys. Geosyst.* 19 (9), 3164–3188. doi:10.1029/2018GC007686

Métrich, N., Zanon, V., Créon, L., Hildenbrand, A., Moreira, M., and Marques, F. O. (2014). Is the 'Azores Hotspot' a Wetspot? Insights from the Geochemistry of Fluid and Melt Inclusions in Olivine of Pico Basalts. *J. Petrol.* 55 (2), 377–393. doi:10.1093/petrology/egt071

Mitchell, N. C. (2003). Susceptibility of Mid-ocean ridge Volcanic Islands and Seamounts to Large-Scale Landsliding. *J. Geophys. Res.* 108 (B8). doi:10.1029/2002JB001997

Morisseau, M., and Traineau, H. (1985). Mise en évidence d'une activité hydromagmatique holocène sur l'île de Flores (Açores). *C. R. Acad. Sc. Paris, T* 301 (série II, no 18), 1309–1314.

Pimentel, A., Pacheco, J., and Self, S. (2015). The ~1000-years BP Explosive Eruption of Caldeira Volcano (Faial, Azores): the First Stage of Incremental Caldera Formation. *Bull. Volcanol* 77 (5), 1–26. doi:10.1007/s00445-015-0930-2

Rull, V., Stansell, N. D., Montoya, E., Bezada, M., and Abbott, M. B. (2010). Palynological Signal of the Younger Dryas in the Tropical Venezuelan Andes. *Quat. Sci. Rev.* 29 (23-24), 3045–3056. doi:10.1016/j.quascirev.2010.07.012

Sáez, A., Valero-Garcés, B. L., Moreno, A., Bao, R., Pueyo, J. J., González-Sampériz, P., et al. (2007). Lacustrine Sedimentation in Active Volcanic Settings: the Late Quaternary Depositional Evolution of Lake Chungará (Northern Chile). *Sedimentology* 54 (5), 1191–1222. doi:10.1111/j.1365-3091.2007.00878.x

Stern, C. R. (2008). Holocene Tephrochronology Record of Large Explosive Eruptions in the Southernmost Patagonian Andes. *Bull. Volcanol* 70 (4), 435–454. doi:10.1007/s00445-007-0148-z

Stockhecke, M., Sturm, M., Brunner, I., Schmincke, H. U., Sumita, M., Kipfer, R., et al. (2014). Sedimentary Evolution and Environmental History of Lake Van (Turkey) over the Past 600 000 Years. *Sedimentology* 61 (6), 1830–1861. doi:10.1111/sed.12118

Stuiver, M., Reimer, P. J., and Reimer, R. W. (2021). CALIB 8.2. [WWW program] at: http://calib.org (accessed January 25, 2021).

Sulpizio, R., Mele, D., Dellino, P., and Volpe, L. L. (2005). A Complex, Subplinian-type Eruption from Low-Viscosity, Phonolitic to Tephri-Phonolitic Magma: the AD 472 (Pollena) Eruption of Somma-Vesuvius, Italy. *Bull. Volcanol* 67 (8), 743–767. doi:10.1007/s00445-005-0414-x

Van Daele, M., Moernaut, J., Silversmit, G., Schmidt, S., Fontijn, K., Heirman, K., et al. (2014). The 600 Yr Eruptive History of Villarrica Volcano (Chile) Revealed by Annually Laminated lake Sediments. *Geol. Soc. America Bull.* 126 (3-4), 481–498. doi:10.1130/B30798.1

Vázquez-Loureiro, D., Gonçalves, V., Sáez, A., Hernández, A., Raposeiro, P. M., Giralt, S., et al. (2019). Diatom-inferred Ecological Responses of an Oceanic lake System to Volcanism and Anthropogenic Perturbations since 1290 CE. *Palaeogeogr. Palaeoclimatol. Palaeoecol.* 534, 109285. doi:10.1016/j.palaeo.2019.109285

Wulf, S., Kraml, M., Brauer, A., Keller, J., and Negendank, J. F. W. (2004). Tephrochronology of the 100ka lacustrine sediment record of Lago Grande di Monticchio (southern Italy). *Quat. Int.* 122 (1), 7–30. doi:10.1016/j.quaint.2004.01.028

Zanon, V., Pimentel, A., Auxerre, M., Marchini, G., and Stuart, F. M. (2020). Unravelling the Magma Feeding System of a Young Basaltic Oceanic Volcano. *Lithos* 352-353, 105325. doi:10.1016/j.lithos.2019.105325

Zanon, V., and Pimentel, A. (2015). Spatio-temporal Constraints on Magma Storage and Ascent Conditions in a Transtensional Tectonic Setting: the Case of the Terceira Island (Azores). *Am. Mineral.* 100 (4), 795–805. doi:10.2138/am-2015-4936

Conflict of Interest: The authors declare that the research was conducted in the absence of any commercial or financial relationships that could be construed as a potential conflict of interest.

Publisher's Note: All claims expressed in this article are solely those of the authors and do not necessarily represent those of their affiliated organizations, or those of the publisher, the editors and the reviewers. Any product that may be evaluated in this article, or claim that may be made by its manufacturer, is not guaranteed or endorsed by the publisher.

Copyright © 2021 Andrade, Ramalho, Pimentel, Hernández, Kutterolf, Sáez, Benavente, Raposeiro and Giralt. This is an open-access article distributed under the terms of the Creative Commons Attribution License (CC BY). The use, distribution or reproduction in other forums is permitted, provided the original author(s) and the copyright owner(s) are credited and that the original publication in this journal is cited, in accordance with accepted academic practice. No use, distribution or reproduction is permitted which does not comply with these terms.

frontiers in Earth Science

ORIGINAL RESEARCH
published: 18 October 2021
doi: 10.3389/feart.2021.713444

Eruption Sequences and Characteristics of Weizhou Island Volcano, Guangxi Province, South of China

Hongmei Yu[1,2]*, *Wenjian Yang*[1,2], *Bo Zhao*[1,2], *Zhengquan Chen*[1,2], *Bin Zhou*[3], *Guanjun Nie*[3] *and Hao Luo*[4]

[1]National Observation and Research Station of Jilin Changbaishan Volcano, Institute of Geology, China Earthquake Administration, Beijing, China, [2]Key Laboratory of Seismic and Volcanic Hazards, China Earthquake Administration, Beijing, China, [3]Guangxi Earthquake Agency, Nanning, China, [4]China Earthquake Disaster Prevention Center, Beijing, China

Weizhou island, located in the north margin of the South China Sea (SCS), is characterized by multi-stage volcanism, several eruption styles and eruption craters, and is also the youngest Quaternary volcanic island in China. An eruption on this island may pose high risk to life and property. However, the eruptive history of Weizhou island, the craters number and location, and their eruptive sequence and characteristics are still being debated, which are important for potential volcanic hazard assessment. In the present study, field surveys, $^{40}Ar/^{39}Ar$ and ^{14}C geochronological studies and whole rock composition analysis of volcanic rock are used to investigate the eruption sequences associated with Weizhou island and the characteristics of each period. Four volcanoes were discovered at Henglushan, Hengling, Nanwan and Daling. The Henglushan and Hengling volcanoes were produced by early weak explosive and late effusive eruptions, and lavas from these volcanoes represent the foundation of island. Conversely, the Nanwan and Daling volcanoes are linked to multiple explosive eruption phases, with hydromagmatic eruptions in the first and last phase and a magmatic explosive eruption in the second phase. The pyroclastic density currents (PDCs) deposits of the Nanwan and Daling volcanoes virtually cover the entire island. Volcanic activity in Weizhou island started in Early Pleistocene and ended in Late Pleistocene. This can be divided into the following distinct periods: 1,420–1,260, 870–740, 600–480, 283–222 ka, and 33.7–13 ka. The first four periods were dominated by effusive eruptions associated with the Henglushan and Hengling volcanoes, which peaked between 870 and 740 ka. After this period, explosive eruptions began at around 33.7 ka because of magma–water interactions. These explosive eruptions then created the Nanwan and Daling volcanoes. Early effusive lava flows in Weizhou island are characterized by basaltic compositions and are linked with a small amount of fractional crystallization. Magmas in later eruptions contained slightly lower SiO_2 and involved some basanite. Fractional crystallization was also less pronounced in these lavas because of their rapid ascent.

Keywords: eruption sequence, effusive eruption, explosive eruption, base-surge deposits, Weizhou Island volcano

OPEN ACCESS

Edited by:
Joan Martí,
Consejo Superior de Investigaciones Científicas (CSIC), Spain

Reviewed by:
Dario Pedrazzi,
Instituto de Ciencias de la Tierra Jaume Almera (ICTJA), Spain
Marie-Noelle Guilbaud,
National Autonomous University of Mexico, Mexico

****Correspondence:***
Hongmei Yu
yuhongmei@ies.ac.cn

Specialty section:
This article was submitted to Volcanology, a section of the journal Frontiers in Earth Science

Received: *23 May 2021*
Accepted: *01 October 2021*
Published: *18 October 2021*

Citation:
Yu H, Yang W, Zhao B, Chen Z, Zhou B, Nie G and Luo H (2021) Eruption Sequences and Characteristics of Weizhou Island Volcano, Guangxi Province, South of China. Front. Earth Sci. 9:713444. doi: 10.3389/feart.2021.713444

1 INTRODUCTION

The area around Leiqiong (Leizhou Peninsula and Hainan Island) and Beibu Gulf in the north margin of the South China Sea (SCS) was formed during the late expansion stage of the SCS Basin **(Figures 1A,B)**. This region is the largest Quaternary volcanic field in South China and includes Weizhou island in Beibu Gulf (Fan et al., 2006), which is approximately 37 km (20 sea mile) away from Beihai city in Guangxi province **(Figure 1B)**. This island is the youngest Quaternary volcanic islands in China (Li et al., 2005; Huang and Li, 2007), and it covers an area of approximately 25 km^2 and reaches a maximum elevation of 79 m asl. The Xieyang island, a small (< 2.0 km^2) associated island, is approximately 14 km southeast of Weizhou island. Both islands contain hydromagmatic and ocean erosion features which are exploited for tourism. Consequently, the Weizhou island Volcano National Geopark was established in 2004 to preserve these unique features. Weizhou island hosts almost 20,000 residents and it is visited by thousands of tourists daily, and thus an eruption on the island may pose high risk to life and property.

Understanding the history, sequences, and characteristics of eruptions that occurred in Weizhou island is necessary for volcanic hazard assessment. Small oceanic islands are particularly vulnerable to explosive eruptions and the risk is potentially aggravated by their geographical isolation and the weak socioeconomic conditions of local communities (Pimentel et al., 2021). Therefore, detailed studies are needed to widen our understanding of Weizhou island eruptions and their potential impacts.

Weizhou island is characterized by elevated terrain in the south and low-lying terrain in the north. Volcanic rocks in Weizhou island are dominated by alkaline basalts, which exhibit the Dupal isotopic anomaly and geochemical characteristics that are consistent with those of ocean island basalts (OIBs) formed by mixing of the DM and EMII mantle components (Fan et al., 2008; Xu et al., 2012; Yang et al., 2020; Zhang et al., 2020). According to previous studies (Li and Liu, 1991; Lu, 1993; Li and Fang, 2004; Fan et al., 2006), the formation of Weizhou island involved multi-stage volcanism, characterized by several eruption styles, which produced several volcanoes. Rao (1988) suggested the presence of two volcanoes in Weizhou island, with one at sea level, 500 m away from the south of Nanwan, and another in Hengling in the east of the island. Based on the distribution, tectonic characteristics, and topographic features associated with volcanic rocks in Weizhou island, Lu (1993) reported three volcanoes in Henglushan, Nanwan, and Daling. However, Li et al. (2005) proposed that the craters locations are at Henglushan, Nanwan, and Eyuzui (also called Eyushan). Thus, the number, locations, and association between these volcanoes are still being debated.

Based on their characteristics and relationships, volcanic strata in Weizhou island can be partitioned into the following groups: 1) Early Pleistocene Zhanjiang Formation volcano-sedimentary rocks, 2) Middle Pleistocene Maoling Formation flood basalts and pyroclastics, 3) Late Pleistocene Huguangyan Formation basaltic pyroclastics, and 4) Holocene Eyushan Formation flood basalts and pyroclastics (Li and Fang, 2004; Li et al., 2005). Because chronological evidence is generally lacking in previous studies, the assigned volcanic-activity periods in Weizhou island require additional investigation.

In the present study, field surveys, geochronological study and whole rock composition analysis of volcanic rock are used to investigate the eruption sequences associated with Weizhou island and the characteristics of each period, and to reconstruct the eruptive history and evolution of Weizhou island. The findings of the present study provide a scientific basis for eruption forecasting for this island.

2 GEOLOGICAL BACKGROUND

The SCS is the largest marginal sea in East Asia. It is in the convergence area of the Indo–Australian, Eurasian, and Pacific plates, which represents the junction between the Pacific and Tethyan Tectonic Domains (Zhou et al., 2008). Expansion of the SCS started at around 32 Ma and lasted until 16 Ma (Briais et al., 1993). Owing to mid-oceanic ridge assimilation processes, expansion basalts (32–16 Ma) are rare around the SCS (Huang et al., 2013; Zeng et al., 2017). Conversely, in the north periphery of the SCS and Indochina region, wide distribution of post-expansion volcanic rocks (<16 Ma) is present (Yan et al., 2014, 2018; **Figure 1A**). The southeast end of the major right lateral-slip Red River Fault originating from the southeast margin of the Tibetan Plateau traverses the study area, and extends to the north margin of the SCS Basin (Chung et al., 1997; Hao et al., 2001; Yan et al., 2006). According to Jia et al. (2003), basalts in the Beibu Gulf Basin and volcanic rocks of the Red River Fault originate from the same mantle source. The Red River Fault was transformed from a left lateral-slip to a right lateral-slip fault around 5.5 Ma (Leloup et al., 1995; Replumaz et al., 2001; Clift and Sun, 2006; Wang et al., 2016), and this tectonic change likely caused mantle perturbations, which triggered magmatic activities to form Weizhou island (Jia et al., 2003). However, the Hainan mantle plume revealed by geophysical and geochemical data likely influenced Late Cenozoic magmatism in the SCS and its periphery significantly (Montelli et al., 2006; Lei et al., 2009; Yan and Shi, 2007; Yan et al., 2008; Wang et al., 2012; Xia et al., 2016; Kimura et al., 2018).

Based on a comparison of rocks and lithologic characteristics of the Nanwan and Huguangyan volcanoes in Zhanjiang, Guangdong, Liu (1986) indicated that the former likely formed during Pleistocene but the exact period was undetermined. In a study involving boreholes (Bureau of Geology and Mineral Resources of Guangxi, 1985; Li and Liu, 1991; Lu, 1993), the onset of volcanism in Weizhou island is assigned to Early Pleistocene, with distinct evolution in the Early, Middle, and Late Pleistocene. However, because the boreholes did not penetrate igneous rocks, the occurrence of volcanic eruptions prior to the Pleistocene in the island remains undetermined. Based on basalt samples from the intertidal zone in Weizhou island, Long et al. (2004) attributed the earliest volcanic activities in the island to the Neogene or slightly later. Field surveys, volcanic rock characteristics, K–Ar dating, optically stimulated

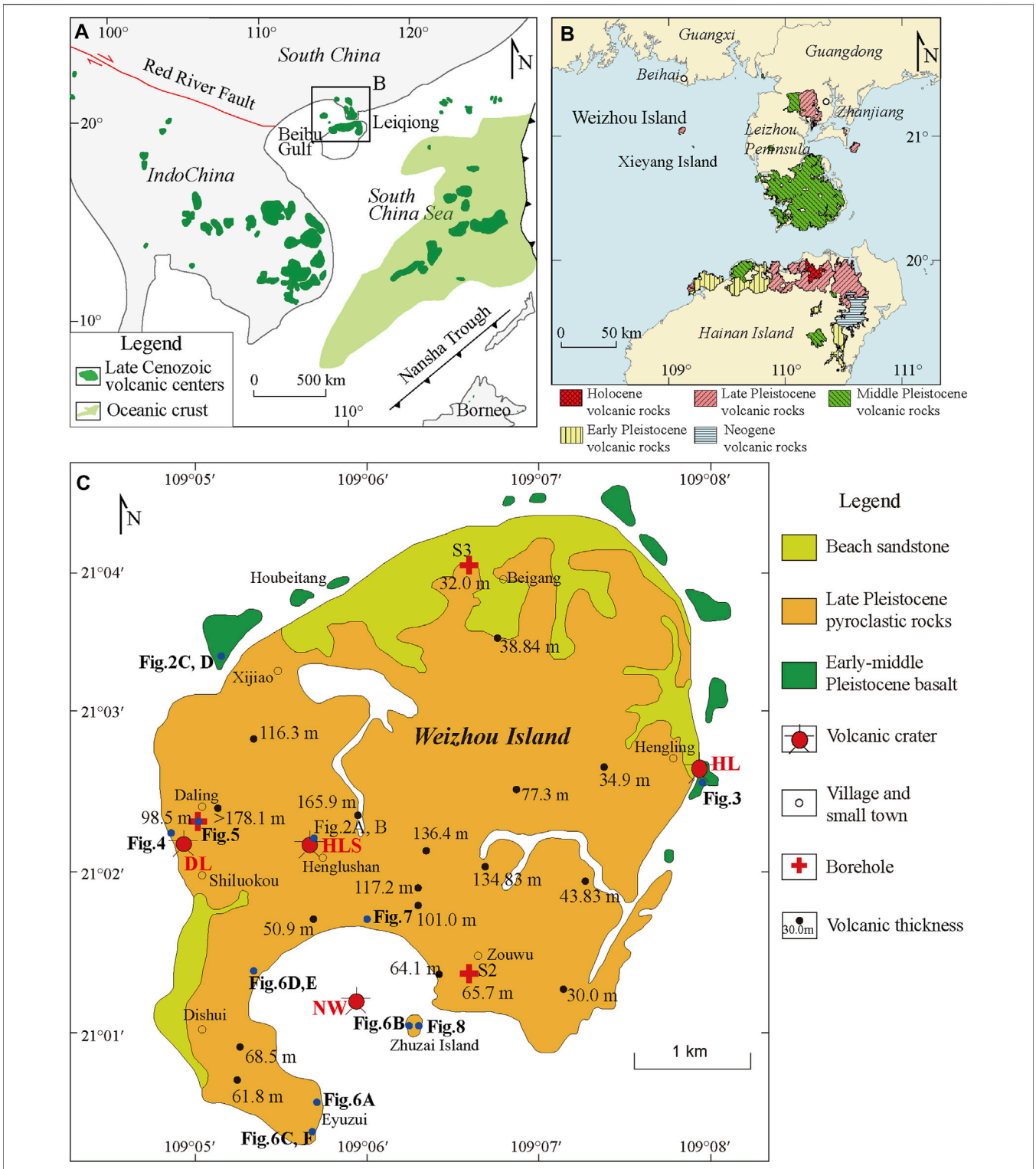


FIGURE 1 | (A) Distribution of Late Cenozoic basalts in the SCS and its periphery (Yan et al., 2018). **(B)** Quaternary volcanic rocks distribution of Leiqiong and the surrounding area of Beibu Gulf, southern China (modified from) **(C)** Geological map of volcanoes on Weizhou island (modified from Fan et al., 2006; parts of the drilling depths are from Lu, 1993). HLS-Henglushan volcano, HL-Hengling volcano, DL-Daling volcano, NW-Nanwan volcano.

luminescence (OSL) dating of sandstone xenoliths, and mollusk shell ^{14}C dating data were used by Fan et al. (2006) to divide volcanic eruptions in Weizhou island into the following: Early–Late Pleistocene effusive (1.42 Ma–0.49 Ma) and Late Pleistocene hydromagmatic (36–33 ka) styles (**Figure 1C**). Further, Xu et al., 2020 used electron spin resonance (ESR) to date PDCs deposits and obtained ages between 33 and 13 ka. Based on these data, they suggested that the last volcanic eruption in Weizhou island occurred during the Late Pleistocene.

3 MATERIALS AND METHODS

3.1 Field Survey and Sampling

Field surveys were conducted to determine the locations and number of volcanoes in Weizhou island based on indicators, such as scoria cones, welded agglomerates, welded breccia and volcanic bombs. Profile maps were created by mapping the distribution of ejecta, and these were used to analyze the eruption sequences and characteristics in Weizhou island. According to the volcanic strata, clastic grain size and petrographic characteristics, we have defined the eruption style. The products from each volcano were then systematically sampled. Three drill cores were also acquired from Daling, Zouwu (**Figure 1C**, S2), and Beigang (S3).

3.2 Dating Methods

The ages of Weizhou island volcanoes were constrained using the $^{40}Ar/^{39}Ar$ and ^{14}C geochronological methods.

3.2.1 $^{40}Ar/^{39}Ar$ Dating

Eleven basalts and basalts xenoliths from PDCs deposits were selected for the $^{40}Ar/^{39}Ar$ dating. A cutting machine was used to scrape weathered and potentially contaminated surfaces of the basalts, followed by crushing. Particles with sizes between 180 and 250 μm were then screened, and phenocrysts were removed using a magnetic separator, leaving behind just the matrix. Next, the matrix particles were digested using HCl, HNO_3, and HF, followed by drying in an oven at 50°C for 24 h. The dried samples were then screened again to obtain particles with sizes between 180 and 250 μm, and remnants of phenocrysts were removed with the aid of a microscope. Samples were then cleaned using acetone and stored in a glass jar for subsequent analyses. Samples were analyzed by irradiation in a TRIGA reactor and Ar–Ar geochronology using an ARGUS-VI mass spectrometer in Oregon State University (OSU). All ages were calculated using ArArCALC v.2.7.0 software (Koppers, 2002), and uncertainties are reported at the 2σ confidence limits.

3.2.2 ^{14}C Dating

Charcoal clasts measuring approximately 5 cm in diameter were encountered at a depth of 175.7 m in the borehole drilled in Daling. Some of these clasts were sent to the BETA Laboratory in Miami, Florida United States for ^{14}C dating, where measurements were performed using a NEC accelerator mass spectrometer and a Thermo Fisher isotope ratio mass spectrometer. The age was calibrated based on the INTCAL13 database on BetaCal3.21 software with 2σ (95% confidence limits). The age in this paper is calendar year obtained from conventional radiocarbon ages.

4 RESULTS

4.1 Weizhou Island Volcanoes and Eruption Styles

In the present study, the four volcanoes identified during field surveys are the Henglushan, Hengling, Nanwan, and Daling, and these exhibit distinct eruption characteristics and are associated with different eruption styles.

4.1.1 Henglushan Volcano

The Henglushan volcano is a central volcano, and located near Guogailing, Henglushan in the mid-western part of Weizhou island (**Figure 1C**). Guogailing is a shield-like plateau with a diameter of approximately 1 km and an elevation of 60 m. Welded agglomerates with the pyroclastic size between 2 and 10 cm are present on top of Guogailing, while volcanic bombs approximately 60 cm in diameter are near Guogailing (**Figures 2A,B**); these are typical features of proximal faces. The Henglushan volcano was formed mainly by effusive central eruptions. Borehole data reveal a maximum basalt thickness of 165 m, and this is characterized by thinning with increasing distance from the volcano (**Figure 1C**). Lavas from this volcano likely provided the foundation for the formation of Weizhou island. Lava flows in intertidal zones in the southwest and north parts of Weizhou island were mostly derived from eruptions of the Henglushan volcano, with the significant weathering of these spheroidal lava bodies indicating that they originated from ancient volcanic eruptions (**Figures 2C,D**).

4.1.2 Hengling Volcano

Hengling volcano is located near Hengling in the central eastern part of Weizhou island (**Figure 1C**). Indurated volcanic breccias with size of 0.5–2 cm extending for approximately 100 m are observed at a beach near Hengling. These breccias display banded distribution and contain volcanic bombs with diameters ranging between 10 cm and 1 m (**Figures 3A,B**), indicating a location near a vent or crater. Although the indurated volcanic breccias are rounded by weathering, breccias with centimetric lengths remain clearly visible (**Figures 3C,D**). Owing to severe weathering and erosion, distinguishing bombs from spheroidal weathered basalts is difficult. This probably explains the rare mention of a volcano in this location except by Rao (1988) among previous studies. The vent(s) may be eroded or under the sea level. Eruptions associated with the Hengling volcano were also dominantly effusive and the lava can be seen around Hengling volcano.

4.1.3 Daling Volcano

The Daling volcano is in the mid-western part of Weizhou island (**Figure 1C**), near the shore, and the base of the volcano is at an elevation of 50 m. Welded agglomerates and large volcanic bombs are present in the Shiluokou beach, near Daling (**Figure 4A**);

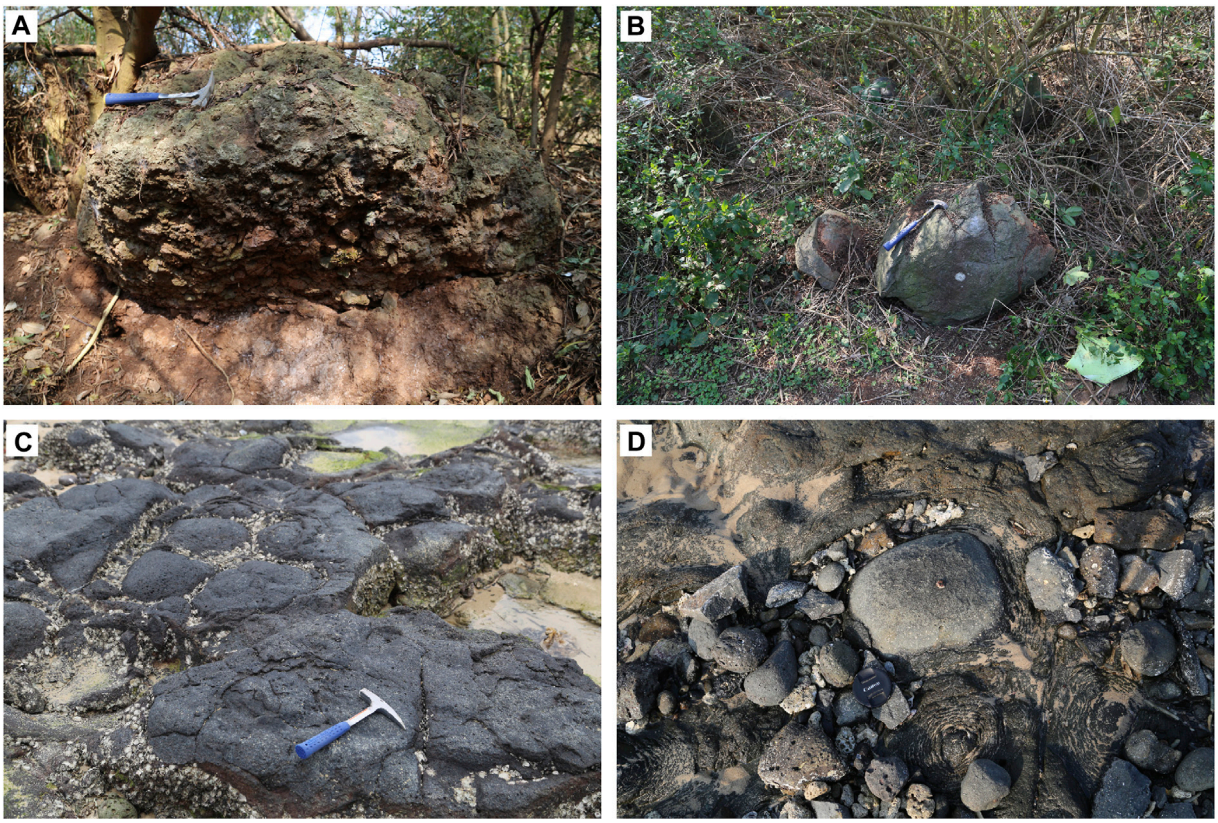


FIGURE 2 | Field photographs of volcanic products from Henglushan Volcano. **(A)** Welded agglomerates on the top of Guogailing at Henglushan. **(B)** Volcanic bomb with a diameter around 60 cm close to Guogailing. **(C)** Outcropping lava bodies in Xijiao intertidal zone. **(D)** Outcropping spheroidal weathered basalts in Xijiao intertidal zone.

these features are indicators of a nearby volcano. Lu (1993) used geomorphological features, fault structures, and drill core data to confirm the presence of a volcano in this location. The vent(s) of Daling volcano may also be eroded or under the sea level. In the southwestern shore, thick PDCs deposits (from hydromagmatic eruptions) characterized by numerous cross-bedding, oblique bedding, and U-shaped grooves are present (**Figures 4B–D**). In addition, palagonitized brown–yellow tephra clasts are observed in the fallout strata produced by magmatic eruption (**Figure 4B**).

A borehole with depth of 391 m was drilled in Daling and the observed stratigraphy is as follows (**Figure 5**): Dark red clays are present at between 0 and 33 m depth, followed by pyroclastic layers at between 33 and 132.5 m depth, with yellow/grey–yellow strongly weathered layer at the shallow level and grey/grey–black slightly weathered layer at the deeper level, and soft mudstones, sandstones, and clay below 132.5 m.

4.1.4 Nanwan Volcano

The Nanwan volcano in the southern part of Weizhou island is almost circular, with a diameter of approximately 2 km, and it represents a maar formed by a hydromagmatic eruption. The south crater wall is missing, probably because of wave erosion or later volcanic activity, whereas well-preserved north, west, and east crater walls appear as vertical cliffs, thereby imparting an armchair-like shape to the volcano. PDCs deposits from the hydromagmatic eruption are distributed around the preserved crater walls. Proximal spatter deposits, such as lava cakes, volcanic bombs and welded volcanic breccias (**Figures 6A,B**) are also present around the crater walls as well as bean-sized accretionary lapilli (**Figure 6C**) and bomb sags (**Figures 6D,E**). Climbing structure was observed in Eyuzui in the south of Nanwan, and the change of the strata inclinations supports that Nanwan is a volcano with several vents (**Figure 6F**). Considering that the Tianhougong and Zhuzai island profiles in the north and east, respectively, of the Nanwan volcano are the nearest well-preserved stratigraphic profiles, these were analyzed to decipher the eruption sequences of the Nanwan volcano.

4.1.4.1 Tianhougong Stratigraphic Log

The Tianhougong stratigraphic log comprises thick PDCs deposits, scoria, and spatter deposits, with a thickness of approximately 24 m. This stratigraphic log can be separated into the following three layers (**Figure 7**):

Layer I: This layer involves yellow PDCs deposits, which consist of quartz, feldspar and a little black scoria. It is consolidated and develops multiple coarse and fine-grained rhythmic characteristic. It has typical base-surge deposits

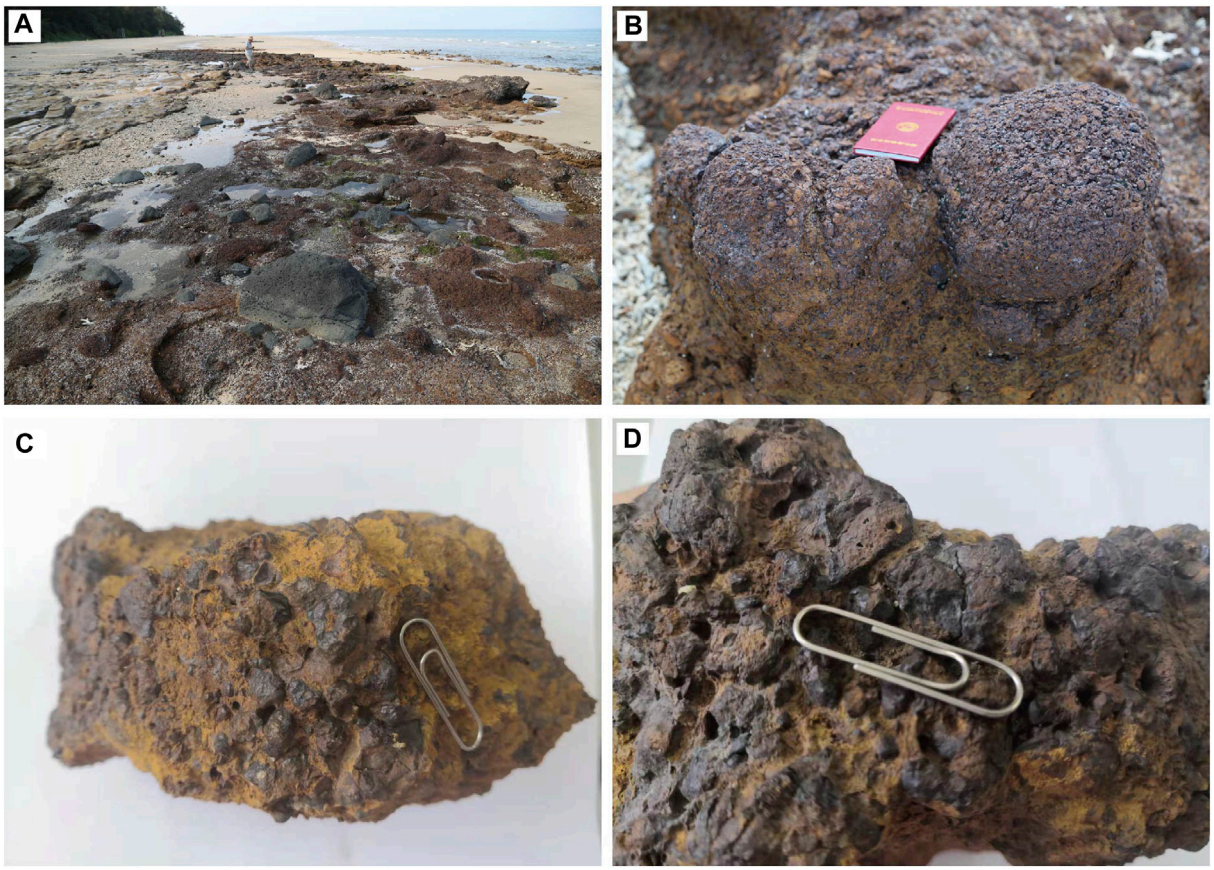


FIGURE 3 | Field photographs of Hengling volcano products. **(A)** Banded volcanic breccias and volcanic bombs inside the breccias. **(B)** Spheroidal weathered indurated volcanic breccias. **(C)** Indurated volcanic breccias with weathered matrix. **(D)** Volcanic breccias with diameter of 0.5–2 cm.

structures, such as cross- and oblique bedding, bomb sag structures. It is approximately 18 m thick.

Layer II: The top part of this layer consists of grey–black scoria and volcanic bombs, and exhibits non-uniform thickness (approximately 2 m on average). The bottom part contains a brown–yellow scoria stratum that is approximately 2 m thick. This layer was formed by an explosive eruption. A palagonitized brown–yellow surface was created by early interactions between hot scoria and water, but this scoria–water interaction significantly decreased later, thereby producing a grey–black scoria stratum.

Layer III: This layer contains 1–2 m thick brown–yellow base-surge deposits, characterized by weathering at the top. The degree of consolidation is weaker than layer I and the content of quartz reduces.

4.1.4.2 Zhuzai Island Stratigraphic Log

The Zhuzai island stratigraphic log is thinner than the one Tianhougong, with a thickness of 10.2 m (**Figure 8**). It also comprises PDCs deposits, scoria, and spatter deposits, which also produce three layers.

Layer I: This 3.5 m thick layer contains PDCs deposits involving cross- and oblique bedding, bomb sags but the bottom part of the layer is unexposed. It is consolidated and develops multiple rhythem.

Layer II: This layer involves proximal faces tephra deposits, with the top 2 m comprising grey–black scoria, volcanic bombs, and lava cakes, while the bottom 2.2 m contain brown–yellow scoria. The scoria is fused together in a plastic state, which formed welded volcanic breccias (**Figure 6B**).

Layer III: This 2.5 m thick layer contains base-surge deposits characterized by cross-and oblique bedding and weathering at the top.

The layers are consistent with those in the Tianhougong stratigraphic log and indicate that the Nanwan volcano is associated with three phases of activity, with the first and third being hydromagmatic, while the second was magmatic.

4.2 S2 and S3 Boreholes

The stratigraphy of the S2 borehole (**Figure 9A**), which extends to a depth of 73.4 m is as follows: Thick grey–yellow and grey–black tuff with bedded and tuff structures are present at 5.0–37.5 m, followed by a thick basalt layer at 37.5–70.7 m, and which is characterized by severe weathering and cracks filled with welded volcanic breccia at 37.5–40 m. In fact, some breccia has been weathered to soil, with widespread joints and fractures at

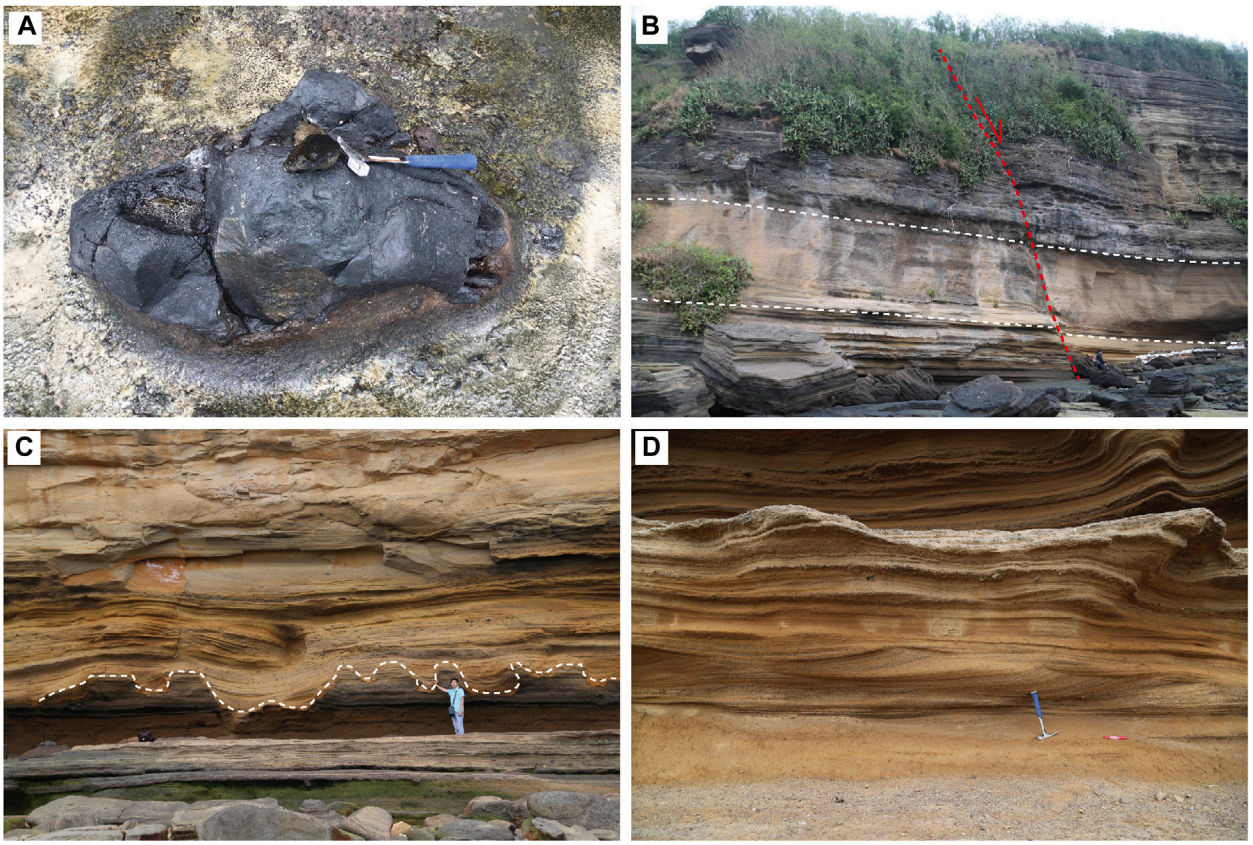


FIGURE 4 | Field photographs of Daling volcano deposits. **(A)** Indurated agglomerates with a baking layer. **(B)** An approximately 30 m-thick profile of Shiluokou, with PDCs deposits on the top and bottom of the profile and tephra-fall pyroclastics in between. These strata are separated by a normal fault. **(C)** U-shaped grooves. **(D)** Cross and oblique beddings in the PDCs strata.

40.0–43.8 m causing fragmentation of cores at this depth interval. Highly dense grey–black basalts with localized vesicles occur at 43.8–45 m, while the interval at 45.0–62.1 m contains yellow–brown vesicular basalts with localized vesicles. Beneath this layer, dense basalts are present at 62.1–63.5 m, while grey–green basalts with cracks and joints are present at 63.5–67.0 m, and grey–green dense basalts involving joints and cracks are present at 67.0–70.7 m.

Borehole S3 (**Figure 9B**) was drilled to a depth of 66.8 m and it revealed grey–yellow and grey–black tuff at 2.1–9.5 m, while interbedded vesicular basalts approximately 23 m thick occur at 9.5–31.8 m. The interval at 9.5–12.7 m is dominated by grey–black vesicular basalts, while dense block-like basalts dominate at 12.7–22.0 m. In the interval at 22.0–25.5 m, purple–red and yellow–brown vesicular basalts filled with green mudstone are prevalent, whereas at 25.5–31.8 m, grey–black dense block-like basalts predominate, and yellow–grey tuffs and breccias occurring are present at 31.8–34.1 m.

These boreholes reveal that earlier volcanic activities in Weizhou island were mainly associated with effusive eruptions which generated lava flows, whereas later volcanic activities were linked to explosive eruptions which produced pyroclastics. The lavas split into different units during cooling, with the top portion forming vesicular basalts while the bottom portion produced dense basalts.

4.3 Dating Results

The basalt $^{40}Ar/^{39}Ar$ dating data for Weizhou island that were generated in the present study are presented in **Table 1**. The $^{40}Ar/^{39}Ar$ ages are in range of 868.5 ± 25.4 ka–222.1 ± 14.3 ka and most are 762.6 ± 7.3–740.5 ± 3.4 ka, which are consistent with the results of previous K-Ar ages (Feng, 1992; Fan et al., 2006). The ages of dense basalt are general 740.5–744.3 ka, but the basalt xenolith ages in pyroclastic rocks are in a wide range. Charcoal clasts collected at a depth of 42 m from a borehole in the Daling volcano yielded a ^{14}C age of 33,390 ± 200 years BP (**Figure 5**).

5 WEIZHOU ISLAND LAVA COMPOSITIONS

Here, we analyze the compositions of lavas in Weizhou island based on whole-rock data reported in previous studies (Li et al., 2005; Fan et al., 2008; Yang et al., 2020). Owing to difficulty to distinguish products from the Henglushan and Hengling volcanoes, and as their eruption periods are comparable, their lavas are simply referred as

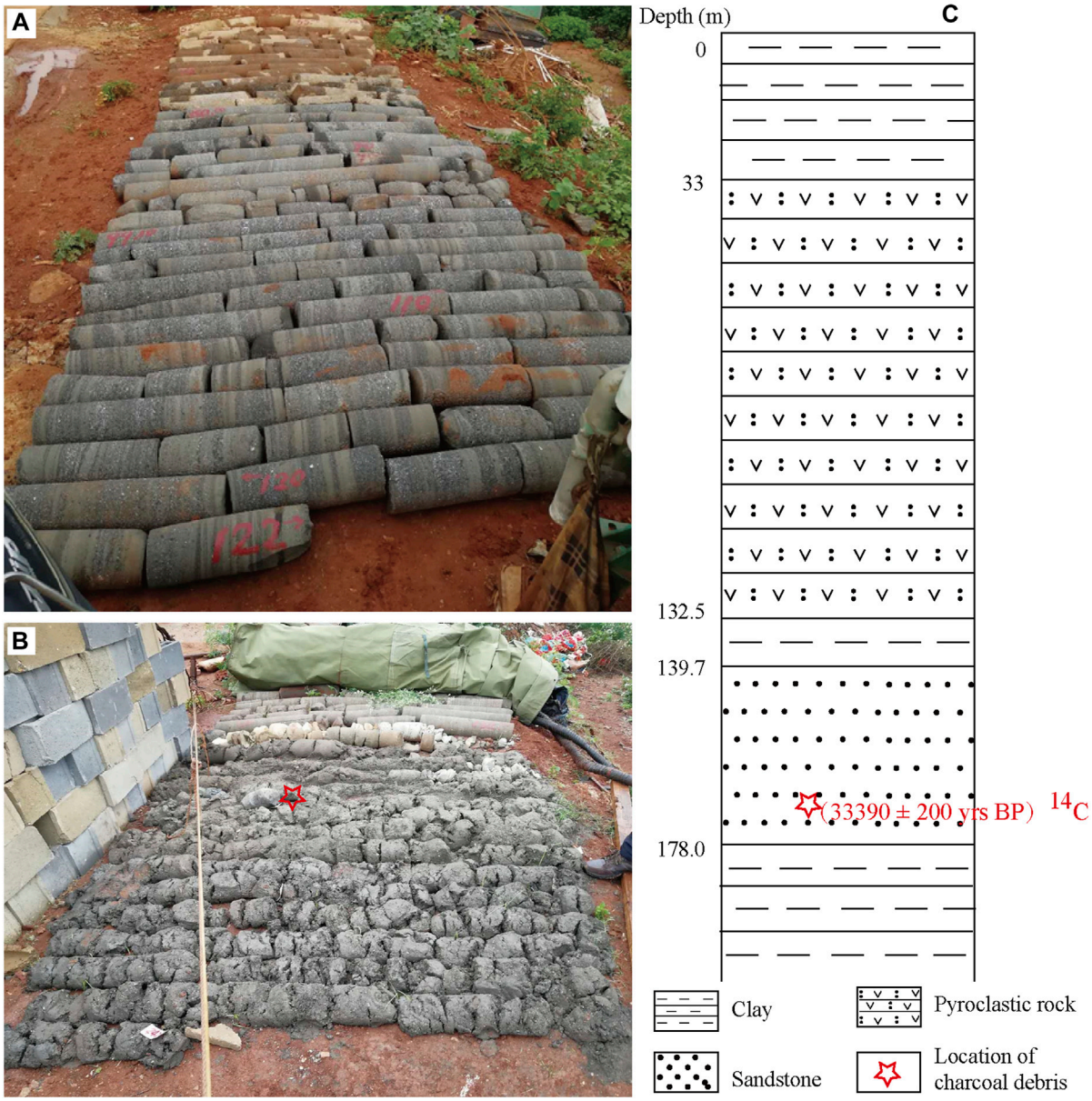


FIGURE 5 | Drilled core from Daling. **(A)** Upper part of the core. **(B)** Lower part of the core. **(C)** Stratigraphic column of the Daling borehole.

"Henglushan lava" in the present analysis. The major element measurements of Daling volcano samples are excluded because of significant high ignition loss (Yang et al., 2020). The Henglushan and Nanwan lavas exhibit some compositional differences. Whole-rock SiO_2 and $Na_2 + K_2O$ contents rocks from the Henglushan volcano range between 44.79–50.56 wt% and 3.25–5.45 wt%, respectively, which correspond to trachybasalt and basalt in the total–alkali–silica (TAS) diagram (**Figure 10A**). Nanwan igneous rocks show overlapping to lower SiO_2 contents (41.61–48.67 wt%) and overlapping to higher $Na_2O + K_2O$ contents (3.75–6.01 wt%), and these fall within the trachybasalt and basanite fields (**Figure 10A**). Microscopy revealed a basaltic matrix with an intergranular texture and rich in olivine (about 5–10%), pyroxene (<5%), and plagioclase (about 5%) microcrystals (**Figure 10B**). In contrast, the basanite matrix is vitreous and pitch black under crossed polarized light, and it contains few microcrystals (**Figure 10C**). Earlier lavas likely experienced fractional crystallization (Yang et al., 2020), but the impact was significantly diminished in later lavas because of the rapid rising and ejection.

Chondrite-normalized rare earth element (REE) diagrams show that data for samples from the Nanwan and Henglushan volcanoes coincide and exhibit light REEs enrichment; the rocks display no significant Eu anomaly (**Figure 11A**). The Henglushan basalts show slightly lower total REE ($\sum$REE) and $(La/Yb)_N$ values compared to the Nanwan volcano rocks, which suggest primitive magmas of the later were associated with higher partial melting. In the primitive mantle-

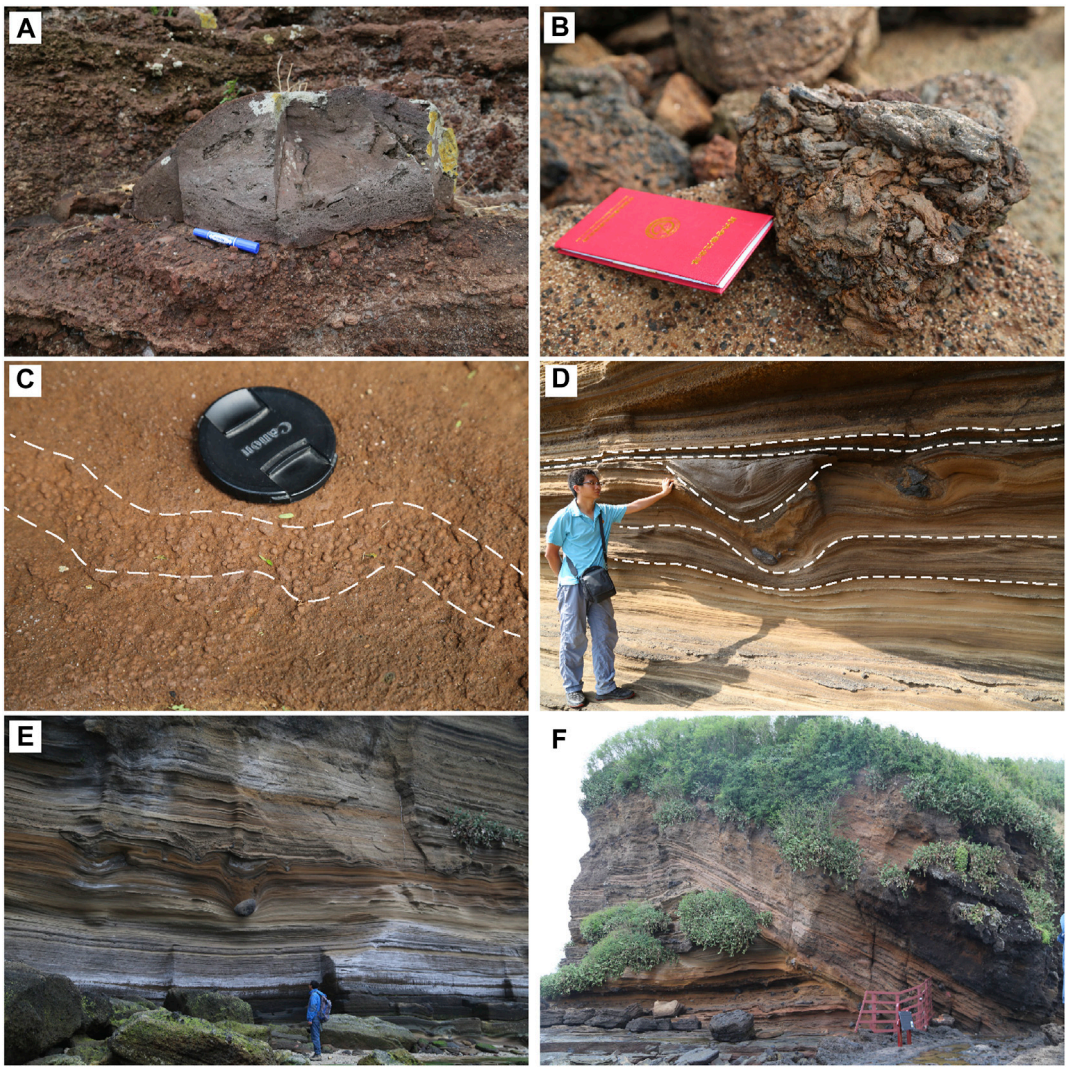


FIGURE 6 | Field photographs of Nanwan volcano deposits. **(A)** Volcanic bomb in brick-red spatter deposits inside the crater walls of Nanwan Volcano. **(B)** Welded breccias on the eastern side of Zhuzai island. **(C)** Outcropping accretionary lapilli at the bottom of the PDCs deposits at Eyuzui; Accretionary lapilli are spherical aggregates of volcanic ash, commonly having a concentric structure and formed by clumping of moist ash (Yan et al.,2008; Sigurdsson et al., 2015). **(D)** Bomb sag structure near Dishui, where volcanic bombs fell into the underlying plastic layer and created cratered surfaces. **(E)** Thick PDCs deposits and bomb sag structure. **(F)** Climbing structure at Eyuzui.

normalized trace element spider diagram, data for rocks in the region display significant positive Nb–Ta anomalies and negative Pb anomalies, with the later quite prominent in data from the Henglushan basalts (**Figure 11B**). These characteristics are consistent with OIBs devoid of crustal magma contamination.

6 DISCUSSION

6.1 Weizhou Island Volcanic Eruption Styles and Sequences

The welded agglomerate, volcanic bombs at the top of Guogailing and large areas of lava indicating the eruption styles of Henglushan were early weak explosive and late effusive eruptions. Based on the borehole data, the thickest igneous rocks deposits in the island are in Henglushan, and thinning with increasing distance away (**Figure 1C**). Therefore, the earliest lavas in Weizhou island probably originate from the Henglushan volcano. The average $^{40}Ar/^{39}Ar$ age of dense basalts near the Henglushan volcano is 762.6 ± 7.3 ka, while that for lavas in the intertidal zone near Xijiao (western shore) is 744.3 ± 5.1 ka, and these ages are consistent with K–Ar ages (0.79–0.60 Ma) measured by Fan et al. (2006) for the Guogailing basalts. $^{40}Ar/^{39}Ar$ ages of basalt samples from a depth of 43.8 in Borehole S2 and 26 m in Borehole S3 are 745.0 ± 6.1 ka and 760.0 ± 4.4 ka, respectively. Therefore, these samples are most likely volcanic products belonging to contemporaneous volcanic activities in the island. Although Lu (1993) reported thick basalts in a borehole

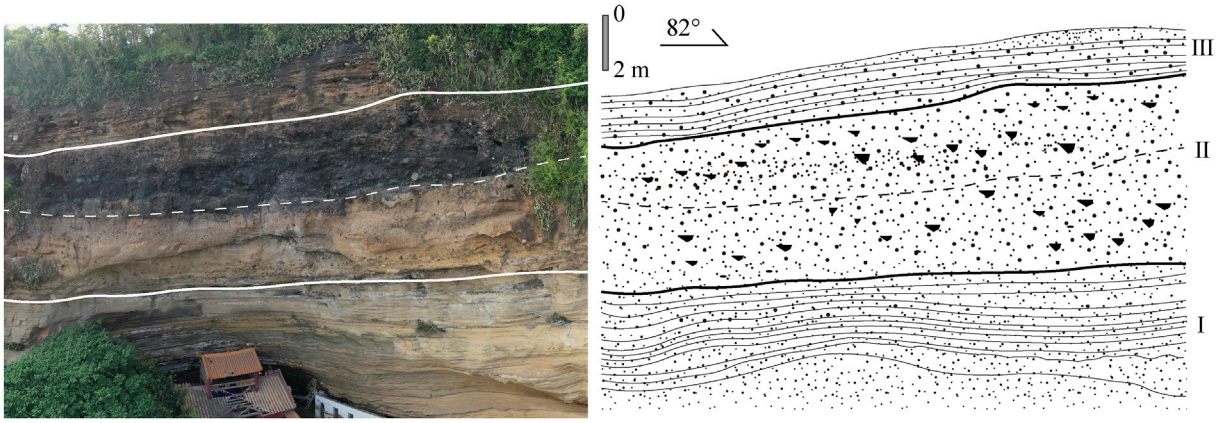


FIGURE 7 | Stratigraphic log at Tianhougong.

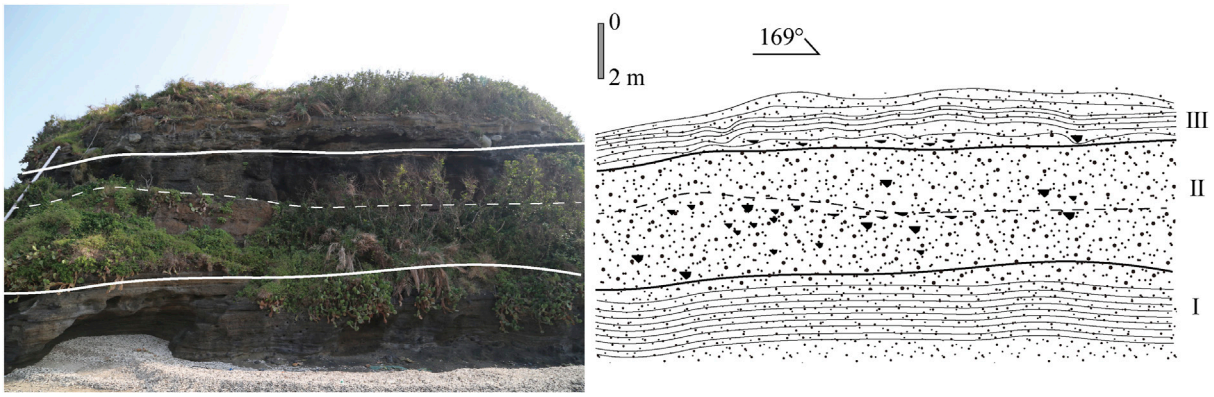


FIGURE 8 | Stratigraphic log at Zhuzai island.

near Daling, the borehole drilled in Daling in the present study revealed only pyroclastics. Considering the proximity of Daling to Henglushan, the lavas which solidified near Daling likely flowed from the Henglushan volcano. Fan et al. (2006) measured a K–Ar age of 1.42 ± 0.12 Ma using basalt xenoliths from clasts in Shiluokou, Daling; these products are likely from the earliest eruption in Henglushan. Since the $^{40}Ar/^{39}Ar$ ages of basalt xenoliths from the Daling borehole (depth of 73.6 m) and Shiluokou clasts are 868.5 ± 25.4 ka and 870.3 ± 34.3 ka, these were probably formed after eruption of the Henglushan volcano. Since eruptions in the Nanwan volcano were explosive and the lava thicknesses in the Nanwan borehole are consistent with effusive lava flows from the Henglushan volcano, the basalt xenoliths in the Nanwan pyroclastics may also originate from the Henglushan volcano. $^{40}Ar/^{39}Ar$ ages of these basalt xenoliths represent eruptions in the Henglushan volcano during different periods. Hence, the Henglushan volcano is linked to multiple effusive eruptions, and the earliest and latest eruptions likely occurred at around 1.42 ± 0.12 Ma and 222.1 ± 14.3 ka, respectively. The most voluminous among these eruptions occurred between 870 and 740 ka.

The products of Hengling volcano are similar to Henglushan volcano, and the eruption styles were also early weak explosive and late effusive eruptions. Although proximal features are present in Hengling, the distribution range of lava flows generated by this volcano still requires accurate determination. Owing to its proximity to the shore, some of its lavas are probably on the seafloor. The $^{40}Ar/^{39}Ar$ age of the dense lavas that were sampled in this location is 747.4 ± 10.4 ka; this age is comparable to that obtained for the most voluminous eruption in the Henglushan volcano. Therefore, intense volcanic activity occurred in Weizhou island between 870 and 740 ka, and two active volcanoes were present in the island during this period.

Data from the Daling borehole reveal that the two hydromagmatic and one magmatic explosive eruption occurred at the Daling volcano. Pyroclastics produced in these eruptions are mainly in the southwest of the island. Considering that pyroclastics in the Daling borehole are almost 100 m thick (**Figure 1C**), the volcano is probably linked to major eruptions. However, most of the ejecta may be covered the sea because of its proximity to the coast. According to ^{14}C dating on charcoal clasts beneath the pyroclastics, the Daling volcano eruptions were younger than 33 ka.

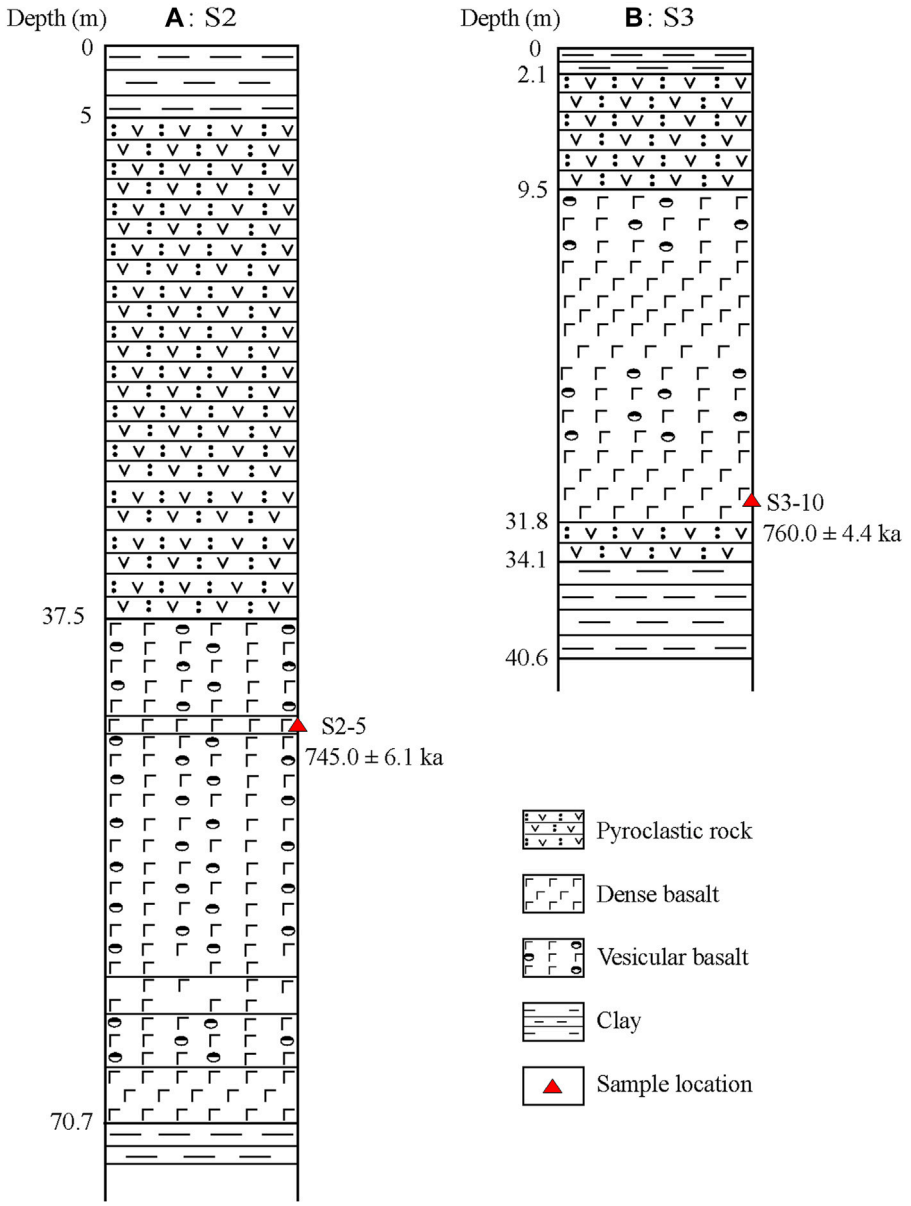


FIGURE 9 | Stratigraphic columns boreholes. **(A)** S2 borehole. **(B)** S3 borehole.

The Nanwan volcano involved major eruptions associated with multiple phases, and the pyroclastics from this volcano are found throughout Weizhou island. Eruptions that occurred in the initial period of activity were hydromagmatic and these produced mainly PDCs deposits. The period that followed was dominated by magmatic explosive eruptions and these formed mainly scoria and spatter deposits. In the late -period, eruptions were hydromagmatic, and these also produced mainly PDCs deposits. Fan et al. (2006) reported OSL ages of 33.7 ± 1.8 ka and 33.7 ± 0.4 ka from sandstone xenoliths embedded in the Nanwan pyroclastics, while Xu et al. (2020) dated ejecta samples from deposits in Nanwan using ESR and reported ages between 33 and 13 ka. Therefore, the latest eruption in the Nanwan volcano occurred during the Late Pleistocene, and this is the most recent eruption in Weizhou island. It's necessary to note that the assignment of a Holocene age to the Nanwan Volcano based on its unconformable presence on the Eyuzui in Nanwan by Li and Wang (2004) and Li et al. (2005) is erroneous. More chronological evidence is needed to determine whether Nanwan is a Holocene volcano.

6.2 Eruptive History and Evolution of Weizhou Island Volcano

According to the dating data (**Figure 12**), volcanic activities in Weizhou island can be divided into 5 periods. The first four

TABLE 1 | Weizhou island igneous rock samples that were used for $^{40}Ar/^{39}Ar$ dating and their ages.

Sample no	Sampling location	Description of sample	Plateau age/ka	2σ/ka	MSWD
ZK-23	Daling borehole, burial depth: 73.6 m	basalt xenolith in pyroclastic rocks	868.5	25.4	1.16
WZ-4	Shiluokou beach at Daling	basalt xenolith in pyroclastic rocks	870.3	34.3	0.36
HLS-5	Summit of Henglushan	dense basalt	762.6	7.3	1.18
18WZ-4	Xijiao beach	spheroidal weathered basalt	744.3	5.1	0.36
19WZ-17	Hengling beach	spheroidal weathered basalt	747.4	10.4	0.73
S2-5	S2 borehole, burial depth: 43.8 m	dense basalt	745.0	6.1	0.80
S3-10	S3 borehole, burial depth: 26 m	dense basalt	760.0	4.4	0.92
19WZ-23	Nanwan market beach	dense basalt	740.5	3.4	1.13
19WZ-18	Nanwan Volcano	basalt xenolith in pyroclastic rocks	487.8	12.0	1.78
19WZ-1	Danping in Dishui, Nanwan	basalt xenolith in pyroclastic rocks	282.9	32.5	0.63
WZ-1	Entrance of Nanwan Park	basalt xenolith in pyroclastic rocks	222.1	14.3	0.84

Note: The $^{40}Ar/^{39}Ar$ ages were measured in the OSU Argon Geochronology Lab in the United States.

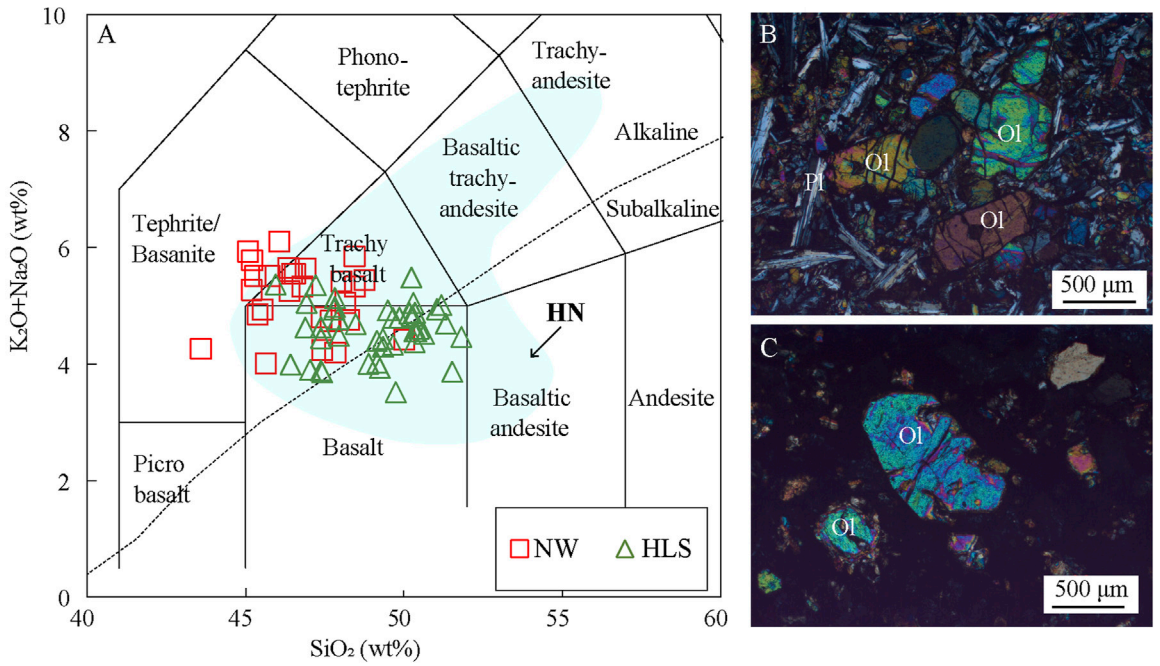


FIGURE 10 | (A) TAS diagram of Weizhou volcanic rocks. Classification boundaries are from Le Maitre et al., 1989. Weizhou island data are from (Li et al., 2005; Fan et al., 2008; Yang et al., 2020); The compositions of Hainan (HN) island volcanic rocks are from Ho et al. (2000), Zou and Fan (2010), Wang et al. (2012) and Liu et al. (2015). NW- Nanwan volcano, HLS-Henglushan volcano, HN-Hainan island volcano. **(B)** Photomicrographs of basalts in Weizhou island, crossed polarized light. **(C)** Photomicrographs of basanite in Weizhou island, crossed polarized light, Ol-olivine, Pl-plagioclase.

periods were dominated by effusive eruptions, while the eruptions in the last period were predominantly explosive. Period I occurred during the Early Pleistocene (1,420–1,260 ka) and it was characterized by minor eruptions, with the lavas limited to the east and west shores of the island. Period II occurred during the Early to Middle Pleistocene (870–740 ka) and it involved major eruptions, which produced lavas exposed throughout the island. In Period III, which occurred during the Middle Pleistocene (600–480 ka), eruptions were relatively minor and localized, and the associated lavas outcrop near Henglushan and Hengling, while basalt xenoliths in the Nanwan pyroclastics also contain products from this period. Period IV is attributed to the Middle to Late Pleistocene (283–222 ka), which was characterized by minor eruptions which produced deposits that are restricted to xenoliths in the Nanwan pyroclastics, without major lava flow. Period V is assigned to the Late Pleistocene (33.7–13 ka), and the associated eruptions produced the Nanwan and Daling volcanoes.

Period V coincides with the Last Glacial Maximum, during which sea level was low (Harrison et al., 2019). Therefore, Weizhou island probably subsided after the eruptions that occurred 220,000 years ago, which transformed the area of

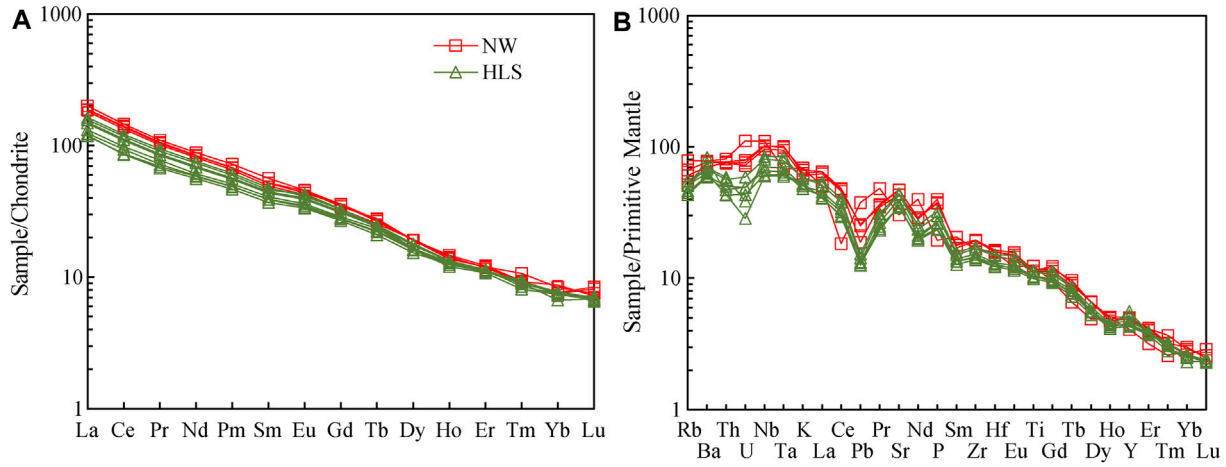


FIGURE 11 | Distribution of rare earth **(A)** and trace element contents **(B)** in Weizhou volcanic rocks. Chondrite standard value and original mantle standard value data are from Sun and McDonough (1989). Rare earth and trace data of volcanic rocks from (Yang et al., 2020).

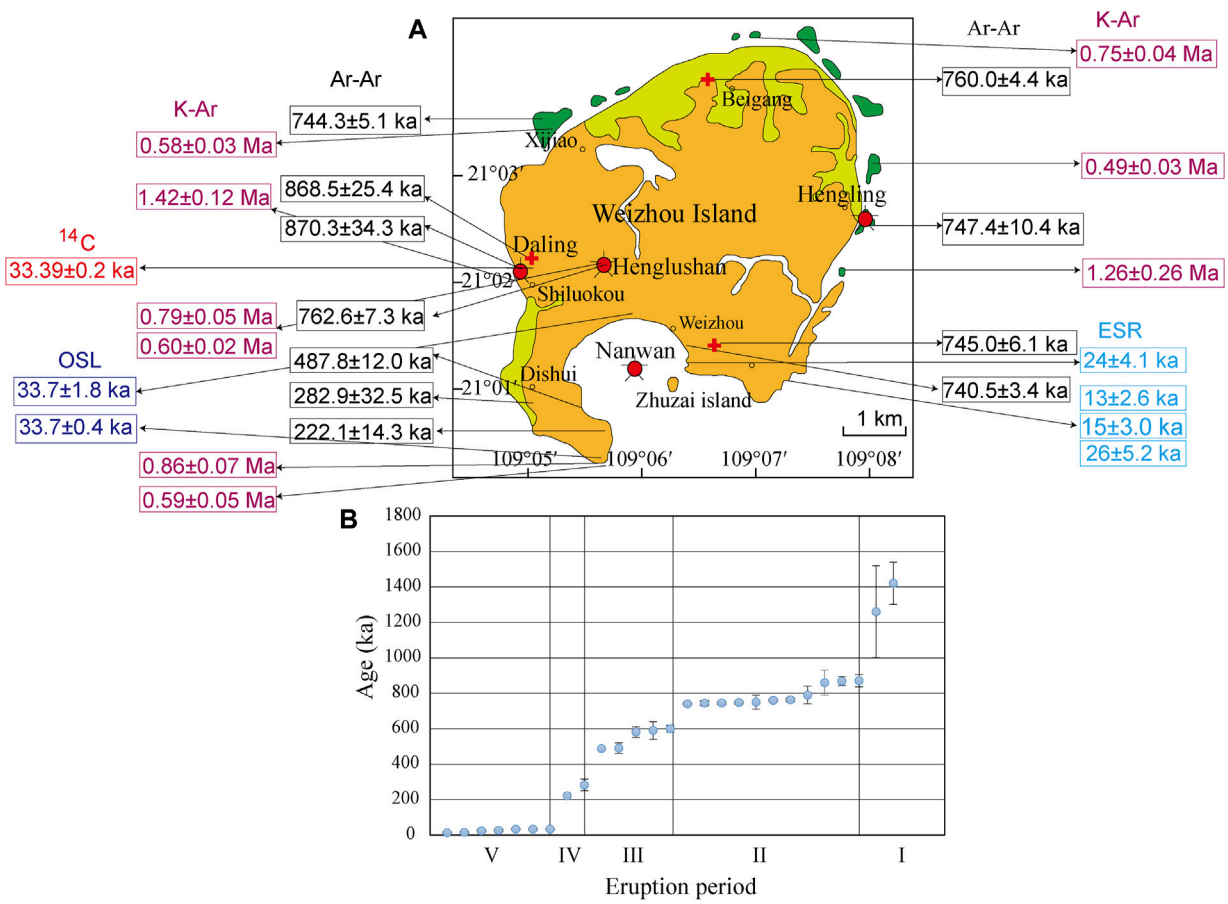


FIGURE 12 | (A) Ages of Weizhou island igneous rocks. **(B)** A statistical graphic of the dating data. K-Ar ages are from Fan et al. (2006) and Feng (1992), OSL ages are from Fan et al. (2006), ESR ages are from Xu et al. (2020). Legends are same as **Figure 1C**.

the island into a coastal or shallow water marine environment. Around 30,000 years ago, explosive eruptions occurred when rising magmas encountered the seawater. However, because sea level rose after the end of the last glacial period, most of the ejecta from these eruptions are presently under the sea.

6.3 Comparison With Surrounding Volcanoes

There are a small volcano called Xieyang island and a large volcanic field in the northern Hainan island surrounding Weizhou island volcano. Similar to Weizhou island, the lower part of Xieyang island volcano is basaltic rocks and the upper part of the island is the PDCs deposits. Fan et al. (2006) tested the K-Ar age of the basalt in the lower part is 0.57 ± 0.05 Ma and the ^{14}C age of the shell in the upper PDCs deposits is 36,135 ± 185 years BP.

A large area of volcanic rocks is distributed in northern Hainan island (**Figure 1B**), and the volcanic rocks are mainly basalt with a small amount of intermediate rocks (**Figure 10A**). The eruptive period is divided into six stages (Fan et al., 2004): Miocene stage (5.43–3.04 Ma), Pliocene stage (3.82–3.68 Ma), Early Pleistocene stage (2.11–0.77 Ma), Middle Pleistocene stage (0.73–0.21 Ma), Late Pleistocene stage (0.11–0.06 Ma), Holocene stage (~0.01 Ma). In the late Pleistocene, a large number of low level craters and base-surge deposits produced by hydromagmatic eruptions were developed (Bai et al., 2003; Sun et al., 2003). We can see from the comparison that the eruption time and eruption styles Qieyang island volcano and northern Hainan Island volcano in Pleistocene correspond well with those of Weizhou island volcano.

6.4 Implications for Hazard Assessment of Weizhou Island Volcano

The above study shows that there are effusive and explosive eruptions on Weizhou island volcano, and a future eruption could strongly impact the island, with devastating and long-term socio-economic consequences for its 20,000 inhabitants. The extent of the lava flows suggests that effusive eruption can also affect the entire island. Explosive eruptions include hydromagmatic eruptions and magmatic eruptions. The range of base-surge deposits produced by hydromagmatic eruptions can be several times the diameter of the crater (Crowe and Fisher, 1973; Fisher and Schmincke, 1984), so a hydromagmatic eruption may also radiate the entire Weizhou Island (5–6 km long from north to south). The magma explosive eruption produced airborne accumulation in the vicinity of Daling with a thickness of about 4–5 m, indicating a large eruption scale. The possibility of other similar eruptions in the future cannot be ruled out. Although the current data cannot determine the eruption column and volume of the magmatic eruption, the eruption column produced by the magma explosive eruption can spread to a far area under the action of wind. According to numerical simulations, if there is an explosive eruption in Weizhou island involving volcanic ash reaching a height of 23 km, the ash will spread to Hainan, Guangxi, and Guangdong, China under SSW or NNW wind direction (Ma et al., 2008). Despite the relatively low probability of such an event, this worst-case scenario should be considered by regional and national authorities in risk management plans.

7 CONCLUSION

Four volcanoes were discovered at Henglushan, Hengling, Nanwan and Daling in Weizhou island. The Henglushan and Hengling volcanoes were produced predominantly by early weak explosive and late effusive eruptions, and these lavas represent the foundation of Weizhou island. Conversely, the Nanwan and Daling volcanoes are linked to multiple eruption phases, with hydromagmatic eruptions in the first and last phase and a magmatic explosive eruption in the second phase. The PDCs deposits of the Nanwan and Daling volcanoes virtually cover the entire Weizhou island.

Volcanic activity in Weizhou island can be divided into the following distinct periods: 1,420–1,260, 870–740, 600–480, 283–222, and 33.7–13 ka. The first four periods were dominated by effusive eruptions associated with the Henglushan and Hengling volcanoes. After this period, explosive eruptions began at around 33.7 ka because of magma–water interactions. These explosive eruptions then created the Nanwan and Daling volcanoes. Sea level rose after the end of the last glacial period, which resulted in that most of the products from these eruptions are presently under the sea.

Early effusive lava flows in Weizhou island are characterized by basaltic compositions and are linked with a small amount of fractional crystallization. Magmas in later eruptions contained slightly lower SiO_2 and involved some basanite. Fractional crystallization was also less pronounced in these lavas because of their rapid ascent.

DATA AVAILABILITY STATEMENT

The original contributions presented in the study are included in the article/Supplementary Materials, further inquiries can be directed to the corresponding author.

ETHICS STATEMENT

Written informed consent was obtained from the relevant individuals for the publication of any potentially identifiable images or data included in this article.

AUTHOR CONTRIBUTIONS

HY and BoZ: designing work plan. WY and HL: Pre-processing of chronological tests and whole-rock analysis. ZC, BiZ and GN: field geological survey and sampling. All authors contributed to interpretation and discussion of the results.

FUNDING

This work is supported by the National Nonprofit Fundamental Research Grant of China, Institute of Geology, China Earthquake Administration (Grant No: IGCEA1712).

ACKNOWLEDGMENTS

Thanks to Guangxi Beihai Hydrological Engineering Mineral Geological Survey Institute for providing S2 and S3 drilling data and core samples. We would like to thank Editage (www.editage.cn) for English language editing.

REFERENCES

Bai, Z. D., Xu, D. B., Wei, H. Q., and Hu, J. C. (2003). Division of the Active Period of Quaternary Volcanism Maanling, Northern Hainan Province. *Seismology Geology*. 25 (Suppl. l), 12–20. (in Chinese with English abstract). doi:10.1023/a:1026276925649

Briais, A., Patriat, P., and Tapponnier, P. (1993). Updated Interpretation of Magnetic Anomalies and Seafloor Spreading Stages in the South China Sea: Implications for the Tertiary Tectonics of Southeast Asia. *J. Geophys. Res.* 98 (B4), 6299–6328. doi:10.1029/92JB02280

Bureau of Geology and Mineral Resources of Guangxi (1985). *Regional Geology of Guangxi Zhuang Nationality Autonomous Region*. Beijing: Geological Publishing House. (in Chinese).

Chung, S. L., Cheng, H., Jahn, B. M., O'Reilly, S. Y., and Zhu, B. (1997). Major and Trace Element, and Sr-Nd Isotope Constraints on the Origin of Paleogene Volcanism in South China Prior to the South China Sea Opening. *Lithos* 40 (2-4), 203–220. doi:10.1016/S0024-4937(97)00028-5

Clift, P. D., and Sun, Z. (2006). The Sedimentary and Tectonic Evolution of the Yinggehai-Song Hong basin and the Southern Hainan Margin, South China Sea: Implications for Tibetan Uplift and Monsoon Intensification. *J. Geophys. Res.* 111 (B6), a–n. doi:10.1029/2005JB004048

Crowe, B. M., and Fisher, R. V. (1973). Sedimentary Structures in Base-Surge Deposits with Special Reference to Cross-Bedding, Ubehebe Craters, Death Valley, California. *Geol. Soc. America Bull.* 84, 663–682. doi:10.1130/0016-7606(1973)84<663:ssibdw>2.0.co;2

Fan, Q. C., Sun, Q., Li, N., and Sui, J. L. (2004). Periods of Volcanic Activity and Magma Evolution of Holocene in North Hainan Island. *Acta Petrologica Sinica* 2093, 533–544. (in Chinese with English abstract). doi:10.1016/j.sedego.2004.01.009

Fan, Q. C., Sun, Q., Long, A. M., Yin, K. J., Sui, J. L., Li, N., et al. (2006). Geology and Eruption History of Volcanoes in Weizhou Island and Xieyang Island, Northern Bay. *Acta Petrologica Sinica* 22 (6), 1529–1537. (in Chinese with English abstract). doi:10.1016/j.sedgeo.2006.03.014

Fan, Q. C., Sun, Q., Sui, J. L., and Li, N. (2008). Trace Element and Isotopic Geochemistry of Volcanic Rocks and It's Techtonic Implications in Weizhou Island and Xieyang Island, Northern Bay. *Acta Petrologica Sinica* 24 (6), 1323–1332. (in Chinese with English abstract).

Feng, G. R. (1992). *Basic Characteristics and Relationship to Tectonic Environment of the Late Cenozoic Basalts along the Coast of South China Sea*. Supplement to the Journal of Sunyatsen University, 1, 93–103. (in Chinese with English abstract).

Fisher, R. V., and Schmincke, H. U. (1984). *Pyroclastic Rocks*. Heidelberg: Springer-Verlag.

Hao, F., Li, S. T., Gong, Z. H., and Yang, J. M. (2001). Development Mechanism of Diapir and Episodic Fluid Charge in Yingge basin. *Sci. China (Series D)* 31, 471–476. (in Chinese)10.1007/BF02879792.

Harrison, S., Smith, D. E., and Glasser, N. F. (2019). Late Quaternary Meltwater Pulses and Sea Level Change. *J. Quat. Sci.* 34 (1), 1–15. doi:10.1002/jqs.3070

Ho, K. S., Chen, J. C., and Juang, W. S. (2000). Geochronology and Geochemistry of Late Cenozoic Basalts from the Leiqiong Area, Southern China. *J. Asian Earth Sci.* 18, 307–324. doi:10.1016/S1367-9120(99)00059-0

Huang, L. P., and Li, C. N. (2007). Peridotite Xenolith Fragments from Late Quaternary Pyroclastic Flow in Weizhou Island, Beihai, Guangxi. *Acta Petrologica et Mineralogica* 26 (4), 321–328. (in Chinese with English abstract).

Huang, X. L., Niu, Y., Xu, Y. G., Ma, J. L., Qiu, H. N., and Zhong, J. W. (2013). Geochronology and Geochemistry of Cenozoic Basalts from Eastern Guangdong, SE China: Constraints on the Lithosphere Evolution beneath the Northern Margin of the South China Sea. *Contrib. Mineral. Petrol.* 165 (3), 437–455. doi:10.1007/s00410-012-0816-7

Jia, D. C., Qiu, X. L., Hu, R. Z., and Lu, Y. (2003). Geochemical Nature of Mantle Reservoirs and Tectonic Setting of Basalts in Beibu Gulf and its Adjacent Region. *J. Trop. Oceanography* 22 (2), 30–39. (in Chinese with English abstract)

JianDong, X., Yu, H. M., HongMei, Y., Bo, Z., JianPing, L., FeiXiang, W., et al. (2020). The Chronology of Last Eruption of Weizhou Island Volcano in Northern Bay of Guangxi Province. *Acta Petrologica Sinica* 36 (7), 2111–2115. (in Chinese with English abstract)doi:10.18654/1000-0569/2020.07.12

Kimura, J.-I., Sakuyama, T., Miyazaki, T., Vaglarov, B. S., Fukao, Y., and Stern, R. J. (2018). Plume-stagnant Slab-Lithosphere Interactions: Origin of the Late Cenozoic Intra-plate Basalts on the East Eurasia Margin. *Lithos* 300-301, 227–249. doi:10.1016/j.lithos.2017.12.003

Koppers, A. A. P. (2002). ArArCALC-software for 40Ar/39Ar Age Calculations. *Comput. Geosciences* 28, 605–619. doi:10.1016/S0098-3004(01)00095-4

Le Maitre, R. W., Streckeisen, A., Zanettin, B., Le Bas, M. J., Bonin, B., Bateman, P., et al. (Editors) (1989). *Igneous Rocks: A Classification of Igneous Rocks and Glossary of Terms* (Oxford: Blackwell), 193.

Lei, J., Zhao, D., Steinberger, B., Wu, B., Shen, F., and Li, Z. (2009). New Seismic Constraints on the Upper Mantle Structure of the Hainan Plume. *Phys. Earth Planet. Interiors* 173 (1-2), 33–50. doi:10.1016/j.pepi.2008.10.013

Leloup, P. H., Lacassin, R., Tapponnier, P., Schärer, U., Zhong, D., Liu, X., et al. (1995). The Ailao Shan-Red River Shear Zone (Yunnan, China), Tertiary Transform Boundary of Indochina. *Tectonophysics* 251 (1-4), 3–10. doi:10.1016/0040-1951(95)00070-4

Li, C. N., and Wang, F. Z. (2004). Holocene Volcanic Effusion in Weizhou Island and its Geological Significance. *J. Mineralogy Petrology* 24 (4), 28–34. (in Chinese with English abstract).

Li, C. N., Wang, F. Z., and Zhong, C. S. (2005). Geochemistry of Quaternary Basaltic Volcanic Rocks of Weizhou Island in Beihai City of Guangxi and a Discussion on Characteristics of Their Source. *Acta Petrologica et Mineralogica* 24 (1), 1–11. (in Chinese with English abstract).

Li, X. M., and Liu, C. Z. (1991). Preliminary Study on the Petrological Characteristics of Alkali-Basalts in Weizhou Island, Guangxi. *Geology. Guangxi* 4 (1), 43–51. (in Chinese with English abstract).

Liu, C. Z. (1986). Geological and Geomorphological Characteristics of the Crater in south bay of Weizhou Island. *Geology. Guangxi* 1, 57–64. (in Chinese with English abstract).

Liu, J. Q., Ren, Z. Y., Nichols, A. R. L., Song, M. S., Qian, S. P., Zhang, Y., et al. (2015). Petrogenesis of Late Cenozoic Basalts from North Hainan Island: Constraints from Melt Inclusions and Their Host Olivines. *Geochimica et Cosmochimica Acta* 152, 89–121. doi:10.1016/j.gca.2014.12.023

Long, A. M., Fan, Q. C., Sun, Q., Yin, K. J., Li, N., and Wang, T. H. (2004). Volcano Eruption Features in Weishou Island of Guangxi. *South China J. Seismology* 24 (2), 22–27. (in Chinese with English abstract).

Lu, J. L. (1993). The Characteristics of Volcanic Eruption in Weizhou Island, Beihai City, Guangxi. *Guangxi Geology*. 6 (3), 53–58. (in Chinese with English abstract).

Ma, B. J., Zhao, Y., and Fan, Q. C. (2008). Numerical Simulation on the Airborne Ash of the Weizhou Island Volcanic Activity. *Seismological Res. Northeast China* 24 (1), 71–80. (in Chinese with English abstract).

Montelli, R., Nolet, G., Dahlen, F. A., and Masters, G. (2006). A Catalogue of Deep Mantle Plumes: New Results from Finite-Frequency Tomography. *Geochem. Geophys. Geosyst.* 7(11), a-n. doi:10.1029/2006GC001248

Pimentel, A., Self, S., Pacheco, J. M., Jeffery, A. J., and Gertisser, R. (2021). Eruption Style, Emplacement Dynamics and Geometry of Peralkaline Ignimbrites: Insights from the Lajes-Angra Ignimbrite Formation, Terceira Island, Azores. *Front. Earth Sci.* 9, 673686. doi:10.3389/feart.2021.673686

Replumaz, A., Lacassin, R., Tapponnier, P., and Leloup, P. H. (2001). Large River Offsets and Plio-Quaternary Dextral Slip Rate on the Red River Fault (Yunnan, China). *J. Geophys. Res.* 106 (B1), 819–836. doi:10.1029/2000JB900135

Sigurdsson, H., Houghton, B., and Mcnutt, S. (2015). *The Encyclopedia of Volcanoes*. Second Edition. Academic Pressdoi:10.1016/C2015-0-00175-7

Subba Rao, M. V., and Rao, V. D. (1988). Chemical Constraints on the Origin of the Charnockites in the Eastern Ghat mobile belt, India. *Chem. Geology*. 69, 37–48. (in Chinese). doi:10.1016/0009-2541(88)90156-8

Sun, Q., Fan, Q. C., Wei, H. Q., Sui, J. L., Bai, Z. D., Xu, D. B., et al. (2003). Preliminary Study on Late Pleistocene Phreatomagmatic Eruption of Northern Hainan Island. *Seismology Geology*. 25 (2), 289–297. (in Chinese with English abstract).

Sun, S.-s., and McDonough, W. F. (1989). Chemical and Isotopic Systematics of Oceanic Basalts: Implications for Mantle Composition and Processes. *Geol. Soc. Lond. Spec. Publications* 42 (1), 313–345. doi:10.1144/GSL.SP.1989.042.01.19

Wang, D., Wu, S., Li, C., and Yao, G. (2016). Submarine Slide Evidence for Late Miocene Strike-Slip Reversal of the Red River Fault. *Sci. China Earth Sci.* 59 (11), 2231–2239. doi:10.1007/s11430-015-5534-9

Wang, X. C., Li, Z. X., Li, X. H., Li, J., Liu, Y., Liu, Y., et al. (2012). Temperature, Pressure, and Composition of the Mantle Source Region of Late Cenozoic Basalts in Hainan Island, SE Asia: a Consequence of a Young Thermal Mantle Plume Close to Subduction Zones?. *J. Petrology* 53 (1), 177–233. doi:10.1093/petrology/egr061

WenJian, Y., Yu, H. M.*, HongMei, Y., Bo, Z., ZhengQuan, C., and Xiang, B. (2020). Mantle Sources and Magma Genesis of Late Cenozoic Basalts in Weizhou Island, Guangxi, China. *Acta Petrologica Sinica* 36 (7), 2092–2110. (in Chinese with English abstract). doi:10.18654/1000-0569/2020.07.11

Xia, S., Zhao, D., Sun, J., and Huang, H. (2016). Teleseismic Imaging of the Mantle beneath Southernmost China: New Insights into the Hainan Plume. *Gondwana Res.* 36, 46–56. doi:10.1016/j.gr.2016.05.003

Xu, Y., Wei, J., Qiu, H., Zhang, H., and Huang, X. (2012). Opening and Evolution of the South China Sea Constrained by Studies on Volcanic Rocks: Preliminary Results and a Research Design. *Chin. Sci. Bull.* 57 (24), 3150–3164. (in Chinese with English abstract). doi:10.1007/s11434-011-4921-1

Yan, P., Deng, H., Liu, H., Zhang, Z., and Jiang, Y. (2006). The Temporal and Spatial Distribution of Volcanism in the South China Sea Region. *J. Asian Earth Sci.* 27 (5), 647–659. doi:10.1016/j.jseaes.2005.06.005

Yan, Q., Shi, X., and Castillo, P. R. (2014). The Late Mesozoic-Cenozoic Tectonic Evolution of the South China Sea: A Petrologic Perspective. *J. Asian Earth Sci.* 85, 178–201. doi:10.1016/j.jseaes.2014.02.005

Yan, Q., Shi, X., Metcalfe, I., Liu, S., Xu, T., Kornkanitnan, N., et al. (2018). Hainan Mantle Plume Produced Late Cenozoic Basaltic Rocks in Thailand, Southeast Asia. *Sci. Rep.* 8, 2640. doi:10.1038/s41598-018-20712-7

Yan, Q., Shi, X., Wang, K., Bu, W., and Xiao, L. (2008). Major Element, Trace Element, and Sr, Nd and Pb Isotope Studies of Cenozoic Basalts from the South China Sea. *Sci. China Ser. D-earth Sci.* 51 (4), 550–566. (in Chinese with English abstract). doi:10.1007/s11430-008-0026-3

Yan, Q. S., and Shi, X. F. (2007). Hainan Mantle Plume and the Formation and Evolution of the South China Sea. *Geol. J. China Universities* 13 (2), 311–322. (in Chinese with English abstract).10.16108/j.issn1006-7493.2007.02.014.

Zeng, G., Zheng, L. B., Chen, L. H., Liu, J. Q., Zhang, H., Zhang, Y. J., et al. (2017). Influence of Ridge Suction on Cenozoic Basaltic Magmatism in the Surroundings of the South China Sea. *Geol. J. China Universities* 23, 373–382. (in Chinese with English abstract).10.1007/s11434-011-4921-1.

Zhang, Y., Yu, K., Fan, T., Yue, Y., Wang, R., Jiang, W., et al. (2020). Geochemistry and Petrogenesis of Quaternary Basalts from Weizhou Island, Northwestern South China Sea: Evidence for the Hainan Plume. *Lithos* 362-363, 105493. doi:10.1016/j.lithos.2020.105493

Zhou, H., Xiao, L., Dong, Y., Wang, C., Wang, F., and Ni, P. (2009). Geochemical and Geochronological Study of the Sanshui basin Bimodal Volcanic Rock Suite, China: Implications for basin Dynamics in southeastern China. *J. Asian Earth Sci.* 34 (2), 178–189. doi:10.1016/j.jseaes.2008.05.001

Zou, H., and Fan, Q. (2010). U-th Isotopes in Hainan Basalts: Implications for Sub-asthenospheric Origin of EM2 Mantle Endmember and the Dynamics of Melting beneath Hainan Island. *Lithos*, 116, 145–152. doi:10.1016/j.lithos.2010.01.010

Conflict of Interest: The authors declare that the research was conducted in the absence of any commercial or financial relationships that could be construed as a potential conflict of interest.

Publisher's Note: All claims expressed in this article are solely those of the authors and do not necessarily represent those of their affiliated organizations, or those of the publisher, the editors and the reviewers. Any product that may be evaluated in this article, or claim that may be made by its manufacturer, is not guaranteed or endorsed by the publisher.

Copyright © 2021 Yu, Yang, Zhao, Chen, Zhou, Nie and Luo. This is an open-access article distributed under the terms of the Creative Commons Attribution License (CC BY). The use, distribution or reproduction in other forums is permitted, provided the original author(s) and the copyright owner(s) are credited and that the original publication in this journal is cited, in accordance with accepted academic practice. No use, distribution or reproduction is permitted which does not comply with these terms.

frontiers in Earth Science

ORIGINAL RESEARCH
published: 06 December 2021
doi: 10.3389/feart.2021.786021

Gas Emissions From the Western Aleutians Volcanic Arc

Tobias P. Fischer[1], Taryn M. Lopez[2], Alessandro Aiuppa[3], Andrea L. Rizzo[4], Tehnuka Ilanko[5], Katherine A. Kelley[6] and Elizabeth Cottrell[7]*

[1]Department of Earth and Planetary Sciences, University of New Mexico, Albuquerque, NM, United States, [2]Geophysical Institute, University of Alaska Fairbanks, Fairbanks, AK, United States, [3]Dipartimento di Scienze Della Terra e Del Mare, Università di Palermo, Palermo, Italy, [4]Istituto Nazionale di Geofisica e Vulcanologia, Sezione di Palermo, Palermo, Italy, [5]Te Aka Mātuatua - School of Science, University of Waikato, Hamilton, New Zealand, [6]Graduate School of Oceanography, University of Rhode Island, Washington County, RI, United States, [7]Department of Mineral Sciences, National Museum of Natural History, Smithsonian Institution, Washington, VA, United States

The Aleutian Arc is remote and highly active volcanically. Its 4,000 km extent from mainland Alaska to Russia's Kamchatka peninsula hosts over 140 volcanic centers of which about 50 have erupted in historic times. We present data of volcanic gas samples and gas emission measurements obtained during an expedition to the western-most segment of the arc in September 2015 in order to extend the sparse knowledge on volatile emissions from this remote but volcanically active region. Some of the volcanoes investigated here have not been sampled for gases before this writing. Our data show that all volcanoes host high-temperature magmatic-hydrothermal systems and have gas discharges typical of volcanoes in oceanic arcs. Based on helium isotopes, the western Aleutian Arc segment has minimal volatile contributions from the overriding crust. Volcanic CO_2 fluxes from this arc segment are small, compared to the emissions from volcanoes on the Alaska Peninsula and mainland Alaska. The comparatively low CO_2 emissions may be related to the lower sediment flux delivered to the trench in this part of the arc.

Keywords: Aleutians, volcano, gas, volatiles, geochemistry

OPEN ACCESS

Edited by:
Antonio Paonita, Istituto Nazionale di Geofisica e Vulcanologia (INGV), Italy

Reviewed by:
Franco Tassi, University of Florence, Italy
Philipson Bani, UMR6524 Laboratoire Magmas et Volcans (LMV), France

****Correspondence:***
Tobias P. Fischer
fischer@unm.edu

Specialty section:
This article was submitted to Volcanology, a section of the journal Frontiers in Earth Science

Received: *29 September 2021*
Accepted: *18 November 2021*
Published: *06 December 2021*

Citation:
Fischer TP, Lopez TM, Aiuppa A, Rizzo AL, Ilanko T, Kelley KA and Cottrell E (2021) Gas Emissions From the Western Aleutians Volcanic Arc. Front. Earth Sci. 9:786021. doi: 10.3389/feart.2021.786021

INTRODUCTION

The Aleutian Arc is one of the most volcanically active and remote arcs in the world. The arc extends ~4,000 km from mainland Alaska to Russia's Kamchatka Peninsula and separates the Bering Sea to the North from the Pacific Ocean to the South (**Figure 1**). The eastern 2,500 km of the arc represents the region of active volcanism and is undergoing subduction of the Pacific plate beneath the North American plate. The arc has ~142 volcanic centers, of which 54 volcanoes have been historically active (Cameron et al., 2020). At the time of writing (2021), Semisopochnoi, Great Sitkin and Pavlof volcanoes are currently erupting, and Gareloi and Cleveland volcanoes have shown signs of unrest (GVP, 2015; GVP, 2019; GVP, 2021a; GVP, 2021b; GVP, 2021c; GVP, 2021d). The type of volcanic activity is highly variable throughout the arc, with eruptions ranging from nearly continuous Strombolian-style basaltic eruptions (e.g. Pavlof 2014) to infrequent, discrete Plinian events such as the 1912 Katmai/Novarupta eruption (Fierstein and Hildreth, 1992). The frequent eruptions occurring in the Aleutian Arc often produce high-altitude ash clouds that are hazardous to the numerous aircraft that fly over the North Pacific Ocean. Previous studies have investigated volcanic gas emissions from many Eastern and Central Aleutian volcanoes; however at the time of this study little was known about volcanic gas emissions from the Western Aleutian volcanoes.

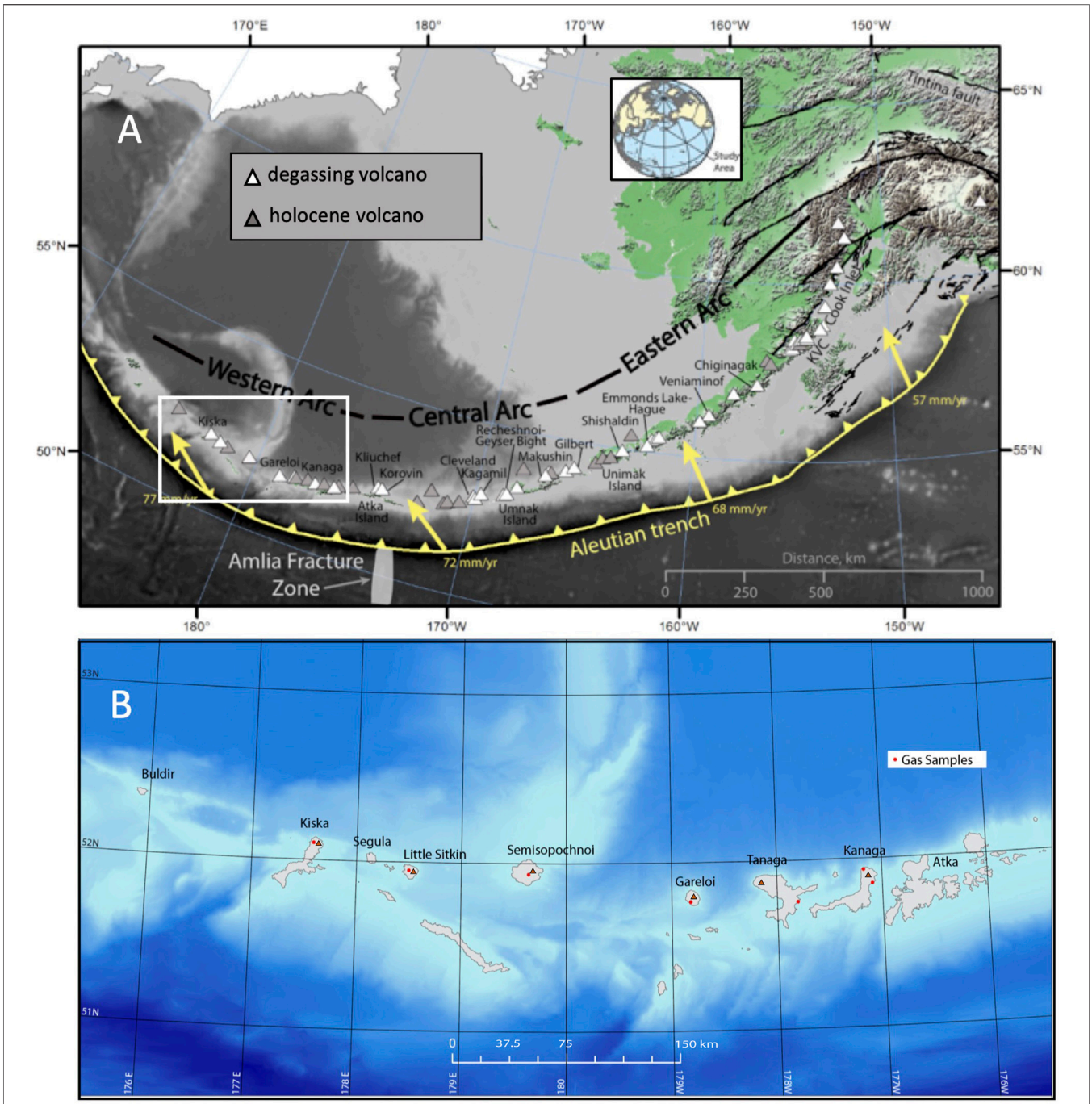


FIGURE 1 | (A) Map of the Aleutian Arc showing degassing volcanoes and volcanoes active in the Holocene. Note that the degassing volcanoes are also active in the Holocene. **(B)** shows the locations that were sampled for this study. Map provided by Dan Cole, Smithsonian Institution.

We characterize volcanic gas emissions from the sparsely studied and highly remote Western Aleutians volcanic islands (from west to east) of Kiska, Little Sitkin, Semisopochnoi, Gareloi, Tanaga and Kanaga (**Figure 1B**). These volcanoes are all considered to be historically active by the Alaska Volcano Observatory, defined as having a known or suspected eruption, persistent fumaroles, a volcanic deformation signal, and/or seismic swarm of volcanic origin since 1700 (Cameron et al., 2020). Because the Western Aleutians volcanoes are some of the most remote in Alaska, many eruptions in this region have been poorly documented throughout historic time and little is known in general about these volcanic systems.

In this publication we present the first constraints on the chemical composition of volcanic gases from Western Aleutians

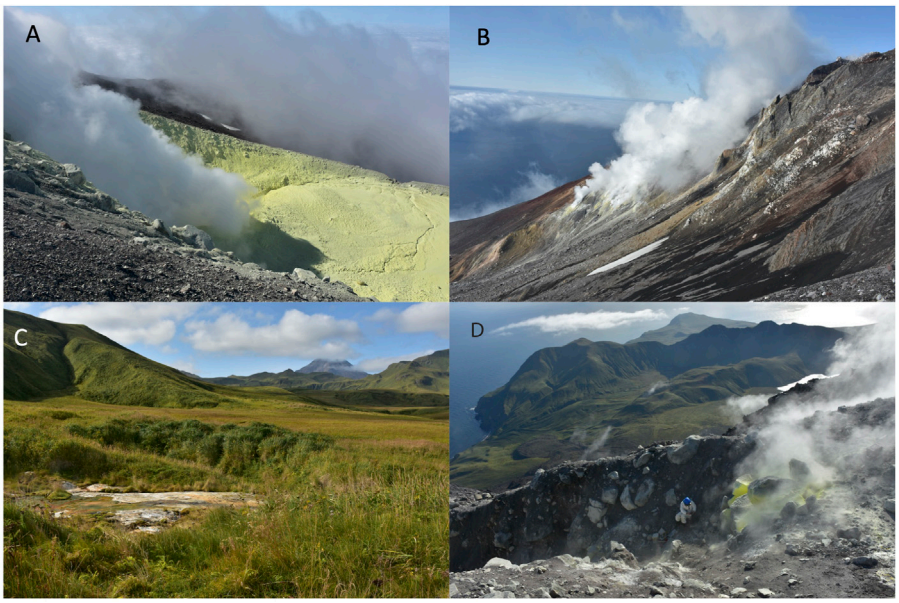


FIGURE 2 | Examples of degassing features in the Western Aleutians. **A:** Fumarole at the flank of Kiska Volcano with native sulfur deposits. The fumarole seen here is about 10 m in diameter and the plume is about 100 m tall. **B:** Fumaroles (100–270°C) at the summit of Gareloi volcano. The fumarole field is about 100 m wide. **C:** Hot spring (62°C) on the flanks of Tanaga volcano; **D:** Fumaroles (boiling temperature) at summit of Kanaga Volcano.

volcanoes of Gareloi, Kiska and Kanaga. We also present new measurements from hydrothermal gas discharges from Semisopochnoi, Tanaga and Little Sitkin volcanoes to complement previous studies. We targeted these volcanoes during an expedition that was jointly supported by NSF, the USGS and the Deep Carbon Observatory in 2015 and involved transportation by a combination of boat, helicopter and foot to reach most of the volcanic centers. Prior to this study, several field efforts since the 1980s have been aimed at measuring volatile emissions within the Aleutian Arc, including collection and analysis of Eastern and Central Aleutian volcanic gas and water samples for chemical and isotopic composition (Motyka et al., 1993; Symonds et al., 2003a; Symonds et al., 2003b; Evans et al., 2015); annual to bi-weekly surveys of plume composition and flux for volcanoes within the Cook Inlet and Katmai Volcanic Cluster regions were performed by Alaska Volcano Observatory scientists (Casadevall et al., 1994; Gerlach et al., 1994; Doukas, 1995; Doukas and McGee, 2007; McGee et al., 2010; Werner et al., 2011; Werner et al., 2013) and targeted gas composition and flux measurements at the individual volcanoes of Akutan (Bergfeld et al., 2013), Ukinrek-Maars (Evans et al., 2009) and Mount Martin, Mount Mageik, and Trident (Lopez et al., 2017). While these studies provide significant information on volcanic gas discharges from the Aleutians and the processes controlling the compositions of these emissions, the main degassing features from the Western Aleutian arc segment were virtually uncharacterized before this work. We also present the first SO_2 flux measurements obtained from Gareloi and Kiska volcanoes. Together, these new constraints on volcanic gas composition and flux allow us to make inferences about the subsurface volcanic systems and current state of volcanic activity at these remote volcanoes. The Western Aleutians, like other remote island arcs that are built on oceanic crust (i.e. Kuril, Izu-Bonin Marianas), have gas compositions that appear to be minimally affected by contributions from the overriding arc crust, providing a relatively undistorted view into slab- and mantle-derived volatiles.

MATERIALS AND METHODS

Volcano Settings

Figure 1B shows the location of Western Aleutian volcanoes sampled in this study and **Figure 2** shows some of their fumaroles and thermal features. Kiska Volcano is the westernmost historically active volcano within the Aleutian Arc (**Figure 1B**). Kiska is a stratovolcano with volcanic rocks of basaltic to andesitic composition (Miller et al., 1998). Confirmed historic eruptions consisted of ash and gas emissions in 1990 and lava effusion in 1962, 1964, 1969 and 1990 (https://volcano.si.edu/volcano.cfm?vn=31102). Other reported volcanic activity has comprised primarily volcanic gas emissions. This study sampled volcanic fluids from Kiska Volcano (52.1056 N, 177.5994 E, 1,049 m) that were emanating from a roaring ~10 m diameter fumarole vent on the upper west flank of the volcanic edifice. The vent consisted of a depression containing ~10–20 vigorously-degassing and audibly-jetting fumaroles whose emissions coalesced into a coherent plume (**Figure 2A**). The ground surrounding the vent was yellow in color and contained native sulfur deposits. The apparent high gas flux and confined emission location prevented safe access to sample the fumaroles by inserting a titaneum tube directly into the vents when we visited this site.

Due to this situation, we were able to approach the site only to collect a gas sample from the plume above the vents that was affected by atmospheric contamination.

Little Sitkin volcano is a stratovolcano within a system of nested calderas (Miller et al., 1998). No confirmed eruptions from Little Sitkin have occurred in historic time, though observations are limited for this remote location. Volcanic rocks are primarily andesitic in composition, and range from basalt to dacite (Snyder, 1959; Larsen et al., 2020). Gas emissions from Little Sitkin emanate primarily from a geothermal region located on the western flank of the volcanic edifice (51.96117 N, 178.49226 E, 166 m), and this was the target of our study. Gas emissions in this region were released via three degassing manifestations: fumarolic emissions, bubbling springs and mud pools. Fumarolic regions near the summit and the northwest shore of the island have been previously reported (Snyder, 1959), but were not sampled during this study.

Semisopochnoi island is composed of scattered volcanic vents, the prominent caldera of Semisopochnoi volcano, and older, ancestral volcanic rocks. Volcanic rocks on Semisopochnoi range from basalt to dacite in composition (Miller et al., 1998; Coombs et al., 2007). Reports of volcanic eruptions prior to our 2015 field study occurred in 1772, 1790, 1792, 1830, 1873, and 1987 (https://volcano.si.edu/volcano.cfm?vn=311060) The 1987 eruption occurred from the extracaldera Sugarloaf Peak. Since 2018 Semisopochnoi has been undergoing intermittent eruptive activity from Mount Cerberus (GVP, 2021d). At the time of our study the volcano was in a period of quiescence, with no persistent fumaroles present to our knowledge. Water samples were collected from a warm spring next to Fenner Creek in the caldera with no visible bubbles (51.93636 N, 179.65459 E, 1,332 m).

Gareloi volcano is a stratovolcano comprising two overlapping volcanic edifices, referred to as the South and North Peaks, respectively. It is one of the most active volcanoes of the Western Aleutians with at least nine confirmed eruptions since 1791 (https://volcano.si.edu/volcano.cfm?vn=311070). Gareloi has also had persistent abundant seismicity since a seismic network was installed in 2005 (Coombs et al., 2008). Gareloi's erupted products are potassium rich in composition and range primarily from shoshonite to latite in composition, with sparse andesite (Coombs et al., 2012). Gareloi's largest historical eruption occurred in 1929 (Coombs et al., 2008) and likely formed the South Peak's asymmetrical crater that opens to the southeast. The South Peak Crater (51.7646 N, 178.80697 W, 1,326 m) is the home of the primary degassing region on Gareloi, an active fumarole field on the crater wall, whose gas emissions coalesce into a coherent plume (**Figure 2B**). These gases were targeted during this study. The North Peak contains a steeply walled crater that was observed to contain a crater lake and potentially an active fumarole field at the lake's edge at the time of our study, but was not targeted here.

Tanaga Island is home to three volcanic centers: Tanaga, Sajaka and Takawangha. Of these Tanaga is thought to be the youngest and only historically active vent of the three. The only confirmed historic eruption from Tanaga occurred in 1914, with suspected eruptions occurring in 1773–1770, 1791 and 1829 (www.alaska.edu). Little information is available on these eruptions, and they may have originated from the other volcanic centers (Miller et al., 1998). The erupted products from the three volcanic centers range from basalt to dacite in composition. While no known fumarole fields exist on Tanaga Island, natural hot springs (**Figure 2C**) are located on the edge of Hot Springs Bay (51.77175 N, 177.79955 W, 1 m), southeast of Takawangha. These hot springs were targeted during our study.

Kanaga volcano is the easternmost volcano discussed here. It is a stratovolcano within an older caldera on the north end of Kanaga island (Miller et al., 1998). Kanaga has had several confirmed historic eruptions including 1786, 1904, 1906, 1942, 1994–95 and most recently in 2012 (GVP, 2013). Erupted products range from basalt to andesite. Volcanic fluids from Kanaga Volcano (51.9230167 N, 177.161,083 W, 1,237 m) were released from two main sources in 2015: 1) numerous individual fumaroles dispersed along the ~10 m wide southwest to southeast trending fracture that has dissected the summit since its 2012 eruption (**Figure 2D**); and 2) hot springs located ~7.3 km southeast of the summit. Yellow sulfur deposits surround the active fumaroles and travertine deposits are prominent in the hot springs region.

Sampling and Analytical Techniques

We utilized a number of techniques for the collection of gas samples depending on the specific situation at the volcano. When possible, we collected direct gas samples from vents or bubbling springs in the crater or on the volcano's flanks using pre-evacuated Giggenbach bottles containing NaOH (Giggenbach and Goguel, 1989b). Where vents were not accessible, we measured plume gas composition by Multi-GAS (Aiuppa et al., 2005) and collected gas samples in Tedlar Bags for immediate subsequent carbon isotope analysis by Infrared Isotope Ratio Analyzer (Delta Ray) located on our boat (Rizzo et al., 2014; Fischer and Lopez, 2016). If there was a substantial plume, we made SO_2 flux measurements using a miniDOAS system (Galle et al., 2002) from the ground or helicopter. We collected water and gas samples from hot springs where no fumaroles were present or accessible.

Direct fumarole sampling involves inserting a titanium tube into a volcanic vent and drawing gases directly into previously evacuated glass bottles (i.e. Giggenbach bottles). The bottles contain a 5N NaOH solution that absorbs the acid gases (CO_2, SO_2, H_2S, HCl, HF) and water vapor allowing the non-reactive gases (noble gases, H_2, N_2, O_2, CH_4, CO) to accumulate in the head space. This technique has been described in Giggenbach and Gougel (1989a) and more recently in Oppenheimer et al. (2014). Gas and water samples were also collected in copper tubes clamped or crimped at both ends for noble gas analyses (Sano and Fischer, 2013). The gas composition of Giggenbach bottles was analyzed in the Volatiles Laboratory at UNM using a combination of gas chromatography and quadrupole mass spectrometry following established procedures (de Moor et al., 2013a; Lee et al., 2017; Ilanko et al., 2019).

Helium isotopes were analyzed in splits from the Giggenbach bottles or from separately collected copper tubes. The samples were analyzed in the noble gases isotope laboratory at INGV,

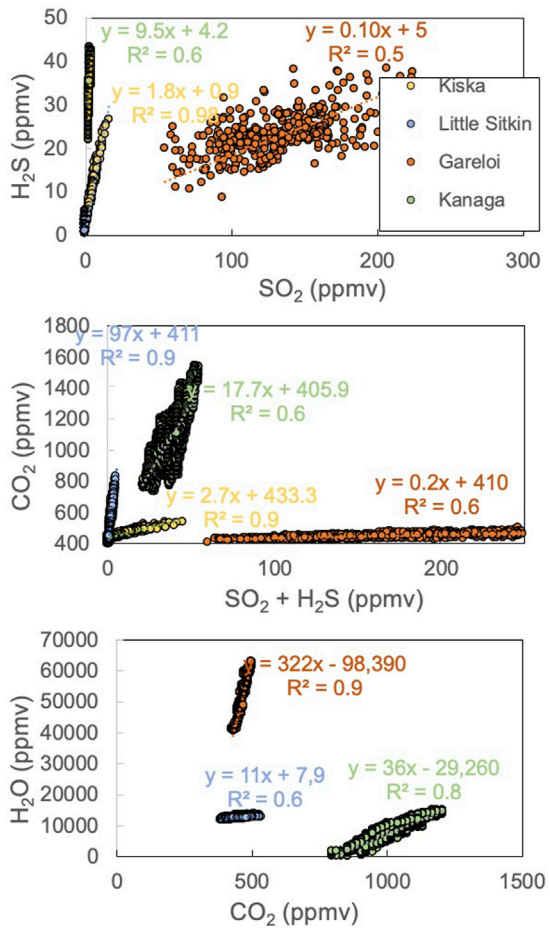


FIGURE 3 | Plume and fumarole gas compositions measured by multiGAS.

Sezione di Palermo (Italy), following the analytical procedures outlined in e.g. Rizzo et al. (2016). The $^{3}He/^{4}He$ ratio is expressed as R/Ra (where Ra is the ratio in air and equal to 1.39×10^{-6}) and was corrected for air contamination (Rc/Ra) using the He/Ne ratio following the equation proposed by Sano et al. (1987).

Nitrogen isotopes were analyzed for select gas samples at the University of New Mexico using a stable isotope ratio mass spectrometer with gas bench following the techniques described in Ilanko et al. (2019). Air standards were analyzed every 3–4 analyses to correct raw $\delta^{15}N$ values. A blank was also run for each sample or air standard and the peak areas were subtracted from those subsequently measured in the sample. The blank-corrected air values were then subtracted from the blank-corrected sample values. Reported errors are given in 1 s.d. over 4–6 peaks. Although the number of peaks for calculations varies between samples, the same peak numbers were used for the blank corrections and the air standard associated with each sample. Unfortunately, as shown in the results section, $\delta^{15}N$ values for these samples are burdened with high standard deviations due to interferences with unidentified peaks or low signals, making the data of limited value.

Water samples for water anion and cation analyses were collected at warm and hot spring sites using standard collection procedure that involved transfer of water into a 60 ml plastic syringe, and filtering through 0.2 micron millipore filters into Nalgene bottles. Samples were analyzed at the analytical chemistry laboratory in the Department of Earth and Planetary Sciences at the University of New Mexico using established IC and ICP OES methods (i.e. ASTM 300.1 and US EPA 200.7).

Multi-GAS

The Multi-GAS used in the work was provided by Alessandro Aiuppa (University of Palermo) and was equipped with an infrared CO_2 sensor and electrochemical sensors for SO_2 and H_2S (Aiuppa et al., 2014). The sensor unit was placed close to the fumarolic vents in campaign style while other samples were collected, usually for 1–2 h. The derived concentration data (acquired at 0.5 Hz) were post-processed to derive ratios between volatile species, using a routine procedure (Aiuppa et al., 2014). In brief, co-acquired gas concentration data for pairs of gas species were compared in scatter plots (see **Figure 3**), and the gas/gas ratios were derived from the slopes of the best fit linear regression lines for each volcano's dataset.

miniDOAS

The miniDOAS used in this work follows the design and approach of Galle et al. (2002) and has previously been used at Anatahan volcano, Mariana Islands (Hilton et al., 2007) at Erta Ale volcano, Ethiopia and Masaya, Nicaragua (de Moor et al., 2013b). The data processing is performed using DOASIS software (Kraus, 2006) that enables real-time calculation of the plume SO_2 burden. The SO_2 burden combined with constraints on windspeed allow emission rates to be calculated (Stoiber et al., 1983). At Kiska Volcano we performed several walking traverses along the crater rim on September 10 and measured wind-speed using a hand-held anemometer at the same time we measured plume SO_2 burden. At Gareloi we mounted the miniDOAS in the helicopter with the telescope positioned vertically out the small window and performed flight traverses under the plume on September 14 at an average altitude of 470 m above sea level. We had measured wind speed using the wind circle method (Doukas, 2002) during a previous trip to the summit (September 13) and asked the pilot to estimate wind speed during the flight. At Kanaga we performed a helicopter traverse as well as a walking traverse and constrained wind speed via the wind circle method at the same time as the plume SO_2 burden measurements (September 21). During the walking traverse, we were only able to partially capture the plume, due to inaccessible terrain.

RESULTS

Generally speaking, our results presented in this section show that the SO_2 fluxes were quite low and typical for volcanoes at a low state of activity (Fischer et al., 2019; Werner et al., 2019). Gas discharges are dominated by H_2O, followed by CO_2 and the sulfur species. Except for Gareloi, which has a fumarole temperature up

TABLE 1 | Gas chemical composition in mmol/mol total gas. All samples were collected in September 2015.

Volcano/sample ID	Temp.°C	H_2O	CO_2	S_t	SO_2	H_2S	HCl	HF	He	H_2	Ar	O_2	N_2	CH_4	CO
Kanaga Fum 1a S21	95	921.03	34.55	3.60	2.13	1.47	0.09	<0.001	0.0015	0.561	0.624	0.001	39.54	0.00082	0.00081
Kanaga Fum 1b S27	95	971.58	9.059	n.a	n.a	n.a	n.a	n.a	0.0007	0.267	0.289	0.008	18.79	0.00039	0.00039
Kanaga Fum 2a S10	n.d	908.06	24.71	0.44	0.41	0.03	2.08	<0.001	0.0008	0.124	0.693	11.90	51.99	<0.0002	<0.0002
Kanaga Fum 2 S11	n.d	927.51	14.97	n.d	n.d	n.d	1.89	<0.001	0.0007	0.044	0.452	8.028	47.11	<0.0002	<0.0002
Gareloy Fum 1a S1	102	985.51	1.982	7.17	5.81	1.36	2.80	0.001	0.0001	1.572	0.013	0.000	0.935	0.00400	0.01195
Gareloy Fum 1b S14	102	983.52	4.130	7.47	5.99	1.48	2.11	0.001	0.0001	1.512	0.015	0.000	1.232	0.01358	0.00025
Gareloy Fum 2a S8	270	983.46	4.185	10.1	9.05	1.07	0.60	0.27	0.0001	0.697	0.006	0.015	0.647	0.00458	0.00012
Gareloy Fum 2b S29	270	953.64	11.30	28.1	24.1	4.02	0.40	0.45	0.0004	3.003	0.037	0.000	3.024	0.02407	0.00170
Little Sitkin 1a S5	66	795.80	164.9	10.7	0.96	9.74	0.65	<0.001	0.0231	0.808	0.050	0.093	20.10	6.84929	<0.0002
Little Sitkin BS2 S26	55	446.49	492.4	16.2	0.84	15.4	0.32	<0.001	0.0209	1.194	0.184	0.054	32.10	11.0480	<0.0002
Little Sitkin Fum 1a S3	97	893.18	98.00	1.91	0.24	1.66	0.07	<0.001	0.0030	0.148	0.013	0.000	5.148	1.52506	<0.0002
Little Sitkin Fum 1b S9	97	878.77	115.0	n.a	n.a	n.a	n.a	n.a	0.0054	0.172	0.016	0.000	4.324	1.72416	<0.0002
Kiska Fumarole KIF1 S16	n.d	536.94	44.59	8.77	n.a	n.a	11.96	<0.001	0.0059	<0.001	2.258	69.76	325.7	<0.0002	<0.0002
Tanaga Hot Spring Gas 1 S22	62	970.00	1.048	0.16	n.a	n.a	1.41	<0.001	0.0001	<0.001	0.043	1.336	4.727	<0.0002	<0.0002

n.a, not analyzed; n.d. not determined.

TABLE 2 | Noble gas and nitrogen stable isotopes.

	Noble gases						Nitrogen	
	R/Ra	He/Ne	Rc/Ra	+/−	Ar^{40}/Ar^{36}corr	+/−	$\delta^{15}N$	±
Kanaga Fum 1a S21	5.95	1.1	7.96	0.0662	295.32	0.16	−0.42	0.10
Kanaga Fum 1b S27	5.99	1.13	7.93	0.0657	294.61	0.16	−0.45	0.08
Kanaga Fum 1c[a]	5.76	0.95	8.14	0.0589	295.55	0.15	—	—
Kanaga Fum 2a S10	n.a	n.a	—	—	n.a	—	0.39	0.12
Kanaga Fum 2 S11	n.a	n.a	—	—	n.a	—	0.30	0.09
Gareloy Fum 1a S1	7.76	5.88	8.15	0.0658	295.31	0.07	−1.59	0.76
Gareloy Fum 1b S14[a]	7.71	3.82	8.31	0.0674	293.85	0.26	−1.63	1.01
Gareloy Fum 2a S8	6.80	4.74	7.22	0.0581	279.03	0.08	—	—
Gareloy Fum 2b S29[a]	6.91	6.63	7.20[a]	0.0515	294.19	0.21	—	—
Little Sitkin 1a S5[a,b]	0.88	0.35	n.d	—	297.67	0.16	—	—
Little Sitkin BS2 S26	7.08	93.12	7.10	0.0557	299.30	0.09	—	—
Little Sitkin Fum 1a S3	7.02	325.44	7.02	0.0566	301.19	0.09	—	—
Little Sitkin Fum 1b S9	n.a	n.a	—	—	n.a	—	—	—
Kiska Fumarole KIF1 S16	n.a	n.a	—	—	n.a	—	—	—
Tanaga Hot Spring Gas 1 S22 [b]	0.97	0.39	n.d	—	296.16	0.15	—	—

[a]*Noble gas isotopes and He/Ne from Cu tube.*
[b]*Heavily air contaminated samples - unreliable values due to analytical issues.*

TABLE 3 | Multi GAS data collected in September 2015.

	Molar ratios									mole %		
	H_2/SO_2	H_2S/SO_2	CO_2/SO_2	CO_2/H_2S	CO_2/S_T	H_2O/SO_2	H_2O/CO_2	H_2O/H_2S	H_2O	CO_2	SO_2	H_2S
Kiska	Nd	1.8	6.9	3.8	2.5	nd	Nd	nd	—	71	10.3	18.6
Little Sitkin	Nd	nd	nd	98	98	nd	11	1,078	91.6	8.3	—	0.08
Gareloi	0.11	0.1	0.26	2.6	0.2	83	320	832	98.4	0.3	1.2	0.12
Kanaga	Nd	9.5	186	19.6	18	6,696	36	705	97.1	2.7	0.015	0.14

to 270°C and displays a magmatic gas composition, all other volcanoes discharge gases that have a mixed magmatic-hydrothermal character. Helium isotopes of gas samples are within the MOR range (Graham, 2002) implying no or only minor contributions of radiogenic helium from the overriding crust. CO_2-N_2-^{3}He relative abundances allow for the assessment of the contributions of these volatiles from of from the mantle wedge and subducted materials (Sano and Marty, 1995; Sano et al., 2001). Our data of gas chemistry are consistent with minor slab-derived volatile contributions to a predominantly mantle-derived source for CO_2 and N_2. A detailed evaluation of the carbon contributions from the subducted slab and how it varies along the entire Aleutian volcanic arc is presented in Lopez et al. (in prep.). The results from direct gas samples are shown in

TABLE 4 | SO_2 fluxes measured by miniDOAS and calculated CO2 fluxes using indicated gas ratios from direct samples or MultiGAS.

	SO_2 flux t/day	±	MG	Direct	MG	Direct	SO_2 (mol/yr)	CO_2 (mol/yr)	CO_2 (mol/yr)	CO_2 (Tg/yr)	±
	—	—	C/St M	C/St M	C/SO_2	C/SO_2	—	MG CO_2/St	MG CO_2/SO_2	MG CO_2/SO_2	—
Kanaga	70	30	18	9.6	186.0	16.2	12,775	229,950	2,376,150	1.05E-04	4.5E-05
	—	—	—	56.5	—	60.5	—	—	—	—	—
Gareloi	320	80	0.20	0.28	0.20	0.34	58,400	11,680	11,680	5.1E-07	1.3E-07
	—	—	—	0.55	—	0.69	—	—	—	—	—
	—	—	—	0.41	—	0.46	—	—	—	—	—
	—	—	—	0.40	—	0.47	—	—	—	—	—
Kiska	3.6	0.1	2.5	5.09	6.9	n.d	657	1,643	4,533	2.0E-07	6E-08
Total	—	—	—	—	—	—	—	—	—	0.00011	0.00004

Tables 1 and **2**, water chemistry of spring samples is in **Supplementary Table S1** and the results of the Multi-GAS and SO_2 flux measurements are shown in **Table 3** and **Table 4**, respectively.

Direct Samples of Gas and Water Phase

The complete gas chemistry is shown in **Table 1** and compositions are typical of magmatic and hydrothermal gas discharges from volcanoes in arc settings (Fischer and Chiodini, 2015). We obtained gas samples from the plume formed above the fumarolic vents at Kiska (unknown temperature), Little Sitkin (97°C), Gareloi (102°C and 270°C), and Kanaga (95°C). We also obtained gas samples from bubbling hot springs at Little Sitkin (55°C and 66°C) and Tanaga (62°C). The sample from Kiska is heavily air contaminated and is not discussed further because we have reliable Multi-GAS data for this plume/vent. All fumarole gases are dominated by H_2O (879–986 mmol/mol), followed by CO_2 (4–115 mmol/mol) and total Sulfur (S_t = SO_2 + H_2S, 0.4–28 mmol/mol). Kanaga and Gareloi had comparatively high HCl contents of up to 2 mmol/mol. Trace gases include He, H_2, CH_4, CO. CH_4 reached up to 1.7 mmol/mol at Little Sitkin. The gases from bubbling springs and extracted from the water phase are dominated by CO_2 with minor H_2S and CH_4.

Noble gas and nitrogen isotope data are reported in **Table 2**. The $^3He/^4He$ ratios corrected for air contamination range from 7.0 to 8.3 R_a. These values are within the MORB range (8 ± 1 Ra; Graham (2002), and at the high end of values typical for arc volcanoes (Hilton et al., 2002; Sano and Fischer, 2013). Although the Gareloi samples are somewhat air contaminated, with He/Ne of 3.8–6.6, the corrected value of 8.3 Ra approaches some of the highest measured values at arcs to date: 8.6 Ra at Goryachii Klyuch in the Kurile Islands (Taran, 2009; Tolstikhin, 1986), 8.8 Ra at Galeras Volcano, Colombia, although the latter sample is highly air contaminated, resulting in a large correction (Sano et al., 1997), and 9.0 Ra at Pacaya volcano, Guatemala, in olivine-hosted fluid inclusions (Battaglia et al., 2018). The helium isotope ratios of our samples indicate that the Western Aleutian volcanoes are among the least influenced by crustal helium of any arc volcano. Two samples from bubbling springs at Tanaga and Little Sitkin are heavily air contaminated and not further discussed. The $^{40}Ar/^{36}Ar$ ratios of gas samples are similar to the air value of 295 with the highest ratio reaching 301, typical of arc gases (Sano and Fischer, 2013). As can be seen from **Table 2**, duplicate samples (e.g. Gareloi Fum 1a and 1b; and 2a and 2b) from the same fumarole with one collected in a Cu-tube and the other in a Giggenbach bottle, followed by splitting in the lab, have indistinguishable He- and Ar- isotope values. This underscores the notion that both types of samples are valid for noble gas isotope sampling; however, if highly acid gases are sampled, Cu-tubes are better to be clamped in the field, rather than cold-welded (Sano and Fischer, 2013).

Nitrogen isotope data were only obtained from two localities. The Kanaga fumaroles have values of $\delta^{15}N$ from–0.4 to +0.4‰, consistent with significant air contamination ($\delta^{15}N_{air}$ = 0.0‰) while the Gareloi fumarole gas has a value of -1.6 ± 0.9‰, also within error of air but potentially more negative. As mentioned above, these analyses were burdened with significant analytical issues, due to low signal and unidentified peaks resulting in high standard deviations, making them of limited value.

Water cation and anion data are shown in **Supplementary Table S1**. We collected water samples from springs on Kanaga, Little Sitkin, Semisopochnoi and Tanaga. Prior to our expedition, the only reported water sample data were from Semisopochnoi and Little Sitkin (Evans et al., 2015). Water temperatures range from 23°C for Semisopochnoi to 86°C at Kanaga, pH varies from acid at Little Sitkin to neutral at Semisopochnoi. Kanaga and Tanaga springs are located on the volcanoes' flanks and characterized by high Na, K, and Ca values while Semisopochnoi and Little Sitkin springs are located within the volcanoes' craters or calderas and characterized by lower, Na, K, and Ca values. SO_4 contents are highest at Little Sitkin and Cl is highest at Tanaga and Kanaga.

Multi-GAS Major Gas Ratios

We obtained Multi-GAS data from Kiska, Little Sitkin, Gareloi and Kanaga volcanoes. The results are shown in **Table 3**. Consistent with direct gas samples, the dominant gas species is H_2O, followed by CO_2 or SO_2. CO_2/S_t ratios show a wide range from 0.2 at the high-temperature vents of Gareloi to 98 at the low-temperature hydrothermal system of Little Sitkin. Kiska (2.5) and Kanaga 18) have intermediate CO_2/S_t ratios. Notably, at Gareloi,

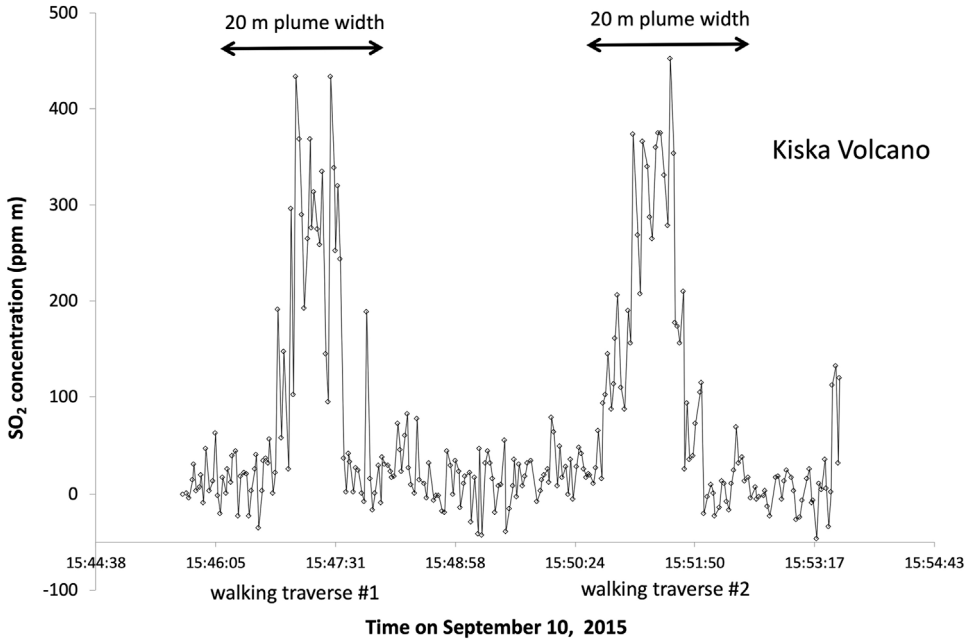


FIGURE 4 | Example of one walking traverse using the miniDOAS to measure SO_2 concentration in the Kiska fumarole plume.

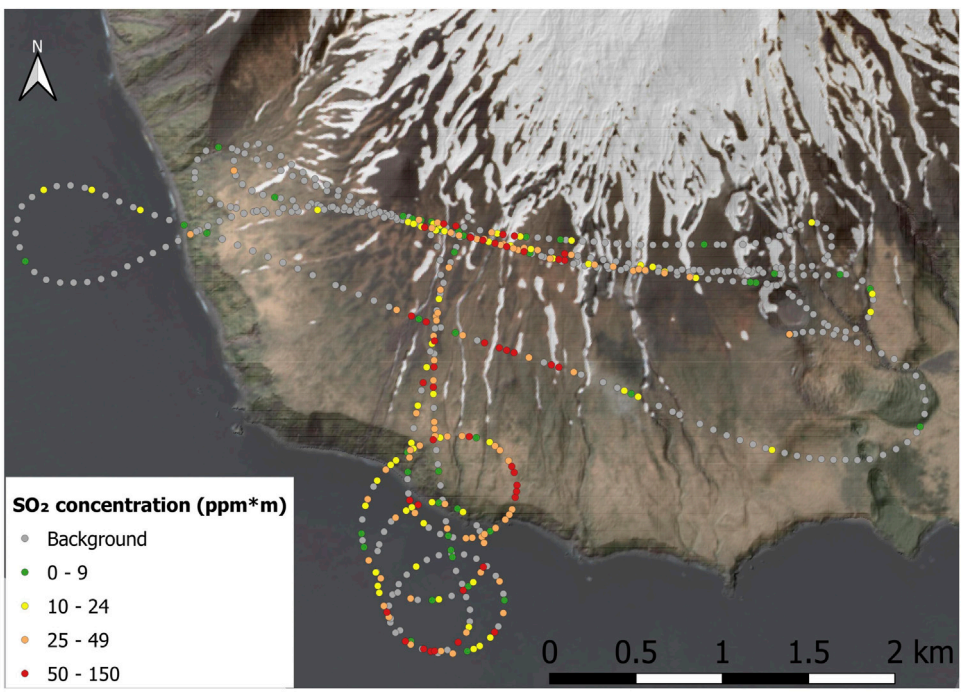


FIGURE 5 | Example of a flight path performed at Gareloi volcano for helicopter-based SO_2 concentration measurements in the plume. The Sentenial image used here was provided by Chris Waythomas, USGS.

the amount of SO_2 detected by Multi-GAS in the gas plume was higher than the mean fumarole composition, resulting in lower average H_2O/SO_2 of 83 than that of the direct gas samples (average H_2O/SO_2 = 120). We were not able to reliably measure H_2O at Kanaga. **Figure 3** shows the Multi-GAS correlation plots with R^2 values as a measure of data quality.

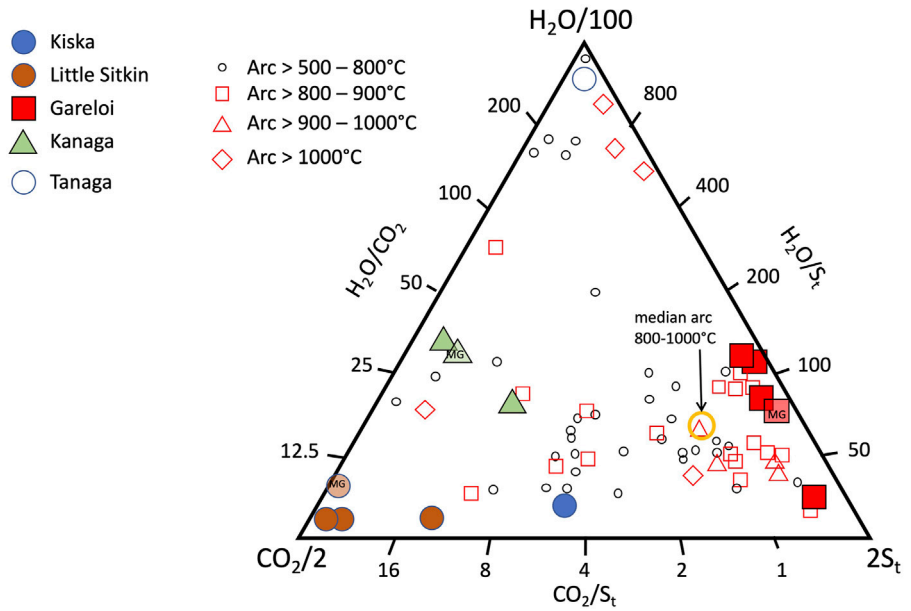


FIGURE 6 | H_2O, CO_2 and S_t (SO_2+H_2S) relative abundances of gas samples collected in this study. Also shown are high temperature gas data from arc fumaroles (Taran and Zelenski, 2015) for comparison.

SO_2 Fluxes

We successfully obtained SO_2 fluxes from Gareloi and Kanaga by helicopter traverse and from Kiska by walking traverse. The SO_2 flux data are summarized in **Table 4** and **Figure 4** shows an example of the two walking traverses performed at Kiska volcano.

At Kanaga wind speed of 12 m/s was measured and the SO_2 flux calculated by averaging 7 helicopter traverses was 70 ± 30 tons SO_2/day. At Kiska the average flux of two walking traverses was only 3.6 ± 0.1 tons SO_2/day, using a measured wind speed of 4.6 m/s. For Gareloi, we use the wind speed of 13.6 m/s to obtain a SO_2 emission rate of 320 ± 80 tons SO_2/day, averaged over 5 helicopter traverses. This was the highest average flux observed during our field campaign. The flight path of the helicopter and obtained SO_2 burdens are shown in **Figure 5**.

DISCUSSION

Major Gases

The compositions of the major gases are shown in **Figure 6**, along with a compilation of high-temperature arc gases from the literature (Henley and Fischer, 2021; Taran and Zelenski, 2015). Notably, the ratios obtained by the Multi-GAS are within the range of gas compositions obtained by direct fumarole sampling, supporting the notion that the two measurement and sampling approaches are complementary and can be used interchangeably depending on which approach is more feasible in a given situation. At Gareloi (270°C) the CO_2/S_t ratio between the four collected samples ranges from 0.3–0.6 while the H_2O/S_t ratio of three direct gas samples ranges from 97 to 137, with the fourth sample being an outlier with much lower H_2O/S_t ratio of 35. Given that the Multi-GAS recorded a H_2O/St ratio of 75, we attribute the low H_2O/S_t ratio of sample 2bS29 to water loss during sampling, consistent with significantly lower water contents of that sample compared to the three others (953 mmol/mol vs 983 mmol/mol). The low CO_2/SO_2 ratio signature is consistent with that previously proposed for the Aleutian-Kamchatka Pacific arc segment indicating relatively low slab-derived carbon contribution to gas discharges compared to other arcs (Aiuppa et al., 2017; Aiuppa et al., 2019). Low CO_2/S_t ratios may also indicate an extensively degassed magma that has lost most of its CO_2 compared to S (Giggenbach, 1996). The low temperature (~boiling point) samples from Kiska, Kanaga, and Little Sitkin display significantly higher CO_2 contents and CO_2/S_t ratios in excess of 4 with most samples' CO_2/S_t > 8. Little Sitkin gases are typical low temperature hydrothermal gases dominated by H_2O and CO_2. In terms of their H_2O/S_t ratios, Little Sitkin, Kiska and Gareloi fall within 40–150, a typical range for arc gases. Notably, the Multi-GAS data set collected for Little Sitkin has a higher H_2O/S_t (~1,000) compared to the gas samples (~50). This is likely due to the high and variable humidity at Little Sitkin fumarole and spring area that may have compromised the Multi-GAS H_2O measurements, as suggested by the low R^2 value (**Figure 3**). Kanaga gases have the highest H_2O/S_t ratios of all the gases sampled or measured, likely due to the addition of significant meteoric water in the subsurface. The sample collected at the bubbling spring of Tanaga is dominated by H_2O. Gareloi and Kiska gas compositions lie in the typical range of high temperature arc gases, even though they have significantly lower outlet temperatures (although we were not able to measure Kiska temperature), suggesting that these volcanic

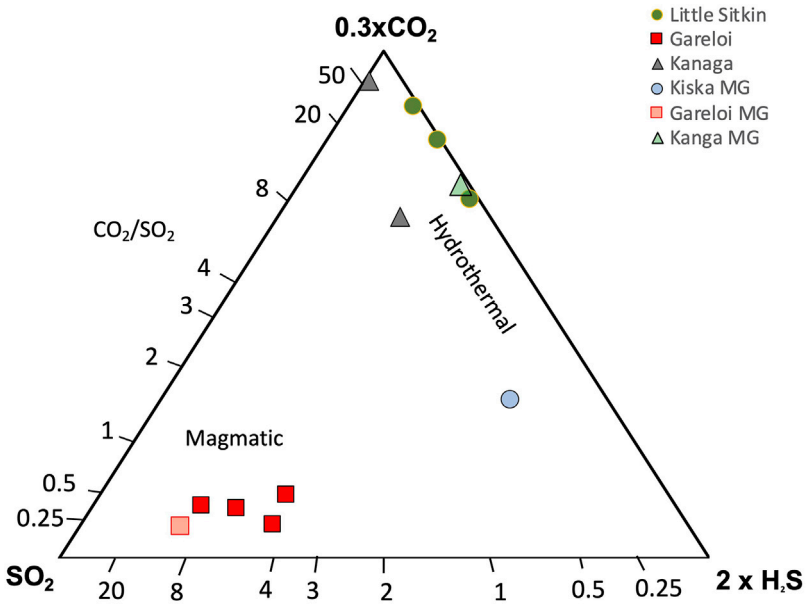


FIGURE 7 | CO_2, SO_2 and H_2S relative abundances of gases collected during this study. Magmatic gases are characterized by relatively high SO_2 contents while hydrothermal gases are dominated by CO_2 and H_2S (Giggenbach, 1996).

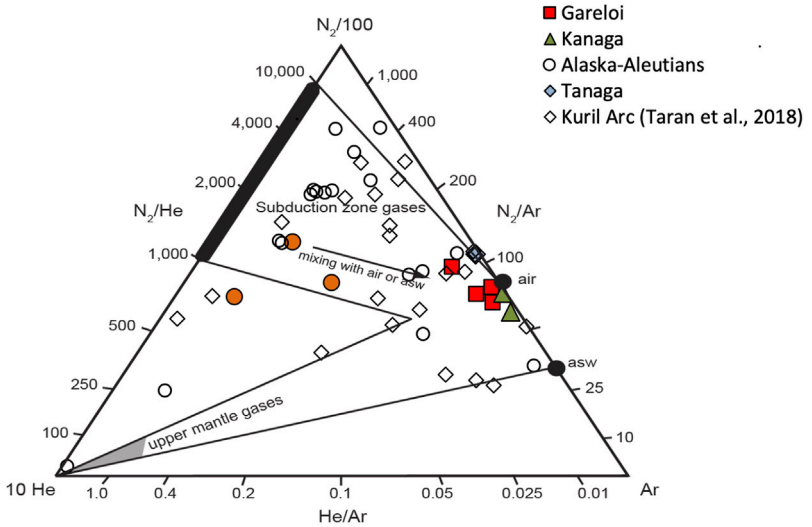


FIGURE 8 | N_2, He, Ar relative abundances of gas samples collected in this study. Also shown are data from volcanoes in Alaska and the Aleutians (Symonds et al., 2003b; Evans et al., 2015). Subduction zone gases are characterized by high N_2/He, while upper mantle gases have low N_2/He at high He/Ar (Giggenbach, 1996).

gases have had minimal interaction with hydrothermal systems (Giggenbach, 1996). This notion is also supported by data presented in **Figure 7** that show the highest SO_2/H_2S ratios for Gareloi, indicating a stronger magmatic gas signature, and significantly lower SO_2/H_2S for Little Sitkin and Kanaga, indicating mixed magmatic-hydrothermal signatures. Multi-GAS data from Kiska shows significantly lower SO_2/H_2S than Gareloi but overall higher sulfur contents than the two volcanoes dominated by hydrothermal gas discharges (Little Sitkin and Kanaga). In summary, there is good agreement between data collected by Multi-GAS and by direct gas sampling of fumaroles irrespective of gas outlet temperature or magmatic/hydrothermal character of the gases. Gareloi and Kiska have the most magmatic major gas compositions of the Western Aleutians volcanoes investigated and their compositions overlap with global high temperature arc gases from the literature.

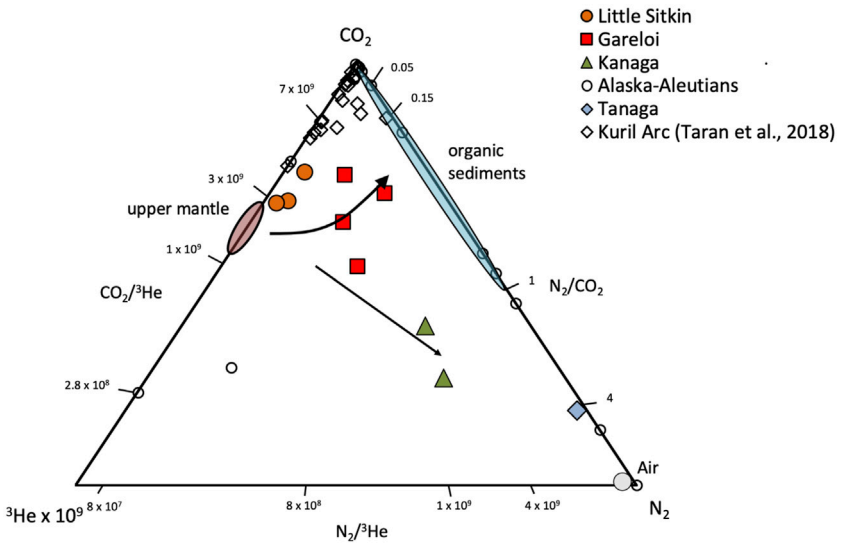


FIGURE 9 | CO_2, ^3He, ^4He relative abundances of gases sampled in this study. Upper mantle gases are characterized by $CO_2/^3He$ of ~2×10^9 and $N_2/^3He$ of ~1×10^6 Subducted organic sediments have significantly higher $CO_2/^3He$ and $N_2/3He$ and are dominated by N_2 over CO_2 (Marty and Jambon, 1987; Sano et al., 2001), resulting in molar $N_2/CO_2 < 1$. Subducted carbonates have $CO_2/^3He$ of 1×10^{13} (Sano and Marty, 1995) and the N content of AOC is on the order of 2–20 ppm (Li et al., 2007) while CO_2 in the AOC is around 2000 ppm (Alt and Teagle, 1999). Assuming a 10 ppmw N content and a 2,000 ppmw CO_2 content of the AOC would result in a N_2/CO_2 molar ratio of ~0.02 or less.(Taran et al., 2018).

Minor Gases and Redox Pairs

Trace gas N_2, He, and Ar of Western Aleutian samples are shown in **Figure 8** along with data from gas samples collected at other Alaska-Aleutian volcanoes (Evans et al., 2015; Symonds et al., 2003a) and from the geographically similar Kuril Island Arc (Taran et al., 2018). Our data display a range in compositions typical of arc gases world-wide (Giggenbach, 1996) with N_2/He ratios generally >1,000 and He/Ar ratios affected by variable amounts of mixing with air or air-saturated water. Gases from Little Sitkin show the lowest N_2/He ratios with samples from both the fumarole and bubbling spring plotting at values close to or below the typical arc-type range. We note that the definition of the arc-type field with N_2/He values from 1,000–10,000 by Giggenbach (1996) was based on significantly fewer data available at the time. More recent additions of data from samples collected from gas discharges of volcanoes in oceanic arc settings (Kurile Islands (Taran et al., 2018), Izu Bonin Marianas (Mitchell et al., 2010), Sangihe (Clor et al., 2005)) display N_2/He values at the lower end of this range, in the mantle field or in some cases between these endmembers. The upper mantle-like $^3He/^4He$ values (7.0–8.3 Ra) that preclude significant crustal contamination of the gases and the higher than mantle N_2/He ratios are indicative of N_2 addition from the subducted slab. Recent thermochemical modeling work by Epstein et al. (2021) in the Hikurangi margin suggests that N generally is better retained than C during subduction an observation that may explain some of the lower N_2/He ratios in some arcs and supports the idea of subduction of some of the N past the zone of arc magma generation (Busigny et al., 2003; Mitchell et al., 2010). The Western Aleutians data also overlap with the Kuril Islands data; however, some of the Kuril volcanoes indicate a more dominant mantle source for N_2, i.e. low N_2/He at high He/Ar values, displacing them close to the mantle gas field (**Figure 8**). Like the Western Aleutians gases, the Kuril $^3He/^4He$ values of the least air contaminated samples have air-corrected values ranging between 7.0 and 8.3 Ra (Taran et al., 2018). This consistency in $^3He/^4He$ ratios between these two oceanic arcs implies that oceanic arc gases are generally less affected than those from continental arcs by contributions of volatiles from crustal sources (Sano and Fischer, 2013), providing the opportunity to investigate slab-derived volatile sources.

Figure 9 shows relative abundances of ^3He, N_2 and CO_2. The upper mantle has $CO_2/^3He$ of ~2×10^9 and $N_2/^3He$ of ~1×10^6. Subducted organic sediments have significantly higher $CO_2/^3He$ (1×10^{13}) and $N_2/^3He$ (1×10^{12}) (Marty and Jambon, 1987; Sano and Marty, 1995; Sano et al., 2001), resulting in molar $N_2/CO_2 < 1$. Subducted carbonates sourced either from the altered oceanic crust (AOC) or sedimentary carbonates have $CO_2/^3He$ of 1×10^{13} (Sano and Marty, 1995). As the Aleutians are located in northern latitudes, there is minimal subducted sedimentary carbonate delivered to the trench (Plank and Langmuir, 1998) and it can be ruled out as contributing significantly to volcanic gas discharges, leaving the AOC as the only potential source of carbonate-derived carbon to Aleutian gas discharges. The N content of AOC is generally assumed to be quite low, on the order of 2–20 ppm (Li et al., 2007) while CO_2 in the AOC is around 2,000 ppm (Alt and Teagle, 1999). Assumption of a 10 ppmw N content and a 2000 ppmw CO_2 content for the AOC would result in a molar N_2/CO_2 ratio of ~0.02 or less, overlapping with the lower end of the organic sediment field in **Figure 9**. The diagram illustrates that gases from Little Sitkin lie closest to the mantle endmember, with a composition reflecting a

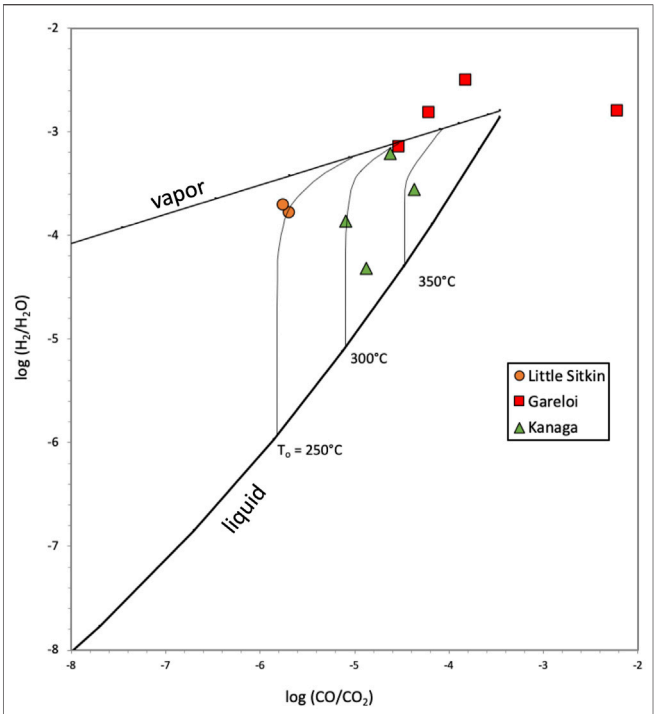


FIGURE 10 | Diagram of relavant redox pairs in hydrothermal gases showing the equilibrium compositions of liquid and vapor and relevant initial liquid temperatures (T_o) (Chiodini and Marini, 1998). The redox conditions are controlled by the f_{O2} buffer of D'Amore and Panichi (1980). Most samples lie in the liquid + vapor field suggesting a two-phase high temperature hydrothermal system at depth.

mixture of predominantly mantle and AOC sources. Gases from Gareloi have the most organic sedimentary ± AOC contributions, based on their relatively high $N_2/^3He$ and high N_2/CO_2, while gases from Kanaga and Tanaga can be explained by a predominantly mantle source mixing with air. It is also apparent that gases from Little Sitkin and Gareloi have $CO_2/^3He$ ratios that overlap with or are only slightly higher than the mantle endmember, indicating that slab-derived carbon addition in this part of the arc is likely minor. However, we note that samples from Gareloi display N_2-He-Ar relative abundances (**Figure 8**) that indicate significant air contamination and therefore, N_2 and CO_2 sources need to be treated with caution. Samples from Kanaga and Tanaga are also displaced towards the air component in **Figure 8**, compromising any evaluation of deep source contributions of N_2 to these gas discharges. Our samples from the Western Aleutians generally display lower $CO_2/^3He$ ratios than the samples from the Kuril arc (Taran et al., 2018), suggesting that gases in the Western Aleutians have a lower slab CO_2 contribution than gases from the Kuril Islands. Lopez et al (in prep) utilize C-isotopes to investigate in detail the contribution of slab derived carbon and how it varies along the Aleutian Arc, and find predominantly mantle and/or AOC carbon sources in the Western Aleutians.

Figure 10 shows that for commonly used redox pairs for H_2/H_2O and CO/CO_2 (Chiodini and Marini, 1998) and using the buffer system of D'Amore and Panichi (1980), the samples for which CO was detected (Kanaga and Gareloi) would have equilibrium temperatures of around 350°C. We note, however, that both Kanaga and Gareloi gas compositions are widely dispersed on this diagram making this assessment qualitative only. If correct, the high equilibrium temperatures in the liquid plus vapor field for Kanaga are consistent with the comparatively high CO_2/S_t and low SO_2/H_2S ratios (**Figures 6**, **7**) that suggest S deposition at depth and production of H_2S according to the following from (Giggenbach, 1996):

$$3SO_2 + 2H_2O = 2H_2SO_4 + S(0) \quad (1)$$

$$SO_2 + 2H_2S = 3S(0) + 2H_2O \quad (2)$$

$$4S(0) + 4H_2O = 3H_2S + H_2SO_4 \quad (3)$$

Therefore, Kanaga likely remains a highly active volcano with a high temperature magmatic-hydrothermal system just below the surface, although SO_2 degassing levels are low (70 ± 30 t SO_2/day) and fumaroles are diffuse. For Gareloi, one sample (1a S1) has unusually high CO contents, compared to the duplicate sample (1b S14) and the other samples from Gareloi that were collected at higher temperature sites (2a and 2b), resulting in unrealistically high $\log(CO/CO_2)$ values of −2.2. We assume that this is likely due to an analytical issue. All other Gareloi samples lie within the vapor field at high temperatures (>350°C) consistent with the magmatic character of these fumarole gases. Unfortunately, the inaccessibility of the Kiska fumarole precluded adequate collection of gas samples, making an evaluation of the equilibrium temperatures impossible. However, the extensive deposition of native sulfur around the vent area (**Figure 2A**) strongly suggests reactions of SO_2 according to 1) and 2) implying that Kiska also hosts pressurized magmatic-hydrothermal system, which is emitting roaring gases at the one fumarole. We also plotted the data for the Little Sitkin fumarole gas using the detection limit for CO (0.0002 mmol/mol), and the resulting minimum equilibrium temperatures are 250°C in a mixed liquid + vapor phase. We note that CO contents of Little Sitkin gases could be lower resulting in temperatures below 250°C. Therefore, quantitative assessment of Little Stitkin deep temperatures in not possible with these data.

Thermal Waters

Thermal water from the Western Aleutians are shown in the classic plot of Giggenbach (1988) in **Figure 11** with the theoretical lines representing equilibrium compositions with a typical hydrothermal mineral composition including K- and Na feldspars, micas and chloride. The intersection of each isotherm with the full equilibrium line indicates that the waters are in full equilibrium with this mineral assemblage at the indicated temperature. Displacement towards the Mg-rich corner of the diagram indicates that the sampled waters are either mixtures of hydrothermal fluids with shallow ground-waters or that the reactions involving Mg have quickly equilibrated during ascent of the thermal waters to the surface (i.e. Chiodini et al. (2015). In both instances, as long as the waters lie between the fully and partially equilibrated curves, the Na-Mg and Na-K

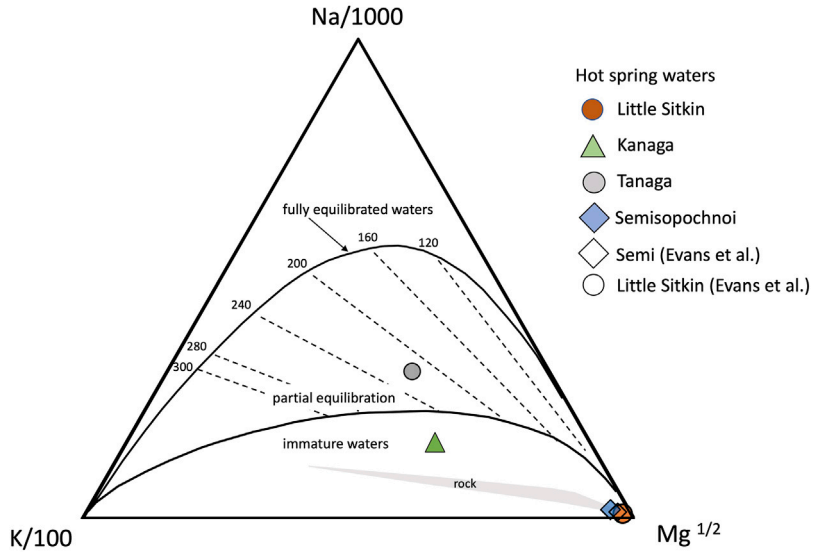


FIGURE 11 | Diagram showing the relative abundances of Na, K and Mg with lines indicating the compositions of waters partially or fully equilibrated with typical rock alteration mineral assemblages at the given temperatures (Giggenbach, 1988). Also shown is the field for a typical rock composition. Our samples are dominated by compositions that reflect immature waters not yet equilibrated with these mineral assemblages.

geothermometers still provide a valid estimate of the hydrothermal temperatures. The Mg-rich waters of Semisopochnoi and Little Sitkin lie close to the Mg-apex and overlap with the typical rock composition, indicating that these waters are immature waters and have not equilibrated with the alteration mineral assemblage. The Kanaga water sample approaches the partial equilibrium line but its composition also suggests immature water composition, out of equilibrium with relevant alteration mineral assemblages. Only Tanaga has a composition that lies in the field of partially equilibrated waters. Its Na-Mg temperature is around 220°C, consistent with a high temperature hydrothermal system at depth. Tanaga water temperature was measured at 62°C but no fumaroles were available for gas sampling to evaluate deep temperatures using gas geothermometry.

SO_2 and CO_2 Fluxes

SO_2 fluxes from Western Aleutian volcanoes are 3.6 ± 0.1 t/day (Kiska), 70 ± 30 t/day (Kanaga) and 320 ± 80 t/day (Gareloi) and are typical of the low to moderate fluxes similar to many passively degassing arc volcanoes (Shinohara, 2013; Carn et al., 2017; Fischer et al., 2019; Werner et al., 2019). CO_2 fluxes can be estimated by combining the CO_2/SO_2 ratios of direct gas emissions with measured SO_2 fluxes (Fischer et al., 1998; Aiuppa et al., 2019; Fischer et al., 2019). While this common approach provides reasonable estimates, it has been pointed out that crater plume or fumarole C/S ratios may not always be representative of the overall C/S ratios in the plume, especially if not measured at the same time as SO_2 flux, and may lead to erroneous CO_2 fluxes (Burton et al., 2013). These authors argue that direct airborne measurements of CO_2 in the plume and contemporaneous C/S ratio measurements improve the accuracy of the CO_2 estimates. Recently Fischer and Aiuppa (2020) showed that high-temperature fumarole compositions and multi-GAS measurements obtained from crater plumes combined with ground-based or satellite-based SO_2 emission provide robust CO_2 fluxes for volcanoes where degassing is dominated by crater emissions. However, estimating the CO_2 fluxes of volcanoes that have SO_2 emissions that are not detectable by satellite, and therefore are likely dominated by hydrothermal and diffuse emissions rich in H_2S and CO_2, provides a significant challenge in estimating a global CO_2 flux that also includes low emitters (Fischer et al., 2019; Werner et al., 2019; Fischer and Aiuppa, 2020). Due to constraints on time and access, we were unable to measure diffuse CO_2 emissions by accumulation chamber (Chiodini et al., 1998) and we did not have the necessary instrumentation to measure CO_2 concentrations in the plume by airborne techniques (Werner et al., 2009). However, our data from direct fumarole samples and from crater plume multi-GAS measurements enable the estimation of CO_2 flux from these volcanoes while addressing some of the issues mentioned above. For Gareloi, the high temperature (270°C) fumarole and multi-GAS CO_2/SO_2 and CO_2/S_t ratios agree well (**Table 4**). The direct fumarole samples have a CO_2/S_t of 0.41 ± 0.11while the Multi-GAS shows 0.20 for that same ratio. The Multi-GAS CO_2/SO_2 ratio (0.26) is essentially identical to that CO_2/S_t ratio (0.20) and the direct samples' CO_2/SO_2 and CO_2/S_t ratios (0.34–0.69 and 0.28 to 0.55, respectively) due to the predominance of SO_2 as the S species degassing from high T fumaroles. Using these ratios, we obtain a CO_2 flux from Gareloi of 1.17×10^4 mol C/yr or 5.14×10^5 g/yr ($5.14 \pm 1.3 \times 10^{-7}$ Tg/yr). Similarly for Kiska, where we observed degassing from one massive fumarole, the CO_2/S_t and CO_2/SO_2 ratios obtained by Multi-GAS are within a factor of two (2.5 and 5.09, respectively). Using this ratio, the CO_2 flux from Kiska is 3,090 ± 1,445 mol/yr or $1.3 \pm 0.6 \times 10^{-7}$ Tg/yr.

For Kanaga, the Multi-GAS CO_2/S_t ratios and CO_2/SO_2 ratios differ significantly (18 and 186, respectively). Likewise, CO_2/S_t and CO_2/SO_2 ratios from direct samples differ significantly and differ between gases collected from different fumaroles. At Kanaga, H_2S is a significant sulfur species and ten times more abundant than SO_2 as measured by Multi-GAS. Notably, the direct samples have variable H_2S contents, likely due to the low overall S concentrations in the gas, making SO_2 versus H_2S distinction challenging using our wet-chemistry based analytical methods. We therefore consider the Multi-GAS CO_2/SO_2 and CO_2/H_2S ratios more reliable. While it has been shown that H_2S will readily oxidize to SO_2 during high temperature (1,000 °C) mixing of magmatic gases with the atmosphere (Martin et al., 2006), low temperature oxidation is likely to be much slower. Because Kanaga equilibrium temperatures are ~300 °C and outlet temperatures are only boiling, extensive high temperature oxidation of H_2S to SO_2 is unlikely and we therefore use the Multi-GAS CO_2/SO_2 ratio for our flux estimate. This approach results in a Kanaga CO_2 flux of 2.38×10^6 mol/yr or $1.05 \pm 0.45 \times 10^{-4}$ Tg/yr. Our data show that while Gareloi is the largest SO_2 emitter of the Western Aleutians, Kanaga is the largest CO_2 emitter. Our data do not include any diffuse degassing or any flank degassing, only crater degassing.

The volcanoes of the Western Aleutians emit about $1 \pm 0.4 \times 10^{-4}$ Tg CO_2/yr, a small fraction of the 1.66 Tg CO_2 (taking into account extrapolations of non-measured volcanoes) emitted by the entire Alaska-Aleutian volcanic arc (Fischer et al., 2019). Using these workers' data, it is interesting to note that the volcanic CO_2 emissions increase significantly from the Western Aleutians (0.0001 $TgCO_2$/yr) to the Central (0.1 ± 0.09 $TgCO_2$/yr) and Eastern Aleutians (0.12 ± 0.08 $TgCO_2$/yr) and to the Alaska Peninsula (1.03 ± 0.48 $TgCO_2$/yr). When we normalize these fluxes by approximate arc segment lengths (Western Arc 500 km, Central Arc 750 km, Eastern Arc 1,100 km, **Figure 1**), we notice orders of magnitude changes in CO_2 fluxes per km with the Western Arc emitting only 2.2×10^{-7} $TgCO_2$/yr/km, the Central Arc emitting 1.3×10^{-4} $TgCO_2$/yr/km and the Eastern Arc emitting 1.05×10^{-3} $TgCO_2$/yr/km. The above values take into account only the volcanoes that have been measured and reported in Fischer et al. (2019). Applying these authors' extrapolation method, to include not measured volcanoes does not significantly change these fluxes for the eastern and central segments (1.13×10^{-3} $TgCO_2$/yr/km for eastern, 1.46×10^{-4} $TgCO_2$/yr/km for central) but increases the flux of the western segment to 1.04×10^{-4} $TgCO_2$/yr/km. The remote western segment has four volcanoes that are hydrothermally active (Great Sitkin, Moffet, Tanaga and Little Sitkin) but have not been measured for CO_2 emissions. As these volcanoes have been ascribed a flux of 0.013 $TgCO_2$/yr each in (Fischer et al., 2019), this extrapolated flux of 0.052 $TgCO_2$/yr is larger than what we measured for all western Aleutian volcanoes combined (0.001 $TgCO_2$/yr/km), leading to a significantly higher estimated flux. Future studies should focus on measuring CO_2 fluxes from these volcanoes.

Plate convergence is near orthogonal in the eastern and central portion of the arc and gradually becomes more oblique in the western region of the Aleutian Arc, with plate motion eventually transitioning to strike-slip near ~170°E (**Figure 1**) (DeMets et al., 1990; Buurman et al., 2014). The varying convergence angles, combined with the thickness of subducted sediment, result in highly variable subducted sediment fluxes along the length of the arc, with a maximum in the central Aleutians and a minimum in the western Aleutians (Kelemen et al., 2003). The Eastern Aleutians are characterized by thicker continental crust (Fliedner and Klemperer, 2000). These along-strike variations in subduction parameters and crustal thickness may potentially affect the observed volcanic CO_2 output along the strike of the arc as is discussed in more detail in (Lopez et al., in preparation).

CONCLUSION

Our new data of gas and spring discharges from the Western Aleutian volcanoes provide key information about the nature of the volcano-hydrothermal systems in this region. The results indicate that all the volcanoes investigated host high-temperature mixed liquid-vapor systems that are fed by volatiles primarily sourced from the mantle wedge and the subducted slab, with negligible crustal contamination. In particular, Kiska, Kanaga and Gareloi have gas compositions that indicate a significant magmatic degassing component. Our measured SO_2 and CO_2 fluxes provide background values during a low-level of activity that provide a baseline against which future fluxes can be compared and evaluated in light of changes in volcanic activity. The Aleutian Arc is well known for its along-strike variations in subduction parameters such as convergence angle, amount of sediment delivery to the trench and crustal thickness. While more work on volcanic gas fluxes is needed, especially in the remote regions of the arc, our data suggests that volcanic CO_2 fluxes are lowest where convergence angle is most oblique and sediment delivery to the trench is at its minimum.

DATA AVAILABILITY STATEMENT

The original contributions presented in the study are included in the article/**Supplementary Material**, further inquiries can be directed to the corresponding author.

AUTHOR CONTRIBUTIONS

TF helped obtain the funding, collected most of the samples and data, coordinated the analyses, made most of the figures and wrote the article. TL helped obtain the funding collected some of the samples and data, performed most of the analyses and contributed to the article. AA provided instrumentation to make some of the measurements, plotted some of the data and contributed to the article AR analyzed some of the samples and contributed to the article TI analyzed some of the samples and contributed to the article KK obtained funding, was co-Scientist in Charge of the cruise and contributed to the article EC obtained funding, was co-Scientist in Charge of the cruise, provided a figure and contributed to the article.

FUNDING

This work was funded by NSF EAR GeoPRISMS 1347248 to EC, a Smithsonian Scholarly Studies Grant to EC, NSF EAR GeoPRISMS 1347330 to KK, by NSF GeoPRISMS grant 1551978 to TF and TL and by support form the Deep Carbon Observatory-DECADE Initiative to TF and TL.

ACKNOWLEDGMENTS

We thank the individuals and organizations that made the summer field season of 2015 possible aboard the third leg of the NSF GeoPRISMS shared platform for Aleutians research, including Captain Raines and the crew of the R/V Maritime Maid, pilot Dan Leary and Maritime Helicopters, Christie Haupert at Polar Field Services, EAR NSF program officers, the USGS Natural Hazards Program, the Deep Carbon Observatory, DECADE Initiative, and the shipboard scientific party. We thank Michelle Coombs for comments on the manuscript and Samantha Wolf for help with the figures. The thank Viorel Atudorei, UNM Center for Stable isotopes for help with nitrogen isotope measurements.We thank Antonio Paonita for handling this masuscript as editor and two reviewers for comments on an earlier version of this manuscript.

SUPPLEMENTARY MATERIAL

The Supplementary Material for this article can be found online at: https://www.frontiersin.org/articles/10.3389/feart.2021.786021/full#supplementary-material

REFERENCES

Aiuppa, A., Fischer, T. P., Plank, T., and Bani, P. (2019). CO2 Flux Emissions from the Earth's Most Actively Degassing Volcanoes, 2005-2015. *Sci. Rep.* 9, 5442. doi:10.1038/s41598-019-41901-y

Aiuppa, A., Frederico, C., Giudice, G., and Gurrieri, S. (2005). Chemical Mapping of a Fumarolic Field: La Fossa Crater, Vulcano Island (Aeolian Islands, Italy). *Geophys. Res. Lett.* 32, L13309. doi:10.1029/2005GL023207

Aiuppa, A., Robidoux, P., Tamburello, G., Conde, V., Galle, B., Avard, G., et al. (2014). Gas Measurements from the Costa Rica-Nicaragua Volcanic Segment Suggest Possible Along-Arc Variations in Volcanic Gas Chemistry. *Earth Planet. Sci. Lett.* 407, 134–147. doi:10.1016/j.epsl.2014.09.041

Alt, J. C., and Teagle, D. A. H. (1999). The Uptake of Carbon during Alteration of Ocean Crust. *Geochimica et Cosmochimica Acta* 63, 1527–1535. doi:10.1016/s0016-7037(99)00123-4

Battaglia, A., Bitetto, M., Aiuppa, A., Rizzo, A. L., Chigna, G., Watson, I. M., et al. (2018). The Magmatic Gas Signature of Pacaya Volcano, with Implications for the Volcanic CO2 Flux from Guatemala. *Geochem. Geophys. Geosystems* 19, 667–692. doi:10.1002/2017gc007238

Bergfeld, D., Lewicki, J. L., Evans, W. C., Hunt, A. G., Revesz, K., and Huebner, M. (2013).Geochemical Investigation of the Hydrothermal System on Akutan Island, Alaska. U.S. Geological Survey Scientific Investigation Report 2013-5231. Reston, Virginia: U.S. Geological Survey, 1–19.

Burton, M. R., Sawyer, G. M., and Granieri, D. (2013). Deep Carbon Emissions from Volcanoes. *Rev. Mineralogy Geochem.* 75, 323–354. doi:10.2138/rmg.2013.75.11

Busigny, V., Cartigny, P., Philippot, P., Ader, M., and Javoy, M. (2003). Massive Recycling of Nitrogen and Other Fluid-mobile Elements (K, Rb, Cs, H) in a Cold Slab Environment: Evidence from HP to UHP Oceanic Metasediments of the Schistes Lustres Nappe (Western Alps, Europe). *Earth Planet. Sci. Let.* 215, 27–42. doi:10.1016/S0012-821X(03)00453-9

Buurman, H., Nye, C. J., West, M. E., and Cameron, C. (2014). Regional Controls on Volcano Seismicity along the Aleutian Arc. *Geochem. Geophys. Geosyst.* 15, 1147–1163. doi:10.1002/2013gc005101

Cameron, C. E., Schaefer, J. R., and Ekberg, P. G. (2020). Historically Active Volcanoes of Alaska. Alaska Division of Geological & Geophysical Surveys Miscellaneous Publication 133 v. 4, 2 sheets.

Carn, S. A., Fioletov, V. E., McLinden, C. A., Li, C., and Krotkov, N. A. (2017). A Decade of Global Volcanic SO2 Emissions Measured from Space. *Sci. Rep.* 7, 44095. doi:10.1038/srep44095

Casadevall, T. J., Doukas, M. P., Neal, C. A., McGimsey, R. G., and Gardner, C. A. (1994). Emission Rates of Sulfur Dioxide and Carbon Dioxide from Redoubt Volcano, Alaska during the 1989-1990 Eruptions. *J. Volcanology Geothermal Res.* 62, 519–530. doi:10.1016/0377-0273(94)90050-7

Chiodini, G., Cioni, R., Guidi, M., Raco, B., and Marini, L. (1998). Soil CO2 Flux Measurements in Volcanic and Geothermal Areas. *Appl. Geochem.* 13 (5), 543–552. doi:10.1016/s0883-2927(97)00076-0

Chiodini, G., Liccioli, C., Vaselli, O., Calabrese, S., Tassi, F., Caliro, S., et al. (2015). The Domuyo Volcanic System: An Enormous Geothermal Resource in Argentine Patagonia. *J. Volcanol. Geotherm. Res.* 274, 71–77. doi:10.1016/j.jvolgeores.2014.02.006

Chiodini, G., and Marini, L. (1998). Hydrothermal Gas Equilibria: the H2O-H2-CO2-CO-CH4 System. *Geochim. Cosmochim. Acta* 62, 2673e2687. doi:10.1016/s0016-7037(98)00181-1

Clor, L. E., Fischer, T. P., Hilton, D. R., Sharp, Z. D., and Hartono, U. (2005). Volatile and N Isotope Chemistry of the Molucca Sea Collision Zone: Tracing Source Components along the Sangihe Arc, Indonesia. *Geochem. Geophys. Geosyst.* 6, a–n. doi:10.1029/2004GC000825

Coombs, M. L., McGimsey, R. G., and Browne, B. L. (2008). Preliminary Volcano-hazard Assessment for Gareloi Volcano, Gareloi Island, Alaska. *U.S. Geol. Surv. Scientific Invest. Rep. 2008–5159*, 26. doi:10.3133/sir20085159

Coombs, M. L., McGimsey, R. G., and Browne, B. L. (2007). Preliminary Volcano-hazard Assessment for the Tanaga Volcanic Cluster, Tanaga Island, Alaska. *U.S. Geol. Surv. Scientific Invest. Rep. 2007-5094*, 36, 2007 . Available at: http://pubs.usgs.gov/sir/2007/5094/.

de Moor, J. M., Fischer, T. P., Sharp, Z. D., Hilton, D. R., Barry, P. H., Mangasini, F., et al. (2013a). Gas Chemistry and Nitrogen Isotope Compositions of Cold Mantle Gases from Rungwe Volcanic Province, Southern Tanzania. *Chem. Geology.* 339, 30–42. doi:10.1016/j.chemgeo.2012.08.004

de Moor, J. M., Fischer, T. P., Sharp, Z. D., King, P. L., Wilke, M., Botcharnikov, R. E., et al. (2013b). Sulfur Degassing at Erta Ale (Ethiopia) and Masaya (Nicaragua) Volcanoes: Implications for Degassing Processes and Oxygen Fugacities of Basaltic Systems. *Geochem. Geophys. Geosyst.* 14, 4076–4108. doi:10.1002/ggge.20255

DeMets, C., Gordon, R. G., Argus, D. F., and Stein, S. (1990). Current Plate Motions. *Geophys. J. Int.* 101, 425–478. doi:10.1111/j.1365-246x.1990.tb06579.x

Doukas, M., and McGee, K. (2007).A Compilation of Gas Emission-Rate Data from Volcanoes of Cook Inlet (Spurr, Crater Peak, Redoubt, Illiamna, and Augustine) and Alaska Peninsula (Douglas, Fourpeaked, Griggs, Mageik, Martin, Peulik, Ukinrek Maars, and Veniaminof), Alaska, from 1995-2006. Open-File Report 02-395. Reston, Virginia: U.S. Geological Survey.

Doukas, M. P. (1995).A Compilation of Sulfur Dioxide and Carbon Dioxide Emission-Rate Data from Cook Inlet Volcanoes (Redoubt, Spurr, Iliamna, and Augustine), Alaska during the Period from 1990-1994. USGS Open-File Report, 95-55. Reston, Virginia: U.S. Geological Survey.

Doukas, M. P. (2002).A New Method for GPS-Based Wind Speed Determinations during Airborne Volcanic Plume Measurements. USGS Open-File Report 02-395. Reston, Virginia: U.S. Geological Survey.

Epstein, G. S., Bebout, G. E., Christenson, B. W., Sumino, H., Wada, I., Werner, C., et al. (2021). Cycling of CO2 and N2 along the Hikurangi Subduction Margin,

New Zealand: An Integrated Geological, Theoretical, and Isotopic Approach. *Geochem. Geophys. Geosys.* 22, e2021GC009650. doi:10.1029/2021GC009650

Evans, W. C., Bergfeld, D., McGimsey, R. G., and Hunt, A. G. (2009). Diffuse Gas Emissions at the Ukinrek Maars, Alaska: Implications for Magmatic Degassing and Volcanic Monitoring. *Appl. Geochem.* 24, 527–535. doi:10.1016/j.apgeochem.2008.12.007

Evans, W. C., Bergfeld, D., Neal, C. A., McGimsey, R. G., Werner, C. A., Waythomas, C. F., et al. (2015). Aleutian Arc Geothermal Fluids: Chemical Analyses of Waters and Gases Sampled in Association with the Alaska Volcano Observatory. *U.S. Geol. Surv. Data Release*. doi:10.5066/F78G8HR1

Fierstein, J., and Hildreth, W. (1992). The Plinian Eruptions of 1912 at Novarupta, Katmai National Park, Alaska. *Bull. Volcanol* 54 (8), 646–684. doi:10.1007/bf00430778

Fischer, T. P., and Aiuppa, A. (2020). AGU Centennial Grand Challenge: Volcanoes and Deep Carbon Global CO2 Emissions from Subaerial Volcanism: Recent Progress and Future Challenges. *G-cubed* 21 (3), e2019GC008690. doi:10.1029/2019gc008690

Fischer, T. P., Arellano, S., Carn, S., Aiuppa, A., Galle, B., Allard, P., et al. (2019). The Emissions of CO2 and Other Volatiles from the World's Subaerial Volcanoes. *Sci. Rep.* 9, 18716. doi:10.1038/s41598-019-54682-1

Fischer, T. P., and Chiodini, G. (2015). Volcanic, Magmatic and Hydrothermal Gases. *Encyclopedia of Volcanoes*. 2nd Edition, 779–797. doi:10.1016/B978-0-12-385938-9.00045-6

Fischer, T. P., Giggenbach, W. F., Sano, Y., and Williams, S. N. (1998). Fluxes and Sources of Volatiles Discharged from Kudryavy, a Subduction Zone Volcano, Kurile Islands. *Earth Planet. Sci. Lett.* 160, 81–96. doi:10.1016/s0012-821x(98)00086-7

Fischer, T. P., and Lopez, T. M. (2016). First Airborne Samples of a Volcanic Plume for d13C of CO2 Determinations. *Geophys. Res. Lett.* 43, 3272–3279. doi:10.1002/2016gl068499

Fliedner, M. M., and Klemperer, S. L. (2000). Crustal Structure Transition from Oceanic Arc to continental Arc, Eastern Aleutian Islands and Alaska Peninsula. *Earth Planet. Sci. Lett.* 179, 567–579. doi:10.1016/s0012-821x(00)00142-4

Galle, B., Oppenheimer, C., Geyer, A., McGonigle, A. J. S., Edmonds, M., and Horrocks, L. (2002). A Miniaturised Ultraviolet Spectrometer for Remote Sensing of SO2 Fluxes; a New Tool for Volcano Surveillance. *J. Volcanol. Geotherm. Res.* 119, 241–254. doi:10.1016/S0377-0273(02)00356-6

Gerlach, T. M., Westrich, H. R., Casadevall, T. J., and Finnegan, D. L. (1994). Vapor Saturation and Accumulation in Magmas of the 1989-1990 Eruption of Redoubt Volcano, Alaska. *J. Volcanology Geothermal Res.* 62, 317–337. doi:10.1016/0377-0273(94)90039-6

Giggenbach, W. F. (1996). "Chemical Composition of Volcanic Gases," in *IAVCEI-UNESCO: Monitoring and Mitigation of Volcano Hazards*. Editors R. Scarpa and R. Tilling, 221–256. doi:10.1007/978-3-642-80087-0_7

Giggenbach, W. F. (1988). Geothermal Solute Equilibria. Derivation of Na-K-Mg-Ca Geoindicators. *Geochimica et Cosmochimica Acta* 52, 2749–2765. doi:10.1016/0016-7037(88)90143-3

Giggenbach, W. F., and Goguel, R. L. (1989a). Collection and Analysis of Goethermal and Volcanci Water and Gas Discharges. Report, No. 2401. Department of Scientific and Industrial Research, Chemistry Division.

Giggenbach, W. F., and Goguel, R. L. (1989b). Methods for the Collection and Analysis of Geothermal and Volcanic Water and Gas Samples. CD 2387. Department of scientific and industrial research, chemistry devision.

Graham, D. W. (2002). "8. Noble Gas Isotope Geochemistry of Mid-ocean Ridge and Ocean Island Basalts: Characterization of Mantle Source Reservoirs," in *MSA Special Volume: Noble Gases*. Editors D. Porcelli, C. Ballentine, and R. Wieler, 47, 247–318. doi:10.1515/9781501509056-010

GVP (2013). "Report on Kanaga (United States)," in *Bulletin of the Global Volcanism Network*. Editor R. Wunderman (Washington, DC: Smithsonian Institution), 38, 3. Available at: https://volcano.si.edu/E3/. Sep Accessed 25, 2019).

GVP (2015). "Report on Pavlof (United States)," in *Bulletin of the Global Volcanism Network*. Editor R. Wunderman (Washington, DC: Smithsonian Institution), 40, 4. Available at: https://volcano.si.edu/E3/. Sep Accessed 25, 2019).

GVP (2021a). "Report on Cleveland (United States)," in *Weekly Volcanic Activity Report, 24 March-30 March 2021*. Editor S. K. Sennert (Washington, DC: Smithsonian Institution and US Geological Survey). GVP.WVAR20210324-311240.

GVP (2021b). "Report on Gareloi (United States)," in *Weekly Volcanic Activity Report, 28 July-3 August 2021*. Editor S. K. Sennert (Washington, DC: Smithsonian Institution and US Geological Survey). doi=GVP.WVAR20210728-311070.

GVP (2021c). "Report on Pavlof (United States)," in *Weekly Volcanic Activity Report, 18 August-24 August 2021*. Editor S. K. Sennert (Washington, DC: Smithsonian Institution and US Geological Survey). doi=GVP.WVAR20210818-312030.

GVP (2021d). "Report on Semisopochnoi (United States)," in *Bulletin of the Global Volcanism Network*. Editors J. B. Krippner and E. Venzke (Washington, DC: Smithsonian Institution), 46, 6. doi:10.5479/si.GVP.BGVN202106-311060

GVP (2019). "Report on Great Sitkin (United States),"in. *Bulletin of the Global Volcanism Network*. Editor E. Venzke (Smithsonian Institution), 44, 7. doi:10.5479/si.GVP.BGVN201907-311120

Henley, R. W., and Fischer, T. P. (2021). Sulfur Sequestration and Redox Equilibria in Volcanic Gases. *J. Volcanology Geothermal Res.* 414, 107181. doi:10.1016/j.jvolgeores.2021.107181

Hilton, D. R., Fischer, T. P., and Marty, B. (2002). "9. Noble Gases and Volatile Recycling at Subduction Zones," in *MSA Special Volume: Noble Gases in Geochemistry and Cosmochemistry*. Editors D. Porcelli, C. Ballentine, and R. Wieler, 47, 319–370. doi:10.1515/9781501509056-011

Hilton, D. R., Fischer, T. P., McGonigle, A. J. S., and de Moor, J. M. (2007). Variable SO_2 Emission Rates for Anatahan Volcano, the Commonwealth of the Northern Mariana Islands: Implications for Deriving Arc-wide Volatile Fluxes from Erupting Volcanoes. *Geophys. Res. Lett.* 34. doi:10.1029/2007GL030405

Ilanko, T., Fischer, T. P., Kyle, P., Curtis, A., Lee, H., and Sano, Y. (2019). Modification of Fumarolic Gases by the Ice-Covered Edifice of Erebus Volcano, Antarctica. *J. Volcanol. Geotherm. Res.* 381, 119–139. doi:10.1016/j.jvolgeores.2019.05.017

Kelemen, P. B., Yogodzinski, G. M., and Scholl, D. W. (2003). Along-strike Variation in the Aleutian Island Arc: Genesis of High Mg# Andesite and Implications for continental Crust. *Geophys. Monogr.* 138, 223–276. doi:10.1029/138gm11

Kraus, S. (2006). DOASIS a Framework Design for DOAS. Ph.D. Thesis Thesis (Mannheim: Universitaet Mannheim).

Larsen, J. F., Neal, C. A., and Cameron, C. E. (2020). Major-oxide and Trace-Element Geochemical Data from Rocks Collected on Little Sitkin Island, from Little Sitkin Volcano, Alaska. *Alsk. Division Geol. Geophys. Surv. Raw Data File 2020-4*, 4. doi:10.14509/30440

Lee, H., Fischer, T. P., Muirhead, J. D., Ebinger, C. J., Kattenhorn, S. A., Sharp, Z. D., et al. (2017). Incipient Rifting Accompanied by the Release of Subcontinental Lithospheric Mantle Volatiles in the Magadi and Natron basin, East Africa. *J. Volcanology Geothermal Res.* 346, 118–133. doi:10.1016/j.jvolgeores.2017.03.017

Li, L., Bebout, G. E., and Idleman, B. D. (2007). Nitrogen Concentration and δ15N of Altered Oceanic Crust Obtained on ODP Legs 129 and 185: Insights into Alteration-Related Nitrogen Enrichment and the Nitrogen Subduction Budget. *Geochimica et Cosmochimica Acta* 71, 2344–2360. doi:10.1016/j.gca.2007.02.001

Lopez, T., Tassi, F., Aiuppa, A., Galle, B., Rizzo, A. L., Fiebig, J., et al. (2017). Geochemical Constraints on Volatile Sources and Subsurface Conditions at Mount Martin, Mount Mageik, and Trident Volcanoes, Katmai Volcanic Cluster, Alaska. *J. Volcanology Geothermal Res.* 347, 64–81. doi:10.1016/j.jvolgeores.2017.09.001

Martin, R. S., Mather, T. A., and Pyle, D. M. (2006). High-temperature Mixtures of Magmatic and Atmospheric Gases. *Geochem. Geophys. Geosyst.* 7, Q04006. doi:10.1029/2005gc001186

Marty, B., and Jambon, A. (1987). C3He in Volatile Fluxes from the Solid Earth: Implications for Carbon Geodynamics. *Earth Planet. Sci. Lett.* 83, 16–26. doi:10.1016/0012-821x(87)90047-1

McGee, K. A., Doukas, M. P., McGimsey, R. G., Neal, C. A., and Wessels, R. L. (2010). "Emission of SO2, CO2, and H2S from Augustine Volcano, 2002-2008: Chapter 26 in the 2006 Eruption of Augustine Volcano, Alaska," in *The 2006 Eruption of Augustine Volcano, Alaska*. Editors J. Power, M. Coombs, and J. Freymueller (Reston, Virginia: U.S. Geological Survey Professional Paper 1769), 609–627. doi:10.3133/pp176926

Miller, T. P., McGimsey, R. G., Richter, D. H., Riehle, J. R., Nye, C. J., Yount, M. E., et al. (1998).Catalog of the Historically Active Volcanoes of Alaska. U.S. Geological Survey Open-File Report 98-0582. Reston, Virginia: U.S. Geological Survey, 104.

Mitchell, E. C., Fischer, T. P., Hilton, D. R., Hauri, E. H., Shaw, A. M., de Moor, J. M., et al. (2010). Nitrogen Sources and Recycling at Subduction Zones: Insights from the Izu-Bonin-Mariana Arc. *Geochem. Geophys. Geosyst.* 11, a–n. doi:10.1029/2009GC002783

Motyka, R. J., Liss, S. A., Nye, C. J., and Moorman, M. A. (1993). *Geothermal Resources of the Aleutian Arc*. Reston, Virginia: USGS Professional Report, 114.

Oppenheimer, C., Fischer, T. P., and Scaillet, B. (2014). Volcanic Degassing: Processes and Impact. *Treastise Geochem.* 4, 111–179. doi:10.1016/B1978-1010-1008-095975-095977.000304-095971

Plank, T., and Langmuir, C. H. (1998). The Chemical Composition of Subducting Sediment and its Consequences for the Crust and Mantle. *Chem. Geology.* second edition 145, 325–394. doi:10.1016/s0009-2541(97)00150-2

Rizzo, A. L., Caracausi, A., Chavagnac, V., Nomikou, P., Polymenakou, P. N., Mandalakis, M., et al. (2016). Kolumbo Submarine Volcano (Greece): An Active Window into the Aegean Subduction System. *Sci. Rep.* 6, 28013. doi:10.1038/srep28013

Rizzo, A. L., Jost, H. J., Caracausi, A., Paonita, A., Liotta, M., and Martelli, M. (2014). Real-time Measurements of the Concentration and Isotope Composition of Atmospheric and Volcanic CO 2 at Mount Etna (Italy). *Geophys. Res. Lett.* 41, 2382–2389. doi:10.1002/2014gl059722

Sano, Y., and Fischer, T. P. (2013). "The Analysis and Interpretation of noble Gases in Modern Hydrothermal Systems," in *Noble Gases as Geochemical Tracers (Peter Burnard, Editor). Series: Advances in Isotope Geochemisrty*. Editors J. Hoefs (Heidelberg: Springer-Verlag). ISBN 978-3-642-28835-7. doi:10.1007/978-3-642-28836-4_10

Sano, Y., Gamo, T., and Williams, S. N. (1997). Secular Variations of Helium and Carbon Isotopes at Galeras Volcano, Colombia. *J. Volcanology Geothermal Res.* 77, 255–265. doi:10.1016/s0377-0273(96)00098-4

Sano, Y., and Marty, B. (1995). Origin of Carbon in Fumarolic Gas from Island Arcs. *Chem. Geology.* 119, 265–274. doi:10.1016/0009-2541(94)00097-r

Sano, Y., Takahata, N., Nishio, Y., Fischer, T. P., and Williams, S. N. (2001). Volcanic Flux of Nitrogen from the Earth. *Chem. Geology.* 171, 263–271. doi:10.1016/s0009-2541(00)00252-7

Shinohara, H. (2013). Volatile Flux from Subduction Zone Volcanoes: Insights from a Detailed Evaluation of the Fluxes from Volcanoes in Japan. *J. Volcanology Geothermal Res.* 268, 46–63. doi:10.1016/j.jvolgeores.2013.10.007

Snyder, G. L. (1959). Geology of Little Sitkin Island, Alaska. In Investigations of Alaskan Volcanoes. U.S. Geological Survey Bulletin 1028-H. Reston, Virginia: U.S. Geological Survey, 169–210.

Stoiber, R. E., Malinconico, L. L. J., and Williams, S. N. (1983). "Use of the Correlation Spectrometer at Volcanoes," in *Forecasting Volcanic Events*. Editors H. Tazieff and J. Sabroux (New York: Elsevier), 425–444.

Symonds, R. B., Janik, C. J., Evans, W. C., Ritchie, B. E., Counce, D., Poreda, R., et al. (2003a). Scrubbing Masks Magmatic DegassingDuring Repose at Cascade-Range andAleutian-Arc Volcanoes. USGS Open File report, 03-435. Reston, Virginia: U.S. Geological Survey.

Symonds, R. B., Poreda, R. J., Evans, W. C., and Janik, C. J. (2003b). Mantle and Crustal Sources of Carbon, Nitrogen, and noble Gases in Cascade-Range and Aleutian-Arc Volcanic Gases. U.S. Geological Survey Open-File Report 03-436. Reston, Virginia: U.S. Geological Survey.

Taran, Y. A. (2009). Geochemistry of Volcanic and Hydrothermal Fluids and Volatile Budget of the Kamchatka-Kuril Subduction Zone. *Geochimica et Cosmochimica Acta* 73 (4), 1067–1094. doi:10.1016/j.gca.2008.11.020

Taran, Y., Zelenski, M., Chaplygin, I., Malik, N., Campion, R., Inguaggiato, S., et al. (2018). Gas Emissions from Volcanoes of the Kuril Island Arc (NW Pacific): Geochemistry and Fluxes. *Geochem. Geophys. Geosyst.* 19, 1859–1880. doi:10.1029/2018gc007477

Taran, Y., and Zelenski, M. (2015). Systematics of Water Isotopic Composition and Chlorine Content in Arc-Volcanic Gases. *Geol. Soc. Lond. Spec. Publications* 410 (1), 237–262. doi:10.1144/sp410.5

Tolstikhin, I. N. (1986). *Isotope Geochemistry of Helium Argon and Rare Gases*. Leningrad: Nauka, 200. in Russian.

Werner, C. A., Doukas, M. P., and Kelly, P. J. (2011). Gas Emissions from Failed and Actual Eruptions from Cook Inlet Volcanoes, Alaska, 1989-2006. *Bull. Volcanol* 73, 155–173. doi:10.1007/s00445-011-0453-4

Werner, C., Evans, W. C., Poland, M., Tucker, D. S., and Doukas, M. P. (2009). Long-term Changes in Quiescent Degassing at Mount Baker Volcano, Washington, USA; Evidence for a Stalled Intrusion in 1975 and Connection to a Deep Magma Source. *J. Volcanology Geothermal Res.* 186 (3-4), 379–386. doi:10.1016/j.jvolgeores.2009.07.006

Werner, C., Fischer, T. P., Aiuppa, A., Edmonds, M., Cardellini, C., Carn, S., et al. (2019). "Carbon Dioxide Emissions from Subaerial Volcanic Regions," in *Deep Carbon: Past to Present*. Editors B. N. Orcutt, I. Daniel, and R. Dasgupta (Cambridge, United Kingdom: Cambridge University Press). doi:10.1017/9781108677950.008

Werner, C., Kelly, P. J., Doukas, M., Lopez, T., Pfeffer, M., McGimsey, R., et al. (2013). Degassing of CO2, SO2, and H2S Associated with the 2009 Eruption of Redoubt Volcano, Alaska. *J. Volcanology Geothermal Res.* 259, 270–284. doi:10.1016/j.jvolgeores.2012.04.012

Conflict of Interest: The authors declare that the research was conducted in the absence of any commercial or financial relationships that could be construed as a potential conflict of interest.

Publisher's Note: All claims expressed in this article are solely those of the authors and do not necessarily represent those of their affiliated organizations, or those of the publisher, the editors and the reviewers. Any product that may be evaluated in this article, or claim that may be made by its manufacturer, is not guaranteed or endorsed by the publisher.

Copyright © 2021 Fischer, Lopez, Aiuppa, Rizzo, Ilanko, Kelley and Cottrell. This is an open-access article distributed under the terms of the Creative Commons Attribution License (CC BY). The use, distribution or reproduction in other forums is permitted, provided the original author(s) and the copyright owner(s) are credited and that the original publication in this journal is cited, in accordance with accepted academic practice. No use, distribution or reproduction is permitted which does not comply with these terms.

frontiers in Earth Science

ORIGINAL RESEARCH
published: 24 December 2021
doi: 10.3389/feart.2021.773819

Intermittent Growth of a Newly-Born Volcanic Island and Its Feeding System Revealed by Geological and Geochemical Monitoring 2013–2020, Nishinoshima, Ogasawara, Japan

Fukashi Maeno[1]*, *Atsushi Yasuda*[1], *Natsumi Hokanishi*[1], *Takayuki Kaneko*[1], *Yoshihiko Tamura*[2], *Mitsuhiro Yoshimoto*[3], *Shun Nakano*[4], *Akimichi Takagi*[5], *Minoru Takeo*[1,5] and *Setsuya Nakada*[1,6]

[1]Earthquake Research Institute, The University of Tokyo, Tokyo, Japan, [2]Japan Agency for Marine-Earth Science and Technology, Yokosuka, Japan, [3]Mount Fuji Research Institute, Yamanashi Prefectural Government, Fujiyoshida, Japan, [4]Geological Survey of Japan, National Institute of Advanced Industrial Science and Technology, Tsukuba, Japan, [5]Japan Meteorological Agency, Tokyo, Japan, [6]National Research Institute for Earth Science and Disaster Resilience, Tsukuba, Japan

OPEN ACCESS

Edited by:
Joan Marti,
Spanish National Research Council (CSIC), Spain

Reviewed by:
Corrado Cimarelli,
Ludwig Maximilian University of Munich, Germany
Heather Michelle Wright,
United States Geological Survey (USGS), United States

***Correspondence:**
Fukashi Maeno
fmaeno@eri.u-tokyo.ac.jp

Specialty section:
This article was submitted to Volcanology, a section of the journal Frontiers in Earth Science

Received: 10 September 2021
Accepted: 06 December 2021
Published: 24 December 2021

Citation:
Maeno F, Yasuda A, Hokanishi N, Kaneko T, Tamura Y, Yoshimoto M, Nakano S, Takagi A, Takeo M and Nakada S (2021) Intermittent Growth of a Newly-Born Volcanic Island and Its Feeding System Revealed by Geological and Geochemical Monitoring 2013–2020, Nishinoshima, Ogasawara, Japan. Front. Earth Sci. 9:773819. doi: 10.3389/feart.2021.773819

The island-forming Nishinoshima eruptions in the Ogasawara Islands, Japan, provide a rare opportunity to examine how the terrestrial part of Earth's surface increases *via* volcanism. Here, the sequence of recent eruptive activity of Nishinoshima is described based on long-term geological and geochemical monitoring of eruptive products. Processes of island growth and temporal changes in the magma chemistry are discussed. The growth of Nishinoshima was sustained by the effusion of low-viscosity andesite lava flows since 2013. The lava flows spread radially with numerous branches, resulting in compound lava flows. Lava flows form the coherent base of the new volcanic edifice; however, pyroclastic eruptions further developed the subaerial volcanic edifice. The duration of three consecutive eruptive episodes decreased from 2 years to a week through the entire eruptive sequence, with a decreasing eruptive volume and discharge rate through time. However, the latest, fourth episode was the most intense and largest, with a magma discharge rate on the order of 10^6 m^3/day. The temporal change in the chemical composition of the magma indicates that more mafic magma was involved in the later episodes. The initial andesite magma with ~60 wt% SiO_2 changed to basaltic andesite magma with ~55 wt% SiO_2, including olivine phenocryst, during the last episode. The eruptive behavior and geochemical characteristics suggest that the 2013–2020 Nishinoshima eruption was fueled by magma resulting from the mixing of silicic and mafic components in a shallow reservoir and by magma episodically supplied from deeper reservoirs. The lava effusion and the occasional explosive eruptions, sustained by the discharge of magma caused by the interactions of these multiple magma reservoirs at different depths, contributed to the formation and growth of the new Nishinoshima volcanic island since 2013. Comparisons with several examples of island-forming eruptions in shallow seas indicate that a long-lasting voluminous lava effusion with a discharge rate on the order of at least 10^4 m^3/day (annual average) to 10^5 m^3/day (monthly average) is

required for the formation and growth of a new volcanic island with a diameter on km-scale that can survive sea-wave erosion over the years.

Keywords: volcanic island, Nishinoshima, lava flow, pyroclast, monitoring, andesite

1 INTRODUCTION

Volcanic eruptions occur in shallow-water environments in active volcanic regions, such as at convergent plate boundaries, and in hot spots and rift zones in and along oceanic plates. These submarine eruptions often result in a change in the eruptive environment from submarine to subaerial and the production of a new island. The emergence and growth of a new volcanic island provide a rare opportunity to examine how the terrestrial part of the Earth surface increases *via* volcanism. Such events also provide fundamental knowledge concerning the very early stages of growth of a large volcanic island edifice. Our current understanding is limited because only a few examples of volcanic island formation have been documented in historical times. One famous example is Surtsey in Iceland in the 1960s, where the creation and growth of a new volcanic island were observed and summarized in detail (e.g., Thorarinsson et al., 1964; Thordarson and Sigmarsson, 2009). Although submarine eruptions in shallow seas have been recently observed in volcanically active regions, e.g., the Zubair archipelago in the southern Red Sea (Xu et al., 2015) and the Tonga archipelago (Cronin et al., 2017), detailed observations are rarely achieved because tiny new islets can easily be eroded by waves and disappear in a short period without the supply of a large volume of magma to the surface. Even in the Japanese archipelago, only two cases have created new long-lasting (decadal-year-old) islands in historical times before the 2013–2020 Nishinoshima eruption: the eruptions in Nishinoshima, Ogasawara, from 1973 to 1974

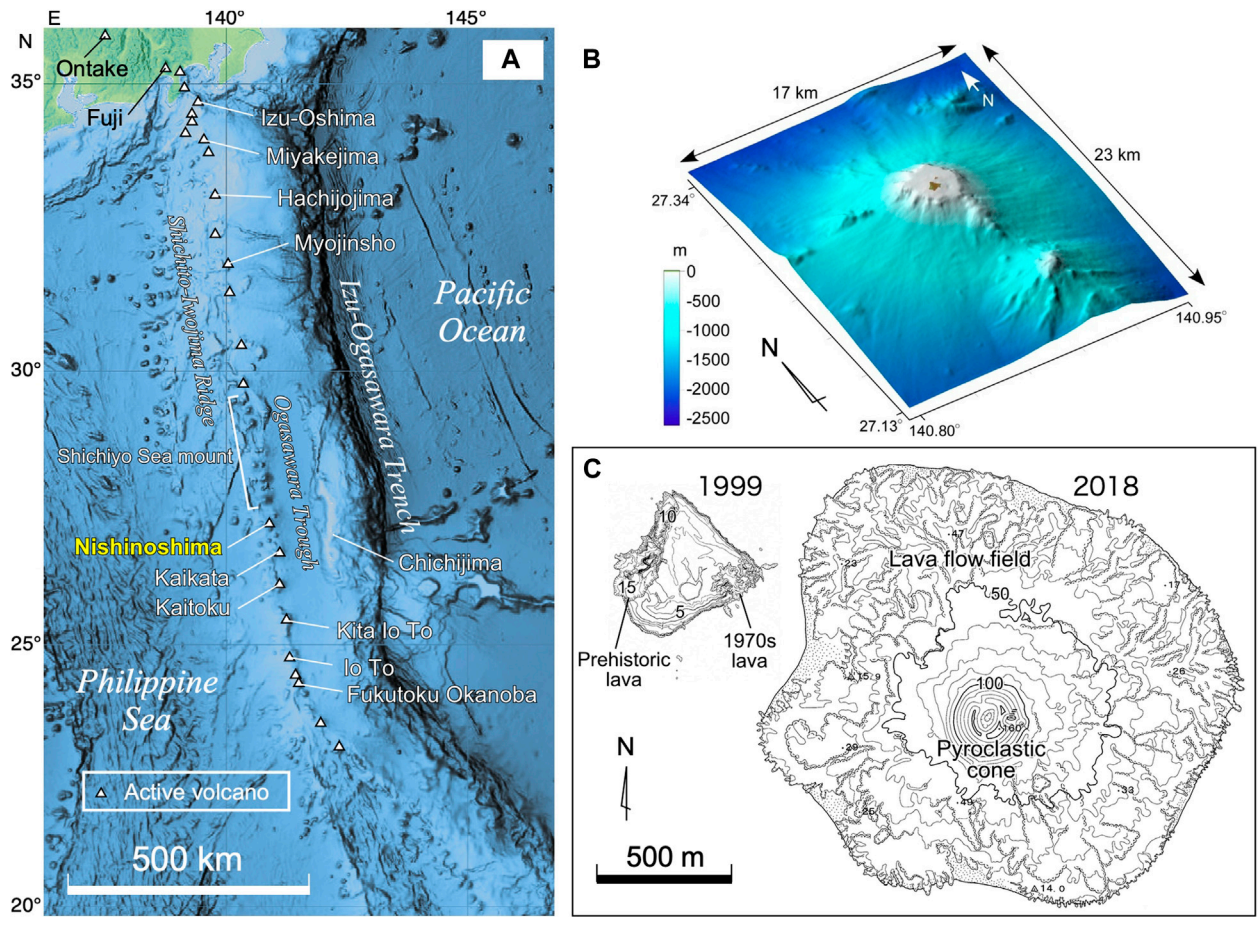


FIGURE 1 | (A) Location map of Nishinoshima. Bathymetry data from NOAA's National Centers for Environmental Information. **(B)** Bathymetry around Nishinoshima before the recent eruptions. Bathymetry data (M7023 ver 2.0) from the Marine Information Research Center, Japan Hydrograph Association. **(C)** Topographical maps drawn before and during the recent eruptions obtained by the Japan Coast Guard in 1999 (Umino and Nakano, 2007) and by the Geospatial Information Authority of Japan in 2018, respectively. The unit of height is meters for topographic contours, and the zero contour represents sea level.



FIGURE 2 | Photos of the recent Nishinoshima eruptive sequence. **(A)** Very initial phase of the volcanic-island formation with phreatomagmatic explosions, taken on November 21, 2013. The old Nishinoshima island is on the left. **(B)** Surtseyan eruption with "cocks' tail" jets, taken on November 21, 2013. **(C)** A small cone ejecting ballistics, which made splashing of water, taken on November 23, 2013. **(D)** The new growing island (below), approaching the old island (above), taken on December 20, 2013. **(E)** The new island with a Strombolian eruption almost contacting the old island, taken on December 25, 2013. **(F)** Lava flows in the northeast, contacting seawater, generating smoke, and reclaiming land, taken on March 4, 2014. **(G)** The pyroclastic cone and part of the old island, late Episode 1, taken on November 17, 2015. **(H)** Lava flows in the southwest spreading into the sea during Episode 2, taken on April 21, 2017. **(I)** Strombolian eruption and lava flows at night during Episode 2, taken on May 25, 2017, by H. Abe. **(J)** Lava flow effusing from the central vent to the south during Episode 3, taken on September 8, 2018. **(K)** Ash plume observed during late Episode 4, taken on July 30, 2020. **(L)** Tephra blanket (pyroclastic fallout deposits) from Episode 4, covering lava flows and smoothing the surface, taken on July 30, 2020. **(M)** The ~250-m-high pyroclastic cone that grew during Episode 4, taken on December 23, 2020, from the west.

(previous activity) (Ossaka et al., 1974; Ossaka, 1991) and in Showa Iwo-jima, southern Kyushu, from 1934 to 1935 (Tanakadate, 1934; Maeno and Taniguchi, 2006). Furthermore, many active island or submarine volcanoes exist in remote areas, making it difficult to comprehensively observe detailed processes.

Nishinoshima in Ogasawara, Japan, has continued its eruptive activity through four eruptive episodes since 2013 and this latest

activity created a new volcanic island (**Figures 1**, **2**). Episode 1 occurred from November 2013 to December 2015, as summarized by Maeno et al. (2016); then, the eruptive activity continued intermittently. Episodes 2 and 3 occurred in April–August 2017 and July 2018, respectively, (Kaneko et al., 2019). Then, Episode 4 occurred from December 2019 to August 2020. The size of the new island increased incrementally to 2.5 km × 2.5 km at the end of the most recent Episode 4 in 2020. This series of volcanic activity at Nishinoshima provides an important opportunity to study the birth, growth, and development of a new volcanic island. Several previous studies deal with specific topics concerning these recent Nishinoshima eruptions (Maeno et al., 2016; Sano et al., 2016; Shinohara et al., 2017; Maeno et al., 2018; Takeo et al., 2018; Kaneko et al., 2019; Tamura et al., 2018; Baba et al., 2020; Tada et al., 2021); however, the entire sequence of these eruptions, including the variation in the eruptive style and magma chemistry, has not yet been summarized and discussed. In this paper, we study the 2013–2020 Nishinoshima eruption and discuss the formation process for the new volcanic island and the magma supply system beneath the island based on time series of geological and geochemical data obtained *via* remote observations and land surveys at the volcano.

2 NISHINOSHIMA VOLCANO

Nishinoshima is located approximately 1,000 km south of Tokyo and 130 km west of Chichijima, Ogasawara (**Figure 1**). It is an active volcano that consists of a volcanic front (Shichito-Iwojima Ridge) of the Izu-Bonin arc, trending in the north–south direction parallel to the Ogasawara Trench. Nishinoshima consists of a main peak that appears as an island and two submarine peaks that are located west and south of the island. There is a small cone on the northeast flank of the main peak, which may be a satellite cone (Yuasa et al., 1991). The volcanic activity in this region is caused by the subduction of the Pacific Plate beneath the Philippine Sea Plate. North of Nishinoshima, large submarine stratovolcanoes, with basal diameters of 20–30 km, reaching heights of 2,200–2,800 m above their base, form the chain called the Shichiyo Seamount (Yuasa et al., 1991; Ishizuka et al., 2007). South of Nishinoshima, the volcanic front includes the Kaikata and Kaitoku seamounts and the volcanic islands of Kita Io To, Io To, and Minami Io To. Although there are studies on magma genesis related to subduction in this region (Yuasa and Nohara, 1992; Ishizuka et al., 2007; Sano et al., 2016; Tamura et al., 2018), the detailed eruptive histories of these active volcanoes, including Nishinoshima, have not been established because of the submarine nature of the major volcanic products and edifices.

Prior to 1973, Nishinoshima was a tiny island consisting of andesite lava, which was the remnant of an old volcanic edifice of unknown age with a length of 200 m, width of 50 m, and height of 25 m extending in the northeast–southwest direction (**Figure 1**), being this the tip of a much larger submarine volcanic edifice. Before the recent 2013 eruptive event, the volcanic eruptions occurred from 1973 to 1974 were the only known historical eruptive activity at Nishinoshima since its discovery in 1702 (Aoki and Ossaka, 1974). During 1973–1974, a new island was formed to the southeast, offshore of the old Nishinoshima island. This was likely the latest eruptive episode experienced by the volcano. However, the small magnitude of the eruptions and the subsequent erosion and sedimentation of reworked volcanic material, did change the dimension of the island considerably (Ossaka, 1991). Although the magma erupted during the 1970s was andesitic in composition, it did slightly differ from the composition of the prehistoric lava, as shown later.

Immediately prior to 2013, the Nishinoshima island consisted of three major areas: a western hill consisting of prehistoric lavas with an unknown age, a height of 25 m, and a flat top; younger lava flows erupted from 1973 to 1974 to the east; and a middle low land consisting of reworked sand and gravel (Umino and Nakano, 2007). The island at this time had a trapezoidal shape with a maximum length of ~600 m and an extension of c.a. 0.2 km^2 (**Figure 3**). Although there are no historical records of eruptions, exception made for those in the 1970s and 2010s, the size of the entire Nishinoshima edifice, which elevates more than ~2,500 m from the sea bottom, indicates that this volcano must have experienced many repeated magmatic eruptions over a long period of time.

3 MATERIALS AND METHODS

3.1 Remote Surveys

Throughout the four episodes of the 2013–2020 Nishinoshima eruption, remote observations from satellites, airplanes, and research vessels were used to monitor the volcano. Not only optical satellite images but also synthetic aperture radar satellite data (TerraSAR-X, ALOS-2) were used to constrain the temporal changes in the eruption processes. The SAR observations are not affected by clouds or eruption plumes because they use electromagnetic waves with long wavelengths. Such observations of a fixed point in a fixed interval allow analyses of the detailed growth process *via* comparisons of time-series images (Maeno et al., 2016; Kaneko et al., 2019[1]). The airplanes (operated by Asahi Shimbun, Yomiuri Shimbun, and Mainichi Shimbun) and research vessels (*Kairei, Natsushima, Shinseimaru, Keifumaru, and Ryofumaru*) were occasionally used for visual observations of the eruptions on-site and to confirm observations from satellites. The research vessels were also used to collect ash samples during the eruption. The remotely controlled aerial vehicles, which were operated from the research vessels, were used to observe the eruptive activities and geological features in more detail, as well as to obtain ash and lapilli samples from the volcanic edifice (**Table 1**). The remote observations by the Japan Coast Guard (JCG), the Japan Meteorological Agency (JMA), and the Geospatial Information Authority of Japan (GSI) were considered in construction of the eruption process. On the basis of these surveys and data, the surface morphology, area, volume, discharge rate, and their changes were quantitatively estimated and used to explore the origins of their variations.

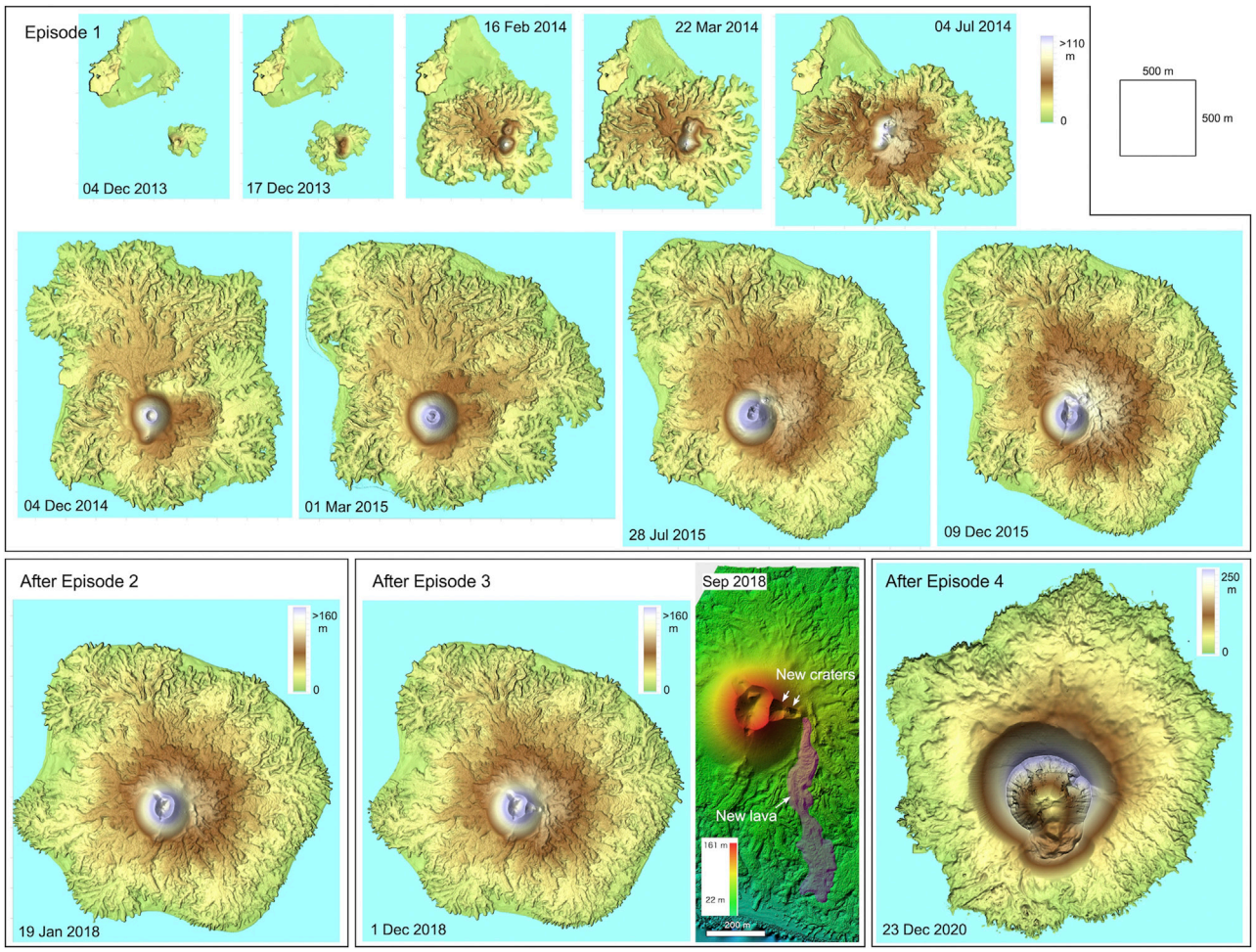


FIGURE 3 | Temporal change in the topography of Nishinoshima since the beginning of the recent eruptions in 2013. The original topographic data for 2013–2018 were provided by the Geospatial Information Authority of Japan. The detailed topography of the central cone and new lava after Episode 3 and the topography of the entire island after Episode 4 were obtained *via* aerial drone surveys.

TABLE 1 | Samples obtained from Nishinoshima and sampling methods.

Episode	Eruption date	Sampling location	Sample type	Sampling date	Sampling methods
1	2014-Jan to 2015-Nov	West coast	Lava, bomb, lapilli	2016/10/20, 21	Land survey, R/V Shinseimaru (KS16-16)
1	2014–2015	Western foot of cone	Lapilli	2016/6/7, 8	UAV from R/V Keifumaru (KS16-05)
1	2015-Feb-27	Off shore	Ash	2015/2/27	On R/V Kairei (KR15-03)
1	2015-Jun-15	Off shore	Ash	2015/6/15	On R/V Natsushima (NT15-E02)
1	2015-Jun to Jul	South coast	Lava	2016/10/28	Land survey by JCG (sampled by JCG)
2	2017-May-28	Off shore	Ash	2017/5/28	On R/V Keifumaru (KS17-04)
2	2017-Apr to Aug	Summit	Lapilli	2018/5/30	Drone from R/V Ryofumaru (KS18-04)
2	2017-Apr to Aug	West coast	Lava	2019/9/3, 4	Land survey (CSR)
2	2017-Apr to Aug	Southwest coast	Lava	2019/9/5	Land survey (CSR)
3	2018-mid Jul	Summit	Lapilli	2018/9/8	Drone from R/V Keifumaru (KS18-07)
3	2018-mid Jul	Summit	Lapilli	2019/6/8	Drone from R/V Ryofumaru (KS19-05)
4	2020-end of Jun	Southwest coast	Lapilli (scoria raft)	2020/12/23	Drone from R/V Kairei (KR20-E06)
4	2020-eartly Jul	West coast	Lapilli, ash	2020/12/21	Drone from R/V Kairei (KR20-E06)
4	2020-Jul-11	Off shore	Ash	2020/7/11	On R/V Ryofumaru (sampled by JMA)
4	2020-Jul-20	Off shore	Ash	2020/7/20	On R/V Keifumaru (sampled by JMA)

JCG, Japan Coast Guard; JMA, Japan Meteorological Agency; JAM, Japan Agency for Marine-Earth Science and Technology; CSR, comprehensive scientific research operated by the Ministry of the Environment Japan; KS (KR, NT) xx-xx: Cruise number.

3.2 Land Surveys

During the 2013–2020 eruption, for safety reasons, access to Nishinoshima was strictly prohibited, with the restricted area being larger than the island. Therefore, remotely controlled aerial vehicles were the only method available to directly approach the island for observation and sampling. However, during the quiet periods, the restricted area was reduced to 0.5 km from the center of the island, making it possible to conduct land surveys. In October 2016 and September 2019, we carried out land surveys on the western and southwestern coasts, where sandy and gravelly beaches had developed. A multidisciplinary research team including volcanologists, biologists and zoologists participated to the survey. To avoid contamination by external species and to conserve the primitive environmental conditions, all scientists carefully followed the guidelines suggested by the Ministry of the Environment, Japan. On the island, we took rock samples and surveyed the distribution and structure of the lava flows and tephra deposits to characterize the eruptive processes. We sampled rocks whose time of emplacement could be estimated using aerial and satellite images; this allowed us to construct the time-series variation of the chemical compositions of the lava flows and some ballistic ejecta.

3.3 Chemical Composition Analyses

Eruptive products from each episode during 2013–2020 were sampled on land and offshore Nishinoshima by the research vessels, remotely controlled aerial vehicles, and land surveys as mentioned above. The sampling methods and analyzed samples are summarized in **Table 1**. We performed microscope observations, whole rock major and trace element analyses using X-ray fluorescence spectrometry (ZSX Primus II, Rigaku Co., Ltd., Tokyo, Japan), and groundmass and mineralogical analyses using an electron probe micro-analyzer (JXA-8800R, JEOL Ltd., Tokyo, Japan), with an acceleration voltage of 15 kV, a beam current of 12 nA, and a beam diameter of 10 μm, at the Earthquake Research Institute, University of Tokyo.

4 RESULTS

4.1 Outline of the Nishinoshima Eruptive Episodes Since 2013

4.1.1 Episode 1: 2013–2015

The latest eruptive episode began in the shallow sea ~300 m southeast offshore the previous Nishinoshima island in November 2013. The eruption was first noticed in aerial observations by the Japan Marine Self-defense Force on November 20. The depth of the eruptive center was ~30 m below sea level, and its location corresponded to one of the vents formed during the activity in the 1970s. When the eruption was reported, a new islet with a small pyroclastic cone, 150 m × 80 m in size, had already formed. The date of the beginning of the eruption is unknown; however, thermal anomaly data from Moderate Resolution Imaging Spectroradiometer satellite observations suggest that the eruption began in early November 2013. At the beginning of the eruption, magma-water interactions produced characteristic "cock's tail" explosive jets and was classified as a Surtseyan-type eruption (**Figures 2A,B**). The new island with its littoral pyroclastic cone rapidly grew by the effect of continuous eruptions in the shallow marine environment.

In late November, the eruptive style changed to Strombolian with lava flows, likely as a result of the rapid growth of the new islet, which may have prevented seawater accessing to the ascending magma (**Figure 2C**). The new islet grew *via* the continuous effusion of lava, which reclaimed the shallow sea and rapidly increased the size of the pyroclastic cone (**Figures 2D**, **3**). The pyroclastic cone was formed by ballistically ejected coarse clasts, including fluidal meter-sized bombs, from Strombolian explosions and by their rolling, which resulted in symmetrical shape with the angle of repose. In late December, the islet connected to the previous Nishinoshima island (**Figure 2E**) and grew further by emplacement of new lava flows and further growth of its pyroclastic cone (**Figure 2F**). By October 2014, most of the old island was covered by new products, except a very small plateau of the prehistoric lava to the west. Also most of the small reefs to the northeast and south were covered by new lava flows by 2015.

New lava flows then further extended the area of the new island, changed their flow direction, and formed the new Nishinoshima island, with a diameter of approximately 2 km (2.7 km^2 in area) and a height of ~150 m (**Figures 2G**, **3**, **4**). Just before this eruptive episode ended, the style of the explosions changed from prevalently Strombolian to Vulcanian. Discrete explosions produced large ballistic blocks and slightly reduced the height of the cone (**Figure 4**). The frequency of the Vulcanian explosions decreased, and the activity finally ceased at the end of 2015. After this first episode, Nishinoshima was quiet for approximately 16 months, during which the first land survey was made in October 2016.

4.1.2 Episode 2: 2017

On April 20, 2017, an eruption was confirmed through aerial observations by JCG. As in Episode 1, the activity was characterized by Strombolian activity with lava flow effusions (**Figures 2H,I**). The lava flows headed west, preferentially along topographic lows. Thermal anomalies were detected by the Himawari-8 satellite at 11:50 Japan Standard Time (JST) on April 17, and acoustic signals and intermittent tremors were detected by a seismo-acoustic station starting at 7:37 JST on April 18. Therefore, this episode is thought to have started on April 17, 2017 (Takeo et al., 2018; Kaneko et al., 2019).

In 1 week, the area covered by new lava and the additional erupted volume had reached 2.4×10^4 m^2 and 1.0×10^6 m^3, respectively. The magma discharge rate during this period was estimated to be 1.9×10^5 m^3/day on average, smaller than the values recorded during Episode 1 (**Figure 4**). This eruption continued until August 2017 and increased the land area to the west and the southwest (**Figure 3**). Although the erupted volume of this episode was smaller than that of Episode 1, due to its shorter duration, the eruptive style was nearly the same, producing Strombolian explosions and lava effusions. The Vulcanian-type explosions were also observed in the late of this episode. The area of the island reached a total of ~2.9 km^2, and

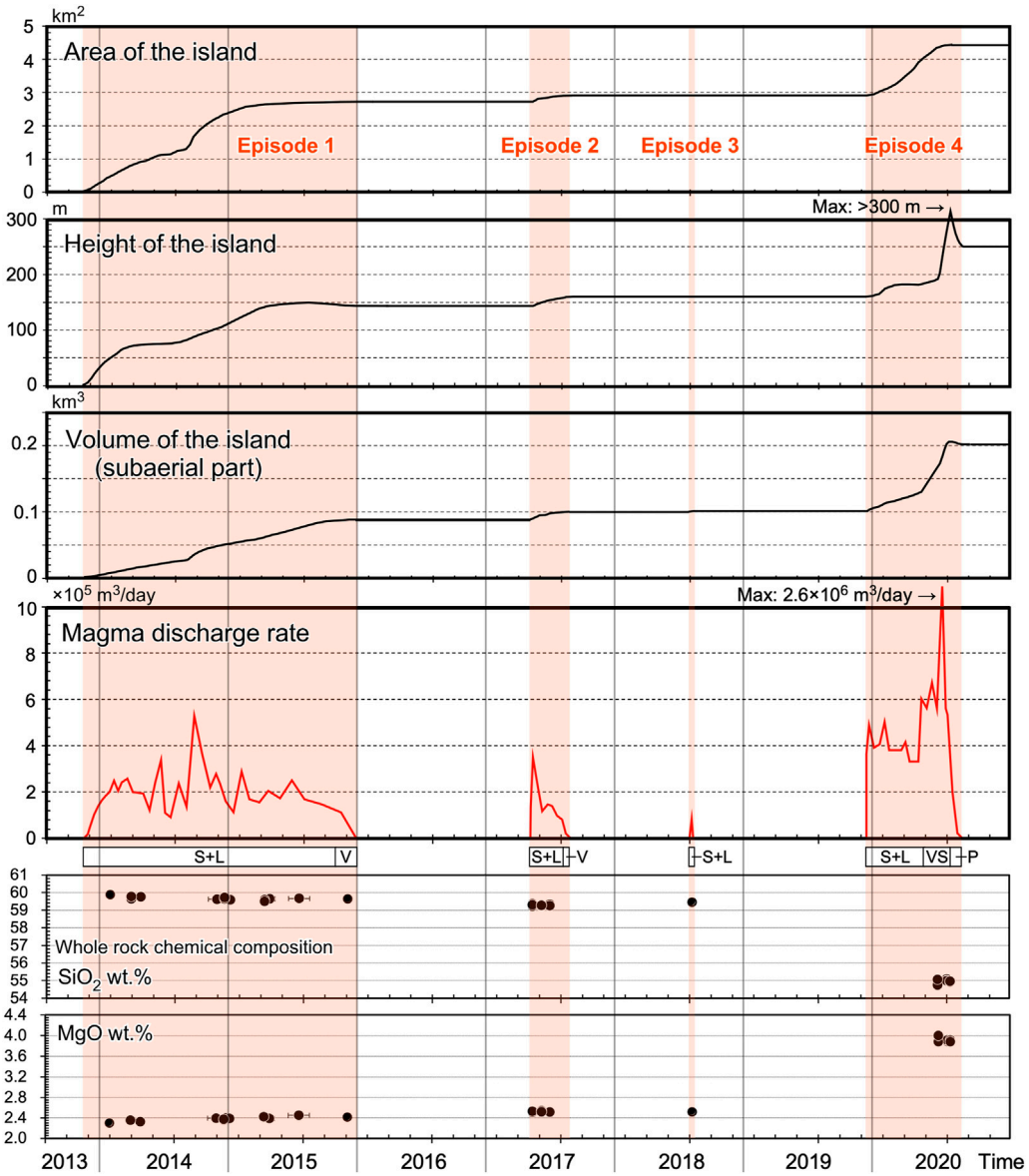


FIGURE 4 | Changes in the area, height, and volume (subaerial part) of the new island, magma discharge rate, and representative whole rock major element chemical compositions (SiO_2 and MgO) of the erupted magma during the four recent Nishinoshima eruptive episodes. Major eruption styles are also indicated below magma discharge rate: S, Strombolian; V, Vulcanian; L, Lava flow; VS, Violent Strombolian; P, Phreatomagmatic.

the height of the cone reached ~160 m (**Figure 4**). During this 4-month period, the prehistoric lavas were partially buried by new lava flows. The 2016 land survey points and a seimo-acoustic station on the west coast were also buried.

4.1.3 Episode 3: 2018

This episode began on July 12, 2018 and ceased within a week. It was characterized by Strombolian activity and lava effusion and had a much smaller scale (shorter duration and smaller volume) than that of Episode 2. New craters were produced on the eastern side of the cone, and lava exiting the cone was directed to the south (**Figures 2J**, **3**). This small-scale single-lobe lava flow did not reach the southern coast only affecting a small part of the eastern and the southern sides of the island, thus leaving the total area of the island unchanged (**Figure 4**). The additional erupted volume of the new lava was estimated to be ~2.5×10^5 m^3. If we assume that the effusive activity lasted less than a week, the magma discharge rate for the lava was $3–4 \times 10^4$ m^3/day (**Figure 4**), which is smaller than those of Episodes 1 and 2. After Episode 3, the volcano became quiet. During this period, we carried out a second land survey in September 2019.

4.1.4 Episode 4: 2019–2020

Episode 4 began in early December 2019, just 3 months after the second land survey. The eruption followed a similar pattern to the

previous episodes in its early months, being characterized by Strombolian eruptions and lava effusion with a discharge rate on the order of 10^5 m^3/day. However, the eruptive style changed dramatically from late June to early July 2020. The recent eruptive activity at Nishinoshima had mainly produced lava flows and intermittent Strombolian eruptions; however, during this period, explosive activity characterized by lava fountains and dark-colored ash plumes, similar to those often observed at basaltic volcanoes such as Etna and Hawaii, were reported by a JCG airplane and a JMA vessel. Satellites also detected an extended ash plume larger than those previously observed. From early June 2020, the height of the eruption column reached 2–6 km (~8 km in maximum on July 4, 2020), based on satellite data (Yanagisawa et al., 2020). The pyroclastic material produced by the prevalent explosive activity rapidly increased the height of the central cone to more than 300 m, as well as its diameter. Furthermore, the southern part of the cone was eventually destroyed by the issuing of new lava flows. Large blocks and fragments, that had originally made up the cone, were rafted toward the sea by the lava flows. During this period, the magma discharge rate was on the order of 10^6 m^3/day, based on thermal anomaly data captured by Himawari-8 and optical satellite images (**Figure 4**)[1]. This discharge rate was the highest recorded for Nishinoshima since 2013. After this most intense phase of Episode 4 in the middle of July 2020, the activity decreased and the eruptive style changed to continuous and vigorous ash emission. A large, light-gray colored eruptive plume was produced during this stage (**Figure 2K**), and associated fine ash entirely covered the new island (**Figure 2L**). No thermal anomalies were detected during the ash plume stage. Our later drone survey and sampling of the deposit confirmed that the topmost part of the deposits from this stage is characterized by consolidated and aggregated fine ash. These observations indicate that fragmentation mechanism that promotes finer granulation, possibly such as magma–water interactions, was involved in generating fine ash, although a thorough textural analysis of the tephra is needed to clarify its mechanism. This type of change in the eruptive style had never occurred during the past eruptive activity at Nishinoshima. However, a similar explosive activity had characterized the later explosive phase of the 2000 Miyakejima eruption, where large amounts of fine ash were generated by phreatomagmatic activity (Nakada et al., 2005). In summary, Episode 4 was first characterized as Strombolian with lava effusion, then lava-fountain eruptions, and lastly ash emission likely generated by phreatomagmatic eruptions. A more detailed sequence of this episode captured by satellites is summarized by[1]. The area of the island, at this point, had increased from 2.9 to 4.4 km^2, and its volume increased from ~0.1 to ~0.2 km^3 (**Figure 4**). The old 160-m-high pyroclastic cone was destroyed, and a new cone had grown up to a height of 250 m (**Figure 2M**). The crater diameter had been enlarged from 150 to 570 m, and the elevation of the crater floor had dropped to ~50 m above sea level. The uneven terrain of the lava flows was flattened by the tephra deposition (**Figure 3**). The change in the eruptive style in Episode 4 was due likely to the change in the magma composition from andesite to basaltic andesite, as shown later, and to the enlargement and deepening of the central crater, which resulted in magma–water interactions. The 2019 land survey points (Maeno and Yoshimoto, 2020) and the seimo-acoustic station installed during the 2019 land survey (Ohminato and Watanabe, 2020) on the west coast were buried by the new lava flows during the earlier eruptive phase.

4.2 Constraints From Remote Observations

The magma discharge rate, estimated based on the morphological changes of the island, was approximately 2.0 × 10^5 m^3/day (2.3 m^3/s) on average during Episode 1. The order of magnitude of the magma discharge rate (~10^5 m^3/day) was similar for all episodes, except Episode 3. In fact, the new island had grown stepwise with magma discharge rate fluctuations since the beginning of Episode 1. In September 2014, the magma discharge rate reached ~5.0 × 10^5 m^3/day and the northern part of the island increased very rapidly its extension (**Figure 4**). An estimation of the magma discharge rate based on the morphological change was used to correlate the magma discharge rate and the satellite-obtained thermal anomaly data (Kaneko et al., 2019). For Episode 4, the temporal variation of the magma discharge rate was estimated based on both the morphological change and the correlation between the magma discharge rate and the thermal anomaly data[1]. By the middle of June 2020, the magma discharge rate was estimated to be on the order of 10^5 m^3/day, as in earlier episodes; however, it increased to 10^6 m^3/day during the lava-fountain eruptions in June and July 2020.

Remote observations captured the dynamic behavior of the lava flows. Newly formed lava flows branched repeatedly, resulting in the formation of multiple lobe structures (**Figure 3**). This type of lava flow structure is referred to as compound lava flows (Walker, 1971; Kilburn and Lopes, 1988; Calvari et al., 2002). Analyses of satellite data confirmed that the lava flow fronts slowly advanced with a maximum speed of ~20 m/day during Episode 1. Groups of neighboring lava lobes were often inflated with time, suggesting that the lobes were interconnected and pressurized by a further supply of low-viscosity magma beneath the solidified crust (Maeno et al., 2016).

According to the aerial observations, large amounts of steam rose from the lava flow front that entered the sea. The flow front rapidly cooled as it came into contact with the seawater, and was brecciated, or auto-brecciated by the motion of the lava flow. On the surface of the lava lobes, which had already ceased to move, clefts developed, parallel to the flow direction and gradually opened and enlarged with time. These clefts were visually detected by airplanes and research vessels, as well as by land surveys, and are interpreted as being lava inflation clefts (Walker, 1991; Hon et al., 1994), which are thought to form *via* the inflation and breakage of the solid lava

[1]Kaneko, T., Maeno, F., Ichihara, M., Yasuda, A., Ohminato, T., Nogami, K., et al. (in review). Episode 4 (2019-2020) Nishinoshima Activity: Abrupt Transitions in the Eruption Style Observed by Image Datasets from Multiple Satellites. Earth Planet. Space.

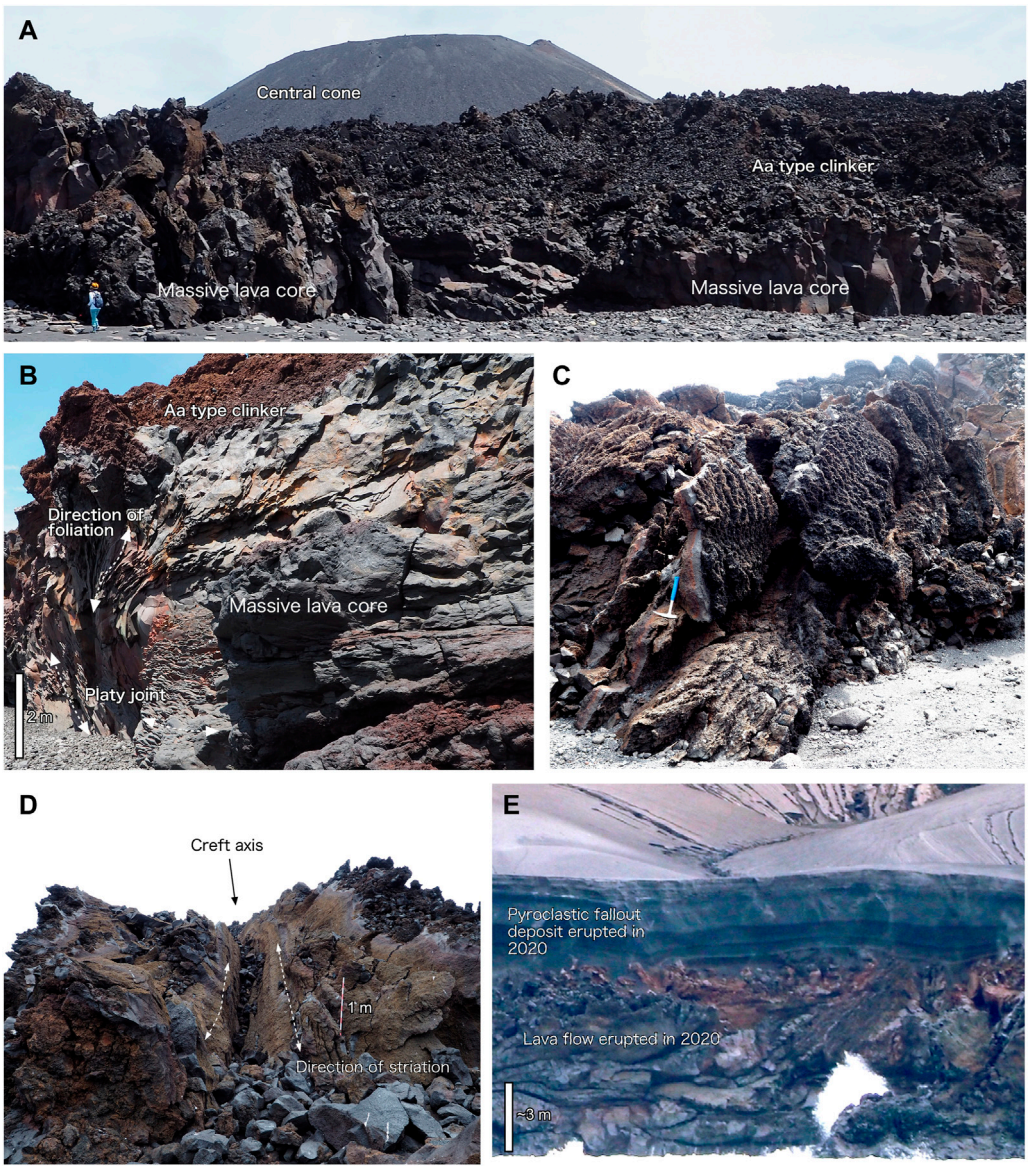


FIGURE 5 | Geological features formed by the recent Nishinoshima eruptions. **(A)** Lava flow field in the southwest of the island. The massive part of the lava (a few meters thick) is covered by aa-type clinker. **(B)** Typical massive andesite lava exposing an onion-like internal structure at a sea cliff. The platy joint developed and surrounds the core of the massive lava lobe. **(C)** Vesiculated lava clinker consisting of an andesite lava flow surface with fine protrusions. **(D)** Inflation cleft developed on the lava lobe. The black arrow shows the axial trough of the cleft, from which massive lava is thought to have fractured and opened to the left and right, as the result of inflation due to increased internal pressure during lava flowage. **(E)** Cross section of stratified pyroclastic fallout tephra deposits from late Episode 4, covering lava flows effused in early Episode 4, observed on the northwestern side of the island. The thickness of the deposit is > 3 m. Photos **(A–D)** were taken during the September 2019 land survey, and photo **(E)** was taken from research vessel *Kairei* in December 2020.

surface because of increases in the internal pressure caused by the continuous supply of still-molten lava.

The coasts of the new Nishinoshima island just after the lava emplacement in each eruptive episode were steep and rocky and consisted of irregular-shaped and complicated patterns reflecting the emplacement of multiple lava lobes. However, the shape of the island has been smoothed by erosion and the sedimentation of reworked materials and has changed with time to form a gravelly and sandy beach. On the western and northern sides of the island, a wide beach developed as the result of the competition between erosion and sedimentation.

4.3 The 2016 and 2019 Land Surveys

4.3.1 Lava Flows

The morphology, internal structure, and distribution of the lava flows were investigated along the western and southwestern coasts. There, the massive dense interiors of the lava effused during

Episodes 1 and 2 have been exposed by wave erosion. Some of them show platy, circularly developed cooling joints surrounding the massive core of the lava lobe (**Figures 5A,B**). North of the western coast, the lava shows cooling joints with a glassy surface, indicating rapid quenching of the lava flows operated by the seawater (Maeno et al., 2017). The lava surface is composed of several types of blocky or aa-type clinker (**Figures 5A,B**): a glassy type with black to dark gray colors, partially reddish due to oxidation; a massive pumiceous and dense type; and a flat-shaped type with a rough surface and fine protrusions (**Figure 5C**). Lava inflation clefts, inferred from satellite images, were also observed at several locations on the Episode 1 and 2 lava lobes (**Figure 5D**). These clefts are more prominent in the western and southwestern base of the cone and expose the massive dense interiors of the lava. We confirmed that the geological features, such as the lava-inflation clefts, internal structure of the lava lobes, and surface morphology, observed in the products of the Episode 1 were very similar to those produced during Episode 2.

4.3.2 Tephra

Before Episode 4, the flat top surface of the prehistoric lava, ~600 m from the vent, was the only place where tephra deposits could be preserved. The 2016 land survey confirmed the presence of ~10-cm-thick pyroclastic fallout deposits on the soil on the old flat lava surface. The lowermost part of the tephra layer is coarse ash mixed with fresh scoria lapilli (less than 1-cm diameter), the middle part of the deposit is composed of gray ash, and the uppermost part of fine laminated ash. This fallout deposit is thought to be derived primarily from the Episode 1 Strombolian activity. Ballistic bombs with >10-cm in diameter are also present on top of the prehistoric lava and surrounding coastal area. These bombs resulted from the Vulcanian activity in the later stage of Episode 1; during this period, JCG observed large bombs ejected toward the west, some of which crossed over the coastline and hit the sea surface causing splashing of water. The 2019 land survey confirmed that the pyroclastic fallout deposits on the old flat lava surveyed in 2016 were covered by a later ash and scoria layer, which resulted from the Episode 2 Strombolian eruptions.

4.4 Research Vessel Observations After Episode 4

Episode 4 caused the most significant change in the geology of the new island. We surveyed the topography and deposits of the island and obtained samples from representative locations using a drone in December 2020. Except for few locations on the southwest and northwest coasts, nearly the entire lava flow field had been covered by pyroclastic deposits. At the sea cliff, we observed a cross section of the stratified pyroclastic fallout tephra covering the lava flows effused during the early activity of Episode 4. In the north, the tephra deposit was more than 5-m thick (**Figure 5E**), reflecting the northward direction of the major tephra dispersal axis during the explosive phase, as observed by satellites. All the tephra layers were originated during the most intense explosive phase accompanying the lava-fountain activity and later phreatomagmatic explosions that occurred after June 2020.

4.5 Chemical Composition of Eruptive Products and Magma Reservoir Conditions

4.5.1 Chemical Characterization of the Eruptive Products

On the basis of the microscope observations, all the products from Episode 1–3 include phenocrysts of plagioclase, clinopyroxene (augite, pigeonite only for the phenocryst rims and groundmass), orthopyroxene, and Fe-Ti oxides less than 1 mm in length, while products of the Episode 4 exclude orthopyroxene and include olivine phenocrysts (**Figure 6**). Some of these phenocrysts appear as aggregates (glomeroporphyroclasts). The total phenocryst content was less than 10 vol% for all the products. The whole rock chemical compositions of the Episode 1–3 products are 59.2–59.9 wt% SiO_2, 2.3–2.5 wt% MgO, and 5.2–5.5 wt% $Na_2O + K_2O$ (**Figure 7**, **Table 2**, **Supplementary Table 1**) and are classified as andesite (Le Bas et al., 1986). Compared with rocks effused before 2013 (Ossaka et al., 1974; Ossaka, 1975, Umino and Nakano, 2007; Sano et al., 2016), all the products have a chemical composition intermediate between that of the products of the 1973–1974 eruptions with 58.6–59.1 wt% SiO_2 and that of the prehistoric (prior to 1702) lava with 60.1–60.8 wt% SiO_2. Conversely, the products of the late Episode 4 have 54.8–55.1 wt% SiO_2, 3.9–4.0 wt% MgO, and 4.0–4.1 wt% $Na_2O + K_2O$ (**Figure 7**) and are classified as basaltic andesite. Such chemical characteristics of magma with lower SiO_2 (higher MgO, **Table 2**) content in the whole rock chemical composition have never been reported before for on-land products from the recent Nishinoshima eruptions, although there is a report of the presence of mafic rocks with unknown ages in the submarine flank and satellite cones of the Nishinoshima (Tamura et al., 2018). Furthermore, the chemical composition trend observed throughout Episodes 1–3, which becomes more mafic with time, does not project to the whole rock compositions observed for Episode 4 (**Figure 7**).

The time-series whole rock chemical compositions of the erupted magma plot along a single trend, where the SiO_2 content gradually decreased with time before dramatically changing before or during Episode 4 (**Figures 4**, **8**). The tendencies of the other elements are similar (**Figure 8**). A few samples obtained by remotely controlled aerial vehicles, with unknown eruption dates, do not plot in this trend; however, most of lava samples fall along this trend and are temporally correlated. Furthermore, incompatible element concentration ratios, such as K_2O/TiO_2, Zr/Y, and Ba/Zr, in the whole rock composition mostly did not change after Episode 3 but increased before or during Episode 4 (**Figure 8**).

Throughout Episodes 1–3, the scoria and ash groundmass consist of glass that is black or brown in color with microlites of plagioclase and pigeonite. The Episode 4 groundmass has similar characteristics to those of Episodes 1–3, except for the absence of pigeonite microlites. The chemical

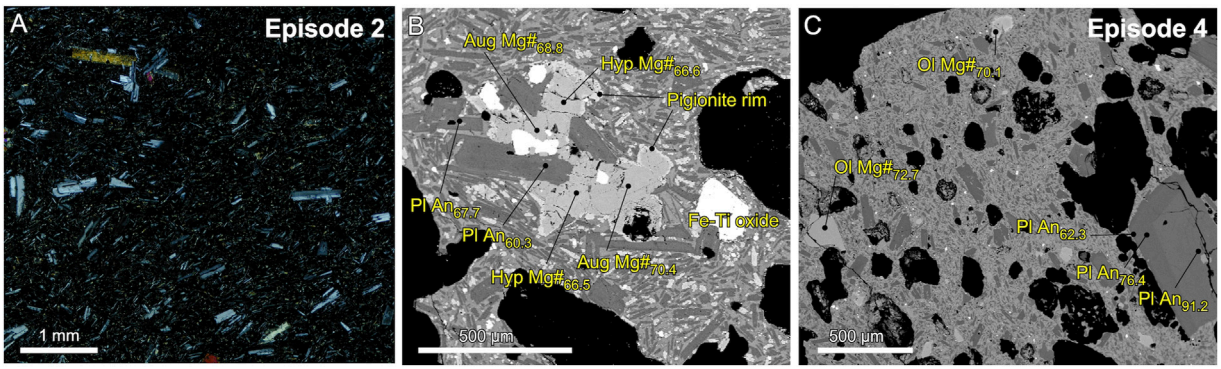


FIGURE 6 | (A) Microphotograph of lava from the 2017 eruption (Episode 2); **(B)** scanning electron microprobe image of a typical early-episode glomeroporphyroclast in scoria lapilli; and **(C)** scanning electron micro-image of scoria lapilli from the 2020 Nishinoshima eruption. Aug, Augite; Hyp, Hypersthene; Pl, Plagioclase; and Ol, Olivine are indicated with major chemical compositions.

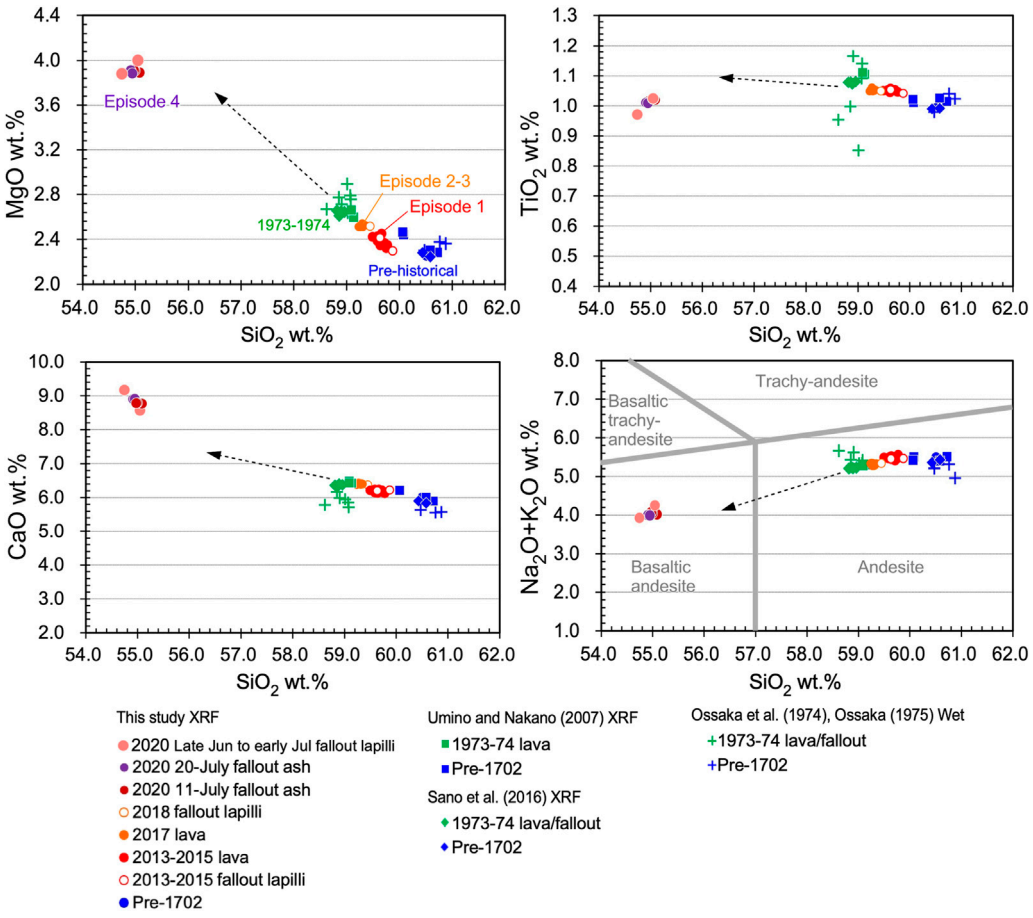


FIGURE 7 | Whole rock major element chemical compositions for representative samples from different Nishinoshima eruptions. Classification from Le Bas et al. (1986). Arrows indicate the direction of the mixing endmember component for the Episode 1–3 magma, which is slightly different from that of Episode 4.

composition of the groundmass glass of each sample varies with crystallinity; however, there is also a variation between Episode 1–3 and 4 that cannot be explained by the degree of crystallization (**Figure 9**). Most of the Episode 1–3 products have 62–69 wt% SiO_2; however, the Episode 4 products have 56–60 wt% SiO_2 (**Supplementary Table 2**). A compositional gap therefore exists in the groundmass glass, as in the whole rock chemical compositions.

TABLE 2 | Whole rock major and trace element compositions for representative samples from Nishinoshima volcano.

Sample name	NSN19090302a	NSN161020-07	NSN161020-10a	NSN19090303a	NSN19090509a	NSN201906	201223 HX01	201223 HX03-01
	Episode 1	Episode 1	Episode 1	Episode 2	Episode 2	Episode 3	Episode 4	Episode 4
Eruption date (from)	2013/11/22	2014/10/16	2015/3/23	2017/4/17	2017/5/1	2018/7/12	2020/6/1	2020/6/1
(to)	2014/3/1	2014/12/4	2015/3/25	2017/4/28	2017/6/5	2018/7/18	2020/6/30	2020/6/30
Major element (wt%)								
SiO_2	59.88	59.62	59.58	59.31	59.30	59.45	54.74	55.05
TiO_2	1.04	1.05	1.06	1.06	1.05	1.05	0.97	1.02
Al_2O_3	15.32	15.42	15.42	15.46	15.48	15.45	16.76	15.97
tFeO	9.15	9.34	9.30	9.46	9.46	9.34	10.17	10.75
MnO	0.21	0.21	0.21	0.21	0.21	0.21	0.20	0.21
MgO	2.30	2.39	2.43	2.51	2.54	2.51	3.88	4.00
CaO	6.22	6.17	6.25	6.39	6.41	6.38	9.17	8.57
Na_2O	4.21	4.30	4.26	4.17	4.13	4.17	3.13	3.47
K_2O	1.25	1.21	1.22	1.16	1.14	1.16	0.79	0.78
P_2O_5	0.43	0.29	0.29	0.28	0.28	0.28	0.18	0.19
FeO/MgO	3.98	3.90	3.83	3.77	3.72	3.72	2.62	2.69
Total	100.00	100.00	100.00	100.00	100.00	100.00	100.00	100.00
Trace element (ppm)								
Sc	19	20	19	20	19	20	32	33
V	161	166	172	183	186	181	317	335
Co	19	20	20	21	22	20	28	32
Cu	133	140	135	141	119	122	160	152
Zn	105	103	102	99	104	100	87	91
Ga	16	17	18	18	18	17	17	16
Rb	20	20	22	18	17	19	12	12
Y	39	39	39	37	37	37	28	30
Sr	226	226	227	224	225	224	241	232
Zr	116	119	119	111	111	113	72	75
Nb	3	3	3	3	3	4	2	2
Ba	291	290	281	273	279	264	190	188
Pb	4	3	3	3	1	3	2	2
La	9	5	4	10	7	9	3	5
Ce	28	29	26	22	28	24	10	16

The plagioclase phenocrysts (0.1–0.2-mm long axis) were divided into two types: Ca-rich cores with An_{80-95} (type 1) [An, anorthite content: 100 × Ca/(Ca + Na)] and Ca-poor cores with An_{55-80} (type 2) (**Figure 10**). Type 2 was further divided into type 2A, which has sodic rims with $An_{<60}$, and type 2B, which does not have sodic rims (**Figure 10**). The groundmass plagioclase has nearly the same composition ($An_{<60}$) as the type 2A rims. Type 2 is often characterized by multiple zoning and appears to be one of the glomeroporphyroclast phases. All of these types of plagioclase phenocrysts are observed throughout the recent eruptions; however, their ratio changes with the eruptive episode (**Figure 10**): for Episodes 1 and 2, type 2A is dominant and a small amount of types 1 and 2B appears; for Episode 3, type 2A decreases while type 1 and 2B slightly increase; and for Episode 4, types 1 and 2B become dominant and there is a decreased amount of type 2A.

The clinopyroxene and orthopyroxene phenocrysts of Episodes 1–3 are divided into two types: 1) a small amount of isolated microphenocrysts and 2) one of the glomeroporphyroclast phases, which is the more abundant and coexists with type 2A plagioclase and Fe-Ti oxides (**Figure 6B**). The microphenocrysts are finer in size (0.1–0.2-mm long axis) than the glomeroporphyroclast phases, while the glomeroporphyroclast phases are coarser (0.5–1-mm long axis). The chemical composition of the clinopyroxene (augite) is $Mg\#_{63-73}$ [Mg#: 100 × Mg/(Fe + Mg)] with a smaller Mg# for the microphenocrysts ($Mg\#_{63-68}$) and a higher Mg# for the glomeroporphyroclasts ($Mg\#_{66-72}$), many of which have pigeonite rims with $Mg\#_{54-60}$ (**Figure 10**). During Episode 4, more Mg-rich augite (average ~$Mg\#_{72}$) appeared and pigeonite disappeared. The chemical composition of the orthopyroxene is $Mg\#_{62-71}$ with a smaller Mg# value for the microphenocrysts ($Mg\#_{62-66}$) and a higher Mg# for the glomeroporphyroclasts ($Mg\#_{65-71}$). Some orthopyroxenes also have a pigeonite rim with $Mg\#_{54-60}$. During Episode 4, the orthopyroxene phenocrysts disappeared (**Figure 10**).

Olivine phenocrysts (0.1–0.4-mm long axis) only appear in the Episode 4 products. The most abundant chemical composition of olivine is $Mg\#_{68-70}$; however, higher $Mg\#_{>80}$ olivine also appears (**Figure 10**). Some of the olivines are characterized by normal zoning and have a rim with lower Mg#.

Melt inclusions (MIs) in plagioclase, pyroxene, and olivine phenocrysts also display a compositional gap as in the whole rock

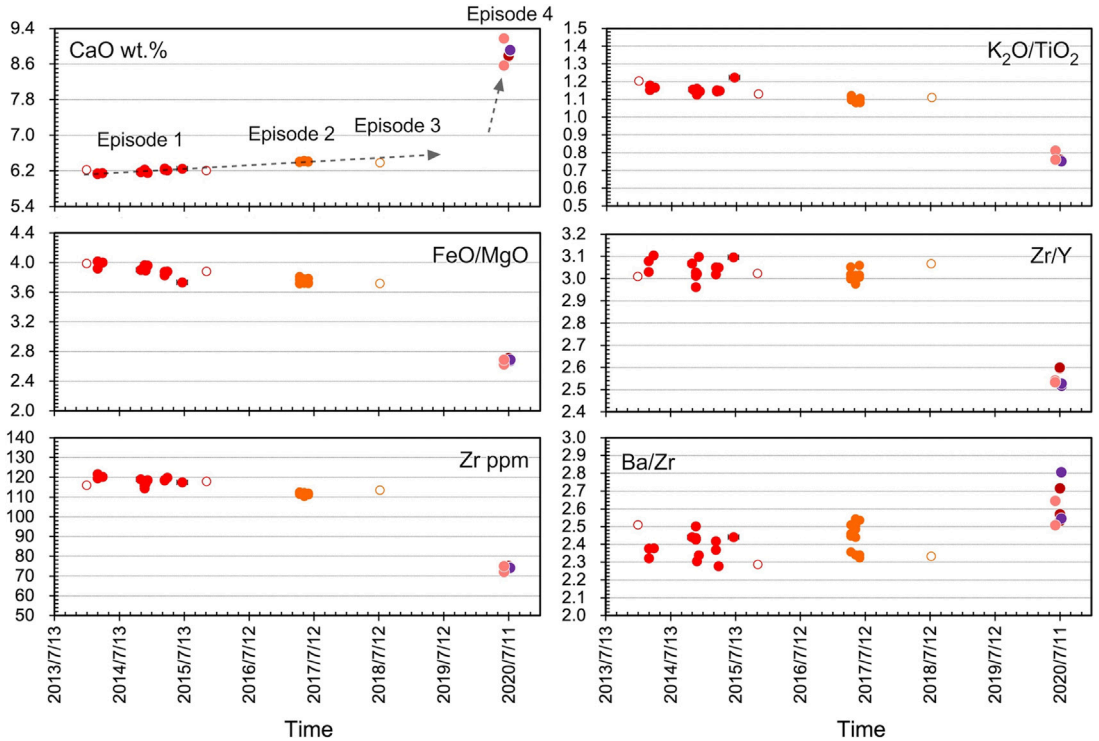


FIGURE 8 | Temporal variation in the whole rock major and trace element chemical compositions and their ratios throughout the recent Nishinoshima eruptive episodes.

and groundmass glass chemical compositions. Most of the Episode 1–3 MIs have 60–68 wt% SiO_2; however, the Episode 4 MIs have 55–59 wt% SiO_2, making them slightly more mafic than the groundmass glass (**Figure 11**, **Supplementary Table 3**). Some MIs in the Episode 4 olivine have undifferentiated features. The most mafic MI (46.8 wt% SiO_2 and 11.2 wt% MgO) was used to estimate the crystallization process of the mafic melts, as shown in **Figure 11**.

4.5.2 Magma Storage Conditions

The variation in the geochemical data suggest that the recent Nishinoshima eruption was linked to multiple magma reservoirs. In this section, magma storage conditions are estimated based on the chemical compositions of phenocrysts, groundmass glass, and MIs.

For Episode 1–3 magma with higher SiO_2 content, the magma temperature and water content were investigated using the MELTS program (Gualda et al., 2012) for a pressure range 0.5–1.5 kb. The MELTS fractionation models for the melt with a whole rock composition in Episode 1–3 best fit the compositional variation of MIs and groundmass in Episode 1–3 using a temperature and water content of ~1,050°C and 0.5–1.5 wt%, respectively (Maeno et al., 2018) (thick arrow A in the SiO_2-TiO_2 field in **Figure 11**). Furthermore, the MI water content in the type 2 plagioclase (abundant in Episodes 1–3 products) was estimated to be 1.5–2.0 wt% *via* direct measurements with Fourier-transform infrared spectroscopy (FTIR) (Maeno et al., 2018). The saturation pressure for these water contents corresponds to a depth of ~1.5–2 km. Using a pyroxene-melt geothermometer (Putirka, 2008) and the water content (by FTIR), the magma temperature of individual clinopyroxene phenocrysts was estimated to be ~1,050°C. This result is consistent with that of Maeno et al. (2016), where a similar temperature (1,050–1,090°C) was estimated for the crystallization temperature of groundmass crystals in volcanic ash from Episode 1, based on chemical compositions of the clinopyroxene (pigeonite) and groundmass glass. Conversely, the pyroxene phenocrysts in the glomeroporphyroclasts showed a lower magma temperature, ~970°C, using a two-pyroxene thermometer (Putirka, 2008). This result suggests different crystallization temperatures for the two types of pyroxene phenocrysts. This temperature is consistent with the results of Sano et al. (2016), who estimated a magma temperature of 970–990°C using a two-pyroxene thermometer for the products of Episode 1; this temperature is thought to correspond to the conditions of the highly crystallized part of the shallow magma reservoir. Type 2A plagioclase is also thought to form in this shallow reservoir.

However, the linear chemical trend that formed progressively from Episodes 1 to 3 (**Figures 7**, **11**) and the multimodal composition of the plagioclase and clinopyroxene phenocrysts and its change toward more mafic composition with time (**Figure 10**) suggest that there

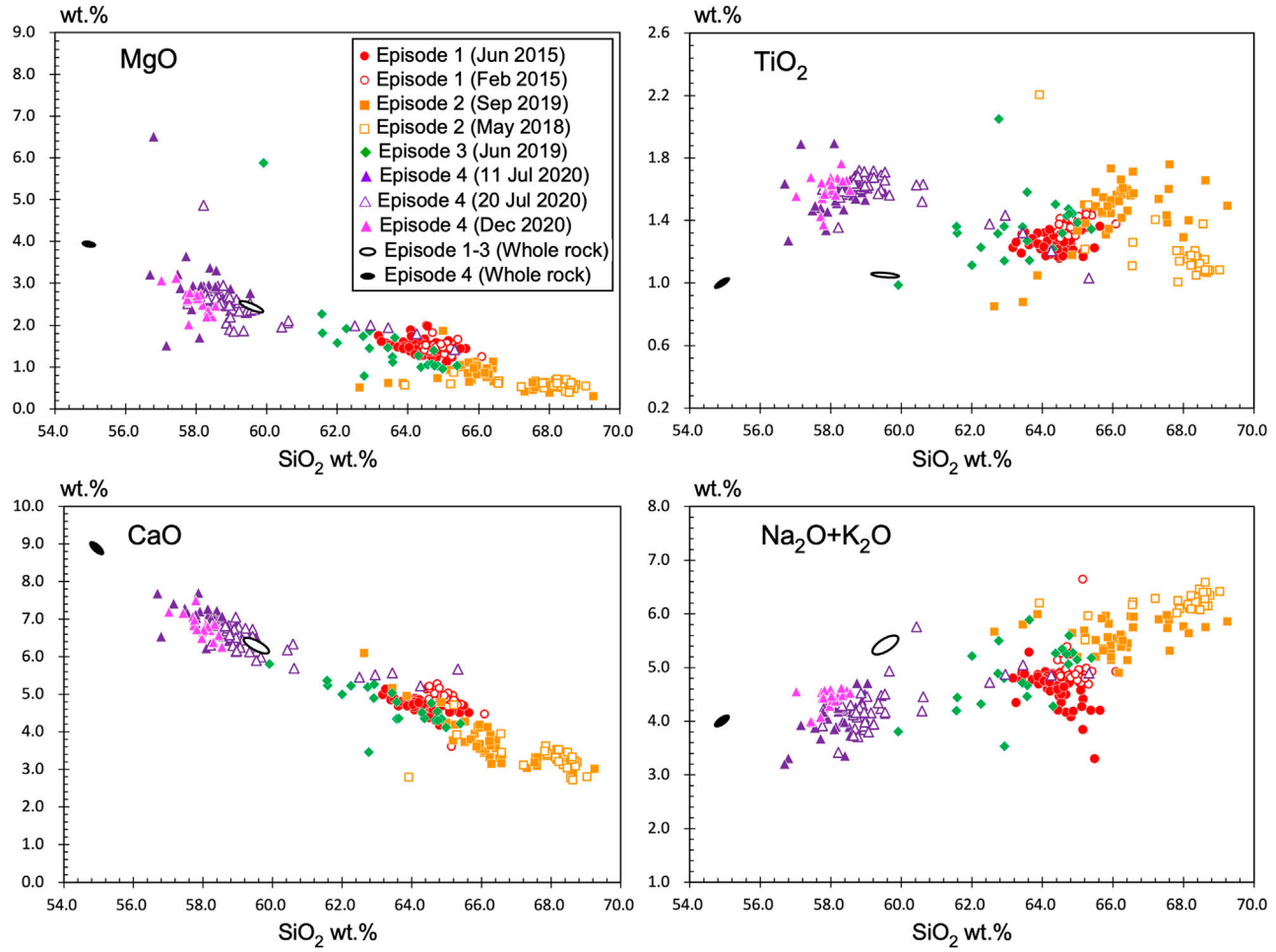


FIGURE 9 | Major element chemical compositions of the groundmass glass of representative samples from the recent Nishinoshima eruptions. Whole rock chemical compositions are also indicated. Dates in parentheses indicate those sampled.

is an endmember component that mixed with the silicic magma in the shallow reservoir. This endmember component is slightly different from the whole rock composition of the Episode 4 magma (**Figure 7**) but is assumed to be a magma having the average composition of the major Episode 4 MI (green field in **Figure 11**). The Episode 4 groundmass glass compositions can be explained by the fractionation of magma with a melt composition that is the same as the Episode 1–3 endmember component (thick arrow B in **Figure 11**). In this case, a similar magma temperature and water content to those of the Episode 1–3 magma (1,050–1,100°C and 0.5–1.5 wt% H_2O) are estimated, while the pressure is not constrained.

The Episode 4 magma also contains high-Mg# olivine (>80) with MIs more mafic than the whole rock chemical composition (**Figures 10**, **11**). Because this high-Mg# olivine cannot be equilibrated with most of the Episode 4 melt, a more mafic magma must have been included with the mixture. The MI compositional variation, which is more mafic than the Episode 4 whole rock composition, also indicates the mixture of a range of mafic melts.

As an attempt to explain these geochemical features, assuming the most mafic MI (46.8 wt% SiO_2 and 11.2 wt% MgO), which is hosted in olivine with $Fo_{87.6}$ as the undifferentiated basaltic magma, we investigated if the observed compositional variation of the plagioclase and olivine phenocryst cores could be explained (**Figures 11**, **12**). In **Figure 11**, the equilibrium and fractional crystallization paths (liquid lines of descent) calculated using the MELTS program (Smith and Asimow, 2005; Gualda et al., 2012) for different initial conditions (water content and pressure) buffered by FMQ are shown. In this calculation, olivine with Fo > 85 appears at temperatures of > 1,170°C for 1 wt% H_2O and > 1,120°C for 3 wt% H_2O (**Figure 12**). Olivine with Fo~70, which is the compositional majority in Episode 4, is explained by fractional crystallization at a temperature 1,050–1,080°C at 1–3 kbar in the case of 1 wt% H_2O. If the water content increases to 3 wt%, a lower pressure of 1–2 kbar is acceptable to form Fo~70 olivine. High-An (>90) plagioclase can crystallize at >1,150°C for 1 wt% H_2O and at 1,010–1,140°C for 2–3 wt% H_2O; however, higher An plagioclase can more easily crystallize

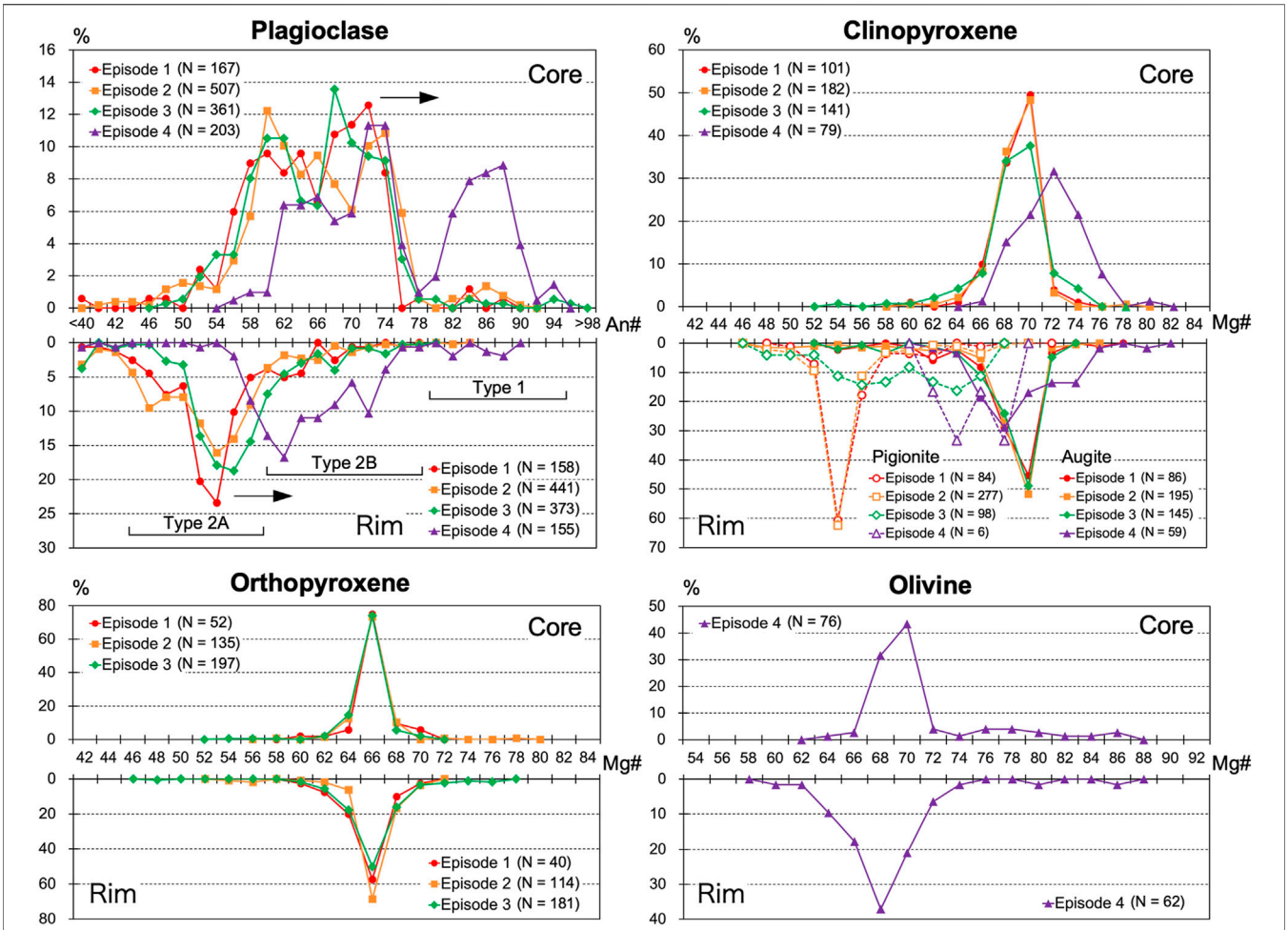


FIGURE 10 | Variation in the chemical composition of the phenocryst core and rim for Episodes 1–4. Black arrows in the plagioclase show the direction of the temporal change.

at lower pressures (1–2 kbar) and higher water contents: An_{95}, which is the highest observed, appears at 1,090–1,110°C and 1–2 kbar for 3 wt% H_2O. Type 1 ($An_{80\text{-}90}$ core) plagioclase can be explained by a temperature range of 1,000–1,100°C (**Figure 12**).

At this stage, we have no further constraints; however, we can infer that plausible conditions for the deep reservoir are 1,050–1,110°C and 1–2 kbar, which can explain major olivine (Fo~70) and plagioclase (type 1) compositions in Episode 4. Furthermore, the water content 2–3 wt% H_2O is required to explain the presence of high-An plagioclase in Episode 4. Therefore, it is possible that the water content increased in the deep reservoir before or during Episode 4. The absence of orthopyroxene in Episode 4 can be explained by the crystallization process assumed here because it first appears at temperatures of <1,050°C under conditions with ≤3 wt% H_2O and pressures of ≤2 kbar, while clinopyroxene appears at >1,100°C. This phase relationship is consistent with the observations.

The equilibrium or fractional crystallization paths calculated using the most mafic MI can produce a range of chemical compositions that might correspond to the mafic endmember melt (**Figure 11**), where the observed high-Mg# olivine and high-An plagioclase are survival crystals in the most mafic melt (**Figure 12**). Mixing of the differentiating mafic melt and the silicic melt (with the groundmass glass composition of Episode 4) may explain the MI compositional variation during Episode 4. It may also control the whole rock chemical composition of the Episode 4 magma, which is slightly different from the endmember component in Episodes 1–3. Some mafic MIs (outliers with 51 wt% SiO_2) cannot be explained by this mixing process, and it is thought that another mafic melt was also involved.

5 DISCUSSION

5.1 Variation in the Eruptive Style

A major characteristic of the Nishinoshima eruptive activity is that the growth of the island was largely dominated by lava effusion but also pyroclastic cone formation, which indicate the

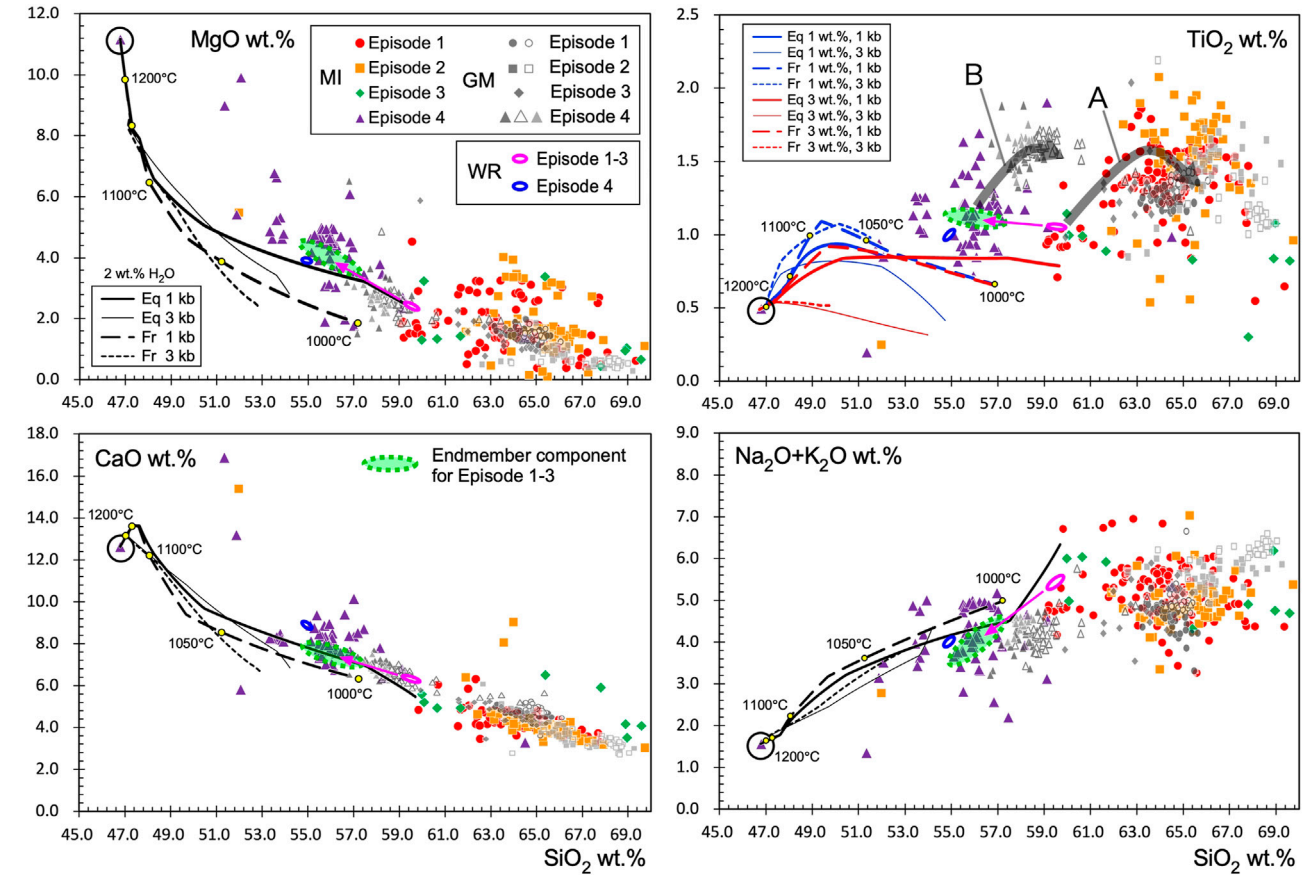


FIGURE 11 | Major element chemical compositions of melt inclusions (MIs, olivine-hosted and plagioclase-hosted) for representative samples from the recent Nishinoshima eruptions (colored symbols), plotted with the groundmass glass (GM) and whole rock (WR) chemical compositions. Symbols for GM are the same as in **Figure 9**, but grayscale is used; dark and light gray filled triangles: Jul 11, 2020 and Dec 2020, respectively. Arrows from the WR (the same as in **Figure 7**) indicate the direction of mixing of the endmember compositions (green area) in Episodes 1–3. Equilibrium (Eq) and fractional (Fr) crystallization paths (liquid lines of descent, LLDs) for the basaltic MI in olivine (denoted by the large circle) calculated using the MELTS program for different initial conditions (water content and pressure) buffered by FMQ are shown (black lines for MgO, CaO, and $Na_2O + K_2O$ and colored lines for TiO_2). For the black lines, only cases with 2 wt% H_2O are shown. Yellow dots indicate the temperatures every 50°C for 1 kbar and 2 wt% H_2O. The thick gray arrows A and B in TiO_2 show the approximate LLDs for water contents of <1.5 wt%, assuming the initial melt compositions of Episodes 1–3 and 4, respectively.

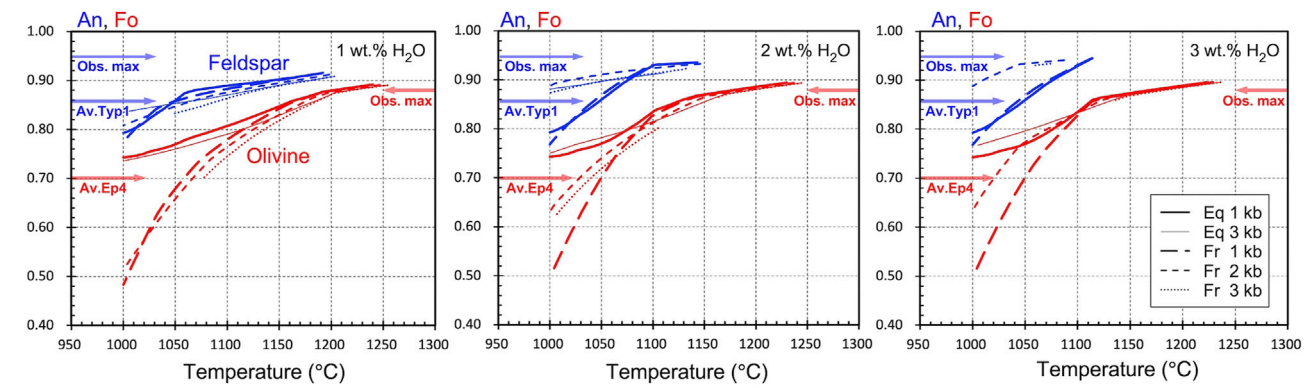


FIGURE 12 | Relationships between the anorthite (An) or forsterite (Fo) contents of feldspar and olivine, respectively, and the temperature down to 1,000°C for different initial water contents calculated using the MELTS program assuming equilibrium (Eq) and fractional (Fr) crystallization of the most mafic olivine-hosted MI in Episode 4 (the same as that circled in **Figure 11**). For feldspar, the observed maximum An (obs. max: ~0.95) and averaged An of type 1 plagioclase (av. typ 1: ~0.85) are indicated. For olivine, the observed maximum Fo (obs. max: ~0.88) and averaged Fo of Episode 4 olivine (av. Ep4: ~0.70) is indicated.

hybrid activity by effusive and explosive eruptions (**Figures 2**, **3**). The lava flows branched repeatedly and formed a large number of small and large lava lobes, namely, compound lava flows. Compound lava flows are generally observed in low-viscosity basaltic lava (Walker, 1971; Kilburn and Lopes, 1988; Calvari et al., 2002). The intermittent explosive activity characterized by Strombolian eruptions (from Episode 1 to early Episode 4) also suggests low-viscosity flows. In low-viscosity magma, efficient gas–melt segregation can occur, which may cause moderately explosive behavior due to the expansion of the gas-rich part of the magma (e.g., Edmonds, 2008; Taddeucci et al., 2013). Conversely, degassed magma, which has high density, may move laterally and yield lava flows if the conduit pressure overcomes the strength of the scoria cone. This type of hybrid activity has been recorded for pyroclastic cone formation by mafic magmas (Valentine et al., 2005; Pioli et al., 2008; Rowland et al., 2009).

Looking only at the whole rock chemical composition, andesite magma with 59–60 wt% SiO_2 may cause explosive activity or viscous lava flows/domes than more mafic compositions, as observed in many andesitic arc volcanoes (e.g., Murphey et al., 2000; Suzuki et al., 2013); however, this is not the case for Nishinoshima. This is because the Nishionoshima magma has a relatively high temperature (1,050–1,100°C) and lower phenocryst content (< 10 vol.%). These conditions can cause a minimum estimate of viscosity of 10^4 Pa s (Maeno et al., 2016) and may cause eruptive behavior similar to basaltic volcanism. Maeno et al. (2016) proposed that the lava flow dynamics of Nishinoshima is primarily controlled by the low magma viscosity, low magma discharge rate, and a higher cooling efficiency compared with terrestrial lava flows based on a theoretical consideration by Blake and Bruno (2000). In fact, the chemical composition of the magma gradually changed with time, becoming increasingly mafic. However, before Episode 4, the change in SiO_2 content was only ~1 wt %, corresponding to only a ~0.2 log unit in viscosity based on the model of Giordano et al. (2008). Such a change would not be able to cause the significant observed changes in the physical properties of the magma, eruptive style, and lava emplacement processes. Our land surveys and remote observations also suggest that there are no differences between Episodes 1 and 2 in the external/internal structures of their lava flows and that they reflect their emplacement processes.

The change in the chemical composition of the magma in Episode 4 might have significantly affected the eruptive style. In June–July 2020, there was a dramatic change in the style from lava flow-dominated to pyroclast-dominated, causing the cone to rapidly grow to a height of 250 m and a diameter of 570 m within a single month. Before 2020, the pyroclastic cone was only <10% of the island volume; however, after June 2020, the volume ratio of the cone increased to 60%. The entire island was also covered by thick pyroclastic fallout deposits. The eruptive style of this explosive type was interpreted to be violent Strombolian (Yanagisawa et al., 2020) as in geological and historical records of explosive basaltic eruptions (Arrighi et al., 2001; Valentine et al., 2007; Pioli et al., 2008; Di Traglia et al., 2009), and suggests that magma fragmentation was more efficient and caused the significant morphological change of the island.

The explosivity of low-viscosity magma is controlled by the degree of gas–melt segregation and the magma ascent velocity (e.g., Parfitt, 2004; Edmonds, 2008; Gonnermann and Manga, 2013; James et al., 2013; Taddeucci et al., 2013). Lava fountains with vigorous ash plumes, as observed during Episode 4, are generally thought to represent the closed-system degassing end member at high magma ascent rates. During the Episode 4, the magma discharge rate (ascent rate if conduit radius not changed) higher than those of the previous activities was estimated from the thermal anomaly intensity and optical satellite observations (**Figure 4**)[1]. Thus, the transition of eruption style from intermittent Strombolian to more continuous and intense lava fountaining is thought to have been caused by the increase of magma ascent rates. The gas–melt segregation efficiency might be also affected by the melt viscosity and its change during ascent, such as *via* microlite crystallization (Polacci et al., 2006; Houghton and Gonnermann, 2008; Cimarelli et al., 2011), but the eruption style and explosivity can be primarily controlled by elementary factors such as the volatile content in the reservoir (e.g., Sides et al., 2014). The higher initial volatile content can contribute to make higher exit velocity at vent, thus resulting in higher fountains (e.g., Wilson and Head, 1981; Parfitt, 2004).

The dramatic change in the chemical composition of the magma in the later phase of Episode 4 suggests that there was a large amount of mafic magma recharge from the deeper part of the magma system (**Figure 13**). This is consistent with the apparent increase in the sulfur component of the satellite-observed volcanic gas, indicating the recharge of volatile-rich mafic magma[1]. Our geochemical monitoring data also showed the possibility of increased volatile content in the magma, as indicated by the increase in higher-An (type 1, An > 90) plagioclase (**Figures 10**, **12**). These observational and geochemical data suggest that the major factors in the explosivity increase observed during Episode 4 were the change in the volatile (vapor phase) content in the magma-storage region, the increase in the mass discharge rate, or both, resulted from mafic magma recharge in depth. More direct evidence for the transition of eruption style and its causes is required to provide better constraints. They might be recorded in micro-scale rock textures or volatile species and their concentrations in crystal and melt phases.

During the period just before the cessation of each eruptive episode, Vulcanian-type explosions were observed. This change in the eruptive style is a common characteristic of Nishinoshima magma. Regardless of the chemical compositions of the erupting magma, the decrease in the average rates of magma ascent may allow an increase in the magma viscosity in shallow conduits because of slow magma ascent, or a longer residence time, which causes more extensive degassing and crystallization. This eventually inhibits two-phase flow and causes the formation of an impermeable plug on top of the conduit, decreasing degassing and increasing the overpressure in the shallow magma, resulting in an intense explosion (Sparks, 1997; Stix et al., 1997). This type of Vulcanian activity caused by mafic magma was also observed in the 1943–1952 eruption of the Paricutin volcano, Mexico (Pioli et al., 2008).

The change in the eruptive style from Strombolian to Vulcanian was observed in Episodes 1 and 2. During this

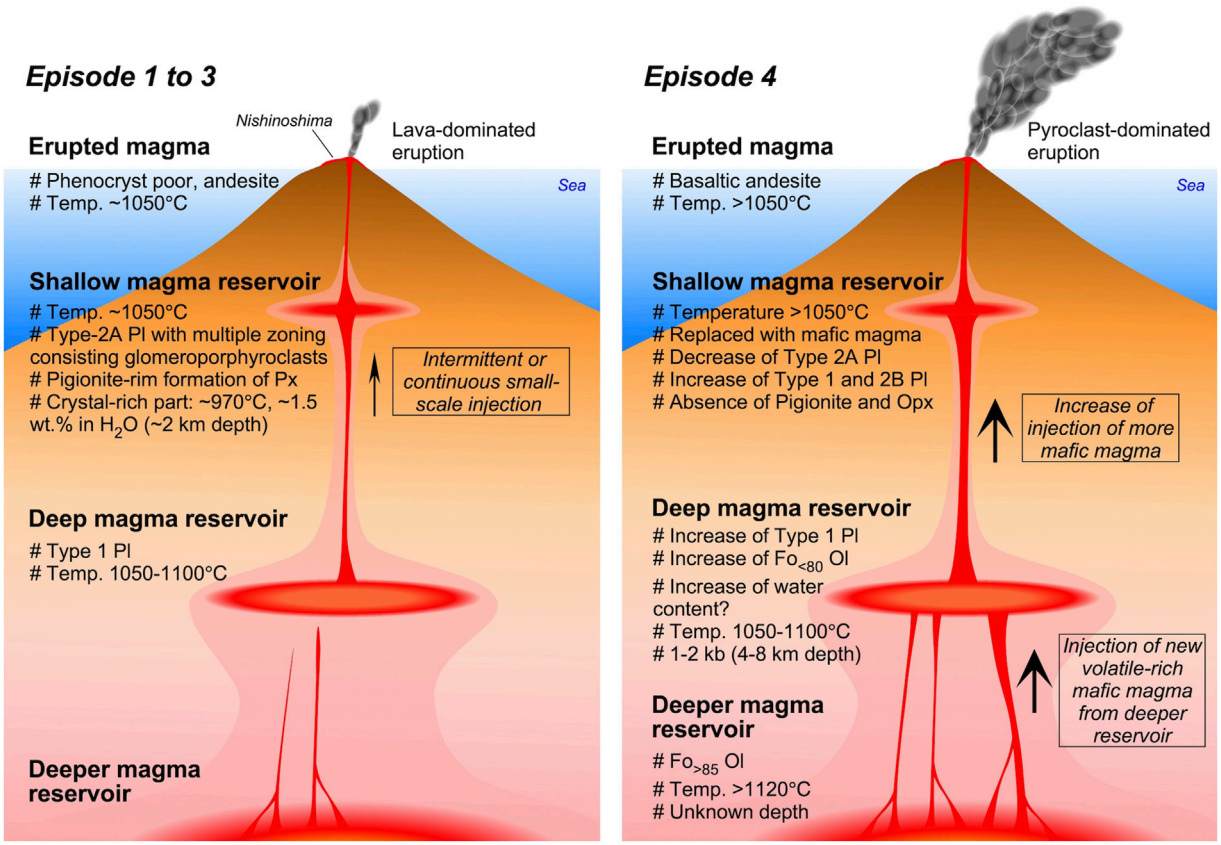


FIGURE 13 | Schematic diagram of the magma reservoirs and feeding system thought to have developed beneath Nishinoshima volcano.

period, the summit crater was enlarged and the height of the cone slightly decreased (**Figures 3**, **4**) as a result of the expulsion of the summit rocks by intense explosions. For Episodes 3 and 4, whether Vulcanian-type explosions occurred is unknown.

5.2 Implication for the Magma Feeding System

The erupted volume gradually decreased during the three episodes from 2013 to 2018. Before 2019, we interpreted this observation as indicating that the recent Nishinoshima activity was headed toward cessation in the long term as a result of the decreasing overpressure in the magma reservoir. However, the erupted magma shows evidence of an increased contribution of magma mixing; for example, the whole rock chemical compositions have become more mafic in the later activity and there was an increase in type 1 plagioclase with high-An cores. In just Episode 1, the mafic component in the whole rock major element composition gradually increased. These data indicate that the ratio of the mafic component increased as the result of multiple and intermittent mafic magma recharge from a deep reservoir (4–8 km) into a shallow magma reservoir (1.5–2 km) or a decrease in the volume of the silicic component in the shallow magma reservoir (**Figure 13**). Baba et al. (2020) estimated the demagnetization source and pressure source depths to be 2.6 km below sea level (b.s.l.) and 6.6 km b.s.l., respectively, using ocean bottom electromagnetometers installed offshore the island from 2016 to 2017. The depths of the deep and shallow reservoirs may be related to these magnetic and pressure sources, although there is a little discrepancy for the shallow source.

The onset of Episode 4 in December 2019, with more explosive eruptions and a higher magma discharge rate, and the change of magma from andesite to basaltic andesite suggest that the recent activity was not actually declining but that there was a large mafic magma recharge. In addition to a large amount of volatile release during the most intense phase of Episode 4, previously unrecognized olivine phenocrysts have been incorporated into the magma and incompatible element concentration ratios, such as Zr/Y, in the whole rock compositions have changed. Therefore, we suggest that a new undifferentiated, volatile-rich magma, different from the mafic magma that was involved in the earlier eruptive episodes, ascended from an additional source (deeper than 8 km) and dramatically changed the eruptive style to be more explosive in Episode 4.

The observations are difficult to explain using only the magma reservoirs that caused Episodes 1–3. Undifferentiated magma might have ascended from depth, or the discharge of a large volume of magma from the shallow magma reservoir might have triggered the movement, redistribution and ascent of deeper magma. If we assume that the endmember mafic magma in

Episode 4 exists on the calculated LLDs and that the temperature is 1,050–1,100°C (**Figure 11**), the weight ratio of the mixed endmember mafic magma will be approximately 20–30%. This probably caused a significant change in magma reservoir condition, hence the change in eruptive behavior, although the relationship between the volume of mafic magma involved and the eruption style and magnitude may not be straightforward. Geochemical monitoring data suggests that the recent eruptive activity and growth of Nishinoshima have been fueled by intermittent or continuous mixing in the shallow reservoir and more episodic and large-scale magma recharge from deeper parts of the magma-feeding system (**Figure 13**). The temperatures of the shallow and deep reservoirs are not significantly different, meaning that deep magma can be supplied to shallow levels with limited cooling. Therefore, it is thought that deeper magma injection significantly controlled the eruptive activity during Episode 4.

5.3 Morphological Development and Growth of the Island

In the effusive phases by low-viscosity andesitic magma, lava was supplied from the center of the island with some fluctuations in the discharge rate and flowed along topographic lows. It formed both small and large lava lobes, increasing the area of the lava field. This process formed the complicated irregular morphology of Nishinoshima. This was observed particularly in the middle of Episode 1, Episode 2, and the earlier phase of Episode 4 and it is thought to reflect the lava flow dynamics, which is primarily controlled by the lower magma discharge rate (Maeno et al., 2016). Low-viscosity lava basically spreads horizontally and enlarges the area of effusive products, following its gravity flow nature (e.g., Huppert et al., 1982; Griffiths, 2000). The final morphology of the lava flows is controlled by the viscosity, cooling rate, and effusion rate (Griffiths and Fink, 1992; Blake and Bruno, 2000; Anderson et al., 2005; Harris et al., 2007), and lava flows fundamentally contribute to the lateral growth of the volcanic edifice.

The contribution of lava flows to island growth and morphological characteristics on Nishinoshima is observed at other volcanoes where silicic lava flows with multiple lobes, inflation clefts, and breakouts spread onto the shallow seafloor, such as andesite lavas from the Sakurajima volcano, Japan (Omori, 1916), andesite lavas from the Anak Krakatau volcano, Indonesia (Sutawidjaja, 2006), and dacite lavas from the Nea Kameni volcano, Greece (Pyle and Elliot, 2006). As Maeno et al. (2016) noted, the development of a solid crust at the lava flow margins may be pronounced in eruptions in marine and lacustrine settings and may be an enhancing factor in the emplacement processes of lava flows with multiple lobes.

When lava flows enter water, a large amount of steam rises from the front of the lava flow (**Figure 2**). The flow front is rapidly cooled as it comes into contact with the seawater and is presumably brecciated, or auto-brecciated by the motion of the lava flow. The development of platy joints surrounding the massive interior of a lava lobe may reflect rapid cooling in a single lava lobe, as observed in lava flows contacting ice (e.g., Lescinsky and Sisson, 1998). Although the submarine parts of the lava flows are not exposed, the lava-fed delta may be composed of hyaloclastites that are continuously produced at the front and base of the flow. These flows are extending the foreshore, as described for exposed ancient basaltic and andesitic lava flow successions (e.g., Schneider, 2000; Smellie et al., 2013), and contribute to the formation of the foundation of the volcanic island.

In addition to lava effusion, pyroclastic eruptions also contributed to the morphological development. The formation process of a central cone at Nishinoshima can be divided into two stages: the cone-building by accumulation of the ballistically ejected clasts from coarse-grained Strombolian eruptions in early stages (Episode 1 to mid-Episode 4) and the later cone-building by deposition of fine-grained tephra from more explosive eruptions in mid-Episode 4. The growth rate of the later cone was much higher than that of the earlier one (**Figure 4**), reflecting higher depositional (or magma discharge) rate in the middle of Episode 4. The early cone continued to grow upward and outward with a combination of ballistic emplacement and grain avalanching. The latter cone may be explained by the rapid accumulation of fine-grained fallout deposits from the sustained, well-fragmented eruption column, which is significantly different from the early episode. The dramatic changes of eruption style, depositional process, and resulting morphological feature, similar to Nishinoshima, have been reported for Lathrop Wells volcano, southern Nevada, United States (Valentine et al., 2005), where the clear boundary of the two different depositional processes between the early Strombolian eruption and the later violent-Strombolian eruption was identified. Although Valentine et al. (2005) argued that the change of the eruption style might be caused by increase of effective viscosity due to microlite crystallization, this may not be only the mechanism for such an eruption. In Nishinoshima, geochemical characteristics of the magma feeding system and their change by the recharge of more mafic magma played an important role on the eruption transition and the morphological development of the volcanic edifice.

Pyroclastic eruptions will be one of the major contributing factors for the growth of the cone in Nishinoshima. However, if such eruptions occur in a very initial phase of the island formation and pyroclasts mainly shape the island without lava flow effusion, they are likely to be easily and quickly eroded by waves. In the recent Nishinoshima eruption, the situation in which primary loose pyroclastic fall/flow deposits form coast lines was not observed. Rather, the lava flows that can control lateral growth played the most important role on the formation of the foundation of the island. In fact, wave erosion was observed on some near-shore lava lobes, particularly during the calm periods between the eruptive episodes. However, resedimentation of pyroclastic materials by waves also occurred, resulting in the formation of new beaches. These secondary processes of erosion and resedimentation have reshaped the irregular outline of the island to be more rounded with time (**Figure 3**); however, they do not appear to have significantly changed the surface area of the island, at least in the recent years.

5.4 Comparison With Historical Examples

Historical records of failed and successful volcanic island formation are available. The 1952–1953 silicic eruption at Myojinsho in the Izu-Bonin arc, Japan, created a small lava (dome) island in shallow water; however, this island was destroyed by numerous explosion episodes and disappeared because of the lack of further lava effusion, thus failing in forming a volcanic island (Morimoto and Ossaka, 1955; Fiske et al., 1998). The 1986 eruption at Fukutoku Okanoba, 300 km south of Nishinoshima, created a small pyroclastic cone in shallow water as the result of Surtseyan-type eruptions of trachytic magma (Ossaka, 1991). However, the cone was easily eroded within 3 months and no island formed. The ephemeral Ferdinandea Island produced by the 1831 Surtseyan-type eruption in the Strait of Sicily, Italy (Cavallaro and Coltelli, 2019), was also one of examples of failed volcanic island formation. Conversely, in the 1934–1935 eruption at Showa Iwo-jima, silicic lava effusion resulted in a new volcanic island (300 m × 530 m) that has survived 80 years, although wave erosion has decreased the size of the island. The duration of this eruption was only half a year (October 1934–March 1935); however, lava effusion occurred continuously and its effusion rate reached values of the order of 10^5 m^3/day (Maeno and Taniguchi, 2006), the same order observed during the recent Nishinoshima eruptions. During the first 5 months of the 1973–1974 Nishinoshima eruption, submarine eruptions occurred, and their products buried the funnel-shaped crater to a depth of ~100 m and then formed a new island with Surtseyan and Strombolian eruptions with lava effusion (Aoki and Ossaka, 1974; Ossaka et al., 1974; Ossaka, 1991). The eruptions occurred at a similar location to the recent activity since 2013. For this previous Nishinoshima eruption, the discharge rate was estimated to be 1×10^5 m^3/day for the submarine stage during the first 5 months, then decreasing to $2–4 \times 10^4$ m^3/day in the following 11 months of island forming activity. The magma discharge rate during the submarine stage was comparable to that of the recent eruptions. However, multiple subaerial vents and scattered small pyroclastic cones (with maximum heights of ~52 m) formed, confining the lava effusion rates at each vent. Although the eruption created a new island with an area of ~0.25 km^2 and a pre-erosion height of ~50 m (total volume, $\sim 2.4 \times 10^7$ m^3), most of the pyroclast-dominated island was eroded and only small portions of the lava-dominated parts withstood erosion by 2013. This previous Nishinoshima eruption differs from the recent events, in which continuous lava effusion occurred from almost the same location throughout four eruptive episodes over 8 years, resulting in an area of 2.6 km^2 (~10 times larger than the previous area) and a height of ~250 m.

As seen in the Nishinoshima eruption and other historical submarine eruptions in the Japanese archipelago, one of the important factors controlling whether a volcanic island is created is the volume and effusion rate of the lava flows in shallow seas. Large volumes of unerodable lava relative to pyroclastic material contribute to the enlargement of the foundation of a volcanic island. The Episode 1 lava volume of the recent Nishinoshima eruptions reached more than 1×10^8 m^3, corresponding to an eruption magnitude (M: Pyle, 2013) of ~4.5. The average lava effusion rate was $\sim 2.0 \times 10^5$ m^3/day. The magnitude of this eruption was the largest in Japan since the 1991–1996 Unzen eruption (M ~ 4.7) in which 2.1×10^8 m^3 of dacite magma were effused with an average magma discharge rate on the order of $\sim 10^5$ m^3/day (Nakada et al., 1999). In the case of Nishinoshima, long-term but episodic magma discharge has resulted in voluminous lava flows and an extension of the island area. The average magma discharge rate, 2.0×10^5 m^3/day (2.3 m^3/s) of the recent Nishinoshima eruptions is similar to the discharge rate (2–5 m^3/s) during the later phase of the 1964 Surtsey eruption, although the discharge rate of the Surtsey eruption reached 20 m^3/s on average in the early effusive phase with relatively high-intensity activity (Thordarson and Sigmarsson, 2009). Comparing the magma discharge rates at Nishinoshima with those of other island-forming eruptions, it appears that long-lasting lava effusion with a discharge rate on the order of at least 10^4 m^3/day (annual average) to 10^5 m^3/day (monthly average) is required for the formation and long-term survival of a new volcanic island in shallow seas. Specifically, effusive lava flows contribute to increasing the area of the island and to form the solid foundation of the island. Conversely, the vertical growth rate of an island may be controlled by tephra deposition, including pyroclastic cone formation. Explosive activity contributes to increasing the height of a volcano *via* pyroclastic deposits. This order of eruptive products from lava flows to pyroclastic deposits may be essential for the efficient growth of a volcanic island. At the time of writing, there was an explosive eruption at Fukutoku Okanoba volcano in Japan from the shallow sea floor on August 13–15, 2021 (confirmed by Japan Coast Guard), that formed a new island consisting of pyroclastic deposits. This island remains after several months; it will be interesting to see whether this island formation fails or succeeds.

6 CONCLUSION

Here, we reported the detailed sequence of the recent Nishinoshima eruptive events based on long-term geological and geochemical monitoring since 2013 and discussed the formation and growth processes of the new volcanic island and the temporal changes in the magma chemistry. The Nishinoshima eruptive activity can be divided into four episodes. Over the eruptive episodes, the growth of the new volcanic island was sustained by the effusion of andesite lava flows into the shallow sea at a rate of the order of 10^5 m^3/day. The lava flows spread radially with numerous branches, resulting in compound lava flows. This constituted the primary contributor to the construction of the solid foundation of the island; however, deposition of pyroclastic materials also helped expanding the subaerial volcanic edifice. The duration of the eruptive episodes was initially 2 years (Episode 1) but shortened to a week by Episode 3, with decreasing eruptive volume with time. However, the latest episode (Episode 4, 8 months of

activity) was the most intense and the largest episode with a magma discharge rate on the order of 10^6 m^3/day. The size of the new island reached 2.5 km × 2.5 km (~4.4 km^2) with a volume of ~0.2 km^3 by 2020. The eruptive style dramatically changed during Episode 4 from lava-dominated to more explosive pyroclast-dominated, and the volume ratio of the pyroclastic cone increased from <10 to 60%. However, the temporal change in the geochemical characteristics indicates that more mafic magma was involved in the later episode and that the initial andesite magma with ~60 wt% SiO_2 changed to basaltic andesite magma with ~55 wt% SiO_2 in Episode 4. The eruptive behavior and geochemical data suggest that the recent Nishinoshima eruptions were fueled by the intermittent or continuous mixing of silicic and mafic magmas in a shallow reservoir (~2-km depth) and by a more episodic and large-scale magma supply from deeper reservoirs.

Some of the important factors controlling volcanic island formation and growth in shallow seas are the volume and effusion rate of the lava flows. A larger volume of unerodable lavas rather than pyroclastic deposits contributes to enlarging the solid foundation of a volcanic island, as observed in the case of the recent eruption of Nishinoshima volcano. Comparisons with several examples of island-forming eruptions indicate that long-lasting lava effusion with a discharge rate of the order of at least 10^4 m^3/day (annual average) to 10^5 m^3/day (monthly average) is required for the formation and growth of a new volcanic island with a diameter on km-scale that can survive against sea waves over the years.

The longer-term eruptive history of Nishinoshima is not well understood; however, because it is growing a large volcanic edifice, Nishinoshima may continue to be very active over a long time and may repeat eruptive activity, such as the effusion of large amounts of lava, as in the recent eruptions. Most of the volcanic edifice is underwater; therefore, it is unknown whether submarine eruptive activity had recently occurred other than at the summit. To capture a complete view of the recent eruptive activity, it is necessary to perform detailed survey of the changes in the seafloor topography and ejecta. Comprehensive analyses of the eruptive materials are also expected to provide a detailed image of the magma feeding system that caused the recent eruptions and the processes of magma ascent. Further geological and geochemical analysis, as well as geophysical data, is crucial to provide an overall understanding of the Nishinoshima volcano.

DATA AVAILABILITY STATEMENT

The original contributions presented in the study are included in the article/**Supplementary Material**, further inquiries can be directed to the corresponding author.

AUTHOR CONTRIBUTIONS

FM oversaw data collection and analysis and wrote the first draft of the manuscript. NH and AY conducted XRF and EPMA analyses, and FM and AY analyzed the dataset. TK, AY, and FM analyzed the satellite data. FM, TK, and SN (NIED) conducted aerial surveys, analyzed images, and made geological interpretations. FM, MY, and SN (AIST) conducted geological investigations and sampled rocks during the land surveys. YT, AT, and MT led the remote research vessel surveys and contributed to sampling and eruption chronology. All authors discussed the eruption process, cooperated in revisions, and approved this submission.

FUNDING

This research was supported by Grant-in-Aid for scientific research (No. 16H02221, 17H02987 and 21H01195) from the Ministry of Education, Culture, Sports, Science and Technology of Japan (MEXT), by Earthquake and Volcano Hazards Observation and Research Program of MEXT (ERI17) and by ERI JURP 2019-G-05 in Earthquake Research Institute, the University of Tokyo.

ACKNOWLEDGMENTS

We acknowledge the Nishinoshima comprehensive scientific research project led by the Ministry of the Environment Japan, specifically for the land surveys. Sampling of volcanic products from Nishinoshima were carried out in cooperation with shipboard scientists and technical personnel on multiple research vessels (*Kairei, Natsushima, Shinseimaru, Keifumaru, and Ryofumaru*). We also acknowledge the JCG and the GSI for providing their bathymetry data before the eruption and their topography data during the recent eruptions. Our aerial inspections were performed courtesy of Asahi Shimbun, Yomiuri Shimbun, and Mainichi Shimbun who kindly provided their aircrafts. We also thank the editors Joan Marti and Valerio Acocella and two reviewers for constructive comments and suggestions.

SUPPLEMENTARY MATERIAL

The Supplementary Material for this article can be found online at: https://www.frontiersin.org/articles/10.3389/feart.2021.773819/full#supplementary-material

REFERENCES

Anderson, S. W., McColley, S. M., Fink, J. H., and Hudson, R. K. (2005). "The Development of Fluid Instabilities and Preferred Pathways in Lava Flow Interiors: Insights from Analog Experiments and Fractal Analysis," in *Kinematics and Dynamics of Lava Flows*. Editors M. Manga and G. Ventura (Boulder: Geol. Soc. Am. Sp. Pap.), 396, 147–161. doi:10.1130/0-8137-2396-5.147

Aoki, H., and Ossaka, J. (1974). *A Mystery of Submarine Volcanoes – the Exploration Records of Nishinoshima (Kaiteikazan No Nazo)*. Tokyo: Tokai Univ. Press, 250. in Japanese.

Arrighi, S., Principe, C., and Rosi, M. (2001). Violent Strombolian and Subplinian Eruptions at Vesuvius during post-1631 Activity. *Bull. Volcanol.* 63, 126–150. doi:10.1007/s004450100130

Baba, K., Tada, N., Ichihara, H., Hamano, Y., Sugioka, H., Koyama, T., et al. (2020). Two Independent Signals Detected by Ocean Bottom Electromagnetometers during a Non-eruptive Volcanic Event: Ogasawara Island Arc Volcano, Nishinoshima. *Earth Planets Space* 72, 112. doi:10.1186/s40623-020-01240-z

Bas, M. J. L., Maitre, R. W. L., Streckeisen, A., and Zanettin, B. (1986). IUGS Subcomission on the Systematics of Igneous RocksA Chemical Classification of Volcanic Rocks Based on the Total Alkali-Silica Diagram. *J. Petrology* 27, 745–750. doi:10.1093/petrology/27.3.745

Blake, S., and Bruno, B. C. (2000). Modelling the Emplacement of Compound Lava Flows. *Earth Planet. Sci. Lett.* 184, 181–197. doi:10.1016/s0012-821x(00)00278-8

Calvari, S., Neri, M., and Pinkerton, H. (2002). Effusion Rate Estimations during the 1999 summit Eruption on Mount Etna, and Growth of Two Distinct Lava Flow fields. *J. Volcanol. Geotherm. Res.* 119, 107–123. doi:10.1016/S0377-0273(02)00308-6

Cavallaro, D., and Coltelli, M. (2019). The Graham Volcanic Field Offshore Southwestern Sicily (Italy) Revealed by High-Resolution Seafloor Mapping and ROV Images. *Front. Earth Sci.* 7, 311. doi:10.3389/feart.2019.00311

Cimarelli, C., Costa, A., Mueller, S., and Mader, H. M. (2011). Rheology of Magmas with Bimodal crystal Size and Shape Distributions: Insights from Analog Experiments. *Geochem. Geophys. Geosyst.* 12, a–n. doi:10.1029/2011GC003606

Cronin, S., BrennaSmith, M. I. E. M., Smith, I., Barker, S., Tost, M., Ford, M., et al. (2017). New Volcanic Island Unveils Explosive Past. *Eos* 98, 1. doi:10.1029/2017EO076589

Di Traglia, F., Cimarelli, C., de Rita, D., and Gimeno Torrente, D. (2009). Changing Eruptive Styles in Basaltic Explosive Volcanism: Examples from Croscat Complex Scoria Cone, Garrotxa Volcanic Field (NE Iberian Peninsula). *J. Volcanology Geothermal Res.* 180, 89–109. doi:10.1016/j.jvolgeores.2008.10.020

Edmonds, M. (2008). New Geochemical Insights into Volcanic Degassing. *Phil. Trans. R. Soc. A.* 366, 4559–4579. doi:10.1098/rsta.2008.0185

Fiske, R. S., Cashman, K. V., Shibata, A., and Watanabe, K. (1998). Tephra Dispersal from Myojinsho, Japan, during its Shallow Submarine Eruption of 1952-1953. *Bull. Volcanology* 59, 262–275. doi:10.1007/s004450050190

Giordano, D., Russell, J. K., and Dingwell, D. B. (2008). Viscosity of Magmatic Liquids: a Model. *Earth Planet. Sci. Lett.* 271, 123–134. doi:10.1016/j.epsl.2008.03.038

Gonnermann, H. M., and Manga, M. (2013). in *"Dynamics of Magma Ascent in the Volcanic Conduit," in* Modeling Volcanic Processes. Editor S. A. Fagents, T. K. P. Gregg, and R. M. C. Lopes (Cambridge University Press), 55–84.

Griffiths, R. W., and Fink, J. H. (1992). Solidification and Morphology of Submarine Lavas: a Development on Extrusion Rate. *J. Geophy. Res.* 97, 19729–19737. doi:10.1029/92jb01594

Griffiths, R. W. (2000). The Dynamics of Lava Flows. *Annu. Rev. Fluid Mech.* 32, 477–518. doi:10.1146/annurev.fluid.32.1.477

Gualda, G. A. R., Ghiorso, M. S., Lemons, R. V., and Carley, T. L. (2012). Rhyolite-MELTS: A Modified Calibration of MELTS Optimized for Silica-Rich, Fluid-Bearing Magmatic Systems. *J. Petrology* 53, 875–890. doi:10.1093/petrology/egr080

Harris, A. J. L., Dehn, J., and Calvari, S. (2007). Lava Effusion Rate Definition and Measurement: a Review. *Bull. Volcanol.* 70, 1–22. doi:10.1007/s00445-007-0120-y

Hon, K., Kauahikaua, J., Denlinger, R., and Mackay, K. (1994). Emplacement and Inflation of Pahoehoe Sheet Flows: Observations and Measurements of Active Lava Flows on Kilauea Volcano, Hawaii. *Geol. Soc. Am. Bull.* 106, 351–370. doi:10.1130/0016-7606(1994)106<0351:eaiops>2.3.co;2

Houghton, B. F., and Gonnermann, H. M. (2008). Basaltic Explosive Volcanism: Constraints from Deposits and Models. *Geochemistry* 68, 117–140. doi:10.106/j.chemer.2008.04.00210.1016/j.chemer.2008.04.002

Huppert, H. E., Shepherd, J. B., Haraldur Sigurdsson, R., and Sparks, S. J. (1982). On Lava Dome Growth, with Application to the 1979 Lava Extrusion of the Soufrière of St. Vincent. *J. Volcanology Geothermal Res.* 14, 199–222. doi:10.1016/0377-0273(82)90062-2

Ishizuka, O., Taylor, R. N., Yuasa, M., Milton, J. A., Nesbitt, R. W., Uto, K., et al. (2007). Processes Controlling Along-Arc Isotopic Variation of the Southern Izu-Bonin Arc. *Geochem. Geophys. Geosyst.* 8, 6Q06008. doi:10.1029/2006gc001475

James, M. R., Lane, S. J., and Houghton, B. F. (2013). "Unsteady Explosive Activity: Strombolian Eruptions," in *Modeling Volcanic Processes*. Editor S. A. Fagents, T. K. P. Gregg, and R. M. C. Lopes (Cambridge University Press), 107–128.

Kaneko, T., Maeno, F., Yasuda, A., Takeo, M., and Takasaki, K. (2019). The 2017 Nishinoshima Eruption: Combined Analysis Using Himawari-8 and Multiple High-Resolution Satellite Images. *Earth Planets Space* 71, 140. doi:10.1186/s40623-019-1121-8

Kilburn, C. R. J., and Lopes, R. M. C. (1988). The Growth of Aa Lava Flow fields on Mount Etna, Sicily. *J. Geophys. Res.* 93, 14759–14772. doi:10.1029/jb093ib12p14759

Lescinsky, D. T., and Sisson, T. W. (1998). Ridge-forming, Ice-Bounded Lava Flows at Mount Rainier, Washington. *Geology* 26, 351–354. doi:10.1130/0091-7613(1998)026<0351:rfiblf>2.3.co;2

Maeno, F., Nakada, S., and Kaneko, T. (2016). Morphological Evolution of a New Volcanic Islet Sustained by Compound Lava Flows. *Geology* 44, 259–262. doi:10.1130/G37461.1

Maeno, F., Nakano, S., Yoshimoto, M., Ohminato, T., Watanabe, A., Kawakami, K., et al. (2017). First landing and Survey of a New Volcanic Island: Nishinoshima. *J. Geogr. (Chigaku Zasshi)* 126, N1–N13. in Japanese with English abstract.

Maeno, F., and Taniguchi, H. (2006). Silicic Lava Dome Growth in the 1934-1935 Showa Iwo-Jima Eruption, Kikai Caldera, South of Kyushu, Japan. *Bull. Volcanol.* 68, 673–688. doi:10.1007/s00445-005-0042-5

Maeno, F., Yasuda, A., Nakano, S., Yoshimoto, M., Ohminato, T., Watanabe, A., et al. (2018). Formation Process of a New Volcanic Island at Nishinoshima, Ogasawara, Japan, Inferred from Eruptive Products. *J. Adv. Mar. Sci. Tech. Soc.* 24, 35–44. doi:10.14928/amstec.24.1_35 in Japanese with English abstract.

Maeno, F., and Yoshimoto, M. (2020). Characteristics and Change of Geomorphology, Geology and Eruptive Materials in the Eruption of Nishinoshima Volcano, Ogasawara. *Ogasawara Res.* 46, 37–51. in Japanese with English abstract.

Morimoto, R., and Ossaka, J. (1955). The 1952-1953 Submarine Eruption of the Myojin Reef Near the Bayonnaise Rocks, Japan. *Bull. Earthq. Res. Inst. Tokyo Univ.* 33, 221–250.

Murphey, D., Sparks, R. S. J., Barclay, J., Carroll, M. R., and Brewer, D. T. S. (2000). Remobilization of Andesite Magma by Intrusion of Mafic Magma at the Soufriere Hills Volcano, Montserrat, West Indies. *J. Petrol.* 41, 21–42. doi:10.1093/petrology/41.1.21

Nakada, S., Nagai, M., Kaneko, T., Nozawa, A., and Suzuki-Kamata, K. (2005). Chronology and Products of the 2000 Eruption of Miyakejima Volcano, Japan. *Bull. Volcanol.* 67, 205–218. doi:10.1007/s00445-004-0404-4

Nakada, S., Shimizu, H., and Ohta, K. (1999). Overview of the 1990-1995 Eruption at Unzen Volcano. *J. Volcanology Geothermal Res.* 89, 1–22. doi:10.1016/s0377-0273(98)00118-8

Ohminato, T., and Watanabe, A. (2020). Seismic and Infrasound Observation at Nishinoshima Island in 2019. *Ogasawara Res.* 46, 53–68. in Japanese with English abstract.

Omori, F. (1916). *The Sakura-jima Eruptions and Earthquakes III. Bulletin of the Imperial Earthquake Investigation Committee 8*, 181–321.

Ossaka, J. (1975). Activity of Nishinoshima Volcano and its Observation (2). *GSJ Chishitsu News* 246, 1–9. in Japanese.

Ossaka, J. (1991). *Eruptions of Submarine Volcanoes in the Sea Near Japan*. Tokyo: Tokai University Press, 279. in Japanese.

Ossaka, J., Ohira, Y., and Minato, I. (1974). On the Submarine Eruption of Nishinoshima (3). *Bull. Volcanol. Soc. Jap.* 19, 37–38. in Japanese.

Parfitt, E. A. (2004). A Discussion of the Mechanisms of Explosive Basaltic Eruptions. *J. Volcanology Geothermal Res.* 134, 77–107. doi:10.1016/j.jvolgeores.2004.01.002

Pioli, L., Erlund, E., Johnson, E., Cashman, K., Wallace, P., Rosi, M., et al. (2008). Explosive Dynamics of Violent Strombolian Eruptions: The Eruption of Parícutin Volcano 1943-1952 (Mexico). *Earth Planet. Sci. Lett.* 271, 359–368. doi:10.1016/j.epsl.2008.04.026

Polacci, M., Corsaro, R. A., and Andronico, D. (2006). Coupled Textural and Compositional Characterization of Basaltic Scoria: Insights into the Transition from Strombolian to Fire fountain Activity at Mount Etna, Italy. *Geol* 34, 201–204. doi:10.1130/G22318.1

Putirka, K. D. (2008). Thermometers and Barometers for Volcanic Systems. *Rev. Mineralogy Geochem.* 69, 61–120. doi:10.2138/rmg.2008.69.3

Pyle, D. M., and Elliott, J. R. (2006). Quantitative Morphology, Recent Evolution, and Future Activity of the Kameni Islands Volcano, Santorini, Greece. *Geosphere* 2, 253–268. doi:10.1130/GES00028.1

Pyle, D. M. (2013). "Sizes of Volcanic Eruptions," in *The Encyclopedia of Volcanoes*. Editor H. Sigurdsson, B. Houghton, S. R. McNutt, H. Rymer, and J. Stix Second Edition (London: Academic Press), 257–264.

Rowland, S. K., Jurado-Chichay, Z., Ernst, G., and Walker, G. P. L. (2009). "Pyroclastic Deposits and Lava Flows from the 1759-1774 Eruption of El Jorullo, Mexico: Aspects of 'violent Strombolian' Activity and Comparison with Paricutin," in *Studies in Volcanology: The Legacy of George Walker International Association of Volcanology and Chemistry of the Earth's Interior Special Publication 2*. Editor T. Thordarson, S. Self, G. Larsen, S. K. Rowland, and Á. Höskuldsson (London: Geological Society of London), 105–128.

Sano, T., Shirao, M., Tani, K., Tsutsumi, Y., Kiyokawa, S., and Fujii, T. (2016). Progressive Enrichment of Arc Magmas Caused by the Subduction of Seamounts under Nishinoshima Volcano, Izu-Bonin Arc, Japan. *J. Volcanology Geothermal Res.* 319, 52–65. doi:10.1016/j.jvolgeores.2016.03.004

Schneider, J.-L. (2000). "Volcaniclastic Sedimentation in Submarine Settings: Products and Processes," in *Volcaniclastic Rocks, from Magma to Sediments*. Editors H. Leyrit and C. Montenat (Amsterdam: Gordon & Breach Science Publishers), 175–192.

Shinohara, M., Ichihara, M., Sakai, S. i., Yamada, T., Takeo, M., Sugioka, H., et al. (2017). Continuous Seismic Monitoring of Nishinoshima Volcano, Izu-Ogasawara, by Using Long-Term Ocean Bottom Seismometers. *Earth Planets SpaceSpace* 69, 159. doi:10.1186/s40623-017-0747-7

Sides, I. R., Edmonds, M., Maclennan, J., Swanson, D. A., and Houghton, B. F. (2014). Eruption Style at Kīlauea Volcano in Hawai'i Linked to Primary Melt Composition. *Nat. Geosci* 7, 464–469. doi:10.1038/ngeo2140

Smellie, J. L., Wilch, T. I., and Rocchi, S. (2013). 'A'ā Lava-Fed Deltas: A New Reference Tool in Paleoenvironmental Studies. *Geology* 41, 403–406. doi:10.1130/g33631.1

Smith, P. M., and Asimow, P. D. (2005). Adiabat_1ph: A New Public Front-End to the MELTS, pMELTS, and pHMELTS Models. *Geochem. Geophys. Geosyst.* 6, Q02004. doi:10.1029/2004GC000816

Sparks, R. S. J. (1997). Causes and Consequences of Pressurisation in Lava Dome Eruptions. *Earth Planet. Sci. Lett.* 150, 177–189. doi:10.1016/s0012-821x(97)00109-x

Stix, J., Torres, R. C., Narváez M, L., Cortés J, G. P., Raigosa, J. A., Gómez M, D., et al. (1997). A Model of Vulcanian Eruptions at Galeras Volcano, Colombia. *J. Volcanology Geothermal Res.* 77, 285–303. doi:10.1016/s0377-0273(96)00100-x

Sutawidjaja, I. S. (2006). Pertumbuhan Gunung Api Anak Krakatau Setelah Letusan Katastrofis 1883. *J. Geol. Indonesian* 1, 143–153. doi:10.17014/ijog.vol1no3.20063

Suzuki, Y., Yasuda, A., Hokanishi, N., Kaneko, T., Nakada, S., and Fujii, T. (2013). Syneruptive Deep Magma Transfer and Shallow Magma Remobilization during the 2011 Eruption of Shinmoe-Dake, Japan-Constraints from Melt Inclusions and Phase Equilibria Experiments. *J. Volcanology Geothermal Res.* 257, 184–204. doi:10.1016/j.jvolgeores.2013.03.017

Tada, N., Ichihara, H., Nakano, M., Utsugi, M., Koyama, T., Kuwatani, T., et al. (2021). Magnetization Structure of Nishinoshima Volcano, Ogasawara Island Arc, Obtained from Magnetic Surveys Using an Unmanned Aerial Vehicle. *J. Volcanology Geothermal Res.* 419, 107349. doi:10.1016/j.jvolgeores.2021.107349

Taddeucci, J., Edmonds, M., Houghton, B., James, M. R., and Vergniolle, S. (2013). "Hawaiian and Strombolian Eruptions," in *The Encyclopedia of Volcanoes*. Editor H. Sigurdsson, B. Houghton, S. R. McNutt, H. Rymer, and J. Stix Second Edition (London: Academic Press), 485–503.

Takeo, M., Ohminato, T., Maeno, F., Shinohara, M., Baba, K., Watanabe, A., et al. (2018). Geophysical Observations and landing Survey at Nishinoshima Volcano. *J. Adv. Mar. Sci. Tech. Soc.* 24, 45–56. doi:10.14928/amstec.24.1_45 in Japanese with English abstract.

Tamura, Y., Ishizuka, O., Sato, T., and Nichols, A. R. L. (2018). Nishinoshima Volcano in the Ogasawara Arc: New Continent from the Ocean? *Isl. Arc* 28, e12285. doi:10.1111/iar.12285

Tanakadate, H. (1934). Evolution of a New Volcanic Islet Near Io-Zima (Satsuma Prov.). *Proc. Imp. Acad. Jpn.* 11, 152–154.

Thorarinsson, S., Einarsson, T., Sigvaldason, G., and Elisson, G. (1964). The Submarine Eruption off the Vestmann Islands 1963-64. *Bull. Volcanol.* 27, 435–445. doi:10.1007/bf02597544

Thordarson, T., and Sigmarsson, O. (2009). "Effusive Activity in the 1963–1967 Surtsey Eruption, Iceland: Flow Emplacement and Growth of Small Lava Shields," in *Studies in Volcanology: The Legacy of George Walker International Association of Volcanology and Chemistry of the Earth's Interior Special Publication 2*. Editor T. Thordarson, S. Self, G. Larsen, S. K. Rowland, and Á. Höskuldsson (London: Geological Society of London), 53–84.

Umino, S., and Nakano, S. (2007). *Geology of the Chichijima Retto District, Quadrangle Series, 1:50,000*. Tsukuba: Geological Survey of Japan, AIST, 71. in Japanese with English abstract.

Valentine, G. A., Krier, D. J., Perry, F. V., and Heiken, G. (2007). Eruptive and Geomorphic Processes at the Lathrop Wells Scoria Cone Volcano. *J. Volcanology Geothermal Res.* 161, 57–80. doi:10.1016/j.jvolgeores.2006.11.003

Valentine, G. A., Krier, D., Perry, F. V., and Heiken, G. (2005). Scoria Cone Construction Mechanisms, Lathrop Wells Volcano, Southern Nevada, USA. *Geology* 33, 629–632. doi:10.1130/g21459ar.1

Walker, G. P. L. (1971). Compound and Simple Lava Flows and Flood Basalts. *Bull. Volcanol.* 35, 579–590. doi:10.1007/BF0259682910.1007/bf02596829

Walker, G. P. L. (1991). Structure, and Origin by Injection of Lava under Surface Crust, of Tumuli, ?lava Rises?, ?lava-Rise Pits?, and ?lava-Inflation Clefts? in Hawaii. *Bull. Volcanol* 53, 546–558. doi:10.1007/bf00298155

Wilson, L., and Head, J. W. (1981). Ascent and Eruption of Basaltic Magma on the Earth and Moon. *J. Geophys. Res.* 86, 2971–3001. doi:10.1029/jb086ib04p02971

Xu, W., Ruch, J., and Jónsson, S. (2015). Birth of Two Volcanic Islands in the Southern Red Sea. *Nat. Commun.* 6, 7104. doi:10.1038/ncomms8104

Yanagisawa, H., Iino, H., Ando, S., Takagi, A., and Oikawa, T. (2020). Violent Strombolian Eruption from June to August 2020 of Nishinoshima Island, Ogasawara Islands, Japan. *Bull. Volcanol. Soc. Jap.* 65, 119–124. in Japanese. doi:10.18940/kazan.65.4_119

Yuasa, M., Murakami, E., Saito, E., and Watanabe, K. (1991). Submarine Topography of Seamounts on the Volcanic Front of the Izu-Ogasawara (Bonin) Arc. *Bull. Geol. Surv. Jpn.* 42, 703–743.

Yuasa, M., and Nohara, M. (1992). Petrographic and Geochemical Along-Arc Variations of Volcanic Rocks on the Volcanic Front of the Izu-Ogasawara (Bonin) Arc. *Bull. Geol. Surv. Jpn.* 43, 421–426.

Conflict of Interest: The authors declare that the research was conducted in the absence of any commercial or financial relationships that could be construed as a potential conflict of interest.

Publisher's Note: All claims expressed in this article are solely those of the authors and do not necessarily represent those of their affiliated organizations, or those of the publisher, the editors and the reviewers. Any product that may be evaluated in this article, or claim that may be made by its manufacturer, is not guaranteed or endorsed by the publisher.

Copyright © 2021 Maeno, Yasuda, Hokanishi, Kaneko, Tamura, Yoshimoto, Nakano, Takagi, Takeo and Nakada. This is an open-access article distributed under the terms of the Creative Commons Attribution License (CC BY). The use, distribution or reproduction in other forums is permitted, provided the original author(s) and the copyright owner(s) are credited and that the original publication in this journal is cited, in accordance with accepted academic practice. No use, distribution or reproduction is permitted which does not comply with these terms.

frontiers in Earth Science

ORIGINAL RESEARCH
published: 03 March 2022
doi: 10.3389/feart.2022.810790

The Submarine Boundaries of Mount Etna's Unstable Southeastern Flank

Morelia Urlaub[1], Jacob Geersen[2], Florian Petersen[2,3], Felix Gross[2,3], Alessandro Bonforte[4], Sebastian Krastel[2] and Heidrun Kopp[1,2]*

[1]GEOMAR Helmholtz Centre for Ocean Research Kiel, Kiel, Germany, [2]Institute of Geosciences, Christian-Albrechts-Universität zu Kiel, Kiel, Germany, [3]Center for Ocean and Society, Christian-Albrechts-Universität zu Kiel, Kiel, Germany, [4]Istituto Nazionale di Geofisica e Vulcanologia, Section of Catania—Osservatorio Etneo, Catania, Italy

Coastal and ocean island volcanoes are renowned for having unstable flanks. This can lead to flank deformation on a variety of temporal and spatial scales ranging from slow creep to catastrophic sector collapse. A large section of these unstable flanks is often below sea level, where information on the volcano-tectonic structure and ground deformation is limited. Consequently, kinematic models that attempt to explain measured ground deformation onshore associated with flank instability are poorly constrained in the offshore area. Here, we attempt to determine the locations and the morpho-tectonic structures of the boundaries of the submerged unstable southeastern flank of Mount Etna (Italy). The integration of new marine data (bathymetry, microbathymetry, offshore seismicity, reflection seismic lines) and published marine data (bathymetry, seafloor geodesy, reflection seismic lines) allows identifying the lineament north of Catania Canyon as the southern lateral boundary with a high level of confidence. The northern and the distal (seaward) boundaries are less clear because no microbathymetric or seafloor geodetic data are available. Hypotheses for their locations are presented. Geophysical imaging suggests that the offshore Timpe Fault System is a shallow second-order structure that likely results from extensional deformation within the moving flank. Evidence for active uplift and compression upslope of the amphitheater-shaped depression from seismic data along with subsidence of the onshore Giarre Wedge block observed in ground deformation data leads us to propose that this block is a rotational slump, which moves on top of the large-scale instability. The new shoreline-crossing structural assessment may now inform and improve kinematic models.

Keywords: volcano-tectonic structure, flank instability, flank collapse, onshore-offshore, reflection seismic, bathymetry, seafloor geodesy, strike slip fault

OPEN ACCESS

Edited by:
Luis E. Lara,
Servicio Nacional de Geología y Minería de Chile (SERNAGEOMIN), Chile

Reviewed by:
Paraskevi Nomikou,
National and Kapodistrian University of Athens, Greece
Raffaello Cioni,
University of Florence, Italy

****Correspondence:***
Morelia Urlaub
murlaub@geomar.de

Specialty section:
This article was submitted to Volcanology, a section of the journal Frontiers in Earth Science

Received: *07 November 2021*
Accepted: *04 February 2022*
Published: *03 March 2022*

Citation:
Urlaub M, Geersen J, Petersen F, Gross F, Bonforte A, Krastel S and Kopp H (2022) The Submarine Boundaries of Mount Etna's Unstable Southeastern Flank. Front. Earth Sci. 10:810790. doi: 10.3389/feart.2022.810790

1 INTRODUCTION

Most volcanoes form in tectonically active areas on top of deformed continental or oceanic basement. The generally complex structural and morphologic nature of the underlying basement influences the stress regime and thus their seismic and volcanic activity (Cayol et al., 2000; Dieterich et al., 2000). The growth of a volcano over long (geologic) times in turn, alters the regional geologic and tectonic framework which may lead to the generation and reactivation of new or existing fault zones (Walter and Schmincke, 2002). Some of these faults are limited to shallow depth within the volcanic edifice, or at the contact between the edifice and the underlying basement, while others extend to larger depth. The latter faults may provide links between the volcano-tectonic motion and the regional tectonic setting (Bonaccorso et al., 2013). The

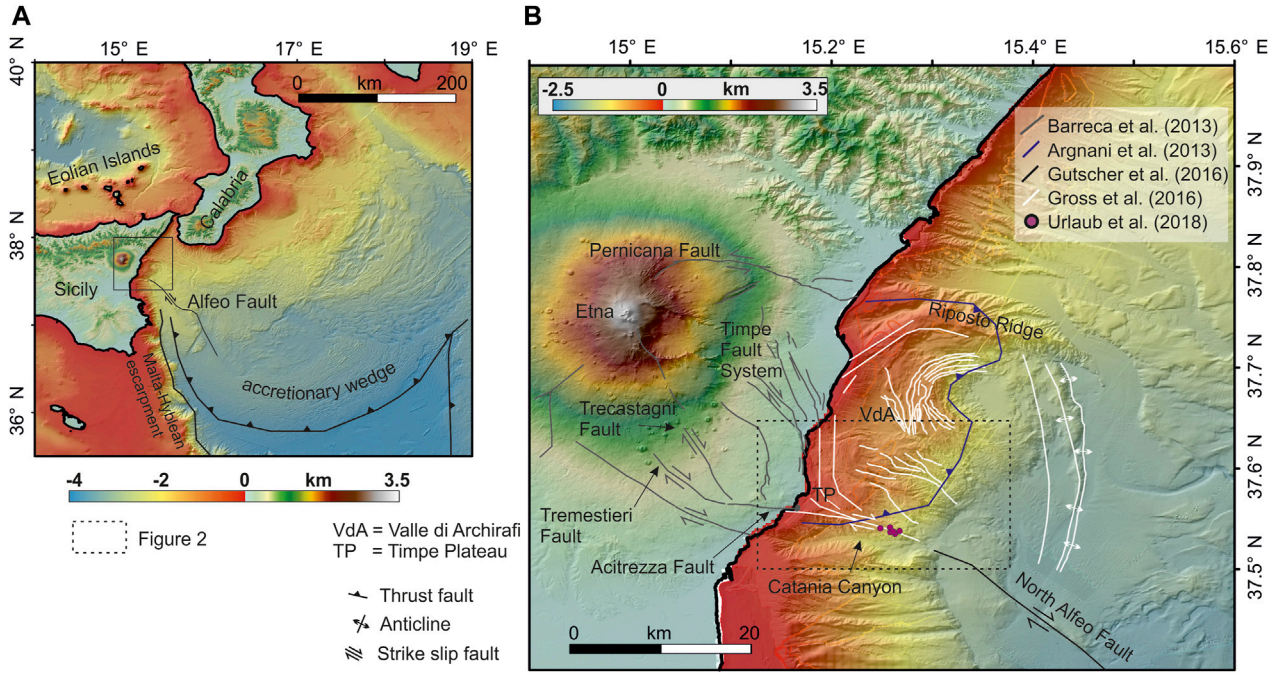


FIGURE 1 | Overview of the study area in South Italy. **(A)** Shaded relief map of the Western Ionian Sea with the Calabrian Arc subduction zone. Bathymetry is that of Gutscher et al. (2017). **(B)** Shaded relief map of the Mount Etna region. Onshore digital elevation data from the Shuttle Radar Topography Mission. Bathymetry from Chiocci et al. (2011). Main structures that are kinematically linked to flank instability are indicated following the respective publications. The grey dashed rectangle shows the focus area of newly acquired bathymetric and microbathymetric data.

complex intertwined relation between local and regional volcanic and tectonic processes can induce instability in the volcanic edifice (Chiocci et al., 2011), raising the potential for hazardous events triggered by flank collapses and their related aseismic (creep) and seismic (earthquake) motion, in addition to those hazards associated with volcanic activity.

Flank instability appears to be even more frequent on coastal and ocean island volcanoes than on fully subaerial ones (Alparone et al., 2013; Poland et al., 2017). This is likely due to the lithological (weak marine sediments) and morphological (seawards inclined) nature of the sedimentary basement that underlies the volcanic edifice and that favours the sliding of the edifice under its own weight. Gravitational flank sliding thus adds to the tectonic setting and to the magma dynamics beneath and inside the volcano (Alparone et al., 2011; Bonforte et al., 2013a; Poland et al., 2017). Yet, the presence of the sea dramatically increases the hazard related to flank instability. Slope failures and partial collapses of coastal and ocean island volcanoes can cause damaging tsunamis as the world recently witnessed when the volcano Anak Krakatau in the Sunda Strait (Indonesia) collapsed catastrophically on 22 December 2018. The resulting landslide caused a tsunami resulting in more than 400 fatalities (Walter et al., 2019). Also, huge intraplate volcanoes, such as Fogo, the Canary Islands, and Hawaii have collapsed in the geological history and pose an ocean-wide hazard (Paris, 2015; Ramalho et al., 2015).

Knowledge of the relationship between volcanic activity and tectonic deformation may put us in a position to recognise potential precursory signals of impending collapses. Kinematic models that seek to explain these relationships require certain boundary conditions, with the geometry of the faults that define the downward movement of an unstable flank, and that accommodate gravitational movement, being a main factor (Solaro et al., 2010; Bonforte et al., 2011; Azzaro et al., 2013). For the onshore part of the volcano edifice, this geometry is often well known from geological, seismic, and geodetic data. In those areas of the volcano edifice covered by water, the geometry of faults and their transient activity is generally poorly constrained. Yet, ocean island volcanoes grow from the bottom of the deep sea and often only a small fraction of the edifice is exposed. In the case of Kilauea (Hawaii), 85% of the volcano is under water. Also, for Mount Etna, which is growing at the edge of continental crust (**Figure 1**), a volumetrically large part of the mobile sector is submerged (Chiocci et al., 2011; Gross et al., 2016). This fact explains that kinematic models of flank deformation often predict the largest deformation to occur in the offshore sectors. For example, the area of maximum co-seismic slip related to the recent moment magnitude (Mw) 6.9 earthquakes at Kilauea in May 2018 was modeled at ~10 km off the coast (Liu et al., 2018). At Mount Etna, kinematic models of slow slip events (Mattia et al., 2015; Palano, 2016; Bruno et al., 2017) also predict maximum slip seawards of the coast, although the ground deformation pattern is different during periods of strong magmatic inflation (Acocella et al., 2003; Neri et al., 2004; Solaro et al., 2010). It is obvious that the submerged flanks of coastal and ocean island volcanoes play important roles in accommodating volcano-tectonic deformation and

gravitational flank movement. Yet, these offshore flanks usually represent the least explored and understood parts of a volcano.

To understand flank collapse hazard at volcanoes whose edifices are, to a large extent, covered by water, the offshore geometry and kinematics of the unstable sector needs to be rigorously understood. This knowledge can then lend constraints to kinematic models that seek to explain observed ground deformation but lack information on the offshore extent, architecture, and geometry of the moving flank. Worldwide, there are only few volcanoes for which the offshore volcano-tectonic structure, deformation, and dynamics are well studied. Kilauea is one example, where this knowledge is available and, indeed, revealed crucial to the understanding of the volcano's overall stability. With seismic, bathymetric, and seafloor geodetic data it was possible to identify a mobile, shallow slump (Hilina Slump) that is riding atop Kilauea's seawards sliding south flank (Morgan et al., 2003; Phillips et al., 2008). Only with this information, it was possible to confirm the origin and underlying processes of the onshore extensional headwall domain (Hilina Fault System).

Here, we focus on the submerged boundaries of the unstable sector of Mount Etna. We present new bathymetric and microbathymetric maps from the continental bulge and the transition to the Ionian basin, as well as new offshore seismicity data from an Ocean Bottom Seismometer network installed from April 2016 to February 2017, and as yet unpublished seismic reflection lines. These new data, in combination with marine geological, geodetic, and geophysical data published in recent years allow us to determine the location of the southern boundary, as well as to discuss the yet widely unexplored northern and seaward boundaries of the unstable flank. We further identify the main uncertainties and key questions that remain unanswered concerning the geometry of Mount Etna's unstable sector, and propose pathways to overcome these.

2 MOUNT ETNA: REGIONAL TECTONIC SETTING AND FLANK INSTABILITY

Mount Etna is a basaltic stratovolcano on the East coast of Sicily, Italy (**Figure 1**). The volcano is located at the edge of the subducting Ionian slab of the Calabrian subduction zone (Gvirtzmann and Nur, 1999a). The crustal deformation rates related to plate convergence in eastern Sicily vary around 3–6 mm/yr (Ventura et al., 2014). A key tectonic element in the larger region is the Subduction Tear Edge Propagator (STEP) fault, which is hypothesised to continue underneath Mount Etna. Possible candidates for the shallow expression of this STEP fault are the Malta Escarpment (Neri et al., 2018, and references therein) or the Alfeo fault system in the Ionian Sea (**Figure 1A**). The Malta Escarpment is a prominent morphological feature offshore eastern Sicily that separates the continental hyblean crust from the oceanic crust of the Ionian Basin (Lanzafame et al., 1996; Neri et al., 2018, and references therein). The Alfeo fault system consists of the normal South Alfeo fault off Southern Sicily and the right-lateral North Alfeo fault off Central and Northern Sicily (Gutscher et al., 2016). It has been suggested that the North Alfeo fault continues underneath Mount Etna (Barreca et al., 2013; Gutscher et al., 2016).

Mount Etna has a prominent morphology resulting from a rapid and complex growth of the volcanic edifice. The summit is 3,350 m above sea level. The volcanic pile is about 2 km thick (Branca and Ferrara, 2013) and grows on the continental margin that dips seawards. The volcano's eastern flank reaches well into the Ionian Sea to ~1,500 m below sea level (**Figure 1B**). The sedimentary basement underneath Mount Etna consists of early Quaternary clays bounded to the north and to the west by flysch units of the Apennine–Maghrebian Chain (Branca et al., 2011). The basement gently dips in SE direction thereby promoting lateral spreading and flank instability of Mount Etna's southeastern sector (Branca and Ferrara, 2013). The deformation of the eastern flank is quite different and often independent of that affecting the northern and western parts of the volcano, showing a different stress state, acting at least on the volcanic pile and the uppermost part of the sedimentary basement, as revealed by geodetic and seismic data (Alparone et al., 2011). Onshore geodetic measurements document large-scale continuous seaward motion of the SE flank at an average rate of 3–5 cm per year since the early 1980s (Patanè et al., 2003; Bonforte and Puglisi, 2006; Solaro et al., 2010). Seawards slip occurs as continuous motion spiked by episodic acceleration that often links to rift zone activity and dike intrusions (Bonforte et al., 2013b; Palano, 2016; Bruno et al., 2017). During rest phases, when the edifice is not affected by magmatic inflation that mainly deforms the central part of the volcano, displacement rates on the southeastern slope generally increase towards the coast and into the Ionian Sea (Bonforte and Puglisi, 2006; De Guidi et al., 2018; Urlaub et al., 2018). Even during deflation phases, characterized by centripetal deformation, the southeasternmost part of the volcano moves eastward (Bonforte et al., 2008). This pattern suggests that the present deformation is driven by gravitational instability, being further promoted by magma dynamics.

The morphologically prominent and seismically active Timpe Fault System, with its NNW-SSE orientation, crosses the eastern slope of Mount Etna for a length of about 30 km (**Figure 1B**). The individual segments of the Timpe Fault System show oblique normal and dextral motion, thus accommodating WNW-ESE oriented extension mostly through shallow (<5 km in depth) earthquakes of moderate magnitudes (Mw < 5) (Alparone et al., 2015). There are contrasting views regarding the origin of the Timpe Fault System. This fault system has been considered one of the northernmost segments of the NNW-SSE oriented Malta Escarpment. Barreca et al. (2018) suggest connection of the Timpe Fault System to the offshore North Alfeo fault. These hypotheses contrast the observation that the hanging wall and the footwall of the Timpe fault system move along with the SE flank, suggesting that the Timpe System is dragged seawards with the mobile flank and then should be confined above the detachment surface of the unstable flank and thus a shallow, second order system (Bonforte and Puglisi, 2006).

2.1 Onshore Boundaries and Volcano-Tectonic Structures

On land, the outline of the unstable flank is well determined by geodetic, geophysical, and geological methods. Along the northern boundary of the unstable flank, deformation focuses

along the transtensive left-lateral Pernicana fault system with average slip rates of 2–3 cm/yr (Neri et al., 2004; Bonforte et al., 2007; Azzaro et al., 2013). The Pernicana fault extends from the NE Rift downslope to the coast (**Figure 1B**). While the western sections of the fault system are seismically very active, its eastern part is almost completely devoid of shallow seismicity (Groppelli and Tibaldi, 1999; Alparone et al., 2013, 2015). The sharp morphologic expression of the Pernicana fault vanishes close to the Ionian coast, where there is a culmination of the sedimentary basement (Bonforte et al., 2007). Here, deformation related to instability of Mount Etna's eastern flank is diffuse and solely expressed as creep along multiple en échelon left-lateral faults (Azzaro et al., 2013).

Extending from the South Rift, the Trecastagni-Tremestieri fault system represents the modern southern boundary of the unstable sector (Bonforte et al., 2013a). The NNW-SSE trending faults appear as pronounced morphological scarps. The faults accommodate normal and right-lateral movements through continuous creep with episodic accelerations accompanied with shallow seismicity (Acocella et al., 2003; Gambino et al., 2011; Bonforte et al., 2013b; De Novellis et al., 2019). Towards the coast, the faults join into one and the southern boundary continues to the coast along the NNW-SSE San Gregorio and then along the WNW-ESE Acitrezza fault systems (Bonforte et al., 2011). These are mostly hidden faults without morphological expressions at the surface affected by continuous creep.

2.2 Offshore Boundaries: A Review of Current Understanding and Uncertainties

The large-scale morphology of the continental margin offshore of Mount Etna is characterized by an east oriented convex bulge that hosts slope gradients of up to 25° (**Figure 1B**). The continental slope reaches down to ~1800 m water depth about 20 km off the coast. A morphological step marked by a sudden decrease in slope angle represents the transition into the Ionian Sea basin. The central realm of the continental bulge is described by the Valle di Archirafi bounded by a structural high, both of which are affected by normal faulting (Gross et al., 2016). A prominent morphological feature offshore Mount Etna is the semi-circular amphitheatre enclosing a local depression. Chiocci et al. (2011) propose that the amphitheater is the result of a large submarine landslide.

The Acitrezza fault marking the southern boundary of the onshore unstable sector in the coastal area continues across the shoreline as a WNW-ESE trending morphological feature at the seafloor (Chiocci et al., 2011; Gross et al., 2016). At about 400 m water depth the offshore continuation of the Acitrezza fault appears to merge with a series of NNW-SSE trending escarpments at the seafloor that bend into the WNW-ESE orientation. It has been suggested that the NNW-SSE trending seafloor escarpments represent the surface expression of the southwards prolongation of the Timpe Fault System (Barreca et al., 2018). Further seawards of where the seafloor escarpments merge into a single fault system, a 30 km long WNW-ESE topographic high on the northern limb of Catania Canyon termed lineament (Chiocci et al., 2011) is visible (**Figure 1B**). Seafloor geodetic measurements conducted between 2016–2017 confirm the lineament as an active right-lateral fault that had experienced at least 4 cm of slip released during a recent slow slip event (Urlaub et al., 2018). The fault slip rate measured in this single location matches the cumulative slip of the linked onshore faults related to flank instability. Hence, the lineament likely represents a section of the southern offshore boundary of the mobile sector (Gross et al., 2016; Urlaub et al., 2018). Some authors hypothesise that this fault at the northern limb of Catania Canyon is the shallow branch of the North Alfeo fault, which would argue for a crustal origin (Gutscher et al., 2017; Barreca et al., 2018). From seismic data there is, however, no indication that the lineament connects to crustal faults, which would suggest that this lateral boundary of the moving flank is not genetically linked to crustal tectonics (Argnani and Bonazzi, 2005; Argnani et al., 2013).

In the north, the transition of the Pernicana fault into the offshore is less obvious. Isolated small NNE–SSW trending seafloor scarps in the shallow offshore realm indicate active deformation (Argnani et al., 2013). Further downslope, the NW-SE trending Riposto Ridge, probably a remnant of Apennine–Maghrebian Chain units, forms a morphological boundary (Chiocci et al., 2011; Gross et al., 2016). There is no evidence for extensive and localized active faulting in the shallow subsurface in seismic data (Argnani et al., 2013; Gross et al., 2016). This stands in contrast to many kinematic models based on onshore ground deformation data that predict largest flank slip within the northern submerged sector of the flank (e.g., Palano, 2016; Bruno et al., 2017; Mattia et al., 2015).

Different hypotheses compete with respect to the location of the distal (seaward) boundary of the unstable volcano pile, mainly based on seismic data of different resolution. Argnani et al. (2013) suggest the offshore bulge is bounded by a thrust fault encircling the offshore bulge (**Figure 1B**), which is related to the intrusion of the magmatic body. Gross et al. (2016) described two anticlines several kilometres seawards of the thrust fault interpreted by Argnani et al. (2013) in seismic reflection data (**Figure 1B**). The authors suggest that compression caused by downwards flank movement forms the anticlines, which thus mark the seaward foot of the volcanic sector.

3 SUMMARY OF DATA SETS AND OBSERVATIONS

In the following, we analyse new bathymetric and microbathymetric maps from the southern part of the offshore flank, unpublished reflection seismic lines as well as 1 year of offshore seismicity recorded by an Ocean Bottom Seismometer network. Previously published marine data complement the new data. We summarise the key implications from each dataset with respect to Etna's flank dynamics and in the context of existing literature.

3.1 Ship-Based Bathymetry

A Multibeam Echo Sounder (MBES) sends acoustic signals in form of a fan, which are reflected/scattered at the seafloor. In addition to the traveltime, which is transferred into water depth, the system also records the strength of the reflected/scattered signal (backscatter). Through emitting a swath of several

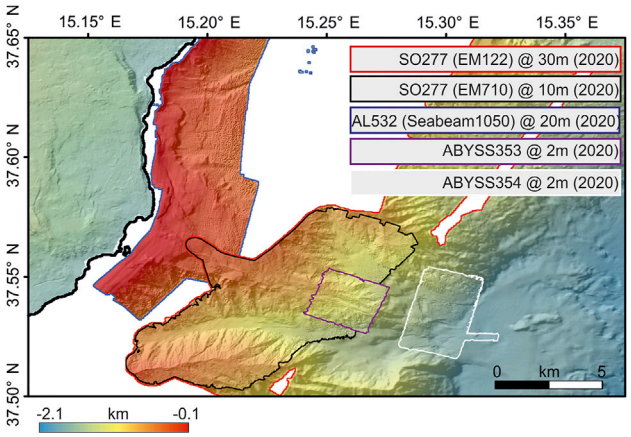


FIGURE 2 | Newly acquired bathymetric data sets presented in this study for the first time. The location is shown in **Figure 1B**.

hundreds of beams at each side, MBES attached to the hull of a ship covers a strip of the seafloor up to six times the water depth wide. The vertical and lateral resolution is primarily dependent on the water depth. The new MBES data off Etna, which were collected in 2020 have a vertical resolution of <10 m and the grid spacing of the bathymetric maps is ≤30 m (**Figure 2**). It includes data from 2020 RV SONNE cruise SO277 (Berndt et al., 2021) and 2020 RV ALKOR cruise AL532 (Urlaub et al., 2020). During SO277, MBES data were acquired with hull-mounted Kongsberg EM122 and EM710 systems. For these data sets, we also show the backscatter intensities (**Figure 3C**). During AL532, bathymetric data were collected in shallow water (<600 m) with an ELAC Seabeam 1050 MBES system installed in the vessel's moonpool. Derivatives of the bathymetry, such as slope gradient (**Figure 3A**) and aspect (**Figure 3B**) help to interpret seafloor morphologies (**Figure 3D**). The new hydroacoustic data are here combined with published data from Chiocci et al. (2011), Gross et al. (2016), and Gutscher et al. (2017) (**Figure 3**).

The combined bathymetric data reveal a suite of seabed morphologies, sedimentary structures and bedforms predominantly related to gravitational sediment transport. We identify canyons, gullies, landslide scars, sediment ponds, and sediment waves (**Figure 3**). Catania Canyon in the south of the study area is just one of several larger canyons, not all of which directly relate to onshore rivers. The major canyon systems dip straight into the Ionian Basin without forming significant meanders. Landslide scars occur along steep canyon walls (e.g., at the south limb of Catania Canyon) and at the foot of the

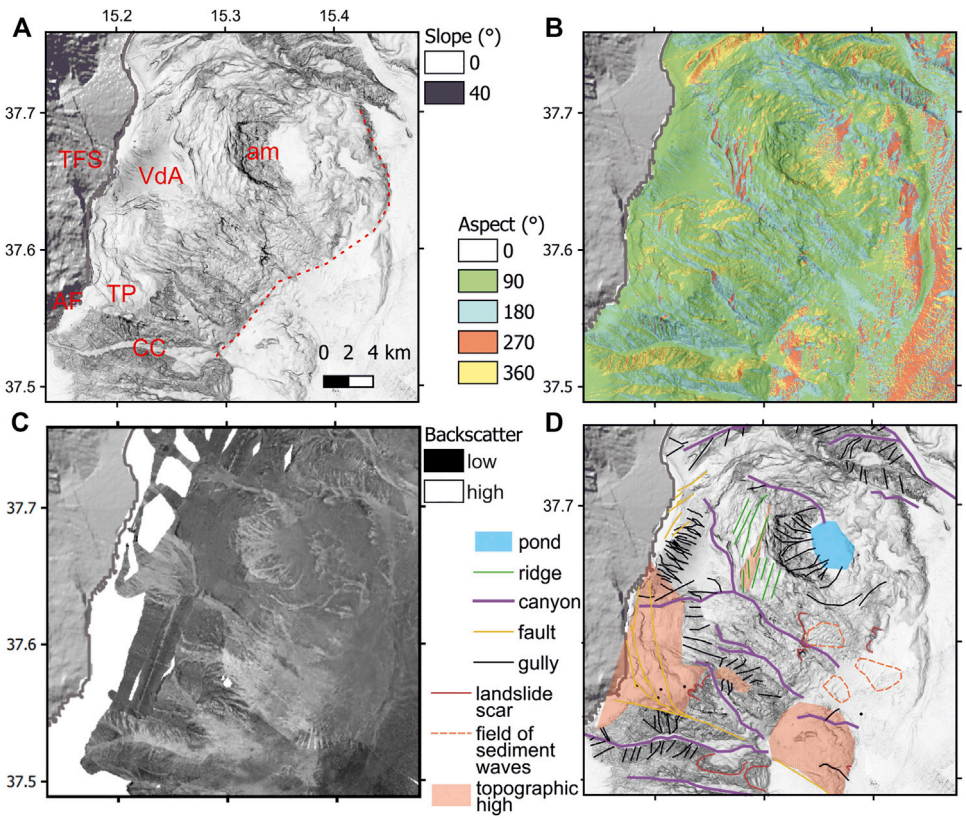


FIGURE 3 | Products and derivatives of the new integrated bathymetric data: **(A)** slope gradient, **(B)** aspect, **(C)** backscatter, **(D)** morphological interpretation. CC, Catania Canyon, TFS, Timpe Fault System, VdA, Valle di Archirafi, TP, Timpe Plateau, AF, Acitrezza fault, am, amphitheatre. The dashed red line marks the seawards edge of the continental bulge, i.e. the transition from the continental slope to the Ionian Basin.

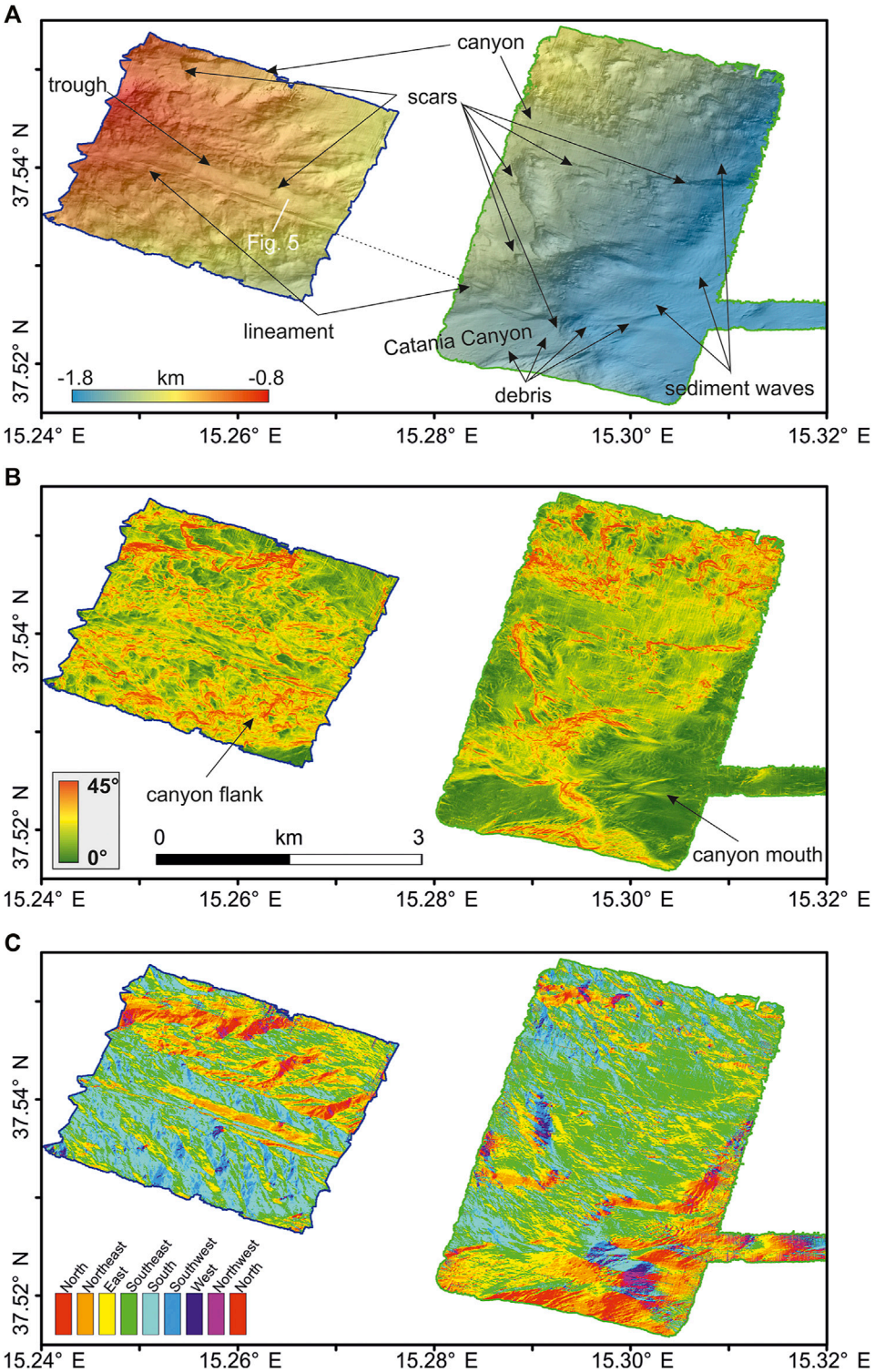


FIGURE 4 | (A) Depth, **(B)** slope, and **(C)** aspect (downhill direction) maps of the multibeam bathymetry data collected with an AUV. See **Figure 2** for location of the maps. Black line in a) marks the prominent surface expression of the offshore extent of the Acitrezza fault.

continental bulge. Numerous smaller scars, partly at the limit of the resolution of the data, cluster in areas of low backscatter (**Figure 3C**) indicating the presence of softer sediments. There are two fields of sediment waves at the seawards edge of the continental bulge, and thus on nearly flat seafloor. A third area of sediment waves is observed upslope, in another area of

low backscatter. Creep of shallow soft sediments is probably forming these waves (Pope et al., 2018).

From analyses of local relief, aspect, and location of gullies (**Figure 3D**), we identify several topographic highs. The Timpe Plateau, described previously by Gross et al. (2016) and Carlino et al. (2019), constitutes the south westernmost topographic high. It is cross-cut by several NW-SE trending escarpments, offsetting the seafloor downwards and in ENE direction in a stepwise fashion. East of the Timpe Plateau a smaller and isolated topographic high is visible surrounded by deeply-cutting gullies. These are signs of long-term erosion, suggesting the topographic feature to be rather old. Within the center of Valle di Archirafi a subtle topographic high dipping landwards deviates the canyon systems to its sides. To the northeast, an elongated topographic high marks the uppermost of a series of coast-parallel elongated features, which we term ridges. The aspect map (**Figure 3B**) depicts the two-sided ridge-shape structure as facing land- and seawards. In contrast to these topographic highs on the upper continental slope, another almost circular topographic high is visible at the foot of the continental bulge in the southeast of the study area. The structure also has a circular shape as highlighted in the aspect map (**Figure 3B**). While its eastern side inclines seawards, its western side inclines landwards. This may be indicative of active uplift in the centre of this structure.

The bathymetric data also show the surficial expression of several faults, which usually show up as linear trending escarpments at the seafloor. In the northern study area, several short seafloor offsets provide a stair step morphology dipping towards the SE (**Figure 3A**). As in the coastal area onshore, no prominent seafloor expression of a northern boundary fault is visible. In the south, the fault that constitutes the seaward extension of the onshore Acitrezza fault has a positive seafloor relief and extends in WNW-ESE direction (**Figure 3A**). North of it, the seafloor shows several parallel NNW-SSE trending escarpments that offset the seafloor downwards towards the ENE in a stepwise fashion. These escarpments continue across the shore and connect to the faults of the onshore Timpe Fault System (**Figure 3A**). Seawards, they appear to bend to an E-W direction before merging with the offshore Acitrezza fault coming from the West. The result of this merging is a prominent feature termed lineament and previously interpreted as the southern boundary of the unstable sector (Chiocci et al., 2011; Gross et al., 2016; Urlaub et al., 2018). The lineament at the northern wall of Catania Canyon continues in distal direction but vanishes at the toe of the continental bulge. About 1 km farther eastwards, the northernmost seafloor expression of the North Alfeo fault appears.

3.2 Microbathymetry

Resolution of shipborne bathymetric surveys is limited, especially in deep water, due to the strong attenuation of high-frequency sound waves and the lateral distance between neighbouring beams. Bathymetric grids in large water depths based on shipborne bathymetric surveys therefore usually have a lateral resolution in the range of several 10 s of meters. One option for increasing lateral resolution is to reduce the distance between the MBES and the seafloor. This approach allows to use higher frequencies while reducing the distance between neighbouring beams at the seafloor. Autonomous Underwater Vehicles (AUVs) are unmanned untethered vehicles that operate fully independent along a pre-programed track and that are capable of carrying multibeam echosounders. In January 2020, during expedition AL532 with RV ALKOR, the deep-water AUV ABYSS performed two dives carrying a Reson SeaBat T50 multibeam echosounder 80 m above the seafloor. The acquired data provide two new microbathymetric maps, each covering an area about 2.5 × 2.5 km of the seafloor with a grid spacing of 2 m (**Figure 4**). See Urlaub et al. (2020) for details on survey design and processing routines.

Both maps image the seafloor across the lineament, i.e. the offshore continuation of the Acitrezza fault. The more proximal located map covers the area of the seafloor geodetic experiment, which recorded right-lateral faulting during a slow slip event in May 2017 (Urlaub et al., 2018). The other map, further downslope, covers the toe of the continental bulge and its transition to the less steep Ionian Basin. Although only 3 km apart, the two maps show very different morphologic expressions of what, from the shipborne bathymetric data, is interpreted as a single fault.

The seafloor in the upslope site is steep and rugged. The area is inclined in ESE direction with average slope gradients between 10–20° following the large-scale configuration of the continental margin. This overall trend is superimposed by multiple linear W-E trending structures. Along the southern margin of the map, a steep (30–40°) southwards facing slope marks the northern flank of the Catania Canyon. Along the northern edge of the canyon, a larger scale topographic high subdivides into two WNW-ESE trending ridges separated by an approximately 100 m wide trough that is 20–60 m deep. The southern ridge morphology is peculiar striking, and presents an almost razor-sharp, about 10 m wide, structure that elevates about 5 m from the surrounding seafloor (**Figure 4**). We interpret this as the surface expression of the active strike-slip fault that ruptured during the May 2017 slow-slip event.

The more distally located microbathymetric map covers the transition from the continental bulge into the Ionian Basin, including the mouth of Catania Canyon. The seafloor inclination is on average about 13° on the continental slope and <5° in the basin on the SE part of the map. Overall, the seafloor morphology in this map is much smoother than farther upslope and dominated by sedimentary features like canyons, landslide scars, canyon debris, and sediment waves. In the southwestern corner of the map a NW–SE oriented elongated positive relief is visible that disappears in the canyon mouth. It matches the downslope continuation of the active strike slip fault observed farther upslope indicating a similar genetic origin. There is no seafloor expression of this fault within the mouth of Catania Canyon as well as farther towards the east. This might be due to active sediments transport through the canyon leading to either deposition of these sediments at the mouth of the canyon, or thalweg erosion, which would both mask the imprint of recent fault activity. Alternatively, the distal part of the fault may not

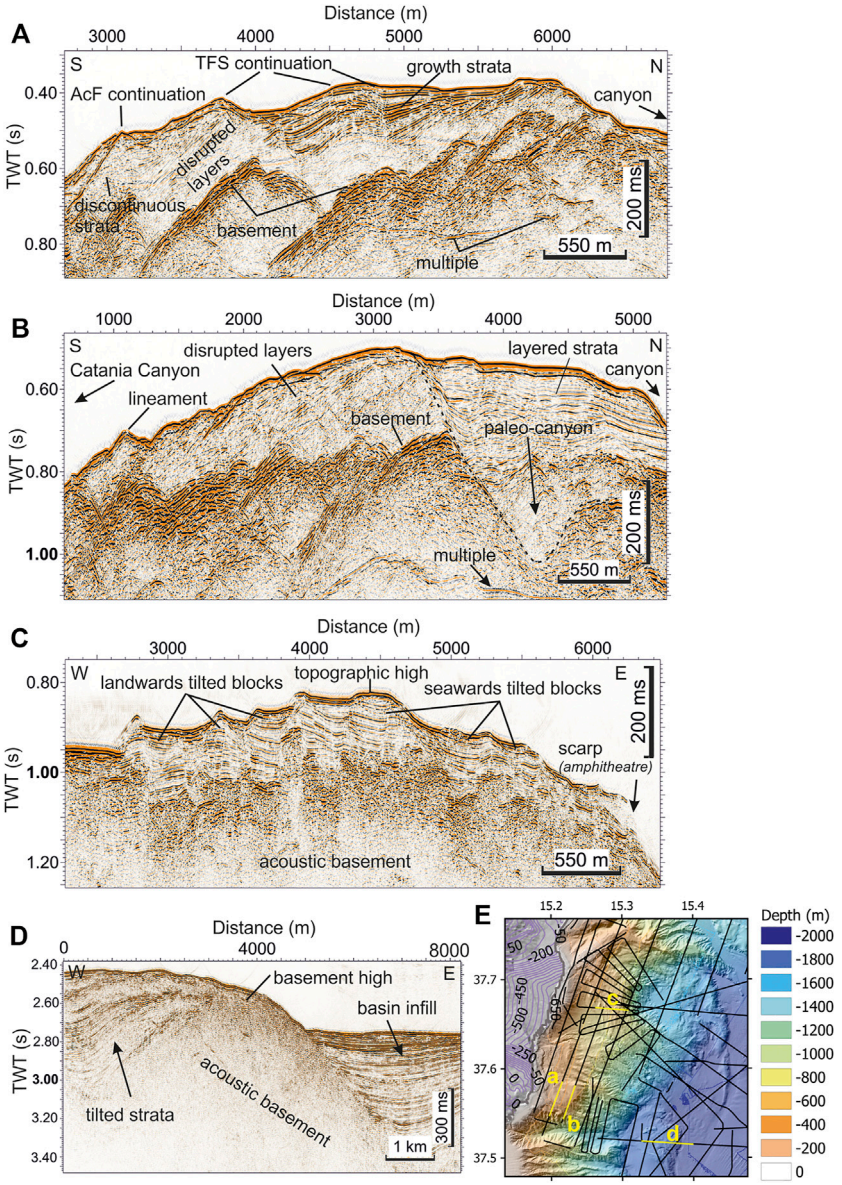


FIGURE 5 | Reflection seismic profiles across **(A,B)** the southern boundary fault, **(C)** the area of ridges and elongated local topographic high, and **(D)** the topographic high at the edge of the continental bulge. Locations are shown in e.

have been active recently. Constraints on the interplay of sedimentary processes linked to Catania Canyon and tectonic processes related to Etna's moving flank are hampered by the limited information that is available regarding the activity of Catania Canyon. While the imprint of debris in the canyon floor suggests a certain degree of canyon activity there is no major river system that connects to the head of the canyon and that could provide sediment input. A steep scar and drop in relief from 1700 to 1790 m water depth in the entire canyon thalweg could be the result of erosion by mass movements or bottom currents. With the available data it is thus not possible to resolve the exact location, offshore extent, and activity of the distal most section of the southern boundary fault of Etnas unstable flank.

3.3 Seismic Reflection Profiles

While bathymetric data provide information on surface morphologies, seismic reflection surveys image the structure of the subsurface. Seismic resolution and penetration depths are primarily controlled by the frequency of the emitted signal and the physical nature of the subsurface. Due to strong attenuation of high-frequency signals, it is difficult to achieve high resolution and deep penetration at the same time. Here, we analyse seismic reflection data yielding a vertical resolution of ~10 m. Subsurface penetration along the submerged flank of Mount Etna strongly depends on the nature of the subsurface and varies between some tens of meters (on the volcanic pile) and up to 1 km (in sedimentary basins). These data are thus particularly well-suited to image shallow sedimentary strata.

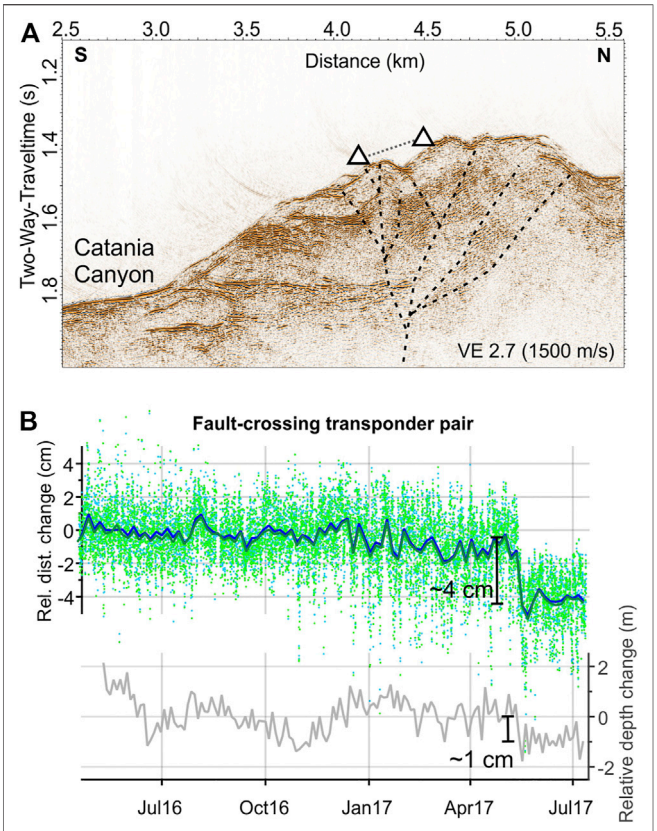


FIGURE 6 | Results from the seafloor geodetic experiment (see **Figure 1B** for location). **(A)** Seismic profile in the area of the seafloor geodetic network, crossing the southern boundary fault. Triangles mark the approximate location of transponders, which are projected onto the profile. **(B)** Time series of relative distance changes and relative depth changes between two transponders that are located on different sides of the boundary fault after Urlaub et al. (2018). Absolute distance between transponders is 840 m. Dots show actual measurements and continuous lines show distance changes averaged over 5 days.

We show unpublished seismic reflection lines (**Figure 5**) from two surveys conducted in 2012 during expedition M86/2 with RV METEOR (Krastel and Cruise, 2012) and in 2016 during expedition POS496 with RV POSEIDON (Krastel, 2016). During the 2012 survey, a Geometrics GeoEel digital streamer including 104 channels and a total length of 162.5 m was used for recording of seismic signals. The source was a 2 × 1.7 L GI gun. For the 2016 survey the seismic source was a Mini GI air gun (2 × 0.2 L) and the receiver a Geometrics GeoEel digital streamer with 80 channels and a total length of 125 m. Standard processing routines were applied with details described in Gross et al. (2016) and Schulze (2017).

Two margin-parallel seismic lines image the offshore continuation of the Acitrezza and Timpe faults, at distances of 3.5 km (**Figure 5A**) and 5 km (**Figure 5B**) off the coast (locations shown in **Figure 5E**). The deepest recognisable unit in both profiles is of high amplitudes with an undulating surface. This unit likely corresponds to the pre-Etnean clay basement as also suggested by Barreca et al. (2018). The overall depth of the inferred basement is consistent with the seaward extrapolation of onshore basement depth shown in **Figure 5E**. The pre-Etnean clay units are overlain by mainly chaotic as well as layered units. While the chaotic strata may correspond to volcanic deposits, the layered reflections are usually interpreted as continental slope sediments (Gross et al., 2016). The latter become progressively more disrupted and offset from N to S, indicating recent and shallow tectonic deformation.

The proximal seismic line (**Figure 5A**) images the offshore continuation of the Acitrezza fault as a vertical divide between shallow discontinuous strata to the S from layered (but disrupted) strata to the N. This may result from significant juxtaposition of geologic units across the strike-slip fault. The seismic data do not resolve whether the fault is limited to shallow depths or if it also affects the underlying stable basement. Farther towards the north, the seismic line reveals the curved seafloor escarpments observed in the bathymetry (**Figure 3D**) that appear to connect the onshore Timpe Fault System with the offshore continuation of the Acitrezza fault. Here, the seafloor escarpments are the surface expression of seaward dipping normal faults, with growth strata in the hanging-wall indicating syn-sedimentary and likely recent extensional deformation. It is possible to trace reflector packages across the faults, suggesting no or little offset by strike slip motion. Again, no significant offsets of the undulated basement are visible. Nevertheless, this may also be an effect of the poor imaging of the basement strata.

About 2 km farther downslope (**Figure 5B**) of the seismic line shown in **Figure 5A**, the surface expressions of the different fault systems have merged into one structure which corresponds to the W-E trending lineament observed at the seafloor (**Figure 5B**, Chiocci et al., 2011; Gross et al., 2016). Here, the lineament is underlain by a local basement high. To the north, disrupted sedimentary layers, likely of volcanic and volcanoclastic origin, cover the undulating basement. In the central part of **Figure 5B** the subsurface strata, including the basement, are cut by a v-shaped paleo-depression filled with continuous and layered strata, partly of undulating nature. We interpret the v-shaped structure as a paleo-canyon that is filled with sedimentary strata that has experienced little or no deformation.

The seismic line shown in **Figure 5C** trends perpendicular to the coast across the continental slope upslope of the amphitheater. Layered continental slope sediments that separate into individual blocks bounded by steeply inclined extensional faults characterize the shallow sub-surface (**Figure 5C**). Tilt of the individual blocks in landward (at the western part of the seismic line) and seaward (eastern part) direction results in the peculiar seafloor morphology of coast-parallel trending ridges (**Figure 3**) that were also observed by Gross et al. (2016). The slope sediments are underlain by a chaotic acoustic basement that may correspond to volcanic and volcanoclastic material. We interpret the shallow extensional deformation of the slope sediments, including the transition from primarily landward dipping faults in upslope direction to primarily seaward dipping faults farther downslope, as the result of localized margin parallel uplift of the continental slope.

The most distal seismic line (**Figure 5D**) images the Ionian Basin just seaward of the mouth of Catania Canyon in W-E

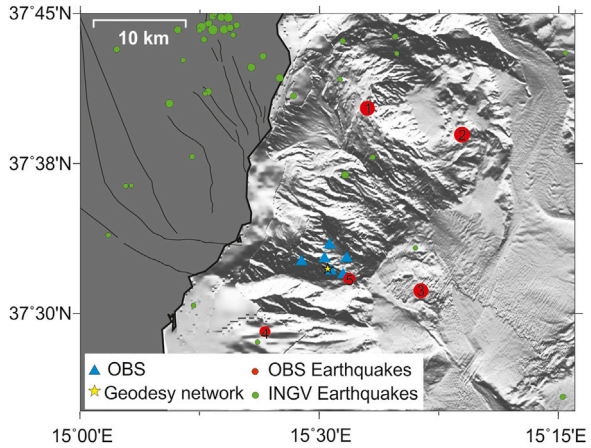


FIGURE 7 | Seismicity on Mount Etna's submarine southeastern flank between April 2016 and February 2017, during which an Ocean Bottom Seismometer array consisting of six instruments (blue triangles) was installed. See **Table 1** for details on the events detected by the OBS array.

direction. Along the central part of the line, the acoustic basement crops out at the seafloor (**Figure 5D**). It separates folded and deformed sedimentary strata to the west from layered and largely undeformed sedimentary strata to the east. On the western side of the line, the dip of the sedimentary layers increases with depth, indicating syn-sedimentary deformation. Although the genetic origin of the acoustic basement in the central part of the line remains unresolved, it seems to mark the transition of compressional deformation at the margin of Mount Etna into the Ionian Basin.

3.4 Seafloor Geodesy

The above data sets all show compelling evidence for long-term deformation across the southern boundary of Mount Etna's moving flank. There is also evidence for active (short-term) movement along this boundary from a seafloor geodetic experiment (Urlaub et al., 2018). Relative seafloor motion across the boundary fault was recorded from April 2016 until January 2018 within the area covered by the proximal microbathymetric AUV map (**Figure 4**) between 800–1,100 m water depth (**Figure 6A**). The direct-path acoustic ranging method provided continuous distance measurements between five transponders at the seafloor in an array configuration. The measurements allowed reconstructing relative seafloor displacement within the array in the respective observation period at sub-centimetre precision (Petersen et al., 2019).

The seafloor network revealed a significant distance change between fault-crossing transponder pairs in May 2017 (**Figure 6B**). Vertical motion makes up only a minor part of these distance changes. Combining the network information, up to 4 cm of right-lateral fault slip was released across the well-defined lineament (**Figure 4**) in a slow-slip event lasting 8 days (Urlaub et al., 2018). This is a minimum estimate of fault slip because activity of other fault branches not covered by the array cannot be excluded. In the same observation period, onshore faults kinematically related to flank instability also accumulated ~4 cm of right-lateral fault slip, providing confidence in the cross-shoreline continuation of these fault systems.

3.5 Offshore Seismicity

In April 2016, six short-period ocean-bottom seismometers (OBS) were deployed around the seafloor geodetic network at the southeastern flank of Mount Etna. Five OBS recorded continuously until their recovery in February 2017 while one instrument ceased to record after 2 months. Each OBS was equipped with a three-component short-period geophone of 4.5 Hz corner frequency and a HiTech Inc. hydrophone. We used an STA/LTA trigger to detect seismic events in the continuous waveforms. After applying a 3–15 Hz bandpass filter to the waveforms, we manually picked the onsets of P and S phase arrivals. The data processing, phase picking and database management were accomplished using the software SEISAN of Havskov and Ottemoeller (1999). Subsequently, we estimated absolute event locations based on a local 1D velocity model, which was extracted from an adjacent 2D refraction seismic profile (Dannowski et al., 2019) using the non-linear oct-tree search algorithm NonLinLoc (Lomax et al., 2000). We located five local earthquakes with phase arrivals on all recording OBS (**Figure 7**; **Table 1**). These events had not been detected by the permanent onshore network maintained by the local Etna Observatory and have not yet been published.

All detected earthquakes occurred outside of the OBS network (GAP >180°) and have not been resolved by the onshore network. The calculated moment magnitudes range from $1.2 < Mw < 2.7$. Four events occurred in depths >35 km and are therefore not associated to Etna's flank. The location of the single shallow event coincides with the seawards extension of the lineament (**Figure 7**), along which the seafloor geodetic array recorded the right-lateral slow slip motion described above. The event occurred 2.4 km depth below sea level, which accounts for only

TABLE 1 | Seismic events detected by the Ocean Bottom Seismometer network from April 2016 until February 2017. Note that we report only those events that were not detected by the permanent onshore network.

Event	Date	Time	Lat (°N)	Long (°E)	Depth b.s.l. (km)	Mw	Water depth (m)
1	08.04.2016	13:17:57.80	37.671	15.300	40.8	2.4	0.65
2	12.04.2016	06:18:09.90	37.649	15.399	41.6	2.7	1.72
3	16.04.2016	00:12:37.60	37.519	15.356	45.8	2.4	1.85
4	27.04.2016	05:08:55.80	37.485	15.193	37.0	1.2	0.58
5	09.06.2016	00:41:47.30	37.529	15.281	2.4	1.5	1.48

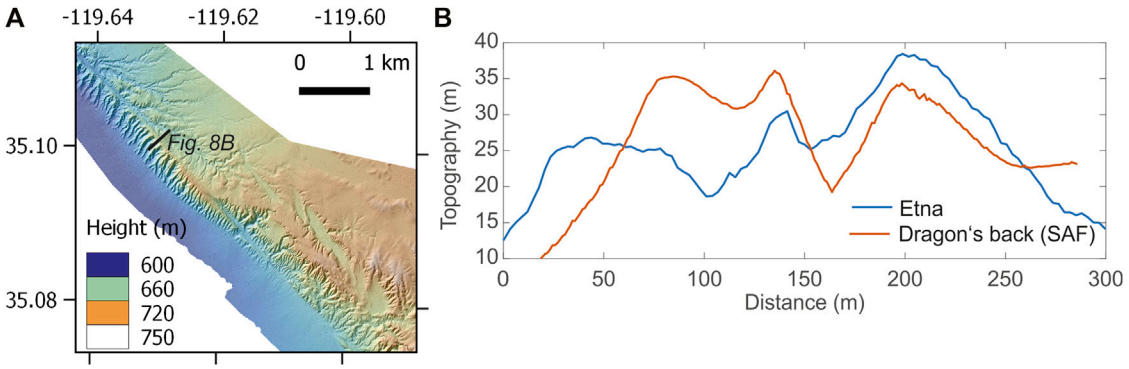


FIGURE 8 | Comparison of the morphology around the San Andreas Fault and the offshore continuation of the Acitrezza fault offshore Mount Etna. **(A)** Topographic map of the Dragon's Back pressure ridge segment of the San Andreas Fault. Data was extracted from the OpenTopography Facility with support from the National Science Foundation under NSF Award Numbers 1833703, 1833643, and 1833632. **(B)** Cross-fault height profiles. Locations are shown in **Figure 8A** and in **Figure 4A**.

900 m below the seafloor. The location uncertainties for this event are low given its proximity to the OBS network. Because of its shallow depth and location, we interpret the event as a manifestation of Etna's flank instability. The earthquake occurred in June 2016 and thus 11 months prior to the geodetically recorded slow slip event.

4 DISCUSSION

Bringing together published (bathymetry, seafloor geodesy) and newly acquired marine geophysical data (reflection seismic lines, bathymetry, microbathymetry, offshore seismicity) yields new insights into the geometry of Mount Etna's submerged unstable southeastern flank. Here, we summarise and discuss our observations in order to define the structures and locations of the boundaries of the moving flank. We identify the gaps that still exist in this definition and describe how they might be overcome in order to further constrain the offshore volcano-tectonic structure.

4.1 Southern Boundary

In the shallow offshore, there is a clear morphological continuation of the onshore Acitrezza fault. In seismic data, this structure (termed lineament) represents a near-vertical divide between different units, as expected for horizontal juxtaposition caused by strike-slip motion (**Figures 5A,B**). This lineament continues downslope as a razor-sharp fault scarp at the seafloor, now resolved for the first time in newly collected microbathymetric data (**Figure 4A**). The fault morphology is almost identical to that of the Dragon's Back segment of the San Andreas fault (**Figure 8**). This part of the San Andreas Fault accommodates dextral slip of 3.5 cm/yr (Jones and Wesnousky, 1992). Hence, the morphology observed at Etna's flank indicates recent and shallow deformation at comparable rates. This is further supported by recent dextral deformation across the fault scarp during a slow-slip event of 4 cm recorded by the seafloor geodetic array in May 2017. The inferred slip rate of the offshore fault is of similar magnitude as displacement rates associated with seaward flank sliding onshore, and thus at least an order of magnitude higher than tectonic rates in the region. We therefore conclude that the offshore continuation of the Acitrezza fault (or lineament) accommodates seaward flank sliding. The lineament is the main volcano-tectonic feature accommodating seaward motion along the southern boundary of the unstable sector. The amount of slip recorded during the May 2017 event is in the same order of magnitude as the cumulative slip measured on all onshore faults across the southern boundary during the same time, all converging to this lineament offshore. From this, and the lack of adjacent offshore fault scarps of similar nature, we suggest that the southern boundary of the mobile sector in the marine realm is described by a single fault, cumulating and releasing the slip that is then partitioned upwards on along all onshore faults dissecting the southeastern flank of the volcano.

The offshore continuation of the faults belonging to the Timpe Fault System accommodates extensional deformation most likely limited to the shallow sedimentary strata (**Figure 5A**). Continuation of sedimentary layers from the footwall into the hanging wall of the faults suggests no or little offset by strike slip motion. These faults bend towards the ESE (**Figure 3D**), i.e. in downslope direction, before merging with the offshore continuation of the Acitrezza fault (or lineament) representing the southern boundary of the moving flank. We interpret the bending and shallow extension as a result of downwards and eastwards sliding of the moving flank. In this model, the offshore branches of the Timpe Fault System are shallow second-order structures that result from extensional deformation within the moving flank.

The active southern boundary fault extends in downslope direction at least to the seawards edge of the continental bulge. This is supported by its prominent morphology (**Figure 4**) and shallow seismic activity (**Figure 7**) along its distal trace. A possible continuation into the Ionian Basin is less clear. The morphological expression of the fault on the seafloor disappears in the mouth of Catania Canyon (**Figure 4A**), where it is most likely masked by sediment deposition or erosion that exceeds fault activity.

A link to regional strike-slip tectonics, i.e. to the North Alfeo fault, is not evident from our data. We therefore propose that the observed southeastern flank motion is primarily gravitationally driven.

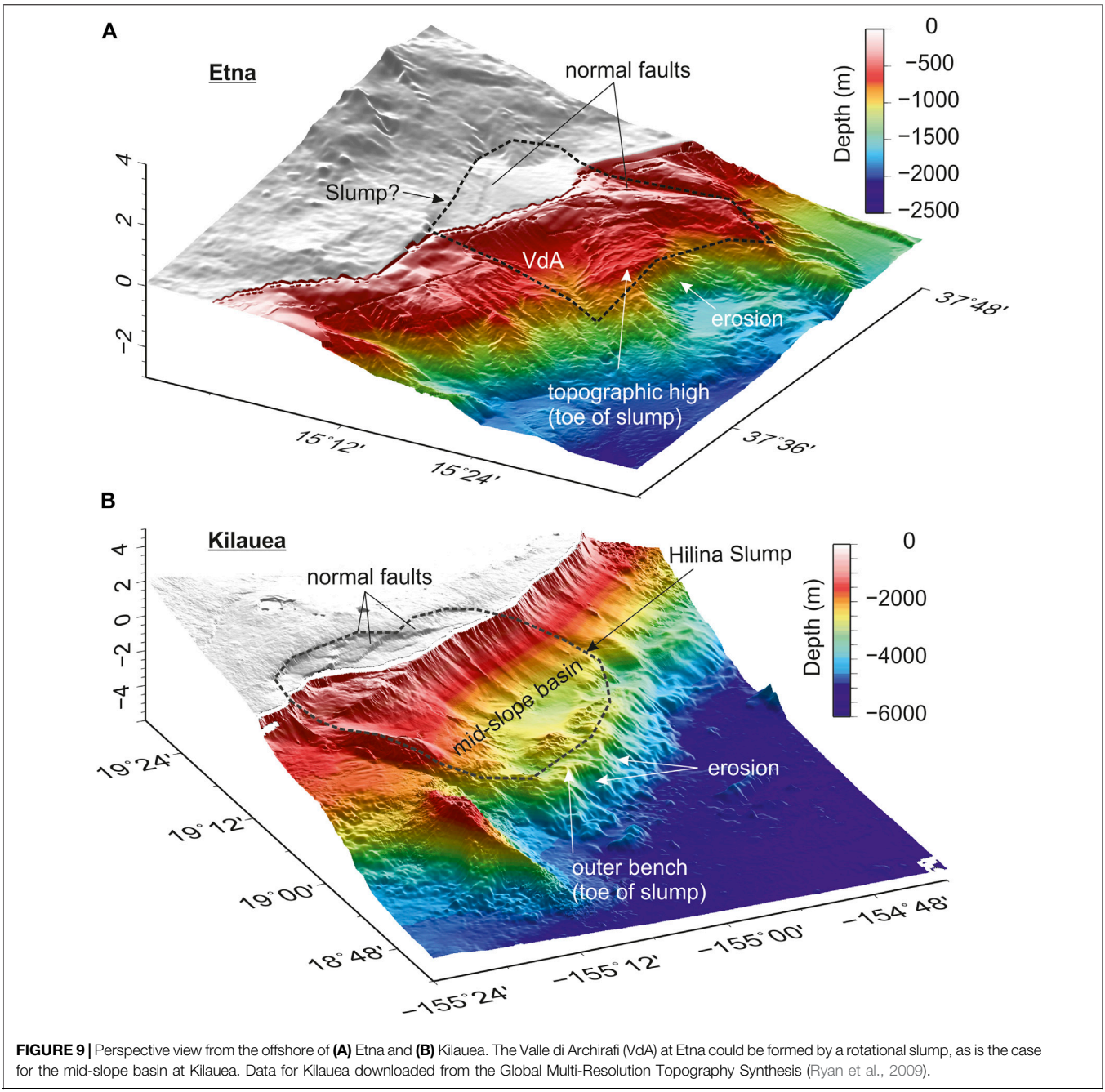


FIGURE 9 | Perspective view from the offshore of **(A)** Etna and **(B)** Kilauea. The Valle di Archirafi (VdA) at Etna could be formed by a rotational slump, as is the case for the mid-slope basin at Kilauea. Data for Kilauea downloaded from the Global Multi-Resolution Topography Synthesis (Ryan et al., 2009).

However, a certain geometric, dynamic, and genetic link to underlying crustal structures, which may act as a nucleus for driving or simply a weak zone for accommodating flank movement, cannot be excluded. Understanding this possible link is important in order to better characterise the hazard posed by this fault as well as the interaction of the volcano with the tectonic setting.

4.2 Seaward and Northern Boundaries

As the southern boundary extends at least to the edge of the continental bulge, also the seawards boundary (foot) of the unstable flank must be located similarly far into the Ionian Sea, at least along its south-eastern edge. Here, a basement high (i.e. the acoustic basement described in **Figure 5D**) separates folded young sediments in the west from unfolded shallow sediments in the Ionian Basin (**Figure 5D**). This area also reveals a local topographic high (**Figures 3B,D**). Folding of shallow strata in the west (0–3,000 m in **Figure 5D**) is likely a result of compression against this basement high. This basement high seems to act as a kinematic boundary because the sediments in the Ionian Basin on the eastern flank of the basement high are undisturbed (5,000–8,000 m in **Figure 5D**). We propose that, as Mount Etna's unstable flank moves seawards, it bulldozes shallow sedimentary strata against the basement high, which forms a stable buttress. This bulldozing induces compressional deformation of shallow sediments leading to folding of these

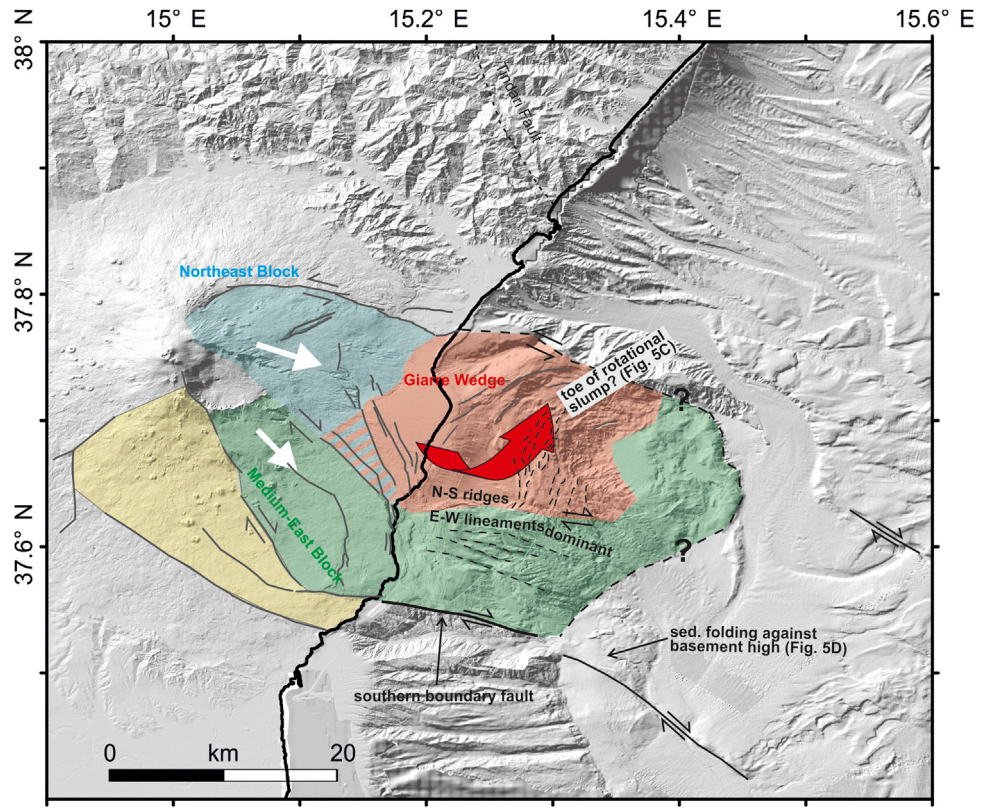


FIGURE 10 | Structural map of Mount Etna's unstable southeastern flank combining the onshore structure and nomenclature proposed by Bonforte et al. (2011) and the offshore structure presented here. Dashed lines with question marks indicate uncertainty in the location of the limit of the unstable sector. The red arrow suggests rotational slump movement of the Giarre Wedge. We infer a slump movement from observations of strong subsidence of the onshore part in InSAR and GNSS data (Bonforte and Puglisi, 2006), and evidence of active uplift in the offshore part in seismic data (**Figure 5C**).

sediments west of the basement high, but not east of it. A similar deformation pattern is absent in seismic data from the toe of the bulge to the north so that the northward continuation of the seaward boundary is still uncertain and needs further investigation.

A region within the northernmost sector of the moving flank that seems to experience uplift is the rim upslope of the amphitheater. The edge of the amphitheatre is described by a N-S elongated topographic high bounded to the west by the Valle di Archirafi and to the east by the amphitheatre. Shallow normal faults accommodate extensional deformation on both sides of the topographic high (**Figure 5C**). The resulting downward movement of shallow sediment blocks produces a stair-step morphology. We suggest that these normal faults form in response to local uplift along a N-S trending axis roughly parallel to the coast. One process that could induce this localized uplift is rotational slumping originating at the western side of the Valle di Archirafi. This would induce contraction at the slump's foot that squeezes up the sediments to form the N-S trending elongated topographic high. In this conceptual model, the Timpe faults would represent the head- and sidewalls of rotational slumping. This model resembles that of the Hilina Slump at Kilauea's submerged flank (**Figure 9**), where onshore normal faults mark the headwall of the slump. Extensional deformation along these faults leads to the formation of the offshore mid-slope basin (equivalent to Valle di Archirafi). In the deep offshore, an uplifting feature known as the outer bench corresponds to the slump's toe (Morgan et al., 2003). At Kilauea, the seaward-facing steep cliff of the outer bench is affected by significant erosion, which probably is a result of oversteepening due to ongoing uplift (Philips et al., 2008). Following this argumentation, the amphitheater at Etna could also be forming by intense erosion. The high backscatter intensity (**Figure 3C**) indicates that the amphitheatre consists of comparatively hard material. Any soft material might have eroded.

This conceptual model explains the uplift and extensional collapse of the continental margin upslope of the amphitheater. It further sheds light on the erosional process that led to the formation and shape of the amphitheater. The model, however, does not resolve the question on the seawards boundary of the unstable flank in the north. It seems possible that uplift of shallow sedimentary strata induced by gravitational slumping at the western side of the Valle di Archirafi is superimposed on a longer (deeper origin) wavelength deformation pattern induced by the distal boundary of the moving flank. This scenario is supported by the fact that south of the area interpreted to be affected by slumping there is no clear seafloor or sub-seafloor structure that may correspond to the

seawards boundary. This includes the lack of evidence for EW compression as well as any sharply defined fault outcrops at the seafloor. In alignment with previous studies (Argnani et al., 2013) we do not observe clear evidence for the location of the northern boundary of the entire mobile flank in our data.

4.3 Overall Structure of Etna's Southeastern Flank

For a synthesis of the above findings, we build on the onshore structural map of Bonforte et al. (2011) and extend it to the offshore flank (**Figure 10**). Based on results from the Permanent Scatterers technique, Bonforte et al. (2011) identify three main structural domains that form Etna's mobile southeastern flank; Northeast Block, Giarre Wedge, and Medium-East Block. The Giarre Wedge (red domain in **Figure 10**) is the sector showing the strongest subsidence, associated with a significant eastward motion that remains outstanding even when the rest of the volcano is deflating. In the model we propose above, this is the extensional and subsiding part at the head of a rotational slump. The compressional part (or toe) of the slump is probably found offshore at the topographic high upslope of the amphitheatre (**Figures 5C**, **10**). This area thus could belong to the Giarre Wedge block (red domain in **Figure 10**). We determine the block's seawards termination to coincide with a break in slope and the disappearance of North-South trending ridges. There is a morphological divide between the North-South trending ridges marking the toe of the slump, and East-West oriented lineaments that shape the south of the study area (**Figures 3D**, **10**). This morphological divide probably forms the southern edge of the area of the unstable flank that is additionally involved in slumping (red domain). Because of the faster movement of the Giarre Wedge with respect to the other blocks, we expect this boundary area to host right-lateral motion but microbathymetric and seafloor geodetic data are needed to confirm this. The area between this divide and the southern boundary fault probably represents the pure eastwards flank movement on seawards inclined basement. We suggest this pattern to be conform to the onshore Medium-East Block (green domain).

Our structural interpretation suggests that also the offshore flank is segmented, similarly to what has been proposed for the onshore part of the southeastern flank based on GNSS and InSAR data (Solaro et al., 2010; Bonforte et al., 2011). What is the reason for this segmentation? Bonforte et al. (2011) propose that basement discontinuities drive segmentation. This is also possible for the offshore flank. However, the hypothesis is difficult to test because of a lack of information on offshore stable basement morphology. The available marine geophysical data do not allow consistent imaging of the stable basement underlying the volcano flank.

5 SUMMARY AND OUTLOOK

The geometry, structure and recent activity of the lateral submerged southern boundary of Mount Etna's unstable flank is now well-defined based on a wealth of different marine geophysical data. Deciphering a link and possible interaction of the volcanic flank with regional tectonic structures requires further investigations. A comparison of fault slip at the continental bulge and at tectonic features in the Ionian Basin will help identify a potential connection. Furthermore, long-term offshore slip rates will provide more confidence on the overall rates and style of deformation. Knowing the depth of the fault will also help discern between tectonic and gravitational origin of fault slip. As seismic imaging is poor due to the nature of the substrate even across different resolutions (Argnani et al., 2013; Gross et al., 2016; Carlino et al., 2019), comparison and integration with other methods or disciplines could help determine whether the faults considered here are crustal structures. Faults are preferred vertical pathways for pore fluids, which carry diagenetic signals from the stratigraphic units they originate from. Hence, geochemical analyses of the composition of sediment pore fluid from faults could be one possibility to constrain fault depth.

From shipborne bathymetric data and seismic reflection lines it was possible to formulate hypothesizes about possible locations of the seawards and northern boundary of the moving flank. It has to be noted, however, that the high level of confidence that now accompanies the location and activity of the southern boundary offshore fault was only achieved through the combination of latest microbathymetry collected with an AUV (in 2020) and a continuous seafloor geodetic survey (2016–2018). Such a combination of latest and state-of-the-art marine geophysical data is, to our knowledge, however, not available for a single other submerged volcanic flank on Earth.

Considering the continuous gravitational downwards and eastwards sliding of the volcano flank, the seawards boundary should be a compressional feature. We show evidence for compression in certain locations but do not succeed to identify a continuous structure in the available seismic data. At Kilauea, monitoring vertical seafloor deformation with pressure gauges revealed active uplift of the volcano's toe (Philipps et al., 2008). The data confirmed the structure and seawards boundary of Kilauea's unstable south flank as Morgan et al. (2003) postulated based on reflection seismic data. Such pressure monitoring at the toe of Mount Etna's flank, which we suspect to actively uplift in response to flank dynamics, may also help to constrain the seawards limit of Mount Etna's flank. Unless such data become available, the location of the offshore northern and seawards boundaries of the mobile sector remain speculative.

Today, the situation at the lateral northern boundary of the moving flank resembles the available knowledge on the southern boundary prior to collection of the AUV microbathymetry and seafloor geodesy data. We expect the northern boundary of the Etna landslide to deform in a left-lateral motion at similar rate and style as the southern boundary. It is also possible that the motion on the offshore northern side is accommodated by a more complex arrangement of structures, as is the case on southern onshore side of the volcano. While we are able to formulate hypothesizes about its location and activity of the boundary faults, a better constrained model will only be possible with comparable data (i.e., with microbathymetry and seafloor geodesy).

DATA AVAILABILITY STATEMENT

The datasets presented in this study can be found in the online repository PANGAEA (https://www.pangaea.de/) as supplement to this publication:

https://doi.pangaea.de/10.1594/PANGAEA.922750
https://doi.pangaea.de/10.1594/PANGAEA.893036
https://doi.pangaea.de/10.1594/PANGAEA.941403

All other data will be made available upon request to the corresponding author.

AUTHOR CONTRIBUTIONS

MU and JG led the conception and design of the manuscript and wrote the first draft. JG wrote sections of the manuscript. FP conducted the seismological analysis. AB and FG contributed to the conception of the study. MU, FP, FG, AB, and SK acquired the data. HK substantially contributed to data acquisition. All authors contributed to manuscript revision, read, and approved the submitted version.

FUNDING

This project has received funding from the European Research Council (ERC) under the European Union's Horizon 2020 research and innovation programme (grant agreement No. 948797).

ACKNOWLEDGMENTS

We thank Marc André Gutscher for providing the CIRCEE bathymetry compilation of the Ionian Sea, Irena Schulten for processing the backscatter data, Bruna Pandolpho for calculating morphometric attributes, Anja Steinführer for processing and editing the AUV bathymetry, and the scientific and nautic crews of expeditions M86/2, M111, POS496, POS509, POS515, AL532, and SO277. Sincere thanks to the Chief Editor Valerio Acocella and two reviewers for thorough reviews that helped improving the manuscript. Figures were created using the Free and Open Source QGIS and GMT, as well as ArcMAP, The Kingdom Software, and Matlab.

REFERENCES

Acocella, V., Behncke, B., Neri, M., and D'Amico, S. (2003). Link between Major Flank Slip and 2002–2003 Eruption at Mt. Etna (Italy). *Geophys. Res. Lett.* 30 (24). doi:10.1029/2003gl018642

Alparone, S., Barberi, G., Bonforte, A., Maiolino, V., and Ursino, A. (2011). Evidence of Multiple Strain fields beneath the Eastern Flank of Mt. Etna Volcano (Sicily, Italy) Deduced from Seismic and Geodetic Data during 2003-2004. *Bull. Volcanol* 73, 869–885. doi:10.1007/s00445-011-0456-1

Alparone, S., Bonaccorso, A., Bonforte, A., and Currenti, G. (2013). Long-term Stress-Strain Analysis of Volcano Flank Instability: The Eastern Sector of Etna from 1980 to 2012. *J. Geophys. Res.* 118, 1–11. doi:10.1002/jgrb.50364

Alparone, S., Maiolino, V., Mostaccio, A., Scaltrito, A., Ursino, A., and Barberi, G. (2015). Instrumental Seismic Catalogue of Mt. Etna Earthquakes (Sicily, Italy): Ten Years (2000-2010) of Instrumental Recordings. *Ann. Geophys.* 58 (4), S0435. doi:10.4401/ag-6591

Argnani, A., and Bonazzi, C. (2005). Malta Escarpment Fault Zone Offshore Eastern Sicily: Pliocene-Quaternary Tectonic Evolution Based on New Multichannel Seismic Data. *Tectonics* 24. doi:10.1029/2004tc001656

Argnani, A., Mazzarini, F., Bonazzi, C., Bisson, M., and Isola, I. (2013). The Deformation Offshore of Mount Etna as Imaged by Multichannel Seismic Reflection Profiles. *J. Volcanology Geothermal Res.* 251, 50–64. doi:10.1016/j.jvolgeores.2012.04.016

Azzaro, R., Bonforte, A., Branca, S., and Guglielmino, F. (2013). Geometry and Kinematics of the Fault Systems Controlling the Unstable Flank of Etna Volcano (Sicily). *J. Volcanology Geothermal Res.* 251, 5–15. doi:10.1016/j.jvolgeores.2012.10.001

Barreca, G., Bonforte, A., and Neri, M. (2013). A Pilot GIS Database of Active Faults of Mt. Etna (Sicily): A Tool for Integrated hazard Evaluation. *J. Volcanology Geothermal Res.* 251, 170–186. doi:10.1016/j.jvolgeores.2012.08.013

Barreca, G., Corradino, M., Monaco, C., and Pepe, F. (2018). Active Tectonics along the South East Offshore Margin of Mt. Etna: New Insights from High-Resolution Seismic Profiles. *Geosciences* 8 (2), 62. doi:10.3390/geosciences8020062

Berndt, C., Urlaub, M., Jegen, M., Zahra, F., Gesa, F., Carolin, K., et al. (2021). RV SONNE Fahrtbericht/Cruise Report SO277 OMAX: Offshore Malta Aquifer Exploration, Emden (Germany) - Emden (Germany), 14.08. - 03.10.2020. *GEOMAR Report, N. Ser.* 057, 139. doi:10.3289/GEOMAR_REP_NS_57_20

Bonaccorso, A., Currenti, G., and Del Negro, C. (2013). Interaction of Volcano-Tectonic Fault with Magma Storage, Intrusion and Flank Instability: A Thirty Years Study at Mt. Etna Volcano. *J. Volcanology Geothermal Res.* 251, 127–136. doi:10.1016/j.jvolgeores.2012.06.002

Bonforte, A., Bonaccorso, A., Guglielmino, F., Palano, M., and Puglisi, G. (2008). Feeding System and Magma Storage beneath Mt. Etna as Revealed by Recent Inflation/deflation Cycles. *J. Geophys. Res. Solid Earth* 113. doi:10.1029/2007jb005334

Bonforte, A., Branca, S., and Palano, M. (2007). Geometric and Kinematic Variations along the Active Pernicana Fault: Implication for the Dynamics of Mount Etna NE Flank (Italy). *J. Volcanology Geothermal Res.* 160, 210–222. doi:10.1016/j.jvolgeores.2006.08.009

Bonforte, A., Carnazzo, A., Gambino, S., Guglielmino, F., Obrizzo, F., and Puglisi, G. (2013a). A Multidisciplinary Study of an Active Fault Crossing Urban Areas: The Trecastagni Fault at Mt. Etna (Italy). *J. Volcanology Geothermal Res.* 251, 41–49. doi:10.1016/j.jvolgeores.2012.05.001

Bonforte, A., Guglielmino, F., Coltelli, M., Ferretti, A., and Puglisi, G. (2011). Structural Assessment of Mount Etna Volcano from Permanent Scatterers Analysis. *Geochem. Geophys. Geosys* 12, Q02002. doi:10.1029/2010gc003213

Bonforte, A., Guglielmino, F., and Puglisi, G. (2013b). Interaction between Magma Intrusion and Flank Dynamics at Mt. Etna in 2008, Imaged by Integrated Dense GPS and DInSAR Data. *Geochem. Geophys. Geosyst.* 14 (8), 2818–2835. doi:10.1002/ggge.20190

Bonforte, A., and Puglisi, G. (2006). Dynamics of the Eastern Flank of Mt. Etna Volcano (Italy) Investigated by a Dense GPS Network. *J. Volcanology Geothermal Res.* 153 (3-4), 357–369. doi:10.1016/j.jvolgeores.2005.12.005

Branca, S., Coltelli, M., Groppelli, G., and Lentini, F. (2011). Geological Map of Etna Volcano, 1: 50,000 Scale. *Ital. J. Geosciences* 130 (3), 265–291. doi:10.3301/ijg.2011.15

Branca, S., and Ferrara, V. (2013). The Morphostructural Setting of Mount Etna Sedimentary Basement (Italy): Implications for the Geometry and Volume of the Volcano and its Flank Instability. *Tectonophysics* 586, 46–64. doi:10.1016/j.tecto.2012.11.011

Bruno, V., Mattia, M., Montgomery-Brown, E., Rossi, M., and Scandura, D. (2017). Inflation Leading to a Slow Slip Event and Volcanic Unrest at Mount Etna in 2016: Insights from CGPS Data. *Geophys. Res. Lett.* 44 (24), 12–141. doi:10.1002/2017gl075744

Cayol, V., Dieterich, J. H., Okamura, A. T., and Miklius, A. (2000). High Magma Storage Rates before the 1983 Eruption of Kilauea, Hawaii. *Science* 288 (5475), 2343–2346. doi:10.1126/science.288.5475.2343

Chiocci, F. L., Coltelli, M., Bosman, A., and Cavallaro, D. (2011). Continental Margin Large-Scale Instability Controlling the Flank Sliding of Etna Volcano. *Earth Planet. Sci. Lett.* 305, 57–64. doi:10.1016/j.epsl.2011.02.040

Dannowski, A., Kopp, H., Klingelhoefer, F., Klaeschen, D., Gutscher, M.-A., Krabbenhoeft, A., et al. (2019). Ionian Abyssal Plain: A Window into the Tethys Oceanic Lithosphere. *Solid Earth* 10 (2), 447–462. doi:10.5194/se-10-447-2019

De Guidi, G., Brighenti, F., Carnemolla, F., Imposa, S., Marchese, S. A., and Palano, M. (2018). The Unstable Eastern Flank of Mt. Etna Volcano (Italy): First Results of a GNSS-Based Network at its southeastern Edge. *J. Volcanology Geothermal Res.* 357, 418–424. doi:10.1016/j.jvolgeores.2018.04.027

De Novellis, V., Atzori, S., De Luca, C., Manzo, M., Valerio, E., and Bonano, M. (2019). DInSAR Analysis and Analytical Modeling of Mount Etna Displacements: The December 2018 Volcano-Tectonic Crisis. *Geophys. Res. Lett.* 46 (11), 5817–5827. doi:10.1029/2019gl082467

Dieterich, J., Cayol, V., and Okubo, P. (2000). The Use of Earthquake Rate Changes as a Stress Meter at Kilauea Volcano. *Nature* 408 (6811), 457–460. doi:10.1038/35044054

Firetto Carlino, M., Cavallaro, D., Coltelli, M., Cocchi, L., Zgur, F., and Patanè, D. (2019). Time and Space Scattered Volcanism of Mt. Etna Driven by Strike-Slip Tectonics. *Sci. Rep.* 9 (1), 15–12215. doi:10.1038/s41598-019-48550-1

Gambino, S., Bonforte, A., Carnazzo, A., Falzone, G., Ferrari, F., Ferro, A., et al. (2011). Displacement across the Trecastagni Fault (Mt. Etna) and Induced Seismicity: the October 2009 to January 2010 Episode. *Ann. Geophys.* 54.

Groppelli, G., and Tibaldi, A. (1999). Control of Rock Rheology on Deformation Style and Slip-Rate along the Active Pernicana Fault, Mt. Etna, Italy. *Tectonophysics* 305 (4), 521–537. doi:10.1016/s0040-1951(99)00035-9

Gross, F., Krastel, S., Geersen, J., Behrmann, J. H., Ridente, D., and Chiocci, F. L. (2016). J. Bialas, C. Papenberg, D. Cukur, M. Urlaub, A. MicallefThe Limits of Seaward Spreading and Slope Instability at the continental Margin Offshore Mt Etna, Imaged by High Resolution 2D Seismic Data. *Tectonophysics* 667, 63–76. doi:10.1016/j.tecto.2015.11.011

Gutscher, M. A., Dominguez, S., Lepinay, B. M. de, Pinheiro, L., and Gallais, F., (2016). Tectonic Expression of an Active Slab Tear from High-Resolution Seismic and Bathymetric Data Offshore Sicily (Ionian Sea). *Tectonics* 35 (1), 39–54. doi:10.1002/2015tc003898

Gutscher, M. A., Kopp, H., Krastel, S., Bohrmann, G., Garlan, T., and Zaragosi, S. (2017). Active Tectonics of the Calabrian Subduction Revealed by New Multi-Beam Bathymetric Data and High-Resolution Seismic Profiles in the Ionian Sea (Central Mediterranean). *Earth Planet. Sci. Lett.* 461, 61–72. doi:10.1016/j.epsl.2016.12.020

Gvirtzman, Z., and Nur, A. (1999a). The Formation of Mount Etna as the Consequence of Slab Rollback,. *Nature* 401, 782–785. doi:10.1038/44555

Havskov, J., and Ottemoeller, L. (1999). SeisAn Earthquake Analysis Software. *Seismological Res. Lett.* 70, 532–534. doi:10.1785/gssrl.70.5.532

Jones, C. H., and Wesnousky, S. G. (1992). Variations in Strength and Slip Rate along the San Andreas Fault System. *Science* 256 (5053), 83–86. doi:10.1126/science.256.5053.83

Krastel, S., and Cruise, P. (2012). Seismogenic Faults, Landslides, and Associated Tsunamis off Southern Italy. Cruise No. M86/2 – November 21, 2011 – January 17, 2012 – Cartagena (Spain) – Brindisi (Italy). *METEOR-Berichte* M86/2, 49. DFG-Senatskommission für Ozeanographie. doi:10.2312/cr_m86_2

Krastel, S. (2016). RV POSEIDON-CRUISE POS496, Malaga – Catania, 24.03.2016-04.04.2016, Short Cruise Report: MAGOMET - Offshore flank movement of Mount Etna and associated landslide hazard in the Ionian Sea (Mediterranean Sea). Christian-Albrechts-Universität zu Kiel. *Inst. Geosciences* 8. doi:10.3289/SCR_POS_496

Lanzafame, G., Neri, M., and Rust, D. (1996). A Preliminary Structural Evaluation of Recent Tectonic Activity on the Eastern Flank of Mount Etna, Sicily., West Lond. Pap. Environ. *Stud.* 3, 73–90.

Liu, C., Lay, T., and Xiong, X. (2018). Rupture in the 4 May 2018 MW 6.9 Earthquake Seaward of the Kīlauea East Rift Zone Fissure Eruption in Hawaii. *Geophys. Res. Lett.* 45 (18), 9508–9515. doi:10.1029/2018gl079349

Lomax, A., Virieux, J., Volant, P., and Berge-Thierry, C. (2000). Probabilistic Earthquake Location in 3D and Layered Models. *Adv. seismic event location*18, 101–134. doi:10.1007/978-94-015-9536-0_5

Mattia, M., Bruno, V., Caltabiano, T., Cannata, A., Cannavo, F., D'Alessandro, W., et al. (2015). A Comprehensive Interpretative Model of Slow Slip Events on Mt. Etna's Eastern Flank. *Geochemistry, Geophys. Geosystems* 16 (3), 635–658.

Morgan, J. K., Moore, G. F., and Clague, D. A. (2003). Slope Failure and Volcanic Spreading along the Submarine South Flank of Kīlauea Volcano, Hawaii. *J. Geophys. Res.* 108. doi:10.1029/2003jb002411

Neri, M., Acocella, V., and Behncke, B. (2004). The Role of the Pernicana Fault System in the Spreading of Mt. Etna (Italy) during the 2002–2003 Eruption. *Bull. Volcanology* 66 (5), 417–430. doi:10.1007/s00445-003-0322-x

Neri, M., Rivalta, E., Maccaferri, F., Acocella, V., and Cirrincione, R. (2018). Etnean and Hyblean Volcanism Shifted Away from the Malta Escarpment by Crustal Stresses. *Earth Planet. Sci. Lett.* 486, 15–22. doi:10.1016/j.epsl.2018.01.006

Palano, M. (2016). Episodic Slow Slip Events and Seaward Flank Motion at Mt. Etna Volcano (Italy). *J. Volcanology Geothermal Res.* 324, 8–14. doi:10.1016/j.jvolgeores.2016.05.010

Paris, R. (2015). Source Mechanisms of Volcanic Tsunamis. Philosophical Transactions of the Royal Society A: Mathematical. *Phys. Eng. Sci.* 373 (2053), 20140380. doi:10.1098/rsta.2014.0380

Patanè, D., De Gori, P., Chiarabba, C., and Bonaccorso, A. (2003). Magma Ascent and the Pressurization of Mount Etna's Volcanic System. *Science* 299, 2061–2063. doi:10.1126/science.1080653

Petersen, F., Kopp, H., Lange, D., Hannemann, K., and Urlaub, M. (2019). Measuring Tectonic Seafloor Deformation and Strain-Build up with Acoustic Direct-Path Ranging. *J. Geodynamics* 124, 14–24. doi:10.1016/j.jog.2019.01.002

Phillips, K. A., Chadwell, C. D., and Hildebrand, J. A. (2008). Vertical Deformation Measurements on the Submerged South Flank of Kīlauea Volcano, Hawai'i Reveal Seafloor Motion Associated with Volcanic Collapse. *J. Geophys. Res.* 113. doi:10.1029/2007jb005124

Poland, M., Peltier, A., Bonforte, A., and Puglisi, G. (2017). The spectrum of persistent volcanic flank instability; A review and proposed framework based on Kilauea, Piton de la Fournaise and Etna. *J. Volcanol. Geother. Res.* 339, 63–80. doi:10.1016/j.jvolgeores.2017.05.004

Pope, E. L., Jutzeler, M., Cartigny, M. J., Shreeve, J., Talling, P. J., Wright, I. C., et al. (2018). Origin of Spectacular fields of Submarine Sediment Waves Around Volcanic Islands. *Earth Planet. Sci. Lett.* 493, 12–24. doi:10.1016/j.epsl.2018.04.020

Ramalho, R. S., Winckler, G., Madeira, J., Helffrich, G. R., Hipólito, A., and Quartau, R. (2015). Hazard Potential of Volcanic Flank Collapses Raised by New Megatsunami Evidence. *Sci. Adv.* 1 (9), e1500456. doi:10.1126/sciadv.1500456

Ryan, W. B. F., CarbotteMelkonian, S. M. A., Arko, R., Weissel, R. A., Ferrini, V., Goodwillie, A., et al. (2009). Global Multi-Resolution Topography (GMRT) Synthesis Data Set. *Geochem. Geophys. Geosyst* 10, Q03014. doi:10.1029/2008GC002332

Schulze, I. (2017). *Continental Margin Deformation Offshore Mt Etna and Potential Landslide Risk*. Kiel, Germany: Christian-Albrechts-Universität zu Kiel. Msc Thesis.

Solaro, G., Acocella, V., Pepe, S., Ruch, J., Neri, M., and Sansosti, E. (2010). Anatomy of an Unstable Volcano from InSAR: Multiple Processes Affecting Flank Instability at Mt. Etna, 1994–2008. *J. Geophys. Res. Solid Earth* 115. doi:10.1029/2009jb000820

Urlaub, M., Bonforte, A., Kurbjuhn, T., Steinführer, A., and Wenzlaff, E. (2020). Monitoring and Mapping Active Deformation Offshore Etna, Cruise No. AL532, 29.01.2020 – 02.02.2020 Catania (Italy) – Catania (Italy), MAPACT-ETNA. *Alkor-Berichte, AL532* 27. GEOMAR Helmholtz-Zentrum für Ozeanforschung Kiel, Kiel, Germany. doi:10.3289/CR_AL532

Urlaub, M., Petersen, F., Gross, F., Bonforte, A., Puglisi, G., Guglielmino, F., et al. (2018). Gravitational Collapse of Mount Etna's southeastern Flank. *Sci. Adv.* 4, eaat9700. doi:10.1126/sciadv.aat9700

Ventura, B. M., Serpelloni, E., Argnani, A., Bonforte, A., Bürgmann, R., and Anzidei, M. (2014). Fast Geodetic Strain-Rates in Eastern Sicily (Southern Italy): New Insights into Block Tectonics and Seismic Potential in the Area of the Great 1693 Earthquake. *Earth Planet. Sci. Lett.* 404, 77–88. doi:10.1016/j.epsl.2014.07.025

Walter, T. R., Haghighi, M. H., Schneider, F. M., Coppola, D., Motagh, M., and Saul, J. (2019). Complex hazard cascade Culminating in the Anak Krakatau Sector Collapse. *Nat. Commun.* 10 (1), 1–11. doi:10.1038/s41467-019-12284-5

Walter, T., and Schmincke, H. U. (2002). Rifting, Recurrent Landsliding and Miocene Structural Reorganization on NW-Tenerife (Canary Islands). *Int. J. Earth Sci.* 91 (4), 615–628. doi:10.1007/s00531-001-0245-8

Conflict of Interest: The authors declare that the research was conducted in the absence of any commercial or financial relationships that could be construed as a potential conflict of interest.

Publisher's Note: All claims expressed in this article are solely those of the authors and do not necessarily represent those of their affiliated organizations, or those of the publisher, the editors and the reviewers. Any product that may be evaluated in this article, or claim that may be made by its manufacturer, is not guaranteed or endorsed by the publisher.

Copyright © 2022 Urlaub, Geersen, Petersen, Gross, Bonforte, Krastel and Kopp. This is an open-access article distributed under the terms of the Creative Commons Attribution License (CC BY). The use, distribution or reproduction in other forums is permitted, provided the original author(s) and the copyright owner(s) are credited and that the original publication in this journal is cited, in accordance with accepted academic practice. No use, distribution or reproduction is permitted which does not comply with these terms.

frontiers in Earth Science

ORIGINAL RESEARCH
published: 04 March 2022
doi: 10.3389/feart.2022.730734

The Volcanic Hazards of Jan Mayen Island (North-Atlantic)

Eirik Gjerløw[1,2]*, *Ármann Höskuldsson*[3], *Stefania Bartolini*[4], *Sebastien Biass*[5], *Sophie Mossoux*[6], *Jennie Gilbert*[7], *Rolf Birger Pedersen*[2] and *Joan Martí*[4]

[1]Department of Building, Energy and Material Technology, UiT the Arctic University of Norway, Narvik, Norway, [2]Department of Earth Sciences, Centre for Geobiology, University of Bergen, Bergen, Norway, [3]Nordic Volcanological Center, Institute of Earth Sciences, University of Iceland, Reykjavik, Iceland, [4]Group of Volcanology, (SIMGEO-UB) CSIC, Institute of Earth Sciences Jaume Almera, Barcelona, Spain, [5]Earth Observatory of Singapore, Nanyang Technical University, Singapore, Singapore, [6]Department of Geography, Cartography and GIS Research Group - Physical Geography, Vrije Universiteit Brussel, Brussels, Belgium, [7]Lancaster Environment Centre, Lancaster University, Lancaster, United Kingdom

Hazard assessment of remote volcanic islands provides many challenges compared to other volcanoes and volcanic fields. Here we present the first systematic volcanic hazard assessment of Jan Mayen Island, a remote island located in the North-Atlantic Ocean and home to the northernmost active subaerial volcano in the world (Beerenberg Volcano), and we discuss some of the challenges and characteristics of performing a volcanic hazard assessment of a remote volcanic island. Jan Mayen has had at least five eruptions since its discovery at the start of the 17th century. Its Holocene volcanism is mainly characterized by eruptions with styles ranging from Hawaiian to Strombolian, but also by lava domes and Surtseyan eruptions. Based on field data, remote images, topographic data, past data, and computer simulations, our study evaluates the spatial probability of new vents opening, estimates eruption recurrence rates, simulates various eruption scenarios, and produces hazard maps for the different scenarios. This work shows where the hazards of ash fall, and lava flows are more likely to affect the built infrastructure on Jan Mayen Island. This hazard assessment will assist emergency planning and the determination of future land use on the island.

Keywords: volcanic hazard, eruptive scenarios, geohazard, hazard models, hazard assesment, volcano

OPEN ACCESS

Edited by:
Valerio Acocella,
Roma Tre University, Italy

Reviewed by:
Paul William Taylor,
Independent researcher, East Maitland, Australia
Laura Sandri,
National Institute of Geophysics and Volcanology, Italy
Jocelyn McPhie,
University of Tasmania, Australia

***Correspondence:**
Eirik Gjerløw
Eirik.Gjerlow@uit.no

Specialty section:
This article was submitted to Geohazards and Georisks, a section of the journal Frontiers in Earth Science

Received: *25 June 2021*
Accepted: *15 February 2022*
Published: *04 March 2022*

Citation:
Gjerløw E, Höskuldsson Á, Bartolini S, Biass S, Mossoux S, Gilbert J, Pedersen RB and Martí J (2022) The Volcanic Hazards of Jan Mayen Island (North-Atlantic). Front. Earth Sci. 10:730734. doi: 10.3389/feart.2022.730734

INTRODUCTION

Remote volcanic islands provide a challenging environment for conducting volcanic hazard assessment. They are often uninhabited and have a limited historical period, meaning that descriptions of and data from past volcanic activity can be scarce or missing. Using currently visible vents to assess the volcanic susceptibility of monogenetic volcanism is a common procedure, but for volcanic islands coastal erosion and submarine volcanism can affect the accuracy of the procedure. Furthermore, a proportion of remote volcanic islands are glaciated which means that vents may be hidden beneath ice or they may have been destroyed by glacier erosion. Our approach to a volcanic hazard assessment highlights and discusses some of the difficulties of conducting hazard assessments on remote volcanic islands with a limited historical period and datasets of past eruptions, and it can be used as an example for how to conduct a volcanic hazard assessment in such a setting.

The Norwegian island of Jan Mayen, located NE of Iceland in the North-Atlantic Ocean (**Figure 1A**), hosts the northernmost active subaerial volcano in the world–Beerenberg Volcano,

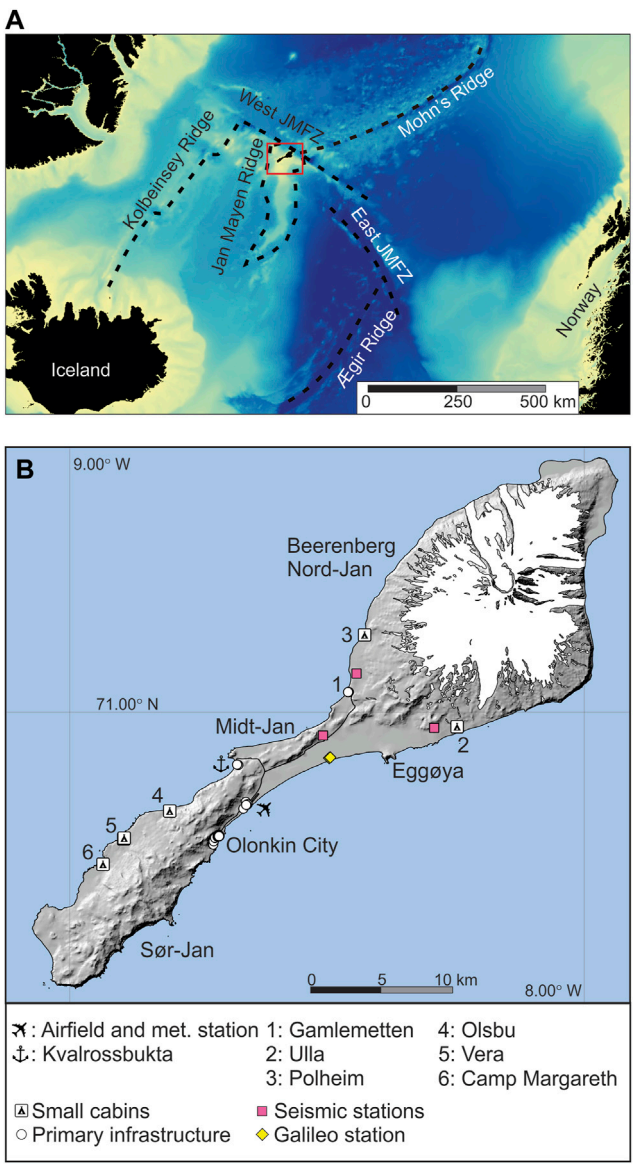


FIGURE 1 | (A) Bathymetric map (Jakobsson et al., 2012) showing the location of Iceland, Norway, the Kolbeinsey Ridge, Mohn's Ridge, Ægir Ridge, Jan Mayen Ridge, and the West- and East-Jan Mayen fracture zones (JMFZ) and Jan Mayen Island (red box). The island is located approximately 600 km NE of Iceland and 950 km W of Norway. **(B)** Key points of interest on Jan Mayen. The white areas in the map are covered by glaciers or permanent snow.

the summit of which is 2,277 m above sea level (European Catalogue of Volcanos). The island is about 53 km long from SW to NE and covers an area of approximately 373 km^2. Sør-Jan is the term given to the southern part of the island which is joined to the northern part (Nord-Jan or Beerenberg) via an isthmus (Midt-Jan).

Dutch whaling companies sent summer expeditions to Jan Mayen from 1,614 until around 1,645 (Barr 2003). When the whaling expeditions ceased there was only intermittent human activity on and around Jan Mayen. During the first International Polar Year in 1882–1883, the Austro-Hungarian navy established a research station on the island and carried out geographic mapping of Jan Mayen. In subsequent years several research expeditions visited Jan Mayen. In 1906, Norwegian trappers began overwinter hunting for arctic foxes, and this resulted in a more established human presence. In 1921, the first permanent meteorological station was installed. Since then, the island has been continuously inhabited. Currently a team of 18 people associated with the Norwegian Meteorological Institute and Norwegian Armed Forces live permanently on Jan Mayen to maintain all infrastructure (i.e., roads, weather observation equipment, houses, and cabins) on the island. During the summer, the number of inhabitants can be significantly higher due to the arrival of scientists, tourists, and maintenance crew.

The infrastructure on Jan Mayen is mainly located along the coastlines of the central parts of the island (**Figure 1B**). The main infrastructure is in Olonkin City, which has living quarters, workshops, and the necessary infrastructure for day-to-day operations. The meteorological station on Jan Mayen lies 3 km NE of Olonkin City. Next to the meteorological station lies the Jan Mayensfield airfield that has an unpaved, 1.6 km long, runway. Kvalrossbukta, about 5 km N of Olonkin City, is used as a natural harbor for landing light boats and military landing crafts that resupply the island. A cabin and a generator are also present at Kvalrossbukta. Other infrastructure on the island consists of the Galileo and EGNOS equipment (used for global navigation satellite purposes) plus three seismometers; these are remotely operated from Olonkin City. Finally, there are several old cabins that are used for recreational purposes. The largest cabin is located at Gamlemetten, and this could be used for evacuation in the event of an eruption on Sør-Jan (**Figure 1B**). Gamlemetten is linked to Olonkin City by roads that are open and maintained during the summer months.

The most recent eruptions on Jan Mayen took place in 1970 (Siggerud 1972) and 1985 (Imsland 1986), both on the NE flank of Mt. Beerenberg approximately 40 km from Olonkin City (**Figure 1**). The 1970 eruption was the larger and produced plumes of steam and ash, reaching altitudes of at least 10 km. At the time, a red volcanic sunset was reported in England (Siggerud 1972). Those working at Olonkin City did not notice the eruption until a few days after it started, when it was spotted by an airplane flying over the island (Siggerud 1972). Prior to 1970, descriptions of eruptions at Jan Mayen were seen as unreliable (Sylvester 1975). However, following the eruptions of 1970 and 1985 these reports were deemed more credible (Sylvester 1975). These eruptions demonstrated that volcanic hazards should be a cause of concern for people and installations on Jan Mayen.

Past work by Sylvester (1975) briefly discussed volcanic hazards on the island. This author suggested that Olonkin City could only be impacted if an eruption broke out in the cliffs above the city or on the lava plateau that the city is built up on. Prior to our study, no attempts have been made to generate hazard maps or conduct a comprehensive analysis of volcanic hazards on the island.

In this paper, we present for the first time a volcanic hazard assessment of Jan Mayen by applying a systematic methodology

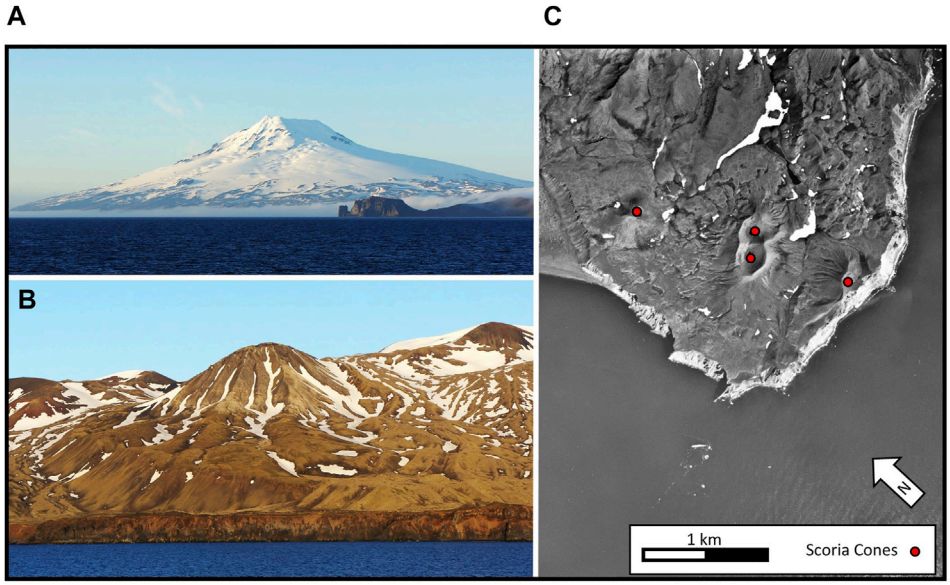


FIGURE 2 | (A) The Beerenberg volcano (2,227 m a.s.l.) constitutes the N part of the island. Note the tuff cone in the foreground. **(B)** Bombellestoppen (606 m a.s.l.), one of the trachytic domes on the S part of Jan Mayen. **(C)** Aerial photograph of the S tip of Jan Mayen showing four scoria cones (marked with red dots). Section of aerial photo JM75 7183, with permission, © Norsk Polarinstitutt.

that includes spatial and temporal analysis and simulation of the hazardous events related to some of the most probable eruptive scenarios (e.g., Martí 2017). In this work we use 1) previously published studies, 2) new data based on fieldwork carried out in 2011 and 2012 and 3) remote imaging. The resulting work leads to 1) a probability density analysis of the distribution of past vents, to identify the most likely location of future ones, and 2) numerical simulations of the various volcanic and associated hazards (tephra fall and lava flow inundation) that may occur during future eruptions. Due to lack of information on major explosive eruptions from Beerenberg, we use data from Hekla volcano to simulate possible future explosive eruptions and tephra fall on the island. The results include volcanic hazard maps for different scenarios from which an exposure-based analysis for the main infrastructure locations on Jan Mayen is conducted. These results further reveal areas on the island that are most likely to be affected by future eruptions, in case one of the explored scenarios occurs. The study is an example on how future hazard assessment of remote volcanic islands can be approached, with the aim of emergency planning and risk mitigation in case of future volcanic eruptions, helping decision making in regard to land use and planning.

GEOLOGICAL SETTING

Jan Mayen (**Figure 1**) is a volcanic island that lies in the Norwegian-Greenland sea at the junction between the Jan Mayen ridge microcontinent, the Jan Mayen fracture zone transform fault and the Mohn's ridge, a continuation of the Mid-Atlantic ridge divergent plate boundary (**Figure 1A**). The most striking feature of the island is the glacier-capped volcano Mt. Beerenberg (**Figure 1B**, **Figure 2A**). Mt. Beerenberg constitutes the N part of Jan Mayen whereas the central and S parts form an isthmus and a ridge extending 30 km towards the SW from Mt. Beerenberg respectively (**Figure 1B**). The S and central parts of Jan Mayen reach a maximum altitude of 769 m and consist of the ridge, coastal lava plateaus and beaches. Two possible origins have been suggested for the volcanism on Jan Mayen, namely, the Mohn's ridge magmatism acting across the Jan Mayen transform fault (Trønnes et al., 1999), or a small mantle plume (Elkins et al., 2016).

Previous paleomagnetic studies show that all exposed rocks on Jan Mayen are normally magnetized. This suggests that all exposed magmatism on the island of Jan Mayen belongs to the Brunhes epoch and is therefore younger than approximately 700 ka (Fitch et al., 1965; Cox 1969; Imsland 1978; Cromwell et al., 2013). Rock samples from Jan Mayen have been dated by the ^{40}Ar/39Ar incremental heating method to give an age range from 460.9 ± 55.8 ka to present day (Cromwell et al., 2013) and agree with the paleomagnetic data.

At least five eruptions have occurred on the island since it was discovered early in the 17th century (Imsland 1978). An eruption is suggested to have taken place on the NE flank of Beerenberg between 1,650 and 1882 based on changes in topographic maps (Imsland 1978). In 1732, a Surtseyan eruption occurred in the sea off the SW flank of Beerenberg and formed the Eggøya tuff cone (Gjerløw et al., 2015) and most of the sandy SE shores of Midt-Jan (**Figure 1B**). This eruption also covered large parts of the island in a blanket of tephra (approximately 10 cm thick at the location of Olonkin City). In 1818, an eruption was reported in the sea off the S flank of Mt. Beerenberg (Scoresby 1820). The 1970 (Siggerud 1972) and the 1985 (Imsland 1986) eruptions were effusive to mixed style eruptions (where lava makes up between 5 and 95%,

and tephra makes up between 5 and 95% of the erupted DRE volume, e.g. Thorarinsson 1981); estimated pyroclastic deposit volume was in excess of 5% of the total DRE volume for the 1970 eruption, and "the volume of tephra was relatively large" (Imsland 1986, page 51) in the 1985 eruption. Both eruptions occurred on the NE flank of Mt. Beerenberg.

Holocene volcanism on Sør-Jan (**Figure 1B**), represented by the Inndalen Formation, mainly consists of lava flows, coulees and domes, scoria cones, and shallow marine to coastal phreatomagmatic deposits (**Figure 2B,C**); one littoral cone has also been identified on a coastal lava plateau on Sør-Jan. The Inndalen Formation on Midt-Jan, the isthmus between Nord- and Sør-Jan, is characterized by scoria cones and shallow marine to coastal phreatomagmatic deposits. On Nord-Jan (**Figure 1B**) the Holocene eruptions were mostly effusive, forming mainly lava flows with some scoria cones, on the flanks of Mt. Beerenberg (Fitch et al., 1965; Imsland 1978). Fumaroles were reported from the central crater of Beerenberg after the eruptions in 1970 and 1985. However, glacial cover and subsequent erosion in the summit regions of Beerenberg make identification of Holocene eruptive products difficult. The composition of the Inndalen formation is mostly in the range of trachybasalt to basalt, but also includes basanite, basaltic trachyandesite, trachyandesite and trachyte (Imsland 1978; Gjerløw et al., 2015). Imsland (1978) estimated that around 5.35 km^3 dense rock equivalent (DRE) has been erupted during Holocene times and single eruption sizes are between 0.007 and 0.5 km^3 DRE (Siggerud 1972).

Investigations of soil sections (Gjerløw et al., 2015) and sediment cores (Gjerløw et al., 2016), indicated that medium to large explosive volcanic eruptions, such as the eruption that produced the Eggøya tuff cone with a Volcanic Explosivity Index (VEI) of 3-4, are a relatively rare phenomenon on Jan Mayen. Only two sediment horizons containing significant concentrations of juvenile tephra originating from Jan Mayen have been found within the Holocene interval in nearby marine sediment cores (Gjerløw et al., 2016). One of these originated from the 1732 Eggøya eruption whereas the other originated from an unidentified source on Jan Mayen dating back to approximately 10.3 ka BP (Gjerløw et al., 2016). Soil sections on Jan Mayen show locally distributed coarse-grained pyroclasts with morphologies consistent with magmatic fragmentation, and more widely distributed fine-grained pyroclasts with morphologies consistent with hydromagmatic fragmentation (Gjerløw et al., 2015). In the Greenland ice cores, several cryptotephra layers allocated to Jan Mayen have been recorded, dating back to 63 ka BP (Abbot and Davies 2012) and it has been shown that remote cryptotephra layers such as these are associated with explosive sub-Plinian to Plinian eruptions (Plunkett et al., 2020 and reference therein). Marine sediment cores from the N and E of Iceland also record cryptotephra layers from Jan Mayen (e.g., Brendryen et al., 2010; Gjerløw et al., 2016). Most of the tephra identified to be from Jan Mayen is of trachybasalt and basaltic trachyandesite compositions; basalt, tephrite/basanite and trachyandesite are also present but are less common. The presence of tephra so far from the source indicates that explosive basaltic eruptions have occurred on Jan Mayen in the past and that the potential for future explosive basaltic eruptions exists.

METHODS AND DATA PRESENTATION

Volcanic Susceptibility

Analysis of volcanic susceptibility, defined as the spatial probability of a vent opening, conditional to eruption occurrence (Martí and Felpeto 2010), is widely accepted to be the first step when preparing mapping of volcanic hazards in an active volcanic field. In this study, we use the QVAST (QGIS for VolcAnic SuscepTibility) tool developed by Bartolini et al. (2013), an open-source plugin for Quantum GIS, to estimate volcanic susceptibility. QVAST requires the coordinates of the structural elements used for spatial modelling as input. In our study, we use the locations of Holocene mafic vents and trachyte domes as input. These coordinates are included in the **Supplementary Material**. The spatial distribution of volcanic-structural elements was obtained from fieldwork, maps from Imsland (1978), satellite images and aerial photographs from the Norwegian Polar Institute. QVAST uses the location of volcanic vents and structures, such as domes, faults, and dykes, to calculate a Probability Density Function (PDF) that describes the spatial probability of vent opening. QVAST uses a smoothing parameter, or bandwidth, to define how the probabilities should be spread over the susceptibility map. A small bandwidth will concentrate the probability closer to input coordinates whereas a large bandwidth will spread the probability over a larger area. The QVAST tool provides two different methods for estimating the optimal bandwidth: the Least Square Cross Validation (LSCV) and the Sum of Asymptotic Mean Square Error (SAMSE). Both methods have previously been applied in other volcanic areas (Cappello et al., 2012; Connor et al., 2012; Bartolini et al., 2013, 2014, 2015), and in this study both methods are used. After selecting the bandwidth, a PDF is generated for each considered volcanic structure. When multiple sources are considered, the final PDF for the entire area is obtained by combining them in a non-homogenous Poisson process with different weights assigned to each PDF (Bartolini et al., 2013). **Table 1** contains the various input parameters used for the QVAST tool. Through an expert elicitation process (Aspinall 2006; Neri et al., 2008), we decided to assign equal weight to each vent, fissure, and dome location, since most of them do not have accurate formation dates. To give each vent location equal weight, the two input layers, "mafic vents" and "trachyte vents" were given 95.1 and 4.9% weights respectively (based on the number of input co-ordinates in each of the layers) when they were combined into the final PDF.

Recurrence Rate

The temporal recurrence rate of a volcanic system or volcanic field is estimated based on the number of eruptions and time (where the average recurrence rate between eruptions λ_t is the number of eruptions divided by time) (Connor and Conway 2000). The eruption record of Jan Mayen is incomplete, but the calculations still provide constraints for the minimum recurrence

TABLE 1 | Input parameters used for the QVAST (QGIS for VolcAnic SuscepTibility) tool.

QVAST input	Input file/value
Digital elevation model (DEM)	DEM from the Norwegian Polar Institute, see references
Vent co-ordinates	File containing input co-ordinates of Holocene mafic vents
Vent co-ordinates 2	File containing input co-ordinates of trachytic domes
Weights	95.1% for file 1 and 4.9% for file 2
Least square cross validation (LSCV)	
Bandwidth basalt LSCV (m)	1805
Bandwidth trachyte	2856
LSCV (m)	
Sum of Asymptotic Mean Square Error (SAMSE)	
Bandwidth basalt	4266
SAMSE (m)	
Bandwidth trachyte	1,067
SAMSE (m)	

rates. The recurrence rate for the 10,000-year period of the Holocene was calculated using 82 eruptions, based on the currently visible monogenetic vents. The historical time was set to 370 years (because the first historical map was published around 1,650) and the recurrence rate was calculated with five eruptions because at least five eruptions have been documented in this period. In some contexts, the probability of occurrence of different eruptive scenarios can be estimated using a Poisson distribution (e.g., Dzierma and Wehrmann, 2010; Biass and Bonadonna, 2013). It should be noted that the use of a Poisson distribution in such a manner is a simplification and requires that eruptions are strictly independent of each other, can occur only one at a time and that the probability of an event occurring does not depend on the time that has already elapsed since the last event occurred (Biass and Bonadonna 2013). With these considerations in mind, the probability of a volcanic eruption within a selected forecast time window can thus be estimated according to the exponential distribution in the equation below.

$$F_{exp}(t) = 1 - e^{-\lambda t}$$

Where t is the time window we want to forecast for, and λ is the annual eruption rate calculated for Holocene and historic time. By using this equation, we can calculate the probability of occurrence for a given volcanic eruption scenario on Jan Mayen for a chosen forecast period.

The vents were characterized according to eruptive style as effusive, Strombolian to Vulcanian, Surtseyan and dome forming. Probabilities were calculated based on eruptions during the Holocene and eruptions in historical times extending back to 1,650, and the probability of different eruptive styles was also calculated.

Eruption Scenarios

Previous published work on the volcanism of Jan Mayen (Siggerud 1972; Imsland 1978; Gjerløw et al., 2015) coupled with this study suggests the following likely eruption scenarios: Strombolian to Vulcanian eruptions, effusive lava forming (including lava domes) eruptions, Surtseyan eruptions and sub-Plinian to Plinian eruptions from Beerenberg. Secondary, or littoral, explosions can also occur where lava flows enter the sea. With these eruption styles, we would expect the following volcanic hazards: ash fall (i.e., tephra fall), lava flows, lahars and jökulhlaups, pyroclastic density currents and ballistic projectiles. Ballistic projectiles are not included in this hazard assessment due to the scarcity field of data. Lahars and jökulhlaups are not included since the thickness of the glaciers and the subglacial topography of Beerenberg is unknown, and this leads to great uncertainties in the source parameters and input data for computer simulations. Volcanic islands such as Jan Mayen can also be susceptible to flank collapse and associated hazards, such as tsunamis and lateral blasts (Paris et al., 2017 and references therein). However, the scope of this paper is to focus on the most common volcanic scenarios based on geological observations on the island and in distal tephra records. The whole marine shelf of Jan Mayen has not been mapped in a sufficient detail to recognize offshore volcanic formations or massive gravity currents deposits. Thus, in this hazard assessment we exclude major events like gravity collapse of the flanks of Beerenberg and offshore eruptions as we believe these subjects deserve further study.

Accumulation of Ash Fall on the Ground

TephraProb is a Matlab toolbox used to produce scenario–based probabilistic hazard assessments for tephra accumulation on the ground for Plinian-type and Vulcanian-type eruptions (Biass et al., 2016a). The toolbox is based on the advection diffusion model "Tephra2" (Bonadonna et al., 2005). The model requires the following input parameters: vent location, wind data (direction, altitude, and speed), plume height, eruption mass, total grain size distribution, pumice and lithic density, a distribution of mass in the plume and other parameters such as particle aggregation, eddy constant, diffusion coefficient and fall-time threshold. For a more detailed description of the toolbox, see Biass et al. (2016b). For each scenario, ranges of critical input parameters are identified. TephraProb then runs Tephra2 in a probabilistic way, stochastically sampling eruption and wind conditions at each run of Tephra2. Outputs are scenario-based probabilistic hazard maps that contour the spatial probability of exceeding a fixed threshold of tephra accumulation.

From distal tephra records it is clear that there is potential for explosive eruptions from Mt. Beerenberg. However, we have no eruption source parameters relating directly to these eruptions. We have created two different eruption scenarios for explosive eruptions from Mt Beerenberg and we have chosen to use the 1947 and 2000 eruptions of Hekla (Biass et al., 2014) in Iceland as analogues for explosive Mt. Beerenberg eruptions. The first scenario is a mixed style eruption on the flank of Mt. Beerenberg, such as the 1970 eruption. This scenario represents the larger end of explosive flank eruptions. Descriptions of the 1970 eruption of Jan Mayen (Siggerud 1972) demonstrate similarities to the Hekla 2000 eruption (Höskuldsson et al., 2007); both eruptions started with an explosive phase, with plume heights of at least 11 km (Jan

TABLE 2 | Input values for the Tephraprob toolbox. The input includes grainsize information (in phi scale), aggregation coefficient (the percentage of grains below four phi/63 micron grain size that aggregate to form larger grains), diffusion coefficient and fall time threshold; see Biass and Bondanna, 2013 for more detail regarding Tephraprob.

Tephraprob input	Hekla 2000	Hekla 1947	Vulcanian 1 km	Vulcanian 5 km	Vulcanian 10 km
Plume height (km asl)	6–16	16–30	1	5	10
Mass (x109 kg)	6.9–69	69–351	2×10^{-5}	5×10^{-2}	0.9
Grain size range (phi scale)	–6-11	–5-11	–4-8	–4-8	–4-8
Median grain size (phi scale)	–3-3	–1-1	–1-1	–1-1	–1-1
Standard deviation (phi scale)	1–2	1–2	1–3	1–3	1–3
Aggregation coefficient (%)	0.2–0.8	0.2–0.8	0.3–0.7	0.3–0.7	0.3–0.7
Density lithic (kg/m^3)	2600	2600	2700	2700	2700
Density pumice (kg/m^3)	1,000	1,000	1,000	1,000	1,000
Density deposit (kg/m^3)	—	—	1,200	1,200	1,200
Diffusion coefficient (m/s^2)	112.5	112.5	4900	4900	4900
fall time threshold (s)	1,563	1,563	5000	5000	5000
Duration (h)	0.5–1	0.5–1	—	—	—

Mayen) and 12 km (Hekla), they were both fissure eruptions and, following the initial explosive phase, produced lava flows (0.5 km^3 in the case for Jan Mayen and 0.188 km^3 in the case for Hekla). For this scenario, the summit region was chosen as the vent since the volcanic susceptibility in the glaciated regions of Beerenberg is highly uncertain, and since this allows for easier comparison with the second scenario. The second scenario is for an explosive summit eruption. Such eruptions are expected to occur less frequently than flank eruptions (Gjerløw et al., 2016) and have more evolved composition, as seen both in the composition of rocks near the summit and in the steeper slopes close to the summit region (Fitch et al., 1964). The Hekla 1947 eruption was used as an analogue for larger summit eruptions since this represents an eruption with longer repose time, larger volume and more evolved composition than the Hekla 2000 scenario.

Historic volcanism on Jan Mayen (effusive, mixed, and explosive) indicates that the mass ranges for the eruptions ranges between 1.85×10^{10} to 1.32×10^{12} kg. Simulations of the Hekla 2000 and 1947 eruption scenarios by Biass et al. (2014) provide good analogues for VEI 2-3 mixed eruptions in case of the Hekla 2000 scenario and VEI 3-4 eruptions in the case of the Hekla 1947 scenario (with masses of 6.9×10^9 kg to 6.9×10^{10} kg and 6.9×10^{10} kg to 3.5×10^{11} kg respectively). The plume heights of the Hekla 2000 and Hekla 1947 eruption scenarios (measured to 6–16 km and 16–30 km respectively), when combined with Jan Mayen wind patterns, also allow us to determine the effect of wind directions at different altitudes and during different seasons. Wind conditions for Jan Mayen were obtained from the National Oceanic and Atmospheric Administration, National Centers for Environmental Prediction/National Center for Atmospheric Research (NOAA NCEP/NCAR) reanalysis database (Kalnay et al., 1996) for a 10-year period from 2005 to 2015. This database provides four daily measurements of wind velocity and direction for 17 pressure levels at a resolution of 2.5°latitude x 2.5°longitude.

The Hekla 2000 and 1947 scenarios were run to simulate an eruption with Mt. Beerenberg as the source vent, input parameters are given in **Table 2**. Wind conditions at Mt. Beerenberg show little seasonality below 15 km altitude (see **Supplementary Material**), so for the Hekla 2000 scenario we used 1,000 runs (to achieve stable and reproducible results) using all year wind data. From 15 to 20 km altitude there is a change in wind directions and speeds in summer (May to August). During the summer months, the median wind velocity drops from 15 to 20 m/s to <10 m/s, and the median wind direction (the direction the wind is blowing towards) also changes from around 90° to around 270°. Therefore, the Hekla 1947 scenario, with a plume height of up to 30 km, was separated into three parts featuring 1,000 runs each. The first part used wind conditions from all the seasons, the second part used wind conditions for the summer season (May-August) and the third part used the wind conditions for the rest of the year (September-April).

On Sør-Jan, Strombolian to Vulcanian tephra producing eruptions are the most frequent style of eruption (Imsland 1978). A soil section from Jan Mayensfield (**Figure 3A**) shows that at least four eruptions of this type have occurred near the airfield during the Holocene. These tephra layers have thicknesses of 7–13 cm and consist mainly of coarse ash to lapilli. They killed the vegetation that they covered, and most likely originate from vents and fissures around 2–4 km distance away from the soil section. None of these eruptions have been studied in sufficient detail to obtain eruption source parameters, thus the La Fossa volcano, Vulcano, Italy, was used as an analogue for a single Vulcanian eruption on Sør-Jan with eruption source parameters from Biass et al. (2016b) (**Table 2**). For this scenario, the highest probability cell given by the QVAST analysis was selected as the vent location. This eruption scenario uses three different plume-heights, 1, 5 and 10 km (above sea level), and the simulations were run 1,000 times for each plume height using all year wind data. The Tephra2 simulations for these scenarios yield almost circular distribution and show mostly local distribution of tephra within a few km of the vent. For the 10 km plume, the radius of the zone around the eruptive vent having 50% probability or more of tephra accumulation reaching more than 10 kg/m^2 in a violent Strombolian to Vulcanian eruption is 2 km. This distance is similar to the distance from vents seen at the soil section by Jan Mayensfield with similar tephra accumulation. Since the Vulcanian to Strombolian eruptions can occur all over the island it is unfortunately very time consuming and hardware dependent to be able to produce probabilistic maps (with simulations of many different vent locations and then weighing the simulations according to the spatial probability).



FIGURE 3 | (A) Soil section near Jan Mayensfield airfield. The orange-brown layers are vegetation that was buried by tephra. The top of this section is around half a meter of reworked tephra from the Eggøya eruption. **(B)** Satellite photo (source: Google, DigitalGlobe) of the area surrounding Olonkin City with the main infrastructure (white square). Trolldalen (orange lines), the east side of Borga (white lines) and Borgdalen (purple lines) depict the boundaries of small valleys that serve as natural drainage paths. The anchor shows Båtvika that serves as a landing site for small boats. The valleys have lava flows running through them. These lavas have constructed the coastal plateau that Olonkin City stands on and another plateau S of Båtvika.

Because of this we instead made a qualitative map using the spatial probability from the SAMSE map, and then applied a 2 km buffer to each of the hazard levels. This allows visualization of both the spatial probability and the localized and circular tephra dispersal seen both in the simulations and fieldwork.

Tephra fall maps were compiled for tephra accumulations of 1, 10 and 100 kg/m2, corresponding to ash accumulation thicknesses of 1 mm, 1 cm, and 10 cm respectively. The highest threshold would be expected to seriously disrupt road and air transport, produce loss of visibility, and have implications for health. Equipment with external cooling would require frequent cleaning of intake filters (Wilson et al., 2012; Scaini et al., 2013) and that exposed to ash would experience abrasion and increased wear. The lowest level of ash accumulation would also be expected to cause equipment damage, reduce visibility, and impede air traffic to the island (Guffanti et al., 2010).

Lava Inundation

Q-LavHA (Quantum-Lava Hazard Assessment) is an open-source GIS plugin to simulate lava flow inundation probability from regularly distributed eruptive vents on a Digital Elevation Model (DEM) (Mossoux et al., 2016). For this study, version 2.0 of Q-LavHA was used alongside a DEM from the Norwegian Polar Institute with a spatial resolution of 25 m (Norwegian Polar Institute 2014). Q-LavHA requires a probability density function map (such as those generated by QVAST) to weight the probability of lava flows at a particular vent location. All the input co-ordinates used to generate the PDF maps are shown in **Figure 4A**. The LSCV susceptibility map (**Figure 4B**) concentrates the volcanic susceptibility in a smaller area around the volcanic vents than the SAMSE susceptibility map (**Figure 4C**). We therefore chose to use the SAMSE PDF as input for the lava inundation simulations, because this PDF can compensate for vents destroyed by erosion and hidden by glaciers or younger volcanic units. Before starting, the lava flows in the simulation must be characterized. The height correction factor Hc, which represents the average thickness of the lava flow front, was set at 5 m. The correction factor Hp, representing the maximum thickness of the lava flow, was set to 10 m. These factors allow the simulated lava flows to overcome small topographic obstacles and depressions. The program was set to make it more likely that the simulated lava would follow the steepest downward slope. In order to stop the simulations, a maximum flow length of 3,500 m was selected. Lava flows on Sør-Jan typically reach distances of 2.5–3.5 km before entering the sea, and lava flows from the 1970 eruption on Nord-Jan reached up to 3 km length. Finally, the minimum susceptibility value from the PDF map to simulate vents was set to zero so that all vents were simulated and the distance between all simulated vents was set to 100 m. The model was then run for 1,500 iterations to achieve stable and reproducible results, as recommended by Mossoux et al. (2016). The various input parameters for Q-LavHA are shown in **Table 3**.

Pyroclastic Density Currents From Surtseyan Eruptions

Deposits of previous eruptions have shown that pyroclastic density currents affected areas up to 2 km distance from Surtseyan eruptive vents. This type of eruption could occur all

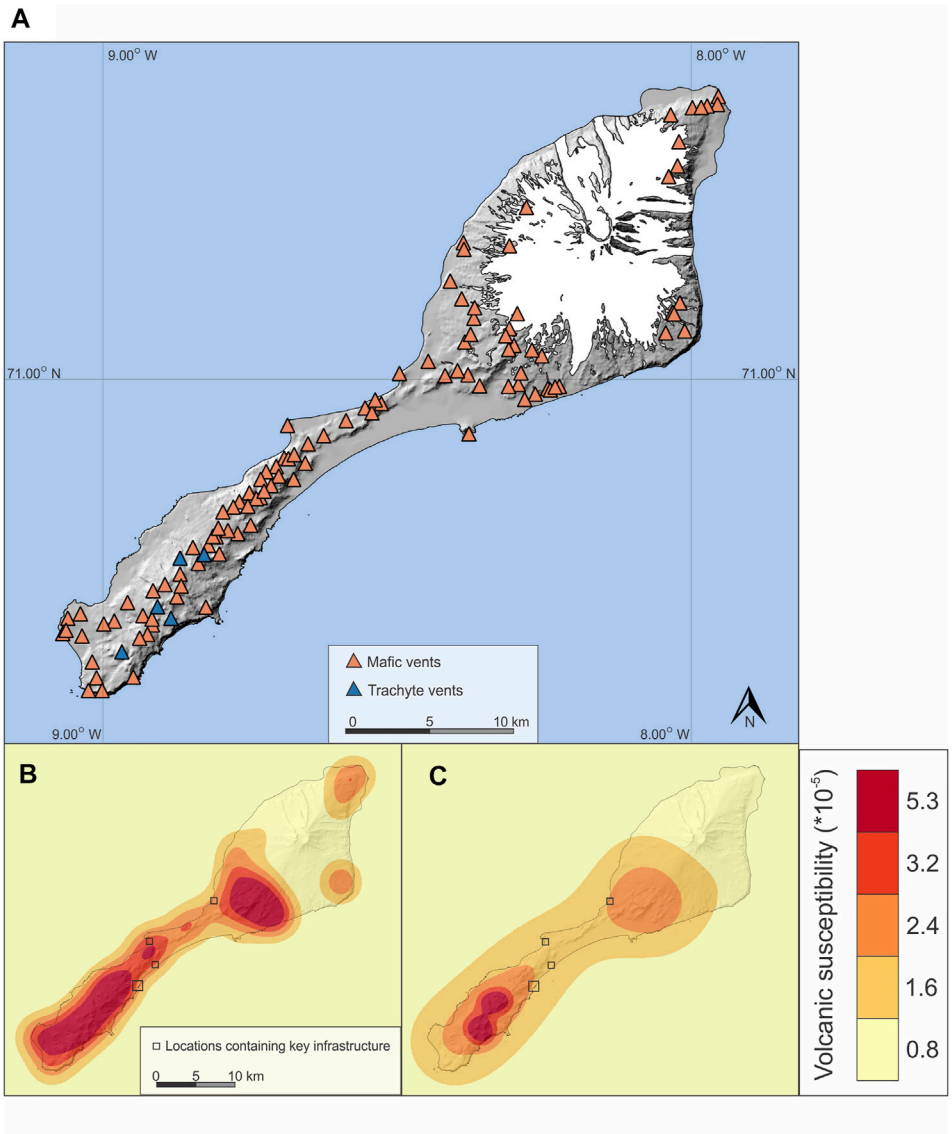


FIGURE 4 | (A) Location of trachyte domes and mafic vents used as input for the volcanic susceptibility maps. Spatial probability maps using: **(B)** a Least Square Cross Validation bandwidth and **(C)** a Sum of Asymptotic Mean Square Error bandwidth). Small black squares represent four locations (Olonkin City, Jan Mayensfield and meteorological station, Kvalrossbukta, and Gamlemetten) containing key infrastructure. The volcanic susceptibility used as a scale in B and C is the probability, in the case of a volcanic eruption, that a given 25 × 25 cm cell will host an eruption. All the cells are colored based on the assigned threshold values.

around the shoreline of Jan Mayen. However, the SE and NW flanks of Beerenberg seem less susceptible to such hazards due to a smaller amount of visible recent volcanic vents in these areas. A susceptibility zone for pyroclastic density currents from Surtseyan eruptions was created in QGIS by defining areas within 2 km of the shoreline and below 200 m altitude in order to eliminate areas located above steep sea cliffs.

Volcanic Threat Analysis

To assess whether or not the monitoring of a volcano is sufficient, it is essential to quantify the threat posed by the volcano to its surroundings. Volcanoes with low threat require less monitoring than volcanoes with high threat. We have applied the method of the National Volcano Early Warning System (NVEWS) devised by Ewert et al., 2005 for this purpose. The NVEWS was originally developed for volcanoes in the United States but has, in recent years, been applied to other volcanic areas such as Nisyros (Kinvig et al., 2010), Tenerife (Martí et al., 2012) and Deception Island (Bartolini et al., 2014). The NVEWS requires a systematic assessment of various exposure and hazard factors and multiplies these factors to produce a threat score. The final threat score was used to characterize single volcanoes into one out of five different threat categories ranging from very high to very low. The NVEWS also suggests appropriate monitoring for each of the different threat categories.

TABLE 3 | Input for the Q-LavHA (Quantum-Lava Hazard Assessment) plugin.

Q-LavHA input	Input file/value
Digital elevation model (DEM)	DEM from the Norwegian Polar Institute, see references
Probability density function (PDF)	Sum of Asymptotic Mean Square Error PDF
Minimum PDF value to simulate	0
Height correction (Hc in m)	5
Lava flow thickness (Hp in m)	10
Probability to the square	Enabled
Maximum length (m)	3500
Iterations	1,500
Vent distance (m)	100

Qualitative Volcanic Hazard Map

An integrated qualitative hazard map was produced using the hazard maps created for lava inundation and qualitative Vulcanian to Strombolian tephra hazard. The hazard zones in each of these maps were given values (described in the following paragraph) and these values were summed to produce the final qualitative hazard map. This methodology has been used in other locations and volcanic islands such as Deception Island (Bartolini et al., 2014), El Hierro (Becerril et al., 2014), San Miguel in El Salvador (Jiménez et al., 2020) and La Garrotxa in Spain (Bartolini et al., 2015).

For lava flows, areas were given scores based on the lava flow inundation probability. Areas with probability scores $<0.075 \times 10^{-07}$ were given a score of 1, areas with $0.075–0.15 \times 10^{-07}$ were given a score of 2, areas with $0.15–0.225 \times 10^{-07}$ were given a score of 3, areas with $0.225–0.3 \times 10^{-07}$ were given a score of four and areas above 0.3×10^{-07} were given a score of 5. For qualitative Vulcanian to Strombolian tephra hazard, the hazard levels were given scores from one to 5 (1 for lowest, 5 for highest). Four different hazard levels are used in the integrated qualitative hazard map: three or less, 4–5, 5–6 and 7 and more.

RESULTS

Volcanic Susceptibility

The volcanic susceptibility maps produced by QVAST (**Figure 4**), using vent locations as input (**Figure 4A**), represent areas with a range of probabilities of hosting a new vent. Pixels with a high probability value have a high chance of hosting the next eruptive vent and vice versa. Two spatial probability maps were produced, one using LSCV (**Figure 4B**) and one using SAMSE (**Figure 4C**) bandwidth calculations. The maps show a high probability of vent openings on Sør-Jan due to the presence of many vents along the volcanic ridge. On Mt. Beerenberg, probabilities have only been calculated on the lower elevations where volcanic vents are visible. Current glacier cover masks possible existing Holocene vents. Furthermore, the Mt. Beerenberg summit crater is not included in these calculations since we do not have any accurate estimates of how often it has erupted during the Holocene.

Recurrence Rate

The recurrence rate of eruptions on Jan Mayen during the Holocene is calculated to be between 7.5×10^{-3} and 8.5×10^{-3} volcanic events per year, and the average repose time is between 133 and 117 years. With a 370-year historical period and five eruptions, we calculate 1.35×10^{-2} volcanic events per year and an average repose time of 73 years.

Eruption Scenarios

The Holocene eruptions on Jan Mayen can be divided into two main groups based on composition - mafic (alkali-basaltic) and trachytes. The mafic eruptions occurred all over Jan Mayen and produced lava flows, scoria cones and tuff cones (**Figure 2A,C**, **Figure 4A**). Based on the currently visible vents, between two and seven eruptions have been Surtseyan and have produced tuff cones. Approximately 20 have produced only scoria cones whereas around 50 have produced lava flows with varying amounts of spatter and scoria. From the 75 to 85 eruptions that have been estimated to have occurred during the Holocene, seven produced trachyte domes (**Figure 2C** and **Figure 4A**) and these domes have been observed on only Sør-Jan. For an estimated 75–85 Holocene eruptions based only on counting the currently visible vents, the average eruption volume is 0.06–0.07 km^3 DRE. Of the Holocene eruptions, approximately 61% are classified as mainly effusive, approximately 24% are classified as Strombolian to Vulcanian, approximately 8% are classified as dome forming and approximately 6% are classified as Surtseyan (**Table 4**). During the historical period of Jan Mayen, from 1,650 up to the present day, there have been at least five eruptions, one of which was mostly effusive but also had significant explosive phases, and it is thus characterized as having a mixed style of eruption. In the historical period 60% of the eruptions are classified as effusive, 20% as Surtseyan, and 20% as mixed eruptions (**Table 4**).

Accumulation of Ash Fall on the Ground

Results from TephraProb calculations are presented in **Figure 5** using eruption parameters from the Hekla 2000 and 1947 eruptions in case of an eruption from Mt. Beerenberg (Biass et al., 2014) and Vulcanian eruptions with 5 and 10 km plume heights. The 1 km plume simulations for Vulcanian eruptions did not produce tephra fall exceeding the chosen thresholds and are therefore excluded from the maps. **Figure 5A,B** show the results from calculations using all year wind data, whereas **Figure 5C,D** use wind data from May-August and September-April respectively. A comparison of the probability isolines in **Figure 5C,D** shows that a summer eruption gives more circular isolines versus oval isolines for the rest of the year. The seasonality shows that a Mt. Beerenberg eruption occurring in the summer months (May, June, July, and August) is more likely to distribute tephra towards the SW (i.e., in the direction of Olonkin City) than a similar eruption occurring during the rest of the year. The likelihood of ash fall exceeding 10 kg/m^2 is shown in **Figure 5** A-E, whereas the likelihood of exceeding ash fall of 1 kg/m^2 is shown in **Figure 5F**. The qualitative hazard from tephra fall from Strombolian to Vulcanian eruptions based on a circular distribution and the spatial probabilities is shown in **Figure 5G**. In **Table 5** results from TephraProb on the probability of airborne volcanic ash exceeding 1 kg/m^2, 10 kg/m^2 and 100 kg/m^2 for the

TABLE 4 | The probability (in %) of occurrence of eruptions with given eruption scenarios for the next 10 and 100 years (P10 and P100, respectively), based on Holocene and historical volcanism. * The non-historical records are most likely not complete and the number of events, λ, P10 and P100 therefore represent minimum values.

Holocene Scenario	*Completeness (year)	Number of events	% Of total	λ	P10	P100
Eruption	10000	82	100.00	0.0082	0.0787	0.5596
Effusive	10000	50	60.98	0.0050	0.0480	0.3412
Strombolian/Vulcanian	10000	20	24.39	0.0020	0.0192	0.1365
Hydromagmatic	10000	5	6.10	0.0005	0.0048	0.0341
Trachyte dome	10000	7	8.45	0.0007	0.0067	0.0473
Historical						
Eruption	370	5	100	0.0135	0.1264	0.7411
Effusive	370	3	60	0.0081	0.0758	0.4447
Mixed eruption	370	1	20	0.0027	0.0253	0.1482
Hydromagmatic	370	1	20	0.0027	0.0253	0.1482

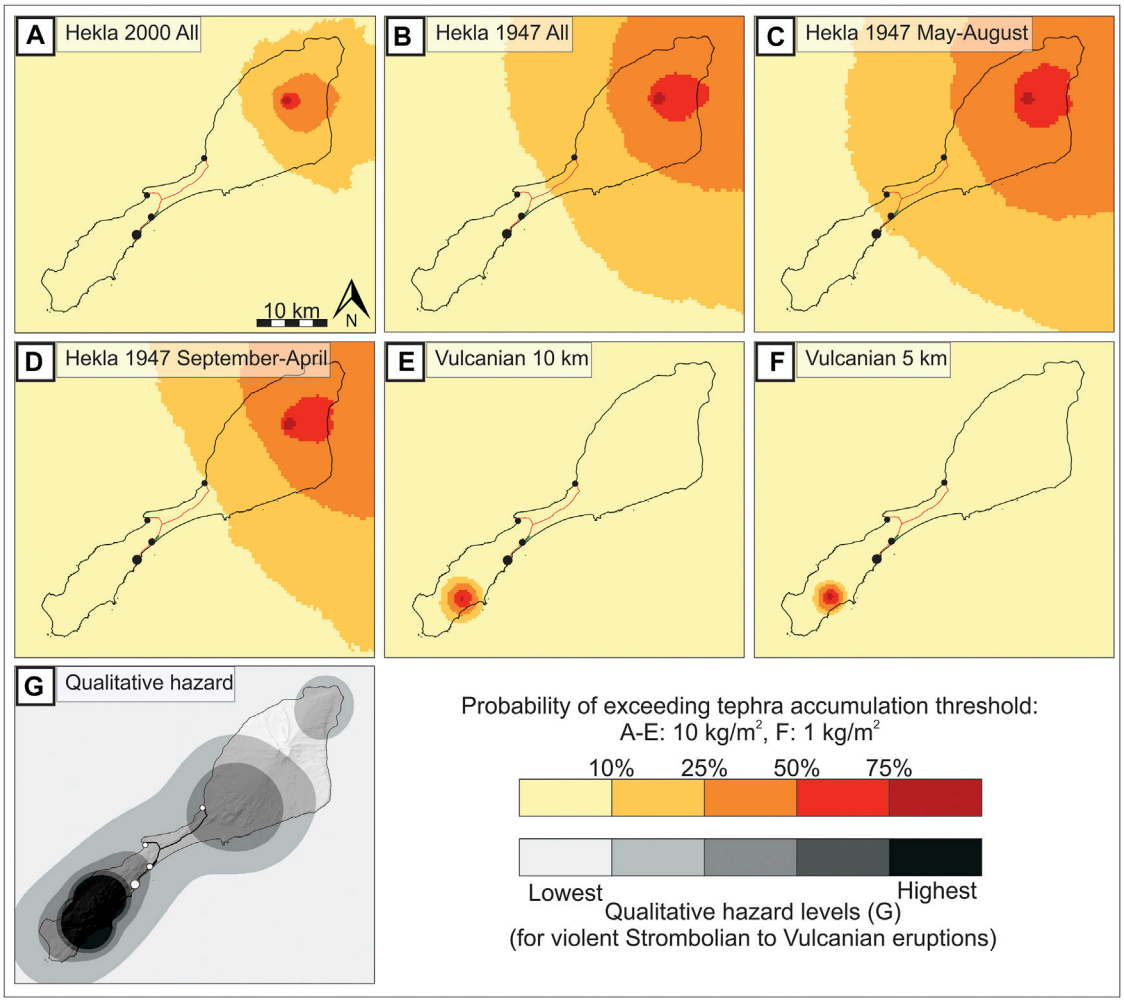


FIGURE 5 | The probability of exceeding an accumulation of 10 kg/m^2 of tephra fall deposit for the following eruption scenarios from the Beerenberg central crater: **(A)** Hekla 2000 all seasons, **(B)** Hekla 1947 all seasons, **(C)** Hekla 1947 May-August, and **(D)** Hekla 1947 September-April. **(E)** and **(F)** represent Vulcanian eruption scenarios involving a single Vulcanian explosion and a plume height of 10 and 5 km respectively. For (F) the threshold for tephra accumulation was set at 1 kg/m^2 because there was no probability of exceeding a 10 kg/m^2 threshold. Black dots represent primary infrastructure locations and red lines represent the road network. **(G)** Represents the qualitative tephra hazard for Vulcanian to Strombolian eruptions. White dots represent primary infrastructure locations and black lines represent the road network.

TABLE 5 | The probability of exceeding given mass loads for the different eruptive scenarios at four locations containing key infrastructure on Jan Mayen.

	—	Olonkin city	Jan mayensfield	Kvalrossbukta	Gamlemetten
Hekla 2000	100 kg/m^2	0.0%	0.0%	0.0%	0.2%
	10 kg/m^2	0.3%	0.7%	0.9%	3.8%
	1 kg/m^2	4.7%	5.7%	6.0%	11.6%
Hekla 1947 all year	100 kg/m^2	0.9%	0.9%	1.0%	4.7%
	10 kg/m^2	5.5%	7.2%	7.6%	15.3%
	1 kg/m^2	14.5%	16.4%	16.6%	25.8%
Hekla 1947 summer	100 kg/m^2	1.4%	1.8%	2.0%	8.0%
	10 kg/m^2	9.3%	10.9%	11.2%	20.4%
	1 kg/m^2	20.0%	22.4%	22.5%	35.2%
Hekla 1947 September-April	100 kg/m^2	0.0%	0.3%	0.3%	2.6%
	10 kg/m^2	3.8%	4.4%	4.4%	9.8%
	1 kg/m^2	9.0%	11.0%	11.0%	20.1%
Vulcanian 5 km	10 kg/m^2	0.0%	0.0%	0.0%	0.0%
	1 kg/m^2	0.0%	0.0%	0.0%	0.0%
	0.05 kg/m^2	22.4%	11.0%	6.1%	0.1%
Vulcanian 10 km	10 kg/m^2	0.0%	0.0%	0.0%	0.0%
	1 kg/m^2	27.7%	18.2%	11.1%	2.3%
	0.05 kg/m^2	55.5%	43.6%	35.7%	23.4%

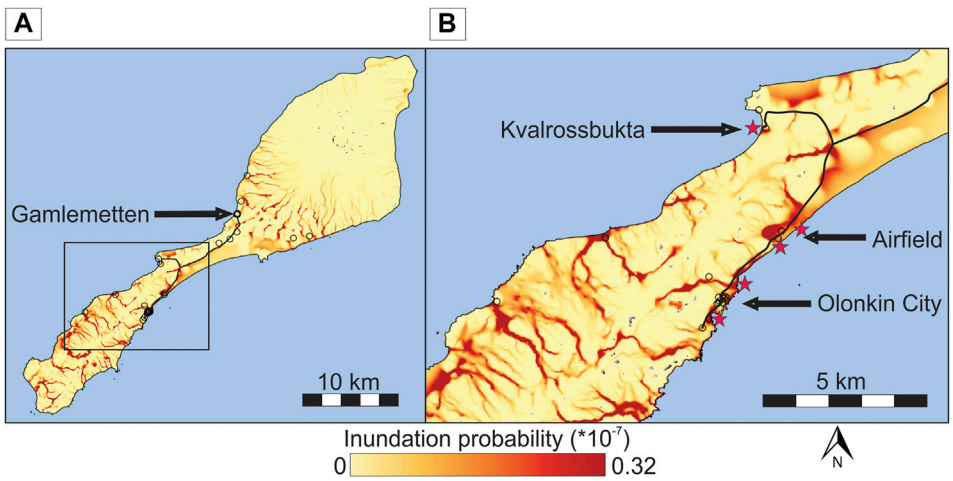


FIGURE 6 | Maps showing the probability of lava flow inundation, where pale yellow represents a lower probability of inundation and red represents a higher probability. Locations with infrastructure are represented with black circles, and stars show areas with a relatively high likelihood of lava flows entering the sea. The black box in shows the location of the inset map.

locations of Olonkin City, Jan Mayen airfield, Kvalrossbukta and Gamlemetten are given.

Lava Inundation

The lava flow hazard map produced with Q-LavHA (**Figure 6A**) shows the relative probability of single cells to be inundated by lava flows. Lava flow inundation is controlled by topography, resulting in an increased probability of lava inundation in natural watersheds due to channeling effects. The map also shows locations near Olonkin City and the airfield with high inundation probability that could serve as entry points for lava flows entering the sea (**Figure 6B**), that could produce littoral explosions (Mattox and Mangan 1997). The highest probabilities are found along the central ridge in Sør-Jan, where the volcanic susceptibility is highest (**Figure 4**).

Pyroclastic Density Currents From Surtseyan Eruptions

The entire primary infrastructure on Jan Mayen lies within the susceptibility zone for pyroclastic density currents from Surtseyan eruptions (**Figure 7**), but Gamlemetten (**Figure 1B**) is probably the least susceptible of the infrastructure locations since it stands at a height of 40 m above sea level on a plateau with steep cliffs down to the sea.

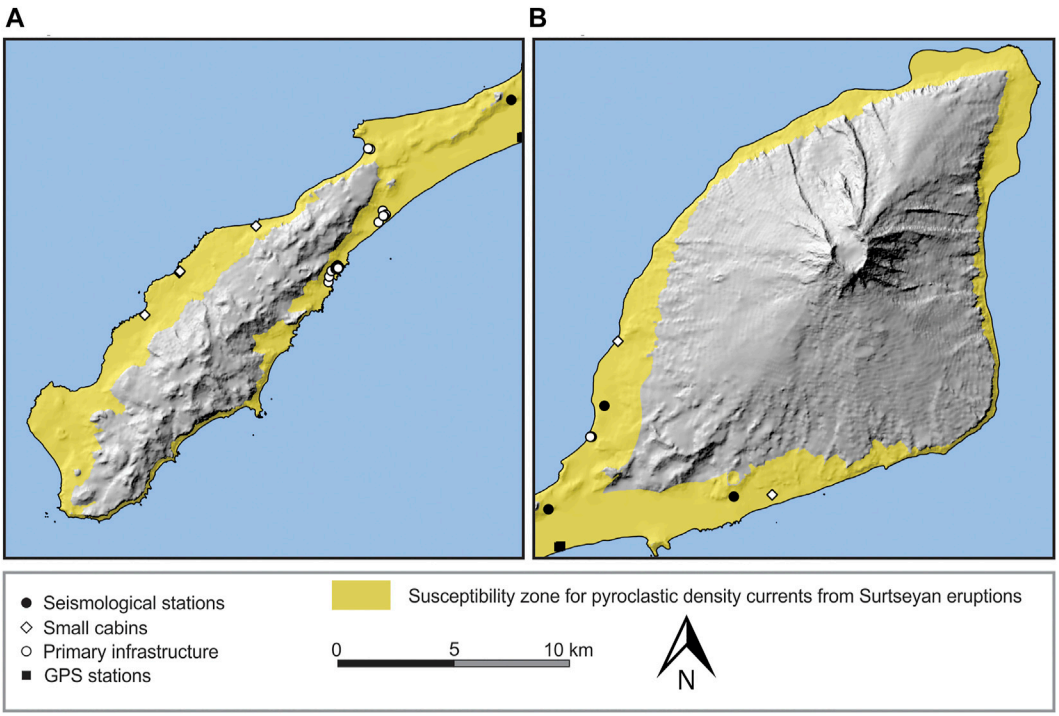


FIGURE 7 | (A and B) Zones within 2 km of the coastline and below 200 m a.s.l. that are most susceptible to pyroclastic density currents from Surtseyan eruptions.

National Volcano Early Warning System

The following section describes the scoring factors used for the NVEWS threat rating and shows the criteria used for determining each of the scores (**Table 6**); each number in the table corresponds to the same number in the text. For a more detailed description of the scoring system, the reader is referred to Ewert et al., 2005. Lack of data caused uncertainty in some of the parameters, and for these scores we have assigned maximum and minimum scores in an attempt to quantify the uncertainty.

Hazard Factors

Jan Mayen Island comprises volcanic domes, monogenetic fissures and lavas, and the summit region of Beerenberg has a morphology akin to a stratovolcano (1). One Holocene Surtseyan eruption has been reconstructed and has a VEI of 3–4 2) and 3) (Gjerløw et al., 2015). In addition, although no deposits from large explosive eruptions (VEI >4) have been found, the possibility of such eruptions cannot be excluded (4).

The historical period for Jan Mayen starts in the early 17th century, and during this time at least five eruptions have occurred on the island (Gjerløw et al., 2015). During the Holocene, 75–85 eruptions are estimated to have occurred (5). Pyroclastic density currents have been documented from an eruption in 1732 (Gjerløw et al., 2015) (6) and several recent lava flows extend to the current coastline of the island (7). Lahar and tsunami deposits have not been documented during the Holocene (8) and (9). The 1732 eruption was Surtseyan and several tuff cones along the coastline show that this type of eruption has occurred multiple times in the past (10). Sector collapse has not been documented from Jan Mayen, but the shape of the eastern and northern flanks of Beerenberg suggest that sector collapse could have occurred in the past (11). Beerenberg is covered by glaciers that could serve as a source of water for lahars and glacier floods (12) in the event of a subglacial eruption. Since the last eruption in 1985 (Imsland 1986), there have been several earthquakes (13), but no ground deformation has been documented (14), and fumaroles were observed from the summit region of Beerenberg for a few years following the eruption (15).

Exposure Factors

The first exposure factors consider the population on or near the volcano. The first factor is the volcano population index within 30 km of the volcano. The population usually consists of 18 people and can reach as high as 100 when cruise ships stop and allow tourists ashore: the Volcano Population Index ranges from 1.25 to 2 (16). There is no population directly downslope of the glaciers of Beerenberg (17) and no fatalities have been recorded during the eruptions on Jan Mayen (18). When the 1970 eruption was first observed, Olonkin City was evacuated for a short period while the possible threat to the population and infrastructure was evaluated (19). There are no airports for jet-airplanes near Jan Mayen (20), but international flight corridors pass within 200 km of Jan Mayen (21). Power and transport infrastructure on Jan Mayen is of limited scope and only intended for local use (22) and (23). Finally, most of the island is a nature reserve (s4) and Holocene volcanic deposits cover more than 25% of the exposed area of the island (25).

TABLE 6 | Jan Mayen National Volcano Early Warning System (NVEWS) scoring factors.

Hazard factors	Score high	Score low
(1) Volcano type	1	1
(2) Maximum known VEI	1	1
(3) Explosive (VEI>3) activity past 5 ka	1	1
(4) Major explosive VEI>4) past 5 ka	1	0
(5) Recurrence rate	4	3
(6) Holocene pyroclastic flows	1	0
(7) Holocene lava flows	1	1
(8) Holocene lahars	0	0
(9) Holocene tsunamis	0	0
(10) Hydrothermal explosion potential	1	1
(11) Sector collapse	1	0
(12) Primary lahar source	1	1
(13) Observed seismic unrest	1	1
(14) Observed ground deformation	0	0
(15) Observed fumarolic or magmatic degassing	1	0
Sum of hazard factors	15	10
Exposure factors		
(16) Population within 30 km	2	1.25
(17) Population downslope	0	0
(18) Historical fatalities	0	0
(19) Historical evacuations	1	1
(20) Local aviation	0	0
(21) Regional aviation	3.73	3.43
(22) Power infrastructure	0	0
(23) Transport infrastructure	0	0
(24) Sensitive areas	1	1
(25) Volcano area of island	1	1
Sum of exposure factors	8.73	7.68
Threat rating	130.05	76.8
Score level	Very high	High

The scores for Beerenberg, and for Jan Mayen as a whole, are the same and the final threat score calculated for the high values was 130, whereas the final threat score for the low values was 77. The low value falls within the high threat rating (64–123, Ewert et al., 2005), whereas the high value falls within the very high threat rating (123–324). These values are compared here with volcanoes in the United States. The high score is similar to Long Valley Caldera, the low score is similar to Mount Cleveland and in between these scores, are volcanoes such as Mount Katmai, Novarupta and Pavlof (Ewert et al., 2005).

Qualitative Volcanic Hazard Map

The qualitative hazard map (**Figure 8**) based on tephra fall from Strombolian to Vulcanian eruptions and lava flow inundation shows that the highest hazard levels are in the valleys and watersheds on Sør-Jan and on the SW flank of Beerenberg. The highest hazard areas (that score >7) comprise mainly natural drainages and topographic depressions with high scores 5) for lava inundation that also score 3 or higher for Vulcanian to Strombolian tephra hazard. Areas with hazard scores of 6-7 comprise areas with the highest score in Vulcanian to Strombolian tephra hazard, as well as natural drainages and topographic depressions in areas with a score of three for Vulcanian to Strombolian tephra hazard. The areas with hazard scores of four to five comprise mostly areas with a score of three–four in Vulcanian to Strombolian tephra hazard. The lowest hazard areas, with scores of 0–3, generally score lowest in lava inundation and in the two lowest categories for qualitative Vulcanian to Strombolian tephra hazard. Due to the lack of data, and therefore possible underestimation of the hazard from the glaciated regions of Beerenberg, this part of the island is excluded from the qualitative hazard map.

Areas on Midt-Jan where the roads between Kvalrossbukta, Olonkin City and Gamlemetten run have scores in the two lowest categories (<3 and 4–5). Olonkin City is mainly located in an area with hazard scores of four to five but contains parts with scores of 6-7, and the roads leading from Olonkin City run through areas with hazard scores >7. The meterological station NE of Olonkin City lies in an area with hazard score >7, whereas Jan Mayensfield airfield lies mostly in an area with a hazard score of 4–5. Kvalrossbukta is in an area with hazard score of 0–3 and the plateau where Gamlemetten is located is in an area with a hazard score of four to five.

DISCUSSION

Exposure Based Analysis

Based on past activity on Jan Mayen, the most likely future eruption scenarios are effusive eruptions and Strombolian to Vulcanian explosive eruptions. Surtseyan eruptions producing large amounts of tephra, such as the Eggøya eruption in 1732 (Gjerløw et al., 2015), are less common but have occurred a few times during the Holocene. The trachyte domes on Sør-Jan are interpreted to be of Holocene age (Imsland 1978), and this form of volcanism is less common. Gjerløw et al. (2016) did not find evidence for explosive summit eruptions at Beerenberg. There was fumarolic activity from the summit crater after the 1970 and 1985 eruptions, but the eruptions themselves were fissure eruptions on the flank of the volcano. Although no evidence for Holocene eruptions from the summit vent has been found, the volcano is most likely not extinct. Following the volcanic eruptions of 1970 and 1985, fumarolic activity was seen located on the inner rim of the central crater (Gjerløw et al., 2016), and steam was seen rising from the central crater during the 1970 eruption (Siggerud 1972), indicating some degree of volcanic activity from the central crater of Beerenberg. The frequency of sub-Plinian to Plinian eruptions from the Beerenberg summit is most likely low, but the hazards from such an eruption still need to be considered. An exposure-based analysis of volcanic hazards on Jan Mayen Island shows that the main infrastructure at risk is: Olonkin City, the Jan Mayensfield airfield and meteorological station, the cabin and natural harbor at Kvalrossbukta, the cabins at Gamlemetten, and the road network of the island.

Olonkin City (**Figure 1B**) is in an area with an intermediate probability of vent opening (**Figure 4B,C**), but it is also proximal to areas with high probabilities and lies approximately 3 km from one of the areas with highest probability (to the SW). Multiple fissure eruptions have occurred along the center of the ridge, just 1.5 km NE of Olonkin City, during the Holocene and Olonkin City is located on a lava flow from one of these (**Figure 4A**). If a violent Strombolian to Vulcanian eruption occurred in this area,

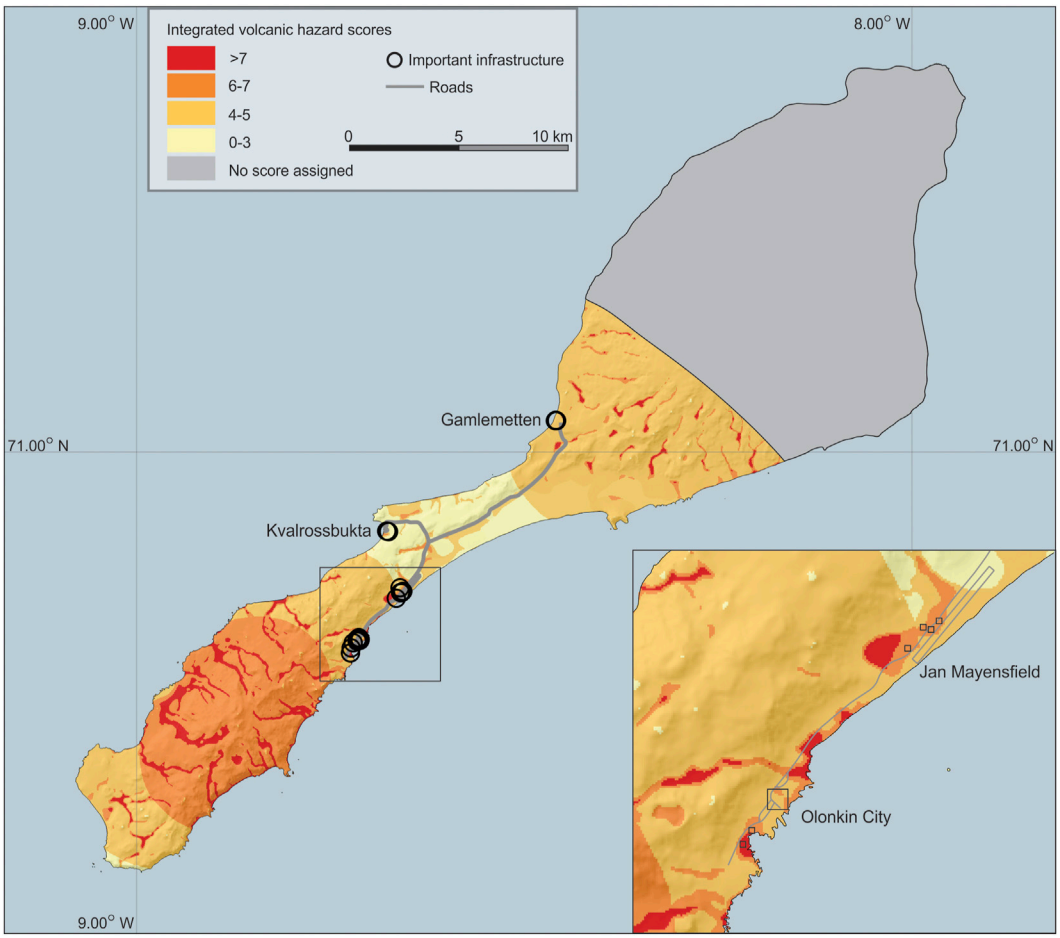


FIGURE 8 | Qualitative volcanic hazard map for Jan Mayen (based on tephra fall from Strombolian to Vulcanian eruptions and lava flow inundation). The expanded section of the map shows the airfield (elongated rectangle), Olonkin City (large square) and other buildings (small squares). Scores of >7 are given to areas with high scores in two or more of the other hazard maps. Scores of 5-6 are given to areas with high scores in one hazard and intermediate in one. Scores of four to five are given to areas that have intermediate scores in one hazard. Scores of three or less are given to areas with low scores in both hazards. The grey area is excluded from the scoring due to lack of data in the subglacial parts of Beerenberg.

tephra fall would be expected in Olonkin City (**Figure 5**). The Hekla 2000 scenario for a Beerenberg explosive eruption (**Table 5**) gives a 4.7% probability of exceeding a mass load of 1 kg/m^2, 0.3% probability of exceeding a mass load of 10 kg/m^2 and 0% of exceeding 100 kg/m^2. The Hekla 1947 scenarios (all year, summer, and September-April) give 9–20% probability of exceeding a mass load of 1 kg/m^2, 3.8–9.3% probability of exceeding a mass load of 10 kg/m^2 and 0.0–1.4% probability of exceeding 100 kg/m^2. In terms of the possibility of lava inundation, the SW part of Olonkin City is in a low probability area whereas the NE part is in a medium probability area. As seen in **Figure 6**, Olonkin City has areas with high probability located both on the NE and on the SW sides. The steep cliffs to the NW and shoreline to the SE mean that the Olonkin City is effectively surrounded by areas with high probability of lava inundation. An eruption starting at Trolldalen, located N of Olonkin City, could potentially inundate Olonkin City, and cut off evacuation routes. A lava flow coming from the NE side of Borga (**Figure 3B**) could cut off on-foot evacuation routes or by boat in Båtvika, directly S of Olonkin City, (**Figure 3B**). A lava flow in Borgdalen (**Figure 3B**) would also cut off on-foot evacuation routes but would keep Båtvika and the possibility of evacuation by small boats open. As seen in **Figure 6**, both Båtvika and the area NE of Olonkin City have domains with high lava flow inundation probabilities, which could serve as points for lava flows entering the sea. Should such a scenario occur, Olonkin City could also be subjected to tephra fall and ballistic projectiles from littoral explosions (e.g., Mattox and Mangan 1997).

The Jan Mayensfield airfield and meteorologic station (**Figure 1B**) are in an area with an intermediate probability of vent opening (**Figure 4B,C**). If a violent Strombolian to Vulcanian eruption occurs within a few kilometers of these locations, tephra fall would be expected. The Hekla 2000 scenario for a Beerenberg explosive eruption (**Table 5**) gives a 5.7% probability of exceeding a mass load of 1 kg/m^2, 0.7% probability of exceeding a mass load of 10 kg/m^2 and 0% of exceeding 100 kg/m^2. The Hekla 1947 scenarios (all year,

summer, and September-April) give 11–22.4% probability of exceeding a mass load of 1 kg/m^2, 4.4–10.9% probability of exceeding a mass load of 10 kg/m^2 and 0.3–1.8% probability of exceeding 100 kg/m^2. With respect to the possibility of lava inundation, there are natural drainage paths on the NE and SW sides, and both the meteorological station and the airfield are in high probability areas. These sites are vulnerable if an effusive eruption occurs on the ridge to the NE near these locations (**Figure 6**). The Jan Mayensfield airfield and meteorologic station are both situated on Holocene lava flows that entered the sea. The lava inundation probability map shows that nearby areas have high inundation probabilities near the sea (**Figure 6**). Therefore, both locations could also be subjected to tephra fall and ballistic projectiles from littoral explosions if nearby lava flows reach the sea.

Kvalrossbukta (**Figure 1B**) has an intermediate probability of vent opening (**Figure 4B,C**) and, should a violent Strombolian to Vulcanian eruption occur within a few kilometers of Kvalrossbukta, tephra fall would be expected. The Hekla 2000 scenario for a Beerenberg explosive eruption (**Table 5**) gives a 6.0% probability of exceeding a mass load of 1 kg/m^2, 0.9% probability of exceeding a mass load of 10 kg/m^2 and 0% probability of exceeding 100 kg/m^2. The Hekla 1947 scenarios (all year, summer, and September-April) give 11.0–22.5% probability of exceeding a mass load of 1 kg/m^2, 4.4–11.2% probability of exceeding a mass load of 10 kg/m^2 and 0.3–2.0% probability of exceeding 100 kg/m^2; higher probabilities apply for an eruption during the summer months. Kvalrossbukta has a low probability of lava inundation (**Figure 6**), but towards the center of the bay the probability increases in a small area and reaches a high probability. The cabin in Kvalrossbukta is in an area with intermediate probability.

Gamlemetten (**Figure 1B**) is located on a plateau with intermediate probability of vent openings (**Figure 4B,C**). For the Beerenberg explosive scenarios, Gamlemetten has the highest probabilities of experiencing significant tephra fall due to its location on the flank of Beerenberg (**Table 5**; **Figure 5**). The Hekla 2000 scenario gives an 11.6% probability of exceeding a mass load of 1 kg/m^2, 3.8% probability of exceeding a mass load of 10 kg/m^2 and 0.2% probability of exceeding 100 kg/m^2. The Hekla 1947 scenarios (all year, summer, and September-April) give 20.1–35.2% probability of exceeding a mass load of 1 kg/m^2, 9.8–20.4% probability of exceeding a mass load of 10 kg/m^2 and 2.6–8.0% probability of exceeding 100 kg/m^2; the probabilities are higher during the summer months. The plateau that Gamlemetten stands on has a low probability of being inundated by lava flows (**Figure 6**), due to the natural watersheds running on either side of it.

The road network on Jan Mayen is located along the coastal cliffs and crosses the island in two locations (**Figure 1B**). The spatial probability of vent openings is low to intermediate along the road network (**Figure 4B,C**). The probabilities for tephra fall vary with distance from Beerenberg; higher probabilities apply closer to Beerenberg for the Hekla 1947 and Hekla 2000 scenarios. For Vulcanian eruptions the probabilities vary with distance from the source (**Figure 5**). The roads pass through areas with high probability of lava inundation (**Figure 6**) between Olonkin City, Jan Mayensfield and Kvalrossbukta, and an effusive eruption on the ridge between Kvalrossbukta and Olonkin City could block the road between these points.

The cabins on the S flank of Beerenberg (**Figure 1B**) are more exposed to tephra fall from the Beerenberg summit eruption scenarios than any other infrastructure (**Figure 5**); probabilities exist of exceeding the 10 kg/m^2 thresholds of more than 25% for the May-August Hekla 1947 scenario. Some of the cabins located on the SW coast of Jan Mayen are in areas with high probabilities of lava inundation (**Figure 6**).

Qualitative Volcanic Hazard

From the qualitative volcanic hazard map (**Figure 8**), we find the highest volcanic hazard in the central parts of Sør-Jan where valleys and watersheds are in proximity to the highest concentration of Holocene volcanic vents. Fieldwork revealed several coarse-grained tephra layers, and several lava flows forming coastal plateaus on Sør-Jan. On Midt-Jan, the hazard level is generally low; there are no Holocene lava flows in this area and only a few scoria cones. On the SW flank of Beerenberg, the hazard score is four to five whereas watersheds and valleys have higher scores, but there is higher uncertainty in these hazard scores due to the glacier cover on Beerenberg. In this area, there are several young lava flows, coarse-grained tephra layers and scoria cones.

NVEWS

The minimum and maximum scores assigned to Jan Mayen and Beerenberg in the NVEWS methodology (**Table 6**) are in the category of a high to very high threat volcano although, if the international flight corridor near Jan Mayen is excluded, the threat rating is moderate for the minimum and high for the maximum score. The scores in **Table 6** represent maximum and minimum values. With a more complete knowledge regarding past eruptions and precursors it would be possible to narrow the gap between these scores, and most likely conclude with a moderate score in between the two extreme values. Furthermore, the fact that a remote island with a small population such as Jan Mayen could result in a high to very high threat rating, points to issues with the NVEWS system. The solution to this may be to remove the factor "regional aviation" from the equation. This reduces the maximum and minimum scores to result in a moderate to high threat. This air corridor is quite isolated and it should be possible to re-route the traffic in it to other locations in the case of an eruption providing justification for this approach. According to Ewert et al., 2005 (page 20), high and very high threat volcanoes should be "well monitored in real time". More specifically, they suggest that the monitoring network should provide the ability to track changes in real-time and to develop, test, and apply models of ongoing and expected activity. For moderate threat volcanoes the "monitoring should provide the ability detect and track pre-eruptive and eruptive changes in real-time, with a basic understanding of what is occurring" (Ewert et al., 2005 page 20), and include a seismic network with at least six stations, continuous deformation measurements with at least six stations as well as regular surveys in addition to monitoring gas and hydrology. The current

network on Jan Mayen consists of four seismological stations and a single deformation monitoring point. The recommendations from the NVEWS guidelines show that the volcano monitoring on Jan Mayen is closer to the recommendations for a low threat volcano and not sufficient for a moderate threat volcano.

Hazard Assessment on Remote Volcanic Islands

Hazard assessments on volcanic islands are like other volcanic areas in many aspects, but some special considerations need to be done compared to other locations:

- A major part of conducting hazard assessment is to study the past activity of the volcano or volcanic field (Marti, 2017). This can be difficult in remote islands due to limited historical data (for example Deception Island was discovered in 1820 and Jan Mayen in 1,608). There are often large holes in the historical records due to their remoteness and the records that do exist can often be inaccurate or limited. Furthermore, it can be difficult and even dangerous to conduct fieldwork to study past eruptions; on Jan Mayen the NE flank of Beerenberg is only accessible by boat, and 5 people from the University of London died when their boat capsized due to fall winds in 1961 (Barr 2003). The remoteness also often means that strict safety measures are required, and this can set limitations to what kind of studies can be performed.
- When conducting spatial analysis and volcanic susceptibility these islands have the added consideration of vents obscured by the sea and vents removed by coastal erosion. In addition, volcanic islands in the Arctic and Antarctic can also have glacier cover capable of obscuring vents underneath the ice. Due to these issues volcanic susceptibility maps from volcanic islands should be interpreted with care as they can be inaccurate due to the missing and obscured vents.
- As mentioned in the 2018 update to the NVEWS scores (Ewert et al., 2005), many volcanic islands have high to moderate scores due to aviation. In the update they have shown aviation scores in addition to the total threat scores NVEWS scores. However, when remote volcanic islands such as Jan Mayen (this study) and Deception Island (Bartolini et al., 2014) end up in the high-to very-high threat ratings it can be useful to further separate the scores since they can be inflated due to tourism and aviation. One suggestion could be to also create a local hazard score (where the impact of regional aviation and tourism is removed).
- The use of qualitative volcanic hazard maps is a topic of debate for the scientific community, and some would argue that qualitative maps can be misleading for decision makers in risk assessment (Thompson et al., 2015). However, volcanic islands such as Jan Mayen and Deception Island often have scarce or missing data of past eruptions, and as such it is not possible to produce detailed and precise quantitative maps (Marti, 2017). In these cases, the use of qualitative maps can be appropriate and provide guidance on future land use and planning (e.g., Bartolini et al., 2015; Jiménez et al., 2020).

Recommendations

Our suggestion is to improve the volcano monitoring on Jan Mayen to bring it more in line with the recommendations from the NVEWS. Installing additional monitoring equipment prior to the next eruption could help improve the knowledge of expected precursors. Improving the monitoring would potentially assist with early eruption-detection, give the team on the island time to evacuate and help to issue aviation warnings, especially considering that the high-threat score achieved for Jan Mayen results mostly from the proximity of the island to polar air routes. There are arguments for relocating Olonkin City from its current location to areas less exposed to lava inundation and tephra fall from Strombolian to Vulcanian eruptions (**Figure 8**). However, most of the low hazard areas have other issues (such as wave erosion, topographic constraints, exposure to extreme wind and the presence of ephemeral lakes and streams) that complicate such a relocation. We therefore recommend that emergency response plans are made for the volcanic hazards most likely to affect Olonkin City, namely lava flows and tephra fall from Strombolian to Vulcanian eruptions.

Caveats

All the probabilities and hazard maps shown in this study are conditional on the occurrence of a specific eruption scenario, which differs among the different hazardous events considered (lava inundation, tephra fallout, etc...). For example, **Table 5** shows the probability of exceeding thresholds of tephra accumulation for different eruption scenarios, but the probabilities in this table are conditional upon the assumption that the associated eruption scenario occurs.

Since our source parameters are limited to volume, we use analogues for sub-Plinian or Vulcanian eruptions from Jan Mayen. The proximal deposits show that Strombolian to Vulcanian eruptions do occur and, due to the presence of pre-Holocene Jan Mayen tephra in distal regions, we include sub-Plinian to Plinian eruptions to account for potentially larger eruptions. There is, however, no guarantee that future eruptions on Jan Mayen will fit with the selected scenarios and input parameters; eruptions with different source parameters and vent locations could have different hazard patterns to the simulated ones, thus it is important to run short time hazard analysis once unrest is detected. Future work should also take into considerations the vents susceptibility calculations (and its effect on eruptive styles such as in case of Surtseyan eruptions) with lava and tephra modelling (Becerril, 2009, 2017; Selva et al., 2010; Bartolini et al., 2015; Thompson et al., 2015; Sandri et al., 2016).

This study focuses on the spatial probability of vent openings, lava flows and tephra fall on Jan Mayen, but the selected eruption scenarios can also generate additional hazards such as ballistic projectiles, pyroclastic density currents, lahars and volcanic gases. The spatial maps could underestimate the probability of vent openings on Nord-Jan due to glacier cover and all around the island along the coastlines due to erosion, and thus overestimate the probability of vent opening along the ridge on Sør-Jan. Because of this, we chose to use the SAMSE probability map for modeling the lava inundation probability (**Figure 4C**); this spreads the probability over a larger area than the LSCV map, and should give more accurate spatial

probabilities on Sør-Jan. However, this approach also results in decreased probabilities of vent openings on the SW and NE flanks of Beerenberg and decreases the probability of lava flow inundation in the Q-LavHA simulations in these areas.

The number of vents used in calculating the recurrence rates for the Holocene represents the number of vents that are visible at the surface at the present. However, there is no guarantee that this represents the true number of Holocene eruptions as older vents might have been eroded or have been obscured by glaciers or newer eruptions. And as we have mentioned above, the submarine shelf of Jan Mayen has not been mapped in sufficient details to draw any conclusion on number of vents offshore.

On Beerenberg, the DEM represents the glacier surface. However, since studies have shown that lava flows with access to a snow/ice boundary and its substrate tend to flow along this contact (e.g., Edwards et al., 2015; Oddsson et al., 2016), simulated lava flows from the glaciated parts of Beerenberg must be carefully interpreted since this fact is not integrated in the present version of Q-LavHA.

CONCLUSION

We present a volcanic hazard assessment of Jan Mayen Island. The most likely hazards to occur on the island, based on past activity, are tephra fall and lava flows. The qualitative hazard and probability maps show that both hazards could affect Olonkin City and the rest of the infrastructure on Jan Mayen if an eruption occurred in their vicinity. We recommend that volcano monitoring on Jan Mayen is enhanced. Explosive eruptions from the Beerenberg summit vent are low frequency events and give low probabilities of significant ash-fall on Sør-Jan. However, it should be kept in mind that that such events can quickly become cross border hazard with special attention of the aviation industry (Titos et al., 2021). The results of this study are useful for hazard assessment and risk mitigation, planning of evacuation routes for different eruption scenarios, and designation of future land use on the island. The results should be interpreted with care because 1) they depend on an incomplete catalogue of historical and Holocene eruptions, 2) some scenarios are based on analogues with other volcanoes and 3) the qualitative map is based on hazard scores that are conditional to different scenarios. This study exemplifies a hazard assessment approach for remote volcanic islands.

DATA AVAILABILITY STATEMENT

The original contributions presented in the study are included in the article/**Supplementary Material**, further inquiries can be directed to the corresponding author.

AUTHOR CONTRIBUTIONS

ÁH, RP and EG, are responsible for the project idea behind this article. EG, SBa, SBi and SM prepared the input data and ran the computer models. EG drafted the manuscript and designed figures. EG, ÁH, SBa, SBi, SM, JG, RP and JM contributed with writing, feedback and suggestions to the article and approved the submitted manuscript.

FUNDING

This study was part of EG's Ph.D. project and was financed by the Centre for Geobiology at the University of Bergen and the Nordic Volcanological Center at the University of Iceland. This paper has been written while the lead author has been employed at UiT the Arctic University of Norway. This study has also been part of the VeTools and EVE projects (EC ECHO Grants SI2.695524 and 826292).

ACKNOWLEDGMENTS

We want to acknowledge the Jan Mayen personnel for their hospitality and assistance during fieldwork, and the Norwegian Polar Institute for supplying aerial photos and map data. We thank Antonio Paonita and Valerio Acocella for the editorial handling and the three reviewers for comments that helped us improve the quality of this article.

SUPPLEMENTARY MATERIAL

The Supplementary Material for this article can be found online at: https://www.frontiersin.org/articles/10.3389/feart.2022.730734/full#supplementary-material

REFERENCES

Abbot, P. M., and Davies, S. M. (2012). Volcanism and the Greenland Ice-Cores: the Tephra Record. *Earth. Sci. Rev.* 115, 179–193. doi:10.1016/j.earscirev.2012.09.001

Aspinall, W. P. (2006). "Structured Elicitation of Expert Judgment for Probabilistic hazard and Risk Assessment in Volcanic Eruptions," in *Statistics in Volcanology. Special Publication of IAVCEI 1*. Editors H. M. Mader, S. G. Coles, C. B. Connor, and L. J. Connor (Geological Society of London, UK.

Barr, S. (2003). *Jan Mayen Norges Utpost I Vest, Øyas Historie Gjennom 1500 År. Schibsted Forlag*. Oslo, Norway.

Bartolini, S., Bolós, X., Martí, J., Pedra, E. R., and Planagumà, L. (2015). Hazard Assessment at the Quaternary La Garrotxa Volcanic Field (NE Iberia). *Nat. Hazards* 78, 1349–1367. doi:10.1007/s11069-015-1774-y

Bartolini, S., Cappello, A., Martí, J., and Del Negro, C. (2013). QVAST: a New Quantum GIS Plugin for Estimating Volcanic Susceptibility. *Nat. Hazards Earth Syst. Sci.* 13, 3031–3042. doi:10.5194/nhess-13-3031-2013

Bartolini, S., Geyer, A., Martí, J., Pedrazzi, D., and Aguirre-Díaz, G. (2014). Volcanic hazard on Deception Island (South Shetland Islands, Antarctica). *J. Volcanology Geothermal Res.* 285, 150–168. doi:10.1016/j.jvolgeores.2014.08.009

Becerril, L. (2009). *Volcanic hazard Approach and Their Effects on Coastal Areas in Canary Islands*. Master Thesis book.ISBN: 978-84-694-0895-7

Becerril, L., Bartolini, S., Sobradelo, R., Martí, J., Morales, J. M., and Galindo, I. (2014). Long-term Volcanic hazard Assessment on El Hierro (Canary Islands). *Nat. Hazards Earth Syst. Sci.* 14, 1853–1870. doi:10.5194/nhess-14-1853-2014

Becerril, L., Martí, J., Bartolini, S., and Geyer, A. (2017). Assessing Qualitative Long-Term Volcanic Hazards at Lanzarote Island (Canary Islands). *Nat. Hazards Earth Syst. Sci.* 17, 1145–1157. doi:10.5194/nhess-17-1145-2017

Biass, S., and Bonadonna, C. (2013). A Fast GIS-Based Risk Assessment for Tephra Fallout: the Example of Cotopaxi Volcano, Ecuador. *Nat. Hazards* 65, 477–495. doi:10.1007/s11069-012-0378-z

Biass, S., Bonadonna, C., Connor, L., and Connor, C. (2016a). TephraProb: a Matlab Package for Probabilistic hazard Assessment of Tephra Fallout. *J. Appl. Volcanol* 5, 10. doi:10.1186/s13617-016-0050-5

Biass, S., Bonadonna, C., di Traglia, D., Pistolesi, M., Rosi, M., and Lastuzzi, P. (2016b). Probabilistic Evaluation of the Physical Impact of Future Tephra Fallout Events for the Island of Vulcano. *Italy. Bull. Vulcanol* 78, 37. doi:10.1007/ss0445-016-1028-1

Biass, S., Scaini, C., Bonadonna, C., Folch, A., Smith, K., and Höskuldsson, A. (2014). A Multi-Scale Risk Assessment for Tephra Fallout and Airborne Concentration from Multiple Icelandic Volcanoes - Part 1: Hazard Assessment. *Nat. Hazards Earth Syst. Sci.* 14, 2265–2287. doi:10.5194/nhess-14-2265-2014

Bonadonna, C., Connor, C., Houghton, B. F., Connor, L., Byrne, M., Laing, A., et al. (2005). Probabilistic Modeling of Tephra Dispersal: Hazard Assessment of a Multiphase Rhyolitic Eruption at Tarawera, New Zealand. *J. Geophys. Res.* 110. doi:10.1029/2003JB002896

Brendryen, J., Haflidason, H., and Sejrup, H. P. (2010). Norwegian Sea Tephrostratigraphy of marine Isotope Stages 4 and 5: Prospects and Problems for Tephrochronology in the North Atlantic Region. *Quat. Sci. Rev.* 29, 847–864. doi:10.1016/j.quascirev.2009.12.004

Cappello, A., Neri, M., Acocella, V., Gallo, G., Vicari, A., and Del Negro, C. (2012). Spatial Vent Opening Probability Map of Etna Volcano (Sicily, Italy). *Bull. Volcanol* 74, 2083–2094. doi:10.1007/s00445-012-0647-4

Connor, C. B., and Conway, F. M. (2000). "Basaltic Volcanic fields," in *Encyclopedia of Volcanoes*. Editors H. Sigurdsson, B. F. Houghton, S. R. McNutt, H. Rymer, and J. Stix (Academic Press), 330–343.

Connor, L. J., Connor, C. B., Meliksetian, K., and Savov, I. (2012). Probabilistic Approach to Modeling Lava Flow Inundation: a Lava Flow hazard Assessment for a Nuclear Facility in Armenia. *J. Appl. Volcanol* 1, 1–19. doi:10.1186/2191-5040-1-3

Cox, A. (1969). Geomagnetic Reversals. *Science* 163, 237–245. doi:10.1126/science.163.3864.237

Cromwell, G., Tauxe, L., Staudigel, H., Constable, C. G., Koppers, A. A. P., and Pedersen, R.-B. (2013). In Search of Long-Term Hemispheric Asymmetry in the Geomagnetic Field: Results from High Northern Latitudes. *Geochem. Geophys. Geosyst.* 14, 3234–3249. doi:10.1002/ggge.20174

Dzierma, Y., and Wehrmann, H. (2010). Eruption Time Series Statistically Examined: Probabilities of Future Eruptions at Villarrica and Llaima Volcanoes, Southern Volcanic Zone, Chile. *J. Volcanology Geothermal Res.* 193, 82–92. doi:10.1016/j.jvolgeores.2010.03.009

Edwards, B. R., Belousov, A., Belousova, M., and Melnikov, D. (2015). Observations on Lava, Snowpack and Their Interactions during the 2012-13 Tolbachik Eruption, Klyuchevskoy Group, Kamchatka, Russia. *J. Volcanology Geothermal Res.* 307, 107–119. doi:10.1016/j.jvolgeores.2015.08.010

Elkins, L. J., Hamelin, C., Blichert-Toft, J., Scott, S. R., Sims, K. W. W., Yeo, I. A., et al. (2016). North Atlantic Hotspot-ridge Interaction Near Jan Mayen Island. *Geochem. Persp. Let.* 2, 55–67. doi:10.7185/geochemlet.1606

Ewert, J. W., Guffanti, M., and Murray, T. L. (2005). An Assessment of Volcanic Threat and Monitoring Capabilities in the United States: Framework for a National Volcanic Early Warning System, NVEWS. *US Geol. Sur. Open-file Rep.* 1164, 1–62. doi:10.3133/ofr20051164

Fitch, F. J., Nairn, A. E. M., and Talbot, C. J. (1965). Paleomagnetic Studies on Rocks from North Jan Mayen. *Nor. Polarinst. Aarb* 1963, 49–60.

Fitch, F. J. (1964). The Development of the Beerenberg Volcano, Jan Mayen. *Proc. Geologists' Assoc.* 75, 133–IN9. doi:10.1016/s0016-7878(64)80002-x

Gjerløw, E., Haflidason, H., and Pedersen, R. B. (2016). Holocene Explosive Volcanism of the Jan Mayen (Island), Volcanic Province, North-Atlantic. *J. Volcanol. Geotherm. Res.* 321, 31–44. doi:10.1016/j.jvolgeores.2016.04.025

Gjerløw, E., Höskuldsson, A., and Pedersen, R. B. (2015). The 1732 Surtseyan Eruption of Eggøya, Jan Mayen, North-Atlantic: Deposits, Distribution, Chemistry and Chronology. *Bull. Volcanol* 77, 14. doi:10.1007/s00445-014-0895-6

Guffanti, M., Casadevall, T. J., and Wunderman, R. (2010). Encounters of Aircraft with Volcanic Ash Clouds: A Compilation of Known Incidents, 1953-2009, ver. 1.0, 12 p. *US Geol. Surv. Data Ser.* 545. (plus 4 appendixes including the compilation database). doi:10.3133/ds545

Höskuldsson, A., Óskarsson, N., Pedersen, R., Grönvold, K., Vogfjörd, K., and Ólafsdóttir, R. (2007). The Millennium Eruption of Hekla in February 2000. *Bull. Volcanol.* 70 (2), 169–182. doi:10.1007/s00445-007-0128-3

Imsland, P. (1978). The Geology of the Volcanic Island Jan Mayen, Arctic Ocean. Nordic Volcanol. *Inst. Res. Rep.* 78, 13.

Imsland, P. (1986). The Volcanic Eruption on Jan Mayen, January 1985: Interaction between a Volcanic Island and a Fracture Zone. *J. Volcanology Geothermal Res.* 28, 45–53. doi:10.1016/0377-0273(86)90004-1

Jakobsson, M., Mayer, L., Coakley, B., Dowdeswell, J. A., Forbes, S., Fridman, B., et al. (2012). The International Bathymetric Chart of the Arctic Ocean (IBCAO) Version 3.0. *Geophys. Res. Lett.* doi:10.1029/2012GL052219

Jiménez, D., Becerril, L., Bartolini, S., Escobar, D., and Martí, J. (2020). Making a Qualitative Volcanic-Hazards Map by Combining Simulated Scenarios: An Example for San Miguel Volcano (El Salvador). *J. Volcanol. Geotherm. Res.* 395, 106837. doi:10.1016/j.jvolgeores.2020.106837

Kalnay, E., Kanamitsu, M., Kistler, R., Collins, W., Deaven, D., Gandin, L., et al. (1996). The NCEP/NCAR 40-year Reanalysis Project. *Bull. Amer. Meteorol. Soc.* 77 (3), 437–471. doi:10.1175/1520-0477(1996)077<0437:tnyrp>2.0.co;2

Kinvig, H. S., Winson, A., and Gottsmann, J. (2010). Analysis of Volcanic Threat from Nisyros Island, Greece, with Implications for Aviation and Population Exposure. *Nat. Hazards Earth Syst. Sci.* 10, 1101–1113. doi:10.5194/nhess-10-1101-2010

Martí, J. (2017). Assessing Volcanic Hazard: A Review. Oxford Handbooks Online. Available at: http://www.oxfordhandbooks.com/view/10.1093/oxfordhb/9780190676889.001.0001/oxfordhb-9780190676889-e-32.

Martí, J., and Felpeto, A. (2010). Methodology for the Computation of Volcanic Susceptibility. *J. Volcanology Geothermal Res.* 195, 69–77. doi:10.1016/j.jvolgeores.2010.06.008

Martí, J., Sobradelo, R., Felpeto, A., and García, O. (2012). Eruptive Scenarios of Phonolitic Volcanism at Teide-Pico Viejo Volcanic Complex (Tenerife, Canary Islands). *Bull. Volcanol* 74, 767–782. doi:10.1007/s00445-011-0569-6

Mattox, T. N., and Mangan, M. T. (1997). Littoral Hydrovolcanic Explosions: a Case Study of Lava–Seawater Interaction at Kilauea Volcano. *J. Volcanol. Geotherm. Res.* 75, 1–17. doi:10.1016/s0377-0273(96)00048-0

Mossoux, S., Saey, M., Bartolini, S., Poppe, S., Canters, F., and Kervyn, M. (2016). Q-LAVHA: a Flexible GIS Plugin to Simulate Lava Flows. *Comput. Geosciences* 97, 98–109. doi:10.1016/j.cageo.2016.09.003

Neri, A., Aspinall, W. P., Cioni, R., Bertagnini, A., Baxter, P. J., Zuccaro, G., et al. (2008). Developing an Event Tree for Probabilistic hazard and Risk Assessment at Vesuvius. *J. Volcanology Geothermal Res.* 178, 397–415. doi:10.1016/j.jvolgeores.2008.05.014

Norwegian Polar Institute (2014). Terrengmodell Jan Mayen (J0 Terrengmodell) [Data Set]. *Norwegian Polar Inst.* doi:10.21334/npolar.2014.e2b2417e

Oddsson, B., Gudmundsson, M. T., Edwards, B. R., Thordarson, T., Magnússon, E., and Sigurðsson, G. (2016). Subglacial Lava Propagation, Ice Melting and Heat Transfer during Emplacement of an Intermediate Lava Flow in the 2010 Eyjafjallajökull Eruption. *Bull. Volcanol* 78, 48. doi:10.1007/s00445-016-1041-4

Paris, R., Coello Bravo, J. J., Bravo, J. J. C., González, M. E. M., Kelfoun, K., and Nauret, F. (2017). Explosive Eruption, Flank Collapse and Megatsunami at Tenerife Ca. 170 Ka. *Nat. Commun.* 8, 15246. doi:10.1038/ncomms15246

Plunkett, G., Sigl, M., Pilcher, J. R., McConnell, J. R., Chellman, N., Steffensen, J. P., et al. (2020). Smoking Guns and Volcanic Ash: the Importance of Sparse Tephras in Greenland Ice Cores. *Polar Res.* 39, 3511. doi:10.33265/polar.v39.3511

Sandri, L., Costa, A., Jacopo, S., Tonini, R., Macedonio, G., Folch, A., et al. (2016). Beyond Eruptive Scenarios: Assessing Tephra Fallout hazard from Neapolitan Volcanoes. *Sci. Rep.* 6, 24271. doi:10.1038/srep24271

Scaini, C., Biass, S., Galderisi, A., Bonadonna, C., Folch, A., Smith, K., et al. (2014). A Multi-Scale Risk Assessment for Tephra Fallout and Airborne Concentration from Multiple Icelandic Volcanoes - Part 2: Vulnerability and Impact. *Nat. Hazards Earth Syst. Sci.* 14, 2289–2312. doi:10.5194/nhess-14-2289-2014

Scoresby, W., Jr (1820). *An Account of the Arctic Regions, with a History and Description of the Northern Whale-Fishery*. Edinburgh: A Constable & Co.

Selva, J., Costa, A., Marzocchi, W., and Sandri, L. (2010). Multiple Hazards and Paths to Eruptions: BET_VH: Exploring the Influence of Natural Uncertainties on Long-Term hazard from Tephra Fallout at Campi Flegrei (Italy). *Bull. Volcanol.* 72. doi:10.1007/s00445-010-0358-7

Siggerud, T. (1972). The Volcanic Eruption on Jan Mayen 1970. *Nor. Polarinst. Årb* 1970, 5–18.

Sylvester, A. G. (1975). History and Surveillance of Volcanic Activity on. *Jan Mayen Isl. Bull. Volcanol* 39, 1–23. doi:10.1007/bf02597834

Thompson, M. A., Lindsay, J. M., and Gaillard, J. (2015). The Influence of Probabilistic Volcanic hazard Map Properties on hazard Communication. *J. Appl. Volcanol.* 4 (1). doi:10.1186/s13617-015-0023-0

Thorarinsson, S. (1981). *Náttúra Íslands*. 2nd ed., 81–119. Almenna bókafélagid, Reykjavík.Jardeldasvædi Á Núnatíma (Volcanic Areas of the Holocene)

Titos, M., Martínez Montesinos, B., Barsotti, S., Sandri, L., Folch, A., Mingari, L., et al. (2021). Assessing Potential Impact of Explosive Volcanic Eruptions from Jan Mayen Island (Norway) on Aviation in the North Atlantic, doi:10.5194/nhess-2021-264

Trønnes, R. G., Planke, S., Sundvoll, B., and Imsland, P. (1999). Recent Volcanic Rocks from Jan Mayen: Low-Degree Melt Fractions of Enriched Northeast Atlantic Mantle. *J. Geophys. Res.* 104, 7153–7716. doi:10.1029/1999jb900007

Wilson, T. M., Stewart, C., Sword-Daniels, V., Leonard, G. S., Johnston, D. M., Cole, J. W., et al. (2012). Volcanic Ash Impacts on Critical Infrastructure. *Phys. Chem. Earth, Parts A/B/C* 45-46, 5–23. doi:10.1016/j.pce.2011.06.006

Conflict of Interest: The authors declare that the research was conducted in the absence of any commercial or financial relationships that could be construed as a potential conflict of interest.

The reviewer LS declared a past collaboration with one of the authors SM to the handling Editor.

Publisher's Note: All claims expressed in this article are solely those of the authors and do not necessarily represent those of their affiliated organizations, or those of the publisher, the editors and the reviewers. Any product that may be evaluated in this article, or claim that may be made by its manufacturer, is not guaranteed or endorsed by the publisher.

Copyright © 2022 Gjerløw, Höskuldsson, Bartolini, Biass, Mossoux, Gilbert, Pedersen and Martí. This is an open-access article distributed under the terms of the Creative Commons Attribution License (CC BY). The use, distribution or reproduction in other forums is permitted, provided the original author(s) and the copyright owner(s) are credited and that the original publication in this journal is cited, in accordance with accepted academic practice. No use, distribution or reproduction is permitted which does not comply with these terms.

frontiers in Earth Science

ORIGINAL RESEARCH
published: 24 March 2022
doi: 10.3389/feart.2022.767485

A 1.5 Ma Marine Record of Volcanic Activity and Associated Landslides Offshore Martinique (Lesser Antilles): Sites U1397 and U1399 of IODP 340 Expedition

Benoît Villemant[1], Anne Le Friant[2], Benoît Caron[1], Giulia Del Manzo[2], Sara Lafuerza[1], Laurent Emmanuel[1], Osamu Ishizuka[3], Hervé Guyard[2], Nathalie Labourdette[1], Agnès Michel[2†] and Samia Hidalgo[2]*

[1]Institut des Sciences de la Terre Paris (ISTEP), Sorbonne Université, Paris, France, [2]Institut de Physique du Globe de Paris (IPGP), Paris, France, [3]Geological Survey of Japan, National Institute of Advanced Industrial Science and Technology, AIST, Tsukuba, Japan

OPEN ACCESS

Edited by:
Michel Pichavant,
CNRS Orléans, France

Reviewed by:
Sebastian Watt,
University of Birmingham,
United Kingdom
Armin Freundt,
Helmholtz Association of German
Research Centres (HZ), Germany

***Correspondence:**
Benoît Villemant
benoit.villemant@sorbonne-universite.fr

†AM deceased

Specialty section:
This article was submitted to Volcanology, a section of the journal Frontiers in Earth Science

Received: 30 August 2021
Accepted: 18 February 2022
Published: 24 March 2022

Citation:
Villemant B, Le Friant A, Caron B, Del Manzo G, Lafuerza S, Emmanuel L, Ishizuka O, Guyard H, Labourdette N, Michel A and Hidalgo S (2022) A 1.5 Ma Marine Record of Volcanic Activity and Associated Landslides Offshore Martinique (Lesser Antilles): Sites U1397 and U1399 of IODP 340 Expedition. Front. Earth Sci. 10:767485. doi: 10.3389/feart.2022.767485

The products of eruptive and mass-wasting processes that built island arc volcanoes are better preserved in marine deposits than on land. Holes U1397A and U1399A drilled during IODP Expedition 340 provide a 1.5 Ma record of the volcanic history of Martinique. ^{14}C dating and $\delta^{18}O$ patterns are used to reconstitute the chronostratigraphy of tephra, volcaniclastic turbidites, and mass-wasting events (traced by debris avalanches, debrites, and duplication and deformation of pre-existing sediments), leading to a new volcanic history of Montagne Pelée and Pitons du Carbet volcanoes. The top 50 m of core U1397A provides a continuous high-resolution sedimentation record over the last ~130 ka. The sedimentation record deeper than 50 m in core U1397A and in the whole core U1399A is discontinuous because of the numerous sliding and deformation events triggered by debris avalanches related to flank collapses. Three successive activity periods are identified since ~190 ka: the "Old Pelée" until 50 ka, the "Grand Rivière" (50–20 ka), and the "Recent Pelée" (20 ka—present day). The first two periods have the highest volcanic deposition rates offshore but very little outcrop on land. The whole magmatic activity of Mt Pelée comprises silicic andesites, but mafic andesites were also emitted during the whole "Grand Rivière." At ~115 ka, a major flank collapse ("Le Prêcheur") produced a debris avalanche and submarine landslide that affected sea floor sediments by erosion and deformation up to ~70 km from the shore. The Pitons du Carbet volcano was active from 1.2 Ma to 260 ka with numerous large flank collapses at a mean rate of 1 event every 100 ka. The average deposition rate of tephra fall offshore is much less than that at Mt Pelée. Our data show that correlations between the timing of large landslides or emission of mafic magmas and rapid sea level rise or lowstands suggested by previous studies are not systematic. The reconstituted chronostratigraphy of cores U1397A and U1399A provides the framework necessary for further studies of the magma petrology and production rates and timing of the mechanisms triggering flank collapses and related submarine landslides of Mt Pelée and Pitons du Carbet.

Keywords: *Chronostratigraphy*, volcanic tephra, flank collapse, submarine landslides, Caribbean, Mt Pelée volcano, Martinique (FWI: French West Indies), IODP (integrated ocean drilling program) expedition 340

1 INTRODUCTION

Reconstitution of the history of volcanoes of the Lesser Antilles Arc using on-land data is difficult because of the scarcity of outcrops due to 1) the tropical climate that favors the erosion of volcanic deposits and development of a dense vegetation cover and 2) the specific characters of the andesitic volcanic activity: low eruption rates (some eruptions per ka), recurrence of explosive and destructive phases, recurrence of dome-forming eruptions, and scarcity of lava flows that create highly unstable deposits, easily destroyed by flank collapses. In small island environments, the history of the volcanic activity is generally better preserved in the submarine deposits close to the volcano than on-land. In addition, the ^{14}C and ^{18}O records on foraminifera allow construction of a precise chronostratigraphy of the hemipelagic sedimentation and volcanic tephra and debris avalanche deposits intercalated in the marine sedimentary sequence.

Following the approaches of Keller et al. (1978), Carey and Sigurdsson (1980), Paterne et al. (1986), Reid et al. (1996), and Carey (1999), the IODP 340 expedition on the R/V JOIDES Resolution drilled and cored marine sediments at nine sites located off Montserrat and Martinique islands. The objectives were 1) to study deposits related to volcano flank collapses and 2) document the long-term eruptive history of volcanoes. Previous studies from the Lesser Antilles have identified distinctions of two types of offshore deposits related to flank collapse, based on surface morphology, geophysical data, and core sampling (see, for example, Deplus et al., 2001; Watt et al., 2012; Le Friant et al., 2015): debris avalanche deposits (DADs), that are primary deposits of volcano flank collapse, and submarine landslide deposits (SLDs) that are deformed to remobilized seafloor sediments by secondary failures initiated by the DAD. The timing and emplacement processes of landslide deposits inferred from the IODP 340 expedition and previous studies are summarized in the studies by Le Friant et al. (2013), Le Friant et al. (2015), and Le Friant et al. (2020). A series of articles report the eruptive history of Montserrat inferred from the IODP 340 expedition (Jutzeler et al., 2014; Wall-Palmer et al., 2014; Coussens et al., 2016a; Coussens et al., 2016b; Fraass et al., 2017; Jutzeler et al., 2017). Five coring sites (U1397 to U1401) were chosen on the Caribbean western flank of Martinique. One site U1397 was dedicated to sediment chronostratigraphy, and the other sites were dedicated to investigate the SLDs generated by flank collapses of Mt Pelée, the most recent volcano north of Martinique (Lafuerza et al., 2014; Hornbach et al., 2015; Le Friant et al., 2015; Brunet et al., 2016; Brunet et al., 2017; Llopart et al., 2018; Knappe et al., 2020; Le Friant et al., 2020; Mencaroni et al., 2020), combining description of the types of cored sediments (composition, deformation, distribution, and physical properties), high-resolution seismic reflection data, and physical modeling. Only the short (~15 m) core U1401A has been investigated for tephrostratigraphy using a high-resolution ^{14}C and ^{18}O chronology (0 to ~36 ka; Solaro et al., 2020).

This study contributes to the reconstruction of the volcanic history of Martinique using two IODP sites: U1397 close to the coast expected to have the most extensive and better preserved record of the volcanic activity and U1399 at the distal part of the main SLD. ^{14}C and ^{18}O records on Foraminifera (*Globigerinoides ruber* white and pink) provide a precise chronostratigraphy of hemipelagic sediments and document the volcanic activity and flank collapses related to recent activity of Mt Pelée over the last 130 ka. For older periods, despite the disturbance of the sedimentary sequences caused by turbidity currents and landslides driven by gravity or by volcanic activity and flank collapses, it is possible to propose a reconstitution of the history and emplacement mechanisms of these events over ~1.5 Ma as they are recorded in offshore sediments. These new results are compared to on-land data with a special emphasis on the relationship between flank collapses and magmatic evolution of the volcanoes.

2 PREVIOUS WORKS

2.1 Geological Setting and On-Land Volcano History

The Lesser Antilles Arc results from the subduction of the Atlantic oceanic plate beneath the Caribbean Plate, at ~2 cm/yr (Wadge, 1984). North of Dominica, it is divided in two distinct arcs due to the westward migration of the volcanic activity (**Figure 1A**). To the southwest, it is bordered by the 2,900-m deep back-arc Grenada Basin and, to the east, by a large plateau that is cut in the northeast by deep trenches perpendicular to the arc (Feuillet et al., 2002). The volcanic activity started at the north of the arc ~40 Ma ago and progressively migrated to the southwest (Martin-Kaye, 1969; Bouysse et al., 1990). The inner arc includes all active volcanoes of the last 20 Ma. Martinique is located at the junction between the two arcs. The volcanic activity migrated from southeast to northwest of the island since the Early Miocene (Westercamp et al., 1989; Germa et al., 2010, Germa et al., 2011b; Labanieh et al., 2012). Since the Pliocene, the northern part of Martinique was built by the successive activities of Morne Jacob (5.2–1.5 Ma) to the east, Pitons du Carbet (998–322 ka) to the south, Mont Conil (543–127 ka) to the north, and Montagne Pelée (126 ka–present day) located between the last two edifices (Samper et al., 2008; Germa et al., 2011b, Germa et al., 2015; **Figure 2A**). Mt Pelée eruptions have been the subject of numerous studies in volcanology (Lacroix, 1904; Westercamp and Traineau, 1983a; Jaupart and Allègre, 1991; Tanguy, 1994, Villemant and Boudon, 1998; Tanguy, 2004; Carazzo et al., 2012) and petrology (Roobol and Smith, 1976; Bourdier et al., 1985; Gourgaud et al., 1989; Traineau et al., 1989; Fichaut et al., 1989; Villemant et al., 1996; Martel et al., 1998; Pichavant et al., 2002; Annen et al., 2008; Labanieh et al., 2010; Boudon et al., 2013). The recent activity of Mt Pelée from the last eruption in 1929 to about 20 ka is well-established (Westercamp and Traineau, 1983a, Westercamp and Traineau, 1983b; Traineau et al., 1989; Michaud-Dubuy et al., 2019; **Figure 2B**). In addition, the volcanic record is more fragmentary due to the rarity of outcrops and poor dating resolution. Between ~20 and 40 ka, the "Grand Rivière" events are characterized by specific eruptive style and petrology (Bourdier et al., 1985; Boudon et al., 2013). The older activity period (~40–130 ka) called 'Paleo Pelée' is identified

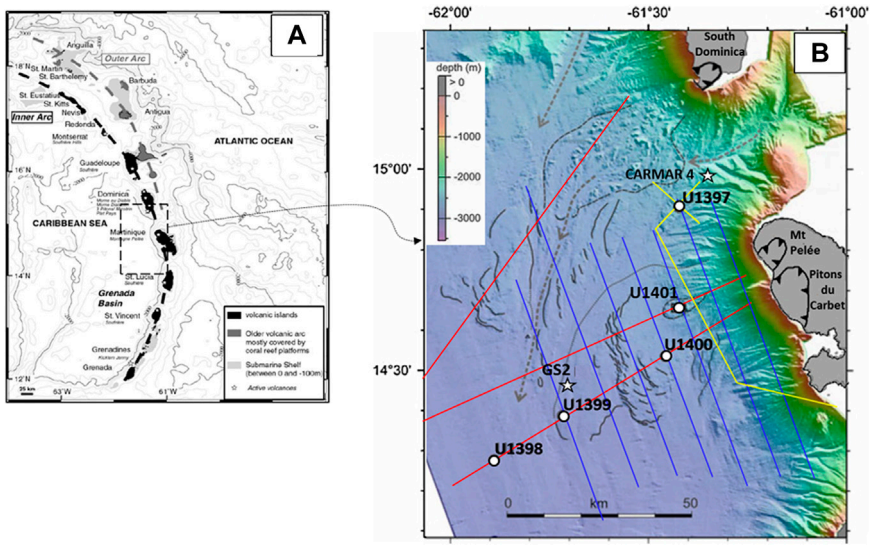


FIGURE 1 | Lesser Antilles Arc, landslide deposits, and IODP 340 coring sites offshore Martinique. **(A)** Two island arcs. The inner arc is the active volcanic arc (modified from Boudon et al. (2007)). **(B)** IODP 340 drilling sites and extent of chaotic units. Submarine topography: swath bathymetry illuminated from the North; gray lines: topographic scarps (DAD3 is the blocky unit above which is located the U1401 site; other scarps correspond to SLDs limits); gray arrows: main deep sea channels. Colored lines are seismic reflection lines used to locate the coring sites (blue: AGUADOMAR cruise, 1999, Red: CARAVAL cruise, 2002, Yellow: GWADASEIS cruise, 2009, Deplus et al., 2001; Le Friant et al., 2003). Drilling sites: open circles: IODP 340 cores; stars: CARMAR-4 (CARAVAL cruise) and GS-2 (Gs7605 cruise; Reid et al., 1996). On-land black scars: flank collapse structures of Martinique (Mt Pelée and Pitons du Carbet) and South Dominica (modified from Boudon et al. (2013)).

in very few outcrops on land. Older volcanic complexes (Mt Conil, Pitons du Carbet, and Morne Jacob) have only been the subject of few petrological or volcanological studies (Westercamp and Traineau, 1983a; Westercamp et al., 1989; Labanieh et al., 2010, Labanieh et al., 2012; Boudon et al., 2013; **Figure 2B**).

Numerous flank collapses have been identified on volcanoes of the Lesser Antilles Arc (Deplus et al., 2001; Le Friant et al., 2002, Le Friant et al., 2003; Boudon et al., 2005, Boudon et al., 2007). Their emplacement and time constraints have been established from offshore drilling data (Le Friant et al., 2013; Wall-Palmer et al., 2014, Le Friant et al., 2015; Brunet et al., 2016; Coussens et al., 2016a; Coussens et al., 2016b; Le Friant et al., 2020). At Mt Pelée, at least three flank collapses have created large horseshoe-shaped structures on the western flank of the volcano and produced DADs on land and offshore (Vincent et al., 1989; Le Friant et al., 2003, Boudon et al., 2005, Boudon et al., 2007, Le Friant et al., 2008; Le Friant et al., 2015; **Figure 2B**). They were identified and first dated by the scars of the collapse structures (Le Friant et al., 2003; Boudon et al., 2005; Germa et al., 2011a; Boudon et al., 2013): "Le Prêcheur" event (between 70 and 127 ka), "Saint Pierre" event (between 30 and 45 ka), and 'Rivière Sèche' event (~10 ka). Recent investigations have questioned this chronology (Le Friant et al., 2015, Brunet et al., 2016; Le Friant et al., 2020; Solaro et al., 2020). At the Pitons du Carbet volcanic complex, a large collapse structure corresponds to one or more flank collapses of the minimum age ~337 ka (Westercamp et al., 1989; Boudon et al., Boudon et al., 2007; Samper et al., 2008, Boudon et al., 2013; **Figure 2B**). Triggering mechanisms of flank collapses and their consequences on volcanic activity have been discussed in a number of articles (see, for example, Quidelleur et al., 2008; Boudon et al., 2013; Le Friant et al., 2015; Coussens et al., 2016b; Brunet et al., 2016; Watt, 2019; Le Friant et al., 2020).

2.2 Submarine Record of the Volcanic History of Martinique

The Endeavour cruise in 1979 gathered a regional collection of piston cores allowing assessments of rates of volcanism and sedimentation, dating of major eruptions, recognition of submarine pyroclastic flow deposits, and establishment of a biostratigraphic framework for the eastern Caribbean (Sigurdsson et al., 1980; Sparks et al., 1980a, Sparks et al., 1980b; Reid et al., 1996). Cruises offshore Montserrat and Martinique islands collected short cores (<10 m) that record the volcanic activity since ~110 ka for Montserrat (Le Friant et al., 2008; Trofimovs et al., 2013) and ~30 ka for Mt Pelée (CARAVAL cruise, Deplus et al., 2001; Boudon et al., 2013). Drillings of the IODP 340 expedition in 2012 considerably widen the studied age ranges (Le Friant et al., 2013). Sites U1394 to U1396 were used to reconstitute the volcanic history of Montserrat over ~1 Ma (Wall-Palmer et al., 2014; Coussens et al., 2016a; Coussens et al., 2016b). Five sites (U1397 to U1401) were drilled offshore Martinique. To better record the volcanic activity, site U1397 is located north-west of the island, close to the coast (~20 km) but far enough from the DADs and SLDs from Mt Pelée and South Dominica (**Figure 1B**). It is located on a topographic high bound by large canyons to be as undisturbed as possible by marine and turbidity currents. It is also close to the piston core CARMAR 4 of the CARAVAL cruise

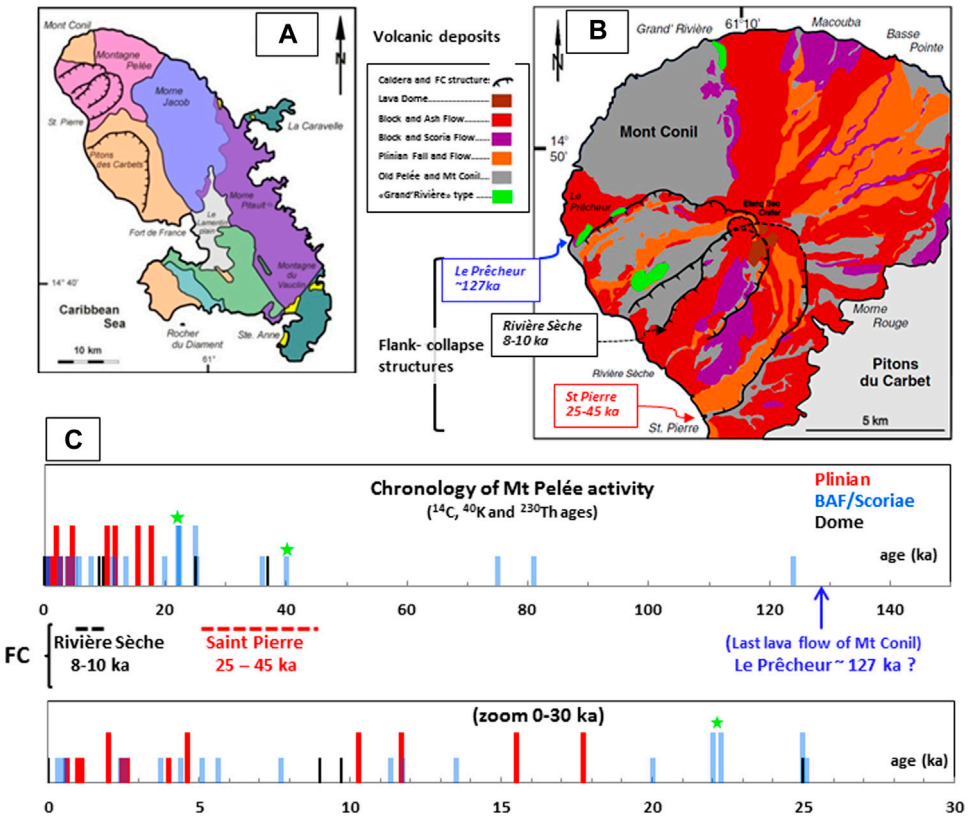


FIGURE 2 | Chronology of the volcanic activity of Martinique. **(A)** Volcanic centers of Martinique (from Germa et al. (2011a)). **(B)** Volcanic deposits and flank collapse structures of Mt Pelée (modified from Le Friant et al., 2003 and Boudon et al., 2013). Flank collapse structures are dated by bracketing with ages of domes grown inside the collapse scarps or cut at collapse structure edges: "Le Prêcheur" (K-Ar[3]); "Rivière sèche" (U-Th[2,5]); and "St Pierre" (K-Ar[3],U-Th[2,5],^{14}C[1]). **(C)** Chronology of the volcanic activity and flank collapse structures of Mt Pelée. Eruptive styles: Dome: lava dome; BAF: block and ash flow; scoriae: scoria fall or flow; Plinian: plinian fall or flow; FC: flank collapses. The height of the bars relates to the relative intensities of the eruptions. Green stars: the two dated "Grand Rivière" events that produced mafic scoriae. Data sources: (1) Westercamp et al., 1989 (^{14}C); (2) Le Friant et al., 2002 (^{14}C-U/Th); (3) Germa et al., 2011a (K-Ar); (4) Michaud-Dubuy (^{14}C), 2019, (5) Villemant et al. (U/Th, unpublished); (6) Ishizuka et al., (^{14}C-K/Ar unpublished); see also **Supplementary Table S3**.

(2002, ~15 km to the NE of site U1397) that collected 7 m of well-bedded sediments with around 50 tephra layers (Boudon et al., 2013). The four other sites are aligned with the flank-collapse structures of Mt Pelée on the seismic line 16 of the CARAVAL cruise (**Figure 1B**). Sites U1399 to U1401 are located on deposits characterized by chaotic facies in seismic reflection (for definition see, for example., Deplus et al., 2001; Lebas et al., 2011; Watt et al., 2012). Site U1398 is the most distant (~80 km) from the shore, beyond the chaotic facies deposits (**Figure 1B**). It mainly contains volcaniclastic turbidites (>70%–95%, Le Friant et al., 2013; Breitkreuz et al., 2021) due to its location on the low slopes inside the Grenada Basin which channeled most turbidity currents from the western flank of the Arc (**Figure 1**). The composition of volcanic clasts, age range, and isotopic and trace element compositions of zircons suggest that the majority of these turbidites originate from Dominica (Breitkreuz et al., 2021). Site U1401, the closest to the shore, penetrates the sediments over 15 m down to the blocky deposit whose drilling was unsuccessful due to its high content in large volcanic blocks, characteristic of a DAD (DAD 3; **Figure 1B**; Le Friant et al., 2015). This DAD is related to the "St Pierre" flank collapse (Brunet et al., 2016) and is older than 36 ka (Solaro et al., 2020).

Compaction of sediments in the upper 200 m of the IODP 340 cores west of Martinique was evaluated from the normalized undrained shear strength measurements on the hemipelagic intervals and correlated with consolidation tests on whole round samples (Lafuerza et al., 2014). Most sediments (except at site U1400) are normally or slightly under-consolidated. High abundance of thick turbidites and coarser tephra explains the pore fluid pressures in slight excess of hydrostatic. However, the upper 120 m of core U1400 and some intervals in the other cores are over-compacted due to vertical erosion and/or deformation. Cores U1399 and U1400 penetrate more than 200 m within sediments typical of SLDs with only few well-bedded sediments interspersed in turbidites and highly deformed

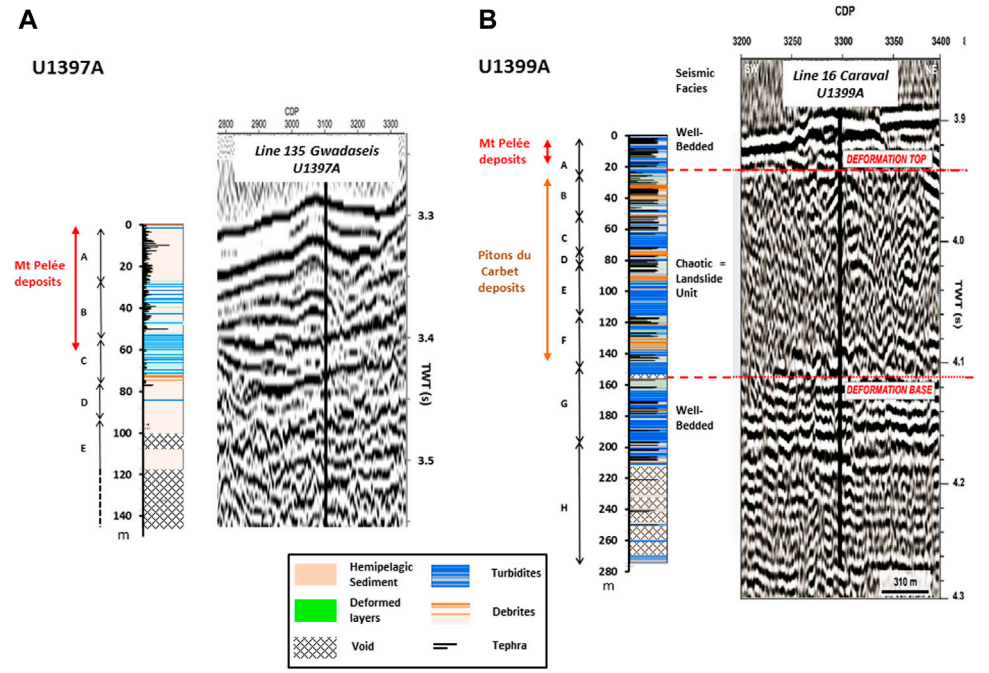


FIGURE 3 | Simplified lithology, deformation figures, and seismic facies of holes 1397A **(A)** and 1399A **(B)**. Seismic data from Brunet et al. (2016) and Le Friant et al. (2015), Le Friant et al. (2020). Depth in core in meter. Letters: lithological units defined on board (Le Friant et al., 2013). The reader is referred to **Supplementary Figure S1** for high-resolution stratigraphic logs on the web version of this article for benefit.

sediments (Le Friant et al., 2013; Lafuerza et al., 2014, Brunet et al., 2016, Le Friant et al., 2020; **Figure 1B**). The deformation microstructures in cores U1399 and U1400 range from brittle to ductile and polyphasic (mixed), with inclined or contorted beds in highly variable degrees and directions. They are acquired after sediment deposition and may be the result of multiple successive but independent episodes of stress (Hornbach et al., 2015; Brunet et al., 2016). Laboratory experiments and numerical models show that lower permeability and high fluid pore pressures exist in some discrete units in the core, where slight changes in the stress regime may have triggered motion and local deformation (Lafuerza et al., 2014; Hornbach et al., 2015). A comprehensive model of emplacement of the debris avalanches and associated submarine landslides was proposed combining data of the IODP 340 expedition and geophysical data of three cruises (AGUADOMAR held in 1999, CARAVAL held in 2002 and GWADASEIS held in 2009; see Deplus et al., 2001; Le Friant et al., 2003; Brunet et al., 2016): the overload generated by the accumulation of debris flows produced by flank collapses at the break in slope on the seafloor triggers the sliding of pre-existing sediments along décollement surfaces and induces deformation of high-pore pressure units distributed within the submarine landslide thus created (Le Friant et al., 2015; Brunet et al., 2016; Le Friant et al., 2020). Core U1399 is less deformed than core U1400 and contains a large section of undeformed well-bedded sediments at the top. The existence of such undeformed layers at the top of the SLDs in all cores shows that deformation stopped over 50 ka ago (Brunet et al., 2016; Le Friant et al., 2020; **Figure 3**). Site U1399 is close to the site GS 2 of the 1976 cruise Gs7605 (Carey and Sigurdsson, 1980; Reid et al., 1996; **Figure 1B**).

3 MATERIALS AND METHODS

Cores U1397A and U1399A are simultaneously studied in this research to complete the chronostratigraphic information available in published studies on land and in marine cores and make an attempt to interpret the distal deposits of SLDs.

3.1 Lithostratigraphic Facies Analysis

At the studied sites, the sedimentary units consist of various combinations of hemipelagic sediments, tephra fall deposits, turbidites (bioclastic and volcaniclastic), debris flow deposits, and homogenized sandy-mud lithofacies (both referred here as debrites). The distinction between the different sedimentary facies is often a complex task due to their large variability and numerous artifacts due to piston coring (Cassidy et al., 2014; Jutzeler et al., 2014). Therefore, we use the nomenclature defined on-board and reported in the visual core descriptions (VCDs, Le Friant et al., 2013). Detailed descriptions and interpretations of these lithostratigraphic facies can be found in the studies by Talling et al. (2012), Trofimovs et al. (2013), Cassidy et al. (2014), Coussens et al. (2016a), Jutzeler et al. (2017) and for cores offshore Martinique in the studies by Le Friant et al. (2013),

Lafuerza et al. (2014) Brunet et al. (2016), and Le Friant et al. (2020). The distinction between turbidites and tephra layers, critical for the current investigation, is not always straightforward. Tephra layers consist of thin (centimeter to tens of centimeter) and fine grained (<1 cm) deposits either well-sorted and normally graded or massive with sharp contacts with sediments. They contain different types of volcanic clasts and separated minerals. The content in biogenic and other non-volcanic material is <10%. Different types of tephra deposits have been defined on-board based on deposit characteristics (fallout or volcaniclastic deposit) and nature of volcanic fragments (pumice, black scoriae, dome fragments, and separated minerals). The most frequent types are pumice clasts and separated minerals (mainly plagioclase and, to a lesser extent, pyroxenes and more rarely amphibole, biotite, olivine, or quartz). Glass shards are almost absent. Laboratory analysis of tephra layers identified on-board in the upper ~10 m of the core U1397A indicates that most of them (~60%) actually contain more than 50% of fresh pumice clasts and/or scoriae and separated minerals, but ~20% are not of direct volcanic origin but are remobilized deposits, for example, in some turbidites (Del Manzo et al., in prep). Here, we use on-board identifications of tephra layers, with some addition or exclusion after careful examination of VCDs. No attempt has been made to distinguish the different volcanic or magmatic types which require much more detailed investigations (Del Manzo et al., in prep) that are beyond the scope of this study.

The volcaniclastic turbidites have similar lithology and are also normally graded (segregation and sorting) by transport in the sea, but they are generally much thicker (tens of centimeter to tens of meter) and contain much coarser fragments (>1 cm). Pumice clasts most frequently represent the highest volcanic fraction. They are sometimes marked by an erosive base and may incorporate a significant fraction of pre-existing sea floor sediments. Volcanoclastic turbidity deposits may result from pyroclastic density currents (mainly pumice flows) entering into the sea or from remobilization of pyroclastic deposits on the submarine slopes or on land (Cassidy et al., 2014; Jutzeler et al., 2017). Debrites are deposits of submarine flows of debris avalanches. Homogenized muddy sand layers observed in some IODP 340 cores could not only result from mixing of pre-existing stratigraphy within the localized zones of intense shear (Brunet et al., 2016) but can also represent distal deposits of submarine debris flows (Talling et al., 2010; Talling, 2013; Talling, 2014).

3.2 Biostratigraphy

Planktonic foraminifers collected on board in both cores are characteristic of Upper Miocene to Upper Pliocene (Le Friant et al., 2013). An overall trend to older material with depth is observed in core U1397A, with an age younger than 220 ka for the top 25 m, younger than 250 ka from ~50 to 100 m, and younger than ~350 ka from ~100 m to ~400 ka at the bottom of this site (Le Friant et al., 2013). In core U1399A, the same fossils were only found in low numbers, and no reliable planktonic foraminiferal data were found.

3.3 Chronostratigraphy: $\delta^{18}O$ Measurements and ^{14}C Dating

The combined use of ^{14}C dating and variations of oxygen isotopes of marine foraminifers makes it possible to establish a reliable chronostratigraphy of marine sediments (Keller et al., 1978; Paterne et al., 1986; Lowe 2011; Griggs et al., 2014; Lowe 2014). *Globigerinoides ruber* was collected in hemipelagic layers of both cores for $\delta^{18}O$ analyses (611 in the upper 95 m of U1397A and 911 in the upper 150 m of U1399A). The collection was as systematic as possible at a depth interval ranging between 2 and 20 cm depending on lithology, with a mean interval of ~10 cm. Stable oxygen isotope analyses were carried out at the Laboratory ISTeP (Institut des Sciences de la Terre de Paris, Sorbonne-Université, Paris, France). No chemicals were used to disaggregate the sediments, and at all stages in the processing, deionized water was used to ensure no dissolution of the carbonate microfossils. The samples were sieved by washing on a stainless steel sieve and slowly dried at 35–40°C. Pristine test samples of white and pink *Globigerinoides ruber* > 150 μm in size were picked (~10 mg) and sonically cleaned. The samples were reacted with 100% H_3PO_4 acid under vacuum in a Kiel IV automatic preparation device at 70°C, and the resulting CO_2 was analyzed using a ThermoFisher Delta V Advantage IRMS mass spectrometer. Oxygen isotope values ($\delta^{18}O$) are reported as per mil (‰) deviation in the isotope ratio ($^{18}O/^{16}O$) standardized to the Vienna Peedee belemnite—VPDB scale using an internal standard (Marceau marble: $\delta^{18}O$ = −1.83‰ V-PDB) calibrated against NBS-19 using the classical method. The analytical reproducibility (1σ) on replicate analyses was 0.1‰. The mean bulk reproducibility is ~0.27‰. It includes the variability in sampled sediment and was estimated from two to three replicates in ~40 sediment layers of core U1397A. $\delta^{18}O$ data are reported in **Supplementary Tables S1A,B**.

For ^{14}C dating, approximately 800 specimens (~10 mg) of *G. Ruber* of a size >150 μm were picked in each of the selected hemipelagic sediment layer. AMS analyses were performed by Artemis National Platform LMC14 (CEA Saclay, Gif sur Yvette, France) or by Beta Analytics Inc. (FL, United States, www.radiocarbon.com) using their in-house protocols. Thirteen samples were selected in the upper 7 m of U1397A and seven samples in the upper 3 m of U1399A. ^{14}C dating results are reported in **Supplementary Tables S2A,B** as conventional radiocarbon years BP, expressed at the ±1σ level for overall analytical confidence. The AMS dates are calibrated against the Marine13 dataset using CALIB 7.0 Radiocarbon Calibration software (Stuiver and Reimer, 1993; Reimer et al., 2013a; Reimer et al., 2013b).

4 RESULTS

4.1 Lithology, Deformation, and Seismic Facies of Cores U1397A and U1399A

Simplified lithology (hemipelagic sediments, tephra layers, turbidites, and debrites) and possible deformation figures established on board from visual core descriptions (VCD's; Le

Friant et al., 2013) are compared to seismic facies (Brunet et al., 2016) for both cores in **Figure 3**. For interpretation of the stratigraphic sections reported in **Figure 3**, high-resolution logs are reported in **Supplementary Figure S1**.

4.1.1 Site U1397

Two holes have been cored on this site (**Figures 1B**, **3A**). The top 50 m of core U1397A contains a slightly higher proportion of tephra and hemipelagic sediments and a lower proportion of turbidites than in core U1397B distant about 15 m to the south (see **Supplementary Figure S2**). The general distribution of hemipelagic and tephra layers is, however, similar. This indicates that turbidity currents are strongly channelized and may partially and superficially erode pre-existing sediments. The core U1397A (Lat 14°54.4081N, Long. 61°25,3530W, water depth 2,482.2 m) reached 265.5 m bsf (meters below sea floor), but only the uppermost 120 m has good recovery. Seismic data indicate that at least the upper 90 m of the core penetrates regular reflectors that correspond to undisturbed well-bedded sediments; below, numerous chaotic reflectors are visible. At least 300 tephra layers have been recognized in the top 50 m. Numerous thick turbidites are intercalated between thick well-bedded sediment layers in the intervals ~50–65 m, ~95–120 m, and below 140 m bsf. Six different lithostratigraphic units (A to H) are recognized (**Figure 3A**). Unit A (0–28 m bsf) comprises a sequence of hemipelagic sediments with interbedded tephra layers and few thin and poorly sorted turbidites. Unit B (28–53 m bsf) comprises the same material but with numerous volcaniclastic turbidites, particularly in the upper 5 m. Unit C (53–76 m bsf) is mainly a turbidite sequence of mixed (bioclastic–volcaniclastic) composition. Turbidites are normally graded and contain variable amounts of fresh pumice. The turbidite layers are most often in direct contact with no separating hemipelagic layer. The basal zone of unit C (<3 m thick) contains a debrite and a section of deformed sediment. Unit D (76–91 m bsf) comprises a series of volcaniclastic turbidites (more abundant from ~83 m bsf) and a few tephra layers which are interbedded in a hemipelagic mud. The proportion of hemipelagic sediment is lower than that in unit C. Unit E (91–120 m bsf) comprises a series of thick massive to normally graded volcaniclastic turbidites containing a large amount of massive to poorly vesiculated lava fragments. Below ~120 m bsf, the core recovery was very low, and the stratigraphy is uncertain. The recovered sediments are significantly and increasingly compacted from this depth. Three different units were successively sampled: 1) between ~150 and ~170 m, two sequences of hemipelagic sediments weakly compacted at the top with a progressive lithification into mudstones with depth; 2) between ~170 and 230 m bsf, many sequences of mud-rich sandstone layers and semi-consolidated, highly fractured, and contorted mudstones with abundant lava clasts, few pebbles, and a larger block comprising andesitic lava containing large phenocrysts of amphibole and quartz; 3) between ~230 and ~265 m bsf, a sequence of heavily bioturbated hemipelagic mud with few interbedded layers of bioclastic sandstone.

4.1.2 Site U1399

Site U1399A (Lat 14°23,2419N, Long. 61°42,6833W, water depth 2,900.8 m) reached 274.7 m bsf (**Figures 1B**, **3B**). Cored sediments are dominated by a combination of hemipelagic mud with interbedded tephra and volcaniclastic turbidites and various types of deformed sedimentary intervals that occur at different depths. Some units contain debrites. Seismic data indicate a thick zone (~25–150 m bsf) with chaotic reflectors intercalated between two zones with typical well-bedded facies (0–25 m bsf, and below ~150 m bsf, **Figure 3B**). The chaotic facies correspond to locally highly deformed sediments. Eight different lithostratigraphic units (A–H) are defined based either on changes in the cored material characteristics or a distinct marker layer (Le Friant et al., 2013; **Figure 3B**). Unit A (0–24 m bsf) mainly comprises hemipelagic mud with abundant tephra layers and several small turbidites. Unit B (24–50 m bsf) is a sequence of variably deformed and contorted hemipelagic sediment and debrites with a muddy sand matrix. Unit C (50–72 m bsf) consists of hemipelagic mud with interbedded tephra layers and thin turbidites (<1 m thick). The base of unit C comprises a 1-m-thick interval of hemipelagic mud overlain by a thick turbidite (~8 m). Unit D (72–80 m bsf) comprises highly deformed sediments in the upper part and weakly deformed hemipelagic mud in the lower part. Unit E (80-112 m bsf) consists of a succession of alternating layers of undeformed hemipelagic mud with interbedded tephra layers and thin turbidites, deformed pelagic mud, debrites, and turbidites. Unit F (112–150 m bsf) comprises a sequence of highly deformed and contorted hemipelagic sediment with turbidites and contorted tephra layers. Unit G (150–192 m bsf) comprises sequences of pumice-rich turbidites with few interbedded hemipelagic mud and tephra layers. Unit H (192–270 m bsf) has very low recovery and consists of hemipelagic mud with interbedded tephra layers and pumice-rich turbidites.

4.2 Chronostratigraphic Data and Model Ages

The patterns of $\delta^{18}O$ vs. hemipelagic sediment thickness compared to standard $\delta^{18}O$ vs. age curves allows to establish the age ("model age") of hemipelagic sediments as a function of depth in the core. The mean time resolution ($\pm 1\sigma$) of the chronological reconstructions is theoretically ~1 ka for U1397A and ~4 ka for U1399A, as estimated from the mean sedimentation rates and sampling interval (~10 cm). In many cases, however, (no recovery, gaps in hemipelagic sedimentation), the age can only be bracketed in a much larger time interval. The large differences between the $\delta^{18}O$ depth patterns of U1397A and U1399A are due to differences in both sedimentation rates and post deposition perturbations (mass transport, deformations etc.).

4.2.1 Core U1397A

Lithology of core U1397A is compared to the $\delta^{18}O$ patterns in **Figure 4**. $\delta^{18}O$ data obtained at approximately the same depth resolution in two other cores drilled near site U1397 (**Figure 1B**) are also reported for comparison: the ~10-m-long core CARMAR 4

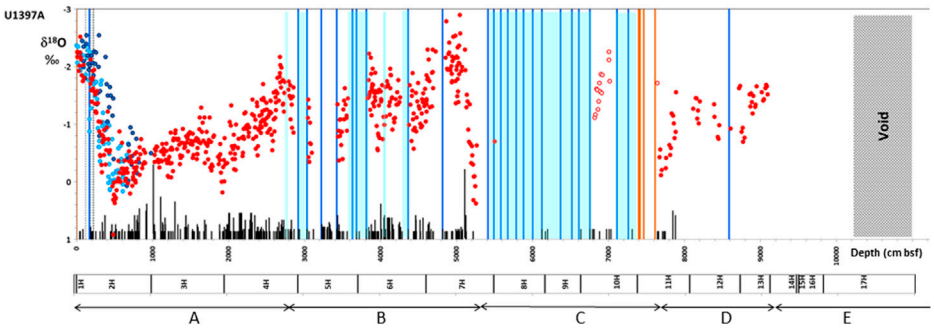


FIGURE 4 | Synthetic logs and $\delta^{18}O$ values of core U1397A. Comparison with cores U1401A and CARMAR-4. $\delta^{18}O$ data: red dots U1397A; light blue dots: CARMAR-4 (Boudon et al., 2013); dark blue dots: U1401A (Solaro et al., 2020). Blue domains: turbiditic zones; blue bars: turbidites >50 cm; black bars: tephra units; orange bars: debrites. The height of the bars relates to the relative thicknesses of the deposits. Gray domains: void in core; dots: $\delta^{18}O$ values; open circles: series of samples of which the $\delta^{18}O$ pattern is not consistent with the stratigraphic position in the core. They correspond to sedimentary units displaced by submarine sliding ("duplicate units"). Letters are the different core section labels and lithological units (see **Figure 3A**).

(Boudon et al., 2013) and the ~15-m-long core U1401A (Solaro et al., 2020). The three datasets are consistent in absolute values and dispersion, indicating that the relatively high dispersion of $\delta^{18}O$ values is mainly due to the natural heterogeneity of sediments rather than analytical. This natural heterogeneity is likely due to the sedimentation conditions in an agitated marine environment on steep volcano slopes. $\delta^{18}O$ data for U1401A display a slightly higher dispersion than those for U1397A, though performed in the same conditions (**Figure 4**): it is likely due to its location at the outlet of Mt Pelée collapse structures, leading to significant disturbance of the sedimentation (**Figure 1B**).

$\delta^{18}O$ data of core U1397A display a continuous trend over the upper 28 m of the core (unit A). Below, the $\delta^{18}O$ record is discontinuous due to the abundance of thick turbidite layers or poor recovery (**Figure 4**). The $\delta^{18}O$ pattern over the upper 28 m reproduces the typical isotopic variations since the last interglacial low-stand to the present day, with maximum $\delta^{18}O$ values at ~18 ka. The age–depth calibration is estimated using both ^{14}C dating and $\delta^{18}O$ measurements (see **Supplementary Tables S1A, S2A**). Due to the volcanic environment and the proximity to the coast, the sedimentation may be disturbed by volcanic events (such as large eruptions, volcaniclastic turbidity currents, or debris avalanches) or climatic events (such as strong floods or storms). These events may be considered instantaneous compared to the time resolution, and their deposits can be relatively easily identified. Due to relatively low frequency of such events and the low thickness of volcaniclastic layers in the upper 28 m of the core, we assume in first approximation a constant hemipelagic sedimentation rate. The thickness of hemipelagic sediments is estimated by subtracting the thickness of volcanic (VL), turbidite (Tu), or debrite (D) layers as reported in the VCD from the depth in core (see **Supplementary Table S1A**). Then, the use of ^{14}C dating (**Supplementary Table S2A**) leads to a mean sedimentation rate of ~23 cm/ka (**Figure 5A**). This rate is lower (~9–10 cm/ka) for the upper meter of the core, but then increases rapidly. It may be due to coring under-recovery of the upper unconsolidated sediments. From this first estimate, a new mean sedimentation rate is obtained (**Figure 5B**) by fitting "by eye" the $\delta^{18}O$ pattern to a reference pattern derived from the following well-constrained $\delta^{18}O$ age curves (see **Supplementary Figure S3**): SPECMAP LR-04 (Lisiecki and Raymo, 2005), ODP999, and VM78-122 in the Caribbean Sea (Broecker W. et al., 1988; Broecker W. S. et al., 1988; Broecker et al., 1990) and CARMON-2 offshore Montserrat (Le Friant et al., 2008). A compaction factor k^0 to take into account for sediment pile overload is defined as follows: $Vs = Vs^0\ (1 - k^0\ d)$, where Vs^0 and Vs are, respectively, the actual and the apparent sedimentation rates and d is the depth expressed in centimeter (bsf). The best fit is obtained for $Vs^0 = 28$ cm/ka and $k^0 = 2.5{\cdot}10^{-5}$ cm^{-1} (**Figure 5A**). The calibration curve is consistent with that of core U1401A (Solaro et al., 2020) and with the hemipelagic sedimentation rates deduced from biochronology in cores En 46 and GS 27 cored near the Caribbean coasts of St Lucia and the Grenadines (Reid et al., 1996; **Figure 5A**).

Sediment erosion and sliding and doubling of sediment packages as discussed below inhibit application of the same fitting method to core sections older than 130 ka (**Figure 4**). In unit C (~53–76 m bsf) in core U1397A, the sediments mainly consist of a series of volcaniclastic turbidites, representing a total thickness of ~15 m ~ 2 m at 53 m, ~5.5 m at 55.5 m, ~4.5 m at 61.5 m, ~2 m at 66.5 m, and ~0.4 m at 70 m bsf (**Figure 4**). This sequence of turbidites lies on top of a debrite-like deposit between 74 and 76 m bsf. Only a ~1.6 m thick continuous sequence (68.4–70 m bsf) of hemipelagic sediments is preserved within the turbidite sequence. It displays a $\delta^{18}O$ pattern that is not consistent with possible nearby reference patterns, that is, older than 130 ka. This pattern is, however, similar to that of a shallower section (46–48 m bsf, in unit B), which corresponds to the 115–121 ka time period (**Figures 4**, **5B**). We assume that this sedimentary sequence is a duplicate unit and that its stratigraphic position is controlled by the emplacement of the complex system comprising thick turbidites and debrites of unit C (53 and 76 m bsf; **Figure 5B**).

To fit the $\delta^{18}O$ measured in the series of hemipelagic sediments of unit D (between 76.7 and 90.2 m bsf, the

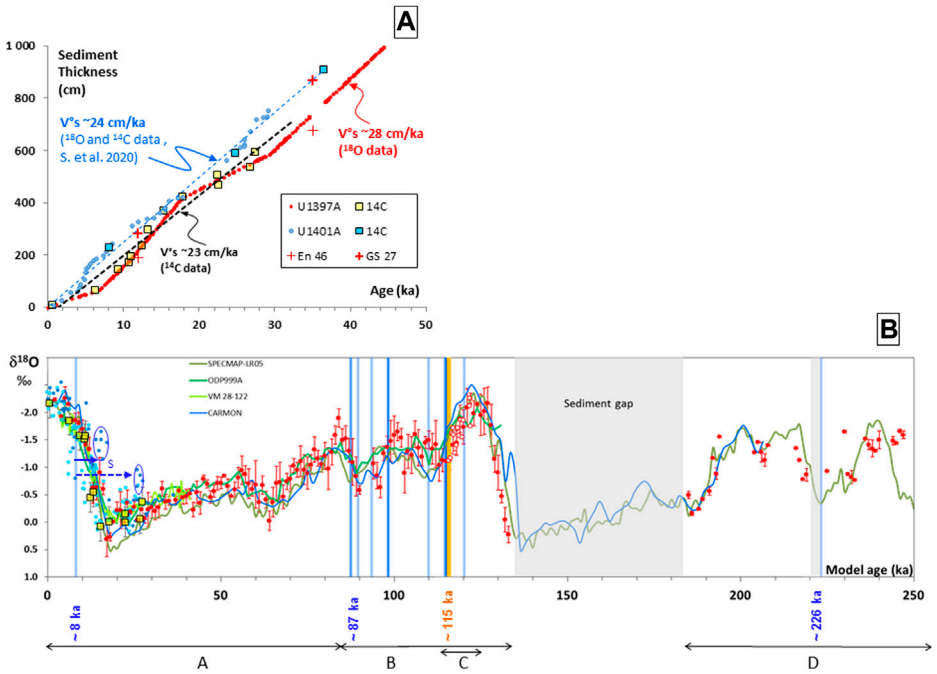


FIGURE 5 | Model age and sedimentation rate of core U1397A. Comparison with core U1401A. **(A)** Sedimentation rates: $\delta^{18}O$ data; red dots: U1397A; blue dots: U1401A (data from Solaro et al. (2020)). Squares: ^{14}C data; yellow: U1397A; blue: U1401A. V°_{S}: mean hemipelagic sedimentation rates. Crosses: data of cores En 46 and GS 27 (biochronology, two values per core; Reid et al., 1996; see also **Figure 8**). **(B)** Model age of core U1397A $\delta^{18}O$ data: red dots: U1397A (mean values with error bars for a sampling step of 1 cm); open red circles: sedimentary units displaced by submarine sliding ("duplicate units"); light blue dots: CARMAR-4 (Boudon et al., 2013); dark blue dots: U1401A (model age from Solaro et al., 2020); continuous green and blue lines: standard $\delta^{18}O$–age patterns (SPECMAP, ODP-999, VM 28-122, CARMON). Yellow squares: ^{14}C data (age errors are within symbol size). Blue bars: turbidites >50 cm; orange bars: debrites; gray domain: erosion or sedimentation gaps; open circles: duplicate hemipelagic unit. Blue ellipses: the two anomalous $\delta^{18}O$ patterns in core U1401A considered stratigraphically discordant units. Letters are the different lithological units (see **Figure 3A**). See also **Figure 4** and the text for further explanations.

maximum depth of $\delta^{18}O$ measurements, **Figure 4**) with the isotopic reference patterns, it is necessary to assume a large gap of hemipelagic sediments at the base of unit B (from 53 m bsf), which corresponds to the turbidites of unit C (**Figure 4**). The missing sediments correspond to a time period of ~50 ka (between 135 and 185 ka; **Figures 5A,B**) and theoretical thickness of hemipelagic sediments of ~14 m estimated from the hemipelagic sedimentation rate. Another but smaller sedimentation gap likely exists at ~85.8 m (in unit D) and is also contemporaneous (at ~226 ka) of a ~1.5 m-thick turbidite. The overall fit with isotopic reference curves for the time period 185–250 ka is less satisfactory than for shallower sediments. The core U1397 provides the longest time interval (~1–133 ka) of continuous sedimentation collected offshore Martinique. The $\delta^{18}O$ record and the corresponding model ages are wholly consistent with those of the CARMON 2 piston core offshore SW Montserrat (**Figure 5B**), which records a continuous sedimentation over ~250 ka, but with much lower sedimentation rates (~2–4 cm/ka; Le Friant et al., 2008).

4.2.2 Core U1399A

Lithology and $\delta^{18}O$ measurements of core U1399A are compared in **Figure 6**. Site U1399A is located further from the coast (~70 km) and at a much greater water depth (2,900 m) than site U1397A (located at ~20 km and 2,480 m water depth), but far from the main marine streams: the mean hemipelagic sedimentation rate should be much lower. Because the U1399A core was drilled through the SLDs, it contains numerous turbidites and debrites and intense deformation over large depth intervals that are related to the volcanic activity and flank collapses of Mt Pelée and possibly Pitons du Carbet (**Figure 3B**). Large perturbations in the hemipelagic sedimentation record are expected. Of the seven ^{14}C dates performed in this core, only three are below the upper age limit of the method (<45 ka; **Supplementary Table S2B**). At the top of unit A, there is a large gap between the ^{14}C dates (~25 ka; **Supplementary Table S2B**) of the two hemipelagic sediment layers 1H1 80-82 and 1H2 60-62 (at depths 82 and 212 cm bsf, respectively), which bracket a 1.2-m-thick turbidite (vertical gray arrows in **Figure 6A**). In the nearby site GS 2, a coarse pyroclastic deposit (75-cm thick) was also reported at a similar depth and attributed to the volcanic activity of Dominica (Reid et al., 1996). The different ^{14}C dates obtained in sediments collected below this turbidite (>210 cm bsf, unit A; **Supplementary Table S2B**) are inconsistent, even considering the large age uncertainties (**Figure 7A**). The existence of a thick turbidite and chaotic distribution of ^{14}C dates in sediment layers below it argue in favor of a strong disturbance of the original sedimentary pile below 80 cm bsf.

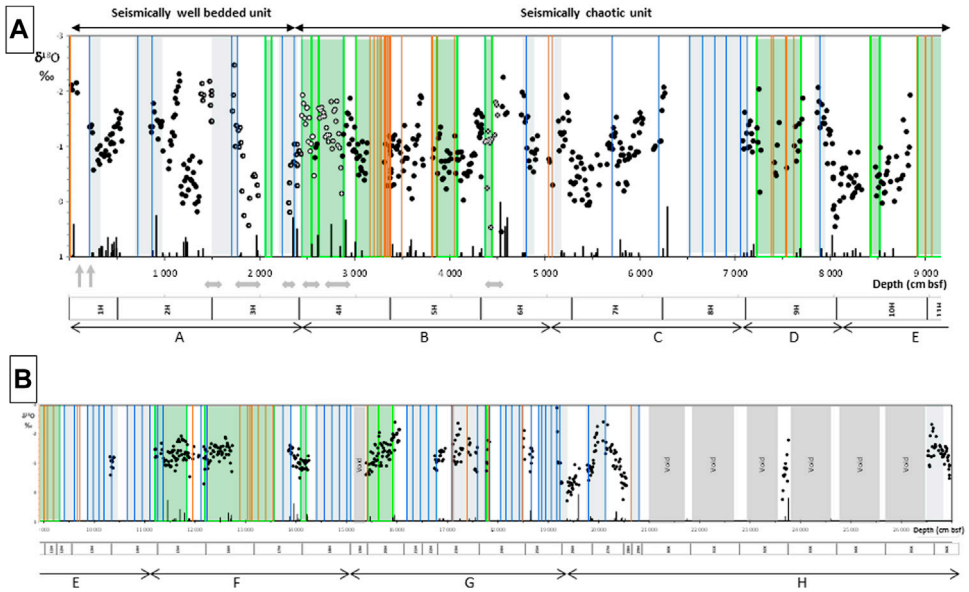


FIGURE 6 | Synthetic logs and $\delta^{18}O$ values of core U1399A. **(A)** 0–90 m bsf. **(B)** 90–270 m bsf. $\delta^{18}O$ data: dots U1399A; open circles: sedimentary units displaced by submarine sliding ("duplicate units"). Blue domains: turbiditic zones; blue bars: turbidites >50 cm; black bars: tephra units; orange bars: debrites. The height of the bars relates to the relative thicknesses of the deposits. Green domains: deformed zones; gray domains: void in core. Gray arrows: the horizontal arrows indicate the duplicate units, and the vertical arrows indicate the first two sediment gaps identified in the upper part of the core (they correspond to the gray domains in **Figure 7A**; see the text for further explanations). Letters are the different core section labels and lithological units (see **Figure 3B**). The reader is referred to high-resolution figure on the web version of this article for benefit.

The $\delta^{18}O$ patterns of the next 2.5–4.2 m in core U1399A (**Figure 6A**), and of the 12.5–17.5 m in core U1397A (base of unit A; **Figure 5B**), are similar and correspond to the age range ~43–60 ka (**Figure 7A**). This confirms the existence of a large sediment gap corresponding to the age range ~12–43 ka and equivalent to ~1.5 m of hemipelagic sediments in core U1399A (gray domain in **Figure 7A**). The few significant ^{14}C data (layers shallower than 80 cm bsf, **Figure 7B**) provide a rough estimate of the hemipelagic sedimentation rate Vs^0 ~ 9 cm/ka. This value is consistent with the biostratigraphic estimate of Vs°~8 cm/ka at the site GS 2 nearby (Reid et al., 1996). As for the core U1397A, a compaction factor of $k^0 = 10^{-6}\,cm^{-1}$ is estimated from the comparison of the first well-identified continuous sediment units. The fit of the $\delta^{18}O$ pattern of core U1399A with reference isotopic curves over the last 150 ka (**Figure 7A**) provides a more confident estimate of the mean hemipelagic sedimentation rate of ~5.2 cm/ka (**Figure 7B**).

For greater depths, we investigate step by step, with increasing depth, the different continuous series of hemipelagic sediments using the VCDs (**Figure 6**). The $\delta^{18}O$-age pattern of each continuous series is established using the estimate of the hemipelagic sediment thickness and mean sedimentation rate. As for core U1397A, these patterns are compared and fit to reference isotopic curves considering possible duplicates or gaps in the sedimentary sequence. Duplicates and gaps are generally bracketed by thick turbidite, debrite, or deformation zones (**Figure 6**). In deformed zones, the actual thickness of sediments is lower than that measured by depth variations because of folding or tilting of the sedimentary layers. The apparent sedimentation rate is $Vs = Vs^0\ (1 - k^0\ d)\ k^1$, with $k^1 > 1$. For all deformed zones, we adopted, in first approximation, an elongation factor of 10%, let $k^1 = 1.1$, which is consistent with observations (Lafuerza et al., 2014; Brunet et al., 2016).

The resulting age model for the core section down to 210 m bsf is reported in **Figure 7C**. The consistency between the SPECMAP curve and the $\delta^{18}O$ model age of U1399A is relatively satisfying up to ~1.2 Ma (~120 m bsf). Beyond this, especially for ages >1.6 Ma (>190 m bsf), the poor recovery, the scarcity of continuous sedimentary piles and the almost systematic deformation prevent confident fitting. On the basis of $\delta^{18}O$ patterns, many duplicate units are identified in the upper 45 m of the core (base of unit A and the whole unit B; **Figures 6**, **7C**); they probably also exist at greater depths in the sediments but are not identifiable. The origin of such chronological discrepancies will be discussed below in the context of stratigraphic disturbances caused by erosion and sliding sediment packages. The decrease in the amplitude of $\delta^{18}O$ variations for ages older than 1 Ma is well-known (Mid-Pleistocene transition; see, for example, Clark et al., 2006) and consistent with the $\delta^{18}O$ patterns between ~95 and 175 m bsf (units E and F; **Figures 6B**, **7**). On the contrary, the $\delta^{18}O$ pattern between 195 and 210 m (unit H; **Figure 6B**) is characterized by a broad peak with large variations in $\delta^{18}O$ values (range: [−2.5; 0.3‰]), which is inconsistent with ages older than 1 Ma. This range of $\delta^{18}O$ values is typical of the time periods 0–250 ka or 350–750 ka, which suggests that this sediment package could represent a 10-m-thick duplicate unit of a relatively recent material overlain by a very thick pile of at least 100 m of older sediments.

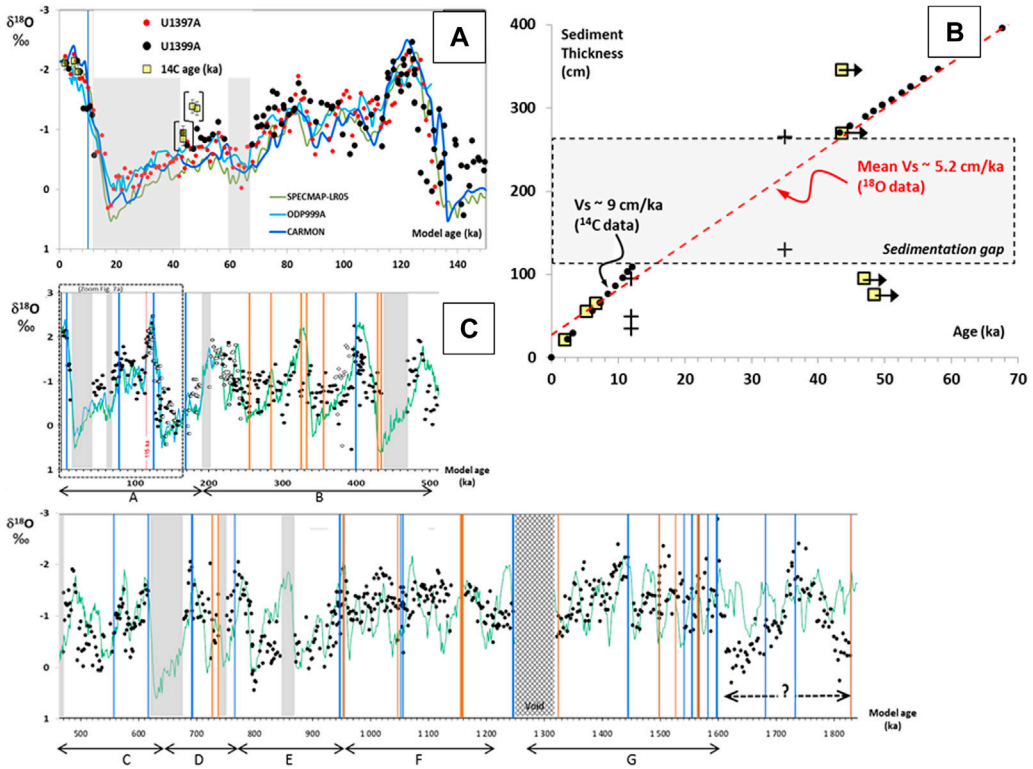


FIGURE 7 | Model age and sedimentation rate of core U1399A. **(A)** Model age for the time period 0–150 ka. Dots: $\delta^{18}O$ data of cores U1399A (black) and U1397A (red). Squares: ^{14}C data of core U1399A; error bars are within symbol size; black arrows: data out of ^{14}C dating range. Continuous lines: standard $\delta^{18}O$—age patterns. Blue bars: turbidites >50 cm; orange bars: debrites. Gray domain: erosion or sedimentation gaps (identified by arrows in **Figure 6A**). **(B)** Sedimentation rate. Black dots: U1399A; squares: ^{14}C data. V°_{S}: mean hemipelagic sedimentation rates. Crosses: data of cores En 6, GS 2 and GS 18 (biochronology, Reid et al., 1996; see also **Figures 1**, **8**). **(C)** Model age for the time period 0–1.8 Ma. $\delta^{18}O$ data: black dots; open circles: sedimentary units displaced by submarine sliding ("duplicate units"). Reference curves: SPECMAP (green) and CARMON (blue). Other symbols as in **(A)**. Letters are the different core section labels and lithological units (see **Figure 3B**). For ages older than ~1 Ma, the proposed chronology has a low confidence due to large deformation and low recovery. No attempt has been made to interpret data for sediments deeper than 200 m (i.e., older than >1.6 Ma).

5 DISCUSSION

5.1 Preservation of Sedimentary Deposits and Chronostratigraphy

The Caribbean flank of the southern part of the Lesser Antilles Arc is characterized by high sedimentation rates of both hemipelagic and volcanic origin. The volcanic supply is high and variable along the Caribbean coasts because of the distribution of the active volcanic centers on the western side of the islands and of the western vergence of the horseshoe-shaped structure generated by flank collapses that channel the pyroclastic flows and debris avalanches (**Figure 1**; Deplus et al., 2001). The distribution and thickness of volcaniclastic turbidites and debrites are also extremely variable as indicated by the VCDs of the different cores offshore Martinique (**Figure 3**; Le Friant et al., 2002; Le Friant et al., 2013). Two factors favor erosion of the sedimentary deposits: 1) the local sea floor morphology with very steep submarine slopes and deep canyons related to regional and local fracturing (Feuillet et al., 2002) which favor the sliding of sediment piles and erosion by powerful turbidity currents, and 2) the volcanic activity itself through potentially erosive debris avalanches and related submarine landslides (Le Friant et al., 2015; Le Friant et al., 2020). On the contrary, on the eastern (Atlantic) side of the islands, the hemipelagic and volcanic sedimentation rates are much lower (Reid et al., 1996; Le Friant et al., 2008), and volcanic deposits almost exclusively consist of small volcanic clasts transported in volcanic plumes, but the preservation of sediments over long periods of time is much better (Reid et al., 1996).

The hemipelagic and volcanic sediments recorded in cores offshore Martinique generally consist of a series of continuous and well-preserved units of highly variable thicknesses (from typically 10 m–50 m, but sometimes some meters only) separated by volcaniclastic turbidites or more rarely by debrites. No erosion features at the top or the bottom of these units are identified in VCDs (Le Friant et al., 2013), but a fine analysis of $\delta^{18}O$ patterns suggests that some rare debrites may have had a significant erosive effect as, for example, at ~50 m bsf in core U1399A (unit C, 435 ka; **Figures 6**, **7C**). All along the core U1399A (**Figure 7C**) and below ~52 m bsf in core U1397A (**Figures 4**,

5B), many large hemipelagic sedimentation gaps are identified through $\delta^{18}O$ chronostratigraphy. Finally, numerous duplicate sedimentary units are also identified in core U1399A (**Figure 6A**) and one in core U1397A (unit C and following; **Figure 4**) that result from slumping of coherent sediment slices down steep canyon flanks (U1397A) or at the front of large submarine landslides (U1399A). Thus, the sedimentary records of both cores reflect continuous hemipelagic sedimentation with discrete volcanic deposits, turbidites, and more rarely debrites producing sedimentary piles that are periodically destabilized or eroded. Potential triggering processes are various: sediment overload and slope failure, large volcanic events or flank collapses (Le Friant et al., 2015; Brunet et al., 2016; Le Friant et al., 2020), earthquakes, etc.

Three factors affect the $\delta^{18}O$ correlations and age models: inconsistent $\delta^{18}O$ values (i.e., duplicates), sediment gaps (by erosion), and recovery gaps. The continuous hemipelagic sediment record in the upper 28 m (Unit A) of core U1397A allows the reconstitution of a precise chronostratigraphy over ~135 ka in both cores (**Figures 5B**, **7A**). On the basis of reference $\delta^{18}O$ age curves, the age resolution is ~2 and ~5 ka in cores U1397A and U1399A, respectively (see **Supplementary Figure S3**). In core U1399A, this reconstitution is possible up to ~1.5 Ma but with a much lower age resolution and large discontinuities especially from ~450 ka; poor recovery, erosion, and slumping and deformation of sediments strongly affect the age model. All events recorded by well-identified deposits can then be dated. Tephra layers, despite some evidences of post-deposition transport on short distances, do not significantly disturb the hemipelagic sedimentation and are accurately dated. Since volcaniclastic turbidites and debrites are discontinuities in sedimentation, only maximum or minimum ages of emplacement can be estimated.

5.2 Sedimentation Rates

The hemipelagic sediments on the eastern side of the Grenada Basin consist of a dominant fraction of terrigenous (volcanic clay and silts) sediments supplied by island rivers and a low fraction of pelagic sediments produced *in situ* but also transported from the Atlantic Ocean by the powerful submarine currents through island passages (South Dominica, South Martinique, and South St Lucia; Reid et al., 1996; **Figure 8A**). In the Caribbean Sea, along the western coasts of the Lesser Antilles Arc, the hemipelagic sedimentation rates are variable in space and time; they are high close to the islands at the mouth of inter-island submarine channels and rapidly decrease away into the Grenada Basin (Reid et al., 1996). The pure hemipelagic sedimentation rates measured close to the shore (~25 km) in cores CARMAR-4 (upper 7 m; Boudon et al., 2013), U1401A (upper 8 m; Solaro et al., 2020), and U1397A (upper ~25 m) are similar, varying between 24 and 28 cm/ka (**Figure 5A**). The location of sites CARMAR-4 and U1397A at the mouth of the Dominica channel explains their slightly higher hemipelagic sedimentation rates than those of U1401A (**Figure 8A**). The sedimentation rates decrease rapidly with distance from the Grenada Basin with a mean value of ~5.2 cm/ka at ~70 km (site U1399A; **Figure 7B**). These low sedimentation rates are consistent with biostratigraphic estimates in the Grenada Basin (e.g., 8 cm/ka at site GS 2; Reid et al., 1996; **Figure 8A**). More generally, they are consistent with estimates in most sites in the Lesser Antilles Backarc, Forearc, or Volcanic Platform ranging between 2 and 8 cm/ka for at least the last 80 ka (Reid et al., 1996, **Figure 8A**). They are also consistent with recent estimates (3–4 cm/ka) using $\delta^{18}O$ and ^{14}C chronostratigraphy on cores offshore SW Montserrat (CARMON-2, Le Friant et al., 2008; U 1396, Wall-Palmer et al., 2014; Fraass et al., 2017; **Figure 8A**). The background hemipelagic sedimentation rates are, thus, generally <8 cm/ka in the whole east Caribbean Sea except along the flanks of the southern islands (sites U1397A and U1401A offshore Martinique and En46, ~60 km S offshore St Lucia) and in site GS-27, 220 km SW-offshore Grenadines, where they are 3–4 times higher (**Figure 8A**). The distribution of these sites suggests that the most active volcanoes in the southern Antilles Arc provide a higher supply of volcanic silts and clays and that there is an active transport of terrigenous sediments by the N–S surface coastal currents in the south Grenada Basin. Finally, there is no evidence of large variations in the hemipelagic sedimentation rate during the last glacial period in cores U1397A and U1401A (**Figure 8B**). This is consistent with the study of Reid et al. (1996) showing that in the southern part of the Antilles backarc, hemipelagic sedimentation rates are weakly dependent on sea level height, contrary to those in the northern regions.

The variations in sedimentation rates (in cm/ka) of every type of sediment (hemipelagic, volcanic, turbidites, and debrites) are estimated using model ages and sediment thicknesses corrected, if necessary, for deformation and discarding duplicate units (**Figure 8B**). Though some significant biases may occur for core U1399A due to underestimation of duplicate units and large chronology uncertainties for ages >450 ka, some robust observations can be highlighted. In both cores, hemipelagic sedimentation is largely dominant (~70% in U1397A and ~50% in U1399A). In core U1399A, sedimentation rates of volcaniclastic turbidites and debrites are largely dominant over those of tephra. In core U1397A, the turbidites and tephra sedimentation rates are similar. In core U1397A, the total sedimentation rate of ~43 cm/ka is roughly constant over the last ~150 ka (**Figure 8B**). The sedimentation rate of turbidites is highly variable and dominated by some discrete major events in a short interval of time between 90 and 120 ka (unit C; **Figure 8B**). In core U1399A, the total sedimentation rate is ~11 cm/ka over the last 1.5 Ma, and the sedimentation rates of turbidites and debrites are highly variable in time. All these observations are consistent with the location of the two sites: U1397A is close to the coast but far from the outlet of flank collapse structures and, thus, collects a significant fraction of erupted products but a low fraction of volcaniclastic turbidites. Site U1399A is located on the submarine landslides far from the coast: it collects much less volcanic tephra but is supplied by reworked material transported by submarine landslides and turbidity currents (Le Friant et al., 2020). Finally, no correlations exist between variations in sedimentation rates and changes in sea level, which suggests that volcanic products constitute the dominant supply of all types of sediment, which are therefore independent of sea level changes.

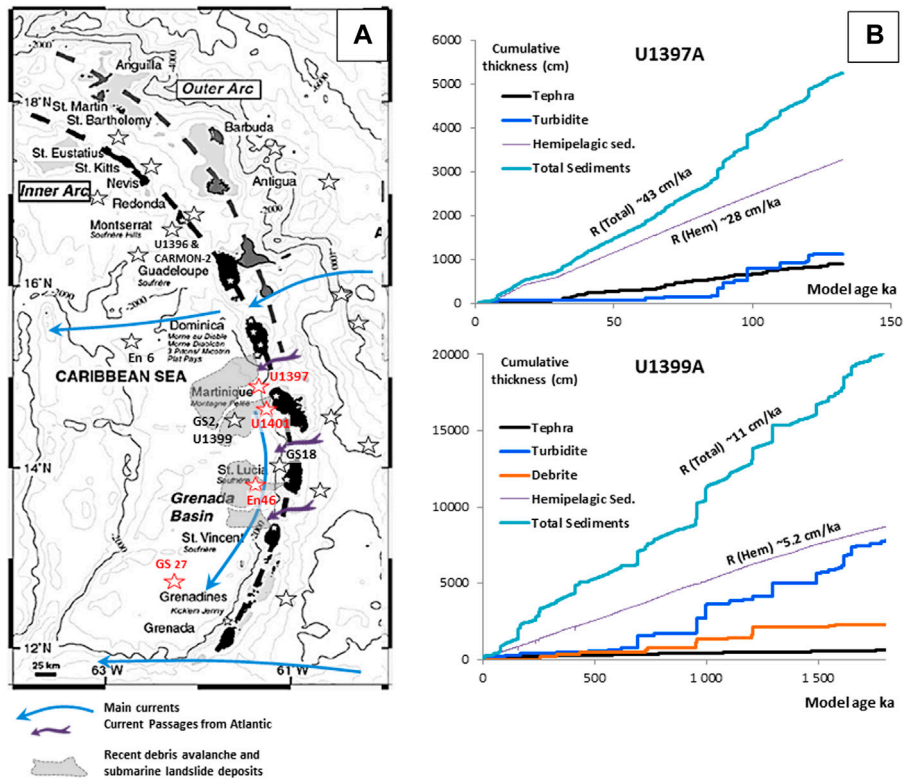


FIGURE 8 | Sedimentation rates. **(A)** Hemipelagic sedimentation rates in the South Caribbean Sea (Grenada Basin). Red stars: V˚s > 15 cm/ka; black stars V˚s < 8 cm/ka. Data sources: U1397A, U1399 (this work); U1401 (Solaro et al., 2020, modified); U1396 and CARMON-2 and NE Montserrat; Le Friant et al., 2008; Wall-Palmer et al., 2014 and Fraass et al., 2017); En 6, En 46, GS 2, GS 27, and other coring sites north Guadeloupe: biostratigraphic estimates (Broecker et al., 1990; Reid et al., 1996; Carey 1999). **(B)** Cumulative sediment thicknesses with time: sites U1397A and U1399A. R (Total) and R(Hem) values are the mean sedimentation rates of hemipelagic and total sediments. It is to be noted that hemipelagic curves are used as a reference (rates are estimated from ^{14}C and $\delta^{18}O$ dating for age <50 ka and beyond are assumed constant; see **Figures 5A**, **7B**).

5.3 Eruptive Activity

Depending on the eruptive style, volcanic deposits at sea are very variable in nature and thickness. Plinian and sub-Plinian eruptions producing pumice clasts and scoriae that are widely dispersed in the atmosphere are most likely to be registered at sea and are better represented on the eastern side of the arc due to dominant easterly winds. Dome-forming eruptions generally produce pyroclastic flows that also generally reach the sea but have limited aerial extent. Almost all eruptive episodes have significant phreatic activity which widely disperses a large amount of very fine material. This material, however, is very quickly transformed into clay during sedimentation in the sea and extremely difficult to distinguish from hemipelagic material from another origin. To reconstruct the volcanic history, the sedimentary record must not only be as complete as possible but also as least disturbed as possible by the numerous processes that may affect the submarine flanks of Lesser Antilles volcanoes: volcano flank collapses, turbidity currents generated by sediment failures on the steep submarine slopes (especially on the western coasts), and erosion by the strong deep sea currents. Due to the steep slopes of the western flanks of the volcanoes and existence of strong marine currents, the products of volcanic eruptions are rarely deposited by fallout on the sea floor without some lateral transport or reworking. In most cases, volcanic material has been reworked after initial deposition, leading to more or less blunt magmatic fragments. In addition, due to the high crystallinity of most andesitic material, glassy material is rare. Consequently, submarine sediments are considered representative of an eruptive episode if they contain volcanic material that has been only slightly modified by post-depositional transport, that is, with a significant fraction of pumice or scoria fragments that are extremely fragile and cannot be preserved over long transport distances or angular dome fragments.

Core U1397A provides a continuous record of tephra layers over the first 130 ka, with a time resolution ~2 ka. Over the top 50 m (approximately the first 110 ka), the two cores U1397A and U1397B display similar distributions of tephra layers despite significant differences in the distribution of turbidites (see **Supplementary Figure S2**), which confirms the good volcanic record at this site. Although more fragmentary, the tephra record in core 1399A allows reconstruction of the volcanic activity from

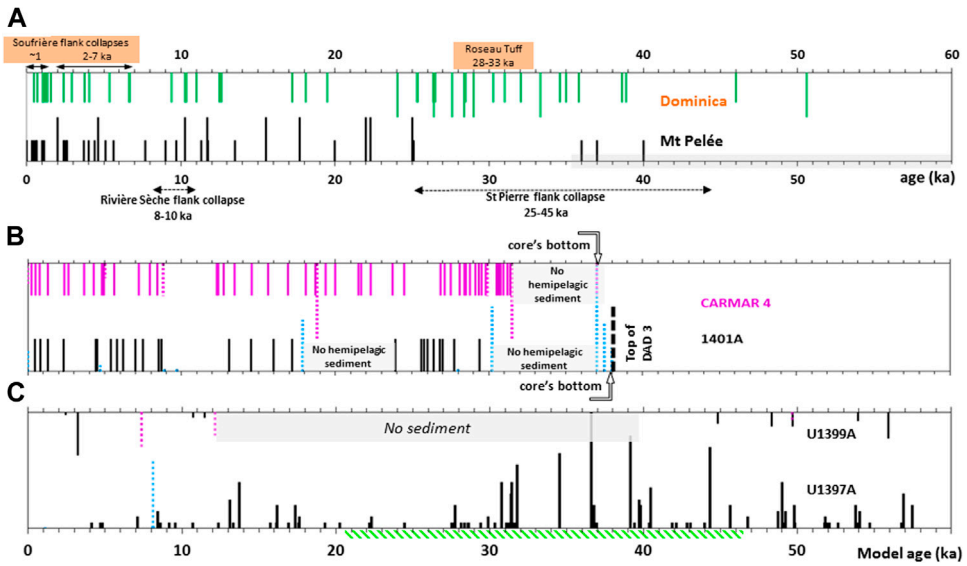


FIGURE 9 | Volcanic records on land (Mt Pelée and Dominica) and in cores U1397A, U1399A, U1401A, and CARMAR 4: 0–60 ka. **(A)** On-land dating. Data sources: 1) Dominica: flank collapses Soufrière (^{14}C; Le Friant et al., 2002), Plat Pays (K-Ar; Samper et al., 2008), and eruptions (^{14}C, Carey and Sigurdsson, 1980, Lindsay et al., 2005, Boudon et al., 2017; U-Th/He Howe et al., 2014). 2) Mt Pelée: flank collapses: "Le Prêcheur" and "St Pierre" (K-Ar, Germa et al., 2011a), "Rivière Sèche" and "St Pierre" (U-Th, Le Friant et al., 2002, Le Friant et al., 2015 and Villemant, unpublished; ^{14}C, Westercamp et al., 1989 and Boudon et al., 2013). Eruptions ages: most ^{14}C dates for Mt Pelée are relatively old measurements by bêta counting (gray zone: all ages out of ^{14}C dating range; Traineau et al., 1989); recent ^{14}C data: Michaud-Dubuy et al., 2019; others: K-Ar, Germa et al., 2011a; U-Th, Le Friant et al., 2002 and Villemant, unpublished. Age ranges of flank collapses are estimated using bracketing ages of pre- and post-flank collapse dome-forming eruptions (see also **Figure 2**). The height of the bars relates to the relative intensities of the eruptions (on-land data). **(B)** Cores U1401 A and CARMAR –4 (from Solaro et al. (2020) and Boudon et al. (2013), modified). Lines: tephra; dotted lines: turbidites (the height of the bars relates to the relative thicknesses of the turbidites). Gray domains: hemipelagic sedimentation gaps. Thick dashed line: end of core U1401A on top of the most recent DAD offshore Mt Pelée (DAD3; see **Figure 1**); its age of ~36 ka (minimum value, Solaro et al., 2020) is still questioned (see text for explanations). **(C)**: Cores U1397A and U1399A (this study). Tephra (lines) and turbidites (dotted lines) are represented with their relative thicknesses. Gray domain: sedimentation gap between 12 and 40 ka (U1399A). The green dashed domain (~20–47 ka) corresponds to the presence of large fractions of mafic scoriae in core U1397A (Del Manzo et al., in prep.). Scales are arbitrary and different for tephra layers, turbidites, and debrites.

~45 ka to ~1.5 Ma. The time resolution varies from ~4 ka for the first 450 ka to much higher values and higher uncertainties in age calibration, beyond.

In **Figure 9**, for the time period 0–60 ka, volcanic records in cores U1397A and U1399A are compared to the data of cores U1401A (Solaro et al., 2020) and CARMAR 4 (Boudon et al., 2013) and to on-land data for the eruptions of Mt Pelée and the most intense ones of South Dominica. The core U1399A does not contain significant information on that time period because of a sedimentation gap (~10–45 ka; **Figure 7A**). The site U1401A, the closest to the coast, suffers from large bias in the volcanic record because of its location in front of the flank collapse structures of Mt Pelée. Channelized pyroclastic and debris flows reaching the sea or remobilized by riverine erosion have produced the numerous turbidites recorded in this core (Solaro et al., 2020). The site CARMAR-4, close to site U1397, displays many more tephra layers than other cores during the first 5 ka likely because deposits are much less disturbed by piston coring than most other drilling techniques (**Figure 9**). The submarine cores clearly provide more complete information on the frequency of volcanic activity than on-land data that suffer from limitations in sampling and dating.

The volcanic activity in Dominica is the main activity that can interfere with Mt Pelée deposits in these cores because of its proximity and intensity. In particular, the "Roseau Tuff" eruption (28 ± 3 ka, Carey and Sigurdsson, 1980, Lindsay et al., 2005; 33.3 ± 0.4 ka Boudon et al., 2017) was the largest explosive eruption since 200 ka in the Antilles Arc (**Figure 9A**). However, the air-fall products of this eruption are mostly dispersed eastward from the Lesser Antilles Arc and almost absent on the western side of the islands (Carey and Sigurdsson, 1980). On the contrary, the voluminous pyroclastic flows of this eruption have triggered submarine pyroclastic and debris flows channelized southward to the Grenada Basin (Sparks et al., 1980a; Whitham, 1989; **Figure 1B**). Tephra layer distributions in the cores IODP340 (U1397A and U1401A) and CARMAR 4 display apparent increase in activity at that period (~25–32 ka; **Figure 9B**). Volcanic products of Dominica compared to those of other nearby islands are typically more K-rich (Carey and Sigurdsson, 1980); almost all glass compositions of tephra measured in cores U1401A (Solaro et al., 2020) and U1397A (at least over the top 50 m let ~0–130 ka, Del Manzo et al., in prep.) are typical of Mt Pelée and not of Dominica (**Figure 10A**).

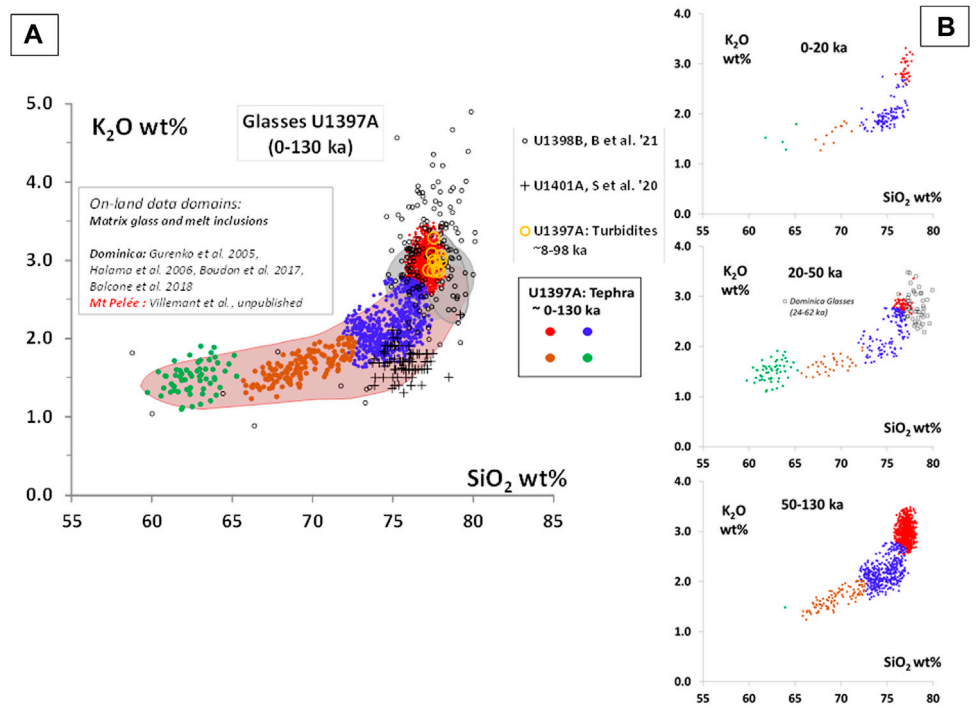


FIGURE 10 | SiO_2 and K_2O compositions of glass from cores of the IODP340 expedition. **(A)** Comparison with on-land samples of Mt Pelée and Dominica. Colored symbols: tephra (dots) and turbidites (open yellow circles) of core U1397A (top 50 m ~ 0–130 ka; Villemant et al., unpublished data and Del Manzo et al., in prep.). Tephra: the different colors correspond to arbitrary subdivisions according to the SiO_2 and K_2O concentrations. Small black circles: tephra and turbidites of core U1398B (0–900 ka, Breitkreuz et al., 2021). Black crosses: tephra and turbidites of core U1401A (0–36 ka; Solaro et al., 2020). Composition domains: matrix glass and melt inclusion compositions (on-land data). Gray domains: South Dominica (0–60 ka, Gurenko et al., 2005; Halama et al., 2006; Boudon et al., 2017; Balcone et al., 2018); red domain: Mt Pelée (0–80 ka, Villemant et al., unpublished data). **(B)** Variations in U1397A glass compositions with time. 0–20 ka: "Recent Pelée"; 20–50 ka: "Grand Rivière"; open squares: glasses from South Dominica (24–62 ka); and 50–130 ka: "Old Pelée."

In core U1397A, only few tephra glasses have Si- and K-rich glass compositions, which may correspond to Roseau Tuff eruption, and the coexistence, in the same tephra layers, of K-poor glasses that are absent in Dominica products also favor the Mt Pelée source (**Figure 10B**). In general, in these cores offshore Martinique, very few tephra deposits originate from Dominica, except in core U1398 at the front of Martinique SLDs in the Grenada Basin, which almost exclusively contains material from Dominica (Breitkreuz et al., 2021). The different types of tephra products (dome or Plinian clasts or scoriae) in cores CARMAR 4 and U1397A are not investigated in this study, but preliminary petrological data on U1397A tephra (Del Manzo et al., in prep.) indicate the presence of abundant scoriae fragments from ~50 to ~20 ka (**Figure 9C**), which is consistent with the observations in core U1401A (Solaro et al., 2020). The glass compositions of these scoriae are typical of the less Si-rich end member of "Grand Rivière" activity (**Figure 10B**).

The total number or thickness of tephra layers, averaged over different time periods (5 or 20 ka), provide estimates of the variations in sedimentation rates of magmatic products (expressed in number/ka or cm/ka; **Figure 11A**). They may also be estimated by the variations in the slopes of cumulative thickness vs. time (**Figures 8B**, **11B**). These parameters are designated under the collective term of mean deposition rate and are used as proxies of the magma production rates. These are minimum values since volcaniclastic turbidites are not included in the balance but may partly be direct products of the volcanic activity. A systematic and detailed study of the turbidites is required to evaluate their actual contribution. In addition, as discussed above, a significant part of the tephra falls (mainly from phreatic and Plinian eruptions) are not recorded in submarine deposits on the western flank of the volcano mainly due to prevailing easterly winds. For the three cores CARMAR-4, U1397A, and U1401A, the recorded activity over the common period of time of ~0–32 ka is low compared to older time periods (**Figure 11C**). In contrast to the large gaps in the tephra succession on land, particularly at > 20 ka (**Figure 9**), the volcanic activity of Mt Pelée recorded offshore is continuous from at least ~130 ka to the present day, with four main periods (**Figure 11A**).

Using cumulative tephra thickness, the most recent period (20 ka—present day) is the less active period with a mean tephra deposition rate of 3 cm/ka. This result contrasts sharply with that of previous evaluation because on-land data are typically biased by better preservation and exposure of the more recent deposits

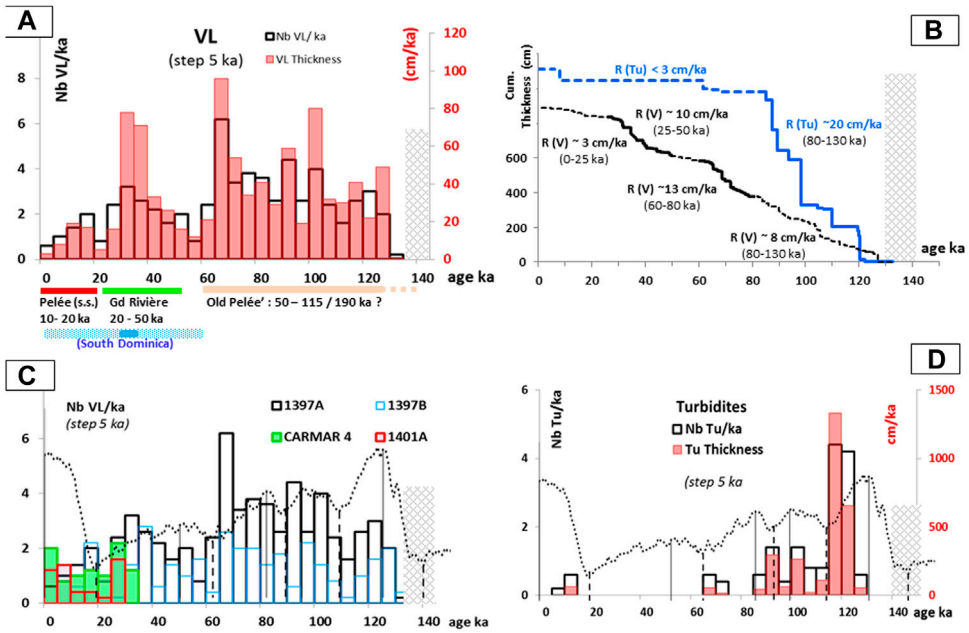


FIGURE 11 | Volcanic tephra deposition rates over the period 0–140 ka (core U1397A). **(A)** Tephra deposition rates. Nb VL/ka: total number of tephra layers (VL) per ka; VL thickness: total thickness of tephra layers per ka. Histograms are drawn with intervals of 5 ka. **(B)** Cumulative thicknesses of tephra and turbidites. R(V) and R(Tu): deposition rates of tephra and turbidites, respectively, in centimeter per ka. In brackets: intervals of time for each deposition rate estimated using a least square regression. **(C)** Comparison of tephra deposition rate estimates in cores U1397A, U1401A, and CARMAR-4. Caption as in **(A)**. Dotted lines: LR04 curves for comparison of deposition rates variations with high and lowstands of the sea level. **(D)** Deposition rates of turbidites. Caption as in **(A)**. Dashed zones: sediment gaps. Dotted lines: LR04 curves for comparison of deposition rates variations with high and lowstands of the sea level.

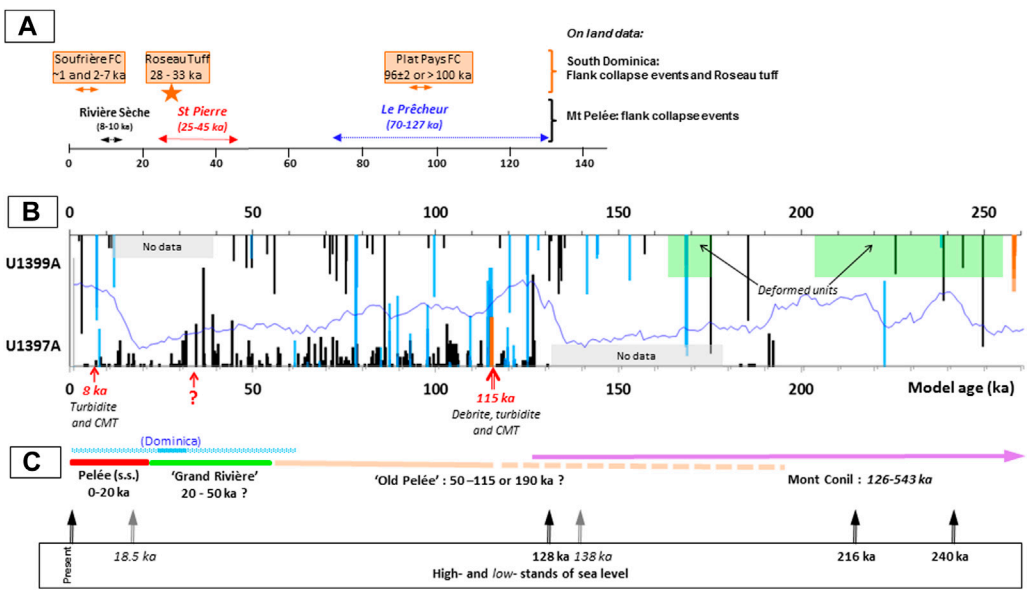


FIGURE 12 | Volcanic records on land (Mt Pelée and Dominica) and in cores U1397A and U1399A: 0–260 ka. **(A)** On-land data. **(B)** Core data. **(C)** Proposed chronology of active volcanic centers. Symbols and data sources as in **Figure 9**. Red arrows in **(B)** refer to possible flank collapses identified on land and offshore. CMT: coherent mass transport (duplicate units). Blue line: LR04 curves for comparison. Dashed lines indicate speculative extent of the volcanic activity.

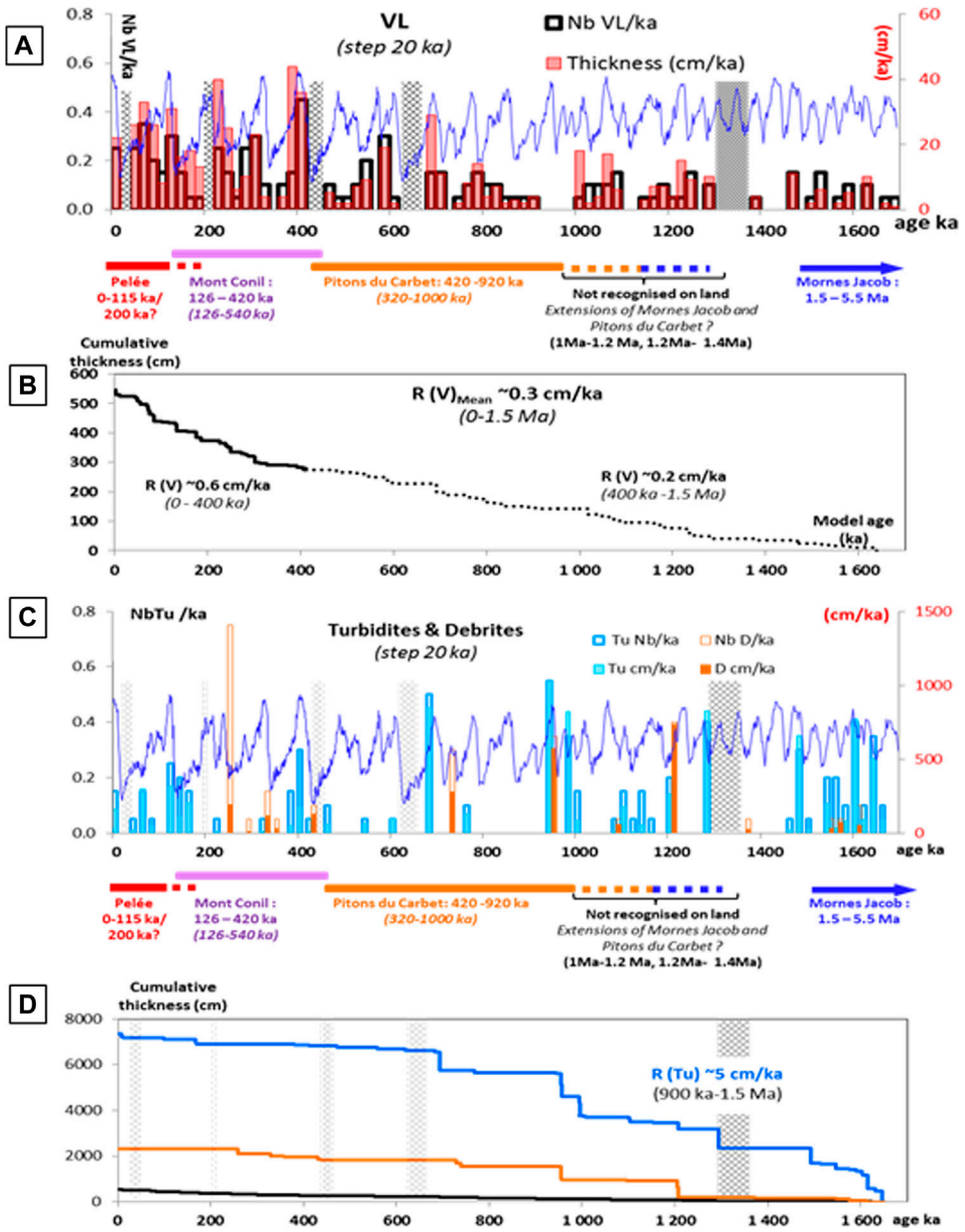


FIGURE 13 | Deposition rates of tephra and turbidites over the period 0–1.5 Ma (core U1399A). Histograms are drawn with intervals of 20 ka. Blue lines: LR04 curves for comparison of deposition rate variations with high and lowstands of the sea level. Dashed zones represent sediment lack (light gray) and void (dark gray) in the core. The height of the bars relates to the relative thicknesses of the deposits. Age ranges: this study; in brackets: previous data (K-Ar dating; Germa et al., 2010; Germa et al., 2011a). **(A)** Tephra deposition rates. Nb VL/ka: total number of tephra layers (VL) per ka; VL thickness: total thickness of tephra layers per ka. **(B)** Cumulative thicknesses of tephra. R(V): mean deposition rates of tephra in centimeter per ka. In brackets: intervals of time for each estimate. **(C)** Turbidite deposition rates. Blue bars: turbidites; orange bars: debrites. Tu Nb/ka and D Nb/ka: total number of turbidites and debrites per ka; Tu cm/ka and D cm/ka: total thickness of turbidites and debrites per ka. **(D)** Cumulative thicknesses of turbidites, debrites, and tephra. Blue line: turbidites; orange line: debrites. R(Tu): mean deposition rate of turbidites in centimeter per ka. In brackets: intervals of time for the estimate.

(see, for example, Traineau et al., 1989 and **Figure 9A**). The periods 50–20 ka and 80–50 ka have the highest mean tephra deposition rates (~10 and 13 cm/ka, respectively) with maximum activities at ~ 30 and ~70 ka, respectively (**Figure 11**). It should be emphasized that the 30–50 ka period of activity which is characterized by the emission of Grand Rivière–type magmas

is much longer and more productive than indicated by on-land investigations (Bourdier et al., 1985). In addition, the model of rejuvenation of the magmatic activity with the emission of more dense mafic magmas triggered by a major flank collapse proposed by Boudon et al. (2013) is incompatible with these new data, which provide no evidence for such triggering event at 50–60 ka, neither on land nor in the cores.

The maximum age of the last period of activity cannot be determined neither in core U1397A because of a large sediment gap (135–185 ka; **Figures 5B**, **12**) nor in core U1399A because of the low age resolution. However, the period of continuous activity lasted at least 50 ka (80–130 ka) with a tephra deposition rate roughly constant ~8 cm/ka (**Figure 11B**). All volcanic activity recorded from 130 ka is by default attributed to Mt Pelée s.l.; the petrological consistency of the whole period still requires confirmation (Del Manzo et al., in prep.).

The core U1399A provides a longer time scale (**Figure 13**). Deposition rates are minimum values since the volcanic units are under-represented in this core because of the great distance to volcanic centers and the fragmentary record. Two main activity periods are evidenced: the recent period, 0 to ~300–400 ka with a mean tephra deposition rate of ~0.6 cm/ka, and the older period (>400 ka) with a deposition rate three times lower (~0.2 cm/ka; **Figure 13B**). Over the last 130 ka, the mean tephra deposition rate at site U1399A is ~10 times lower than that at site U1397A mainly due to the greater distance to volcanic centers and the many missing sedimentary units below 50 m bsf, which lead to a significant underestimate (**Figure 6**). These results, nevertheless, indicate that the volcanic activity in Martinique was almost continuous since at least 1.5 Ma, with a few short rest periods separating several distinct activity periods that roughly correspond to those defined on land (**Figure 13A**). Three successive activity periods at North Martinique are recorded since ~1 Ma, which likely correspond to the three volcanic centers: Pitons du Carbet, Mont Conil, and finally Montagne Pelée (s.l.). In the absence of petrological arguments, it is not possible to identify the possible transition between the activities of Mt Conil and Mt Pelée (s.l.). Volcanic activity older than 1.4 Ma may correspond to that in Morne Jacob. Between 1 and 1.3 Ma, a significant volcanic activity is recorded in core U1399A but not on land. It is separated from the two other periods of activity by rest periods of ~50–100 ka (**Figure 13A**). It could correspond to an extension of the activity of either Morne Jacob or Pitons du Carbet or a still unknown activity.

5.4 Volcaniclastic Turbidites

Almost all turbidites in cores offshore Martinique are volcaniclastic turbidites. Turbidity currents can be generated by voluminous pyroclastic flows entering the sea. They can also be generated on land by remobilization by rivers of pre-existing volcaniclastic deposits (especially during cyclonic periods) or by slope failure within the sea (in that case, the volcanic material is mixed with hemipelagic sediment). The steep slopes of the western coast of Martinique and the strong marine currents favor such submarine remobilizations. The minimum age of emplacement of the turbidite (as well as debrite) is by default approximated by the age of the first overlying hemipelagic layer, but turbidite packages may have been emplaced over large intervals of time (**Figures 12**, **15**). Turbidites have highly variable thicknesses (some cm to 10 m) and are highly heterogenously distributed along the cores. They very often constitute a series of successive turbidites with total thicknesses up to 15–20 m (e.g., unit C; **Figures 4**, **6**). The abundance (or deposition rate) and distribution of turbidites directly depends on the core location. The location of site U1397A on a topographic high strongly prevents it from the influence of turbidity currents; turbidites are almost absent in the upper 30 m and scarce up to a depth of 53 m bsf (**Figures 4**, **5B**). Below, the ~17-m-thick turbidites at the base of unit C are older than 87 ka and have an average accumulation rate of ~20 cm/ka over the time interval 87–130 ka (**Figure 11B**); this suggests that this site before ~87 ka was strongly affected by turbidity currents and probably closer to the channel bed. The core U1398B located in the Grenada Basin outside the SLDs contains at its top a thick series of well-bedded turbidites of total thickness ~30 m, which represent around 2/3 of the total cored sediments (Le Friant et al., 2013). This site collects submarine sediments rich in volcaniclastic material that are remobilized by the strong turbidity currents flowing in deep channels to the Caribbean Sea. The cores U1400A and 1401A located at the outlet of the Mt Pelée collapse structures contain at their top thick turbiditic units (~25 and 50 cm, respectively) almost devoid of hemipelagic sediments (Le Friant et al., 2013); they directly collect pyroclastic material deposited on land and remobilized by rivers draining rainfall in the north of Martinique. On the contrary, core U1399A is located on SLDs, but ~70 km from the coast, contains at its top ~80 cm of hemipelagic sediments (**Figures 3**, **6**) and, in the top 60 m (Units A and B), a low proportion of turbidites with a low deposition rate (<3 cm/ka; **Figure 11B**).

Erosion of pre-existing sediments at the emplacement of turbidites is a well-documented feature (see, for example, Trofimovs et al., 2010; Trofimovs et al., 2013). The $\delta^{18}O$ chronostratigraphy in cores U1397A and U1399A indicates that erosion and/or duplication of large sedimentary units may occur at the emplacement of thick turbidite units. In core U1397A, at the base of unit C, a thick sedimentary unit comprises a sequence of turbidites that includes a 4.5-m-thick hemipelagic duplicate unit and overlays a ~1.5-m-thick series of debrites (**Figure 4**). The whole of this sedimentary unit is intercalated between two units of hemipelagic sediments separated by an interval of time of ~50 ka (**Figure 5B**). This gap is equivalent to ~14 m of hemipelagic sediment. This sediment may have been eroded by the turbidity currents that emplaced this complex sequence, or it may have slid away down slope before. On the contrary, none of the shallower and thinner turbidites in core U1397A does significantly erode pre-existing sediments. Many similar features are also observed in core U1399A below 60 m bsf; long periods of hemipelagic sedimentation (~200–430 ka, ~470–600 ka, ~780–950 ka) alternate with thick series of turbidites with large gaps in hemipelagic sedimentation that could correspond to erosion or sliding down slope at emplacement of the turbidites (**Figure 7**). In addition to low coring recovery, erosion or

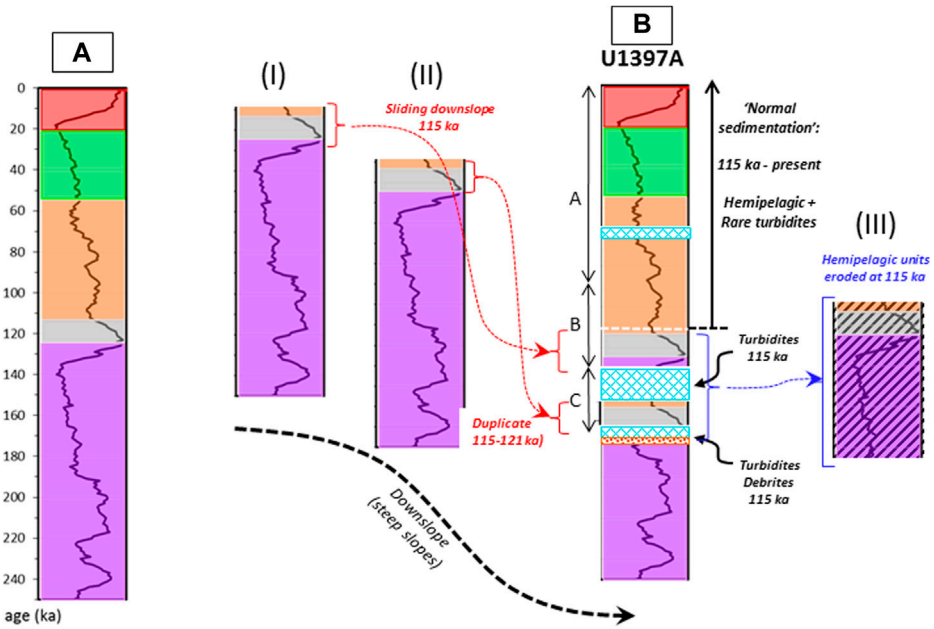


FIGURE 14 | Coherent mass transport model. **(A)** $\delta^{18}O$ stratigraphy with color codes. Black line: LR04 curve. Color codes are arbitrary (see also **Figure 15**). (I) and (II) are hypothetic logs (120–250 ka) of two sites upstream the U1397 site. Color codes from section **(A)**. **(B)** U1397A log interpretation. Color codes from section **(A)**. Dashed blue zones: turbidites. Letters are stratigraphic units defined by Le Friant et al. (2013). (III) Sediment package eroded at the emplacement of the duplicate unit and turbidites (Unit C). At ~115 ka at site U1397A, a large section of sediments deposited between 180 and 115 ka (III) was eroded, a debrite probably generated by a flank collapse, and a series of turbidites with the intercalated duplicate unit were emplaced on the remaining sediments older than 180 ka. These material slided down slope from upstream sites (I and II). Then, sedimentation continued without significant disruption since ~115 ka. This event has likely been triggered by "Le Prêcheur" flank collapse and related landslides.

duplication of hemipelagic sediment related to turbidite and debrite emplacement makes the chronostratigraphic reconstruction less robust beyond 130 ka in core U1397A and 400 ka in core U1399A.

In the absence of detailed petrological information, the origin of turbidites in cores U1397A and U1399A cannot be unambiguously established (**Figure 10**). Glass compositions of turbidites and tephra layers of core U1401A are close and clearly attributed to Mt Pelée magmas (Solaro et al., 2020; **Figure 10A**). Glass compositions of pumice clasts sampled in seven turbidites of the top 50 m of core U1397A (dated between 8 and 98 ka) have been determined. They are highly differentiated (SiO_2 ~ 77%, K_2O ~3%) and homogenous in composition, suggesting a common magma source which, however, cannot be attributed unambiguously to Mt Pelée or Dominica (**Figure 10A**). No turbidite having the same age and composition than that of Roseau Tuff eruption at ~31–33 ka in Dominica (Carey and Sigurdsson, 1980; Boudon et al., 2017) exists in cores U1397A, U1401A, and CARMAR 4 (**Figure 10B**). In core U1399A, a large sediment gap, equivalent to 12–43 ka, is due to erosion by turbidity currents and/or submarine landslides and cannot be solely related to the Roseau Tuff event (**Figure 7A**).

The temporal distribution of the accumulation rates of turbidites offshore Martinique is generally not in phase with the accumulation rates of tephra layers (**Figures 11B**, **13C**). Most eruptions are of low intensity (much less than the exceptional eruption of Roseau Tuff, for example) and pyroclastic flows spread weakly or even do not reach the sea. Most volcaniclastic turbidites are likely the result of the remobilization of pyroclastic deposits on land and on the sea floor, rather than direct deposits of pyroclastic falls or flows. Reid et al. (1996) have suggested that in the back-arc region of the Antilles during low stands of the sea level, volcanic turbidites are thicker and/or more frequent because of the increase of inter-island currents and of erosion of insular shelves. Our results show that it is not the case offshore Martinique and that turbidites are more frequent close to high-stand periods (**Figures 11D**, **13C**). They are not primarily triggered by the variations in sea water level, but highstands naturally increase the probability for pyroclastic falls and flows to reach the sea or for on-land pyroclastic deposits to be transported to the sea by rivers.

5.5 Submarine Landslides: Duplicate Units, Debrites, and Deformed Deposits

The reconstructed chronostratigraphy of cores U1397A and U1399A highlight two main types of sliding of submarine sediments. The first one is a coherent mass transport mainly driven by gravitational failure of steep slope and the second one corresponds to thrusting at the front of large submarine landslides on relatively flat slopes and induces sediment deformation. The first type is favored by the steep slopes of

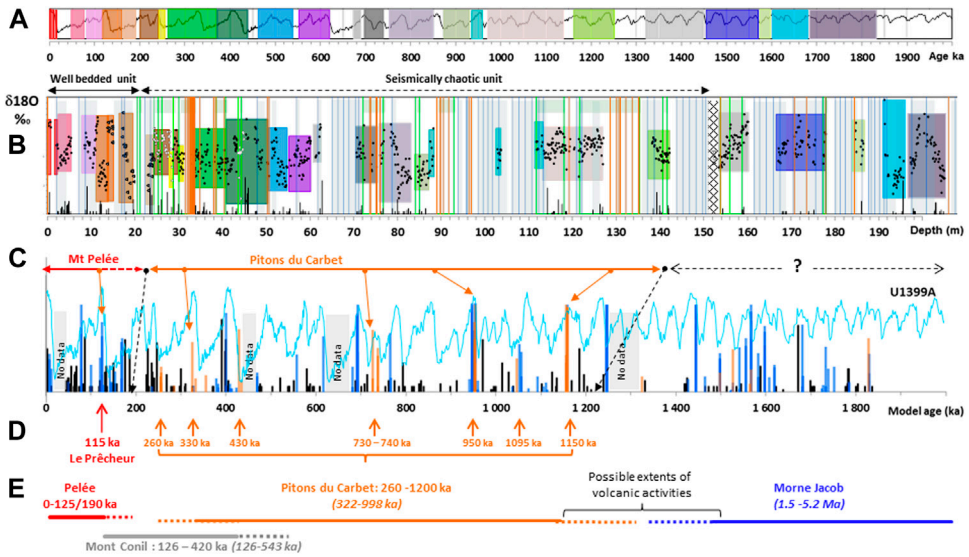


FIGURE 15 | Chronological model of the evolution of volcanic activity in Martinique over the last 1.5 Ma. (The reader is referred to high-resolution figure on the web version of this article for benefit). **(A)** LR04 reference curve for $\delta^{18}O$ evolution of seawater. Color codes are arbitrary and used for comparison with U1399A stratigraphy **(B)**. **(B)** Stratigraphy and $\delta^{18}O$ of hemipelagic sediments of core U1399A. Colored domains correspond to different hemipelagic units characterized by their $\delta^{18}O$ patterns and their age range as defined in **(A)**. Other symbols as in **Figure 6**. **(C)** Reconstituted chronostratigraphy of volcanic events recorded in core U1399A. Symbols as in **Figures 6**, **7C**. Blue line: LR04 curve (unscaled) for comparison of volcanic activity (tephra, turbidites, and debrites) with high and lowstands of the sea level. Orange arrows: main flank collapses identified by debrites and/or turbidites. Black arrows: main rest periods delimiting volcanic activities of Mt Pelée and Pitons du Carbet. **(D)** Scenario of the main flank collapses. Arrows: main flank collapses. **(E)** New model for the volcanic activities of Mt Pelée and Pitons du Carbet. Age ranges in brackets: previous data (K-Ar dating; Germa et al., 2010; Germa et al., 2011b). Mt Pelée activity and "Le Prêcheur" flank collapse are dated from the core U1397A (**Figure 12**). Mt Conil and Morne Jacob activities are not well-constrained by our data.

the volcano close to the shore (as for sites U1397A and U1401A, **Figure 1B**), where sliding is triggered by slope failure and gravity and preserves thick coherent sedimentary units, with no significant internal deformation. Triggering events are various as, for example, high-energy pyroclastic flow entering the sea, debris avalanches generated by flank collapses, intensification of submarine currents during glacial low stands, or high-magnitude earthquakes. On relatively flat slopes at a distance from the shore (as for site U1399A, **Figure 1B**), sliding of very thick sedimentary units implies a significantly different transport mechanism, with deformation of the displaced units.

Such type of behaviors have been proposed by numerous authors for emplacement of SLDs (see, for example., Frey-Martínez et al., 2006; Watt et al., 2012; Le Friant et al., 2015; Brunet et al., 2016; Le Friant et al., 2020); the entrance of debris avalanches in the sea generates debrites and turbidites. It may also generate slope failure and coherent mass transport ('duplicate units') or erosion of pre-existing sediment, especially on steep slopes near the shore. If the accumulated load is large enough, it can induce or reactivate submarine landslides with failure, deformation, and transport of the pre-existing sedimentary units at long distances from the origin (Lafuerza et al., 2014; Hornbach et al., 2015; Le Friant et al., 2020).

The hemipelagic sediments of the top 28 m of core U1397A (unit A) display a continuous $\delta^{18}O$ pattern consistent with the time period 0–87 ka (**Figures 4**, **5B**). Numerous turbidites are intercalated in hemipelagic sediments of unit B (28–53 m bsf; **Figure 4**), but the reconstructed $\delta^{18}O$ pattern is continuous and consistent with the time period 87–132 ka (**Figure 5B**). Unit C (53–76 m bsf) is a complex sequence of turbidites and debrites containing a ~4.5-m-thick unit of hemipelagic sediments which display a $\delta^{18}O$ pattern consistent with the time period 115–121 ka (**Figures 4**, **5B**). We interpret these features as the result of coherent mass transport of pre-existing sediments triggered by a major flank collapse of Mt Pelée at ~115 ka (**Figure 14**). The debris avalanches that entered the sea strongly eroded pre-existing sediments and deposited the debrite units. This event produced large volcaniclastic turbidites possibly containing an eruptive component synchronous of the flank collapse. Simultaneously, the rapid sediment overloading triggered submarine slope failures and coherent mass transports of pre-existing sediments (deposited between 121 and 115 ka) down the slope rather than simply eroding these slope sediments (**Figure 14**). These events were followed by a period of numerous volcaniclastic turbidity currents (between 115 and 87 ka). Thereafter, no other more recent process significantly disturbed the sedimentation at the site U1397A.

The 115 ka event is also recorded in site U1399A at the base of the upper well-bedded seismic facies (**Figure 3B**). At the base of

unit A (14–23 m bsf), a series of three duplicate hemipelagic units is intercalated within turbidites (**Figure 6A**). They represent the sedimentation time interval 115–150 ka (**Figure 7C**). These units likely slided as coherent mass transports simultaneously with a massive turbidite. Debris flows cannot be transported over long distances in the sea, which explains the absence of the debrite at that time in core U1399A. On the contrary, the stress generated by the overload may have propagated over long distances in pre-exiting sediments and activated (or re-activated) sliding and deformation in the thick deformed units existing below unit A (**Figure 6A**). Contrary to shallower well-bedded sediments (cores U1397A, U1401A, and unit A of core U1399A), thick discrete units below 23 m bsf in core U1399A are strongly deformed (**Figure 6A**). They are considered possible zones of décollement favoring landsliding (Lafuerza et al., 2014; Hornbach et al., 2015; Le Friant et al., 2020). These décollement and deformation zones may be reactivated at different periods by successive flank collapses that are necessarily older than the undeformed sediments of the overlying well-bedded unit, that is, older than 150 ka (**Figures 3B**, **13**).

Coherent mass transport processes are likely the cause of the anomalous $\delta^{18}O$ patterns in hemipelagic sediment units at ~4–5 m and ~6–8 m bsf in core U1401A, associated with turbidites (Solaro et al., 2020; **Figure 5B**); they rather correspond to duplicate units. To reconcile their $\delta^{18}O$ patterns with standard reference curves, flank failure should have occurred at 8 and 14 ka. In core U1397A, the youngest turbidite is ~8 ka old (**Figure 5B**), which suggests a common origin of the three events. Because site U1401A is located at the outlet of the Mt Pelée collapse basin, it has better chance to record less intense (and most recent) events than the more distant sites (U1397A and U1399A). This interpretation supports the hypothesis of the existence of a low-magnitude flank collapse at ~8 ka ("Rivière Sèche" flank collapse, Le Friant et al., 2002).

In core U1399A, at least four duplicate units can be identified between ~23 and 45 m bsf in the upper part of the SLDs (**Figures 3B**, **6A**, Le Friant et al., 2015). Their thickness varies from ~1.5 to ~10 m, and they are generally closely associated with turbidites and deformed intervals (**Figures 6A**, **7C**). The maximum ages of transport of these units are 115–150 ka and 210, 220 and 375 ka. Other duplicate units may exist at greater depth, but the low resolution and the sediment gaps prevent any identification. Several debrites are identified inside the landslide (~23–150 m bsf, units B to F), dated at 260, 290, 325–330, 430–440, 730–740, 950, 1,100, and 1,150 ka (**Figure 7C**). Most debrites are closely associated with thick turbidites, which suggests that they correspond to distal deposits of large debris flows (Talling et al., 2010). Finally, the debrite deposits at 430 ka overlay a large sediment gap of ~1.5 m hemipelagic sediments, which is likely an erosive gap. All these features may represent tracers of large flank collapses that occurred between 260 and 1,150 ka and strongly disturbed the sedimentation.

Below ~150 m bsf in the core U1399A, in the seismic well-bedded facies (units G and H), the sediments consist of a succession of thick turbidite sequences (up to 25 m thick) including 5–10 m thick hemipelagic sediment units and some debrite deposits dated at 1.5–1.55 Ma and ~1.8 Ma (confidence upper limit of dating), which could also be the result of large flank collapses.

6 CHRONOLOGY OF THE VOLCANIC ACTIVITY IN MARTINIQUE SINCE 1.5 MA

The reconstructed chronology of volcanic eruptions and flank collapses recorded in cores U1397A and U1399A are summarized in **Figures 12**, **15** (0–1.5 Ma).

6.1 Mt Pelée

6.1.1 Flank Collapses

The major event identified in both cores is dated at 115 ka (**Figure 12**). It corresponds to the "Le Prêcheur" flank collapse of Mt Pelée dated on land between 70 and 127 ka (Le Friant et al., 2003; Germa et al., 2011a; **Figure 2B**). It is the largest flank collapse that affected the Mt Pelée volcano. Its impact on submarine sediments spread over a large sector and at a great distance: ~70 km on-axis of the collapse structure (site U1399A) and at least 30 km off-axis (site U1397A; **Figure 1B**). It represents a much larger area than that defined by the blocky unit (DAD3) and the extent of topographic scarps identified offshore Martinique (Le Friant et al., 2003; Le Friant et al., 2015; **Figure 1B**). However, another interpretation must consider the Plat Pays flank collapse south of Dominica which is at least ~100 ka old (Le Friant et al., 2002; Samper et al., 2008). The estimates of collapse volumes on land (~20–25 km^3) and volumes of chaotic deposits offshore (~250 km^3) are similar for Plat Pays and "Le Prêcheur" events (Le Friant et al., 2002; Le Friant et al., 2003). In addition, distances of both collapse structures to site U1397A are similar (**Figure 1B**). Since the site U1397A is located south of the deep (>3,000 m) submarine channel between Dominica and Martinique, it is likely that most debris flows and submarine landslides originating from Dominica have been channeled toward the Grenada Basin and did not affect the western flank of Martinique.

The existence of two younger flank collapses at Mt Pelée ("St Pierre" and "Rivière Sèche"; Le Friant et al., 2003; Germa et al., 2011a; **Figure 2B**) is still questioned as they are not recorded as specific deposits in both cores (**Figure 9**). Coherent mass transports in core U1401A are contemporaneous of a thick turbidite in core U1397A dated at ~8 ka that could correspond to a low-magnitude flank collapse (**Figure 5B**). The "Rivière Sèche" structure, previously dated at 8–10 ka, was related to the debris avalanche deposit DAD 3 because the missing volume on land and the DAD 3 volume are similar (Le Friant et al., 2003; **Figures 2**, **12**). However, the sediments cored at site U1401A above the DAD 3 are older than 36 ka (Solaro et al., 2020; **Figure 1B**). The DAD 3 could, therefore, result from the "St Pierre" flank collapse structure dated on land at 30–45 ka (Le Friant et al., 2003; **Figure 2**), but the estimated collapse volume is much larger than that of the deposit. Thus, the attribution of DAD 3 to a collapse structure on land remains

an open question: if the DAD 3 is related to the "Rivière Sèche" event and dated older than 36 ka as suggested by Solaro et al. (2020); a younger not yet identified flank collapse occurred at ~8 ka. However, since the U1401A core contains numerous turbidites and likely two duplicate units (see §V-5; **Figure 5B**), we suggest that some of these sedimentary units could have slided over the DAD 3 after its emplacement leading to an erroneous estimate of its actual age.

6.1.2 Volcanic Activity

Three main activity periods are identified at Mt Pelée. Their approximate age limits are "Old Pelée" > 127 ka to 50 ka; the "Grand Rivière" 50–20 ka; and "Recent Pelée" 20 ka to the present day (**Figure 12B**). The "Grand Rivière" and "Old Pelée" activity periods are much more intense than estimated in previous studies on land, and the volcanic activity of Mt Pelée strongly decreased since the last 30 ka. The "Grand Rivière" activity culminates at ~30 ka and is characterized by the emission of scoriae of mafic andesite compositions that were only emitted as enclaves during the other periods (Boudon et al., 2013). The onset of Mt Pelée activity cannot be clearly identified. The first edifice of Mt Pelée, which was at least as large as the present edifice, partially collapsed during the "Le Prêcheur" event at 115 ka, and one can imagine that a time interval of the same order of magnitude was necessary for its construction. Because the tephra records indicate more or less continuous volcanic activity on Martinique since ~190 ka, preceded by a rest period of ~30 ka, we suggest that Mt Pelée activity could have started at ~190 ka (**Figure 12**). On the other hand, the Mt Conil volcano north of Mt Pelée was active between 543 and 126 ka (Germa et al., 2011b), and a partial overlap of the activities of the two edifices must be considered (**Figure 12**). Only detailed petrological investigations are able to resolve this ambiguity.

6.2 Pitons Du Carbet

The submarine landslide units (s.s.) identified from seismic reflexion profiles and core descriptions (Le Friant et al., 2015; Brunet et al., 2016; Le Friant et al., 2020; **Figure 3B**) in core U1399A are covered by well-bedded and undeformed sediments (upper 25 m) younger than ~150 ka. Since that time, there has been no evidence in this core that large submarine landslides were able to displace and deform pre-existing sediments at long distances (>70 km) offshore Martinique. The sediments below 25 m bsf in core U1399A consist of a complex association of debrites, turbidites, and hemipelagic units. The characteristics of these complex sedimentary features are similar to those of the younger deposits related to "Le Prêcheur" flank collapse, except that turbidites are significantly thicker. We propose that they are also the result of high-magnitude flank collapses that produced, transported, or deformed sediments at distances as large as ~70 km from the Martinique shore. Their ages (between 260 and 1,160 ka; **Figure 15**) suggest that they originate from the Pitons du Carbet volcano that was active at least between 322 and 998 ka (Samper et al., 2008; Germa et al., 2011b) and experienced the largest flank collapses of all Lesser Antilles volcanoes (Boudon et al., 2007; Boudon et al., 2013; **Figure 2A**). The topographic scarps identified on submarine topography show that submarine landslides cover a large sector including the outlets of Mt Pelée and Pitons du Carbet collapse basins (**Figure 1B**). Compared to Mt Pelée activity, the tephra deposition rate of Pitons du Carbet eruptions recorded in core U1399A is significantly lower (**Figure 12**). This difference is likely due to the fact that most eruptions produced rhyodacitic lava domes with low dispersion of eruptive products.

7 SUMMARY AND CONCLUSION

The core U1397A provides the longest continuous record offshore Martinique of the hemipelagic sedimentation and volcanic explosive activity over the last 130 ka. The sedimentation along the north western flank of Martinique is dominated by hemipelagic sediments with numerous thin tephra deposits that record the volcanic activity of the volcanic island. The hemipelagic sedimentation is mainly controlled by inputs of the strong marine currents and the volcaniclastic terrigenous sediments. It rapidly decreases with distance from the island, typically from ~30 cm/ka at the shore to 5 cm/ka at 70 km from the shore. In cores U1397 and U1399 to U1401 offshore Martinique, only Mt Pelée activity was recorded in the last 150 ka. Older sediments likely record the activity of Pitons du Carbet. The absence of volcanic deposits from nearby islands, especially Dominica, is explained by the fact that the products of the most explosive phases (Plinian) were mainly dispersed to the east of the islands (due to dominant winds), while the pyroclastic flows entering the Caribbean Sea were channeled westward. The reconstituted tephrostratigraphy indicates more intense and longer activity periods than recorded on land. The volcanic history of Mt Pelée before 20 ka is significantly revised. This activity started ~190 ka ago and strongly decreased since 20 ka ("Recent Pelée" activity). The main activity period between 20 and 50 ka called 'Grand Rivière' is characterized by the emission of large amounts of mafic andesites contrary to other periods which are dominated by silicic andesites. The volcanic history older than 200 ka is less accurately recorded offshore Martinique. The significant volcanic activity recorded between 260 and 1,200 ka likely corresponds to the whole Pitons du Carbet activity. During that period, the volcanic activity recorded offshore Martinique is, however, much less intense than that of Mt Pelée recorded in the more recent deposits.

The hemipelagic and volcanic tephra sedimentation records offshore Martinique are strongly disturbed by numerous instabilities of the sedimentary piles induced by several flank collapses of Mt Pelée and Pitons du Carbet volcanoes. These events produced different deposits and instabilities in sea floor sediments. They were almost systematically accompanied by volcaniclastic turbidity currents and produced debris avalanches of limited extent

in the sea that are only represented in the most proximal cores in front of the collapse structures (cores U1400 and U1401) but could not be penetrated by drilling. Remobilization of these material produced finer deposits (debrites) observed in the cores. Loading of large amounts of collapse material at the slope break probably induced slope failures of the sea floor sediments with small-scale coherent mass transports over relatively limited distances and large-scale sediment failures with generally multiphase episodes of sliding and deformation. These features can be identified in the cores as duplicate layers and deformed sediment intervals. The reconstructed chronostratigraphy facilitates dating the major flank collapses that affected Mt Pelée and Pitons du Carbet volcanoes. The best documented event is the Le Prêcheur event dated at 115 ka, which is the last major flank collapse of Mt Pelée, which has affected the sea floor sediments up to 80 km from the coast. The younger "St Pierre" flank collapse is not clearly evidenced in the studied cores, and its dating is still uncertain. Finally, traces of a 8 ka old, low-amplitude flank collapse ("Rivière Sèche") are found in proximal cores (U1401 and U1397) and could have produced the DAD 3. Pitons du Carbet volcano is characterized by numerous large flank collapses (around 1 every 100 ka over ~1 Ma).

Holes drilled southeast of Montserrat during the IODP 340 expedition show that flank collapses (130 ka and younger) there occurred toward the end of periods of relatively elevated volcanism, and their timing also seemed to coincide with periods of rapid sea level rise (Coussens et al., 2016a; Coussens et al., 2016b). Our data offshore Martinique, however, do not show a clear relationship between the occurrence of flank collapses and the sea level variations, except that they seem to occur more frequent close to sea level highstands (as do emplacements of volcaniclastic turbidites). There is also no evidence for a relationship between the emission of more mafic magmas during "Grand Rivière" activity and a large flank collapse, contrary to previous hypotheses based on the few available data on land (Boudon et al., 2013).

The reconstructed chronostratigraphy of cores U1397 and U1399 constitutes the framework to establish the volcanic history of the volcanoes of the north of Martinique since 1.5 Ma and study the processes that may control the shallow evolution of the volcanic edifices and their instabilities. The detailed study of the petrology of the tephra layers and volcaniclastic turbidites, and of the emplacement and deformation processes within the SLDs, constitute the main methods of investigation using core material, which can be developed from this study.

DATA AVAILABILITY STATEMENT

The original contributions presented in the study are included in the article/**Supplementary Material**; further inquiries can be directed to the corresponding author.

AUTHOR CONTRIBUTIONS

All authors equally contributed to data acquisition. BV and AF were the main contributors to data interpretation and manuscript redaction.

FUNDING

This study was supported by the ANR-13-BS06-0009 CARIB, the Labex UnivEarthS, and by the PREST project co-funded by Interreg Caraibes for the European Regional Development Fund.

ACKNOWLEDGMENTS

We thank the captains, officers, and crews of the R/V JOIDES Resolution and the IODP 340 scientists. Authors are indebted to two reviewers for their detailed and constructive reviews.

SUPPLEMENTARY MATERIAL

The Supplementary Material for this article can be found online at: https://www.frontiersin.org/articles/10.3389/feart.2022.767485/full#supplementary-material

Supplementary Figure 1 | High-resolution stratigraphic logs of cores U1397A and U1399A. Black: tephra; blue: turbidite; orange: debrite. Height of black lines corresponds to the relative thickness of tephra deposits. Only main turbidites are reported as dark blue lines. Light blue zones correspond to the accumulation of numerous thin turbidites. Letters: lithological units defined on board (Le Friant et al., 2013). See also **Figure 3**. The reader is referred to the web version of this article for benefit.

Supplementary Figure 2 | Comparison of tephra layers and turbidite records in cores U1397A and U1397B. Black: tephra; blue: turbidite; orange: debrite. Height corresponds to their relative thickness of tephra layers. Scales are different for each deposit type. **(A)** Distribution as a function of the depth in core (cm). **(B)** Distribution as a function of the model age (in ka). It is to be noted that the same model age (sediments thickness vs. age) has been used for both cores with an additional shift of 9 ka for core U1397B.

Supplementary Figure 3 | Calibration of $\delta^{18}O$—age curves. **(A)** Well-calibrated curves at CARMON-2 site (blue line) offshore Montserrat (Le Friant et al., 2008), ODP999 (light blue line), and VM78-122 (purple line) in the western and eastern Caribbean Sea (Broecker W. et al., 1988; Broecker W. S. et al., 1988; Broecker et al., 1990) are used to calculate a "mean Caribbean" curve over the last 200 ka. The SPECMAP LR-04 reference curve (green line; Liesecki and Raymo, 2005) is used for ages older than 200 ka. **(B)** Reconstructed (best fit) $\delta^{18}O$ age curve for cores U1397A (red dots) and U1399A (black dots) over 0–130 ka. See the text for method description. Open red circles: CARMAR-4 curve (Boudon et al., 2013; Solaro et al., 2020). Age uncertainties are estimated ~2 ka for U1397A and ~5 ka for U1399B over this age range. **(C)** Residues of fits (measured δ18O- calculated δ18O from 'mean Caribbean' curve) for cores U1397A (red dots) and U1398A (black dots) and CARMAR-4 (open circles). Error bars: reproducibility (±1 sigma; two to four determinations per sample) on δ18O measurements in core U1397A. All residues are within ±0.5‰ and within analytical reproducibility.

Supplementary Table 1 | $\delta^{18}O$ data. Depth in core, cumulative hemipelagic sediment thicknesses, $\delta^{18}O$ data, and model ages. **(A)** U1397A. **(B)** U1399A.

Supplementary Table 2 | ^{14}C dating of foraminifers from cores U1397A and U1399A. **(A)** U1397A. **(B)** U1399A. Calibrations from Stuiver and Reimer (1993), Reimer et al. (2013a), Reimer et al. (2013b). Dataset marine 13; ^{14}C Delta R (mean): –27 ± 11 (CALIB Rev 7.0.4 radiocarbon calibration program 1986–2017).

Supplementary Table 3 | Chronology of the volcanic activity and flank collapses at Mt Pelée. Eruptive Style: dome: lava dome; BAF: block and ash flow; Plinian: plinian fall or flow; scoriae: scoria fall or flow; *: major eruption; FC: flank collapse. For sake of simplification, all ages are given in ka (kilo annum) whatever the dating technique; for source data and uncertainties, the reader is referred to references. Data sources: 1) Germa et al. (2011a); 2) Le Friant et al. (2002); 3) U-Th Villemant, unpublished data; 4) Westercamp et al. (1989); 5) Michaud-Dubuy (2019), 6) Ishizuka et al., unpublished data.

REFERENCES

Annen, C., Pichavant, M., Bachmann, O., and Burgisser, A. (2008). Conditions for the Growth of a Long-Lived Shallow Crustal Magma Chamber below Mount Pelee Volcano (Martinique, Lesser Antilles Arc). *J. Geophys. Res.* 113, b07209. doi:10.1029/2007jb005049

Balcone-Boissard, H., Boudon, G., Blundy, J. D., Martel, C., Brooker, R. A., Deloule, E., Solaro, C., and Matjuschkin, V. (2018). Deep Pre-Eruptive Storage of Silicic Magmas Feeding Plinian and Dome-Forming Eruptions of Central and Northern Dominica (Lesser Antilles) Inferred From Volatile Contents of Melt Inclusions. *Contrib. Mineral. Petrol.* 173, 101. doi:10.1007/s00410-018-1528-4

Boudon, G., Balcone-Boissard, H., Solaro, C., and Martel, C. (2017). Revised Chronostratigraphy of Recurrent Ignimbritic Eruptions in Dominica (Lesser Antilles Arc): Implications on the Behavior of the Magma Plumbing System. *J. Volcanology Geothermal Res.* 343, 135–154. doi:10.1016/j.jvolgeores.2017.06.022

Boudon, G., Le Friant, A., Komorowski, J.-C., Deplus, C., and Semet, M. P. (2007). Volcano Flank Instability in the Lesser Antilles Arc: Diversity of Scale, Processes, and Temporal Recurrence. *J. Geophys. Res.* 112, B08205. doi:10.1029/2006JB004674

Boudon, G., Le Friant, A., Villemant, B., and Viodé, J.-P. (2005). "Martinique," in *Volcanic hazard Atlas of the Lesser Antilles*. Editors J. M. Lindsay, R. E. A. Robertson, J. B. Shepherd, and S. Ali (Trinidad and Tobago, West Indies: Seismic Research Unit, The University of the West Indies), 65–102.

Boudon, G., Villemant, B., Friant, A. L., Paterne, M., and Cortijo, E. (2013). Role of Large Flank-Collapse Events on Magma Evolution of Volcanoes. Insights from the Lesser Antilles Arc. *J. Volcanology Geothermal Res.* 263, 224–237. doi:10.1016/j.jvolgeores.2013.03.009

Bourdier, J. L., Gourgaud, A., and Vincent, P. M. (1985). Magma Mixing in a Main Stage of Formation of Montagne Pelée: the Saint Vincent-type Scoria Flow Sequence (Martinique, F.W.I.). *J. Volcanology Geothermal Res.* 25, 309–332. doi:10.1016/0377-0273(85)90019-8

Bouysse, P., Westercamp, D., and Andreieff, P. (1990). The Lesser Antilles Island Arc. *Proc. Ocean Drilling Program B: Scientific Results* 110, 29–44. doi:10.2973/odp.proc.sr.110.166.1990

Breitkreuz, C., Schmitt, A. K., Repstock, A., Krause, J., Schulz, B., Bergmann, F., et al. (2021). Record and Provenance of Pleistocene Volcaniclastic Turbidites from the central Lesser Antilles (IODP Expedition 340, Site U1398B). *Mar. Geology.* 438, 106536. doi:10.1016/j.margeo.2021.106536

Broecker, W., Klas, M., Ragano-Beavan, N., Mathieu, G., Mix, A., Andree, M., et al. (1988). Introduction. *Radiocarbon* 30, 261–263. doi:10.1017/s0033822200044234

Broecker, W. S., Andree, M., Bonani, G., Wolfli, W., Klas, M., Mix, A., et al. (1988). Comparison between Radiocarbon Ages Obtained on Coexisting Planktonic Foraminifera. *Paleoceanography* 3, 647–657. doi:10.1029/PA003i006p00647

Broecker, W. S., Klas, M., Clark, E., Trumbore, S., Bonani, G., Wölfli, W., et al. (1990). Accelerator Mass Spectrometric Radiocarbon Measurements on Foraminifera Shells from Deep-Sea Cores. *Radiocarbon* 32, 119–133. doi:10.1017/s003382220004011x

Brunet, M., Le Friant, A., Boudon, G., Lafuerza, S., Talling, P., Hornbach, M., et al. (2016). Composition, Geometry, and Emplacement Dynamics of a Large Volcanic Island Landslide Offshore Martinique: From Volcano Flank-Collapse to Seafloor Sediment Failure? *Geochem. Geophys. Geosyst.* 17 (3), 699–724. doi:10.1002/2015GC006034

Brunet, M., Moretti, L., Le Friant, A., Mangeney, A., and Fernandez Nieto, E. (2017). Numerical Simulations of 30-45 Ka Debris Avalanche Flow of Montagne Pelee Volcano, Martinique: from Volcano Flank-Collapse to Submarine Emplacement. *Nat. Hazards* 87 (I2), p1189–1222. doi:10.1007/s11069-017-2815-5

Carazzo, G., Tait, S., Kaminski, E., and Gardner, J. E. (2012). The Recent Plinian Explosive Activity of Mt. Pelée Volcano (Lesser Antilles): The P1 AD 1300 Eruption. *Bull. Volcanol* 74, 2187–2203. doi:10.1007/s00445-012-0655-4

Carey, S. N., and Sigurdsson, H. (1980). The Roseau Ash: Deep-Sea Tephra Deposits from a Major Eruption on Dominica, Lesser Antilles Arc. *J. Volcanology Geothermal Res.* 7, 67–86. doi:10.1016/0377-0273(80)90020-7

Carey, S. (1999). "Volcaniclastic Sedimentation Around Island Arcs," in *Encyclopedia of Volcanoes. Part IV. Explosive Volcanism.* Editors H. Sigurdsson, B. Houghton, S. McNutt, H. Rymer, and J. Stix (New York: Academic Press), 627–642.

Cassidy, M., Watt, S. F. L., Palmer, M. R., Trofimovs, J., Symons, W., Maclachlan, S. E., et al. (2014). Construction of Volcanic Records from marine Sediment Cores: A Review and Case Study (Montserrat, West Indies). *Earth-Science Rev.* 138, 137–155. doi:10.1016/j.earscirev.2014.08.008

Clark, P. U., Archer, D., Pollard, D., Blum, J. D., Rial, J. A., Brovkin, V., et al. (2006). The Middle Pleistocene Transition: Characteristics, Mechanisms, and Implications for Long-Term Changes in Atmospheric pCO2. *Quat. Sci. Rev.* 25, 3150–3184. doi:10.1016/j.quascirev.2006.07.008

Coussens, M. F., Wall-Palmer, D., Talling, P. J., Watt, S. F. L., Hatter, S. J., Cassidy, M., et al. (2016a). "Synthesis: Stratigraphy and Age Control for IODP Sites U1394, U1395, and U1396 Offshore Montserrat in the Lesser Antilles," in *Proceedings of the Integrated Ocean Drilling Program, Principal Investigators*. Editors A. Le Friant, O. Ishizuka, and N. A. Stroncik (College Station, Tex: Ocean Drill. Program), 340. doi:10.2204/iodp.proc.340.204.2016

Coussens, M. F., Wall-Palmer, D., Talling, P. J., Watt, S. F. L., Cassidy, M., Jutzeler, M., et al. (2016b). The Relationship between Eruptive Activity, Flank Collapse, and Sea Level at Volcanic Islands: A Long-Term (>1 Ma) Record Offshore Montserrat, Lesser Antilles. *Geochem. Geophys. Geosyst.* 17, 2591–2611. doi:10.1002/2015GC006053

Deplus, C., Le Friant, A., Boudon, G., Komorowski, J.-C., Villemant, B., Harford, C., et al. (2001). Submarine Evidence for Large-Scale Debris Avalanches in the Lesser Antilles Arc. *Earth Planet. Sci. Lett.* 192, 145–157. doi:10.1016/s0012-821x(01)00444-7

Feuillet, N., Manighetti, I., Tapponnier, P., and Jacques, E. (2002). Arc Parallel Extension and Localization of Volcanic Complexes in Guadeloupe, Lesser Antilles. *J. Geophys. Res.* 107, ETG 3-1–ETG 3-29. doi:10.1029/2001JB000308

Fichaut, M., Maury, R. C., Traineau, H., Westercamp, D., Joron, J.-L., Gourgaud, A., et al. (1989). Magmatology of Mt Pele´e (Martinique, F.W.I), III, Fractional crystallisation versus magma mixing. *J. Volcanol. Geotherm. Res.* 38 (1– 2), 189–213. doi:10.1016/0377-0273(89)90037-1

Fraass, A. J., Wall-Palmer, D., Leckie, R. M., Hatfield, R. G., Burns, S. J., Le Friant, A., et al. (2017). A Revised Plio-Pleistocene Age Model and Paleoceanography of the Northeastern Caribbean Sea: IODP Site U1396 off Montserrat, Lesser Antilles. *Stratigraphy* 13, 183–203. doi:10.29041/strat.13.3.183-203

Frey-Martínez, J., Cartwright, J., and James, D. (2006). Frontally Confined versus Frontally Emergent Submarine Landslides: a 3D Seismic Characterisation. *Mar. Pet. Geology.* 23, 585–604. doi:10.1016/j.marpetgeo.2006.04.002

Germa, A., Lahitte, P., and Quidelleur, X. (2015). Construction and Destruction of Mont Pelée Volcano: Volumes and Rates Constrained from a Geomorphological Model of Evolution. *J. Geophys. Res. Earth Surf.* 120 (7), 1206–1226. doi:10.1002/2014jf003355

Germa, A., Quidelleur, X., Labanieh, S., Chauvel, C., and Lahitte, P. (2011b). The Volcanic Evolution of Martinique Island: Insights from K-Ar Dating into the Lesser Antilles Arc Migration since the Oligocene. *J. Volcanology Geothermal Res.* 208, 122–135. doi:10.1016/j.jvolgeores.2011.09.007

Germa, A., Quidelleur, X., Labanieh, S., Lahitte, P., and Chauvel, C. (2010). The Eruptive History of Morne Jacob Volcano (Martinique Island, French West Indies): Geochronology, Geomorphology and Geochemistry of the Earliest Volcanism in the Recent Lesser Antilles Arc. *J. Volcanology Geothermal Res.* 198 (3–4), 297–310. doi:10.1016/j.jvolgeores.2010.09.013

Germa, A., Quidelleur, X., Lahitte, P., Labanieh, S., and Chauvel, C. (2011a). The K-Ar Cassignol-Gillot Technique Applied to Western Martinique Lavas: A Record of Lesser Antilles Arc Activity from 2Ma to Mount Pelée Volcanism. *Quat. Geochronol.* 6, 341–355. doi:10.1016/j.quageo.2011.02.001

Gourgaud, A., Fichaut, M., and Joron, J.-L. (1989). Magmatology of Mt. Pelée (Martinique, F.W.I.), I, Magma Mixing and Triggering of the 1902 and 1292 Pelean Nuées Ardentes. *J. Volcanol. Geotherm. Res.* 38 (1– 2), 143–169. doi:10.1016/0377-0273(89)90035-8

Griggs, A. J., Davies, S. M., Abbott, P. M., Rasmussen, T. L., and Palmer, A. P. (2014). Optimising the Use of marine Tephrochronology in the North Atlantic: a Detailed Investigation of the Faroe Marine Ash Zones II, III and IV. *Quat. Sci. Rev.* 106, 122–139. doi:10.1016/j.quascirev.2014.04.031

Gurenko, A. A., Trumbull, R. B., Thomas, R., and Lindsay, J. M. (2005). A Melt Inclusion Record of Volatiles, Trace Elements and Li-B Isotope Variations in a Single Magma System from the Plat Pays Volcanic Complex, Dominica, Lesser Antilles. *Jour. Petrol.* 46, 2495–2526. doi:10.1093/petrology/egi063

Halama, R., Boudon, G., Villemant, B., Joron, J.-L., Le Friant, A., and Komorowski, J.-C. (2006). Pre-eruptive Crystallization Conditions of Mafic and Silicic Magmas at the Plat Pays Volcanic Complex, Dominica (Lesser Antilles). *J. Volcanology Geothermal Res.* 153, 200–220. doi:10.1016/j.jvolgeores.2005.12.001

Hornbach, M. J., Manga, M., Genecov, M., Valdez, R., Miller, P., Saffer, D., et al. (2015). Permeability and Pressure Measurements in Lesser Antilles Submarine Slides: Evidence for Pressure-driven Slow-slip Failure. *J. Geophys. Res. Solid Earth* 120 (12), 7986–8011. doi:10.1002/2015JB012061

Howe, T. M., Lindsay, J. M., Shane, P., Schmitt, A. K., and Stockli, D. F. (2014). Re-evaluation of the Roseau Tuff Eruptive Sequence and Other Ignimbrites in Dominica, Lesser Antilles. *J. Quat. Sci.* 29, 531–546. doi:10.1002/jqs.2723

Jaupart, C., and Allègre, C. J. (1991). Gas Content, Eruption Rate and Instabilities of Eruption Regime in Silicic Volcanoes. *Earth Planet. Sci. Lett.* 102, 413–429. doi:10.1016/0012-821x(91)90032-d

Jutzeler, M., Manga, M., White, J. D. L., Talling, P. J., Proussevitch, A. A., Watt, S. F. L., et al. (2017). Submarine Deposits from Pumiceous Pyroclastic Density Currents Traveling over Water: An Outstanding Example from Offshore Montserrat (IODP 340). *Geol. Soc. America Bull.* 129 (3_4), 392–414. doi:10.1130/B31448.1

Jutzeler, M., White, J. D. L., Talling, P. J., McCanta, M., Morgan, S., Le Friant, A., et al. (2014). Coring Disturbances in IODP Piston Cores with Implications for Offshore Record of Volcanic Events and the Missoula Megafloods. *Geochem. Geophys. Geosyst.* 15, 3572–3590. doi:10.1002/2014GC005447

Keller, J., Ryan, W. B. F., Ninkovich, D., and Altherr, R. (1978). Explosive Volcanic Activity in the Mediterranean over the Past 200,000 Yr as Recorded in Deep-Sea Sediments. *Geol. Soc. America Bull.* 89, 591–604. doi:10.1130/0016-7606(1978)89<591:evaitm>2.0.co;2

Knappe, E., Manga, M., and Le Friant, A. (2020). Rheology of Natural Sediments and its Influence on the Settling of Dropstones in Hemipelagic Marine Sediment. *Earth Space Sci.* 7 (3), e2019EA000876. doi:10.1029/2019EA000876

Labanieh, S., Chauvel, C., Germa, A., Quidelleur, X., and Lewin, E. (2010). Isotopic Hyperbolas Constrain Sources and Processes under the Lesser Antilles Arc. *Earth Planet. Sci. Lett.* 298, 35–46. doi:10.1016/j.epsl.2010.07.018

Labanieh, S., Chauvel, C., Germa, A., and Quidelleur, X. (2012). Martinique: a clear Case for Sediment Melting and Slab Dehydration as a Function of Distance to the Trench. *Jour. Petrol.* 53 (12), 2441–2464. doi:10.1093/petrology/egs055

Lacroix, A. (1904). *La Montagne Pelée et ses Eruptions*. Paris: Masson, 662.

Lafuerza, S., Le Friant, A., Manga, M., Boudon, G., Villemant, B., Stroncik, N., et al. (2014). "Geomechanical Characterizations of Submarine Volcano Flank Sediments, Martinique, Lesser Antilles Arc, Chap. 7," *Sumarine Mass Movements and Consequences, Advances in Natural and Technological Hazards Research*. S. Krastel, J.-H. Behrmann, D. Völker, M. Stipp, C. Berndt, R. Urgeles, et al. Editors (Cham, Switzerland: Springer International), 73. doi:10.1007/978-3-319-00972-8_7

Le Friant, A., Boudon, G., Deplus, C., and Villemant, B. (2003). Large-scale Flank Collapse Events during the Activity of Montagne Pelée, Martinique, Lesser Antilles. *J. Geophys. Res.* 108 (B1), 2055. doi:10.1029/2001JB001624

Le Friant, A., Boudon, G., Komorowski, J.-C., and Deplus, C. (2002). L'île de la Dominique, à l'origine des avalanches de débris les plus volumineuses de l'arc des Petites Antilles. *Comptes Rendus Geosci.* 334, 235–243. doi:10.1016/s1631-0713(02)01742-x

Le Friant, A., Ishizuka, O., Boudon, G., Palmer, M. R., Talling, P. J., Villemant, B., et al. (2015). Submarine Record of Volcanic Island Construction and Collapse in the Lesser Antilles Arc: First Scientific Drilling of Submarine Volcanic Island Landslides by IODPExpedition 340. *Geochem. Geophys. Geosyst.* 16, 420–442. doi:10.1002/2014GC005652

Le Friant, A., Ishizuka, O., and Stroncik, N. A.; the Expedition 340 Scientists (2013). *Proc. IODP*. Tokyo: Integrated Ocean Drilling Program Management International, Inc., 340. doi:10.2204/iodp.proc.340.109.2013

Le Friant, A., Lebas, E., Brunet, M., Lafuerza, S., Hornbach, M., Coussens, M., et al. and Submarine Landslides Around Volcanic Islands, (2019). Submarine Landslides Around Volcanic Islands: A Review of what Can Be Learned from the Lesser Antilles Arc. AGU Book "*Submarine Landslides: Subaqueous Mass Transport Deposits from Outcrops to Seismic Profiles*" Edited by K. Ogata, A. Festa, and G. A. Pini. (USA: American Geophysical Union, John Wiley & Sons Inc.,), 277-297. doi:10.1002/9781119500513.ch17

Le Friant, A., Lock, E. J., Hart, M. B., Boudon, G., Sparks, R. S. J., Leng, M. J., et al. (2008). Late Pleistocene Tephrochronology of marine Sediments Adjacent to Montserrat, Lesser Antilles Volcanic Arc. *J. Geol. Soc.* 165 (1), 279–289. doi:10.1144/0016-76492007-019

Lebas, E., Le Friant, A., Boudon, G., Watt, S. F. L., Talling, P. J., Feuillet, N., et al. (2011). Multiple Widespread Landslides during the Long-Term Evolution of a Volcanic Island: Insights from High-Resolution Seismic Data, Montserrat, Lesser Antilles. *Geochem. Geophys. Geosystems* 12, Q05006. doi:10.1029/2010gc003451

Lindsay, J. M., Smith, A. L., Roobol, M. J., and Stasiuk, M. V. (2005). "Dominica," in *Volcanic Hazard Atlas of the Lesser Antilles*. Editors J. M. Lindsay, R. E. A. Robertson, J. B. Shepherd, and S. Ali (Trinidad and Tobago, W.I.: Seismic Research Unit. the University of West Indies), 1–48. doi:10.1016/j.jvolgeores.2005.04.018

Lisiecki, L. E., and Raymo, M. E. (2005). A Pliocene-Pleistocene Stack of 57 Globally Distributed Benthic δ18O records18O Records. *Paleoceanography* 20, 1–17. doi:10.1029/2004PA001071

Llopart, J., Lafuerza, S., Le Friant, A., Urgeles, R., and Watremez, L. (2018). "Hydrogeological Evolution as a Pre-conditioning Factor for Slope Failure in a Back-arc Volcanic Setting, W off Martinique Island,". Paper presented at 8th International Symposium on Submarine Mass Movements and their consequences (ISSMMTC), 7–9 May 2018 (Victoria: British Columbia).

Lowe, D. J. (2014). "Marine Tephrochronology: a Personal Perspective," in *Geological Society*. Editors P. M. Abbott, S. M. Davies, N. J. G. Pearce, and S. Wastegard (London: Special Publications), 398, 7–19. doi:10.1144/sp398.11

Lowe, D. J. (2011). Tephrochronology and its Application: a Review. *Quat. Geochronol.* 6, 107–153. doi:10.1016/j.quageo.2010.08.003

Martel, C., Pichavant, M., Bourdier, J., Traineau, H., Holtz, F., and Scaillet, B. (1998). Magma Storage Conditions and Control of Eruption Regime in Silicic Volcanoes: Experimental Evidence from Mt. Pelée. *Earth Planet. Sci. Lett.* 156, 89–99. doi:10.1016/S0012-821X(98)00003-X

Martin-Kaye, P. H. A. (1969). A Summary of the Geology of the Lesser Antilles. *Overseas Geology. Mineral Resour.* 10 (2), 172–206.

Mencaroni, D., Llopart, J., Urgeles, R., Lafuerza, S., Gràcia, E., Le Friant, A., et al. (2020). From Gravity Cores to Overpressure History: the Importance of Measured Sediment Physical Properties in Hydrogeological Models. *Geol. Soc. Lond. Spec. Publications* 500, 289–300. doi:10.1144/SP500-2019-176

Michaud-Dubuy, A., Carazzo, G., Tait, S., Le Hir, G., Fluteau, F., and Kaminski, E. (2019). Impact of Wind Direction Variability on hazard Assessment in Martinique (Lesser Antilles): The Example of the 13.5 Ka Cal BP Bellefontaine Plinian Eruption of Mount Pelée Volcano. *J. Volcanology Geothermal Res.* 381, 193–208. doi:10.1016/j.jvolgeores.2019.06.004

Pamela Reid, R., Carey, S. N., and Ross, D. R. (1996). Late Quaternary Sedimentation in the Lesser Antilles Island Arc. *Geol. Soc. Am. Bull.* 108, 78–100. doi:10.1130/0016-7606(1996)108<0078:lqsitl>2.3.co;2

Paterne, M., Guichard, F., Labeyrie, J., Gillot, P. Y., and Duplessy, J. C. (1986). Tyrrhenian Sea Tephrochronology of the Oxygen Isotope Record for the Past 60,000 Years. *Mar. Geology.* 72 (3-4), 259–285. doi:10.1016/0025-3227(86)90123-4

Pichavant, M., Martel, C., Bourdier, J. L., and Scaillet, B. (2002). Physical Conditions, Structure and Dynamics of a Zoned Magma Chamber: Mount Pelée (Martinique, Lesser Antilles Arc). *J. Geophys. Res.* 107 (B5), 1–25. doi:10.1029/2001jb000315

Quidelleur, X., Hildenbrand, A., and Samper, A. (2008). Causal Link between Quaternary Paleoclimatic Changes and Volcanic Islands Evolution. *Geophys. Res. Lett.* 35, L02303. doi:10.1029/2007GL031849

Reimer, P. J., Bard, E., Bayliss, A., Beck, J. W., Blackwell, P. G., Bronk, H., et al. (2013a). IntCal13 and MARINE13 Radiocarbon Age Calibration Curves 0-50000 Years calBP. *Radiocarbon* 55 (4), 1869–1887. doi:10.2458/azu_js_rc.55.16947

Reimer, P. J., Bard, E., Bayliss, A., Beck, J. W., Blackwell, P. G., Ramsey, C. B., et al. (2013b). Selection and Treatment of Data for Radiocarbon Calibration: an Update to the International Calibration (IntCal) Criteria. *Radiocarbon* 55 (4), 1923–1945. doi:10.2458/azu_js_rc.55.16955

Roobol, M. J., and Smith, A. L. (1976). Mount Pelée, Martinique: A Pattern of Alternating Eruptive Styles. *Geology* 4, 521–524. doi:10.1130/0091-7613(1976)4<521:mpmapo>2.0.co;2

Samper, A., Quidelleur, X., Boudon, G., Le Friant, A., and Komorowski, J. C. (2008). Radiometric Dating of Three Large Volume Flank Collapses in the Lesser Antilles Arc. *J. Volcanology Geothermal Res.* 176, 485–492. doi:10.1016/j.jvolgeores.2008.04.018

Sigurdsson, H., Sparks, R. S. J., Carey, S. N., and Huang, T. C. (1980). Volcanogenic Sedimentation in the Lesser Antilles Arc. *J. Geology.* 88, 523–540. doi:10.1086/628542

Solaro, C., Boudon, G., Le Friant, A., Balcone-Boissard, H., Emmanuel, L., and Paterne, M. (2020). New Insights into the Recent Eruptive History and Collapse History of Montagne Pelée (Lesser Antilles Arc) from Offshore marine Drilling Site U1401A (340 Expedition IODP). *J. Volcanology Geothermal Res.* 403, 107001. doi:10.1016/j.jvolgeores.2020.107001

Sparks, R. S. J., Sigurdsson, H., and Carey, S. N. (1980a). The Entrance of Pyroclastic Flows into the Sea I. Oceanographic and Geologic Evidence from dominica, Lesser Antilles. *J. Volcanology Geothermal Res.* 7, 87–96. doi:10.1016/0377-0273(80)90021-9

Sparks, R. S. J., Sigurdsson, H., and Carey, S. N. (1980b). The Entrance of Pyroclastic Flows into the Sea, II. Theoretical Considerations on Subaqueous Emplacement and Welding. *J. Volcanology Geothermal Res.* 7, 97–105. doi:10.1016/0377-0273(80)90022-0

Stuiver, M., and Reimer, P. J. (1993). Extended 14C Data Base and Revised CALIB 3.0 14C Age Calibration Program. *Radiocarbon* 35, 215–230. doi:10.1017/s0033822200013904

Talling, P. J. (2013). Hybrid Submarine Flows Comprising Turbidity Current and Cohesive Debris Flow: Deposits, Theoretical and Experimental Analyses, and Generalized Models. *Geosphere* 9, 460–488. doi:10.1130/ges00793.1

Talling, P. J., Masson, D. G., Sumner, E. J., and Malgesini, G. (2012). Subaqueous Sediment Density Flows: Depositional Processes and deposit Types. *Sedimentology* 59, 1937–2003. doi:10.1111/j.1365-3091.2012.01353.x

Talling, P. J. (2014). On the Triggers, Resulting Flow Types and Frequencies of Subaqueous Sediment Density Flows in Different Settings. *Mar. Geology.* 352, 155–182. doi:10.1016/j.margeo.2014.02.006

Talling, P. J., Wynn, R. B., Schmmidt, D. N., Rixon, R., Sumner, E., and Amy, L. (2010). How Did Thin Submarine Debris Flows Carry Boulder-Sized Intraclasts for Remarkable Distances across Low Gradients to the Far Reaches of the Mississippi Fan? *J. Sediment. Res.* 80, 829–851. doi:10.2110/jsr.2010.076

Tanguy, J.-C. (2004). Rapid Dome Growth at Montagne Pelée during the Early Stages of the 1902?1905 Eruption: a Reconstruction from Lacroix?s Data. *Bull. Volcanol* 66, 615–621. doi:10.1007/s00445-004-0344-z

Tanguy, J.-C. (1994). The 1902-1905 Eruptions of Montagne Pelée, Martinique: Anatomy and Retrospection. *J. Volcanology Geothermal Res.* 60, 87–107. doi:10.1016/0377-0273(94)90064-7

Traineau, H., Westercamp, D., Bardintzeff, J. M., and Miskovski, J. C. (1989). The recent pumice eruptions of Mt. Pele´e volcano, Martinique, part I, Depositional sequences, description of pumiceous deposits. *J. Volcanol. Geotherm. Res.* 38 (1– 2), 17–33. doi:10.1016/0377-0273(89)90027-9

Trofimovs, J., Fisher, J. K., Macdonald, H. A., Talling, P. J., Sparks, R. S. J., Hart, M. B., et al. (2010). Evidence for Carbonate Platform Failure during Rapid Sea-Level Rise; Ca 14 000 Year Old Bioclastic Flow Deposits in the Lesser Antilles. *Sedimentology* 57, 735–759. doi:10.1111/j.1365-3091.2009.01117.x

Trofimovs, J., Talling, P. J., Fisher, J. K., Sparks, R. S. J., Watt, S. F. L., Hart, M. B., et al. (2013). Timing, Origin and Emplacement Dynamics of Mass Flows Offshore of SE Montserrat in the Last 110 Ka: Implications for Landslide and Tsunami Hazards, Eruption History, and Volcanic Island Evolution. *Geochem. Geophys. Geosyst.* 14, 385–406. doi:10.1002/ggge.20052

Villemant, B., Boudon, G., and Komorowski, J.-C. (1996). U-series Disequilibrium in Arc Magmas Induced by Water-Magma Interaction. *Earth Planet. Sci. Lett.* 140, 259–267. doi:10.1016/0012-821x(96)00035-0

Villemant, B., and Boudon, G. (1998). Transition from Dome-Forming to Plinian Eruptive Styles Controlled by H2O and Cl Degassing. *Nature* 392, 65–69. doi:10.1038/32144

Vincent, P. M., Bourdier, J. L., and Boudon, G. (1989). The Primitive Volcano of Mount Pelée: Its Construction and Partial Destruction by £Ank Collapse. *J. Volcanol. Geotherm. Res.* 38, 1–15.

Wadge, G. (1984). Comparison of Volcanic Production Rates and Subduction Rates in the Lesser Antilles and Central America. *Geol* 12, 555–558. doi:10.1130/0091-7613(1984)12<555:covpra>2.0.co;2

Wall-Palmer, D., Coussens, M., Talling, P. J., Jutzeler, M., Cassidy, M., Marchant, I., et al. (2014). Late Pleistocene Stratigraphy of IODP Site U1396 and Compiled Chronology Offshore of South and South West Montserrat, Lesser Antilles. *Geochem. Geophys. Geosyst.* 15, 3000–3020. doi:10.1002/2014GC005402

Watt, S. F. L., Talling, P. J., Vardy, M. E., Masson, D. G., Henstock, T. J., Hühnerbach, V., et al. (2012). Widespread and Progressive Seafloor-Sediment Failure Following Volcanic Debris Avalanche Emplacement: Landslide Dynamics and Timing Offshore Montserrat, Lesser Antilles. *Mar. Geology.* 323-325, 69–94. doi:10.1016/j.margeo.2012.08.002

Watt, S. F. L. (2019). The Evolution of Volcanic Systems Following Sector Collapse. *J. Volcanology Geothermal Res.* 384, 280–303. doi:10.1016/j.jvolgeores.2019.05.012

Westercamp, D., Andreieff, P., Bouysse, P., Cottez, S., and Battistini, R. (1989). "Martinique," in *Carte géologique à 1/50 000* (Orleans: BRGM).

Westercamp, D., and Traineau, H. (1983b). *Carte géologique au 1/20 000 de la Montagne Pelée, avec notice explicative*. Orleans: BRGM.

Westercamp, D., and Traineau, H. (1983a). The Past 5,000 Years of Volcanic Activity at Mt. Pelee Martinique (F.W.I.): Implications for Assessment of Volcanic Hazards. *J. Volcanology Geothermal Res.* 17, 159–185. doi:10.1016/0377-0273(83)90066-5

Whitham, A. G. (1989). The Behaviour of Subaerially Produced Pyroclastic Flows in a Subaqueous Environment: Evidence from the Roseau Eruption, Dominica, West Indies. *Mar. Geology.* 86, 27–40. doi:10.1016/0025-3227(89)90016-9

Conflict of Interest: The authors declare that the research was conducted in the absence of any commercial or financial relationships that could be construed as a potential conflict of interest.

Publisher's Note: All claims expressed in this article are solely those of the authors and do not necessarily represent those of their affiliated organizations, or those of the publisher, the editors and the reviewers. Any product that may be evaluated in this article, or claim that may be made by its manufacturer, is not guaranteed or endorsed by the publisher.

Copyright © 2022 Villemant, Le Friant, Caron, Del Manzo, Lafuerza, Emmanuel, Ishizuka, Guyard, Labourdette, Michel and Hidalgo. This is an open-access article distributed under the terms of the Creative Commons Attribution License (CC BY). The use, distribution or reproduction in other forums is permitted, provided the original author(s) and the copyright owner(s) are credited and that the original publication in this journal is cited, in accordance with accepted academic practice. No use, distribution or reproduction is permitted which does not comply with these terms.

frontiers | Frontiers in Earth Science

ORIGINAL RESEARCH
published: 01 April 2022
doi: 10.3389/feart.2022.761902

Mantle and Crustal Xenoliths in a Tephriphonolite From La Palma (Canary Islands): Implications for Phonolite Formation at Oceanic Island Volcanoes

Andreas Klügel[1]*, *Elmar Albers*[1] and *Thor H. Hansteen*[2]

[1]Fachbereich Geowissenschaften, Universität Bremen, Bremen, Germany, [2]GEOMAR Helmholtz-Zentrum für Ozeanforschung Kiel, Kiel, Germany

The occurrence of mantle-derived peridotite xenoliths in phonolitic melts is a rare phenomenon, and is commonly ascribed to a mantle origin of the phonolite. The alternative possibility, that xenoliths are transported into evolving phonolite melts by mafic magmas, has received little attention. A unique tephriphonolite lava with phonolitic groundmass composition, from the active Cumbre Vieja volcano of La Palma (Canary Islands), allows to test these models. The lava contains abundant inclusions that represent the island's major xenolith types: kaersutite-dominated cumulates, gabbros from the lower oceanic crust, and peridotites from the mantle. Our petrological investigations indicate that the tephriphonolite magma contained 3–4 wt% H_2O and was stored in the lower crust at around 250–350 MPa and 900–950°C, at oxidized conditions (ΔNNO of 2–3). The peridotite xenoliths are mantled by complex polyphase selvages, with adjacent up to 1.6 mm wide zonations where olivine compositions change from Fo_{78-86} at the selvage contact to Fo_{89-91} inside the xenoliths. We carried out diffusion modelling for Fe-Mg exchange and found that the peridotites had contact with intermediate to evolved alkaline melts over decades to centuries. This timescale is comparable to that inferred for basanite-hosted peridotite xenoliths from Cumbre Vieja. The following model is proposed: differentiation of evolved melts occurs in a magma accumulation zone in the lowermost oceanic crust beneath La Palma. The evolving melts receive periodic recharge by mantle-derived mafic magmas at intervals on the order of decades to a few centuries, comparable to historic eruption recurrences (80 years on average). Some of these recharge pulses carry mantle peridotite fragments that become deposited in the accumulation zone. Thus, these xenoliths do not reflect formation of the evolved melts in the mantle. Final ascent of the tephriphonolite was triggered by magma recharge some weeks before its eruption, resulting in entrainment and thorough mingling of a mixed xenolith population (cumulates, oceanic crust gabbros, peridotites). We infer that formation of phonolites in the lower crust beneath oceanic island volcanoes, and subsequent eruption, requires a balance between rates and volumes of magma recharge pulses and of eruptive events.

Keywords: magma storage, phonolite, differentiation, thermobarometry, intraplate volcanism

OPEN ACCESS

Edited by:
Michel Pichavant, CNRS Orléans, France

Reviewed by:
Abigail Barker, Uppsala University, Sweden
Joan Andújar, UMR7327 Institut des sciences de la Terre d'Orléans (ISTO), France

***Correspondence:**
Andreas Klügel
akluegel@uni-bremen.de

Specialty section:
This article was submitted to Volcanology, a section of the journal Frontiers in Earth Science

Received: *20 August 2021*
Accepted: *18 February 2022*
Published: *01 April 2022*

Citation:
Klügel A, Albers E and Hansteen TH (2022) Mantle and Crustal Xenoliths in a Tephriphonolite From La Palma (Canary Islands): Implications for Phonolite Formation at Oceanic Island Volcanoes. Front. Earth Sci. 10:761902. doi: 10.3389/feart.2022.761902

INTRODUCTION

Phonolites, the differentiated residual end-members of alkaline, SiO_2-undersaturated melts, are typical products of intraplate magmatism. They are widespread on Earth but are volumetrically subordinate to corresponding alkaline basalts in most places, with the Miocene flood phonolites of the Kenya Rift as a notable exception (Hay and Wendlandt, 1995). Phonolite domes, cryptodomes, and lava flows form prominent deposits and outcrops on many volcanic islands, for example La Gomera, La Palma and Tenerife (Canary Islands), Brava and Santo Antão (Cabo Verde Islands), São Tomé, Trindade, Tristan da Cunha, and Kerguelen archipelago (e.g. Mitchell-Thomé, 1970; Schmincke, 1976; Weaver, 1990; Weis et al., 1993). Pyroclastic deposits from strongly explosive phonolite eruptions are major features e.g. on Tenerife, Brava and Santo Antão islands (e.g., Martí et al., 1994; Edgar et al., 2007; Mortensen et al., 2009; Madeira et al., 2010). Phonolites can occur during the early seamount stage of a volcano, such as Cadamosto at Cabo Verde archipelago (Barker et al., 2012) and near Tahiti and the Pitcairn islands (Devey et al., 2003), as well as during later stages or episodes as on Tenerife and Brava (e.g., Ablay et al., 1998; Madeira et al., 2010).

Phonolites are commonly derived from alkaline basaltic melts through extensive, often polybaric fractional crystallization, consistent with observed phenocryst phases and the liquid lines of descent (LLD) for basalt-phonolite series (e.g., Price and Chappell, 1975; Wörner and Schmincke, 1984; LeRoex et al., 1990; Weaver, 1990; Ablay et al., 1998; Johansen et al., 2005; Melluso et al., 2007; Turner et al., 2015; Berthod et al., 2021). U-series isotope studies suggest times of differentiation from basanite to phonolite ranging from ~100 to 1,600 years for small systems (Johansen et al., 2005; Reagan et al., 2008) to 100–230 ka for larger systems (Bourdon et al., 1994; Hawkesworth et al., 2000). Pre-eruptive phonolite evolution at relatively shallow levels (<300 MPa) is indicated by volatile concentrations of trapped melts and mineral barometry (Ablay et al., 1998; Marziano et al., 2007; Schmidt and Behrens, 2008), feldspar fractionation (Price and Chappell, 1975; Kelly et al., 2008), and experimental work (e.g., Berndt et al., 2001; Freise et al., 2003; Harms et al., 2004; Andújar et al., 2008, 2010, 2013; Moussallam et al., 2013). Phonolites may also form at high pressures without feldspar fractionation (1–2 GPa; Kunzmann, 1996; Irving and Price, 1981; Irving and Green, 2008; Grant et al., 2013). In rare cases, phonolites or tephriphonolites carry peridotite xenoliths from the mantle, the only occurrences reported thus far being Phonolite Hill (Australia), Dunedin Volcanic Complex (New Zealand), Bokkos (Nigeria), Heldburg (Germany), Harrat Kishb (Saudi Arabia), and Mayotte Island (Comoros archipelago) (Wright, 1966; Irving and Price, 1981; Irving and Green, 2008; Grant et al., 2013; Berthod et al., 2021).

The occurrence of mantle xenoliths in a phonolite likely reflects a mantle origin of the magma, but unless demonstrated by e.g. barometric data (Grant et al., 2013; Berthod et al., 2021) such an interpretation may be misleading. Recharge events during magma differentiation at shallower levels (e.g., Rout and Wörner, 2020) may also bring deep-seated fragments into an evolving melt. Here we present petrological data from a unique tephriphonolite body on La Palma (Canary Islands), which carries abundant mantle and crustal xenoliths in a phonolitic groundmass. We demonstrate that the magma was stored in the crust and received peridotite fragments by mafic recharge, constrain the timing of recharge events, and discuss the implications for magma storage and eruption.

GEOLOGICAL SETTING

The Canary Archipelago is a chain of seven volcanic islands located off the northwestern African continental shelf (**Figure 1**). They form the western branch of an intraplate hotspot chain with seamount and island ages decreasing from east to west (Geldmacher et al., 2005). All islands are underlain by Jurassic oceanic crust as is indicated by mid-ocean ridge basalt (MORB) gabbro xenoliths occurring on Lanzarote, Gran Canaria, and La Palma (Hoernle, 1998; Schmincke et al., 1998). The age of the crust is 175 Ma between Lanzarote and the African coast (paleomagnetic anomaly S1), and 155 Ma between La Palma and El Hierro, the westernmost and youngest islands (M25; Klitgord and Schouten, 1986).

The geology of La Palma is extensively summarized in Carracedo et al. (2001). Briefly, the island consists of three main units: *1*) the basal complex (4.0–2.9 Ma) which comprises a Pliocene seamount sequence and a plutonic complex; *2*) the older volcanic series (1.7–0.41 Ma) which includes the Taburiente shield volcano and the Bejenado edifice; and *3*) the Cumbre Vieja series (>125 ka to present) confined to the southern half of the island (**Figure 1A**). La Palma is currently in the latter part of its shield-building stage. With seven eruptions recorded since the 15th century, the north-south trending Cumbre Vieja ridge is an active volcanic rift zone along which most scoria cones, eruptive fissures and faults are concentrated (Middlemost, 1972; Hernandéz-Pacheco and Valls, 1982; Carracedo, 1994).

Cumbre Vieja rocks are Si-undersaturated and alkaline, with most compositions following a basanite-phonolite lineage (summarized in Carracedo et al., 2001). The major phenocryst phases are titaniferous clinopyroxene ± olivine + Ti-magnetite ± kaersutitic amphibole in the mafic Cumbre Vieja rocks, and clinopyroxene + kaersutite + magnetite + plagioclase ± haüyne ± titanite ± apatite in the evolved rocks. Xenoliths are commonly found in late erupted basanites, including ultramafic cumulates (the most common type), mafic cumulates, MORB-type gabbros from the Jurassic ocean crust, mantle peridotites, and various types of felsic fragments (Klügel et al., 1999). Whereas phonolites are virtually absent in the older volcanic series and rare at Bejenado volcano, they commonly occur at

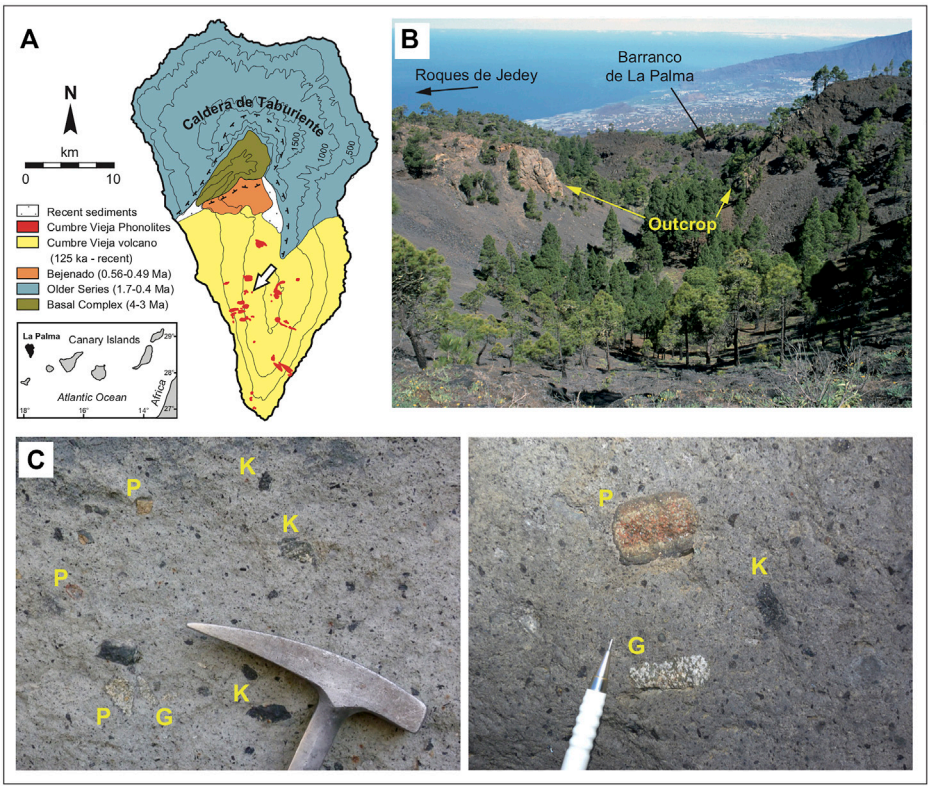


FIGURE 1 | (A) Simplified geological map of La Palma with arrow showing the locality of the tephriphonolite outcrops. **(B)** Photograph towards the northwest, showing the breached 1585 eruption crater with the tephriphonolite outcrops (arrows). **(C)** Outcrop photographs of the tephriphonolite with kaersutitite (K), gabbro (G), and peridotite (P) xenoliths. Note the selvage around the peridotites.

Cumbre Vieja as domes, spines and lava flows (Hernandéz-Pacheco and De la Nuez, 1983) (**Figure 1**). During the catastrophic 1585 eruption, a pre-existing phonolitic dome was uplifted and a juvenile phonolitic cryptodome was emplaced (Day et al., 1999).

The peridotite-bearing tephriphonolite investigated here crops out at the breached wall of the north-easternmost crater of the 1585 Tahuya eruption, 1 km east of the prominent Roques de Jedey phonolite spines and 200 m south of Barranco de La Palma, at 1,200–1,230 m above sea level (**Figure 1B**). The overall joint patterns, flow markers, and steeply west-dipping banks of brecciated rock visible at the northern outcrop cliff suggest that the tephriphonolite was extruded at this site along a N-S trending fissure. This is consistent with the presence of decimeter-sized, partly rounded blocks up to 1 km downslope. Angular tephriphonolite lithic fragments are widespread around the outcrop; apparently they were produced during the 1585 eruption when violent explosions excavated the north-easternmost crater and the tephriphonolite plug (Romero Ruiz, 1991; Day et al., 1999). The tephriphonolite hence pre-dates the 1585 eruption, but its exact age is unknown. Overall, this tephriphonolite is easily recognized in the field due to the abundance of ultramafic cumulate, gabbro, and peridotite xenoliths up to 5 cm in size (**Figure 1C**). A list of the samples from this study and their localities is given in **Supplementary Table S1**.

METHODS

Whole-Rock Analyses

Three selected tephriphonolite samples were crushed and sieved, fragments containing xenoliths were removed, and the remaining separates were powderized using an agate mill. Whole-rock analyses of the tephriphonolite were carried out by X-ray fluorescence spectrometry (XRF) on fused glass beads using a Philips X'Unique PW1480 at GEOMAR (Kiel) calibrated with international standards. H_2O and CO_2 were analysed with a Rosemount CSA 5003 infrared photometer. The samples were also analyzed for trace elements by inductively coupled plasma-mass spectrometry (ICP-MS) at the Department of Earth Science, Memorial University of Newfoundland, following the procedure described in Jenner et al. (1990). Whole-rock analyses of four other tephriphonolites and phonolites were carried out on fused lithium-tetraborate glass beads using a Pananalytical Magix PRO XRF at the Mineralogisch-Petrographisches Institut, Universität Hamburg, Germany. Loss on ignition (LOI) was determined gravimetrically after fusion of a sample aliquot at 1,050°C (Lechler and Desilets, 1987). Analyses of secondary standards

are given in **Supplementary Table S2**. Accuracy of XRF standard data is better than 2 and 10% for concentrations of >1 wt% and >0.1 wt%, respectively. Accuracy of ICP-MS data is better than 5% for most trace elements and better than 10% overall except for Pb (16%).

Groundmass Analyses

The major element composition of groundmass was determined on thin sections by laser ablation ICP-MS at the Faculty of Geosciences, University of Bremen, using a NewWave UP193ss laser coupled to a Thermo Element2. Helium (~0.8 L/min) was used as sample gas and Argon (~0.8 L/min) was subsequently added as make-up gas; plasma power was 1200 W. A laser beam of 100 µm diameter and 5 Hz pulse rate was moved over groundmass at 5–6 µm/s for 60–180 s to give a single analysis; four to eight such analyses were averaged. The isotopes ^{23}Na, ^{24}Mg, ^{27}Al, ^{28}Si, ^{31}P, ^{39}K, ^{44}Ca, ^{48}Ti, ^{55}Mn and ^{56}Fe were analyzed at high resolution with a 150% mass window and a total dwell time of 0.15 s per isotope. Blanks were measured during 25 s prior to ablation. The data were quantified using the Cetac GeoPro™ software with USGS glass BCR-2G as external calibration standard (Jochum et al., 2005) and Ca as internal standard element. The Ca concentration was initially set to an arbitrary value, and calculated concentrations were subsequently normalized to a volatile-free sum of 100 wt% oxides with total Fe as FeO. Analytical precision and accuracy were monitored by regular analyses of USGS basalt glass BHVO-2G (Jochum et al., 2005) along with the samples; both were <2% for most elements and <8% throughout (**Supplementary Table S3**).

Electron Microprobe Analyses

Electron microprobe (EMP) analyses of minerals were carried out on Jeol JXA-8900RL (Geosciences Institute, Universities of Mainz and Kiel), Cameca SX-50 (GEOMAR, Kiel), and Cameca SX-100 instruments (Faculty of Geosciences, Bremen). Analytical conditions included peak counting times of 15–20 s, an acceleration voltage of 15 kV, beam diameter between 1 and 5 µm, and beam currents of 30–50 nA for olivine and 10–15 nA for other minerals. The instruments were calibrated with reference standards mainly from the Smithsonian Institution (Jarosewich et al., 1980). The built-in PRZ (Jeol) and PAP (Cameca) correction methods were applied for data reduction. Analytical precision and accuracy were controlled by regular analyses of secondary standards (**Supplementary Table S4**). Qualitative wavelength-dispersive spectrometer (WDS) analyses of Si, Mg, Fe and Ca along olivine traverses were carried out with 50 nA beam current and dwell times of 1 s per point.

Microthermometry

Fluid inclusions used for barometry were examined in 100 µm thick doubly polished sections. Microthermometric analyses were carried out on small chips from these sections using a Linkam THM 600 heating-cooling stage at GEOMAR, Kiel. The stage was calibrated with SYNFLINC™ fluid inclusion standards at −56.6°C, 0.0°C, and 374.1°C. Accuracy of CO_2 triple-point measurements and reproducibility of melting and homogenization temperatures were within ±0.2°C. Densities of CO_2-dominated inclusions were calculated from measured homogenization temperatures using the auxiliary Eqs 3.14 and 3.15 of Span and Wagner (1996). Isochores were computed with the Sterner and Pitzer (1994) equation of state for the CO_2-H_2O system, following Hansteen and Klügel (2008).

RESULTS

Petrography and Mineral and Melt Compositions

Modal mineral proportions in lavas and xenoliths were determined on thin sections by visual estimates. Whole-rock and groundmass compositions of tephriphonolite and phonolite samples are presented in **Supplementary Table S5**; the compositions of all minerals analyzed are provided in **Supplementary Tables S6–S10**. Scanned images of entire thin sections are presented in **Supplementary Figure S1**.

Host Tephriphonolite

The xenolith-rich tephriphonolite contains up to 10 vol% of irregularly shaped vesicles that were deformed and disrupted by shearing of the viscous magma. The groundmass consists of anorthoclase laths with subordinate Ti-magnetite, clinopyroxene, apatite, minor haüyne, rare zircon (as a late-stage phase occurring close to vesicles), ±glass. The macrocryst phases (>0.1 mm) are kaersutitic amphibole (10–20 vol%, up to 4 mm in size), greenish clinopyroxene (<5%, <1 mm), plagioclase (<5%, <1 mm), haüyne (<5%, <0.5 mm), apatite (<1%, <0.5 mm), and Ti-magnetite (1–2%, <0.5 mm) (**Figures 2A,D** and **Supplementary Figure S1**). Titanite is not present, in contrast to the more evolved Cumbre Vieja phonolites. Most macrocrysts are euhedral to subhedral, but there are also irregularly-shaped crystal fragments and small amphibole/clinopyroxene-rich polycrystalline aggregates, interpreted as xenocrysts and xenolith fragments. Kaersutites commonly display 20–80 µm thick fine-grained opaque reaction rims (opacite), indicating reaction with the host melt (Rutherford and Hill, 1993; De Angelis et al., 2015; France, 2020). Likewise, most haüynes are corroded with 10–60 µm thick opaque reaction rims towards the host melt. Apatite occurs as phenocrysts with locally corroded rims, and as ubiquitous inclusions in kaersutite and clinopyroxene. Locally the feldspar laths and macrocrysts define a flow texture.

Plagioclase has a compositional range $Ab_{48\text{-}60}An_{30\text{-}46}Or_{4\text{-}10}$, showing a gradual transition in composition and size toward the less anorthitic groundmass anorthoclase. Kaersutite has a range in Mg# from 52 to 71 (Mg# = molar Mg/(Mg+Fe_{tot})*100), SiO_2 from 38.6 to 40.9 wt%, and TiO_2 from 4.2 to 5.6 wt% (**Figure 3A**). Many crystals display normal progressive zoning with decreasing Mg# towards the rim (Mg# 66–71 to 52–58; **Figure 3C**); crystals that are more complexly zoned and/or display an optically distinct core are less common. The compositions indicate moderate correlation of Mg# with Na, Al, Ti, and Si with significant scatter, interpreted to reflect a broad fractionation trend (**Figure 3A**). Clinopyroxene is ferrian aluminian diopside

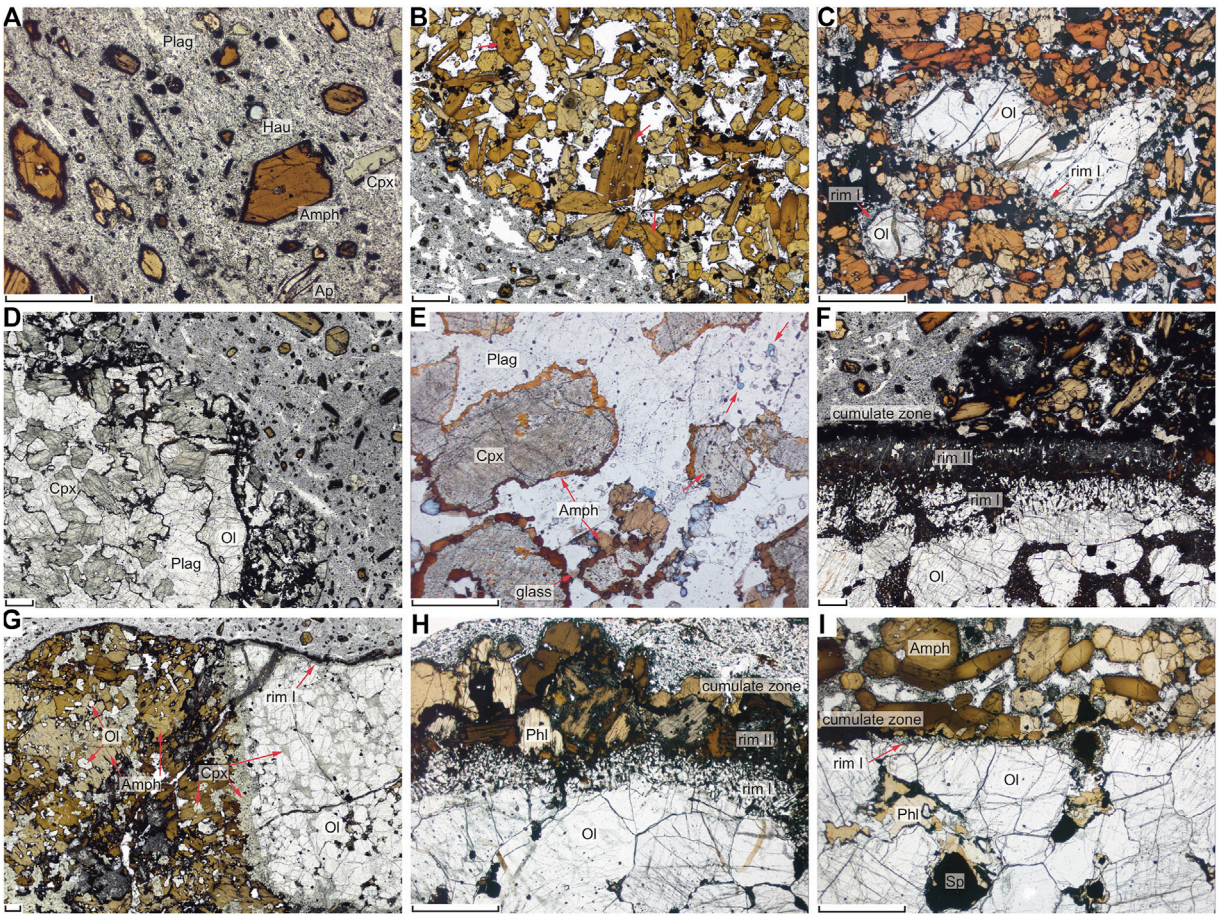


FIGURE 2 | Microphotographs from selected samples taken at plane polarized light; scale bars are 1 mm. Abbreviations: Cpx, clinopyroxene; Amph, amphibole; Plag, plagioclase; Ol, olivine; Phl, phlogopite; Sp, spinel; Ap, apatite; Hau, haüyne. **(A)** Sample KLA1718: tephriphonolite with kaersutite, clinopyroxene, plagioclase, haüyne, and apatite macrocrysts. **(B)** Sample KLA1705: kaersutite-dominated cumulate xenolith with open texture; host tephriphonolite to the lower left. Arrows indicate examples of strongly zoned crystals. **(C)** Sample KLA1709: olivine and small peridotite fragment with reaction rim of Cpx+Mt within kaersutite-dominated cumulate xenolith. **(D)** Sample KLA1701: olivine gabbro xenolith with incipient melting at grain boundaries; degree of melting increases towards the host tephriphonolite contact (upper right). **(E)** Sample KLA1708: strongly metasomatized gabbro xenolith with blue haüyne and brown amphibole around clinopyroxene. Note the presence of glass, euhedral Amph, euhedral haüyne within newly crystallized Plag, and recrystallized Cpx along a NE-SW trending vein (arrows). **(F)** Sample KLA1704: spinel wehrlite xenolith (bottom) with cumulus texture and Cpx that is in large parts replaced by opaque Phl-rich aggregates. The xenolith has a prominent selvage towards the host tephriphonolite (top) consisting of Cpx-Mt-dominated rim I, Phl-dominated rim II, and Amph-rich cumulate zone. **(G)** Sample KLA1735: composite xenolith with veined wehrlite (right) and cumulate dominated by brown Amph oikocrysts, subhedral Ol, and Cpx (left). The wehrlite has a thick Cpx-Mt selvage towards the cumulate, and a thin selvage towards the host tephriphonolite (top). **(H)** Sample KLA1731: dunite xenolith (bottom) with selvage consisting of Cpx-Mt-dominated rim I, Phl-dominated rim II, and Amph-rich cumulate zone. **(I)** Sample KLA1721: peridotite xenolith (bottom) with metasomatic Phl and two-part selvage, consisting of a narrow Cpx+Mt dominated reaction rim I and an Amph-dominated cumulate zone; rim II is absent in this sample.

with considerable variation in composition (Mg# 55–77, SiO_2 43–51 wt%, TiO_2 1.0–3.4 wt%, Na_2O 0.8–2.5 wt%, Al_2O_3 1.7–7.8 wt%; **Figure 3B**). Clinopyroxene macrocrysts can be variably zoned and display complex compositional profiles; reverse and step zoning are not uncommon (**Figure 3D**). The interiors span a larger Mg# range than the rims, with a tendency to higher Si and Na, and lower Al and Ti, at a given Mg#. The interiors and rims broadly define two distinct compositional trends (**Figure 3B**): trend 1) is interpreted to reflect chemical variations during magma evolution and broadly resembles the variations of kaersutite macrocrysts (**Figure 3A**), whilst trend 2) is opposite in some diagrams. Trend 2) can be explained by sector zoning, which produces hourglass {−111} basal sectors that are higher in Mg# and SiO_2, and lower in Al_2O_3 and TiO_2, than {hk0} prism sectors (Ubide et al., 2019). This zoning can be formally expressed by coupled cation exchange between {−111} and {hk0} sectors, resulting in positive correlation of Mg# with Si and negative correlation with Al and Ti (Welsch et al., 2016; Ubide et al., 2019), as observed in **Figure 3B**. Sector zoning can be the dominating trend in clinopyroxene assemblages, making any specific fractionation trend almost unrecognizeable (cf. Ubide et al., 2019). Compared to the rims of macrocrysts in mafic Cumbre Vieja lavas, tephriphonolite clinopyroxenes are more Na-rich and define distinct compositional fields (**Figure 3B**). Overall the large Mg# ranges of the inner regions of clinopyroxene and kaersutite macrocrysts, as well as the reverse and complex zonings observed,

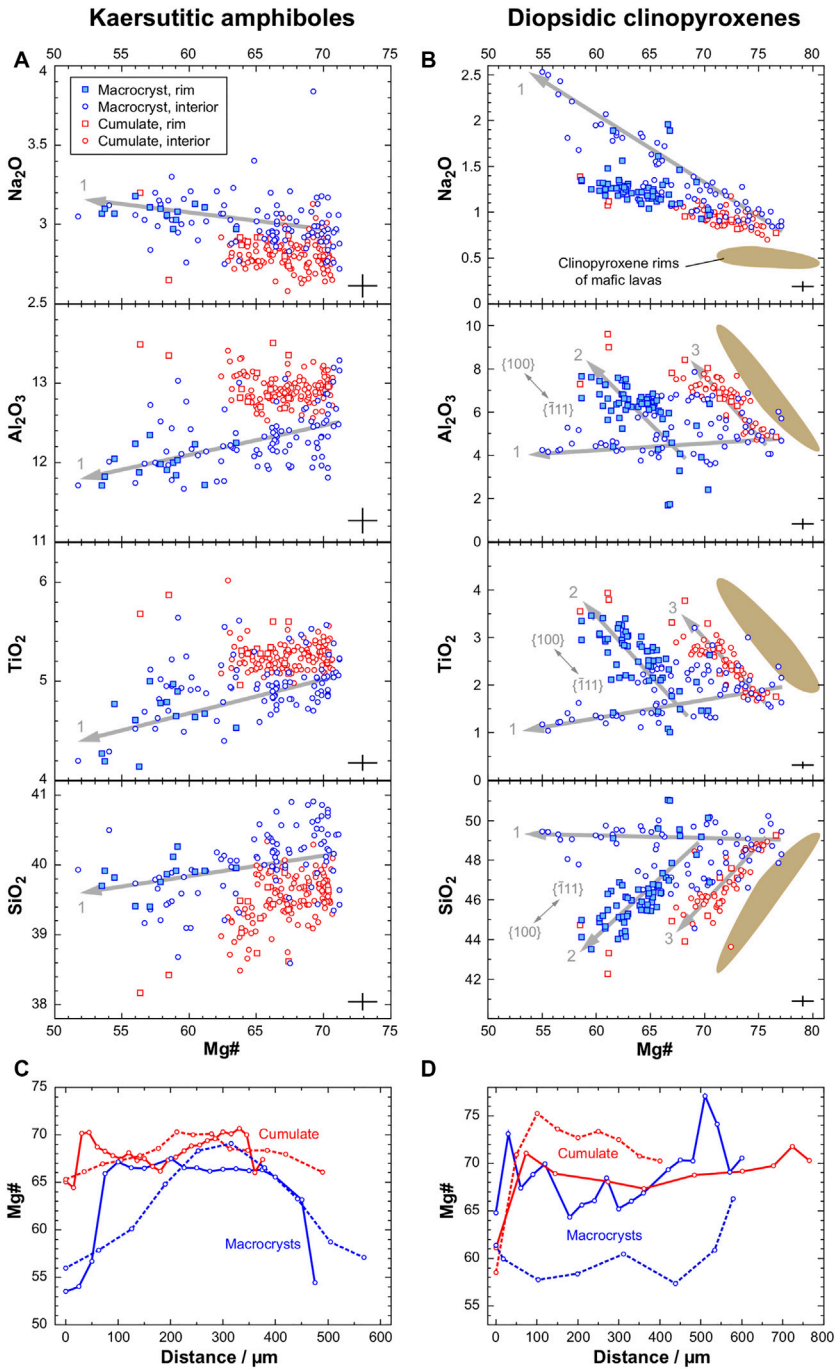


FIGURE 3 | Chemical compositions of **(A)** kaersutite and **(B)** diopside macrocrysts in the host tephriphonolite (blue symbols) and in cumulate xenoliths (red symbols) plotted in bivariate diagrams versus Mg#. Analyses at the outermost crystal rims are indicated by squares, those in the inner regions by circles. Brown fields outline average compositions of rims of clinopyroxene macrocrysts hosted by mafic lavas (basanites and tephrites; Klügel et al., 2000, 2005). Error bars indicate analytical uncertainty (±1 standard deviation) as based on analyses of secondary standards. Cumulate crystals show limited compositional overlap with macrocrysts and a smaller compositional range. Clinopyroxene compositions define three major trends indicated by thick arrows: trend 1) is interpreted to reflect progressive crystal fractionation, whereas trends 2) and 3) show opposite behavior for some elements. These trends are consistent with sector zoning, in which hourglass {−111} basal sectors are higher in Mg# and SiO_2, and lower in Al_2O_3 and TiO_2, than {100} prism sectors (cf. Ubide et al., 2019). The fractionation trend 1) is also broadly recognized in kaersutite macrocrysts. **(C,D)** Compositional profiles showing Mg# of selected kaersutite and diopside crystals, respectively.

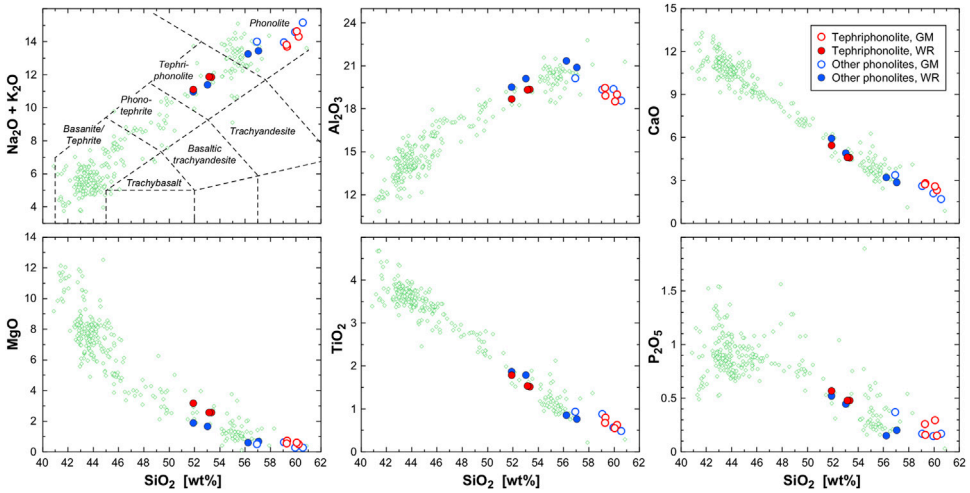


FIGURE 4 | Harker diagrams for samples from the investigated tephriphonolite (red filled circles) and its groundmass (red-white circles), from four other tephriphonolites to phonolites from Cumbre Vieja (blue filled circles) and their groundmass (blue-white circles), and from other historic and prehistoric Cumbre Vieja rocks (green diamonds; data from Hernandéz-Pacheco and Valls (1982), Hernandéz-Pacheco and de la Nuez (1983), Elliott (1991), Klügel et al. (2000); Klügel et al. (2017), Carracedo et al. (2001), Johansen et al. (2005), Day et al. (2010), Turner et al. (2015)). Data are normalized to 100% volatile-free. WR, whole-rock; GM, groundmass. The trends in the diagrams are consistent with fractionation of the phenocryst phases observed.

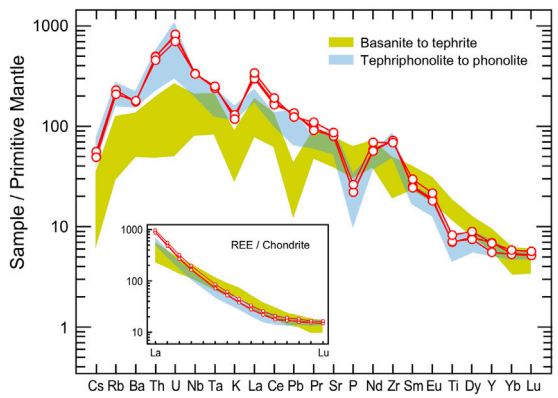


FIGURE 5 | Incompatible-element diagram for three tephriphonolite samples of this study, normalized to primitive mantle. Range for basanites and tephrites (green), and tephriphonolites and phonolites (blue), from Cumbre Vieja are indicated for comparison; data sources as in **Figure 4**. Inset shows the pronounced concave-upward shape of the samples in a chondrite-normalized REE diagram. Normalization values are from Sun and McDonough (1989).

indicate a considerable portion of antecrysts and xenocrysts in the tephriphonolite.

The whole rock contains around 52–53 wt% SiO_2 and falls within the basanite-phonolite lineage of Cumbre Vieja. This lineage is controlled by crystal fractionation and subordinate magma mixing, as is demonstrated by mass-balance calculations (Johansen et al., 2005; Turner et al., 2015). The groundmass of the tephriphonolite has phonolitic composition with around 59–60 wt% SiO_2 (**Figure 4**). The decrease of CaO, TiO_2 and MgO with increasing SiO_2 is consistent with removal of clinopyroxene and kaersutitic amphibole, the main macrocryst phases in tephrites to phonolites from Cumbre Vieja. The depletion in Al_2O_3 of phonolitic groundmass but not in the whole-rock trend (**Figure 4**) suggests that phonolites underwent only little feldspar fractionation. Variations between samples in groundmass composition and macrocryst content indicate some heterogeneities of the tephriphonolite body. Incompatible trace element patterns of the tephriphonolite broadly follow those of other evolved rocks from the Cumbre Vieja (**Figure 5**). Negative Ti anomalies, low Nb/U and Ba/Th ratios, and concave-upward spectra of the rare earth elements (REE) are consistent with extensive kaersutite fractionation, in accordance with the petrographic observations. Likewise, removal of apatite can explain the negative P anomalies observed, as well as decreasing P_2O_5 with increasing SiO_2 (**Figure 4**). In contrast to basanites and tephrites, the tephriphonolite as well as other evolved rocks from the Cumbre Vieja show low Ce/Pb ratios (11–15) and no negative Pb anomalies.

Kaersutitite Xenoliths

These ultramafic xenoliths consist of kaersutitic amphibole as the dominant phase (50–90 vol%, up to 4 mm in size), greenish aluminian diopside (2–30%, <3 mm), apatite (2–5%, <1 mm), anorthoclase feldspar (2–5%, <0.5 mm), Ti-magnetite (1–5%, <0.5 mm), and accessory zircon (**Figure 2B**). Some samples contain olivine xenocrysts or aggregates with symplectitic reaction rims of clinopyroxene and magnetite (**Figure 2C**). The xenoliths show an open cumulus texture with dominantly euhedral to subhedral crystals and up to 20 vol% of voids in the interstices (**Figure 2B**). Much of the interstitial space is filled with anorthoclase and minor zircon representing the last crystallizing phases; we note that zircon is a very rare phase in igneous rocks

from Cumbre Vieja. In thin section, kaersutite and diopside crystals commonly show patchy or concentric zoning, in some cases an optically distinct core, and in many cases a distinct outermost rim (**Figure 2B**). Some kaersutites exhibit opacite rims at the contact to the interstices and to the host tephriphonolite, but not at the contact to other crystals. Apatite occurs as a cumulus phase with marginally corroded crystals similar to those in the host tephriphonolite, and also as ubiquitous inclusions in kaersutite and clinopyroxene. Locally, incipient disintegration at the xenolith surface results in a transition from cumulus texture to macrocrysts in host magma (**Figure 2B**). In contrast to the xenoliths studied here, basanite-hosted kaersutite- and clinopyroxene-dominated cumulate xenoliths that are ubiquitous on Cumbre Vieja have a more primitive character, as is expressed by the presence of olivine and the lack of apatite and anorthoclase feldspar (Muñoz et al., 1974; Klügel et al., 1999; Barker et al., 2015).

Chemical compositions of kaersutite and diopside in the xenoliths partly overlap with those of tephriphonolite macrocrysts and show less variability. Compared to the macrocrysts, xenolith kaersutites tend to be lower in Si and Na, higher in Ti and Al, and more restricted in Mg# (**Figure 3A**). Xenolith diopsides define a unique compositional trend 3) that broadly resembles trend 2) for tephriphonolite macrocrysts, but is shifted to higher Mg# and lower Na (**Figure 3B**). As discussed above, this trend likely reflects sector zonations of the crystals. Diopside rims have a tendency to lower Mg# and Si, and higher Al and Ti than the inner regions, but overall there is strong overlap between interior and outermost rim compositions (**Figures 3A,B**). Cumulus crystals can be variably zoned, including normal zoning with decreasing Mg# from core to rim, or more complex zoning with an increase and subsequent decrease in Mg# from core to rim (**Figures 3C,D**). The compositions of xenolith feldspar ($Ab_{45-65}An_{4-44}Or_{7-43}$) overlap those of the groundmass anorthoclase but extend to less anorthitic and more potassic compositions.

Gabbro Xenoliths

The gabbro xenoliths consist of plagioclase (30–50 vol%), diopsidic clinopyroxene (40–60 vol%), olivine (0–20 vol%), occasional orthopyroxene, and accessory Ti-magnetite (**Figure 2D**). Clinopyroxene commonly shows exsolution lamellae of orthopyroxene. Clinopyroxene compositions differ markedly from those of La Palma lavas (**Figure 3B**) by higher Mg# (80.8–83.6) and SiO_2 (51.7–53.5 wt%), and lower TiO_2 (0.2–0.5 wt%), Al_2O_3 (1.0–2.9 wt%), and Na_2O (0.3–1.2 wt%). These compositions partly overlap with those from MORB-type gabbros of the oceanic crust (Schmincke et al., 1998). Most gabbros are <3 cm in size, medium-grained (0.5–3 mm), and isotropic or mildly foliated. Local intracrystalline deformation is expressed as deformation twins in plagioclase and undulose extinction in plagioclase and olivine. Some gabbros record pervasive overprinting and/or modal metasomatism by alkaline La Palma melts and related fluids (cf. Neumann et al., 2000). This includes ubiquitous fluid and melt inclusions that occur randomly distributed or as trails within and across gabbro crystals (**Figure 2E**). Incipient partial melting of the xenoliths is indicated by sieve textures in clinopyroxene, and by very fine-grained dark zones of recrystallized material along plagioclase-clinopyroxene and plagioclase-olivine contacts. The width and proportion of these dark zones commonly increase towards the host magma contact (**Figure 2D**); locally they form an interconnected network. In some gabbros reaction with alkaline melts resulted in reaction rims of brown Ti-rich amphibole around clinopyroxene, and in the introduction of haüyne within or next to plagioclase (**Figure 2E**). The occurrence of euhedral haüyne crystals within gabbro plagioclase is remarkable, as it indicates a considerable degree of melting with renewed crystallization of plagioclase, and hence a high temperature of metasomatism. The reaction zones of the gabbros toward the host tephriphonolite can grade into cumulate-like zones with open textures and increasing proportion of host magma minerals (**Figure 2E**), marking a precursory stage of xenolith disintegration and assimilation.

Peridotite Xenoliths

Peridotitic xenoliths in the tephriphonolite cover a wide textural and compositional range (**Figures 2F–I**). The xenoliths studied here are spinel- and phlogopite-bearing wehrlite, dunite, and lherzolite with 60–97 percent of modal olivine; this classification uses the original proportions of clinopyroxene before its replacement by other phases. All xenoliths are hydrous, containing up to 25 vol% of phlogopite and in some cases pargasitic to kaersutitic amphibole. Wehrlites commonly show a cumulate-like framework of anhedral to subhedral olivine up to 5 mm in size (samples KLA1704, −1715, −1718, −1735; **Figures 2F,G**). Interstitial and intergranular space makes up to 36 vol%; it is dominated by clinopyroxene, spinel, and complex phlogopite-rich aggregates that appear opaque in thin section where fine-grained phlogopite ± Fe-Ti oxides prevail (**Figure 2F**). In many places clinopyroxene is partly to completely replaced by phlogopite-rich assemblages, as recognized by optical continuity of clinopyroxene remnants. Other samples (KLA1721, -1731) have an olivine grain-supported texture with little interstitial space (**Figures 2H,I**). The investigated spinel lherzolite (sample KLA1736A) is protogranular with olivine, orthopyroxene, and clinopyroxene porphyroclasts (<5 mm). Deformation lamellae, subgrains, and undulose extinction in many olivine and orthopyroxene grains indicate intracrystalline deformation, but local recovery is shown by domains with prevailing mosaic texture. Locally, patches of small olivine + clinopyroxene + colorless silicic glass ± spinel ± phlogopite have replaced orthopyroxene. Spinel (<0.6 mm in size, up to 3 vol%) occurs in all xenoliths and commonly has a corona of phlogopite ± amphibole. Fluid and melt inclusions occurring within groups or along trails that commonly cut grain boundaries are ubiquitous.

Many peridotite xenoliths contain one or more veins or veinlets of phlogopite + clinopyroxene ± amphibole ± spinel ± glass (**Figure 2G**). Veins can be irregularly shaped, and commonly show zonations in modal composition and/or grain size along their length and also in cross section. Locally, the contact between peridotite olivine and vein phlogopite or

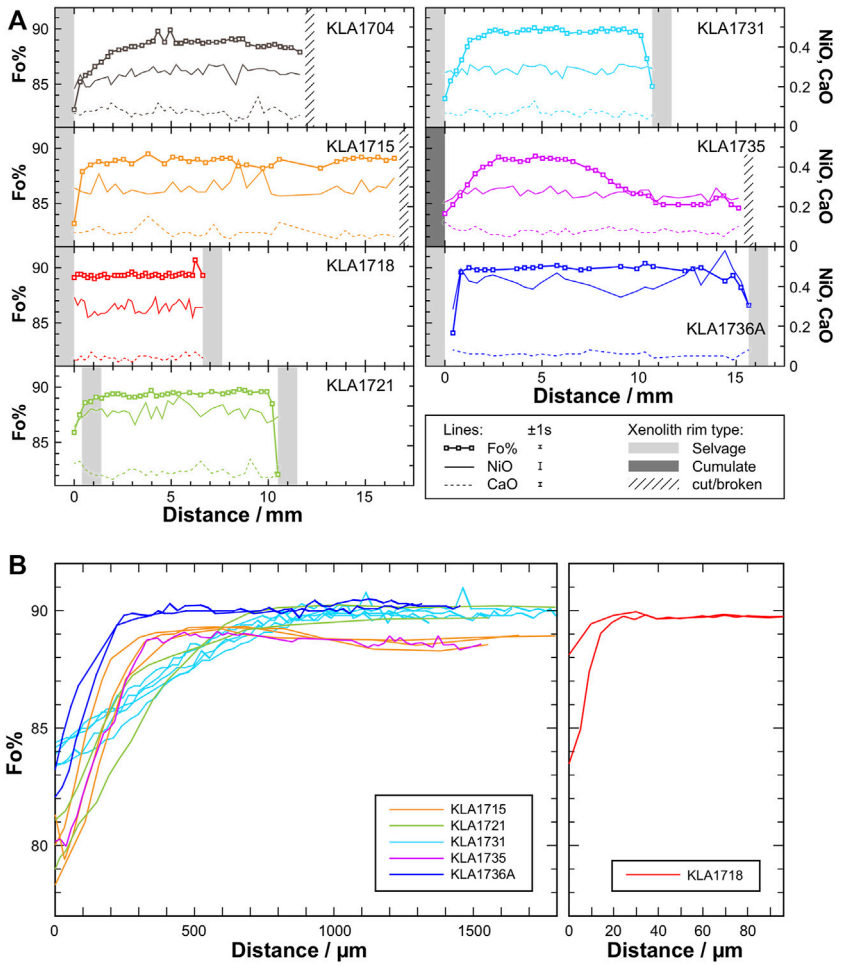


FIGURE 6 | (A) Zonations in forsterite content (Fo%; lines with symbols), NiO (without symbols) and CaO (dashed lines) of olivines across the investigated peridotite xenoliths. Scale on left side of each plot is for Fo%, right side for NiO and CaO in wt%. Error bars in legend indicate analytical uncertainty (±1 standard deviation). Note that most xenoliths show a plateau of broadly constant composition in their central part. **(B)** Zonations in Fo% at the rims of the peridotite xenoliths. The gradual decrease in Fo% extends over 0.3–1.6 mm length, except for sample KLA1718 where gradients are only 0.03–0.04 mm wide.

amphibole is characterized by a reaction zone of fine-grained clinopyroxene. The veins partly resemble the thin "phlog veins" and the broader "phlog-amph veins" and "amph veins" described in detail for basanite-hosted peridotite xenoliths from La Palma (Wulff-Pedersen et al., 1999).

Rare composite xenoliths consist of peridotite fragments and amphibole-clinopyroxene dominated cumulates. In one sample studied here (KLA1735) a wehrlite fragment adjoins a cumulate dominated by oikocrysts of kaersutitic amphibole with euhedral to anhedral olivine, clinopyroxene, and opaques (**Figure 2G**). At the contact to the cumulate, the wehrlite has a reaction rim of clinopyroxene with subordinate magnetite. The cumulate differs from the kaersutitite xenoliths described above by its poikilitic texture and the presence of olivine, and apparently has no direct genetic relationship to the host tephriphonolite. Some veins cut through both the wehrlite and kaersutitite, indicating that they formed by a separate event after cumulate crystallization. Such composite xenoliths are not restricted to the tephriphonolite studied here, but also occur in basanites from Cumbre Vieja (Klügel, 1998; Klügel et al., 2005).

The composition of olivine is $Fo_{88.5\text{-}90.5}$ in the peridotite xenoliths' interior and in most cases shows little variation, except for the strong internal zonation of composite xenolith KLA1735 (**Figure 6A**). Towards the xenoliths' rims and selvages the forsterite content decreases strongly (see below). NiO in the xenolith interior mostly varies between 0.25 and 0.40 wt%, but is higher in the spinel lherzolite KLA1736A (0.30–0.55 wt%). CaO is mostly <0.1 wt% (**Figure 6A**). Peridotite clinopyroxene is diopside with a Mg# of 86–94 and high contents of Cr_2O_3 (0.1–3.0 wt%) and Na_2O (0.4–2.1 wt%), but poor in Al_2O_3 (<2 wt%) and TiO_2 (<1 wt%). Clinopyroxene in veins has similar compositions but a tendency to lower Mg# (84–91; **Figure 7A**). Orthopyroxene of the lherzolite sample is enstatite with a Mg# of 90–91. Peridotite spinel is magnesiochromite and chromite with a Cr# (=molar Cr/

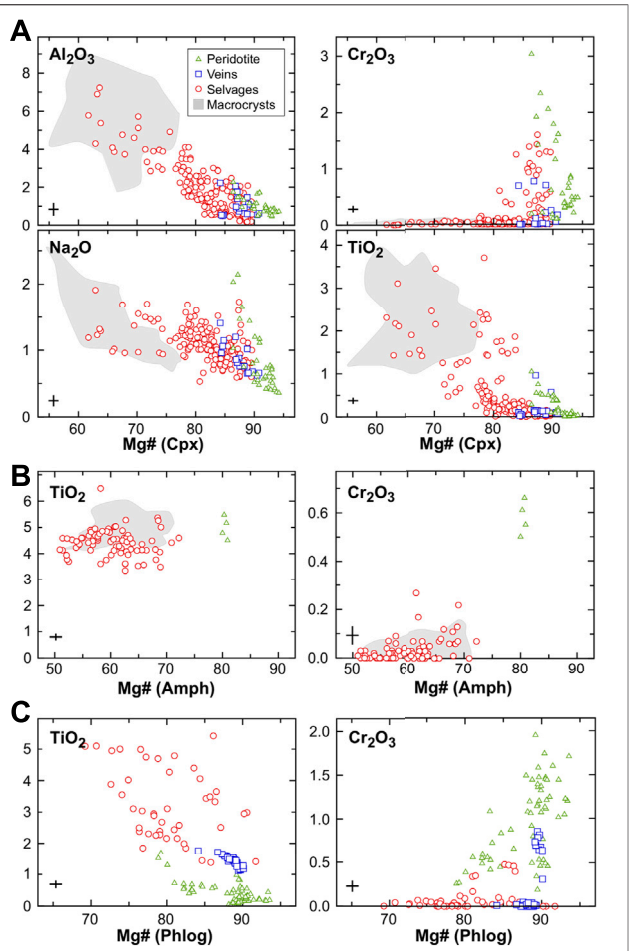


FIGURE 7 | Chemical compositions of **(A)** clinopyroxene, **(B)** amphibole, and **(C)** phlogopite in peridotite xenoliths with their selvages and veins. Peridotite clinopyroxene refers to larger grains in samples with a cumulate-like texture. Gray fields mark the range for clinopyroxene and amphibole macrocrysts in the host tephriphonolite. Error bars indicate analytical uncertainty (±1 standard deviation) as based on the analyses of secondary standards.

(Cr+Al)*100) of 56–96 and low TiO_2 (<2.8 wt%). Phlogopite has Mg# of 79–93, comparatively high Cr_2O_3 (0.2–2.0 wt%), and low TiO_2 (<1.7 wt%); vein phlogopite has a tendency to higher TiO_2 and lower Cr_2O_3 (**Figure 7C**). Amphibole has Mg# around 80, 0.5–0.7 wt% Cr_2O_3, 4.5–5.5 wt% TiO_2, and little variation in CaO, Na_2O and K_2O.

Selvages and Zonations at Peridotite Xenolith Rims

The contact between xenolith olivines and host tephriphonolite is marked by polycrystalline zoned selvages of variable composition and thickness. They cut pre-existing structures and have sharp to convoluted contacts to olivine, and can show considerable textural variation along their length. A selvage typically comprises three parts (**Figures 2F,H**): *1*) a 0–1 mm thick inner reaction rim (termed *rim I*) consisting of fine-grained clinopyroxene + Ti-magnetite ± amphibole ± phlogopite ± glass, commonly with symplectitic texture; *2*) a 0–3 mm thick central zone (termed *rim II*) consisting of phlogopite ± fine-grained clinopyroxene + Ti-magnetite ± olivine ± glass; and *3*) an up to 5 mm thick outer part with cumulus texture (termed *cumulate zone*) consisting of euhedral to subhedral amphibole ± clinopyroxene ± Ti-magnetite ± apatite ± glass. Not all selvages show these three parts; in some samples either rim I or rim II are missing locally or entirely (**Figure 2I**). Phlogopite and amphibole in selvages are locally opacitized and almost opaque. The selvages resemble those commonly present around basanite-hosted peridotite xenoliths from La Palma (Klügel, 1998, 2001), but the latter are typically thinner and lack the phlogopite-rich rim II. The inner selvage (rim I) also has similarities to rims formed by experimental reactions between olivine and evolved melts (Coombs and Gardner, 2004; Grant et al., 2014a).

Clinopyroxene in selvages is compositionally variable (Mg# 62–89), grading from peridotite clinopyroxene-like near the olivine contact in rim I to host macrocryst-like towards the cumulate zone (**Figure 7A**). Similar variations are seen in the inner and outer selvage parts of basanite-hosted peridotite xenoliths (Klügel, 1998, 2001). Amphibole in selvages largely overlaps with host macrocryst composition (Mg# 52–72), but with a tendency to lower TiO_2 (**Figure 7B**). Phlogopite in selvages show almost no compositional overlap with that within the peridotites, being distinguished by lower Cr_2O_3 (<0.5 wt%), higher TiO_2 (1.4–5.4 wt%), and a tendency to lower Mg# (69–91) (**Figure 7C**).

All peridotite xenoliths show a prominent zonation in olivine compositions towards their rims. Typically, the forsterite content decreases steadily from Fo_{88-91} in the xenolith interior to Fo_{78-86} at the selvage boundary over a distance of between 0.3 and 1.6 mm; this distance can vary within a single sample (**Figure 6B**). An exception is sample KLA1718 with much shorter gradients of 0.03–0.04 mm. The selvage of this sample is also significantly thinner (80–200 μm) than at most other samples and lacks rim I, with rim II consisting of microcrystalline phlogopite. The Fo% zonations at xenolith rims are continuous across grain boundaries and are not accompanied by textural changes of the olivines. There is no textural evidence for late olivine growth towards the selvages; rather, olivine was partly consumed during selvage formation. The shape of the Fo% zonations can show irregularities in the vicinity of veins and fine-grained phlogopite-rich aggregates. The zonations are commonly accompanied by decreasing NiO, and increasing CaO and MnO, towards the selvages. The NiO and CaO gradients are shorter than the Fo% zonations, whereas MnO follows FeO. In some compositional profiles NiO and CaO show irregular zonation, and/or strong inflections near veins and fine-grained phlogopite-rich aggregates.

Similar zonations occur at almost every basanite-hosted peridotite xenolith from Cumbre Vieja investigated by us, and were termed diffusion zones in previous studies (Klügel et al., 1997; Klügel, 1998, 2001). The width of the zones (i.e., the length of the Fo% gradient in olivine) ranges between 0.9 and 2.6 mm. Klügel (1998, 2001) argued why

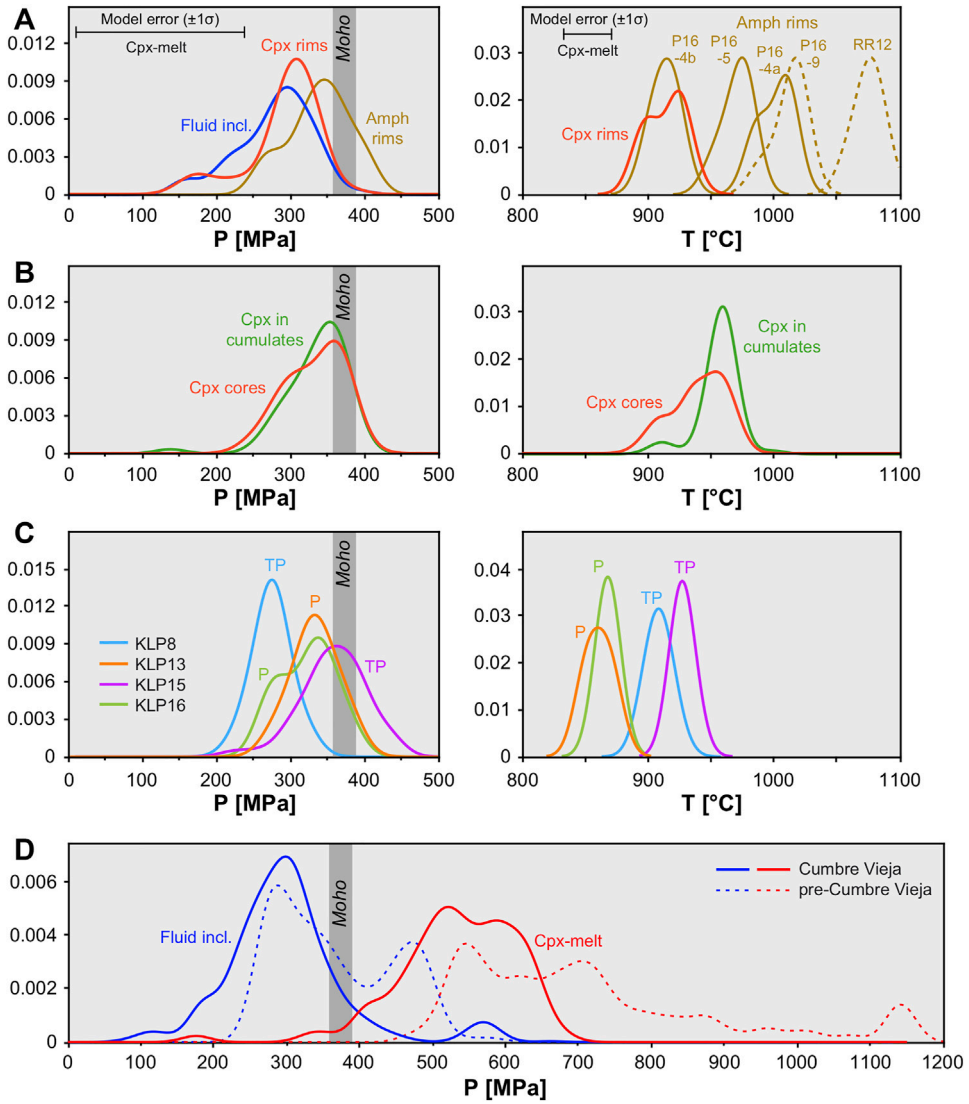


FIGURE 8 | Thermobarometric data displayed as kernel density estimates using bandwiths of 20 MPa for pressure and 10°C for temperature. A sample represents a single fluid inclusion or mineral rim analysis in **(A–C)**, and the mean rim composition of a single crystal in **(D)**. Gray bars show the estimated pressure at Moho depth around La Palma (Ranero et al., 1995). **(A)** Left: Pressure estimates for tephriphonolite macrocryst rims derived from clinopyroxene-melt barometry (red line; model Palk2012 of Masotta et al., 2013), amphibole-melt barometry (brown line; Eq. 7a of Putirka, 2016), and fluid inclusion barometry (blue line). Right: Temperature estimates for the same samples derived from clinopyroxene-melt thermometry (red line; model Talk2012 of Masotta et al., 2013), amphibole-melt thermometry (brown solid lines; Eqs 4a, 4b and 9 of Putirka, 2016), and amphibole-only thermometry (brown dashed lines; Ridolfi and Renzulli, 2012; Eq. 5 of Putirka, 2016). All rim analyses were paired with host groundmass analyses. **(B)** Pressure and temperature estimates for tephriphonolite macrocryst cores and cumulate xenolith crystals derived from clinopyroxene-melt thermobarometry, using the models Palk2012 and Talk2012 of Masotta et al. (2013). All clinopyroxene analyses were paired with suitable whole-rock compositions from Cumbre Vieja (*see* text for details). **(C)** Pressure and temperature estimates for other Cumbre Vieja tephriphonolites (TP) and phonolites (P) derived from clinopyroxene-melt thermobarometry (models Palk2012 and Talk2012 of Masotta et al., 2013). **(D)** Pressure estimates for basalts from Cumbre Vieja (solid lines) and from pre-Cumbre Vieja series (dashed lines), obtained by clinopyroxene-melt barometry on phenocryst rims, and by fluid inclusion barometry (data from compilation in Klügel et al., 2015).

these zones are best explained by diffusive Fe-Mg exchange with mafic melt across the xenolith rims and selvage, and showed that a slight s-shape of some profiles can reflect changing boundary conditions, such as decreasing diffusivity through the selvage. Diffusive exchange can also account for zonations in olivines next to veins (Wulff-Pedersen et al., 1996). By analogy, we propose that the Fo% zonations at the rims of tephriphonolite-hosted peridotite xenoliths have formed in a similar manner.

Geothermobarometry and Hygrometry

Clinopyroxene-Based Thermobarometry

Clinopyroxene-melt equilibria provide a reliable thermometer and the probably most sensitive and accurate mineral-based

barometer (Putirka, 2008). Clinopyroxene-melt thermobarometers that are universally applicable were calibrated on a wide compositional range of experimental liquids (Putirka et al., 1996, 2003; Putirka, 2008), but do not perform well for tephriphonolitic to phonolitic liquids, as these were poorly represented in the experimental data. Masotta et al. (2013) calibrated clinopyroxene-melt thermobarometers specifically for evolved alkaline liquids, which are similar to the groundmass compositions of our study. To constrain pre-eruptive pressure (P) and temperature (T) of the phonolitic melts, we applied the models Palk2012 and Talk2012 of Masotta et al. (2013) to compositions of euhedral macrocryst rims and host groundmass, assuming that the groundmass is the best approximation of the intratelluric melt (**Supplementary Table S6**). Crystal rims were analyzed at ~5 µm distance to planar surfaces. The crystal-melt compositional pairs thus have a well-defined petrographic relationship, and texturally indicate near equilibrium conditions, albeit not necessarily chemical equilibrium. Melt H_2O content was set to 3 wt% based on data from melt inclusions in Cumbre Vieja cumulates (Parat et al., 2011). We note that the dependence of the thermobarometer results on melt H_2O is rather small with −5°C/wt% and +7 MPa/wt%, respectively. The standard error of estimate (SEE) for the thermobarometer is 18°C and 115 MPa, respectively. As chemical equilibrium test, we used 1) $\Delta K_D(Fe\text{-}Mg)^{cpx-liq}$ (hereafter ΔK_D), the difference between the measured Fe-Mg distribution coefficient and that predicted by equation 35alk of Masotta et al. (2013), and 2) ΔDiHd, the difference between measured and predicted diopside-hedenbergite component in clinopyroxene (after Mollo et al., 2013). ΔDiHd is a more robust equilibrium filter than ΔK_D (Mollo et al., 2013), but is not well calibrated for evolved alkaline melts. Both ΔK_D and ΔDiHd should be < 0.1 and <0.12, respectively, corresponding to 2 SEE of the prediction equations.

For the xenolith-rich tephriphonolite, 58 rim analyses of 11 clinopyroxene macrocrysts in two samples give pressures of 297 ± 49 MPa and temperatures of 912 ± 14°C (average and one standard deviation indicated). Kernel density estimates (KDE) show well-defined maxima around 300 MPa and 920°C, respectively (**Figure 8A**). Despite evidence of sector zonations in clinopyroxene rims (**Figure 3B**) the P-T results show limited scatter; pressures <200 MPa are indicated only by few analyses with low Al_2O_3 and high SiO_2. The ΔK_D filter would remove more than half of the data pairs, with little change in pressure KDE and average (270 ± 59 MPa), and no change in temperature. The ΔDiHd filter would have negligible effect, because most data pairs are in the equilibrium range. The clinopyroxene components EnFs and Jd (Putirka, 1999) also show good agreement between measured and predicted values. For these reasons we did not discard any mineral-melt pair. Tentative application of the Putirka et al. (2003) thermobarometer yields 762 ± 139 MPa and 887 ± 20°C for the xenolith-rich tephriphonolite. The pressure estimates show large scatter and are higher than those for basanites and tephrites from Cumbre Vieja (**Figure 8D**), which appears petrologically questionable. This discrepancy corroborates the usage of a specific thermobarometer calibration for evolved alkaline melts.

For clinopyroxene-melt barometry on macrocryst cores and cumulate crystals, the melt composition is basically unknown. We tentatively applied a two-step liquid-matching approach to each clinopyroxene analysis, using a set of ca. 260 published whole-rock compositions from Cumbre Vieja (data sources as in **Figure 4**). In the first step the melts were screened for $K_D(Fe\text{-}Mg)^{cpx-liq}$ to judge whether the thermobarometer calibrations for evolved liquids (Masotta et al., 2013) or primitive to intermediate liquids (Putirka et al., 2003; Putirka, 2008) were appropriate. As all clinopyroxene analyses are best paired with rather evolved melts, we exclusively used the Masotta et al. (2013) models. In the second step we selected all melts that could have been in chemical equilibrium with a given clinopyroxene analysis. As equilibrium filter we used ΔK_D and ΔDiHd as described above, and discarded all melts with <52 wt SiO_2. Between two and 53 putative equilibrium melts passed this filter for any clinopyroxene analyzed; all crystal-melt pairs additionally show agreement between measured and predicted EnFs and Jd components (Putirka, 1999). We then calculated pressure and temperature for each of these melts, and averaged the results to obtain a single P-T estimate. The standard deviations for each P and T estimate so obtained were in the range 34–79 MPa and 11–42°C, respectively (**Supplementary Table S6**).

The inner regions of clinopyroxene macrocrysts from the xenolith-rich tephriphonolite give pressures of 332 ± 39 MPa and temperatures of 941 ± 21°C; KDE curves show maxima around 350 MPa and 950°C, and subordinate maxima around 300 MPa and 910°C. Clinopyroxenes in cumulate xenoliths give 335 ± 42 MPa and temperatures of 956 ± 15°C, overlapping almost perfectly with the macrocryst data (**Figure 8B**). The data distributions essentially overlap with those for clinopyroxene rims, with a slight shift to higher pressure and temperature (**Figure 8A**). The results are to be viewed critically because best-matching melt compositions are not necessarily close to true ones. However, the low dispersion of the data lends credibility to this approach.

Comparison With Other Tephriphonolites and Phonolites From Cumbre Vieja

In order to compare the xenolith-rich tephriphonolite to other evolved Cumbre Vieja rocks in terms of composition and thermobarometric data, we analyzed whole-rock, groundmass and clinopyroxene macrocryst compositions of four additional tephriphonolites to phonolites (samples KLP-8, -13, -15, -16; **Supplementary Table S1**). The macrocryst phases of these rocks are plagioclase + kaersutite + clinopyroxene + Ti-magnetite ± apatite ± titanite; small cumulate aggregates of these phases are common. Their groundmasses are feldspar-dominated and have phonolitic compositions, overlapping with the tephriphonolite from this study. As the groundmass compositions are very similar (**Figure 4**), differences in whole-rock compositions are largely due to the strongly different macrocryst cargos.

Clinopyroxene-melt thermobarometry applied to macrocryst rims and groundmass compositions yields pressures of 229–446 MPa and temperatures of 849–937°C; the respective KDE maxima are in the range 280–360 MPa and 860–930°C (**Figure 8C**). Measured and predicted $K_D(Fe\text{–}Mg)^{cpx-liq}$ agree

within 2 SEE for almost all data pairs. Whereas the pressure distributions overlap strongly and show no systematic dependency on sample type, temperatures for tephriphonolites are some tens of degrees higher than for phonolites, as is petrologically reasonable. Tentative application of the Putirka et al. (2003) thermobarometer gives mean pressures of 815, 930, 641 and 1,153 MPa for samples KLP-8, -13, -15, and -16, respectively, which appear unrealistically high.

Amphibole-Based Thermobarometry

Amphibole composition and amphibole-melt equilibria provide valuable thermometers but have limited potential for barometry, in particular at low pressures (e.g., Shane and Smith, 2013; Erdmann et al., 2014; Putirka, 2016). We used thirteen rim analyses of kaersutite macrocrysts in two tephriphonolite samples and applied the amphibole-only thermobarometer of Ridolfi and Renzulli (2012) (abbreviated as RR12), as well as the pressure-independent thermometers of Putirka (2016) (abbreviated as P16) based on Na partitioning (Eq. 4a), Ti partitioning (Eq. 4b), Na-K exchange (Eq. 9), and amphibole composition only (Eq. 5). These calibrations yield strongly differing temperatures, with a total range of 895–1,089°C (**Supplementary Table S7**) and KDE maxima between 910 and 1,077°C (**Figure 8A**). The high values of RR12 (1,057–1,089°C) do not overlap with results from other thermometers, and are above the temperatures of amphibole saturation calculated by Eq. 3 of Putirka (2016) (**Supplementary Table S5**). Data analysis shows that the high temperatures are due to the pressure-dependency of RR12, in conjunction with an apparent overestimation of pressures by this calibration. The amphibole-only thermometer P16-5 also appears to overestimate temperatures for our sample suite, yet it discriminates between macrocryst rims (1,013 ± 12°C), macrocryst cores (1,040 ± 17°C), and cumulate xenolith crystals (1,057 ± 8°C) (averages and standard deviations indicated). The observed temperature decrease from core to rim is petrologically reasonable for normally zoned crystals, as is a higher temperature indicated by potentially earlier formed cumulates.

Of the different amphibole-melt thermometers, only calibration P16-4b (914 ± 9°C) shows good overlap with the clinopyroxene-melt data (913 ± 14°C); calibrations P16-4a and P16-9 differ from P16-4b by 88 and 57°C on average, respectively. This discrepancy is beyond the thermometers' prediction errors, and may be caused by chemical disequilibrium between crystal rims and liquid (i.e., host groundmass composition). Although the Fe-Mg distribution coefficient for all pairs is within the range of 0.28 ± 0.11 for experimental data, disequilibrium for Na, Al, or Ti exchange due to e.g. different closure temperatures is still possible (Putirka, 2016). Possible disequilibrium is corroborated by significant differences between the predicted SiO_2 of liquids coexisting with amphibole rims (Eq. 10 of Putirka, 2016) of 52.3 ± 1.8 wt%, and the observed values of 59.3–60.2 wt%. In addition, amphibole-thermometers applied to SiO_2-poor and Al_2O_3-rich alkaline magma series are known to overestimate temperatures (Erdmann et al., 2014). For these reasons we view the amphibole-based thermometer data with caution and prefer the clinopyroxene-melt data.

Despite the limitations of amphibole barometry, we tentatively applied Eq. 7a of Putirka (2016) to macrocryst rim and host groundmass compositions of the tephriphonolite (3 wt% H_2O in the melt) and obtained plausible results of 340 ± 42 MPa, overlapping with the clinopyroxene-melt data (**Figure 8A**). The values increase by about 50 MPa per 1 wt% increase in H_2O. In contrast, the amphibole-only barometer of Ridolfi and Renzulli (2012) gives 764 ± 130 MPa for the macrocryst rims, well above the other barometric data. This is in line with earlier studies demonstrating the limited applicability of this barometer (Erdmann et al., 2014; Putirka, 2016).

Oxybarometry

Oxygen fugacities (fO_2) were estimated from kaersutite macrocryst compositions, using the chemometric equations of Ridolfi and Renzulli (2012) calibrated for a wide compositional range. Our analyses yielded near-Gaussian frequency distributions for ΔNNO (log units above the Ni-NiO solid buffer) with averages of 2.5 ± 0.6 for macrocrysts and 1.8 ± 0.4 for cumulate xenolith crystals (**Supplementary Table S7**), indicating relatively oxidizing conditions. We note, however, that the results are slightly beyond the T-fO_2 range used for the Ridolfi and Renzulli (2012) calibration. Moreover, Erdmann et al. (2014) found that the reliability of this oxybarometer is worse than that of the Ridolfi et al. (2010) calibration, which is however calibrated for calc-alkaline magmas only. Our tentative application of the Ridolfi et al. (2010) model yielded ΔNNO values of −0.5 ± 0.3 for both macrocrysts and cumulate xenolith crystals.

In addition we calculated fO_2 from Fe_2O_3/FeO ratios in evolved Cumbre Vieja rocks (>50 wt% SiO_2), using 58 whole-rock analyses in which FeO was determined by potentiometric titration (Hernandéz-Pacheco and De la Nuez, 1983; Carracedo et al., 2001; Praegel and Holm, 2006). Molar Fe_2O_3/FeO of these analyses encompass a considerable range with an average of 0.77 ± 0.32. Following Kress and Carmichael (1991) we obtain average ΔNNO values of 3 ± 1.1. This is in good agreement with the Ridolfi and Renzulli (2012) model applied to our amphibole analyses, considering that whole-rock Fe_2O_3/FeO ratios provide an upper limit for fO_2 due to possible oxidation during and after magma emplacement. The combined data suggest that the crystallization conditions of the tephriphonolite were relatively oxidizing with about two–three log units above the NNO buffer. These oxidizing conditions are consistent with the presence of haüyne in the samples, which requires fO_2 significantly above NNO (Berndt et al., 2001).

Plagioclase-Liquid Hygrometry

In order to obtain a direct estimate for the H_2O content of the studied tephriphonolite samples, we applied the plagioclase-liquid hygrometer of Waters and Lange (2015) to the compositions of groundmass and plagioclase macrocrysts (An_{30-46}). This hygrometer was calibrated with a wide range of melt compositions including mafic alkaline melts, and has a SEE of 0.35 wt% H_2O. For a P-T range of 200–400 MPa and

900–950°C as input (cf. **Figure 8**) we obtained H_2O concentrations between 2.8 and 4.0 wt%. The calculated H_2O contents are essentially independent of pressure, and are in agreement with melt inclusion data in Cumbre Vieja cumulates (Parat et al., 2011). The hygrometer after Ridolfi and Renzulli (2012) applied to kaersutite macrocrysts yields slightly higher H_2O contents of 4.0–4.6 wt%, but these estimates should be treated with caution (Erdmann et al., 2014; Putirka, 2016). For comparison, H_2O contents of Cumbre Vieja basanites that fractionate in the upper mantle were inferred to be 0.8–1.5 wt% (Weis et al., 2015).

Microthermometry

Fluid inclusions are ubiquitous in peridotite and gabbro xenoliths, occurring as trails that can crosscut grain boundaries (secondary inclusions), or randomly in small groups (primary inclusions, cf. Roedder 1984). Fluid inclusions are less common in peridotite xenolith selvages, cumulate xenoliths and macrocrysts; in these cases they occur mostly as single primary inclusions. In order to constrain pressures of inclusion formation or re-equilibration, we investigated primary and secondary fluid inclusions in peridotite olivines (N = 43), kaersutite and clinopyroxene macrocrysts (N = 5), and clinopyroxenes from peridotite selvages (N = 20) by microthermometry (**Supplementary Table S11**).

The investigated inclusions froze to solid CO_2 and vapor during cooling between −80 and −100°C; further cooling to −190°C did not yield additional phase transitions. During reheating, the inclusions showed a melting point between −56.9 and −56.4°C, close to the triple point of pure CO_2 (−56.6°C); no melting interval was observed. The investigated fluid inclusions hence consist of nearly pure CO_2, because significant amounts of additional components would have caused a melting interval with initial melting below −56.6°C (Andersen and Neumann 2001; Frezzotti et al., 2002). As no evidence for H_2O was found in any inclusion observed, it is possible that diffusive H_2O loss had occurred (Hansteen and Klügel, 2008). Upon further heating, all inclusions homogenized into the liquid phase at temperatures between 20.0 and 31.1°C; some inclusions showed critical homogenization behavior. Different microthermometric behavior of primary and secondary inclusions was not recognized, but inclusions in peridotite olivines have a tendency to lower homogenization temperatures, and hence higher densities, than inclusions in selvage clinopyroxenes and macrocrysts. Similar observations were made for fluid inclusions in volcanic rocks from other localities and were assigned to olivine being less prone to re-equilibration than clinopyroxene (Hansteen et al., 1998; Galipp et al., 2006).

Densities of CO_2 inclusions as calculated from measured homogenization temperatures are 0.59–0.77 g/cm³ for peridotite olivines and 0.47–0.72 g/cm³ for selvage clinopyroxenes and macrocrysts. The data for both groups are slightly skewed towards lower densities, which probably reflects volumetric re-equilibration during ascent of the host magma. Pressures of formation or re-equilibration of the inclusions were derived from calculated isochores (Sterner and Pitzer, 1994), using a model temperature of 950°C as based on our thermometry data. The results indicate 200–400 MPa for peridotite olivines and 160–340 MPa for selvage clinopyroxenes and macrocrysts, with averages of 300 and 260 MPa, respectively. These values generally represent lower limits for the trapping pressures of the inclusions, because re-equilibration processes tend to reduce their densities. The influence of model temperature on calculated pressures is almost negligible with about 14 MPa per 50°C increase or decrease. The KDE curve overlaps remarkably well with that for clinopyroxene-melt barometry (**Figure 8A**). It also overlaps with pressure distributions derived from fluid inclusions in basalt-hosted peridotite xenoliths and macrocrysts from La Palma (**Figure 8D**).

Diffusion Modelling of Peridotite Zonations

The time scale to form the rim zonations of peridotite xenoliths (**Figure 6B**), hereafter termed diffusion zones, may be roughly assessed by a simple one-dimensional diffusion model for an infinite half space (Crank, 1975), because the profile depth is short compared to xenolith size. Boundary conditions: peridotite olivine has constant composition C_{core} initially, and at time t = 0 is brought into contact with a source (melt reservoir) of constant Mg# that is in equilibrium with a less magnesian olivine composition C_{rim}. Subsequent Fe-Mg exchange between olivine and melt across a spatially fixed interface at x = 0, and Fe-Mg interdiffusion perpendicular to the interface with constant diffusion coefficient D_{FeMg}, produce the olivine zonations observed. The diffusion equation for composition C at distance x and time t is:

$$(C - C_{rim})/(C_{core} - C_{rim}) = \mathrm{erf}\left[x \Big/ \left(2\sqrt{D_{FeMg}t}\right)\right]$$

This simplified model neglects the formation of a selvage and possible changes in melt composition and temperature over time, both of which influence shape and length of the zonation (cf. Klügel, 1998; Costa et al., 2008). The diffusion time (t) was obtained from the best fit of the measured zonations by the diffusion equation. For D_{FeMg} we used a constant value of 2.5×10^{-17} m^2s^{-1}, calculated after Dohmen and Chakraborty (2007) for T = 1,000°C, p = 300 MPa, fO_2 = NNO +1, Fo_{85} olivine, and diffusion along the [001] direction. Owing to the strong diffusion anisotropy of olivine with D_{FeMg} along [100] and [010] being 1/6 of that along [001] (Dohmen and Chakraborty, 2007), the mean D_{FeMg} for randomly orientated grains is 2/3 of that along [001]. The model temperature was tentatively chosen to be between mafic and evolved Cumbre Vieja melts (Klügel et al., 2005; **Figure 8**), because the actual melt that caused diffusion is not known. Temperature during diffusion was certainly not constant and may have varied between different xenoliths. Based on the temperature dependence of D_{FeMg} after Dohmen and Chakraborty (2007), an increase or decrease of T by 50°C would scale the calculated times by a factor of 0.49 or 2.2, respectively. Hence, the results of our modelling are only an approximation of the timescale involved in the zonations.

Calculated diffusion times for thirteen profiles in five samples range from 13 to 309 years when using the mean D_{FeMg} (**Supplementary Table S12**). Considering the diffusion

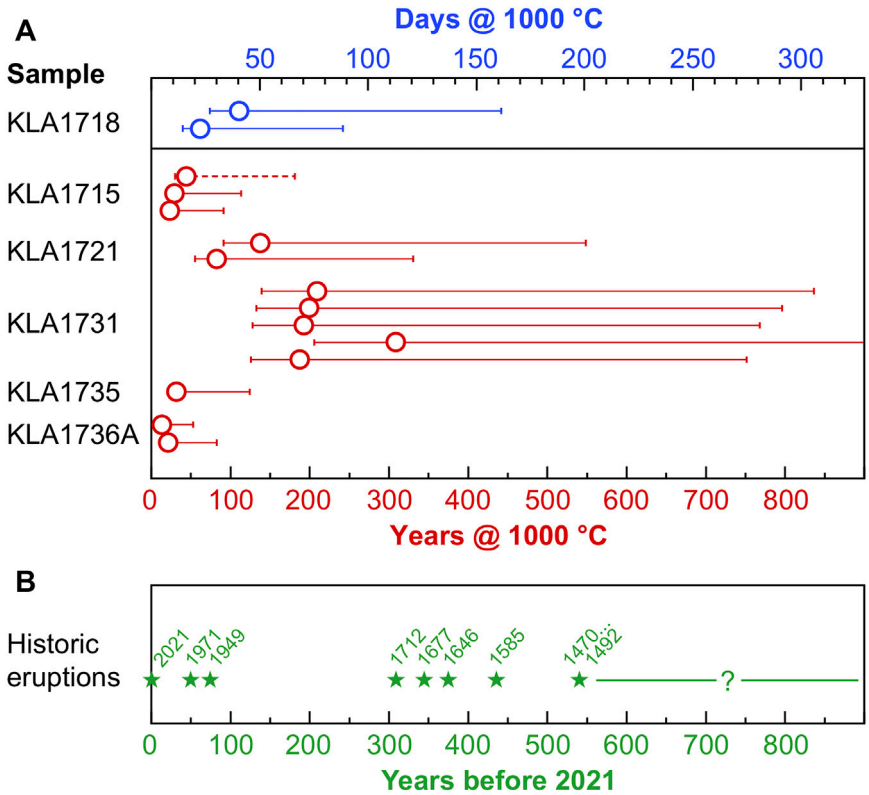


FIGURE 9 | (A) Range of diffusion times for rim zonations of the tephriphonolite-hosted peridotite xenoliths, based on a simple Fe-Mg interdiffusion model in olivine (*see* text for details). Note different scales for sample KLA1718 (blue, top) and the other samples (red, bottom). The large time range for each sample reflects the anisotropy of D_{FeMg} by a factor of six; circles mark the diffusion time for the mean D_{FeMg} of randomly orientated olivine grains (equal to 2/3 the D_{FeMg} along [001]). Diffusion times were calculated for a temperature of 1,000°C; a temperature increase or decrease by 50°C would roughly double or halve the calculated times. **(B)** The diffusion times are compared to a time line for historic eruptions on Cumbre Vieja, applying the same scale as in **(A)**. The eruption ages are summarized in Carracedo et al. (2001).

anisotropy in olivine and the unknown grain orientations in our samples, the total time range may be considerably larger (**Figure 9A**). An exception is sample KLA1718, for which a shorter range of 22–40 days for the mean D_{FeMg} is obtained (maximum range is 15–161 days); this xenolith also has an exceptionally thin selvage. The time ranges illustrated in **Figure 9A** show differences between samples that are beyond the uncertainty related to diffusion anisotropy (e.g., compare KLA1736A to KLA1731, and KLA1718 to all other samples). By considering all uncertainties of the simple diffusion model, we conclude that Fe-Mg exchange between most peridotites and surrounding melt lasted over decades to centuries, which overlaps with the time between historic eruptions on Cumbre Vieja (**Figure 9B**).

DISCUSSION

The petrographical, petrological and geochemical data of the xenolith-rich tephriphonolite provide a wealth of information on the magmatic plumbing system beneath La Palma. We now discuss the crystallization conditions of evolved magmas beneath La Palma, the timescales of their formation, the origin of the different xenolith types, and implications for phonolite generation at other oceanic island volcanoes and seamounts.

Pre-Eruptive Storage Conditions

Based on the thermobarometric and hygrometric data presented above, our best estimates of the pre-eruptive storage conditions of the xenolith-rich tephriphonolite are a pressure range of 250–350 MPa, temperature of 900–950°C, fO_2 of NNO+2 to NNO+3, and H_2O contents of 3–4 wt%. Macrocryst cores and cumulate crystals probably crystallized at slightly higher temperature but below 1,000°C (**Figure 8**). The other tephriphonolites studied here indicate similar temperatures, whereas phonolites were slightly cooler (around 830–880°C). All evolved rocks indicate essentially the same pressures, overlapping within the prediction errors of the barometers (**Figure 8C**). The pressures are equivalent to about 10–13 km depth, using a density of 2,600 kg/m^3 for the volcanic edifice and sediments and 2,900 kg/m^3 for the igneous oceanic crust. As the basement near La Palma extends from about 7 to 13 km depth (Ranero et al., 1995), this places pre-eruptive storage of evolved Cumbre Vieja magmas within the lowermost oceanic crust. This

level is not only reflected in the tephriphonolites to phonolites investigated, but is also indicated by our fluid inclusion data from macrocrysts and xenoliths in basanitic to tephritic magmas from the Cumbre Vieja (**Figure 8D**).

Our clinopyroxene-based pressure estimates are subject to considerable prediction uncertainties of the thermobarometers (**Figure 8A**), and rely on the assumption that the selected melt composition is representative of the composition at depth. For this reason, we validated our data using results from phase equilibrium experiments with evolved alkaline liquids. Of all experiments considered (Berndt et al., 2001; Freise et al., 2003; Harms et al., 2004; Andujar et al., 2008; Andujar et al., 2010; Moussallam et al., 2013; Iacovino et al., 2016), the most similar natural system is the basanite-phonolite series from Ross Island and Mt. Erebus, Antarctica. Other experimentally investigated systems are more evolved than Cumbre Vieja phonolites (Tenerife), do not fall on the Cumbre Vieja LLD (Laacher See, Kerguelen), have different phenocryst assemblages (Vesuvius, Tenerife), and/or are limited to ≤250 MPa. Our thermobarometric results are in agreement with Moussallam et al. (2013), who used Erebus phonolite to produce a phase assemblage comparable to the tephriphonolite studied by us (phonolite melt + kaersutitic amphibole + clinopyroxene + anorthoclase + Ti-magnetite) at 950°C, 100–300 MPa, fO_2 between NNO-0.8 and NNO+2.8, and 1 to 4 wt% H_2O in the melt. The crystallization of anorthoclase in the experiments rather than plagioclase as at Cumbre Vieja may reflect the more evolved bulk composition. Experiments with a Ross Island phonotephrite in the pressure range of 200–400 MPa showed that kaersutite is stable at 1,000°C for oxidized conditions (NNO+1.7 to NNO+3) and 0.7 to 4.8 wt% H_2O in the melt (Iacovino et al., 2016). Kaersutite proportions increased at higher pressure, with up to 60 wt% at 400 MPa. Their compositions overlap with those of Cumbre Vieja but extend to higher TiO_2. One important difference to the Cumbre Vieja tephriphonolite is the lack of co-existing kaersutite and clinopyroxene in the Iacovino et al. (2016) experiments, which may be due to their more primitive bulk composition. The lack of haüyne in the experiments can be ascribed to the low sulfur content of the degassed starting material. However, Moussallam et al. (2013) and Iacovino et al. (2016) found feldspar to be unstable at 250–350 MPa and 3–4 wt% H_2O. Their experimental data rather suggest that the plagioclase macrocrysts in the tephriphonolite crystallized at shallower levels and/or lower H_2O contents.

In summary, the inferred pre-eruptive storage conditions for the xenolith-rich tephriphonolite are in line with data from phase equilibrium experiments. The Moussallam et al. (2013) and Iacovino et al. (2016) experiments show that deeper fractionation levels for the tephriphonolite cannot be ruled out, because kaersutite stability extends to pressures above 400 MPa, and experiments with suitable compositions at this pressure range are lacking. On the other hand, the pressure range of 250–350 MPa inferred for the storage of the tephriphonolite is supported by the abundance of gabbro xenoliths, as these are likely derived from the lower oceanic crust (see below). The crystallization of plagioclase macrocrysts may have occurred at lower pressure, either during gradual ascent of the tephriphonolite or during temporary stagnation in the upper crust. A shallow ponding level cannot be ruled out but is not reflected in our data. The few clinopyroxene analyses indicating <200 MPa (**Figure 8A** and **Supplementary Table S6**) are not representative for the entire crystals, and may reflect limited rim growth during magma ascent.

In contrast to evolved Cumbre Vieja melts, clinopyroxene-melt barometry on basanitic to tephritic magmas indicates pre-eruptive storage and fractionation at around 450–650 MPa (Klügel et al., 2005, Klügel et al., 2015), and at deeper levels within the uppermost mantle at earlier stages of magma evolution (Barker et al., 2015). These magmas also show a bimodality of pressures derived from clinopyroxene-melt and fluid inclusion barometry, whereas the evolved magmas do not (**Figure 8**). This pressure bimodality was explained by short-term magma ponding within the lower crust during an eruption (Hansteen et al., 1998; Klügel et al., 2005). Instead of a continuous vertical ascent in a straight conduit, decompression rates must have slowed down considerably within the lower crust, either by a phase of subhorizontal flow (Klügel et al., 2015) or by slow migration through a complex storage system with limited vertical connectivity (e.g., Cashman et al., 2017). Hansteen et al. (1998) denoted this horizon in the lowermost crust as a *magma accumulation zone*, and Klügel et al. (2015) suggested that highly evolved magmas can be produced within this zone once a critical magma flux is reached. This zone was also locus of intense seismicity before and during the 2021 eruption at Cumbre Vieja (IGN, 2021).

The formation of phonolites at La Palma is not restricted to the lower crust, however. Lavas from Cumbre Vieja commonly contain reversely zoned clinopyroxene macrocrysts with green cores of low Mg# and high Na_2O, which apparently crystallized from highly evolved melts (Klügel et al., 2000). Similar green-core clinopyroxenes are found in alkaline lavas from oceanic and continental intraplate volcanoes worldwide (e.g., Duda and Schmincke, 1985; Dobosi and Fodor, 1992; Pilet et al., 2002; Leite de Oliveira et al., 2021). In many crystals, the green cores are corroded due to dissolution and/or partial melting, and the crystals can be more complexly zoned than a simple core-rim zonation. Reliable barometry on the cores is difficult since compositions of the host melts are not exactly known. However, as the brownish rims of green-core clinopyroxenes from Cumbre Vieja indicate crystallization at mantle depths (**Figure 8D**; Klügel et al., 2000, 2005; Barker et al., 2015), the green cores and the melts from which they crystallized must have formed in the mantle as well.

Provenance of the Xenoliths

Kaersutitite Cumulate Xenoliths

The mineral assemblages of kaersutitite cumulate xenoliths and the host tephriphonolite are similar, except for haüyne. Xenoliths and host also indicate similar pressures of crystallization (**Figure 8**), hence a genetic relationship between both appears likely. This relationship may be simple crystal fractionation in

which the cumulus crystals formed earlier than the host lava macrocrysts. A cognate origin of the xenoliths would agree with the predominance of kaersutite in both the cumulates and in the macrocryst assemblage of the tephriphonolite (**Figures 2A,B**). It would also be consistent with the tendency of kaersutite macrocrysts to higher Na_2O and SiO_2, and lower Al_2O_3 and TiO_2, than cumulus kaersutites with similar Mg# (**Figure 3A**), in agreement with the differentiation trend of evolved Cumbre Vieja rocks (**Figure 4**). The situation is more complicated for clinopyroxenes, however, because the effects of sector zoning are superimposed on any differentiation trend (**Figure 3B**). Yet the restriction of cumulus crystal compositions to the upper range of Mg# (mostly 67–76 for diopsides and 63–71 for kaersutites), in which they overlap with tephriphonolite macrocrysts, is in principal accordance with crystallization from the same initial magma body.

The lack of a coherent fractionation trend in **Figures 3A,B** does not rule out a direct genetic relationship between cumulates and host tephriphonolite. The scatter of the data is partly due to the presence of antecrysts and xenocrysts, as indicated by mineral zonations (**Figures 3C,D**) and by petrographic observations. In addition to kaersutite and diopside xenocrysts, some cumulate xenoliths contain olivine aggregates and single crystals that are reminiscent of mantle fragments (**Figure 2C**). The olivines had reacted with the surrounding melt to form symplectite-like reaction rims (cf. Klügel, 1998). The combined observations suggest that the early evolutionary stage of the tephriphonolite involved mixing with a magma batch from mantle depths, which introduced small mantle fragments and likely additional crystal cargo. These became part of the cumulates that were subsequently formed. In summary, our data suggest that the kaersutitite xenoliths represent cognate cumulates that formed during storage of the host tephriphonolite in a reservoir located in the lowermost crust, i.e., within the magma accumulation zone. The open cumulus texture of the xenoliths, with predominantly euhedral crystals and void space in the interstices (**Figures 2B,C**), indicates that they were not completely crystalline before eruption, but contained a considerable proportion of interstitial melt. This melt vesiculated during xenolith uplift and eruption and was squeezed out, leaving the voids now observed.

Gabbro Xenoliths From the Oceanic Crust

Gabbro xenoliths with Ti- and Al-poor clinopyroxenes are commonly found in basanites from Cumbre Vieja (e.g., Muñoz et al., 1974; Schmincke et al., 1998; Neumann et al., 2000), but to our knowledge have not been described in evolved host rocks. Based on petrography, mineral composition, and whole-rock composition, these gabbros were shown to represent fragments of the Jurassic oceanic crust underlying La Palma (Schmincke et al., 1998; Hoernle, 1998; Neumann et al., 2000). The petrographic characteristics of the tephriphonolite-hosted gabbros of our study, and the Ti-Al-poor nature of their clinopyroxenes, indicate that they are fragments of the oceanic crust as well. Like their basanite-hosted counterparts, the gabbros were metasomatized by alkaline La Palma melts und fluids migrating through the oceanic crust, which resulted in deformation, pervasive recrystallization, partial melting, and introduction of haüyne and Ti-rich amphibole (**Figures 2D,E**). Nevertheless, this late magmatic overprinting was not sufficient to obliterate the tholeiitic MORB-type character of the gabbros (Schmincke et al., 1998; Neumann et al., 2000).

According to our field observations on Cumbre Vieja, such gabbro xenoliths are second in abundance only to ultramafic cumulate xenoliths, and are particularly abundant in the terminal lavas from the 1949 eruption (Klügel et al., 1999). Their abundance is consistent with the existence of a magma accumulation zone within the lower oceanic crust. Gabbro entrainment into the tephriphonolite studied here probably occurred by diking or stoping related to its storage in the lower crust, or to the final ascent to the surface. We note that the oceanic gabbro xenoliths are clearly different from those related to crystallization of intermediate to evolved Cumbre Vieja magmas, which are termed alkaline gabbros (Klügel et al., 1999) or leucogabbros to syenites (Neumann et al., 2000; Barker et al., 2015). These are characterized by cumulus to poikilitic textures, the presence of kaersutitic amphibole ± apatite ± titanite ± haüyne in addition to plagioclase as cumulus crystals, abundant apatite inclusions in pyroxenes and amphiboles, and Ti-Al-rich clinopyroxene compositions.

Peridotite Xenoliths and Their Selvages

Peridotite xenoliths are commonly subdivided into two series, the group I or Cr-Mg series, interpreted as refractory lithospheric mantle that may or may not have been metasomatized, and the group II or Ti-Al series, interpreted as either magmatic cumulates or metasomatically overprinted group I peridotites (Frey and Prinz, 1978; Harte, 1987; Wulff-Pedersen et al., 1996). Clinopyroxenes and spinels in group I peridotites are Cr-rich and Ti-poor, and silicates generally have Mg# >85. In group II peridotites, silicates are less magnesian (Mg# <85), clinopyroxenes are augitic and Al-Ti rich, and spinels are Al-rich and Cr-poor. On La Palma, group I peridotites comprise spinel-bearing harzburgites, dunites, and minor lherzolites, whereas group II peridotites are mostly spinel wehrlites, amphibole wehrlites, and rare dunites (Wulff-Pedersen et al., 1996; Klügel, 1998; Neumann et al., 2004). These xenoliths were all interpreted to be of mantle origin, but does this also apply to the tephriphonolite-hosted peridotites of the present study?

The textures of wehrlite samples KLA1704, -1715, -1718, and -1735 are reminiscent of cumulate rocks (**Figures 2F,G**). However, similar textures can be produced by metasomatic melts that percolate through and react with mantle peridotite, crystallizing new phases that fill the melt porosity in a manner similar to intercumulus melt. Such "metasomatic infill cumulates" are texturally not necessarily distinguishable from "normal" cumulates (Harte et al., 1993). Considering mineral chemistry, clinopyroxene in the wehrlites is higher in Mg# (86–94) and Cr_2O_3, and lower in TiO_2 and Al_2O_3, than macrocrysts (**Figure 7A**). Olivine is around Fo_{89} in the xenoliths' interior (**Figure 6A**); the decrease to Fo_{85} in composite xenolith KLA1735 may reflect Fe-Mg exchange with the surrounding cumulate. Spinel is Cr-rich (Cr# 56–87) and low

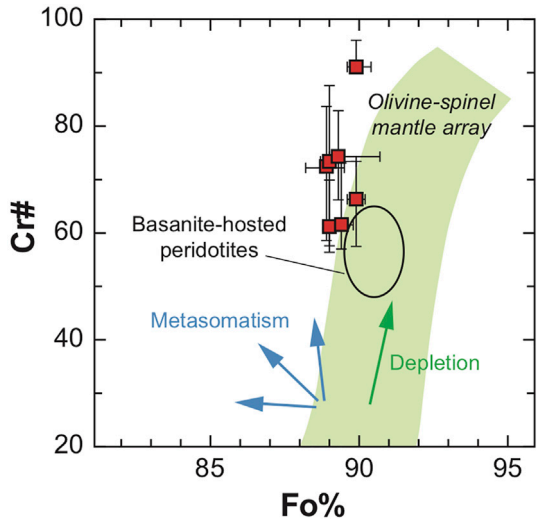


FIGURE 10 | Compositional relationship between Fo% of olivine and Cr# of coexisting spinel in the investigated peridotite xenoliths from La Palma, as compared to the mantle array after Arai (1994). Symbols indicate the average values for the interior parts of each sample; error bars encompass minimum and maximum values. Field for basanite-hosted peridotites based on data from Wulff-Pedersen et al. (1996) and Klügel (1998).

in TiO_2 (mostly <1 wt%). For these reasons the wehrlite xenoliths are unlikely to represent magmatic cumulates, but rather belong to the Cr-Mg series. They may have undergone metasomatic reactions between harzburgite and alkaline melts, leading to the dissolution of orthopyroxene (Kelemen, 1990; Kelemen et al., 1990; Wulff-Pedersen et al., 1996). Of note, Cr-Mg series wehrlite xenoliths are comparatively rare on La Palma and other Canary Islands (Neumann et al., 2004), but common in the tephriphonolite of this study. The dunite (KLA1721, -1731) (**Figures 2H,I**) and lherzolite (KLA1736A) xenoliths petrographically resemble basanite-hosted group I xenoliths from La Palma (Wulff-Pedersen et al., 1996). Their olivine (around Fo_{89-90} in the xenoliths' interior) and spinel (Cr# 57–96, TiO_2 <0.9 wt%) compositions are also consistent with a mantle origin. In a diagram of olivine Fo% versus spinel Cr#, all tephriphonolite-hosted peridotites plot at the boundary of the mantle array after Arai (1994) or slightly off it, in contrast to basanite-hosted peridotite xenoliths from La Palma (**Figure 10**). A shift to lower Fo% and/or higher Cr# likely reflects magmatic overprinting of the peridotites, consistent with the occurrence of phlogopite-clinopyroxene-amphibole veins, interstitial phlogopite, and vermicular or skeletal spinel grains (cf. Wulff-Pedersen et al., 1996, 1999; Klügel, 1998, 2001; Neumann et al., 2004).

The outer parts (cumulate zone) of the selvages encasing most peridotite xenoliths must have formed in the magma accumulation zone where the host tephriphonolite evolved, because the selvage minerals are commonly euhedral towards the host and have compositions approaching those of the macrocrysts (**Figures 7A,B**). The inner selvage parts (rims I and II) likely reflect reactions with intermediate to evolved melts not in equilibrium with forsteritic olivine. Experimental data on reactions between olivine and orthopyroxene with evolved Si-undersaturated melts show that rims some tens of microns thick can form within hours to days, growth rates decreasing strongly with increasing rim thickness (Shaw et al., 1998; Shaw, 1999; Grant et al., 2014a, 2014b). Reaction rates and type of reaction products depend on melt composition and H_2O contents. The presence of two distinct inner selvage zones in some of the peridotites studied here (clinopyroxene-rich rim I and phlogopite-rich rim II; **Figures 2F,H**) likely reflects a rapid change in xenolith environment, i.e., composition of the host melt and/or P-T conditions. Scenario 1: rim I formed within a mantle reservoir after xenolith entrainment, until a magma pulse brought the xenolith into the magma accumulation zone where rim II formed. Scenario 2: rim I and rim II both formed in the magma accumulation zone after the xenolith was brought upward by a mafic magma pulse; the break between both rims reflects injection of new magma into the evolving host melt. In either case, the complex selvages indicate contact of the xenoliths with at least two distinct melt compositions. Based on observations and results from Grant et al. (2013, 2014a, 2014b), we suggest that phlogopite-dominated rims were produced by reaction with H_2O-rich phonolitic melts, whereas clinopyroxene-rich rims indicate reaction with intermediate (tephritic to tephriphonolitic) and/or less H_2O-rich melts.

According to our diffusion modelling, the residence times of the peridotite xenoliths in alkaline magma (that is, the period between xenolith entrainment and host tephriphonolite eruption) were on the order of decades to centuries for most xenoliths (**Figure 9A**). This time scale is significantly longer than that estimated for e.g. mantle-derived fragments in the Heldburg phonolite (several months to a year; Grant et al., 2013). It also exceeds the residence times of 6–100 years calculated for basanite-hosted xenoliths from La Palma (Klügel et al., 1997; Klügel, 1998). These earlier calculations, however, assumed a rather high temperature of 1,200°C during diffusion. Considering that actual temperatures may have been close to 1,100°C (Klügel, 2001), calculated residence times may increase roughly four-fold. It thus appears that basanite- and tephriphonolite-hosted peridotite xenoliths indicate comparable residence times in alkaline magma before eruption. The effect of selvage growth on the lengths of diffusion zones was probably minor, because the selvages were highly permeable for diffusive flux of cations, and diffusion zones essentially formed after the inner reaction rims (Klügel, 2001).

To summarize, the tephriphonolite-hosted peridotite xenoliths are interpreted as mantle fragments that were metasomatized by late-stage reactions with alkaline La Palma melts. They were likely derived from the vicinity of magma reservoirs in the upper mantle decades to centuries before eruption of the host tephriphonolite. After one or more pulses of rising magma brought them into the magma accumulation zone in the lower crust, they became embedded by cumulus crystals, and selvages formed by reaction with evolving melt. The scenario of two-stage xenolith uplift is similar to that for basanite-hosted xenoliths from La Palma (Klügel, 1998), but the presence

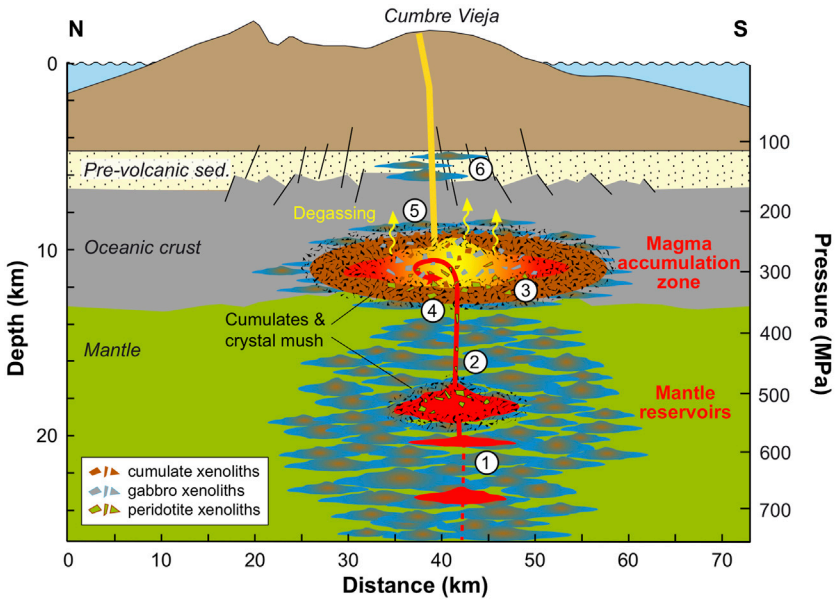


FIGURE 11 | Sketch for phonolite formation beneath La Palma. Magma reservoirs are not to scale but are enlarged to improve clarity; former melt pockets now cooled are drawn in blue, the active system in red to yellow. (1) Magmas rising from depth accumulate and fractionate to various degrees in upper mantle reservoirs. Some phonolite can form in small pockets. (2) Periodically, a reservoir ruptures and a batch of magma rises into the accumulation zone in the lower crust, in some cases carrying peridotite fragments. The magma emplacement may or may not lead to an eruption. (3) Magma in the accumulation zone continues to cool and fractionates towards phonolite. Peridotite xenoliths react with the evolved melts and become deposited in a crystal mush. Further recharge pulses bring new magma from mantle depths. (4) A final recharge event destabilizes the magma accumulation zone, causing rupture of the mafic crystal carapace and of gabbroic wall-rock, and mingling of the xenolith suite. (5) Possibly triggered by overpressurization, the tephriphonolite rises to the surface. (6) Short-term ponding in the upper crust may be possible, but is not reflected by our barometric data.

of three rather than two selvage parts in many xenoliths studied here indicates additional complexity.

Tephriphonolite Evolution and Magma Recharge

Previous studies demonstrated that phonolitic melts from Cumbre Vieja can be produced by 80–85 wt% crystal fractionation from basanitic melts (Johansen et al., 2005; Turner et al., 2015). Additional late-stage mixing with partial melts of earlier formed syenite-like rocks was invoked to explain some trace element characteristics, such as high Ba, Pb, U and Th contents of the most evolved melts (Turner et al., 2015). Our petrographic and mineral data for the xenolith-rich tephriphonolite indicate more than one mixing event. *1*) The diverse crystal cargo of the tephriphonolite and cumulate xenoliths that includes normally, reversely, or more complexly zoned clinopyroxene and kaersutite macrocrysts, partly with corroded cores, indicates magma mixing and/or incorporation of residual crystals of various origin into the evolving melt. *2*) Peridotite xenoliths with two or three distinct selvage zones indicate at least one abrupt change in host melt composition. *3*) The mineralogical variability of selvages between different peridotite xenoliths reflects contact with different alkaline melts and hence a mixed peridotite population. *4*) The large range of residence times of the peridotite xenoliths in host melts (**Figure 9A**) requires xenolith transport by more than one magma pulse. We suggest, therefore, that the petrogenesis of the tephriphonolite involved multiple recharge events in addition to crystal fractionation. The other four tephriphonolites to phonolites studied here also show diverse crystal cargos with variably zoned macrocrysts and small cumulate fragments, suggesting a similarly complex evolution as the xenolith-rich tephriphonolite, even though they lack the xenolith diversity.

Our barometric data substantiate previous suggestions (Johansen et al., 2005; Turner et al., 2015; Klügel et al., 2015) that the evolution of intermediate magmas to phonolites at Cumbre Vieja mainly occurs within a magma accumulation zone in the lower crust to Moho, whereas the more primitive magmas differentiate in the upper mantle (**Figure 11**). Magma mixing or recharge events are common in both mantle and crustal reservoirs, and are recorded as macrocryst zonations in basanites and tephrites (Klügel et al., 2000, 2005) as well as in the more evolved rocks described here. It is likely that a recharge event ultimately caused ascent and eruption of the xenolith-rich tephriphonolite. Recharge by more primitive melts is a common eruption trigger, but is not necessarily apparent in the petrological record (Rout and Wörner, 2020). The actual mechanism for ultimate destabilization and ascent of the tephriphonolite is not known. Plausible possibilities include volume increase and/or thermal disturbance induced by mixing; massive H_2O degassing due to heating by, or CO_2 flushing from, the recharge melt (Caricchi et al., 2018); and

remobilization and partial melting of older cumulates (e.g., Bachmann and Bergantz, 2008; Wolff et al., 2015).

The latest recharge into the magma accumulation zone beneath Cumbre Vieja was associated with the 2021 eruption and began some decades after the 1971 Teneguía eruption. Based on differential interferometric synthetic aperture radar (DInSAR) data, Fernández et al. (2021) inferred that already in 2009–2010 a small volume of magma moved from the mantle storage system to a depth of 8–10 km, i.e., into the accumulation zone. This resulted in fluid migration and subtle surface deformation, as well as in increased CO_2 emission at Cumbre Vieja and an increased magmatic component of helium in a cold spring 1–2 years later (Padrón et al., 2015). A similar event probably occurred in 2011–2012 (Fernández et al., 2021). The first seismic swarms indicative of volcanic unrest were recorded in October 2017 and February 2018 at mostly 15–30 km depth, and were accompanied by changes in helium and CO_2 emissions on La Palma before and after the swarms (Torres-González et al., 2020). Six further seismic swarms occurred between July 2020 and February 2021 at upper mantle depths (IGN, 2021; Longpré, 2021). From 11 September 2021 on, seismicity became more intense and shallower and was accompanied by considerable surface deformation. Hypocenters initially clustered at about 8–13 km depth, within the accumulation zone, and subsequently marked migration of magma towards the eventual eruption site, until the first vents opened on 19 September (IGN, 2021; Longpré, 2021). For the next 3 months, intense pyroclastic and effusive activity was accompanied by seismicity that clustered at about 8–16 km and 30–38 km depth.

The pre- and syn-eruptive seismicity in 2021, the analyses of the initial phase of volcanic unrest, as well as the record of mantle xenoliths from Cumbre Vieja, all indicate temporary magma ponding in the lowermost crust. This zone is periodically recharged by injection of magma from mantle reservoirs; large injections are likely to be accompanied by crustal seismicity and surface deformation. The intense pre- and syn-eruptive seismicity within the magma accumulation zone may reflect limited mobility of magma and brittle response of surrounding rock to changing pressure, as would be the case in a complex system of interconnected mush pockets or compartments (Gudmundsson, 2012; Klügel et al., 2015).

Timescales of Differentiation and Ascent

The tephriphonolite and its xenolith cargo record a succession of events that date back over centuries preceding its eruption (**Figure 9A**), which may be the timescale for differentiation of a more primitive magma to tephriphonolite. This timescale agrees with results from U-series isotope studies, indicating basanite to phonolite differentiation in 1,550–1,750 years for the Jedey phonolite of Cumbre Vieja (Johansen et al., 2005), and a few hundred to 2,000 years for Cumbre Vieja overall (Turner et al., 2015). We now compare these timescales to the recurrence rates for historic eruptions on Cumbre Vieja, which range from 22 to 237 years with an average of broadly 80 years (**Figure 9B**); this record does not take into account possible submarine eruptions. As mantle-derived magmas commonly stall during an eruption within the magma accumulation zone (Hansteen et al., 1998; Klügel et al., 2005, Klügel et al., 2015), the historic activity pattern implies new magma input into this zone every 80 years at least. This has the implication that the century-long differentiation of phonolite in the magma accumulation zone must be accompanied by a number of recharge events, provided that the passing magma batches meet the differentiating melt. In the case of the xenolith-rich tephriphonolite, it is conceivable from the data presented in **Figure 9A** that recharge may have occurred *1*) around two centuries, *2*) some decades, and *3*) some weeks prior to its eruption. These times are not well constrained, but the limited overlap of the calculated diffusion times in **Figure 9A** suggests three recharge events at least.

The timescales for final ascent of the tephriphonolite may be broadly assessed by the width of opacite rims around kaersutite macrocrysts. Experiments with andesitic to dacitic melts have shown that such amphibole reaction rims can form as a result of heating or decompression-induced H_2O degassing of the melt (Rutherford and Hill, 1993; Browne and Gardner, 2006; De Angelis et al., 2015). Both causes cannot be distinguished on the basis of rim thickness and microlite size (De Angelis et al., 2015). By applying the range of experimental growth rates to the observed rim thicknesses of 20–80 μm, we obtain reaction times of 5–102 days for decompression-induced amphibole breakdown (growth rates 9×10^{-10} to 5×10^{-9} cm/s; Browne and Gardner, 2006), and 0.1–11 days for heating-induced breakdown (3×10^{-9} to 2×10^{-7} cm/s; De Angelis et al., 2015). Data on reaction kinetics of amphibole rims in phonolitic melts are lacking, but since reaction rates increase with decreasing melt viscosity (Browne and Gardner, 2006), it is conceivable that reactions are similar or faster in less SiO_2-rich phonolites than in andesites to dacites. In summary, substantial H_2O degassing and/or heating of the tephriphonolite likely occurred days to weeks before eruption, and was possibly related to its final ascent. This timescale is comparable to the inferred diffusion time to produce the rim zonations of peridotite xenolith sample KLA1718 (**Figure 9A**), and to the timescale to form the thin phlogopite reaction rim around this peridotite (according to experimental data from Grant et al., 2014a). Entrainment of some peridotite xenoliths into the rising tephriphonolite and the formation of opacite rims around kaersutite macrocrysts thus seem to be temporally and causally related.

We suggest that the last perturbation of the differentiating tephriphonolite was a small batch of magma from depth weeks to days before eruption. The batch carried some peridotite fragments into the magma accumulation zone in the lower crust, where it mixed with a larger volume of evolved magma (**Figure 11**). However, most of the peridotite xenolith population was carried into this zone by earlier magma pulses, centuries to decades before eruption, as is indicated by diffusion times for their rim zonations (**Figure 9A**) and their thick composite selvages. The diversity of selvage compositions and the wide range of diffusion times indicate that more than one magma was involved. The peridotites carried by each pulse settled and became embedded within a mush of accumulating crystals, a scenario envisaged also for basanite-hosted xenoliths (Klügel, 1998). The last recharge may have triggered a cascade of events, including overpressurization of the magma storage system, rupture of its

mafic crystal carapace and of gabbroic wall-rock from the lower oceanic crust, entrainment of these fragments as xenoliths into the advancing magma, entrainment of peridotite fragments into the magma, and final ascent to the surface (**Figure 11**). The thorough mingling of the xenolith suite suggests a turbulent environment in the magma accumulation zone as the tephriphonolite ascended; in the conduit the viscosity was apparently high enough to prevent settling of the dense xenoliths.

Implications for Phonolite Generation at Ocean Island Volcanoes

Based on geochemical and petrological data it was proposed that the magma storage system beneath Cumbre Vieja is characterized by relatively small magma batches that differentiate in the mantle and pass the magma accumulation zone en route to the surface (Klügel et al., 2000, 2005). A similar model of magma ponding and phonolite differentiation near Moho depths was inferred for Mayotte Island, Comoros archipelago (Berthod et al., 2021). Similar storage horizons in the lower crust seem to exist beneath a number of other oceanic island volcanoes (Hansteen et al., 1998; Klügel et al., 2015), but not all of these erupt evolved magmas. For example, El Hierro Island is located next to La Palma and is of comparable subaerial age, but evolved lavas are rare and are confined to few trachyte flows and minor pyroclastic deposits (Pellicer, 1977; Carracedo et al., 2001; Pedrazzi et al., 2014). The paucity of evolved compositions at El Hierro coincides with a low eruption frequency of around 1,000 years (Becerril et al., 2016), as compared to 80 years at Cumbre Vieja. Magma supply rates are also lower for El Hierro (0.12–0.36 km^3/ka) than for Cumbre Vieja (>0.52 km^3/ka) (Carracedo, 1999; Amelung and Day, 2002). We suspect that the lower crustal magma accumulation zone under El Hierro is less mature than that under Cumbre Vieja, that is, it is cooler, smaller, and also slightly deeper as shown by barometric data (Klügel et al., 2015). In consequence, magmas stalling at this horizon receive less frequent recharge and are more prone to solidifying between recharge events, rather than evolving into trachytes or phonolites. This scenario is consistent with the precursors of the 2011–2012 El Hierro eruption, where almost 10,000 seismic events and gradual surface deformation over 3 months marked magma emplacement and dike propagation at lower oceanic crust to Moho depths (López et al., 2012; González et al., 2013; Martí et al., 2013; Domínguez Cerdeña et al., 2014), suggesting a cold and brittle environment. This contrasts with the situation at Cumbre Vieja in 2021, where intense crustal seismicity with ca. 1,400 events and surface deformation began 8 days before the eruption (IGN, 2021; Longpré, 2021).

Fogo (Cabo Verde islands) is another young volcanic oceanic island that lacks highly evolved compositions almost completely; most of the recent lavas have basanitic to phonotephritic compositions (Hildner et al., 2012, and references therein). Like Cumbre Vieja and El Hierro, Fogo is in its shield-building stage, but is more active with an average of 20 years recurrence rate of historical eruptions (Ribeiro, 1954; Day et al., 2000) and a magma supply rate of >1.7 km^3/ka (Amelung and Day, 2002). Geobarometric data for Fogo magmas strongly resemble those for Cumbre Vieja, with inferred pre-eruptive storage in the mantle at ca. 15–25 km depth, and short-term magma stalling in a magma accumulation zone in the lowermost crust at ca. 8–15 km depth (Hildner et al., 2012; Klügel et al., 2015; Klügel et al., 2020). The magma accumulation zone hence receives fresh magma from mantle reservoirs at least every 20 years on average. The frequency of these pulses keeps the accumulation zone at elevated temperatures, which may prevent significant volumes of unerupted residual melts to differentiate to phonolite. This may explain why the seismic precursors of the latest Fogo eruption in 2014 were located at shallow levels, but not in the hot lower crust where some magma may still have resided (Klügel et al., 2020).

The contrasting situations at La Palma, El Hierro and Fogo suggest that formation of significant amounts of phonolite in the magma accumulation zone in the lowermost crust is facilitated by a thermal and temporal "phonolite window." The thermal state of a storage system depends on several factors including frequency and volume of magma recharge pulses and eruptive events, and ambient temperature (e.g., Annen and Sparks, 2002). Our data for Cumbre Vieja suggest that differentiation of magma batches in the accumulation zone is accompanied by recharge events at rates similar to, or higher than, eruption rates. If recharge rates are high as at Fogo, frequent flushing of the accumulation zone may cause eruption of magma before evolved melts can form. If the rates are low as at El Hierro, unerupted melts that remain in the accumulation zone may solidify between eruptions. At Cumbre Vieja, recharge rates and volumes are balanced, such that phonolites and also intermediate compositions can form and erupt (cf. Menand, 2011). This balance may be one reason why a "Daly Gap" (Daly, 1925) is lacking at Cumbre Vieja (**Figure 4**); another reason can be partial melting of earlier intrusive rocks to produce a geochemical diversity of magmas (Annen and Sparks, 2002; Annen et al., 2006; Turner et al., 2015). Naturally, whether phonolites can form and erupt also depends on other major factors such as composition and volatile contents of the magmas, melt viscosity, storage depths of magmas, and structural regime of the volcano (e.g., Thompson et al., 2001; Gudmundsson, 2012; Andújar et al., 2013).

Sufficient magma supply provided, a magma accumulation zone in the lower crust may eventually evolve into a larger and dynamic crustal storage system that is capable of supporting explosive voluminous eruptions of evolved magma (e.g., Annen and Sparks, 2002; Menand, 2011). Long-lasting shallow storage systems are well described for comparatively thick and hot crust above subduction zones, but less so for ocean islands. The surface manifestation of such a storage system would be the dominance of phonolitic to trachytic rocks during certain evolutionary stages of an ocean island volcano, typically the late shield or post-shield stage. Examples include Brava and Santo Antão islands, Cabo Verde archipelago (Plesner et al., 2002; Holm et al., 2006; Madeira et al., 2010; Mourão et al., 2012), Tenerife and Gran Canaria, Canary Islands (Schmincke, 1976; Ablay et al., 1998; Ancochea et al., 1990, 2006), Trindade (Weaver, 1990), and Rarotonga, Cook Islands (Thompson et al., 2001). On Tenerife, experimental results indicate storage of phonolite prior to voluminous eruptions within the shallow crust, at around 50 and 130 MPa

for flank and central eruptions, respectively (Andújar et al., 2008, 2013). Assuming that phonolite magmas mainly originate by fractional crystallization of mafic magmas, differentiation of large volumes in the shallow crust alone is hardly possible due to the limited crustal space available for storage of cumulates, which can make up around 80–90% of the former melt mass (Wörner and Schmincke, 1984; LeRoex et al., 1990; Ablay et al., 1998; Johansen et al., 2005; Holm et al., 2006; Turner et al., 2015). In addition, gravimetry data for Tenerife do not indicate high density bodies below the Central Volcanic Complex that could be linked to the direct fractionation of mafic magmas at shallow levels (Gottsmann et al., 2008). Thus, a large part of crystal fractionation needs to take place at upper mantle to Moho depths, implying multi-stage differentiation (Ablay et al., 1998). By analogy to the Cumbre Vieja case, we imply that a large shallow storage system beneath an ocean island volcano is preceded by a magma accumulation zone receiving frequent magma recharge. The record of the xenolith-rich tephriphonolite studied here provides a rare opportunity to constrain the frequency of these recharge events (cf. Rout and Wörner, 2020).

CONCLUSIONS

Based on our study of a xenolith-rich tephriphonolite and other evolved rocks on Cumbre Vieja volcano, we arrive at the following conclusions:

- Storage and differentiation of evolved Cumbre Vieja magmas occur in a magma accumulation zone within the lowermost oceanic crust.
- The pre-eruptive storage conditions of a particular xenolith-rich tephriphonolite include a pressure range of 250–350 MPa, temperature of 900–950°C, fO_2 of 2–3 log units above the NNO buffer, and H_2O contents of 3–4 wt%.
- Storage and differentiation of evolved magmas are accompanied by a number of recharge events by mantle-derived mafic magmas. Recharge intervals are on the order of decades to a few centuries, comparable to eruption recurrences in historic times (80 years on average).
- Some recharge events bring mantle-derived peridotite xenoliths into the accumulation zone. Reactions between peridotite fragments and more evolved melt produce selvages around the xenoliths and diffusion zones in olivine. The xenoliths settle and become part of a crystal mush.
- The final recharge event destabilized the tephriphonolite magma in the accumulation zone some weeks prior to final ascent and eruption. This ultimately led to disruption of the surroundings of the storage horizon, entrainment of oceanic crust and cumulate fragments into the magma, and mingling of the xenolith suite during ascent.
- The occurrence of mantle xenoliths in a phonolite may be caused by recharge of mafic magma into a crustal storage system, and does not necessarily imply formation of the evolved melt in the mantle.
- Formation and eruption of phonolites at oceanic island volcanoes depend critically on the thermal regime of crust and uppermost mantle. The evolution of lower crustal storage zones is facilitated by a balance between frequency and volume of magma recharge pulses and of eruptive events. Phonolites are rare if recharge pulses occur too infrequently or too frequently.

DATA AVAILABILITY STATEMENT

The original contributions presented in the study are included in the article/**Supplementary Material**, further inquiries can be directed to the corresponding author.

AUTHOR CONTRIBUTIONS

AK and TH studied the outcrop and collected the samples, AK carried out most of the analyses and led the writing of the manuscript, and EA investigated the peridotite xenoliths and their reaction zones. All authors were actively involved in the discussion and interpretation of the data and participated in the preparation of the manuscript.

FUNDING

Our research was supported by the German Research Foundation (DFG Grant KL1313/13-1) and by department funds.

ACKNOWLEDGMENTS

We thank K. Wolff and M. Thöner (GEOMAR Kiel), B. Schulz-Dobrick and N. Groschupf (University of Mainz), B. Mader and P. Appel (University of Kiel), and S. Jung (University of Hamburg) for support of the EMP and XRF analyses, and M. N. Tubrett for the ICP-MS analyses at Memorial University of Newfoundland. We gratefully acknowledge the staff from the Unidad de Medio Ambiente on La Palma for the permission to take samples. Detailed reviews and comments by J. Andújar, A. Barker and editor M. Pichavant improved the manuscript and are gratefully acknowledged.

SUPPLEMENTARY MATERIAL

The Supplementary Material for this article can be found online at: https://www.frontiersin.org/articles/10.3389/feart.2022.761902/full#supplementary-material

REFERENCES

Ablay, G. J., Carroll, M. R., Palmer, M. R., Marti, J., and Sparks, R. S. J. (1998). Basanite-phonolite Lineages of the Teide-Pico Viejo Volcanic Complex, Tenerife, Canary Islands. *J. Petrol.* 39, 905–936. doi:10.1093/petroj/39.5.905

Amelung, F., and Day, S. (2002). InSAR Observations of the 1995 Fogo, Cape Verde, Eruption: Implications for the Effects of Collapse Events upon Island Volcanoes. *Geophys. Res. Lett.* 29 (12), 10. doi:10.1029/2001gl013760

Ancochea, E., Fuster, J., Ibarrola, E., Cendrero, A., Coello, J., Hernan, F., et al. (1990). Volcanic Evolution of the Island of Tenerife (Canary Islands) in the Light of New K-Ar Data. *J. Volcanol. Geotherm. Res.* 44 (3), 231–249. doi:10.1016/0377-0273(90)90019-C

Ancochea, E., Hernán, F., Huertas, M. J., Brändle, J. L., and Herrera, R. (2006). A New Chronostratigraphical and Evolutionary Model for La Gomera: Implications for the Overall Evolution of the Canarian Archipelago. *J. Volcanol. Geotherm. Res.* 157 (4), 271–293. doi:10.1016/j.jvolgeores.2006.04.001

Andersen, T., and Neumann, E.-R. (2001). Fluid Inclusions in Mantle Xenoliths. *Lithos* 55, 301–320. doi:10.1016/s0024-4937(00)00049-9

Andújar, J., Costa, F., and Martí, J. (2010). Magma Storage Conditions of the Last Eruption of Teide Volcano (Canary Islands, Spain). *Bull. Volcanol.* 72 (4), 381–395. doi:10.1007/s00445-009-0325-3

Andújar, J., Costa, F., Martí, J., Wolff, J. A., and Carroll, M. R. (2008). Experimental Constraints on Pre-eruptive Conditions of Phonolitic Magma from the Caldera-Forming El Abrigo Eruption, Tenerife (Canary Islands). *Chem. Geol.* 257 (3), 173–191. doi:10.1016/j.chemgeo.2008.08.012

Andújar, J., Costa, F., and Scaillet, B. (2013). Storage Conditions and Eruptive Dynamics of central versus Flank Eruptions in Volcanic Islands: The Case of Tenerife (Canary Islands, Spain). *J. Volcanol. Geotherm. Res.* 260, 62–79. doi:10.1016/j.jvolgeores.2013.05.004

Annen, C., Blundy, J. D., and Sparks, R. S. J. (2006). The Genesis of Intermediate and Silicic Magmas in Deep Crustal Hot Zones. *J. Petrol.* 47, 505–539. doi:10.1093/petrology/egi084

Annen, C., and Sparks, R. S. J. (2002). Effects of Repetitive Emplacement of Basaltic Intrusions on thermal Evolution and Melt Generation in the Crust. *Earth Planet. Sci. Lett.* 203, 937–955. doi:10.1016/s0012-821x(02)00929-9

Arai, S. (1994). Characterization of Spinel Peridotites by Olivine-Spinel Compositional Relationships: Review and Interpretation. *Chem. Geol.* 113, 191–204. doi:10.1016/0009-2541(94)90066-3

Bachmann, O., and Bergantz, G. W. (2008). Rhyolites and Their Source Mushes across Tectonic Settings. *J. Petrol.* 49 (12), 2277–2285. doi:10.1093/petrology/egn068

Barker, A. K., Rydeblad, E. M., and Silva, S. M. D. M. (2021). "Magma Storage at Ocean Islands," in *Crustal Magmatic System Evolution*. Editors M. Masotta, C. Beier, and S. Mollo (Washington, DC: American Geophysical Union), 45–78. doi:10.1002/9781119564485.ch3

Barker, A. K., Troll, V., Carracedo, J., and Nicholls, P. (2015). The Magma Plumbing System for the 1971 Teneguía Eruption on La Palma, Canary Islands. *Contrib. Mineral. Petrol.* 170 (5-6), 1–21. doi:10.1007/s00410-015-1207-7

Barker, A. K., Troll, V. R., Ellam, R. M., Hansteen, T. H., Harris, C., Stillman, C. J., et al. (2012). Magmatic Evolution of the Cadamosto Seamount, Cape Verde: beyond the Spatial Extent of EM1. *Contrib. Mineral. Petrol.* 163, 949–965. doi:10.1007/s00410-011-0708-2

Becerril, L., Ubide, T., Sudo, M., Martí, J., Galindo, I., Galé, C., et al. (2016). Geochronological Constraints on the Evolution of El Hierro (Canary Islands). *J. Afr. Earth Sci.* 113, 88–94. doi:10.1016/j.jafrearsci.2015.10.012

Berndt, J., Holtz, F., and Koepke, J. (2001). Experimental Constraints on Storage Conditions in the Chemically Zoned Phonolitic Magma Chamber of the Laacher See Volcano. *Contrib. Mineral. Petrol.* 140, 469–486. doi:10.1007/pl00007674

Berthod, C., Médard, E., Di Muro, A., Hassen Ali, T., Gurioli, L., Chauvel, C., et al. (2021). Mantle Xenolith-Bearing Phonolites and Basanites Feed the Active Volcanic ridge of Mayotte (Comoros Archipelago, SW Indian Ocean). *Contrib. Mineral. Petrol.* 176 (10), 75. doi:10.1007/s00410-021-01833-1

Bourdon, B., Zindler, A., and Wörner, G. (1994). Evolution of the Laacher See Magma Chamber: Evidence from SIMS and TIMS Measurements of U-Th Disequilibria in Minerals and Glasses. *Earth Planet. Sci. Lett.* 126, 75–90. doi:10.1016/0012-821x(94)90243-7

Browne, B. L., and Gardner, J. E. (2006). The Influence of Magma Ascent Path on the Texture, Mineralogy, and Formation of Hornblende Reaction Rims. *Earth Planet. Sci. Lett.* 246 (3-4), 161–176. doi:10.1016/j.epsl.2006.05.006

Caricchi, L., Sheldrake, T. E., and Blundy, J. (2018). Modulation of Magmatic Processes by CO2 flushing. *Earth Planet. Sci. Lett.* 491, 160–171. doi:10.1016/j.epsl.2018.03.042

Carracedo, J. C., Badiola, E. R., Guillou, H., de La Nuez, J., and Pérez Torrado, F. J. (2001). Geology and Volcanology of La Palma and El Hierro, Western Canaries. *Estudios Geológicos* 57, 175–273. doi:10.3989/egeol.01575-6134

Carracedo, J. C. (1999). Growth, Structure, Instability and Collapse of Canarian Volcanoes and Comparisons with Hawaiian Volcanoes. *J. Volcanol. Geotherm. Res.* 94, 1–19. doi:10.1016/s0377-0273(99)00095-5

Carracedo, J. C. (1994). The Canary Islands: An Example of Structural Control on the Growth of Large Oceanic-Island Volcanoes. *J. Volcanol. Geotherm. Res.* 60, 225–241. doi:10.1016/0377-0273(94)90053-1

Cashman, K. V., Sparks, R. S. J., and Blundy, J. D. (2017). Vertically Extensive and Unstable Magmatic Systems: A Unified View of Igneous Processes. *Science* 355 (6331), eaag3055. doi:10.1126/science.aag3055

Coombs, M. L., and Gardner, J. E. (2004). Reaction Rim Growth on Olivine in Silicic Melts: Implications for Magma Mixing. *Am. Mineral.* 89, 748–758. doi:10.2138/am-2004-5-608

Costa, F., Dohmen, R., and Chakraborty, S. (2008). 14. Time Scales of Magmatic Processes from Modeling the Zoning Patterns of Crystals. *Rev. Mineral. Geochem.* 69, 545–594. doi:10.1515/9781501508486-015

Crank, J. (1975). *The Mathematics of Diffusion*. London: Oxford University Press.

Daly, R. A. (1925). The Geology of Ascension Island. *Proc. Am. Acad. Arts Sci.* 60, 1–80. doi:10.2307/25130043

Day, J. M. D., Pearson, D. G., Macpherson, C. G., Lowry, D., and Carracedo, J. C. (2010). Evidence for Distinct Proportions of Subducted Oceanic Crust and Lithosphere in HIMU-type Mantle beneath El Hierro and La Palma, Canary Islands. *Geochim. et Cosmochim. Acta* 74 (22), 6565–6589. doi:10.1016/j.gca.2010.08.021

Day, S. J., Carracedo, J. C., Guillou, H., Pais Pais, F. J., Badiola, E. R., Fonseca, J. F. B. D., et al. (2000). Comparison and Cross-Checking of Historical, Archaeological and Geological Evidence for the Location and Type of Historical and Sub-historical Eruptions of Multiple-Vent Oceanic Island Volcanoes. *Geol. Soc. Lond. Spec. Publications* 171, 281–306. doi:10.1144/gsl.sp.2000.171.01.21

Day, S. J., Heleno da Silva, S. I. N., and Fonseca, J. F. B. D. (1999). A Past Giant Lateral Collapse and Present-Day Flank Instability of Fogo, Cape Verde Islands. *J. Volcanol. Geotherm. Res.* 94, 191–218. doi:10.1016/s0377-0273(99)00103-1

De Angelis, S. H., Larsen, J., Coombs, M., Dunn, A., and Hayden, L. (2015). Amphibole Reaction Rims as a Record of Pre-eruptive Magmatic Heating: An Experimental Approach. *Earth Planet. Sci. Lett.* 426, 235–245. doi:10.1016/j.epsl.2015.06.051

Devey, C. W., Lackschewitz, K. S., Mertz, D. F., Bourdon, B., Cheminée, J.-L., Dubois, J., et al. (2003). Giving Birth to Hotspot Volcanoes: Distribution and Composition of Young Seamounts from the Seafloor Near Tahiti and Pitcairn Islands. *Geology* 31, 395–398. doi:10.1130/0091-7613(2003)031<0395:gbthvd>2.0.co;2

Dobosi, G., and Fodor, R. V. (1992). Magma Fractionation, Replenishment, and Mixing as Inferred from green-core Clinopyroxenes in Pliocene Basanite, Southern Slovakia. *Lithos* 28 (2), 133–150. doi:10.1016/0024-4937(92)90028-W

Dohmen, R., and Chakraborty, S. (2007). Fe-Mg Diffusion in Olivine II: point Defect Chemistry, Change of Diffusion Mechanisms and a Model for Calculation of Diffusion Coefficients in Natural Olivine. *Phys. Chem. Mineral.* 34, 409–430. doi:10.1007/s00269-007-0158-6

Domínguez Cerdeña, I., del Fresno, C., and Gomis Moreno, A. (2014). Seismicity Patterns Prior to the 2011 El Hierro Eruption. *Bull. Seismological Soc. America* 104, 567–575. doi:10.1785/0120130200

Duda, A., and Schmincke, H.-U. (1985). Polybaric Differentiation of Alkali Basaltic Magmas: Evidence from green-core Clinopyroxenes (Eifel, FRG). *Contrib. Mineral. Petrol.* 91, 340–353. doi:10.1007/bf00374690

Edgar, C. J., Wolff, J. A., Olin, P. H., Nichols, H. J., Pittari, A., Cas, R. A. F., et al. (2007). The Late Quaternary Diego Hernandez Formation, Tenerife: Volcanology of a Complex Cycle of Voluminous Explosive Phonolitic Eruptions. *J. Volcanol. Geotherm. Res.* 160 (1), 59–85. doi:10.1016/j.jvolgeores.2006.06.001

Elliott, T. R. (1991). *Element Fractionation in the Petrogenesis of Ocean Island Basalts*. Ph.D (Milton Keynes: The Open University).

Erdmann, S., Martel, C., Pichavant, M., and Kushnir, A. (2014). Amphibole as an Archivist of Magmatic Crystallization Conditions: Problems, Potential, and Implications for Inferring Magma Storage Prior to the Paroxysmal 2010 Eruption of Mount Merapi, Indonesia. *Contrib. Mineral. Petrol.* 167 (6), 1016. doi:10.1007/s00410-014-1016-4

Fernández, J., Escayo, J., Hu, Z., Camacho, A. G., Samsonov, S. V., Prieto, J. F., et al. (2021). Detection of Volcanic Unrest Onset in La Palma, Canary Islands, Evolution and Implications. *Sci. Rep.* 11 (1), 2540. doi:10.1038/s41598-021-82292-3

France, L. (2020). Can Destabilization Rims of Hydrous Minerals Be Used to Constrain Magma Ascent Kinetics at Lava Dome Volcanoes? *Bull. Volcanol* 82 (10), 66. doi:10.1007/s00445-020-01405-4

Freise, M., Holtz, F., Koepke, J. r., Scoates, J., and Leyrit, H. (2003). Experimental Constraints on the Storage Conditions of Phonolites from the Kerguelen Archipelago. *Contrib. Mineral. Petrol.* 145, 659–672. doi:10.1007/s00410-003-0453-2

Frey, F. A., and Prinz, M. (1978). Ultramafic Inclusions from San Carlos, Arizona: Petrologic and Geochemical Data Bearing on Their Petrogenesis. *Earth Planet. Sci. Lett.* 38, 129–176. doi:10.1016/0012-821x(78)90130-9

Frezzotti, M. L., Andersen, T., Neumann, E.-R., and Simonsen, S. L. (2002). Carbonatite melt-CO2 Fluid Inclusions in Mantle Xenoliths from Tenerife, Canary Islands: a story of Trapping, Immiscibility and Fluid-Rock Interaction in the Upper Mantle. *Lithos* 64, 77–96. doi:10.1016/s0024-4937(02)00178-0

Galipp, K., Klügel, A., and Hansteen, T. H. (2006). Changing Depths of Magma Fractionation and Stagnation during the Evolution of an Oceanic Island Volcano: La Palma (Canary Islands). *J. Volcanol. Geotherm. Res.* 155, 285–306. doi:10.1016/j.jvolgeores.2006.04.002

Geldmacher, J., Hoernle, K., Bogaard, P. v. d., Duggen, S., and Werner, R. (2005). New 40Ar/39Ar Age and Geochemical Data from Seamounts in the Canary and Madeira Volcanic Provinces: Support for the Mantle Plume Hypothesis. *Earth Planet. Sci. Lett.* 237, 85–101. doi:10.1016/j.epsl.2005.04.037

González, P. J., Samsonov, S. V., Pepe, S., Tiampo, K. F., Tizzani, P., Casu, F., et al. (2013). Magma Storage and Migration Associated with the 2011-2012 El Hierro Eruption: Implications for Crustal Magmatic Systems at Oceanic Island Volcanoes. *J. Geophys. Res. Solid Earth* 118, 4361–4377. doi:10.1002/jgrb.50289

Gottsmann, J., Camacho, A. G., Martí, J., Wooller, L., Fernández, J., García, A., et al. (2008). Shallow Structure beneath the Central Volcanic Complex of Tenerife from New Gravity Data: Implications for its Evolution and Recent Reactivation. *Phys. Earth Planet. Interiors* 168 (3), 212–230. doi:10.1016/j.pepi.2008.06.020

Grant, T. B., Milke, R., Pandey, S., and Jahnke, H. (2013). The Heldburg Phonolite, Central Germany: Reactions between Phonolite and Xenocrysts from the Upper Mantle and Lower Crust. *Lithos* 182-183 (0), 86–101. doi:10.1016/j.lithos.2013.09.012

Grant, T. B., Milke, R., and Wunder, B. (2014a). Experimental Reactions between Olivine and Orthopyroxene with Phonolite Melt: Implications for the Origins of Hydrous Amphibole + Phlogopite + Diopside Bearing Metasomatic Veins. *Contrib. Mineral. Petrol.* 168, 1073. doi:10.1007/s00410-014-1073-8

Grant, T. B., Milke, R., Wunder, B., Wirth, R., and Rhede, D. (2014b). Experimental Study of Phlogopite Reaction Rim Formation on Olivine in Phonolite Melts: Kinetics, Reaction Rates, and Residence Times. *Am. Mineral.* 99, 2211–2226. doi:10.2138/am-2014-4821

Gudmundsson, A. (2012). Magma chambers: Formation, Local Stresses, Excess Pressures, and Compartments. *J. Volcanol. Geotherm. Res.* 237-238, 19–41. doi:10.1016/j.jvolgeores.2012.05.015

Hansteen, T. H., and Klügel, A. (2008). Fluid Inclusion Thermobarometry as a Tracer for Magmatic Processes. *Rev. Mineral. Geochem.* 69, 143–177. doi:10.2138/rmg.2008.69.1

Hansteen, T. H., Klügel, A., and Schmincke, H.-U. (1998). Multi-stage Magma Ascent beneath the Canary Islands: Evidence from Fluid Inclusions. *Contrib. Mineral. Petrol.* 132, 48–64. doi:10.1007/s004100050404

Harms, E., Gardner, J. E., and Schmincke, H. U. (2004). Phase Equilibria of the Lower Laacher See Tephra (East Eifel, Germany): Constraints on Pre-eruptive Storage Conditions of a Phonolitic Magma Reservoir. *J. Volcanol. Geotherm. Res.* 134, 135–148. doi:10.1016/j.jvolgeores.2004.01.009

Harte, B. (1987). "Metasomatic Events Recorded in Mantle Xenoliths: an Overview," in *Mantle Xenoliths*. Editor P. H. Nixon (Chichester: John Wiley & Sons), 625–640.:

Harte, B., Hunter, R. H., and Kinny, P. D. (1993). Melt Geometry, Movement and Crystallization, in Relation to Mantle Dykes, Veins and Metasomatism. *Philosophical Trans. R. Soc. Lond. A* 342, 1–21.

Hawkesworth, C. J., Blake, S., Evans, P., Hughes, R., Macdonald, R., Thomas, L. E., et al. (2000). Time Scales of Crystal Fractionation in Magma Chambers-Integrating Physical, Isotopic and Geochemical Perspectives. *J. Petrol.* 41 (7), 991–1006. doi:10.1093/petrology/41.7.991

Hay, D. E., and Wendlandt, R. F. (1995). The Origin of Kenya Rift Plateau-type Flood Phonolites: Results of High-Pressure/high-Temperature Experiments in the Systems Phonolite-H2o and phonolite-H2O-CO2. *J. Geophys. Res.* 100 (B1), 401–410. doi:10.1029/94jb02160

Hernandéz-Pacheco, A., and De la Nuez, J. (1983). Las extrusiones sálicas del Sur de la Isla de La Palma (Canarias). *Estudios Geológicos* 39, 3–30.

Hernandéz-Pacheco, A., and Valls, M. C. (1982). The historic eruptions of La Palma Island (Canarias). Arquipelago, Revista da Universidade dos Açores, *Série Ciencias da Natureza* 3, 83–94.

Hildner, E., Klügel, A., and Hansteen, T. H. (2012). Barometry of Lavas from the 1951 Eruption of Fogo, Cape Verde Islands: Implications for Historic and Prehistoric Magma Plumbing Systems. *J. Volcanol. Geotherm. Res.* 217-218, 73–90. doi:10.1016/j.jvolgeores.2011.12.014

Hoernle, K. (1998). Geochemistry of Jurassic Oceanic Crust beneath Gran Canaria (Canary Islands): Implications for Crustal Recycling and Assimilation. *J. Petrol.* 39, 859–880. doi:10.1093/petroj/39.5.859

Holm, P. M., Wilson, J. R., Christensen, B. P., Hansen, L., Hansen, S. L., Hein, K. M., et al. (2006). Sampling the Cape Verde Mantle Plume: Evolution of Melt Compositions on Santo Antão, Cape Verde Islands. *J. Petrol.* 47, 145–189. doi:10.1093/petrology/egi071

Iacono Marziano, G., Schmidt, B. C., and Dolfi, D. (2007). Equilibrium and Disequilibrium Degassing of a Phonolitic Melt (Vesuvius AD 79 "white Pumice") Simulated by Decompression Experiments. *J. Volcanol. Geotherm. Res.* 161, 151–164. doi:10.1016/j.jvolgeores.2006.12.001

Iacovino, K., Oppenheimer, C., Scaillet, B., and Kyle, P. (2016). Storage and Evolution of Mafic and Intermediate Alkaline Magmas beneath Ross Island, Antarctica. *J. Petrol.* 57, 93–118. doi:10.1093/petrology/egv083

IGN (2021). *Earthquake Catalogue*. Madrid: Instituto Geográfico Nacional de España. https://www.ign.es/web/ign/portal/sis-catalogo-terremotos.

Irving, A. J., and Green, D. H. (2008). Phase Relationships of Hydrous Alkalic Magmas at High Pressures: Production of Nepheline Hawaiitic to Mugearitic Liquids by Amphibole-Dominated Fractional Crystallization within the Lithospheric Mantle. *J. Petrol.* 49, 741–756. doi:10.1093/petrology/egm088

Irving, A. J., and Price, R. C. (1981). Geochemistry and Evolution of Iherzolite-Bearing Phonolitic Lavas from Nigeria, Australia, East Germany and New Zealand. *Geochim. et Cosmochim. Acta* 45, 1309–1320. doi:10.1016/0016-7037(81)90224-6

Jarosewich, E. J., Nelen, J. A., and Norberg, J. A. (1980). Reference Samples for Electron Microprobe Analysis. *Geostand. Newsl.* 4, 43–47. doi:10.1111/j.1751-908X.1980.tb00273.x

Jenner, G. A., Longerich, H. P., Jackson, S. E., and Fryer, B. J. (1990). ICP-MS - A Powerful Tool for High-Precision Trace-Element Analysis in Earth Sciences: Evidence from Analysis of Selected U.S.G.S. Reference Samples. *Chem. Geol.* 83, 133–148. doi:10.1016/0009-2541(90)90145-w

Jochum, K. P., Willbold, M., Raczek, I., Stoll, B., and Herwig, K. (2005). Chemical Characterisation of the USGS Reference Glasses GSA-1G, GSC-1G, GSD-1G, GSE-1G, BCR-2G, BHVO-2G and BIR-1G Using EPMA, ID-TIMS, ID-ICP-MS and LA-ICP-MS. *Geostand Geoanal. Res.* 29, 285–302. doi:10.1111/j.1751-908x.2005.tb00901.x

Johansen, T. S., Hauff, F., Hoernle, K., Klügel, A., and Kokfelt, T. F. (2005). Basanite to Phonolite Differentiation within 1550-1750 Yr: U-Th-Ra Isotopic Evidence from the A.D. 1585 Eruption on La Palma, Canary Islands. *Geology* 33, 897–900. doi:10.1130/g21663.1

Kelemen, P. B., Joyce, D. B., Webster, J. D., and Holloway, J. R. (1990). Reaction between Ultramafic Rock and Fractionating Basaltic Magma II. Experimental Investigation of Reaction between Olivine Tholeiite and Harzburgite at 1150-1050 C and 5 Kb. *J. Petrol.* 31, 99–134. doi:10.1093/petrology/31.1.99

Kelemen, P. B. (1990). Reaction between Ultramafic Rock and Fractionating Basaltic Magma I. Phase Relations, the Origin of Calc-Alkaline Magma Series, and the Formation of Discordant Dunite. *J. Petrol.* 31, 51–98. doi:10.1093/petrology/31.1.51

Kelly, P. J., Kyle, P. R., Dunbar, N. W., and Sims, K. W. W. (2008). Geochemistry and Mineralogy of the Phonolite Lava lake, Erebus Volcano, Antarctica: 1972-2004 and Comparison with Older Lavas. *J. Volcanol. Geotherm. Res.* 177, 589–605. doi:10.1016/j.jvolgeores.2007.11.025

Klitgord, K. D., and Schouten, H. (1986). "Plate Kinematics of the Central Atlantic," in *The Geology of North America, Vol. M, the Western North Atlantic Region*. Editors P. R. Vogt and B. E. Tucholke (Boulder, Colorado: Geological Society of America), 351–378.

Klügel, A., Day, S., Schmid, M., and Faria, B. (2020). Magma Plumbing During the 2014–2015 Eruption of Fogo (Cape Verde Islands). *Front. Earth Sci.* 8. doi:10.3389/feart.2020.00157

Klügel, A., Galipp, K., Hoernle, K., Hauff, F., and Groom, S. (2017). Geochemical and Volcanological Evolution of La Palma, Canary Islands. *J. Petrol.* 58, 1227–1248. doi:10.1093/petrology/egx052

Klügel, A., Longpré, M.-A., García-Cañada, L., and Stix, J. (2015). Deep intrusions, lateral magma transport and related uplift at ocean island volcanoes. *Earth Planet. Sci. Lett.* 431, 140–149. doi:10.1016/j.epsl.2015.09.031

Klügel, A., Hansteen, T. H., and Galipp, K. (2005). Magma Storage and Underplating beneath Cumbre Vieja Volcano, La Palma (Canary Islands). *Earth Planet. Sci. Lett.* 236, 211–226. doi:10.1016/j.epsl.2005.04.006

Klügel, A., Hansteen, T. H., and Schmincke, H.-U. (1997). Rates of Magma Ascent and Depths of Magma Reservoirs beneath La Palma (Canary Islands). *Terra Nova* 9 (3), 117–121. doi:10.1046/j.1365-3121.1997.d01-15.x

Klügel, A., Hoernle, K. A., Schmincke, H.-U., and White, J. D. L. (2000). The Chemically Zoned 1949 Eruption on La Palma (Canary Islands): Petrologic Evolution and Magma Supply Dynamics of a Rift Zone Eruption. *J. Geophys. Res.* 105 (B3), 5997–6016. doi:10.1029/1999jb900334

Klügel, A. (2001). Prolonged Reactions between Harzburgite Xenoliths and Silica-Undersaturated Melt: Implications for Dissolution and Fe-Mg Interdiffusion Rates of Orthopyroxene. *Contrib. Mineral. Petrol.* 141, 1–14. doi:10.1007/s004100000222

Klügel, A. (1998). Reactions between Mantle Xenoliths and Host Magma beneath La Palma (Canary Islands): Constraints on Magma Ascent Rates and Crustal Reservoirs. *Contrib. Mineral. Petrol.* 131, 237–257. doi:10.1007/s004100050391

Klügel, A., Schmincke, H.-U., White, J. D. L., and Hoernle, K. A. (1999). Chronology and Volcanology of the 1949 Multi-Vent Rift-Zone Eruption on La Palma (Canary Islands). *J. Volcanol. Geotherm. Res.* 94, 267–282. doi:10.1016/s0377-0273(99)00107-9

Kress, V. C., and Carmichael, I. S. E. (1991). The Compressibility of Silicate Liquids Containing Fe2O3 and the Effect of Composition, Temperature, Oxygen Fugacity and Pressure on Their Redox States. *Contrib. Mineral. Petrol.* 108, 82–92. doi:10.1007/bf00307328

Kunzmann, T. (1996). The Solidus-Liquidus Phase Relations of the Heldburg Phonolite up to 2.5 GPa. *Terra Abstr.* 8, 37–38.

Le Roex, A. P., Cliff, R. A., and Adair, B. J. I. (1990). Tristan da Cunha, South Atlantic: Geochemistry and Petrogenesis of a Basanite-Phonolite Lava Series. *J. Petrol.* 31, 779–812. doi:10.1093/petrology/31.4.779

Lechler, P. J., and Desilets, M. O. (1987). A Review of the Use of Loss on Ignition as a Measurement of Total Volatiles in Whole-Rock Analysis. *Chem. Geol.* 63, 341–344. doi:10.1016/0009-2541(87)90171-9

Leite de Oliveira, A., Costa dos Santos, A., Nogueira, C. C., Maia, T. M., and Geraldes, M. C. (2021). Green Core Clinopyroxenes from Martin Vaz Archipelago Plio-Pleistocenic Alkaline Rocks, South Atlantic Ocean, Brazil: A Magma Mixing and Polybaric Crystallization Record. *J. South Am. Earth Sci.* 105, 102951. doi:10.1016/j.jsames.2020.102951

Longpré, M.-A. (2021). Reactivation of Cumbre Vieja Volcano. *Science* 374 (6572), 1197–1198. doi:10.1126/science.abm9423

López, C., Blanco, M. J., Abella, R., Brenes, B., Cabrera Rodríguez, V. M., Casas, B., et al. (2012). Monitoring the Volcanic Unrest of El Hierro (Canary Islands) before the Onset of the 2011–2012 Submarine Eruption. *Geophys. Res. Lett.* 39 (13), 1–7. doi:10.1029/2012GL051846

Madeira, J., Mata, J., Mourão, C., Brum da Silveira, A., Martins, S., Ramalho, R., et al. (2010). Volcano-stratigraphic and Structural Evolution of Brava Island (Cape Verde) Based on 40Ar/39Ar, U-Th and Field Constraints. *J. Volcanol. Geotherm. Res.* 196, 219–235. doi:10.1016/j.jvolgeores.2010.07.010

Martí, J., Mitjavila, J., and Araña, V. (1994). Stratigraphy, Structure and Geochronology of the Las Cañadas Caldera (Tenerife, Canary Islands). *Geol. Mag.* 131 (6), 715–727. doi:10.1017/S0016756800012838

Martí, J., Pinel, V., López, C., Geyer, A., Abella, R., Tárraga, M., et al. (2013). Causes and Mechanisms of the 2011–2012 El Hierro (Canary Islands) Submarine Eruption. *J. Geophys. Res.* 118, 1–17. doi:10.1002/jgrb.50087

Masotta, M., Mollo, S., Freda, C., Gaeta, M., and Moore, G. (2013). Clinopyroxene-liquid Thermometers and Barometers Specific to Alkaline Differentiated Magmas. *Contrib. Mineral. Petrol.* 166, 1545–1561. doi:10.1007/s00410-013-0927-9

Melluso, L., Morra, V., Riziky, H., Veloson, J., Lustrino, M., Del Gatto, L., et al. (2007). Petrogenesis of a Basanite-Tephrite-Phonolite Volcanic Suite in the Bobaomby (Cap d'Ambre) peninsula, Northern Madagascar. *J. Afr. Earth Sci.* 49, 29–42. doi:10.1016/j.jafrearsci.2007.06.002

Menand, T. (2011). Physical Controls and Depth of Emplacement of Igneous Bodies: A Review. *Tectonophysics* 500, 11–19. doi:10.1016/j.tecto.2009.10.016

Middlemost, E. A. K. (1972). Evolution of La Palma, Canary Archipelago. *Contrib. Mineral. Petrol.* 36, 33–48. doi:10.1007/bf00372833

Mitchell-Thomé, R. C. (1970). *Geology of the Middle Atlantic, Beiträge zur Regionalen Geologie der Erde*. Berlin: Borntrager.

Mollo, S., Putirka, K., Misiti, V., Soligo, M., and Scarlato, P. (2013). A new test for equilibrium based on clinopyroxene-melt pairs: Clues on the solidification temperatures of Etnean alkaline melts at post-eruptive conditions. *Chem. Geol.* 352, 92–100. doi:10.1016/j.chemgeo.2013.05.026

Mortensen, A. K., Wilson, J. R., and Holm, P. M. (2009). The Cão Grande Phonolitic Fall deposit on Santo Antão, Cape Verde Islands. *J. Volcanol. Geotherm. Res.* 179, 120–132. doi:10.1016/j.jvolgeores.2008.10.014

Mourão, C., Mata, J., Doucelance, R., Madeira, J., Millet, M.-A., and Moreira, M. (2012). Geochemical Temporal Evolution of Brava Island Magmatism: Constraints on the Variability of Cape Verde Mantle Sources and on Carbonatite-Silicate Magma Link. *Chem. Geol.* 334, 44–61. doi:10.1016/j.chemgeo.2012.09.031

Moussallam, Y., Oppenheimer, C., Scaillet, B., and Kyle, P. R. (2013). Experimental Phase-Equilibrium Constraints on the Phonolite Magmatic System of Erebus Volcano, Antarctica. *J. Petrol.* 54, 1285–1307. doi:10.1093/petrology/egt012

Muñoz, M., Sagredo, J., and Afonso, A. (1974). Mafic and Ultramafic Inclusions in the Eruption of Teneguía Volcano (La Palma, Canary Islands). *Estudios Geol.*, 65–74.

Neumann, E.-R., Griffin, W. L., Pearson, N. J., and O'Reilly, S. Y. (2004). The Evolution of the Upper Mantle beneath the Canary Islands: Information from Trace Elements and Sr Isotope Ratios in Minerals in Mantle Xenoliths. *J. Petrol.* 45, 2573–2612. doi:10.1093/petrology/egh063

Neumann, E.-R., Sørensen, V. B., Simonsen, S. L., and Johnsen, K. (2000). Gabbroic Xenoliths from La Palma, Tenerife and Lanzarote, Canary Islands: Evidence for Reactions between Mafic Alkaline Canary Islands Melts and Old Oceanic Crust. *J. Volcanol. Geotherm. Res.* 103, 313–342. doi:10.1016/s0377-0273(00)00229-8

Padrón, E., Pérez, N. M., Rodríguez, F., Melián, G. V., Hernández, P. A., Sumino, H., et al. (2015). Dynamics of Diffuse Carbon Dioxide Emissions from Cumbre Vieja Volcano, La Palma, Canary Islands. *Bull. Volcanol.* 77, 1–15. doi:10.1007/s00445-015-0914-2

Parat, F., Holtz, F., and Klügel, A. (2011). S-rich Apatite-Hosted Glass Inclusions in Xenoliths from La Palma: Constraints on the Volatile Partitioning in Evolved Alkaline Magmas. *Contrib. Mineral. Petrol.* 162 (3), 463–478. doi:10.1007/s00410-011-0606-7

Pedrazzi, D., Becerril, L., Martí, J., Meletlidis, S., and Galindo, I. (2014). Explosive Felsic Volcanism on El Hierro (Canary Islands). *Bull. Volcanol* 76, 863. doi:10.1007/s00445-014-0863-1

Pellicer, M. J. (1977). Estudio volcanológico de la Isla de El Hierro, Islas Canarias. *Estudios Geológicos* 33, 181–197.

Pilet, S., Hernandez, J., and Villemant, B. (2002). Evidence for High Silicic Melt Circulation and Metasomatic Events in the Mantle beneath Alkaline Provinces: the Na-Fe-Augitic green-core Pyroxenes in the Tertiary Alkali Basalts of the Cantal Massif (French Massif Central). *Mineral. Petrol.* 76, 39–62. doi:10.1007/s007100200031

Plesner, S., Holm, P. M., and Wilson, J. R. (2002). ^{40}Ar-^{39}Ar Geochronology of Santo Antão, Cape Verde Islands. *J. Volcanol. Geotherm. Res.* 120, 103–121.

Praegel, N. O., and Holm, P. M. (2006). Lithospheric Contributions to High-MgO Basanites from the Cumbre Vieja Volcano, La Palma, Canary Islands and Evidence for Temporal Variation in Plume Influence. *J. Volcanol. Geotherm. Res.* 149, 213–239.

Price, R. C., and Chappell, B. W. (1975). Fractional Crystallisation and the Petrology of Dunedin Volcano. *Contrib. Mineral. Petrol.* 53, 157–182. doi:10.1007/bf00372602

Putirka, K. (2016). Amphibole Thermometers and Barometers for Igneous Systems and Some Implications for Eruption Mechanisms of Felsic Magmas at Arc Volcanoes. *Am. Mineral.* 101, 841–858. doi:10.2138/am-2016-5506

Putirka, K. D. (2008). 3. Thermometers and Barometers for Volcanic Systems. *Rev. Mineral. Geochem.* 69, 61–120. doi:10.1515/9781501508486-004

Putirka, K. D., Mikaelian, H., Ryerson, F., and Shaw, H. (2003). New Clinopyroxene-Liquid Thermobarometers for Mafic, Evolved, and Volatile-Bearing Lava Compositions, with Applications to Lavas from Tibet and the Snake River Plain, Idaho. *Am. Mineral.* 88, 1542–1554. doi:10.2138/am-2003-1017

Putirka, K. (1999). Clinopyroxene + liquid equilibria to 100 kbar and 2450 K. *Contrib. Mineral. Petrol.* 135, 151–163.

Putirka, K., Johnson, M., Kinzler, R., Longhi, J., and Walker, D. (1996). Thermobarometry of Mafic Igneous Rocks Based on Clinopyroxene-Liquid Equilibria, 0-30 Kbar. *Contrib. Mineral. Petrol.* 123, 92–108. doi:10.1007/s004100050145

Ranero, C. R., Torne, M., and Banda, E. (1995). Gravity and Multichannel Seismic Reflection Constraints on the Lithospheric Structure of the Canary Swell. *Mar. Geophys. Res.* 17, 519–534. doi:10.1007/bf01204342

Reagan, M. K., Turner, S., Legg, M., Sims, K. W. W., and Hards, V. L. (2008). 238U- and 232Th-decay series constraints on the timescales of crystal fractionation to produce the phonolite erupted in 2004 near Tristan da Cunha, South Atlantic Ocean. *Geochim. et Cosmochim. Acta* 72, 4367–4378. doi:10.1016/j.gca.2008.06.002

Ribeiro, O. (1954). A ilha Do Fogo e as suas erupçõẽs. *Memórias, Série Geográfica I (Lisbon: Junta de Investigações do Ultramar).*

Ridolfi, F., and Renzulli, A. (2012). Calcic Amphiboles in Calc-Alkaline and Alkaline Magmas: Thermobarometric and Chemometric Empirical Equations Valid up to 1,130°C and 2.2 GPa. *Contrib. Mineral. Petrol.* 163, 877–895. doi:10.1007/s00410-011-0704-6

Ridolfi, F., Renzulli, A., and Puerini, M. (2010). Stability and Chemical Equilibrium of Amphibole in Calc-Alkaline Magmas: an Overview, New Thermobarometric Formulations and Application to Subduction-Related Volcanoes. *Contrib. Mineral. Petrol.* 160, 45–66. doi:10.1007/s00410-009-0465-7

Roedder, E. (1984). "Fluid Inclusions," in *Reviews in Mineralogy* (Mineralogical Society of America), 12, 644. doi:10.1515/9781501508271

Romero Ortiz, J. (1951). La erupción del Nambroque en la isla de La Palma. *Boletín Del. Instituto Geológico y Minero de España* 63, 3–163.

Romero Ruiz, C. (1991). *Las manifestaciones volcanicas historicas del archipielago Canario. El Cedro, S.L.: Gobierno de Canarias, Consejería de Política Territorial.*

Rout, S. S., and Wörner, G. (2020). Constraints on the Pre-eruptive Magmatic History of the Quaternary Laacher See Volcano (Germany). *Contrib. Mineral. Petrol.* 175 (8), 73. doi:10.1007/s00410-020-01710-3

Rutherford, M. J., and Hill, P. M. (1993). Magma Ascent Rates from Amphibole Breakdown; an Experimental Study Applied to the 1980-1986 Mount St. Helens Eruptions. *J. Geophys. Res.* 98 (11), 19667–19685. doi:10.1029/93jb01613

Schmidt, B. C., and Behrens, H. (2008). Water Solubility in Phonolite Melts: Influence of Melt Composition and Temperature. *Chem. Geol.* 256, 259–268. doi:10.1016/j.chemgeo.2008.06.043

Schmincke, H.-U., Klügel, A., Hansteen, T. H., Hoernle, K., and van den Bogaard, P. (1998). Bogaard, P.v.dSamples from the Jurassic Ocean Crust beneath Gran Canaria, La Palma and Lanzarote (Canary Islands). *Earth Planet. Sci. Lett.* 163, 343–360. doi:10.1016/s0012-821x(98)00168-x

Schmincke, H.-U. (1976). "The Geology of the Canary Islands," in *Biogeography and Ecology of the Canary Islands*. Editor G. Kunkel (Netherlands: The Hague), 67–184. doi:10.1007/978-94-010-1566-0_4

Shane, P., and Smith, V. C. (2013). Using Amphibole Crystals to Reconstruct Magma Storage Temperatures and Pressures for the post-caldera Collapse Volcanism at Okataina Volcano. *Lithos* 156-159, 159–170. doi:10.1016/j.lithos.2012.11.008

Shaw, C. S. J. (1999). Dissolution of Orthopyroxene in Basanitic Magma between 0.4 and 2 GPa: Further Implications for the Origin of Si-Rich Alkaline Glass Inclusions in Mantle Xenoliths. *Contrib. Mineral. Petrol.* 135, 114–132. doi:10.1007/s004100050501

Shaw, C. S. J., Thibault, Y., Edgar, A. D., and Lloyd, F. E. (1998). Mechanisms of Orthopyroxene Dissolution in Silica-Undersaturated Melts at 1 Atmosphere and Implications for the Origin of Silica-Rich Glass in Mantle Xenoliths. *Contrib. Mineral. Petrol.* 132, 354–370. doi:10.1007/s004100050429

Span, R., and Wagner, W. (1996). A New Equation of State for Carbon Dioxide Covering the Fluid Region from the Triple-Point Temperature to 1100 K at Pressures up to 800 MPa. *J. Phys. Chem. Ref. Data* 25, 1509–1596. doi:10.1063/1.555991

Sterner, S. M., and Pitzer, K. S. (1994). An Equation of State for Carbon Dioxide Valid from Zero to Extreme Pressures. *Contrib. Mineral. Petrol.* 117, 362–374. doi:10.1007/bf00307271

Sun, S.-s., and McDonough, W. F. (1989). Chemical and Isotopic Systematics of Oceanic Basalts: Implications for Mantle Composition and Processes. *Geol. Soc. Lond. Spec. Publications* 42, 313–345. doi:10.1144/gsl.sp.1989.042.01.19

Thompson, G., Smith, I., and Malpas, J. (2001). Origin of Oceanic Phonolites by crystal Fractionation and the Problem of the Daly gap: an Example from Rarotonga. *Contrib. Mineral. Petrol.* 142, 336–346. doi:10.1007/s004100100294

Torres-González, P. A., Luengo-Oroz, N., Lamolda, H., D'Alessandro, W., Albert, H., Iribarren, I., et al. (2020). Unrest Signals after 46 Years of Quiescence at Cumbre Vieja, La Palma, Canary Islands. *J. Volcanol. Geotherm. Res.* 392, 106757. doi:10.1016/j.jvolgeores.2019.106757

Turner, S., Hoernle, K., Hauff, F., Johansen, T. S., Klügel, A., Kokfelt, T., et al. (2015). ^{238}U-^{230}Th-^{226}Ra Disequilibria Constraints on the Magmatic Evolution of the Cumbre Vieja Volcanics on La Palma, Canary Islands. *J. Petrol.* 56 (10), 1999–2024. doi:10.1093/petrology/egv061

Ubide, T., Mollo, S., Zhao, J.-x., Nazzari, M., and Scarlato, P. (2019). Sector-zoned Clinopyroxene as a Recorder of Magma History, Eruption Triggers, and Ascent Rates. *Geochim. et Cosmochim. Acta* 251, 265–283. doi:10.1016/j.gca.2019.02.021

Waters, L. E., and Lange, R. A. (2015). An Updated Calibration of the Plagioclase-Liquid Hygrometer-Thermometer Applicable to Basalts through Rhyolites. *Am. Mineral.* 100, 2172–2184. doi:10.2138/am-2015-5232

Weaver, B. L. (1990). Geochemistry of highly-undersaturated ocean island basalt suites from the South Atlantic Ocean: Fernando de Noronha and Trindade islands. *Contrib. Mineral. Petrol.* 105, 502–515. doi:10.1007/bf00302491

Weis, D., Frey, F. A., Leyrit, H., and Gautier, I. (1993). Kerguelen Archipelago Revisited: Geochemical and Isotopic Study of the Southeast Province Lavas. *Earth Planet. Sci. Lett.* 118 (1), 101–119. doi:10.1016/0012-821X(93)90162-3

Weis, F. A., Skogby, H., Troll, V. R., Deegan, F. M., and Dahren, B. (2015). Magmatic Water Contents Determined through Clinopyroxene: Examples from the Western Canary Islands, Spain. *Geochem. Geophys. Geosyst* 16, 2127–2146. doi:10.1002/2015gc005800

Welsch, B., Hammer, J., Baronnet, A., Jacob, S., Hellebrand, E., and Sinton, J. (2016). Clinopyroxene in Postshield Haleakala Ankaramite: 2. Texture, Compositional Zoning and Supersaturation in the Magma. *Contrib. Mineral. Petrol.* 171 (1), 1–19. doi:10.1007/s00410-015-1213-9

Wolff, J. A., Ellis, B. S., Ramos, F. C., Starkel, W. A., Boroughs, S., Olin, P. H., et al. (2015). Remelting of Cumulates as a Process for Producing Chemical Zoning in Silicic Tuffs: A Comparison of Cool, Wet and Hot, Dry Rhyolitic Magma Systems. *Lithos* 236-237, 275–286. doi:10.1016/j.lithos.2015.09.002

Wörner, G., and Schmincke, H.-U. (1984). Petrogenesis of the Zoned Laacher See Tephra. *J. Petrol.* 25, 836–851. doi:10.1093/petrology/25.4.836

Wright, J. B. (1966). Olivine Nodules in a Phonolite of the East Otago Alkaline Province, New Zealand. *Nature* 210 (5035), 519. doi:10.1038/210519a0

Wulff-Pedersen, E., Neumann, E.-R., and Jensen, B. B. (1996). The Upper Mantle under La Palma, Canary Islands: Formation of Si–K–Na-rich Melt and its Importance as a Metasomatic Agent. *Contrib. Mineral. Petrol.* 125, 113–139. doi:10.1007/s004100050210

Wulff-Pedersen, E., Neumann, E.-R., Vannucci, R., Bottazzi, P., and Ottolini, L. (1999). Silicic Melts Produced by Reaction between Peridotite and Infiltrating Basaltic Melts: Ion Probe Data on Glasses and Minerals in Veined Xenoliths from La Palma, Canary Islands. *Contrib. Mineral. Petrol.* 137, 59–82. doi:10.1007/s004100050582

Conflict of Interest: The authors declare that the research was conducted in the absence of any commercial or financial relationships that could be construed as a potential conflict of interest.

Publisher's Note: All claims expressed in this article are solely those of the authors and do not necessarily represent those of their affiliated organizations, or those of the publisher, the editors and the reviewers. Any product that may be evaluated in this article, or claim that may be made by its manufacturer, is not guaranteed or endorsed by the publisher.

Copyright © 2022 Klügel, Albers and Hansteen. This is an open-access article distributed under the terms of the Creative Commons Attribution License (CC BY). The use, distribution or reproduction in other forums is permitted, provided the original author(s) and the copyright owner(s) are credited and that the original publication in this journal is cited, in accordance with accepted academic practice. No use, distribution or reproduction is permitted which does not comply with these terms.

frontiers | Frontiers in Earth Science

ORIGINAL RESEARCH
published: 13 September 2022
doi: 10.3389/feart.2022.845544

The Geochemical Evolution of Santa Cruz Island, Galápagos Archipelago

E. L. Wilson[1†], *K. S. Harpp*[2*†], *D. M. Schwartz*[3] *and R. Van Kirk*[2]

[1]Department of Earth and Environment, Franklin and Marshall College, Lancaster, PA, United States, [2]Department of Geology, Colgate University, Hamilton, NY, United States, [3]Department of Geosciences, Boise State University, Boise, ID, United States

Understanding how ocean island volcanoes evolve provides important insight into the behavior of mantle plumes, how plumes interact with mid-ocean ridges, and potential risks posed to inhabitants as the islands age. In this field-based study of the Galápagos Islands, we use radiogenic isotope ratio, major element, and trace element analysis of >70 new lava samples to document the geochemical evolution of Santa Cruz Island over the past ~2 million years, as it has been carried away from the plume. Currently, Santa Cruz is a dormant shield volcano in the central archipelago. Previous work indicates that exposed lavas preserve >1 million years of activity in two eruptive units: *1*) The older Platform Series, exposed primarily in the northeast; and *2*) the Shield Series, which blankets the rest of Santa Cruz and erupted from a WNW trending fissure system. Our new geochemical analyses indicate that the Platform Series lavas are more evolved and isotopically enriched than Shield lavas, but neither as compositionally monotonous nor as isotopically enriched as the younger western Galápagos volcanoes. Santa Cruz formed when the Galápagos Spreading Center (GSC) was closer to the plume than it is today, resulting in enhanced plume-ridge interaction and transport of plume material to the ridge. Consequently, the Platform Series was formed under relatively magma-starved conditions compared to today's western volcanoes. Magma supply was sufficient for partial fractionation and homogenization of melts in shallow reservoirs, but inadequate to support thermochemically buffered networks like those in the present-day western archipelago. The slight depletion of Platform Series lavas relative to Fernandina reflects entrainment of depleted upper mantle and/or diversion of deep, enriched plume melts to the nearby GSC. The younger Shield Series lavas are even more depleted because plate motion has carried the volcano across the compositional boundary of the bilaterally asymmetric plume into its more depleted zone. Shield Series lavas' variable, primitive compositions reflect minimal crustal processing in small, ephemeral, poorly supplied magma reservoirs. Unlike the young western shields, the constructional history of Santa Cruz has been controlled to a significant extent by its proximity to the GSC.

Keywords: mantle plume, Ocean Island Basalt (OIB), volcano evolution, plume-ridge interaction, Galapagos Islands, Galapagos Archipelago, Santa Cruz Island, ocean island evolution

OPEN ACCESS

Edited by:
Michel Pichavant, CNRS Orléans, France

Reviewed by:
Luis E. Lara, Servicio Nacional de Geología y Minería de Chile (SERNAGEOMIN), Chile
Benjamin Bernard, Escuela Politécnice Nacional, Ecuador

***Correspondence:**
K. S. Harpp
kharpp@colgate.edu

†These authors share first authorship

Specialty section:
This article was submitted to Volcanology, a section of the journal Frontiers in Earth Science

Received: *29 December 2021*
Accepted: *29 March 2022*
Published: *13 September 2022*

Citation:
Wilson EL, Harpp KS, Schwartz DM and Van Kirk R (2022) The Geochemical Evolution of Santa Cruz Island, Galápagos Archipelago. Front. Earth Sci. 10:845544. doi: 10.3389/feart.2022.845544

INTRODUCTION

Ocean island volcanoes serve as windows into the composition and behavior of mantle plumes. How the geochemistry of lavas erupted at these volcanoes changes as they are transported downstream provides further insight into temporal and spatial variations of mantle plumes, as well as important constraints on island evolution. The Galápagos Islands are the surface expression of a mantle plume that has been active for at least 14.5 million years (e.g., Werner et al., 1999). Despite both Galápagos and Hawai'i originating as deep mantle plumes (e.g., Morgan, 1972; Wolfe et al., 2009; Weis et al., 2011; French and Romanowicz, 2015), the Galápagos Archipelago is distinct from the Hawaiian mantle plume archetype in multiple ways (Harpp and Weis, 2020). Of most importance for this study, the Galápagos Islands lack a predictable petrologic and geochemical evolutionary sequence like that observed at Hawai'i, in which the islands transition from an alkalic pre-shield to a tholeiitic shield, and eventually to an alkalic post-shield stage, related to changes in magma supply rate as a function of proximity to the Hawaiian plume (e.g., Chen and Frey, 1983; Macdonald et al., 1983; Clague and Dalrymple, 1987, 1988; Geist et al., 2014a).

Furthermore, radiogenic isotopic ratios of Galápagos lavas extend from enriched compositions to signatures indistinguishable from depleted mid-ocean ridge basalt (MORB; e.g., White and Hofmann, 1978; Geist et al., 1988; White et al., 1993; Blichert-Toft and White, 2001; Harpp and White, 2001). In this work, we use "enriched" for material with high time-integrated U/Pb, Th/Pb, and Rb/Sr, as well as low time-integrated Sm/Nd (i.e., high $^{206}Pb/^{204}Pb$, $^{208}Pb/^{204}Pb$, $^{207}Pb/^{204}Pb$, $^{87}Sr/^{86}Sr$, and low $^{143}Nd/^{144}Nd$), and "depleted" for the opposite geochemical systematics. These same adjectives are used as comparative terms for both radiogenic isotope ratios and trace element contents throughout this study. Striking differences distinguish the older, eastern Galápagos Islands from their young western counterparts.

Whereas most of the active western shield volcanoes erupt lavas with a narrow range of major and trace element compositions (e.g., Geist et al., 2014a), the eastern islands exhibit greater compositional variability (e.g., Geist et al., 1986; Harpp and Geist, 2018). Most eastern islands are cut by fissures and faults, many of them trending broadly E-W, instead of the caldera-related structures of the young shields (Chadwick and Dieterich, 1995). The lack of a gravity high corresponding to a residual cumulate body beneath the Santa Cruz and San Cristóbal edifices confirms that these eastern islands do not have buried calderas (Cleary et al., 2020). Consequently, no straightforward evolutionary link between western and eastern Galápagos Islands has been identified to date (Harpp and Geist, 2018), despite detailed geochemical studies on islands and seamounts in the east, including Floreana (Harpp et al., 2014a) and Santiago (Gibson et al., 2012; Schwartz et al., 2020), and in the west (e.g., Geist et al., 1995; Reynolds and Geist, 1995; Allan and Simkin, 2000; Naumann et al., 2002; Geist et al., 2005; Geist et al., 2006; Geist et al., 2014a; Anderson et al., 2018; Schwartz et al., 2020).

Santa Cruz Island is located ~150 km downstream from the presumed plume center between Fernandina and Cerro Azul volcanoes (e.g., Kurz and Geist, 1999; Hooft et al., 2003) and is the second largest island in the archipelago in subaerial extent, covering an area of nearly 1000 km^2 (**Figure 1**). Previous authors have documented the complexity and diversity of Santa Cruz geochemistry (Bow, 1979; White et al., 1993; Kurz and Geist, 1999). For example, $^{87}Sr/^{86}Sr$ ratios in lavas vary from 0.7026 to 0.7031 (White et al., 1993), a significant fraction of the compositional range exhibited by the archipelago (e.g., Harpp and White, 2001). One of the most puzzling aspects of Santa Cruz is that it exhibits such a wide variation in isotopic composition, in striking contrast to the western Galápagos volcanoes, many of which erupt isotopically monotonous lavas and display little elemental variation (e.g., White et al., 1993; Allan and Simkin, 2000; Naumann et al., 2002; Geist et al., 2008; Geist et al., 2014a). An important objective of our study is to explain this dramatic difference in geochemical variation between the older, eastern Galápagos islands such as Santa Cruz and the strongly homogeneous compositions erupted by the young western shield volcanoes, in the context of the Galápagos plume and its compositional structure (e.g., Harpp and Geist, 2018; Harpp and Weis, 2020).

According to the two previous studies of Santa Cruz (Bow, 1979; Schwartz et al., 2022), field evidence indicates that the volcano has experienced two periods of volcanism and two of tectonic activity, spanning at least 1 My (White et al., 1993). Thus, exposed lavas on Santa Cruz provide an opportunity to document the geochemical evolution of Galápagos volcanoes as they have been carried downstream from the plume. In this study, we present new major element, trace element, and radiogenic isotopic data from Santa Cruz Island lavas. Our objectives are to identify the processes responsible for producing some of the most heterogeneous compositions observed at a Galápagos volcano, developing an evolutionary model for the volcanic island, and, at the broadest scale, understanding the compositional structure of the Galápagos plume.

BACKGROUND

Tectonic Setting

The Galápagos Archipelago is located ~1000 km west of South America on the Nazca plate, which is moving eastward at 51 km/Ma (Argus et al., 2011). The east-west trending Galápagos Spreading Center (GSC), where the Nazca and Cocos plates are diverging, is between 150 and 300 km north of the archipelago (**Figure 1A**). The GSC has experienced multiple southward ridge jumps during the last 5 million years, the most recent at ~1 Ma. Consequently, the GSC was closer to the Galápagos plume when the central and eastern islands were forming than it is today (Wilson and Hey, 1995; Mittelstaedt et al., 2012). Santa Cruz is one of several older islands in the central Galápagos, in addition to San Cristóbal, Santiago, Española, Floreana, Rabida,

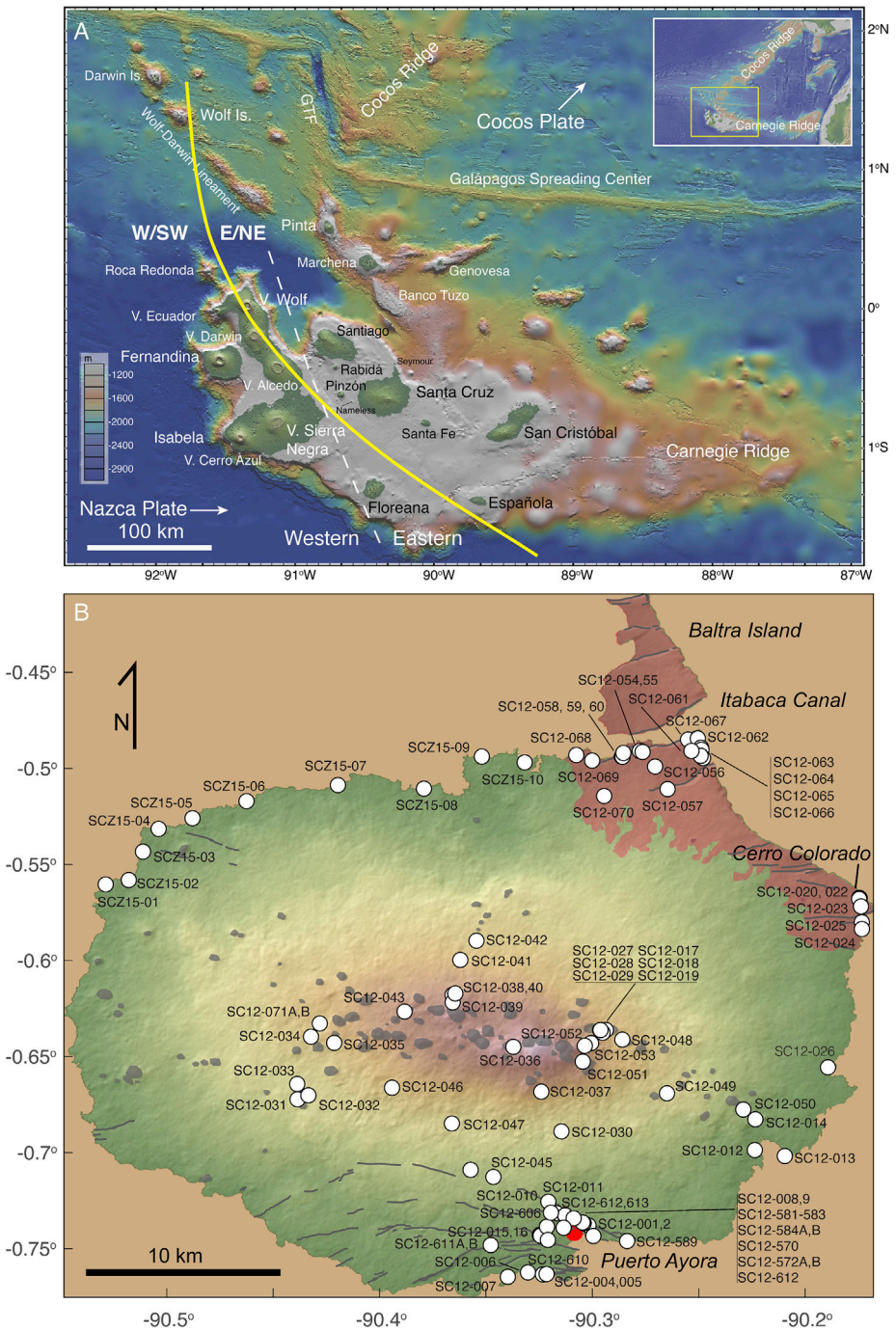


FIGURE 1 | (A) Map of the Galápagos Archipelago. Santa Cruz is located in the central Galápagos. Cocos and Nazca absolute plate motion directions are from Argus et al. (2011). The yellow line denotes the boundary between the enriched, LLSVP-sourced stripe on the W/SW side of the plume and the less enriched, ambient mantle-sourced stripe on the E/NE side of the plume; *see* text for discussion and Harpp and Weis (2020) for further details. The white dashed line indicates the line between the western and eastern volcanic morphologies in the archipelago. **(B)** Digital Elevation Model (DEM) of Santa Cruz with locations for all samples collected during the 2012 and 2015 field excursions to the island. Faults are represented as gray lines. Cinder and tuff cones are colored dark gray. Red circle is the town of Puerto Ayora, and white circles are sampling locations. Light red regions (northeast quadrant and Baltra Island) are Platform Series (Bow, 1979). According to Bow (1979), additional reversely polarized lavas (i.e., >700 ka Ma) are located in the northwest quadrant, but they are not shown here; consequently, it is possible that samples SCZ15-01 through 06 may be Platform Series as well.

Pinzón, and Santa Fe (**Figure 1A**). Santiago, Santa Cruz's neighbor to the northwest, has experienced limited historical activity, having erupted as recently as 1906 (Siebert et al., 2010), and San Cristóbal has ~5 ka lavas along its northern coastline (Geist et al., 1986; Mahr et al., 2016).

Mantle Sources

The geochemistry of Galápagos lavas is complex; lavas ranging from depleted, MORB-like compositions to enriched alkali-olivine basalts have erupted across the archipelago (e.g., White and Hofmann, 1978; Geist et al., 1988; Graham et al., 1993; White et al., 1993; Kurz and Geist, 1999; Blichert-Toft and White, 2001:; Harpp and White, 2001). White and Hofmann (1978) first noted the distinctive, horseshoe-shaped spatial distribution of geochemical signatures in the Galápagos; along the western and southern periphery of the archipelago, volcanoes erupt lavas with geochemically enriched signatures, whereas the central and eastern volcanic centers produce material with depleted, MORB-like signatures (e.g., Geist et al., 1988; White et al., 1993; Harpp and White, 2001).

Initially, the enriched geochemical horseshoe pattern was attributed to plume-asthenosphere mixing (Geist et al., 1988) or thermal entrainment of the asthenosphere into a sheared plume (White et al., 1993; Blichert-Toft and White, 2001; Harpp and White, 2001). Researchers have also invoked a spatially heterogeneous plume, in which multiple mantle reservoirs with different evolutionary histories supply the plume (Hoernle et al., 2000; Gibson et al., 2012; Harpp et al., 2014b; Harpp and Weis, 2020; Gleeson et al., 2021). Harpp and White (2001) established that at least four isotopically distinct mantle endmembers are required to generate the geochemical variation observed across the archipelago: *1*) plume material with primordial helium isotope signatures (PLUME; Graham et al., 1993), supplying the western shields; *2*) ancient recycled material with fluid-mobile element-enriched signatures, concentrated along the southern archipelago near Floreana Island (FLO); *3*) moderately depleted material with elevated $^{207}Pb/^{204}Pb$ and $^{208}Pb/^{204}Pb$ signatures, limited to the northern reaches of the archipelago and whose source remains enigmatic (WD); and *4*) the depleted upper mantle (DUM). Harpp and Weis (2020) proposed that the more enriched signatures originate in the Large Low Shear Velocity Province (LLSVP) at the core-mantle boundary, incorporating ancient, recycled material to provide the enriched signatures, whereas the central and eastern lavas are supplied primarily by less enriched, lower Pacific mantle. They proposed that the compositional boundary between the W/SW enriched and E/NE depleted zones of the bilaterally asymmetric plume runs ~NW-SE, cutting through the archipelago west of Santa Cruz (**Figure 1A**).

Volcanic Evolution

The archetype model for hotspot-generated ocean island evolution is based on Hawai'i (MacDonald and Katsura, 1964; Chen and Frey, 1983; Macdonald et al., 1983; Clague and Dalrymple, 1987; Clague and Dalrymple, 1988). Hawaiian volcanoes experience four lifecycle stages, explained by their proximity to the plume as the edifice is carried northwest by the Pacific plate: *1*) the pre-shield stage, when the volcano is on the upstream periphery of the plume, generating low-degree melts with alkalic compositions; *2*) the shield stage, dominated by high-volume, high-degree melts and tholeiitic lavas; *3*) the post-shield phase, primarily alkalic, low degree melts at the downstream edge of the plume; and *4*) rejuvenated volcanism, which occurs after ~0.25–2.5 Ma of quiescence (e.g., Clague and Dalrymple, 1987, 1988).

Galápagos volcanoes do not conform to the Hawaiian evolutionary sequence (Geist et al., 2014a; Harpp and Geist, 2018; Harpp and Weis, 2020). For example, the central and eastern Galápagos volcanoes do not exhibit clearly defined post-shield or rejuvenation stages (e.g., Geist et al., 1986; Gibson et al., 2012; Harpp et al., 2014a). Furthermore, the eastern Galápagos volcanoes bear little morphological resemblance to the current western shields. The older islands of Santiago, Santa Cruz, San Cristóbal, and Española lack submarine rift zones and calderas characteristic of many western shields (and most Hawaiian volcanoes) and lack buried calderas (Cleary et al., 2020). Like Hawaiian volcanoes, however, the eastern volcanoes also experience extended volcanically active phases, erupting for >2 m.y. beyond when the island was located near the plume center (e.g., Geist et al., 1986; White et al., 1993; Mahr et al., 2016). Finally, petrographic modeling by Geist et al. (1998) indicates that magmatic cooling in the eastern islands, including Santa Cruz, is primarily controlled by clinopyroxene rather than plagioclase. They conclude that the bulk of the fractionation in eastern Galápagos island melts is taking place in the deep crust, at depths within the mantle in the range of 17–23 km. This depth interval is greater than that for the young western shields, whose magmatic plumbing systems are at shallower depths (~10 km; Geist et al., 1998; 2014a) owing to their more robust magma supplies.

As a consequence of the striking differences between the eastern and western Galápagos volcanoes, Harpp and Geist (2018) proposed that the eastern islands are magmatically starved compared to the western shields, preventing development of thermochemically buffered magmatic systems capable of supporting long-lived magma chambers and caldera formation (Geist et al., 2014a). They attribute the lower magma flux to the proximity of the GSC between 1 and 5 Ma (e.g., Wilson and Hey, 1995; Mittelstaedt et al., 2012), which may have diverted plume material toward the ridge, away from the volcanoes developing at the time, which are currently the older, central and eastern Galápagos islands.

Previous Field Studies of Santa Cruz Island

As the largest island in the center of the archipelago, Santa Cruz provides an opportunity to document how ocean islands mature as they are carried downstream from a mantle plume. Three previous field studies of Santa Cruz's development (Bow, 1979; Schwartz, 2014 M.Sc. thesis; Schwartz et al., 2022; the original Masters' thesis of Schwartz is available here: https://drive.google.com/file/d/1iMk9grGWRNORT7K2JxjsoXs4EY6IPKRU/view?usp=sharing), conclude that Santa Cruz has experienced two periods of volcanism and two periods of tectonic activity since

the volcano migrated east from the hotspot center during the last >1 million years, as follows (Ar-Ar ages all from Schwartz et al., 2022):

1. Formation of the Platform Series, emplaced primarily between 1620 ± 15 and 1160 ± 35 ka, with only a trivial volume of activity extending beyond 1160 ka.
2. Normal faulting of the Platform Series, exposed in the NE part of the island and striking sub-parallel to highland vent systems; faulting occurred since 1160 ± 35 ka and likely between 780 and 500 ka (Bow, 1979; Schwartz et al., 2022) and only crosscuts Platform lavas.
3. Formation of the Shield Series between 271 ± 17 and 74 ± 38 ka, erupted from the E-W summit vent system and deposited primarily along the southern flank of the island).
4. Formation of southern flank faults between 274 ± 18 and 38 ± 8 ka, which overlaps with the emplacement of the Shield Series, ending ~20 ka.

The Platform Series consists of lavas exposed primarily along the northeastern coast of Santa Cruz (**Figure 1B**), as well as Baltra and Seymour Islands, which are faulted remains of Santa Cruz (Bow, 1979). Platform Series lavas are both subaerial and submarine, thick (~10 m) pahoehoe flows, and many are interbedded with beach and shallow water deposits (Bow, 1979). Field observations confirm that the Platform Series lies stratigraphically below the Shield Series wherever a contact between the units is exposed. Schwartz et al. (2022) identified Platform Series lavas in several locations (e.g., SC12-572B) along the North Puerto Ayora fault that extends NW from Santa Cruz's largest town, along the south coast of the island. The 416 ± 36 ka (2σ) age of SC12-572B (Schwartz et al., 2022) is anomalously young for a Platform Series lava. Thus, the Platform Series may have been active as recently as ~0.4 Ma (nearly concurrent with some Shield Series flows), and may not have shut down entirely at ~1.1 Ma (White et al., 1993; Schwartz et al., 2022), but the lack of any other Platform Series samples from <1.1 Ma suggests that sample SC12-572B represents only a trivially small-volume tail of activity, and that the bulk of the Platform Series was emplaced between 1.6 and 1.1 Ma.

The Shield Series consists of predominantly pahoehoe flows erupted from the WNW-trending fissure system bisecting the island (**Figure 1B**; Bow, 1979). The fissures are manifested as a quasi-linear arrangement of late-stage cinder cones and pit craters in the highlands and tuff cones near the coast. Gravity studies by Cleary et al. (2020) confirm that they do not define the remnants of an in-filled caldera (Bow, 1979). Shield Series flows exhibit features typical of pahoehoe lava, with inflation lobes and tumuli.

Two Shield Series lavas have been dated using cosmogenic helium techniques, yielding ages between 0.111 ± 0.006 Ma and 0.585 Ma ± 0.013 (Kurz and Geist, 1999). On the basis of Ar-Ar ages and normal paleomagnetic polarity, Schwartz et al. (2022) estimates that the Shield Series became active ~700 ka. Consequently, >1 million years of volcanic and geochemical history are preserved and exposed at Santa Cruz. Unfortunately, dense vegetation severely limits detailed field mapping across most of the island.

Along the northern, eastern, and southern coasts, a series of normal faults strike sub-parallel to the highland cinder cone lineation (Schwartz et al., 2022; **Figure 1B**). Schwartz et al. (2022) proposes that the faults define two distinct periods of tectonic activity. The older faults, limited to the northeast quadrant, only crosscut Platform Series lavas and formed since 1160 ± 35 ka, and likely between 780 and 500 ka (Bow, 1979; Schwartz et al., 2022), as a consequence of regional extension early in the island's construction. The younger faults, along the southern flank, formed contemporaneously with the Shield Series, between 274 ± 18 and 38 ± 8 ka (Schwartz et al., 2022). Schwartz et al. (2022) attributes the younger faults to southward extension of the island caused by E-W-oriented magmatic intrusions that ceased ~20 ka.

MATERIALS AND METHODS

During July and August 2012, we collected >70 samples from Santa Cruz Island (**Figure 1B**), each of which was located by GPS (**Table 1**). An additional 10 samples were collected along the north shore in 2015. Owing to the lack of deeply eroded valleys or a caldera, most samples in this study originate from the uppermost stratigraphic layers of the volcano; only a handful of samples were collected from within pit craters; consequently we have no samples from early in the island's development. The rocks were broken into small chips by a jaw-crusher, and then examined under a binocular microscope to collect ~15 g of fresh material for chemical analysis.

Major and Trace Element Analysis

Samples were analyzed for major elements at Colgate University by X-Ray Fluorescence (XRF) spectroscopy following a method adapted from Norrish and Hutton (1969) on a Philips PW240 instrument. Replicate analyses of USGS Standard Reference Material (SRM) BHVO-2 yielded precision for all major element oxides <0.85% (1σ; **Table 1**). The precision of triplicate analyses of two samples (SC12-001 and SC12-063) yielded <1% relative standard deviation (RSD, 1σ) for all major elements, except P_2O_5 (1.2% RSD, 1σ). A subset of previously collected samples (Bow, 1979) was analyzed by XRF at Washington State University's (WSU) GeoAnalytical Laboratory following procedures described in Johnson et al. (1999). Whole rock major element data were not adjusted for phenocryst content (e.g., crystal accumulation).

Trace element concentrations were determined *via* Inductively Coupled Plasma-Mass Spectrometry (ICP-MS) using a Varian 820MS quadrupole instrument at Colgate University. A 200-ppb internal standard solution of ^{115}In, ^{133}Cs, ^{182}W, and ^{205}Tl was diluted to 1:20 using in-line mixing during analysis. Analyte masses were corrected to the nearest internal standard mass of those listed above to account for instrument drift, according to the method developed by Eggins et al. (1997). External standard curves were created using solutions of USGS SRMs BHVO-2, BIR-1, DNC-1, AGV-2, and W-2. The Pearson correlation coefficients of the standard curves were consistently >0.998. A solution of USGS SRM W-2 was analyzed every five to six samples

TABLE 1 | Santa Cruz sample locations and major element contents.

TABLE 1: Sample location and major element abundances (wt.%)

Sample	Compositional group	Latitude (degrees)	Longitude (degrees)	Altitude (m)	Mg#	SiO_2	TiO_2	Al_2O_3	FeO	CaO	MgO	MnO	K_2O	Na_2O	P_2O_5	Analytical total
SC-194R	Platform	—	—	—	49.74	48.65	2.09	16.84	10.66	11.78	5.92	0.20	0.41	3.14	0.30	96.98
SC-196P	Platform	—	—	—	47.51	47.82	2.76	14.72	13.08	10.89	6.64	0.22	0.36	3.24	0.27	99.19
SC-196R	Platform	—	—	—	47.35	47.78	2.75	14.77	13.12	10.90	6.62	0.22	0.37	3.19	0.27	99.10
SC12-008	Platform exposed in fault	−0.73420	−90.30904	28	63.41	47.07	1.29	16.73	10.44	11.14	10.15	0.18	0.23	2.61	0.17	98.18
SC12-009	Platform exposed in fault	−0.73273	−90.31274	34	52.14	48.46	2.06	17.20	10.13	11.15	6.19	0.17	0.53	3.70	0.40	99.13
SC12-020	Platform	−0.56739	−90.17453	36	45.02	47.57	2.63	14.64	13.28	11.65	6.10	0.23	0.41	3.21	0.29	98.89
SC12-020 re	Platform	−0.56739	−90.17453	36	42.41	46.88	2.59	14.43	14.54	11.48	6.01	0.22	0.40	3.17	0.28	98.89
SC12-022	Platform	−0.56759	−90.17432	28	44.39	46.80	2.67	14.27	14.72	11.07	6.59	0.22	0.37	2.98	0.30	98.16
SC12-025	Platform	−0.58009	−90.17335	27	40.91	49.55	2.26	17.47	10.97	10.75	4.26	0.22	0.56	3.56	0.39	98.77
SC12-054	Platform	−0.49092	−90.27768	50	50.59	46.76	1.96	16.20	12.93	10.80	7.43	0.20	0.35	3.09	0.27	99.24
SC12-055	Platform	−0.49145	−90.27637	40	51.85	46.75	1.87	16.39	12.66	10.81	7.65	0.19	0.33	3.08	0.25	98.94
SC12-056	Platform	−0.49903	−90.27050	48	59.25	47.61	1.77	14.56	12.22	10.22	9.97	0.17	0.35	2.88	0.25	98.83
SC12-057	Platform	−0.51080	−90.26462	88	45.89	46.71	2.36	15.43	13.56	10.82	6.45	0.20	0.45	3.69	0.33	98.73
SC12-058	Platform	−0.49198	−90.28540	14	59.54	46.48	1.64	16.20	11.55	11.44	9.53	0.17	0.25	2.51	0.21	98.70
SC12-059	Platform	−0.49388	−90.28613	28	55.04	47.34	2.09	16.87	11.17	10.91	7.67	0.18	0.33	3.15	0.28	98.57
SC12-059 re	Platform	−0.49388	−90.28613	28	52.41	46.76	2.06	16.66	12.27	10.77	7.58	0.18	0.32	3.11	0.28	98.57
SC12-060	Platform	−0.49394	−90.28582	30	42.17	46.38	2.72	15.18	15.02	10.05	6.14	0.23	0.47	3.44	0.36	98.81
SC12-061	Platform	−0.48504	−90.25501	49	40.95	47.87	3.36	13.08	14.60	11.22	5.68	0.21	0.56	2.97	0.44	98.19
SC12-062	Platform	−0.48445	−90.25042	48	40.68	48.09	3.46	13.12	14.77	10.62	5.68	0.21	0.54	3.07	0.43	98.24
SC12-063	Platform	−0.48924	−90.24891	19	35.02	48.31	3.18	13.49	15.44	9.49	4.67	0.25	0.67	3.85	0.65	98.79
SC12-064	Platform	−0.49030	−90.24870	22	44.26	48.75	3.38	13.49	13.29	10.91	5.92	0.22	0.51	3.06	0.47	99.07
SC12-065	Platform	−0.49461	−90.24798	28	64.02	46.60	1.64	15.57	10.75	11.34	10.73	0.17	0.26	2.68	0.25	98.58
SC12-066	Platform	−0.49347	−90.24911	32	42.13	47.21	2.78	14.39	14.49	10.62	5.92	0.23	0.46	3.53	0.36	99.01
SC12-067	Platform	−0.49090	−90.25342	48	41.18	47.04	2.82	14.58	14.61	10.61	5.74	0.22	0.46	3.54	0.38	99.21
SC12-068	Platform	−0.49303	−90.30752	10	51.39	46.76	2.16	16.54	12.59	10.53	7.47	0.18	0.36	3.11	0.30	98.55
SC12-069	Platform	−0.49594	−90.30007	16	61.38	46.19	1.59	15.26	12.18	10.52	10.86	0.18	0.26	2.71	0.23	99.08
SC12-070	Platform	−0.51437	−90.29446	74	61.61	46.99	1.53	14.55	12.07	10.87	10.87	0.17	0.17	2.58	0.19	98.74
SC12-572B	Platform exposed in fault	−0.73636	−90.30458	38	51.24	48.13	2.09	17.65	9.99	11.34	5.89	0.17	0.54	3.78	0.40	98.97
SC12-572B re	Platform exposed in fault	−0.73636	−90.30458	38	48.62	47.60	2.07	17.46	10.98	11.22	5.83	0.17	0.54	3.74	0.39	98.97
SC-64	Shield Low K/Ti (<0.15)	—	—	—	67.92	46.62	1.06	16.46	10.09	11.06	11.99	0.17	0.09	2.36	0.10	99.27
SC-78	Shield Low K/Ti (<0.15)	—	—	—	67.13	46.46	1.10	15.87	10.71	10.96	12.27	0.17	0.09	2.27	0.09	97.38
SC-163	Shield Low K/Ti (<0.15)	—	—	—	50.38	46.12	2.18	16.61	13.76	9.08	7.84	0.20	0.30	3.63	0.27	99.11
SC-193	Shield Low K/Ti (<0.15)	—	—	—	59.72	46.23	1.59	16.51	11.88	10.23	9.88	0.17	0.23	3.07	0.21	99.00
SC-193 re	Shield Low K/Ti (<0.15)	—	—	—	62.60	47.26	1.60	17.03	10.54	10.05	9.89	0.17	0.22	3.05	0.19	99.66
SC-202	Shield Low K/Ti (<0.15)	—	—	—	66.04	46.88	1.22	16.26	10.65	10.53	11.62	0.17	0.12	2.46	0.10	100.39
SC-206A	Shield Low K/Ti (<0.15)	—	—	—	53.51	46.05	2.70	18.64	11.83	9.67	7.64	0.19	0.14	2.80	0.33	95.94
SC12-001	Shield Low K/Ti (<0.15)	−0.73792	−90.30180	26	60.51	46.11	0.92	17.23	11.32	12.11	9.73	0.17	0.08	2.24	0.08	98.72
SC12-006	Shield Low K/Ti (<0.15)	−0.76233	−90.33024	0	63.79	45.88	1.26	16.07	11.40	11.19	11.27	0.16	0.15	2.46	0.15	98.42
SC12-011	Shield Low K/Ti (<0.15)	−0.73148	−90.31692	47	66.04	45.64	1.14	14.93	11.79	10.79	12.86	0.18	0.15	2.38	0.13	98.83
SC12-013	Shield Low K/Ti (<0.15)	−0.70175	−90.20954	3	61.04	46.06	1.34	15.90	11.79	11.40	10.37	0.17	0.19	2.61	0.17	98.87
SC12-014	Shield Low K/Ti (<0.15)	−0.68263	−90.22337	48	54.85	47.59	1.53	16.15	11.66	11.99	7.95	0.20	0.15	2.56	0.21	99.15
SC12-015	Shield Low K/Ti (<0.15)	−0.74286	−90.32467	41	61.65	46.20	1.29	16.41	11.34	11.52	10.22	0.16	0.16	2.56	0.14	98.80
SC12-015 re	Shield Low K/Ti (<0.15)	−0.74286	−90.32467	41	64.11	46.73	1.30	16.60	10.32	11.65	10.34	0.16	0.16	2.59	0.14	98.80
SC12-016	Shield Low K/Ti (<0.15)	−0.74328	−90.32431	38	58.52	46.63	1.37	16.49	11.73	11.47	9.28	0.17	0.17	2.54	0.15	98.59
SC12-019	Shield Low K/Ti (<0.15)	−0.63662	−90.29538	389	60.03	46.34	1.08	16.91	11.49	11.64	9.68	0.17	0.13	2.42	0.13	99.05
SC12-026	Shield Low K/Ti (<0.15)	−0.65736	−90.18756	18	64.67	46.46	1.28	15.94	10.71	11.88	11.00	0.17	0.09	2.34	0.12	99.30

(Continued on following page)

TABLE 1 | (*Continued*) Santa Cruz sample locations and major element contents.

TABLE 1: Sample location and major element abundances (wt.%)

Sample	Compositional group	Latitude (degrees)	Longitude (degrees)	Altitude (m)	Mg#	SiO_2	TiO_2	Al_2O_3	FeO	CaO	MgO	MnO	K_2O	Na_2O	P_2O_5	Analytical total
SC12-030	Shield Low K/Ti (<0.15)	−0.68891	−90.31452	236	66.24	45.65	1.33	16.24	11.20	10.20	12.33	0.16	0.17	2.50	0.20	98.37
SC12-036	Shield Low K/Ti (<0.15)	−0.64494	−90.33713	794	45.74	46.41	2.61	16.58	13.48	10.11	6.38	0.19	0.33	3.48	0.44	98.64
SC12-042	Shield Low K/Ti (<0.15)	−0.58966	−90.35444	346	64.55	45.46	1.16	15.12	12.23	10.65	12.50	0.17	0.13	2.45	0.12	98.67
SC12-043	Shield Low K/Ti (<0.15)	−0.62654	−90.38822	614	54.76	46.48	1.95	16.06	12.85	9.83	8.73	0.18	0.27	3.34	0.30	98.67
SC12-051	Shield Low K/Ti (<0.15)	−0.65260	−90.30449	540	53.43	46.73	2.25	16.76	12.49	9.44	8.04	0.19	0.31	3.43	0.36	98.83
SC12-071B	Shield Low K/Ti (<0.15)	−0.63275	−90.42808	379	53.50	46.57	2.32	16.56	12.76	9.12	8.24	0.17	0.29	3.64	0.31	98.79
SC12-570	Shield Low K/Ti (<0.15)	−0.73675	−90.30406	—	—	—	—	—	—	—	—	—	—	—	—	—
SC12-581	Shield Low K/Ti (<0.15)	−0.73418	−90.30901	35	60.87	46.09	1.52	15.83	12.17	10.03	10.62	0.17	0.20	3.16	0.21	98.05
SC12-584B	Shield Low K/Ti (<0.15)	−0.73856	−90.32131	31	61.79	46.11	1.29	16.21	11.61	11.27	10.53	0.17	0.16	2.51	0.14	98.23
SCZ15-01	Shield Low K/Ti (<0.15)	−0.56039	−90.52869	0	67.69	46.68	1.05	16.37	10.15	11.21	11.93	0.17	0.09	2.24	0.11	
SCZ15-02	Shield Low K/Ti (<0.15)	−0.55811	−90.51784	0	67.04	46.93	1.03	16.59	9.95	11.39	11.35	0.17	0.11	2.36	0.11	98.78
SCZ15-04	Shield Low K/Ti (<0.15)	−0.53149	−90.50382	0	58.99	47.15	1.50	16.68	11.09	11.61	8.95	0.19	0.15	2.48	0.20	98.33
SCZ15-08	Shield Low K/Ti (<0.15)	−0.51055	−90.37914	0	65.62	46.88	1.28	15.72	11.00	10.41	11.78	0.19	0.15	2.45	0.13	98.22
SCZ15-09	Shield Low K/Ti (<0.15)	−0.49385	−90.35193	0	63.56	47.23	0.97	17.45	10.38	10.98	10.15	0.17	0.10	2.49	0.08	98.61
SCZ15-10	Shield Low K/Ti (<0.15)	−0.49689	−90.33179	0	63.06	47.61	0.99	17.07	10.32	11.31	9.89	0.17	0.10	2.44	0.10	98.42
SC-46	Shield Mid K/Ti (0.15–0.24)	—	—	—	68.44	46.41	1.42	15.92	10.32	10.16	12.56	0.17	0.24	2.61	0.18	100.05
SC-130	Shield Mid K/Ti (0.15–0.24)	—	—	—	55.51	46.86	2.70	15.76	11.84	9.56	8.29	0.20	0.60	3.73	0.45	99.90
SC-135	Shield Mid K/Ti (0.15–0.24)	—	—	—	61.65	47.15	1.94	15.99	10.97	9.43	9.89	0.19	0.44	3.63	0.38	98.58
SC-155	Shield Mid K/Ti (0.15–0.24)	—	—	—	51.87	48.08	2.30	17.53	11.30	9.77	6.83	0.18	0.36	3.27	0.38	98.08
SC12-002	Shield Mid K/Ti (0.15–0.24)	−0.74343	−90.29953	5	58.15	46.37	1.93	15.86	12.33	9.67	9.61	0.17	0.31	3.45	0.29	98.94
SC12-007	Shield Mid K/Ti (0.15–0.24)	−0.76465	−90.33971	0	53.45	46.81	2.08	15.77	12.99	9.15	8.37	0.18	0.41	3.86	0.37	98.81
SC12-010	Shield Mid K/Ti (0.15–0.24)	−0.72552	−90.32068	88	64.76	45.65	1.42	15.77	11.50	10.56	11.85	0.17	0.27	2.54	0.26	98.55
SC12-012	Shield Mid K/Ti (0.15–0.24)	−0.69863	−90.22364	0	57.60	47.27	2.04	16.05	11.44	9.80	8.72	0.19	0.44	3.67	0.38	99.52
SC12-012 re	Shield Mid K/Ti (0.15–0.24)	−0.69863	−90.22364	0	55.02	46.67	2.01	15.85	12.55	9.68	8.61	0.19	0.43	3.63	0.38	99.52
SC12-018	Shield Mid K/Ti (0.15–0.24)	−0.63613	−90.29362	317	58.63	46.09	1.88	15.49	12.40	10.08	9.86	0.19	0.38	3.30	0.31	98.71
SC12-021	Shield Mid K/Ti (0.15–0.24)	−0.56800	−90.17459	33	48.18	47.01	1.98	16.93	12.20	11.53	6.36	0.20	0.32	3.18	0.28	99.02
SC12-023	Shield Mid K/Ti (0.15–0.24)	−0.57188	−90.17373	35	54.39	46.70	2.24	16.31	12.34	9.42	8.26	0.17	0.36	3.81	0.40	98.34
SC12-024	Shield Mid K/Ti (0.15–0.24)	−0.58360	−90.17330	16	53.32	46.67	2.19	16.52	12.48	9.21	8.00	0.17	0.46	3.92	0.39	98.42
SC12-029	Shield Mid K/Ti (0.15–0.24)	−0.63619	−90.29632	455	49.50	46.13	2.30	16.24	13.76	9.16	7.56	0.19	0.43	3.84	0.39	98.50
SC12-031	Shield Mid K/Ti (0.15–0.24)	−0.67224	−90.43854	250	53.11	46.37	2.33	15.84	13.11	8.96	8.33	0.19	0.49	3.92	0.47	98.32
SC12-032	Shield Mid K/Ti (0.15–0.24)	−0.67014	−90.43343	255	55.46	47.14	1.92	17.04	11.50	10.06	8.03	0.16	0.41	3.46	0.28	98.35
SC12-033	Shield Mid K/Ti (0.15–0.24)	−0.66427	−90.43870	227	62.92	46.82	1.38	16.78	10.58	11.12	10.07	0.17	0.22	2.66	0.19	98.76
SC12-034	Shield Mid K/Ti (0.15–0.24)	−0.63963	−90.43221	390	60.10	45.86	1.99	15.74	12.21	10.11	10.32	0.18	0.45	2.80	0.35	98.74
SC12-035	Shield Mid K/Ti (0.15–0.24)	−0.64285	−90.42131	425	54.44	46.23	1.85	16.29	13.17	9.57	8.83	0.18	0.28	3.29	0.29	98.75
SC12-037	Shield Mid K/Ti (0.15–0.24)	−0.66826	−90.32398	480	54.90	45.14	2.48	16.64	13.70	8.76	9.36	0.20	0.48	2.76	0.49	98.32
SC12-038	Shield Mid K/Ti (0.15–0.24)	−0.61789	−90.36569	623	58.42	46.07	2.05	16.98	11.59	10.26	9.13	0.16	0.30	3.21	0.25	98.55
SC12-041	Shield Mid K/Ti (0.15–0.24)	−0.59970	−90.36203	413	53.89	46.33	2.25	16.34	12.70	9.24	8.33	0.18	0.46	3.81	0.37	98.80
SC12-044	Shield Mid K/Ti (0.15–0.24)	−0.70893	−90.35719	145	57.19	46.47	1.84	16.01	12.66	9.03	9.49	0.18	0.34	3.67	0.29	98.62
SC12-046	Shield Mid K/Ti (0.15–0.24)	−0.66620	−90.39413	388	48.23	46.75	2.80	16.29	13.05	8.46	6.82	0.19	0.55	4.56	0.53	99.71
SC12-047	Shield Mid K/Ti (0.15–0.24)	−0.68480	−90.36601	251	54.39	46.94	2.03	16.92	12.06	9.01	8.07	0.16	0.44	4.01	0.36	98.66
SC12-048	Shield Mid K/Ti (0.15–0.24)	−0.64116	−90.28589	434	47.22	46.80	2.77	16.30	13.07	9.03	6.56	0.19	0.62	4.14	0.51	99.05
SC12-050	Shield Mid K/Ti (0.15–0.24)	−0.67753	−90.22904	75	56.83	46.28	2.18	16.43	11.89	10.07	8.78	0.17	0.47	3.40	0.32	98.72
SC12-071A	Shield Mid K/Ti (0.15–0.24)	−0.63275	−90.42808	379	61.37	45.39	1.91	15.69	12.29	10.45	10.95	0.18	0.33	2.50	0.29	98.71
SCZ15-03	Shield Mid K/Ti (0.15–0.24)	−0.54332	−90.51119	0	61.45	47.07	2.03	16.88	10.63	9.68	9.50	0.17	0.36	3.36	0.32	98.39
SCZ15-05	Shield Mid K/Ti (0.15–0.24)	−0.52595	−90.48788	0	57.17	47.47	2.02	17.01	11.27	9.40	8.44	0.18	0.35	3.55	0.33	98.14
SCZ15-06	Shield Mid K/Ti (0.15–0.24)	−0.51707	−90.46250	0	62.57	47.22	1.98	16.78	10.33	9.45	9.69	0.16	0.44	3.60	0.35	98.66

(Continued on following page)

TABLE 1 | (*Continued*) Santa Cruz sample locations and major element contents.

TABLE 1: Sample location and major element abundances (wt.%)

Sample	Compositional group	Latitude (degrees)	Longitude (degrees)	Altitude (m)	Mg#	SiO_2	TiO_2	Al_2O_3	FeO	CaO	MgO	MnO	K_2O	Na_2O	P_2O_5	Analytical total
SCZ15-07	Shield Mid K/Ti (0.15–0.24)	−0.50869	−90.41955	0	56.16	46.81	2.64	16.60	11.74	9.00	8.44	0.17	0.54	3.67	0.39	98.46
SC-151	Shield High K/Ti (>0.24)	—	—	—	45.24	48.24	2.88	17.04	11.58	8.21	5.37	0.20	0.82	4.95	0.71	99.13
SC-164	Shield High K/Ti (>0.24)	—	—	—	47.91	47.56	2.23	16.57	12.55	9.11	6.48	0.20	0.59	4.20	0.51	99.11
SC-172	Shield High K/Ti (>0.24)	—	—	—	50.25	47.71	2.52	16.59	11.68	8.79	6.62	0.20	0.70	4.65	0.53	98.36
SC-203R	Shield High K/Ti (>0.24)	—	—	—	49.69	47.98	2.54	17.11	11.59	8.65	6.42	0.19	0.71	4.28	0.52	98.69
SC-204R	Shield High K/Ti (>0.24)	—	—	—	52.06	47.44	2.59	16.76	11.52	8.81	7.02	0.20	0.78	4.33	0.55	100.62
SC-206B	Shield High K/Ti (>0.24)	—	—	—	46.30	49.04	2.54	17.55	11.22	8.42	5.42	0.20	0.64	4.31	0.65	97.90
SC-48	Shield High K/Ti (>0.24)	—	—	—	49.17	47.76	1.95	17.97	10.57	11.21	5.74	0.17	0.52	3.72	0.38	99.51
SC-48 re	Shield High K/Ti (>0.24)	—	—	—	52.19	48.66	1.99	18.44	9.37	11.09	5.73	0.16	0.51	3.70	0.35	98.87
SC-68	Shield High K/Ti (>0.24)	—	—	—	48.18	48.42	2.68	17.10	11.52	8.18	6.01	0.19	0.77	4.47	0.66	98.20
SC-207	Shield High K/Ti (>0.24)	—	—	—	48.65	48.36	2.43	16.89	11.85	8.16	6.30	0.20	0.63	4.66	0.52	100.31
SC-207 re	Shield High K/Ti (>0.24)	—	—	—	48.53	48.36	2.44	16.85	11.89	8.15	6.29	0.20	0.62	4.67	0.52	99.96
SC12-005	Shield High K/Ti (>0.24)	−0.76335	−90.32322	0	52.34	47.38	1.86	17.56	10.69	11.58	6.58	0.16	0.46	3.39	0.33	98.73
SC12-017	Shield High K/Ti (>0.24)	−0.63613	−90.29362	317	44.35	49.09	2.46	16.26	11.89	8.53	5.31	0.20	0.91	4.79	0.55	101.05
SC12-027	Shield High K/Ti (>0.24)	−0.63759	−90.29519	416	46.22	47.84	2.72	16.64	11.72	8.73	5.65	0.21	0.88	5.01	0.62	98.41
SC12-027 re	Shield High K/Ti (>0.24)	−0.63759	−90.29519	416	43.62	47.22	2.68	16.42	12.85	8.62	5.58	0.20	0.86	4.95	0.61	98.41
SC12-028	Shield High K/Ti (>0.24)	−0.63616	−90.29613	(~450)	53.13	47.60	1.73	16.93	11.52	10.04	7.33	0.18	0.49	3.79	0.39	98.68
SC12-039	Shield High K/Ti (>0.24)	−0.62178	−90.36564	649	49.93	46.99	2.35	16.44	12.71	8.78	7.11	0.19	0.65	4.26	0.51	98.72
SC12-040	Shield High K/Ti (>0.24)	−0.61715	−90.36520	603	49.58	46.70	2.59	16.22	12.68	9.00	7.00	0.20	0.79	4.27	0.56	99.02
SC12-049	Shield High K/Ti (>0.24)	−0.66909	−90.26491	268	49.48	47.58	2.48	15.80	12.87	8.81	7.07	0.19	0.72	3.91	0.55	99.15
SC12-053	Shield High K/Ti (>0.24)	−0.64296	−90.30057	529	45.57	47.64	2.39	16.61	12.69	9.23	5.96	0.20	0.61	4.12	0.54	98.67
SC12-572A	Shield High K/Ti (>0.24)	−0.73636	−90.30458	38	47.58	48.02	2.03	17.65	10.91	11.18	5.55	0.17	0.52	3.56	0.42	98.65
SC12-611B	Shield High K/Ti (>0.24)	−0.74902	−90.34772	31	—	—	—	—	—	—	—	—	—	—	—	—
SC12-004	Shield No K/Ti	−0.76318	−90.32148	6	—	—	—	—	—	—	—	—	—	—	—	—
SC12-045	Shield No K/Ti	−0.71260	−90.34650	137	—	—	—	—	—	—	—	—	—	—	—	—
SC12-052	Shield No K/Ti	−0.64436	−90.30355	554	—	—	—	—	—	—	—	—	—	—	—	—
SC12-582	Shield No K/Ti	−0.73264	−90.31273	—	—	—	—	—	—	—	—	—	—	—	—	—
SC12-583	Shield No K/Ti	−0.73417	−90.30876	41	—	—	—	—	—	—	—	—	—	—	—	—
SC12-584A	Shield No K/Ti	−0.73856	−90.32131	31	—	—	—	—	—	—	—	—	—	—	—	—
SC12-589	Shield No K/Ti	−0.74605	−90.28364	38	—	—	—	—	—	—	—	—	—	—	—	—
SC12-606	Shield No K/Ti	−0.73128	−90.31945	34	—	—	—	—	—	—	—	—	—	—	—	—
SC12-610	Shield No K/Ti	−0.74549	−90.32088	42	—	—	—	—	—	—	—	—	—	—	—	—
SC12-611A	Shield No K/Ti	−0.74902	−90.34772	31	—	—	—	—	—	—	—	—	—	—	—	—
SC12-612	Shield No K/Ti	−0.73911	−90.31348	—	—	—	—	—	—	—	—	—	—	—	—	—
SC12-613	Shield No K/Ti	−0.73911	−90.31348	0	—	—	—	—	—	—	—	—	—	—	—	—

Major element abundances are reported in weight % and normalized to 100%; analytical totals are included for reference. Samples lacking location data were not gathered in the field during our expeditions, but were obtained from existing collections by Bow (1979) and White et al. (1993). Several sample replicates (indicated with "re") for major element analyses are also included. See *text for explanation of compositional groups.*

as an unknown and yielded <4% RSD (1σ) precision for elements with atomic masses greater than 89. Only Sc and Rb registered precisions >8% (1σ) in replicate W-2 solutions run as unknowns; elements with masses less than 89 amu had precisions <8% and usually <5%. Corrections were made for isobaric interferences on Gd.

Radiogenic Isotope Analysis

Strontium, neodymium, and lead radiogenic isotope analyses were performed at the University of Florida's Department of Geological Sciences **Table 3**. Samples were leached aggressively to remove sea salt spray and weathering products according to procedures in Goss et al. (2010). All subsequent chromatographic elemental separations were performed in a class 100 clean laboratory. Samples were diluted with 2% HNO_3 to achieve ~4–6 V total ion current for each solution concentration. To monitor instrument performance, NBS 987 Sr and JNDi Nd standards were analyzed every four samples. External precision for Sr (2σ) is 0.00002 (n = 42) and 0.00002 (n = 91) for Nd. Strontium results were corrected to a $^{88}Sr/^{86}Sr$ value of 0.1194 and neodymium ratios were normalized to a $^{146}Nd/^{144}Nd$ value of 0.7219 using an exponential law for mass bias fractionation. Strontium and neodymium isotope ratios presented here have been corrected to SRM NBS 987 Sr ($^{87}Sr/^{86}Sr$ = 0.710248) and La Jolla ($^{143}Nd/^{144}Nd$ = 0.511858). The Pb standard, NBS 981, achieved a long-term (June 2012–January 2013) average of $^{206}Pb/^{204}Pb$ = 16.938 ± 0.004 (2σ), $^{207}Pb/^{204}Pb$ = 15.488 ± 0.003 (2σ), and $^{208}Pb/^{204}Pb$ = 36.693 ± 0.009 (2σ). The Pb isotopic analyses presented here are corrected to NBS 981 values $^{206}Pb/^{204}Pb$ = 16.9405, $^{207}Pb/^{204}Pb$ = 15.4963, and $^{208}Pb/^{204}Pb$ = 36.7219 (Weis et al., 2006). A subset of Santa Cruz samples were analyzed at the Pacific Centre for Isotopic and Geochemical Research (PCIGR) at the University of British Columbia, according to methods described in Harpp and Weis (2020). All data have been corrected to the same reference values as samples analyzed at the University of Florida.

RESULTS

Petrography

According to thin section observations, lavas in the Platform Series are aphyric to plagioclase-phyric with a subophitic groundmass composed of plagioclase, clinopyroxene, olivine, and opaque oxides. Plagioclase phenocrysts are up to 1 cm long, and constitute 1–3% of Platform Series samples. A plagioclase ultraphyric lava in the Cerro Colorado area contains 25% modal plagioclase, with crystals up to 10 × 5 mm, but its major element composition is not exceptional compared to the others from the same unit. Most lavas have sparse (<2%) olivine phenocrysts ~1 mm in diameter; however, olivine and plagioclase are often present in glomerocrysts up to 1 cm in diameter.

Shield Series lavas include plagioclase- and olivine-phyric rocks. Plagioclase and Ti-rich clinopyroxene are ubiquitous groundmass phases. Olivine is also present in the intergranular to subophitic groundmass. Plagioclase phenocrysts are variable in shape and typically between <1 and 5 mm long. They constitute up to 25% modal abundance in some samples, although the majority have <10% phenocrysts. Olivine phenocrysts are also prevalent in Shield Series lavas, usually <25% modal abundance. Olivine phenocrysts are subhedral to euhedral, ~1–2 mm in diameter, and some contain spinel inclusions. Hawaiites erupted at cinder and tuff cones preserve a pilotaxitic matrix rich in plagioclase microlites, oxidized olivine, and opaque oxides all <1 mm long.

Major Element Compositions

Major element concentrations of Santa Cruz lavas define a wide compositional range that spans values observed across the archipelago (**Figures 2–4**; **Table 1**; e.g., White et al., 1993), despite a relatively small range of SiO_2 contents (45.1–49.6 wt.%); rocks are tholeiitic to weakly alkaline (**Figure 2**). Major element variations do not exhibit any systematic geographic pattern. Santa Cruz lavas have between 4.3 and 12.9 wt.% MgO, extending to both more primitive and evolved compositions than Fernandina and most of the other active volcanoes in the western Galápagos (**Figures 3A–H**; Allan and Simkin, 2000). At a given Mg# value, Santa Cruz has lower TiO_2 and CaO contents than Fernandina, but higher Al_2O_3, FeO_t, Na_2O, and P_2O_5. In general, K_2O values at a given Mg# are higher than those from Fernandina for most of the Shield series, but lower for the Platform Series.

The Platform Series rocks are more fractionated than Shield lavas, but cannot be produced from the more primitive Shield Series samples, owing to their different incompatible element ratios and the distinct trends they define in Harker diagrams. The lack of dominant trends in either the Platform or Shield Series lavas suggests that there is not a single parental melt composition responsible for each geologic unit; instead, there must be an array of primary melt compositions and depths of melt generation within both the Shield and Platform Series. Similarly, the range of FeO_t contents in primitive lavas may signal that the mantle source includes a pyroxenitic component, as has been proposed for other lavas from the central Galápagos (Gleeson et al., 2020).

In CaO-Mg# space (**Figure 3E**), Santa Cruz lavas define two broad trends. The positive trend that includes most of the Shield Series lavas likely reflects control primarily by clinopyroxene fractionation, whereas the shallower trend defined by Platform lavas and a handful of mostly low K_2O/TiO_2 Shield lavas has experienced less clinopyroxene fractionation. The high modal abundance of plagioclase and elevated Al_2O_3 contents of many Shield Series lavas indicates that there has been plagioclase accumulation. In contrast, the Platform Series' lower Al_2O_3 contents suggest greater control by plagioclase fractionation.

The Platform Series defines a horizontal array in Mg#-K_2O/TiO_2 space, varying between ~0.1 and 0.25 in K_2O/TiO_2. The low FeO and MgO values of some Platform Series suggest that a few may have fractionated Fe-Ti oxides, although to a limited extent given that these lavas maintain relatively elevated TiO_2 contents (**Figures 3B,D**). The Shield Series array is negatively sloped in Mg#-K_2O/TiO_2 space; consequently, we have divided the Shield Series into three compositional sub-groups (**Figure 4**). Shield Series lavas with K_2O/TiO_2 <0.15 are classified as the Low K_2O/

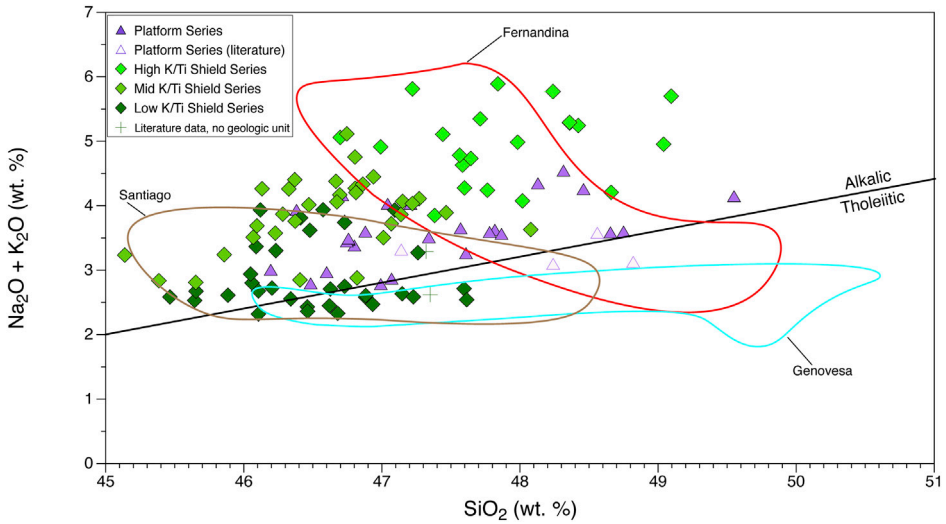


FIGURE 2 | Alkali-silica diagram of Santa Cruz lavas. The alkalic-tholeiitic dividing line is from Macdonald and Katsura, 1964). Fields are literature data. Red: Fernandina, blue: Genovesa, brown: Santiago (White et al., 1993; Harpp et al., 2002; Harpp et al., 2003; Saal et al., 2007; Gibson and Geist, 2010; Gibson et al., 2012; Harpp et al., 2014a). Samples indicated by a cross are literature data from Santa Cruz (White et al., 1993; Kurz and Geist, 1999; Saal et al., 2007); they have not been attributed to either the Platform or Shield Series owing to a lack of GPS coordinates for their origin locations.

TiO_2 suite. These samples have the highest MgO and CaO, and the lowest K_2O, TiO_2, Na_2O, and P_2O_5, of the Shield Series (**Figures 3A,B,E–H**). Samples with K_2O/TiO_2 >0.25 are the High K_2O/TiO_2 suite, and constitute the most evolved lavas within the Shield. Lavas with K_2O/TiO_2 values between 0.15 and 0.25 are designated as the Mid K_2O/TiO_2 suite of the Shield Series (**Figure 4**).

Trace Element Compositions

Broadly, trace element concentrations vary from depleted, near-MORB-like values to more enriched compositions typical of ocean island basalt (**Table 2**; White et al., 1993). The Platform Series exhibits less compositional variability in trace element contents than the Shield Series (**Figures 5–7**).

Rare Earth Elements

Santa Cruz lavas exhibit a wide range of Rare Earth Element (REE) compositions. Chondrite-normalized REE concentrations of Platform Series lavas define nearly linear patterns with slight negative slopes (**Figure 5**). Most Platform Series REE patterns are parallel to each other, with minor variations in slope steepness in the mid-to-heavy REEs. Platform Series lavas mostly have minor negative europium anomalies.

The Shield Series lavas exhibit greater variability than the Platform Series in terms of absolute REE concentrations and their patterns (**Figure 5**). The High K_2O/TiO_2 Shield Series lavas are most similar to the Platform Series, with relatively gentle, negatively sloping patterns and Eu anomalies that range from slightly negative to zero. The Low K_2O/TiO_2 Shield Series has the most depleted REE compositions, with positive light-REE (LREE) slopes for some samples, a common characteristic of MORB (e.g., Workman and Hart, 2005; McLennan and Taylor, 2012); others have gentle negative LREE slopes, more like the High K_2O/TiO_2 suite, but with flatter LREE slopes. The Mid K_2O/TiO_2 Shield lavas resemble the more enriched Low K_2O/TiO_2 group, but several have steeper LREE slopes. A few samples from across the island also exhibit minor negative Ce anomalies.

Incompatible Trace Elements

All three Shield Series K_2O/TiO_2 groups have compositions that overlap significantly but not completely in primitive mantle-normalized trace element contents (**Figure 7**). Generally, the Platform and High K_2O/TiO_2 Shield samples have the highest incompatible trace element (ITE) concentrations, and the Low K_2O/TiO_2 Shield lavas have the lowest. Most Santa Cruz lavas are enriched in the High Field Strength Elements (HFSE; Ti, Nb, Zr, Hf, Ta) compared to less incompatible elements, but the extent of enrichment varies. Within each eruptive unit, ITE concentrations vary by up to a factor of four relative to primitive mantle (**Figure 6**).

The Low K_2O/TiO_2 suite is the least enriched group of the Shield Series, and the High K_2O/TiO_2 lavas are the most enriched (**Figure 6**). Shield Series lavas exhibit positive slopes for the most incompatible trace elements and negative slopes for the less incompatible ones. The Low K_2O/TiO_2 suites have mostly positive Sr anomalies, whereas the High K_2O/TiO_2 and Platform Series lavas' Sr anomalies are negative, and the Mid K_2O/TiO_2 have both types. Many Low and Mid K_2O/TiO_2 suite samples also exhibit small positive Ba anomalies, as is the case for Floreana lavas (e.g., Harpp et al., 2014a). By contrast, the Platform Series has positive Ba but negative Sr anomalies. Taken as a whole, Santa Cruz lavas have ITE contents that span the range between Genovesa's depleted and Fernandina's enriched compositions (**Figure 6**; White et al., 1993; Harpp and White, 2001).

Variations in light (La_n/Sm_n) and heavy REE (HREE) ratios (Sm_n/Yb_n) for Santa Cruz also vary widely (**Figure 7A**). Santa

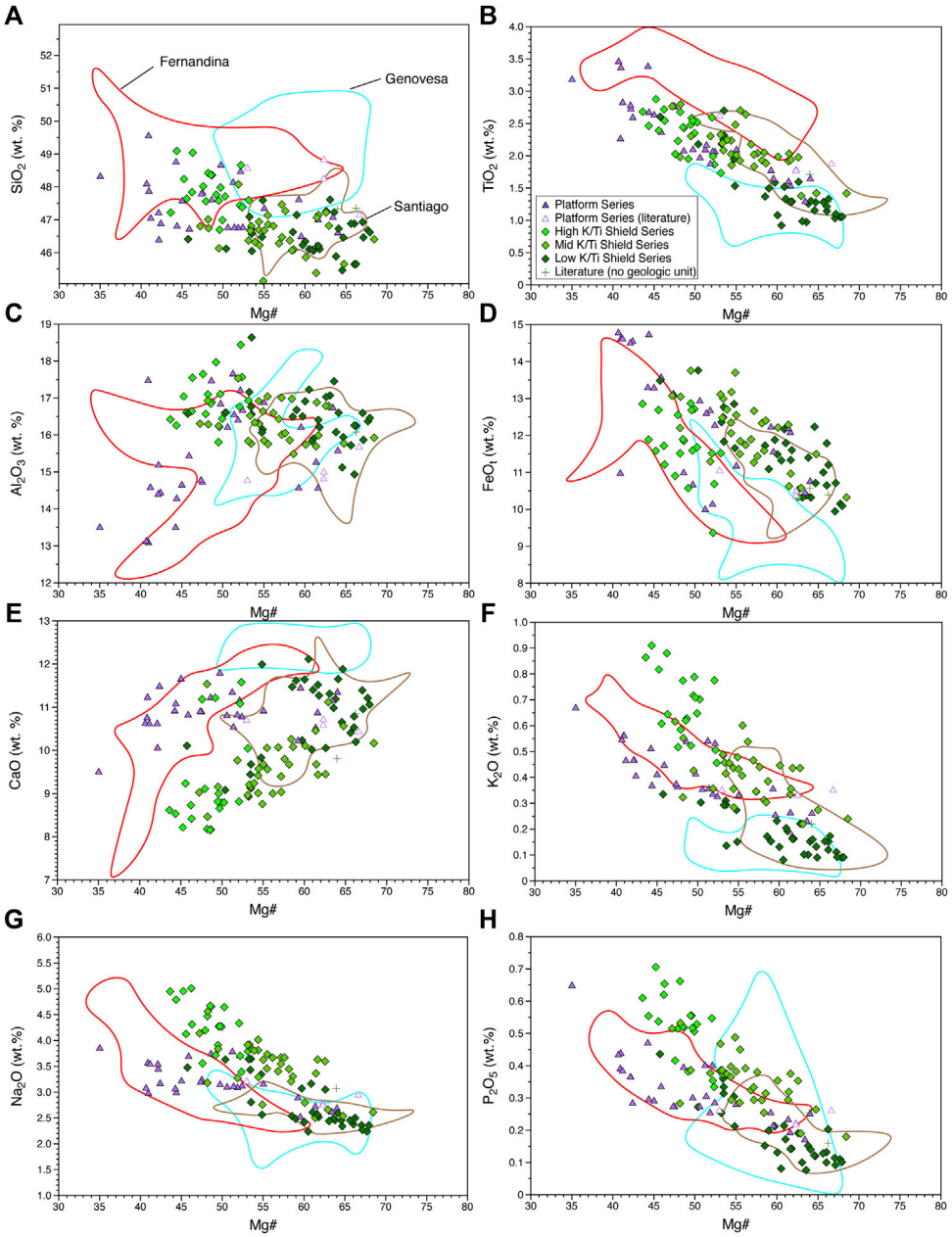


FIGURE 3 | Selected major element variation versus Mg# for Santa Cruz lavas. Fields are literature data. Red: Fernandina, blue: Genovesa, brown: Santiago (White et al., 1993; Harpp et al., 2002; Harpp et al., 2003; Saal et al., 2007; Gibson and Geist, 2010; Gibson et al., 2012; Harpp et al., 2014a). Concentrations are in weight percent (wt.%) and have been normalized to 100%. Mg# = [molar Mg/(Mg + Fe)]. Symbols are larger than 1σ analytical error. Samples indicated by a cross are literature data from Santa Cruz (White et al., 1993; Kurz and Geist, 1999; Saal et al., 2007); they have not been attributed to either the Platform or Shield Series owing to a lack of GPS coordinates for their origin locations. **(A)** SiO_2-Mg#; **(B)** TiO_2-Mg#; **(C)** Al_2O_3-Mg#; **(D)** FeOtotal-Mg#; **(E)** CaO-Mg#; **(F)** K_2O-Mg#; **(G)** Na_2O-Mg#; **(H)** P_2O_5-Mg#

Cruz lavas define a broad range in La_n/Sm_n at $Sm_n/Yb_n < 2.6$. The Shield Series' Low K_2O/TiO_2 lavas have the greatest variability in LREE and HREE ratios, and the Mid K_2O/TiO_2 lavas overlap the Low K_2O/TiO_2 group in all but the lowest values; the Shield's High K_2O/TiO_2 suite exhibits less variation as well as the island's highest La_n/Sm_n values. The Platform Series overlaps the Shield's Mid K_2O/TiO_2 lavas, but also has some of the highest Sm_n/Yb_n observed on the island. Compared to the rest of the Galápagos Archipelago, LREE and HREE ratios of Santa Cruz lavas extend between the fields of Fernandina and Genovesa, with little overlap into the shallow-melting, low Sm_n/Yb_n field of Floreana (White et al., 1993; Harpp et al., 2014a).

Ratios of comparably incompatible trace elements are relatively consistent across Santa Cruz, whereas the Platform

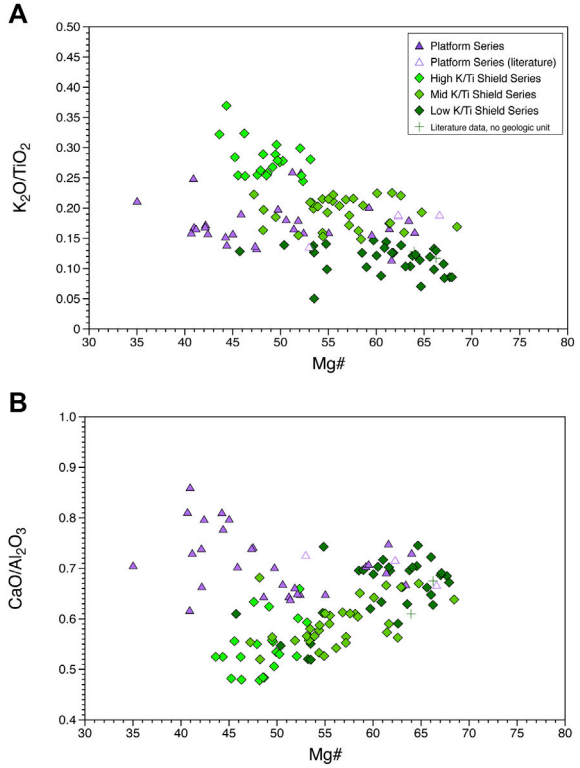


FIGURE 4 | Major element ratio variation with Mg# for Santa Cruz lavas. **(A)** K_2O/TiO_2, to illustrate how Shield Series sub-groups were defined. **(B)** CaO/Al_2O_3. Concentrations are in weight percent (wt.%) and have been normalized to 100%. Symbols are larger than 1σ analytical error. Samples indicated by a cross are literature data from Santa Cruz (White et al., 1993; Kurz and Geist, 1999; Saal et al., 2007); they have not been attributed to either the Platform or Shield Series owing to a lack of GPS coordinates for their origin locations.

Series is slightly more enriched in the more incompatible elements and in fluid-mobile elements. For instance, the Nb/Zr ratio of the Platform Series is 0.064 (± 0.009 1σ; n = 32), and the Shield value is 0.049 ± 0.011 (1σ; n = 93); the Platform Series Ba/La is 7.97 (± 3.89 1σ; n = 32) compared to the Shield Series' 5.34 (± 1.24 1σ; n = 94). Santa Cruz ITE ratios define distinct fields from those of most other Galápagos volcanoes, and usually fall between the Fernandina and Genovesa fields. Across the archipelago, Santa Cruz ITE ratios are most similar to Santiago's less enriched lavas (**Figure 7**; Gibson et al., 2012) and rocks from Volcán Wolf (Geist et al., 2005).

The variation across Santa Cruz in La_n/Sm_n (Platform: 1.17–1.97; Shield: 0.51–2.15) and Sm_n/Yb_n (Platform: 1.67–2.56; Shield: 0.98–2.55) indicates that the island's lavas were generated across a range of extents and depths of melting, similar to those at Santiago Island (Gibson et al., 2012). Comparison of Sm_n/Yb_n values as an indication of depth of melting reveals that the Platform and Shield Series' averages are similar, but the Shield Series varies more than the Platform (Platform average Sm_n/Yb_n = 1.90 ± 0.23 (1σ), n = 31; Shield average Sm_n/Yb_n = 1.91 ± 0.34 (1σ), n = 90). The Shield and Platform Series lavas have nearly identical Sm_n/Yb_n maxima (~2.55), but the Shield minimum indicates shallower melting (0.98) than Platform lavas (1.67). The Shield's Low K_2O/TiO_2 lavas exhibit the shallowest melting, with an average Sm_n/Yb_n of 1.63 (± 0.34 (1σ), n = 32). The Shield Mid and High K_2O/TiO_2 rocks have higher averages, indicative of deeper melting (Shield Mid Sm_n/Yb_n = 2.10 ± 0.20 (1σ), n = 33; Shield High Sm_n/Yb_n = 2.14 ± 0.19 (1σ), n = 16).

Isotopic Ratios

Basalts from Santa Cruz define a wider range of isotopic ratios than those erupted at most other Galápagos Islands (**Figures 8A–D**; **Table 3**, e.g., White et al., 1993). The $^{87}Sr/^{86}Sr$ ratios vary from 0.702633 to 0.702959, and ε_{Nd} values extend from 7.77 to 9.43. Lead isotopic ratio ranges are 18.531–18.947 for $^{206}Pb/^{204}Pb$, 15.519–15.560 for $^{207}Pb/^{204}Pb$, and 38.071–38.515 for $^{208}Pb/^{204}Pb$. Platform Series lavas are generally more enriched than the Shield Series. Even though there is overlap between the two groups, taking into account analytical uncertainty, the averages of the Platform and Shield Series lavas in all isotopic ratios are significantly different from each other at >95% certainty. The enrichment in Platform over Shield Series lavas supports previous observations based on fewer samples (White et al., 1993).

The most depleted signatures of the Shield Series (e.g., $^{87}Sr/^{86}Sr < 0.7027$; $\varepsilon_{Nd} > 9$) resemble material erupted at Genovesa Island in the Northern Galápagos Volcanic Province (NGVP; e.g., Harpp et al., 2003; Harpp et al., 2014c). The most enriched Santa Cruz lavas are comparable to the enriched material erupted at other eastern Galápagos volcanoes, including Santiago and San Cristóbal, which also display comparable ranges in isotopic ratios (e.g., Geist et al., 1986; Gibson et al., 2012). Santa Cruz lavas are not as enriched as those produced at volcanic centers closer to the leading edge of the plume, such as Fernandina, Volcán Sierra Negra, and Volcán Cerro Azul (e.g., White et al., 1993; Allan and Simkin, 2000; Naumann et al., 2002).

Relationship between Incompatible Trace Element Ratios and Isotopic Ratios

Santa Cruz geochemical variations are consistent with the archipelago-wide observation first noted by Kurz and Geist (1999) that ε_{Nd} has a strong negative correlation with Nb/La (**Figure 9**), and therefore that Nb/La can be a proxy for plume material (highest Nb/La = greatest plume contribution). Santa Cruz compositions extend from the depleted Genovesa field and overlap with the depleted end of the Santiago field. Santiago, in turn, extends toward Fernandina's enriched compositions, resulting in a relatively coherent array in Nb/La-ε_{Nd} space. The average Nb/La of the older Platform Series (1.00 ± 0.08 1σ; n = 31) is significantly higher than that of the Shield Series (0.88 ± 0.12 1σ; n = 89), consistent with radiogenic isotope ratio systematics that indicate a decrease in the contribution of enriched plume material to Santa Cruz lavas over time (**Figures 8E,F**; White et al., 1993). Variations in isotopic ratios with ITE ratios such as La_n/Sm_n whose elements differ more in their incompatibility than Nb/La display a different pattern. Most Galápagos lavas define a broadly binary array in ε_{Nd}-La_n/Sm_n

TABLE 2 | Trace element abundances of Santa Cruz lavas, reported in parts per million (ppm). One replicate analysis (indicated by "re") is included.

Sample	Comp. Group	Sc	V	Cr	Co	Ni	Cu	Zn	Rb	Sr	Y	Zr	Nb	Ba	La	Ce	Pr	Nd	Sm	Eu	Gd	Tb	Dy	Ho	Er	Tm	Yb	Lu	Hf	Ta	Pb	Th	U
SC-194	Platform	37.7	305	156	55.7	58.0	76.6	94.5	6.45	322	41.3	199	13.2	67.3	12.5	30.4	4.53	20.6	5.67	1.75	6.13	1.05	6.69	1.38	3.78	0.55	3.41	0.50	4.45	0.80	1.29	1.07	0.33
SC-194R	Platform	35.4	285	134		51.9	74.0	91.2	6.35	315	38.8	194	11.5	64.5	12.4	30.1	4.41	20.7	5.95	2.04	6.85	1.16	7.37	1.52	4.08	0.58	3.59	0.52	4.71	0.77	0.99	1.08	0.33
SC-196	Platform	40.4	393	124	77.2	63.0	99.8	109	5.00	272	40.3	181	11.7	68.6	12.3	28.9	4.45	21.3	6.00	1.98	6.53	1.10	6.95	1.44	4.00	0.58	3.53	0.52	4.13	0.73	1.23	0.82	0.25
SC-196P	Platform	40.3	388	114		60.7	97.4	108	4.93	270	37.5	174	10.5	63.9	11.0	27.9	4.18	19.9	5.86	2.15	6.89	1.18	7.44	1.52	3.99	0.57	3.40	0.48	4.27	1.28	1.00	0.78	0.24
SC-196R	Platform	39.9	389	113		61.4	97.6	108	4.94	270	37.8	176	10.1	63.8	11.0	28.0	4.17	20.0	5.85	2.21	6.85	1.17	7.43	1.52	4.05	0.56	3.37	0.49	4.29	0.72	0.92	0.78	0.25
SC12-008	Platform exp. fault	36.7	248	146	36.9	66.2	51.6	75.2	7.50	308	34.3	222	15.6	88.3	15.3	36.2	4.78	20.2	5.03	1.65	5.42	0.91	5.62	1.18	3.24	0.47	2.95	0.43	4.36	1.00	1.39	1.35	0.47
SC12-009	Platform exp. fault	29.0	240	265	56.8	233	65.7	72.5	2.88	247	23.4	134	6.90	45.7	7.29	18.6	2.69	12.1	3.30	1.13	3.65	0.62	3.98	0.84	2.31	0.34	2.09	0.31	2.72	0.45	0.82	0.53	0.16
SC12-020	Platform	39.5	377	134	47.1	69.6	51.5	101	3.25	279	35.2	158	10.1	67.3	9.70	24.6	3.68	17.7	5.05	1.71	5.55	0.94	5.98	1.24	3.37	0.49	3.01	0.44	3.69	0.64	0.81	0.68	0.11
SC12-022	Platform	41.0	433	123	48.5	64.0	98.8	111	3.73	275	39.5	181	11.5	70.6	10.7	27.4	4.07	19.4	5.60	1.93	6.20	1.06	6.65	1.39	3.83	0.55	3.35	0.49	4.13	0.73	1.23	0.78	0.24
SC12-025	Platform	33.4	302	75.7	35.3	33.7	74.6	108	5.53	279	52.6	269	18.5	101	20.2	48.1	6.70	30.1	8.10	2.37	8.42	1.43	8.86	1.82	5.01	0.73	4.41	0.64	6.16	1.16	1.63	1.68	0.20
SC12-054	Platform	35.0	273	69.0	49.1	102	80.5	94.9	4.18	305	35.5	206	9.69	74.6	9.93	25.2	3.69	17.5	4.91	1.69	5.40	0.93	5.80	1.23	3.40	0.49	3.05	0.46	4.40	0.62	1.13	0.72	0.22
SC12-055	Platform	36.1	280	73.0	52.8	116	91.5	93.3	3.77	315	35.1	166	9.29	59.0	10.5	24.6	3.72	17.7	4.79	1.58	5.19	0.87	5.47	1.14	3.14	0.46	2.88	0.42	3.53	0.58	1.06	0.67	0.21
SC12-056	Platform	28.3	216	414	54.4	278	74.6	89.6	4.52	278	27.4	140	10.3	74.2	9.42	22.7	3.23	14.9	4.03	1.34	4.46	0.74	4.75	0.98	2.63	0.38	2.32	0.34	3.12	0.64	1.09	0.74	0.21
SC12-057	Platform	38.4	307	124	45.6	62.0	77.0	95.8	5.57	366	36.8	210	11.7	80.0	11.9	30.8	4.53	20.8	5.55	1.87	6.01	1.01	6.14	1.28	3.51	0.50	3.11	0.45	4.40	0.74	1.41	0.76	0.24
SC12-058	Platform	33.6	246	299	47.5	150	92.3	74.9	2.54	386	26.8	130	7.27	57.0	7.40	19.1	2.81	13.3	3.80	1.32	4.25	0.71	4.54	0.93	2.58	0.37	2.28	0.33	2.82	0.46	0.96	0.50	0.09
SC12-059	Platform	31.5	256	101	46.1	110	69.1	87.1	4.07	346	34.2	181	10.3	73.4	10.8	26.9	3.92	18.3	4.97	1.70	5.53	0.91	5.68	1.16	3.23	0.46	2.84	0.42	3.80	0.66	1.17	0.71	0.22
SC12-060	Platform	37.2	348	43.0	46.7	62.0	80.7	124	4.30	299	57.1	242	13.5	90.7	15.1	36.7	5.57	26.1	7.30	2.42	8.13	1.38	8.62	1.85	5.20	0.74	4.55	0.67	5.26	0.88	1.44	0.95	0.28
SC12-061	Platform	41.2	422	91.0	48.3	55.0	138	133	8.50	324	53.7	283	22.7	127	20.7	51.1	7.32	33.7	8.86	2.70	8.91	1.48	8.61	1.72	4.53	0.63	3.80	0.55	6.27	1.37	1.48	1.51	0.49
SC12-062	Platform	36.8	413	81.0	44.5	50.0	131	129	8.80	316	47.0	284	22.5	108	18.7	46.3	6.74	31.5	8.60	2.71	8.96	1.44	8.33	1.65	4.44	0.61	3.65	0.52	6.62	1.48	1.54	1.49	0.51
SC12-063	Platform	35.1	303	61.0	37.7	29.0	56.2	148	5.90	296	71.2	334	22.6	464	22.2	53.1	7.80	36.6	10.1	3.36	11.2	1.89	11.6	2.43	6.76	0.96	5.85	0.84	7.26	1.44	1.78	1.65	0.17
SC12-064	Platform	35.1	375	96.7	41.4	49.3	98.9	125	7.43	327	48.6	281	22.2	271	19.1	47.9	7.03	32.0	8.74	2.81	9.13	1.47	8.66	1.74	4.52	0.63	3.74	0.54	6.58	1.46	1.46	1.50	0.47
SC12-065	Platform	30.3	237	418	53.7	228	86.8	77.7	2.67	290	24.9	130	7.53	64.7	7.57	19.1	2.77	13.0	3.63	1.27	4.08	0.68	4.24	0.87	2.40	0.35	2.12	0.32	2.79	0.48	0.95	0.57	0.15
SC12-066	Platform	37.9	427	81.0	42.1	49.0	77.2	111	4.26	276	48.4	242	13.6	112	13.6	34.6	5.09	23.8	6.64	2.21	7.38	1.27	7.87	1.67	4.65	0.67	4.12	0.61	5.32	0.89	1.38	0.97	0.32
SC12-067	Platform	40.4	442	87.0	45.3	52.0	73.8	115	5.06	274	47.6	239	13.5	88.4	13.2	33.6	4.96	23.2	6.51	2.16	7.21	1.24	7.74	1.64	4.57	0.66	4.07	0.60	5.21	0.87	1.37	0.95	0.26
SC12-068	Platform	29.8	250	99.0	47.7	117	70.4	91.1	3.71	339	35.2	186	10.9	74.4	11.4	28.0	4.07	19.1	5.16	1.76	5.57	0.93	5.80	1.19	3.24	0.47	2.91	0.43	3.94	0.71	1.16	0.75	0.20
SC12-069	Platform	32.5	249	402	50.7	201	75.2	82.7	3.59	273	31.0	145	10.7	148	9.47	23.0	3.34	15.5	4.22	1.45	4.79	0.79	5.17	1.08	2.96	0.44	2.71	0.40	3.20	0.69	1.07	0.63	0.18
SC12-070	Platform	31.6	229	493	62.3	325	83.4	89.0	1.93	262	28.8	112	7.09	136	7.40	17.3	2.63	12.1	3.41	1.19	3.89	0.67	4.35	0.92	2.52	0.37	2.22	0.32	2.43	0.43	0.85	0.44	0.13
SC12-572B	Platform exp. fault	38.3	295	172	40.4	69.1	52.2	88.1	9.32	340	40.6	254	18.3	112	18.3	41.6	5.56	24.3	6.06	1.96	6.45	1.08	6.73	1.40	3.87	0.57	3.53	0.52	5.17	1.18	1.80	1.45	0.43
SC-64	Shield Low K/Ti	40.4	393	124	77.2	63.0	99.8	109	5.00	272	40.3	181	11.7	68.6	12.3	28.9	4.47	21.0	6.00	1.98	6.59	1.10	6.95	1.44	3.96	0.58	3.53	0.52	4.13	0.73	1.23	0.82	0.25
SC-78	Shield Low K/Ti	30.0	215	515	76.3	308	80.5	70.7		248	20.1	81.3	4.17	29.4	3.35	10.6	1.74	8.76	2.65	0.93	3.07	0.53	3.43	0.73	2.02	0.30	1.80	0.26	1.86	0.87	0.69	0.22	0.05
SC-163	Shield Low K/Ti	26.4	182	179		140	61.5	85.1	1.78	382	38.0	220	9.19	58.7	13.2	33.4	4.94	23.5	6.10	2.21	6.95	1.16	7.19	1.50	3.99	0.56	3.46	0.52	4.67	0.75	1.07	0.69	0.22

(Continued on following page)

TABLE 2 | (*Continued*) Trace element abundances of Santa Cruz lavas, reported in parts per million (ppm). One replicate analysis (indicated by "re") is included.

Sample	Comp. Group	Sc	V	Cr	Co	Ni	Cu	Zn	Rb	Sr	Y	Zr	Nb	Ba	La	Ce	Pr	Nd	Sm	Eu	Gd	Tb	Dy	Ho	Er	Tm	Yb	Lu	Hf	Ta	Pb	Th	U
SC-202	Shield Low K/Ti	30.0	215	515	76.3	308	80.5	70.7		248	20.1	81.3	4.17	29.4	3.48	11.0	1.81	8.85	2.65	0.93	3.07	0.53	3.43	0.73	2.02	0.30	1.80	0.27	1.86	0.87	0.69	0.22	0.05
SC-206A	Shield Low K/Ti	37.9	260	229	58.9	122	76.6	90.8		403	37.9	240	10.4	59.0	12.1	32.9	4.99	23.1	6.05	2.00	6.27	1.02	6.12	1.26	3.38	0.49	3.05	0.45	4.72	0.77	1.35	0.60	0.19
SC12-001	Shield Low K/Ti	35.6	213	212	54.4	165	92.4	64.7	0.28	172	20.6	47.3	1.62	11.1	1.95	5.51	1.00	5.31	1.85	0.71	2.55	0.46	3.25	0.74	2.15	0.32	2.06	0.30	1.25	0.12	0.27	0.04	
SC12-006	Shield Low K/Ti	32.7	209	399	58.0	237	69.2	70.7	0.65	313	21.2	92.8	3.97	22.6	4.76	12.9	2.02	9.88	2.89	1.04	3.35	0.57	3.60	0.76	2.14	0.30	1.88	0.27	2.12	0.26	0.52	0.21	0.07
SC12-011	Shield Low K/Ti	36.0	229	548	60.4	308	39.2	68.8	1.48	170	22.2	79.1	3.85	20.0	4.02	10.7	1.64	7.91	2.35	0.82	2.93	0.53	3.59	0.79	2.30	0.35	2.21	0.33	1.78	0.26	0.46	0.21	0.05
SC12-013	Shield Low K/Ti	29.8	210	279	51.2	188	83.5	66.8	1.57	285	19.9	95.0	4.57	26.2	4.96	13.4	2.06	9.89	2.85	1.02	3.32	0.55	3.50	0.73	2.00	0.29	1.77	0.25	2.14	0.30	0.58	0.24	0.08
SC12-014	Shield Low K/Ti	44.2	291	234	49.5	111	97.3	78.1	0.62	195	30.5	101	5.43	31.6	5.20	14.1	2.22	10.9	3.34	1.20	4.14	0.73	4.84	1.03	2.96	0.44	2.77	0.41	2.35	0.35	0.43	0.19	0.06
SC12-015	Shield Low K/Ti	34.2	212	309	53.7	184	55.6	62.3	0.97	302	19.1	84.7	3.54	22.6	4.16	11.5	1.82	9.04	2.68	0.98	3.10	0.53	3.32	0.70	1.92	0.28	1.73	0.25	2.00	0.23	0.45	0.18	0.04
SC12-016	Shield Low K/Ti	33.9	248	602	56.5	173	80.6	74.7	1.32	309	22.0	99.2	4.18	22.8	4.75	13.4	2.11	10.3	3.02	1.07	3.54	0.59	3.74	0.79	2.19	0.32	1.94	0.28	2.21	0.27	0.61	0.20	0.08
SC12-019	Shield Low K/Ti	27.5	215	204	49.7	149	76.3	56.8	0.47	232	15.2	58.1	2.53	14.3	2.78	8.15	1.25	6.18	1.92	0.73	2.34	0.40	2.62	0.56	1.57	0.23	1.40	0.21	1.39	0.17	0.32	0.07	
SC12-026	Shield Low K/Ti	36.1	257	380	59.0	219	119	73.1		260	21.8	71.1	2.34	23.3	2.10	8.67	1.55	8.09	2.58	0.94	2.91	0.54	3.50	0.74	2.07	0.30	1.84	0.27	1.79	0.16	0.60	0.10	0.05
SC12-030	Shield Low K/Ti	28.2	170	455	65.0	406	56.5	63.9	0.92	310	22.1	135	5.21	27.1	6.70	18.0	2.74	12.9	3.44	1.18	3.82	0.63	3.91	0.80	2.21	0.32	2.01	0.30	2.71	0.34	0.72	0.33	0.10
SC12-036	Shield Low K/Ti	34.8	242	157	40.8	55.0	51.0	84.4	0.88	389	36.2	242	13.0	73.3	14.4	36.8	5.41	24.8	6.16	2.00	6.49	1.03	6.30	1.28	3.49	0.50	3.08	0.45	4.77	0.79	1.28	0.86	0.27
SC12-042	Shield Low K/Ti	30.7	214	698	69.6	393	85.2	72.2	1.38	230	18.5	74.7	3.36	35.0	3.73	10.4	1.63	7.92	2.39	0.85	2.73	0.48	3.06	0.65	1.80	0.26	1.60	0.24	1.79	0.22	0.65	0.24	0.07
SC12-043	Shield Low K/Ti	28.9	210	263	56.4	177	69.8	88.7	3.09	348	32.6	203	6.45	33.7	8.85	25.0	3.87	18.5	4.96	1.66	5.40	0.87	5.33	1.11	3.12	0.45	2.76	0.41	3.96	0.41	1.09	0.40	0.13
SC12-051	Shield Low K/Ti	27.1	187	179	50.7	138	67.7	82.5	1.61	397	42.0	244	11.4	59.3	15.4	38.9	5.68	25.7	6.44	2.03	6.59	1.10	6.92	1.45	3.99	0.58	3.59	0.53	4.87	0.71	1.54	0.76	0.25
SC12-071B	Shield Low K/Ti	25.8	180	212	49.8	153	58.4	78.5	3.70	545	33.1	245	9.16	63.3	11.7	31.6	4.79	22.1	5.62	1.92	5.82	0.94	5.67	1.14	3.16	0.45	2.76	0.41	4.62	0.60	1.54	0.60	0.19
SC12-570	Shield Low K/Ti	29.6	181	163	51.8	162	65.8	58.4						8.50	1.86	4.85	0.93	4.81	1.67	0.66	2.28	0.42	2.92	0.65	1.92	0.29	1.83	0.28					
SC12-581	Shield Low K/Ti	27.2	197	364	63.0	306	72.2	75.1	1.91	326	23.6	147	4.79	25.5	6.28	18.2	2.84	13.1	3.55	1.23	3.92	0.66	4.08	0.84	2.35	0.34	2.07	0.31	2.88	0.31	0.73	0.26	0.07
SC12-584B	Shield Low K/Ti	37.9	248	499	54.8	181	72.5	72.5	1.50	286	23.9	102	4.27	23.0	4.94	13.8	2.17	10.8	3.23	1.13	3.69	0.64	4.10	0.87	2.43	0.35	2.17	0.32	2.37	0.28	0.54	0.22	0.08
SCZ15-01	Shield Low K/Ti	34.4	215	454	67.1	435	90.2	63.3	1.36	218	18.3	73.3	2.17	22.4	3.05	8.84	1.42	7.05	2.22	0.84	2.75	0.48	3.08	0.65	1.82	0.27	1.66	0.25	1.66	0.15	1.36	0.17	0.05
SCZ15-02	Shield Low K/Ti	28.2	166	471	89.3	866	77.9	60.7	1.40	182	12.7	56.2	1.60	19.3	2.22	6.52	1.03	5.26	1.69	0.63	2.08	0.37	2.35	0.50	1.34	0.20	1.25	0.19	1.23	0.11	1.08	0.13	0.04
SCZ15-04	Shield Low K/Ti	44.6	316	263	59.0	189	93.0	92.8	1.46	204	32.9	149	9.57	38.7	8.60	21.4	3.02	14.0	3.88	1.34	4.46	0.75	4.91	1.03	2.94	0.43	2.70	0.39	3.10	0.57	1.08	0.41	0.17
SCZ15-08	Shield Low K/Ti	41.2	253	382	69.2	364	101	82.3	1.87	226	27.4	88.9	4.42	34.2	4.83	13.0	1.96	9.42	2.78	1.03	3.37	0.59	3.98	0.87	2.48	0.38	2.46	0.37	1.91	0.29	0.84	0.24	0.08
SCZ15-09	Shield Low K/Ti	39.6	264	306	59.6	170	94.7	74.9	1.18	223	23.0	66.3	2.14	18.7	2.86	7.94	1.28	6.47	2.15	0.83	2.84	0.51	3.48	0.76	2.22	0.34	2.18	0.33	1.51	0.15	0.84	0.15	0.12
SCZ15-10	Shield Low K/Ti	39.5	254	347	62.9	200	110	78.0	1.35	232	21.8	61.5	2.08	19.1	2.56	7.33	1.17	5.88	1.95	0.77	2.62	0.47	3.23	0.72	2.08	0.32	2.05	0.31	1.41	0.14	0.71	0.14	0.07
SC-46	Shield Mid K/Ti	29.7	212	584		306	79.4	72.2	2.56	349	20.9	119	5.08	32.5	6.47	17.4	2.62	12.3	3.39	1.34	3.89	0.66	4.14	0.84	2.26	0.33	1.97	0.29	2.72	0.65	0.74	0.39	0.12
SC-130	Shield Mid K/Ti	25.5	194	141	61.5	121	68.7	91.9	9.29	490	49.6	371	22.3	123	29.5	64.4	9.18	38.1	8.57	2.62	8.60	1.38	8.35	1.67	4.63	0.67	4.17	0.61	6.87	1.36	2.62	1.66	0.51
SC-135	Shield Mid K/Ti	29.4	204	485		234	80.9	85.4	5.52	330	34.2	241	10.4	58.9	13.6	33.8	4.86	22.5	5.85	2.02	6.37	1.06	6.56	1.36	3.65	0.53	3.25	0.50	4.87	0.82	1.37	0.83	0.29
SC-155	Shield Mid K/Ti	31.3	213	148	54.1	95.0	75.8	83.5	2.28	434	33.2	234	13.1	78.9	13.4	34.5	4.97	22.7	5.64	1.86	5.75	0.92	5.55	1.14	3.12	0.45	2.76	0.41	4.43	1.15	1.48	0.82	0.25
SC12-002	Shield Mid K/Ti	28.7	188	284	52.0	202	57.2	75.1	3.20	456	30.0	195	6.86	38.5	9.97	25.7	3.81	17.7	4.76	1.61	5.13	0.82	5.00	1.03	2.87	0.41	2.55	0.37	3.93	0.45	1.01	0.47	0.14

(Continued on following page)

TABLE 2 | (*Continued*) Trace element abundances of Santa Cruz lavas, reported in parts per million (ppm). One replicate analysis (indicated by "re") is included.

Sample	Comp. Group	Sc	V	Cr	Co	Ni	Cu	Zn	Rb	Sr	Y	Zr	Nb	Ba	La	Ce	Pr	Nd	Sm	Eu	Gd	Tb	Dy	Ho	Er	Tm	Yb	Lu	Hf	Ta	Pb	Th	U
SC12-007	Shield Mid K/Ti	21.8	154	306	49.8	197	63.8	70.4	4.11	322	29.5	215	9.56	53.5	10.9	27.7	4.05	18.8	4.73	1.57	5.08	0.81	4.94	1.01	2.81	0.40	2.51	0.36	4.09	0.61	1.30	0.62	0.20
SC12-010	Shield Mid K/Ti	30.5	221	722	62.0	285	48.9	74.5	2.78	384	23.5	140	6.50	36.1	7.77	19.1	2.91	13.6	3.63	1.25	3.90	0.64	3.92	0.81	2.22	0.32	2.00	0.29	2.87	0.42	0.80	0.42	0.14
SC12-012	Shield Mid K/Ti	24.8	201	221	48.1	194	61.4	79.5	4.76	281	35.2	238	11.7	67.8	12.0	31.4	4.60	20.2	5.10	1.66	5.58	0.92	5.78	1.21	3.30	0.48	2.99	0.43	4.39	0.75	1.35	0.77	0.26
SC12-018	Shield Mid K/Ti	32.5	235	368	52.6	216	55.2	78.0	5.00	356	32.3	204	10.6	57.9	12.8	30.7	4.64	21.0	5.24	1.67	5.37	0.88	5.64	1.15	3.17	0.46	2.86	0.42	4.08	0.67	1.37	0.75	0.22
SC12-021	Shield Mid K/Ti	42.4	332	216	46.9	69.0	72.5	88.6	2.87	338	37.8	177	9.41	79.2	10.7	26.1	3.96	18.4	5.02	1.65	5.53	0.92	5.91	1.22	3.37	0.50	3.02	0.44	3.76	0.59	1.15	0.58	0.17
SC12-023	Shield Mid K/Ti	26.7	187	205	48.2	147	59.9	82.0	4.08	516	36.0	252	9.76	55.9	12.6	33.7	5.15	24.0	6.09	1.93	6.07	1.00	6.20	1.26	3.45	0.49	3.09	0.46	4.99	0.62	1.45	0.63	0.21
SC12-024	Shield Mid K/Ti	26.0	177	179	50.8	143	63.2	84.2	6.39	516	35.0	249	12.7	73.0	15.0	37.5	5.37	24.3	5.88	1.90	5.84	0.95	5.66	1.16	3.24	0.47	2.92	0.43	4.82	0.79	1.57	0.85	0.27
SC12-029	Shield Mid K/Ti	29.4	192	169	51.5	129	58.1	90.4	5.81	402	40.2	253	11.7	59.6	12.9	33.9	5.07	23.9	6.09	1.93	6.37	1.06	6.50	1.34	3.72	0.54	3.37	0.50	4.90	0.70	1.61	0.73	0.25
SC12-031	Shield Mid K/Ti	26.8	197	250	49.4	169	67.6	92.2	6.88	397	41.8	363	13.7	70.3	17.8	43.8	6.16	27.7	6.80	2.14	6.95	1.14	6.88	1.39	3.81	0.55	3.43	0.51	5.95	0.86	1.73	0.99	0.33
SC12-032	Shield Mid K/Ti	29.3	205	205	44.7	103	75.7	72.8	6.24	458	30.2	189	11.5	73.6	12.6	29.7	4.38	20.0	5.04	1.68	5.26	0.85	5.31	1.08	2.92	0.42	2.58	0.38	3.82	0.71	1.40	0.80	0.21
SC12-033	Shield Mid K/Ti	31.4	215	274	59.6	263	72.0	69.7	1.89	307	23.7	122	4.99	36.6	6.04	16.3	2.51	12.1	3.30	1.13	3.67	0.62	3.96	0.84	2.32	0.34	2.14	0.32	2.54	0.32	0.81	0.37	0.12
SC12-034	Shield Mid K/Ti	32.1	230	389	55.0	209	50.5	84.7	6.23	428	32.2	234	11.9	70.0	13.6	34.1	5.02	22.6	5.55	1.75	5.77	0.93	5.64	1.14	3.14	0.46	2.80	0.40	4.64	0.75	1.36	0.86	0.26
SC12-035	Shield Mid K/Ti	26.8	176	278	52.8	220	77.3	76.4	2.06	357	30.0	185	8.14	41.8	9.73	25.8	3.80	17.6	4.58	1.54	4.99	0.82	5.09	1.04	2.87	0.42	2.61	0.38	3.70	0.53	1.01	0.57	0.14
SC12-037	Shield Mid K/Ti	34.7	259	309	52.9	179	73.0	97.1	2.92	497	44.9	333	16.5	87.5	19.3	47.7	6.85	31.1	7.43	2.27	7.36	1.20	7.28	1.48	4.00	0.57	3.46	0.51	6.16	1.00	1.88	1.15	0.31
SC12-038	Shield Mid K/Ti	29.5	223	248	49.1	140	50.9	71.6	2.92	555	27.2	163	8.31	55.5	9.88	24.0	3.74	17.3	4.50	1.53	4.57	0.73	4.43	0.89	2.41	0.35	2.12	0.30	3.38	0.54	1.12	0.44	0.14
SC12-041	Shield Mid K/Ti	29.1	194	226	53.8	161	61.2	82.9	4.74	495	34.7	247	11.8	66.7	13.0	34.3	5.02	23.0	5.70	1.83	5.84	0.94	5.60	1.16	3.22	0.46	2.89	0.43	4.77	0.72	1.59	0.78	0.25
SC12-044	Shield Mid K/Ti	26.2	166	394	57.7	247	72.4	75.2	3.71	389	29.4	205	9.37	56.5	10.5	28.0	4.07	18.4	4.57	1.50	4.78	0.78	4.80	0.98	2.68	0.40	2.46	0.36	3.78	0.56	1.36	0.60	0.20
SC12-046	Shield Mid K/Ti	24.5	182	132	43.3	109	46.3	88.3	6.93	525	42.9	349	16.0	85.6	21.3	53.0	7.52	33.3	7.89	2.45	7.80	1.25	7.58	1.53	4.17	0.60	3.68	0.54	6.55	1.01	2.20	1.22	0.37
SC12-047	Shield Mid K/Ti	21.3	144	145	38.8	98.0	60.4	67.6	5.61	521	29.7	234	11.7	80.3	13.4	33.9	4.78	21.4	5.34	1.83	5.38	0.86	5.20	1.06	2.90	0.41	2.55	0.38	4.45	0.76	1.69	0.85	0.23
SC12-048	Shield Mid K/Ti	26.4	200	158	44.6	115	55.5	96.5	9.95	465	42.5	324	19.0	92.4	19.9	49.0	6.94	30.6	7.36	2.27	7.48	1.22	7.37	1.48	4.09	0.59	3.63	0.53	6.25	1.20	2.07	1.44	0.45
SC12-050	Shield Mid K/Ti	29.9	233	245	48.0	145	66.4	83.0	6.85	489	31.4	229	14.3	90.9	13.6	34.2	4.82	21.9	5.53	1.84	5.71	0.91	5.35	1.09	2.92	0.41	2.55	0.38	4.62	0.90	1.90	0.99	0.27
SC12-071A	Shield Mid K/Ti	35.9	262	442	57.6	231	51.9	78.3	1.18	446	30.8	209	11.0	72.6	12.9	30.6	4.58	20.9	5.13	1.65	5.28	0.85	5.15	1.04	2.91	0.42	2.53	0.36	4.18	0.69	1.36	0.75	0.15
SCZ15-03	Shield Mid K/Ti	29.9	195	268	53.9	204	61.7	53.0	5.31	493	29.0	237	10.3	74.2	11.7	29.8	4.40	20.3	5.22	1.71	5.49	0.89	5.38	1.10	2.83	0.42	2.46	0.37	4.60	0.68	2.57	0.73	0.25
SCZ15-05	Shield Mid K/Ti	30.6	192	205	54.6	160	75.6	82.9	4.65	444	35.3	227	9.64	55.6	11.0	29.5	4.43	20.0	5.21	1.75	5.47	0.90	5.41	1.14	3.10	0.46	2.81	0.41	4.35	0.60	1.91	0.59	0.19
SCZ15-06	Shield Mid K/Ti	29.7	196	278	56.8	227	64.5	73.5	5.51	526	30.3	223	11.8	65.7	11.6	29.6	4.35	19.6	4.83	1.66	4.99	0.79	4.73	0.96	2.61	0.38	2.26	0.34	4.19	0.72	1.78	0.73	0.26
SCZ15-07	Shield Mid K/Ti	23.9	212	199	53.9	183	59.0	92.2	7.23	550	34.6	233	19.7	95.0	16.4	40.4	5.65	24.7	6.01	2.01	5.97	0.91	5.58	1.08	2.96	0.41	2.56	0.36	4.56	1.19	1.73	1.14	0.37
SC-48	Shield High K/Ti	32.9	254	143		64.3	56.8	74.4	8.42	339	31.7	209	13.8	87.1	15.5	35.7	4.76	20.6	5.31	1.86	5.84	0.97	6.14	1.28	3.40	0.48	3.01	0.45	4.51	1.13	1.26	1.28	0.41
SC-48 re	Shield High K/Ti	37.7	305	156	55.7	58.0	76.6	94.5	6.45	322	41.3	199	13.2	67.3	12.5	30.4	4.53	20.6	5.67	1.75	5.95	1.05	6.56	1.38	3.78	0.56	3.41	0.50	4.45	0.80	1.29	1.07	0.33
SC-68	Shield High K/Ti	24.0	185	94.1		82.5	47.9	92.5	10.7	476	42.2	378	21.5	129	24.3	59.6	8.14	35.2	8.28	2.83	8.38	1.39	8.42	1.69	4.43	0.63	3.94	0.60	7.51	1.54	2.37	1.76	0.56
SC-203R	Shield High K/Ti	25.5	194	141	61.5	121	68.7	91.9	9.29	190	49.6	371	22.3	123	29.5	64.4	9.18	38.1	8.57	2.62	8.60	1.35	8.11	1.64	4.72	0.67	4.09	0.62	6.87	1.36	2.62	1.66	0.51
SC-204R	Shield High K/Ti	24.7	204	182		131	58.0	87.3	11.2	463	39.2	309	20.2	122	22.1	53.7	7.43	32.1	7.66	2.64	7.80	1.29	7.81	1.56	4.10	0.58	3.58	0.54	6.38	1.36	1.58	1.54	0.41

(Continued on following page)

TABLE 2 | (*Continued*) Trace element abundances of Santa Cruz lavas, reported in parts per million (ppm). One replicate analysis (indicated by "re") is included.

Sample	Comp. Group	Sc	V	Cr	Co	Ni	Cu	Zn	Rb	Sr	Y	Zr	Nb	Ba	La	Ce	Pr	Nd	Sm	Eu	Gd	Tb	Dy	Ho	Er	Tm	Yb	Lu	Hf	Ta	Pb	Th	U
SC-206B	Shield High K/Ti	22.2	173	91.3		62.7	46.5	91.4	8.28	489	46.9	446	24.8	149	27.9	66.8	9.23	39.0	9.02	2.97	8.96	1.47	9.10	1.84	4.87	0.70	4.34	0.66	8.43	1.93	2.85	1.97	0.47
SC-207	Shield High K/Ti	22.7	164	138		107	62.8	93.8	7.29	409	42.6	371	15.9	86.2	20.2	51.1	7.15	32.0	7.72	2.63	8.00	1.34	8.37	1.70	4.55	0.66	4.09	0.63	7.22	1.44	2.32	1.39	0.43
SC12-005	Shield High K/Ti	37.1	263	162	41.5	88.0	63.6	80.1	8.19	312	34.4	217	15.4	86.7	15.5	36.1	4.85	20.6	5.18	1.69	5.55	0.91	5.63	1.17	3.35	0.48	2.96	0.44	4.39	0.99	1.43	1.33	0.45
SC12-017	Shield High K/Ti	25.5	204	79.0	34.7	61.0	45.9	91.7	11.2	465	45.3	393	21.1	118	24.1	59.1	8.15	34.2	7.91	2.38	7.79	1.24	7.29	1.50	4.21	0.62	3.83	0.57	7.24	1.32	2.58	1.75	0.52
SC12-027	Shield High K/Ti	24.9	188	84.0	37.2	66.9	34.2	91.4	11.1	461	42.1	389	26.1	131	26.7	65.0	8.69	36.1	8.17	2.44	7.96	1.28	7.61	1.52	4.01	0.58	3.55	0.52	7.09	1.57	2.30	1.65	0.56
SC12-028	Shield High K/Ti	30.0	203	224	43.1	138	57.1	82.4	7.06	343	39.3	291	13.2	72.2	18.1	42.3	5.82	25.1	5.91	1.82	6.06	1.00	6.22	1.29	3.71	0.54	3.38	0.51	5.30	0.82	1.81	1.04	0.34
SC12-039	Shield High K/Ti	27.1	201	180	45.3	152	63.1	92.6	8.92	435	43.4	318	18.1	92.8	21.5	52.3	7.18	30.9	7.20	2.22	7.16	1.15	6.84	1.41	4.04	0.58	3.56	0.53	5.89	1.10	2.04	1.18	0.37
SC12-040	Shield High K/Ti	28.7	228	154	43.1	116	61.8	96.5	11.1	491	44.5	346	24.7	126	24.2	58.1	7.92	34.0	7.78	2.38	7.74	1.24	7.17	1.48	4.09	0.59	3.63	0.54	6.43	1.47	2.21	1.66	0.52
SC12-049	Shield High K/Ti	27.4	253	128	38.7	90.0	75.8	102	10.1	402	43.2	322	23.7	128	21.2	51.7	7.13	30.8	7.38	2.34	7.65	1.22	7.20	1.49	4.17	0.60	3.71	0.56	6.10	1.44	2.64	1.40	0.46
SC12-053	Shield High K/Ti	26.5	183	105	38.1	64.0	57.7	89.2	8.85	392	47.5	380	16.5	87.0	18.7	47.5	6.96	32.0	7.97	2.46	8.21	1.33	8.06	1.65	4.67	0.67	4.23	0.64	7.32	1.08	2.25	1.24	0.42
SC12-572A	Shield High K/Ti	34.0	268	192	38.3	70.0	48.0	84.1	7.37	369	40.6	238	17.2	220	18.7	41.6	5.76	24.3	5.95	1.99	6.47	1.05	6.50	1.35	3.72	0.54	3.35	0.50	4.80	1.11	1.77	1.38	0.42
SC12-611B	Shield High K/Ti	28.4	201	363	47.5	181	53.8	81.2	6.45	353	38.8	270	14.3	82.1	16.1	39.6	5.55	24.6	5.99	1.91	6.13	1.02	6.20	1.27	3.52	0.51	3.17	0.48	4.98	0.91	1.46	1.02	0.34
SC12-004	Shield No K/Ti	36.1	275	170	41.0	79.0	47.1	77.0	7.37	335	34.0	208	14.5	89.4	16.7	34.1	4.97	21.0	5.16	1.66	5.40	0.90	5.53	1.15	3.26	0.47	2.89	0.43	4.15	0.91	1.57	1.17	0.38
SC12-582	Shield No K/Ti	25.6	188	232	48.1	171	59.1	66.4	1.81	312	23.5	150	5.04	26.7	6.34	19.0	2.88	13.4	3.63	1.25	3.83	0.66	4.09	0.85	2.40	0.34	2.12	0.32	3.02	0.33	0.81	0.29	0.09
SC12-583	Shield No K/Ti	27.0	200	326	56.3	239	60.2	70.5	1.81	332	23.4	143	4.67	27.6	6.07	17.9	2.75	12.7	3.47	1.22	3.67	0.63	3.87	0.81	2.28	0.33	2.01	0.30	2.83	0.30	0.75	0.27	0.08
SC12-584A	Shield No K/Ti	34.2	238	459	62.6	246	74.7	71.5	0.88	288	19.9	19.4	3.79	21.1	4.30	12.3	1.96	9.39	2.78	1.00	3.05	0.55	3.42	0.71	1.99	0.29	1.75	0.26	2.07	0.25	0.46	0.19	0.12
SC12-589	Shield No K/Ti	34.3	253	260	53.9	164	93.7	73.6	3.28	324	22.2	131	7.46	40.0	7.96	20.4	2.89	12.7	3.37	1.17	3.62	0.62	3.77	0.78	2.18	0.31	1.90	0.28	2.67	0.46	0.80	0.48	0.13
SC12-606	Shield No K/Ti	31.8	203	612	62.1	311	74.4	65.9	1.70	307	19.3	103	4.60	25.4	5.18	14.3	2.23	10.4	2.90	1.03	3.13	0.55	3.36	0.70	1.95	0.28	1.70	0.25	2.27	0.30	0.60	0.26	0.08
SC12-610	Shield No K/Ti	30.9	196	396	63.1	314	70.4	68.2	1.12	277	19.8	85.0	3.63	20.1	4.15	11.5	1.88	9.06	2.69	0.96	2.96	0.53	3.40	0.72	2.00	0.29	1.78	0.26	1.97	0.24	0.47	0.18	0.05
SC12-611A	Shield No K/Ti	30.8	232	728	63.1	317	71.6	77.3	2.05	278	22.3	112	6.47	33.2	6.59	17.1	2.56	11.6	3.22	1.11	3.51	0.62	3.81	0.79	2.23	0.32	1.96	0.30	2.39	0.40	0.62	0.33	0.10
SC12-612	Shield No K/Ti	30.2	217	283	49.2	140	54.9	67.9	1.32	275	20.7	93.7	4.20	24.4	4.63	13.3	2.10	10.1	2.95	1.06	3.25	0.58	3.64	0.76	2.13	0.31	1.84	0.27	2.17	0.27	0.56	0.21	0.06

space (**Figure 9**). Unlike Santiago (Gibson et al., 2012), isotopic and ITE ratios do not correlate at Santa Cruz.

Mantle Components at Santa Cruz

Isotopic ratios from Santa Cruz define nearly linear arrays, suggesting that mixing between two primary endmembers, PLUME and DUM, controls most of the island's geochemical variation (**Figures 8A–D**; Harpp and White, 2001). We applied a simple two-component mixing calculation (Langmuir et al., 1978) to estimate contributions of DUM and PLUME, using the isotopic ratios and absolute concentrations of Sr, Nd, and Pb from Harpp and Weis (2020).

According to our estimates, Platform Series lavas have higher contributions of PLUME (20–40%) than the Shield Series (5–35%). In this first-order examination of mantle endmembers, we did not model in detail the role of either WD or FLO, given how much of the variation at Santa Cruz can be explained with mixtures of PLUME and DUM. Owing to the fact that the WD endmember is distinctive primarily in its Pb isotope ratios, it is challenging to distinguish unequivocally whether Santa Cruz signatures are the result of mixing among DUM-PLUME and WD or DUM-PLUME and FLO. Mixing curves calculated for $^{207}Pb^*/^{206}Pb^*$-$^{208}Pb^*/^{206}Pb^*$, however, suggest that WD is the likely reservoir augmenting the dominant combination of DUM and PLUME (**Figure 8D**). Santa Cruz exhibits little evidence that FLO, the component thought to consist of ancient recycled material, is contributing significantly to its source (e.g., Harpp and White, 2001; Harpp and Weis, 2020); this conclusion is supported by Santa Cruz's lack of other compositional features characteristic of Floreana, such as concave-up REE patterns or more extreme Sr and Pb isotopic ratios (Harpp et al., 2014a).

The depleted component responsible for Santa Cruz lavas could be the upper mantle (e.g., Geist et al., 1988; White et al., 1993; Harpp and White, 2001; Blichert-Toft and White, 2001), or it could be intrinsic to the plume, with deep mantle origins (e.g., Hoernle et al., 2000). According to studies of the Icelandic plume by Fitton et al. (1997, 2003), lavas generated at mid-ocean ridges from the upper mantle have distinct signatures in Nb/Y-Zr/Y space compared to basalts sourced by mantle plumes. Fitton et al. (1997) define a reference line (ΔNb) in Nb/Y-Zr/Y space that delimits the lower boundary of the Icelandic array. Lavas with ΔNb >0 are thought to be generated from lower mantle sources (i.e., plume), whereas those with ΔNb <0 are derived from the depleted upper mantle. Santa Cruz lavas land primarily in the quadrant defined by Nb/Zr < 0.06 and ΔNb <0, which corresponds to the depleted MORB source (**Figure 7**). Other Galápagos lavas with similar signatures include those from Genovesa (Harpp et al., 2003), many from Santiago (Gibson et al., 2012), a few from San Cristóbal (Geist et al., 1986; White et al., 1993), and numerous from the NGVP (e.g., Harpp and Geist, 2002; Harpp et al., 2014c; Sinton et al., 2014). A handful of Platform and High K_2O/TiO_2 Shield Series lavas have Nb/Zr > 0.06 (but less than 0.09), which qualify as enriched MORB (Fitton et al., 1997). No Santa Cruz samples have ΔNb >0. Thus, consistent with findings based primarily on isotopic data by Harpp and Weis (2020) for the archipelago as a whole, the depleted material contributing to Santa Cruz lavas' geochemical signatures is likely supplied primarily by the depleted upper mantle, rather than a depleted source intrinsic to the plume.

Trace Element Modeling: Depth and Extent of Melting

To constrain melt generation conditions at Santa Cruz, we apply a simple model to a representative subset of samples that assumes equilibrium melting of the dominant PLUME and DUM mantle components (*see* Supplementary Material for details; **Supplementary Table S1**; Harpp and White, 2001). The compositions of most Platform Series samples can be reproduced by melting 1–10% of a mixed DUM-PLUME mantle source, with 10–30% generated in the garnet stability field. All the modeled Platform lavas require small degree melts of their more enriched source (0.1–1%). The Shield Series lavas, on average, need greater contributions from the depleted mantle source and also exhibit more variation in the degree of melting than the Platform Series. Low K_2O/TiO_2 group lavas are generated by the highest melt fractions (1–20%), High K_2O/TiO_2 requires the least melting (0.5–5%), and Mid K_2O/TiO_2 is generated by an intermediate amount of melting (1–7%) of their mixed mantle sources. The Shield Series melts are generated at shallower depths than the Platform Series, with only minor melting (0-<20%) in the garnet stability field. The Low and Mid K_2O/TiO_2 groups are produced at slightly shallower depths than the High K_2O/TiO_2 lavas, but there is considerable variability within each Shield sub-group in all melt parameters (especially the Low and Mid K_2O/TiO_2 sub-units).

Compositional Variation of Santa Cruz Lavas

Across Santa Cruz

To document the variation of Santa Cruz lava compositions and to compare them to other volcanoes in the Galápagos, probability density function and interquartile ranges (Wessa, 2021) were generated for Mg#, La_n/Sm_n, Sm_n/Yb_n, and Nb/La (**Figure 10**). We chose Mg# as an indicator of shallow fractionation, $La_{(n)}/Sm_{(n)}$ as a proxy for extent of melting, $Sm_{(n)}/Yb_{(n)}$ to track depth of melting, and Nb/La as a measure of Galápagos plume contribution, which is rich in the refractory TITAN elements (Jackson et al., 2008; Kurz et al., 2014).

As stated above, the older Platform Series is more evolved and less variable than the Shield Series; Platform Series lavas have a lower Mg# Maximum Density (MD) than the Shield Series, and a slightly lower interquartile range (IR) (**Figure 10**; Platform MD: 44.4, IR: 10.7; Shield MD: 53.9, IR: 11.5). The sub-groups within the Shield Series increase in Mg# MD and IR from the High to Low K_2O/TiO_2 groups (**Figure 10**).

The Platform Series has La_n/Sm_n and Sm_n/Yb_n values that overlap the Shield Series, but the Shield lavas exhibit ~4 times the variability of Platform lavas (Platform La_n/Sm_n MD: 1.36, IR: 0.12; Shield La_n/Sm_n MD: 1.43, IR: 0.50; Platform Sm_n/Yb_n MD: 1.87, IR: 0.10; Shield Sm_n/Yb_n MD: 1.92, IR: 0.44). Within the Shield Series, the High K_2O/TiO_2 group was generated by the smallest extents of melting at the greatest average depths (La_n/Sm_n MD: 1.86, IR: 0.15; Sm_n/Yb_n MD: 2.25, IR: 0.27). Through

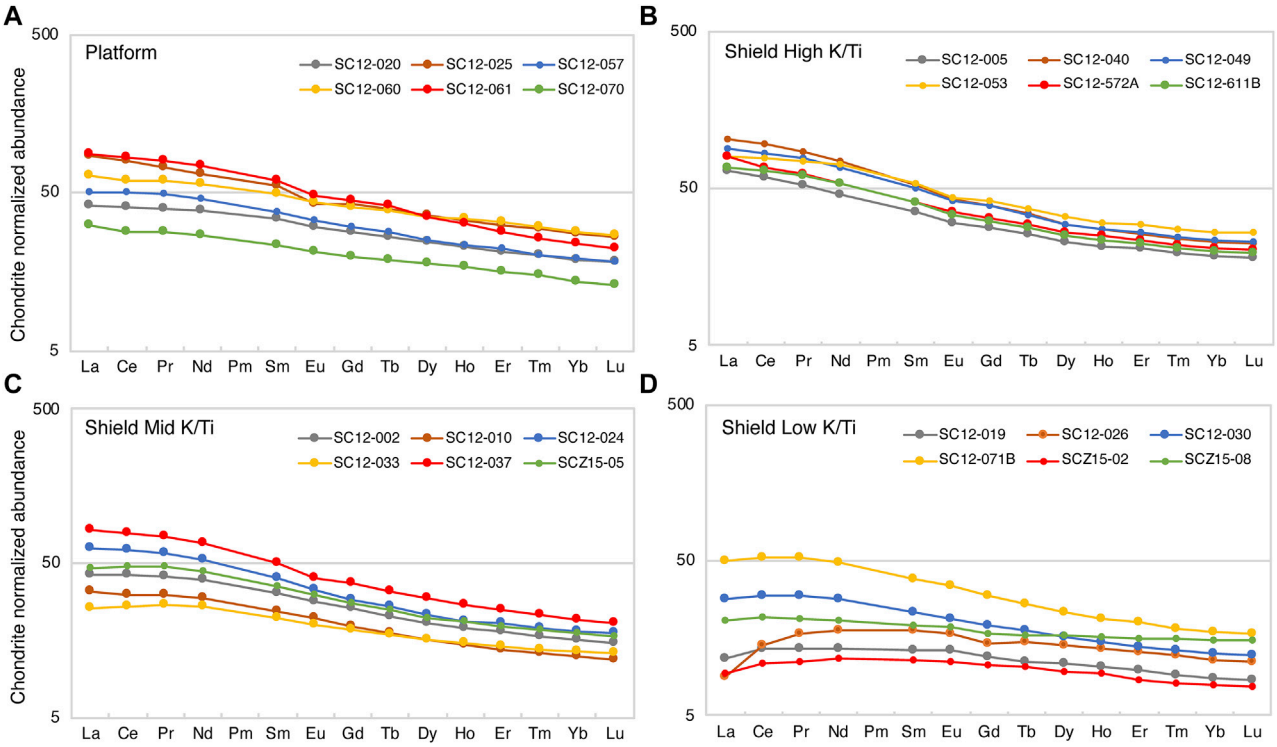


FIGURE 5 | Representative chondrite-normalized rare earth element (REE) values. Normalizing values are from McDonough and Sun (1995). All symbols are larger than 1σ analytical error. **(A)** Platform Series. **(B)** High K_2O/TiO_2 Shield Series. **(C)** Mid K_2O/TiO_2 Shield Series. **(D)** Low K_2O/TiO_2 Shield Series.

the Mid and Low K_2O/TiO_2 groups, extent of melting increases and extends to progressively shallower depths (Mid Shield La_n/Sm_n MD: 1.51, IR: 0.23; Sm_n/Yb_n MD: 2.20, IR: 0.27; Low Shield La_n/Sm_n MD: 0.97, IR: 0.41; Sm_n/Yb_n MD: 1.65, IR: 0.41). The most primitive lavas (Low K_2O/TiO_2 Shield lavas) from Santa Cruz were generated at the shallowest depths and by the greatest extents of melting, on average.

Our proxy for the contribution from the Galápagos plume source, Nb/La, is higher in the Platform than the Shield Series (Platform Nb/La MD: 0.97, IR: 0.08; Shield Nb/La MD: 0.88, IR: 0.13). Platform lavas exhibit less variation in Nb/La than the Shield Series, and the Low K_2O/TiO_2 group has the greatest variability (Nb/La MD: 0.85, IR: 0.16), consistent with radiogenic isotope signatures.

Taken together, the La_n/Sm_n, Sm_n/Yb_n, and Nb/La variations across Santa Cruz suggest that Platform Series lavas were generated by slightly higher extents of melting (on average) at comparable depths to the Shield Series, but with a greater contribution from the enriched PLUME source. Furthermore, Platform Series melts experienced more fractionation than the Shield Series. Platform Series lavas, however, exhibit considerably narrower ranges in incompatible trace element ratios, indicating that they were homogenized significantly more than Shield Series lavas. Within the Shield Series, many of the melts were generated by variable but small degrees of melting of a more depleted source than the Platform Series, likely across a wide range of melt column lengths (Gibson and Geist, 2010), and with little homogenization compared to the Platform Series lavas.

Comparison With Galápagos Archipelago

Probability density functions for the four geochemical metrics Mg#, La_n/Sm_n, Sm_n/Yb_n, and Nb/La from Fernandina, two Isabela volcanoes (Volcán Alcedo and Volcán Sierra Negra), and Santiago are compared to Santa Cruz (**Figure 10**; White et al., 1993; Geist et al., 1995; Reynolds and Geist, 1995; Kurz and Geist, 1999; Allan and Simkin, 2000; Gibson et al., 2012; Geist et al., 2014a). Consistent with previous findings (White et al., 1993; Harpp and Geist, 2018), the older islands in the Galápagos (Santa Cruz and Santiago) produce lava compositions that vary more in all four metrics (Mg#, La_n/Sm_n, Sm_n/Yb_n, and Nb/La) than Fernandina and Volcán Sierra Negra, two of the archipelago's youngest volcanoes.

Santa Cruz Platform lavas have similar Mg# MD values to Fernandina, Volcán Sierra Negra, and Volcán Alcedo, but greater variability than Fernandina and Volcán Sierra Negra (**Figure 10**); the wider interquartile range of Volcán Alcedo reflects its bimodal compositional distribution, which includes rhyolites from an explosive event ~100 ka (Geist et al., 1995). The distribution of Mg# in Shield Series lavas most closely resembles Santiago's geochemical profile (White et al., 1993; Gibson et al., 2012), also with greater variation in Mg# than Fernandina or Volcán Sierra Negra.

Platform Series lavas have an MD for La_n/Sm_n close to that of Fernandina, a Sm_n/Yb_n MD lower than Fernandina's, and more depleted isotopic and Nb/La ratios (**Figures 8**, **10**). Like Fernandina and Volcán Sierra Negra, the Platform Series has a narrow range of

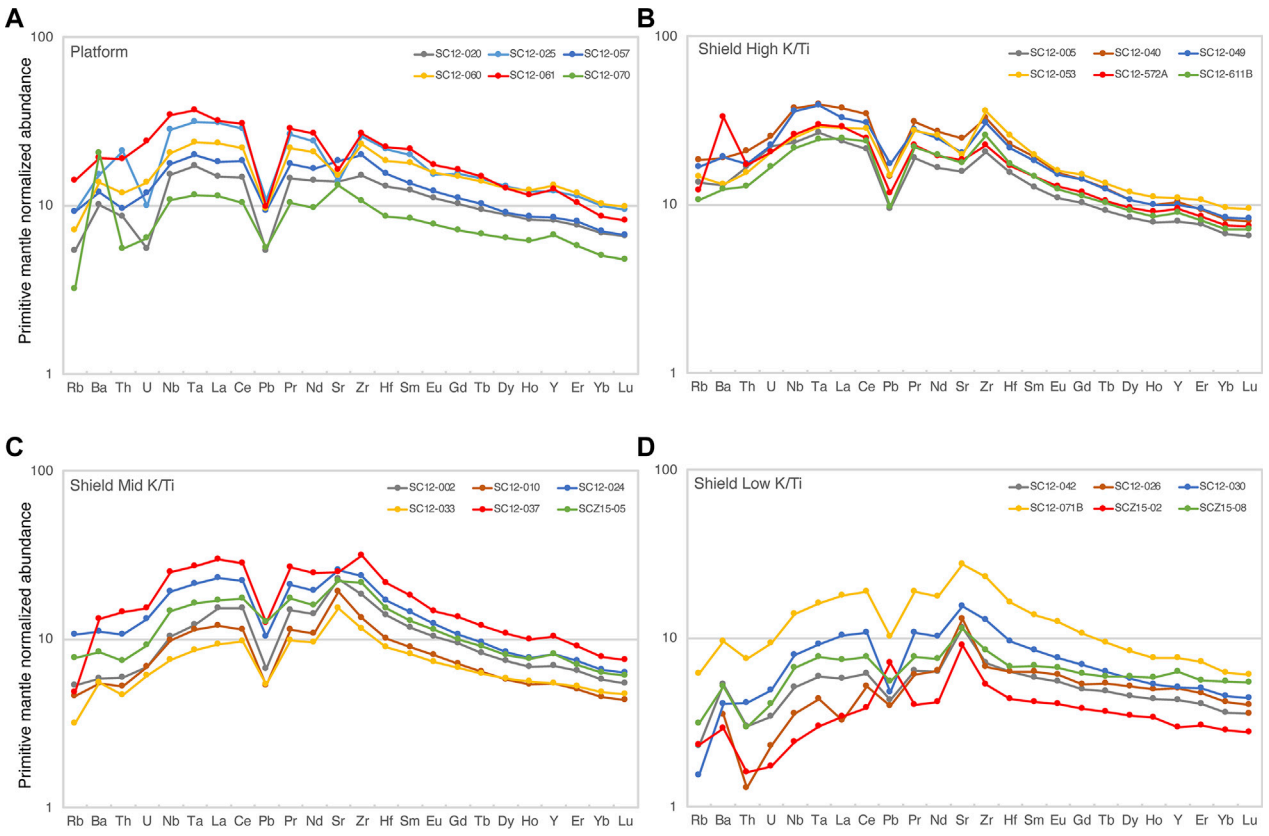


FIGURE 6 | Representative trace element contents of Santa Cruz lavas normalized to primitive mantle (McDonough and Sun, 1995). All symbols are larger than 1σ analytical error. **(A)** Platform Series. **(B)** High K_2O/TiO_2 Shield Series. **(C)** Mid K_2O/TiO_2 Shield Series. **(D)** Low K_2O/TiO_2 Shield Series.

La_n/Sm_n and Sm_n/Yb_n. Thus, compared to Fernandina and Volcán Sierra Negra, Platform melts were generated by broadly similar extents of melting at shallower depths of a more depleted mantle source, which reflect longer melt columns owing to the volcano's proximity to the GSC and therefore its thinner lithosphere (Gibson and Geist, 2010). By contrast, Shield Series samples exhibit greater variation in degree and depth of melting than the Platform Series or the western shields, resembling the more primitive, variable Santiago lavas (**Figure 10**; Gibson et al., 2012).

In terms of Nb/La, the ITE plume proxy, all Santa Cruz lavas exhibit values close to the MD of Santiago and lower than those of the western shields (**Figure 10**). Thus, even though Platform Series lavas are enriched compared to the Shield Series, none of the Santa Cruz lavas are as enriched as those from the western archipelago.

DISCUSSION

Petrogenetic Development of Santa Cruz Island

Melt Generation Processes at Santa Cruz

Geochemical variations in the Platform and Shield Series indicate that melts of the two units were generated under distinct sets of conditions. The key differences between the two units include:

1) The Platform Series requires more melting in the garnet stability field (10–30%) than the Shield Series (0–20%), according to REE systematics (e.g., Gibson and Geist, 2010).
2) Shield Series lavas exhibit more variation than the Platform Series in all melting parameters, including source composition, depth of melting, and extent of melting (**Figure 10**), specifically: a. whereas average depths of melting for both the Shield and Platform Series are comparable, some Shield Series melts were generated at significantly shallower depths, as reflected by the samples with lower Sm_n/Yb_n ratios than the Platform Series; and b. most lavas from the Platform Series result from 1 to 10% melting of a mixed PLUME-DUM source, whereas the Shield Series was produced by a greater range in extents of melting (1–20%) of a more depleted mixed PLUME-DUM source.

In general, depth and extent of melting at hotspot-generated ocean islands are controlled by mantle composition (e.g., Ito and Mahoney, 2005), thickness of the lithosphere (e.g., McKenzie and O'Nions, 1991; Gibson and Geist, 2010), and proximity to the plume (potential temperature; e.g., Herzberg and Gazel, 2009).

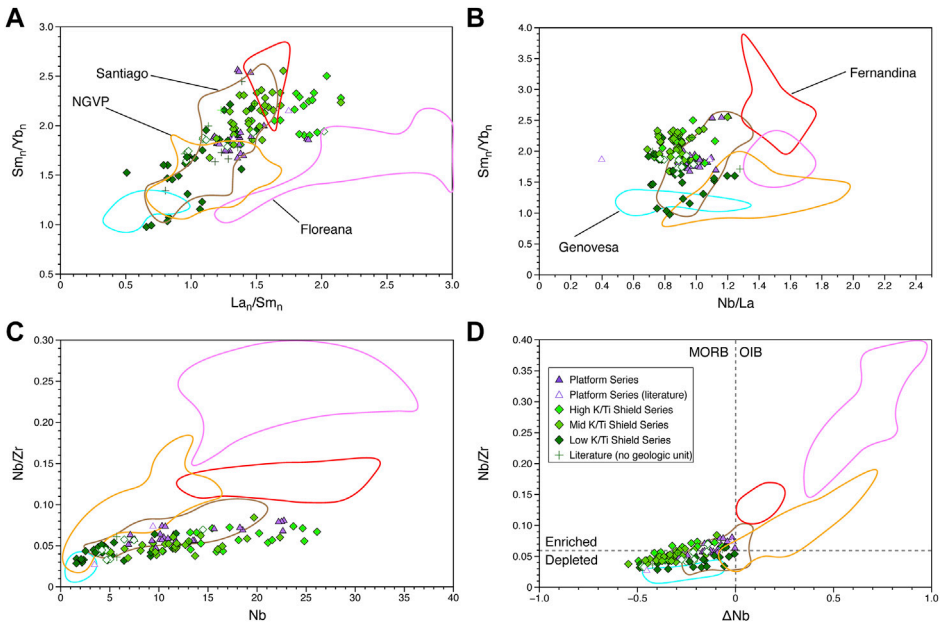


FIGURE 7 | Santa Cruz incompatible trace element ratio variations relative to selected Galápagos Islands. Fields are literature data. Red: Fernandina, blue: Genovesa, brown: Santiago, pink: Floreana, yellow: Northern Galápagos Volcanic Province (Bow and Geist, 1992; White et al., 1993; Harpp et al., 2002; Harpp et al., 2003; Saal et al., 2007; Gibson and Geist, 2010; Gibson et al., 2012; Harpp et al., 2014a; Harpp et al., 2014c). **(A)** Chondrite-normalized La_n/Sm_n and Sm_n/Yb_n ratios (McDonough and Sun, 1995). **(B)** Nb/La versus chondrite-normalized Sm_n/Yb_n ratios. **(C)** Nb versus Nb/Zr. **(D)** ΔNb versus Nb/Zr discrimination diagram to identify origin of depleted signatures. ΔNb (Fitton et al., 1997) = 1.74 + log(Nb/Y) − 1.92 log(Zr/Y). ΔNb >0 is attributed to lower mantle origin (OIB field); ΔNb <0 indicates depleted mantle origin (MORB field). Lavas with Nb/Zr > 0.06 are considered enriched, and those with Nb/Zr < 0.06 are depleted according to Fitton et al. (2003). Several Floreana literature data extend to Nb/Zr = 0.655 and ΔNb = 0.939, but are not shown. Samples indicated by a cross are literature data from Santa Cruz (White et al., 1993; Kurz and Geist, 1999; Saal et al., 2007); they have not been attributed to either the Platform or Shield Series owing to a lack of GPS coordinates for their origin locations.

Variation in mantle composition only explains a small part of the observed melt systematics across Santa Cruz. Enriched mantle sources initiate melting at greater depths than depleted material because they are more fertile and capable of melting at lower temperatures owing to different source lithologies and/or volatile content (e.g., Hirschmann, 2000; Gleeson and Gibson, 2021). Consequently, variable extents of melting of a mixed source result in a direct correlation between incompatible trace element ratios and radiogenic isotope ratios (e.g., at Santiago; Gibson et al., 2012). At Santa Cruz, ITE ratios do not correlate strongly with radiogenic isotope ratios (**Figure 9**), suggesting that a model in which a plum-pudding mantle made of mixed depleted and enriched components becomes progressively depleted with increasing extents of melting is not the dominant process controlling chemical heterogeneity of the island's lavas (e.g., Ito and Mahoney, 2005). We cannot rule out, however, the possibility that chemical and lithologic heterogeneities in the mantle contribute in part to the observed chemical and isotopic variations.

Lithospheric thickness affects the average depth of melting if upwelling and melting continues to the base of the lithosphere (e.g., Klein and Langmuir, 1987; Ellam, 1992; Ito and Mahoney, 2005; Gibson and Geist, 2010). According to Gibson and Geist (2010), typical geochemical estimates for lithospheric thickness are ~57 km in the western Galápagos and ~53 km in the east. Gibson et al. (2012) document a strong correlation between ITE and radiogenic isotope ratios at Santiago, which they attribute to differential melting of a compositionally heterogeneous mantle across an abrupt lithospheric gradient, coupled with a slight shift in bulk source composition across the lithospheric discontinuity. According to their model, enriched and depleted components are intermixed at a short spatial scale beneath Santiago, on the order of kilometers. Beneath the western half of the island, thicker lithosphere limits the top of melt columns so that melts are dominated by the enriched component of the heterogeneous mantle; farther east, where the lithosphere is thinner and melt columns are longer, more of the refractory depleted material melts, diluting the enriched signal. The lack of a correlative relationship between ITE and isotopic ratios on Santa Cruz (**Figure 9**), however, also eliminates lithospheric thickness as a primary control on the geochemical variations on Santa Cruz.

The remaining factor influencing depth and extent of melting at Santa Cruz is distance from the plume center and intensity of magma supply. The potential temperature of the Galápagos plume is ~1350–1400°C (e.g., Ito et al., 1997; Hooft et al., 2003), and thermal anomalies are typically 200–300°C greater than the ambient mantle (Herzberg et al., 2007). Hotter upwelling plumes cause the mantle to intersect the solidus at greater depths than the ambient mantle, supplying overlying volcanoes with higher magmatic fluxes. The oldest recently dated Platform Series

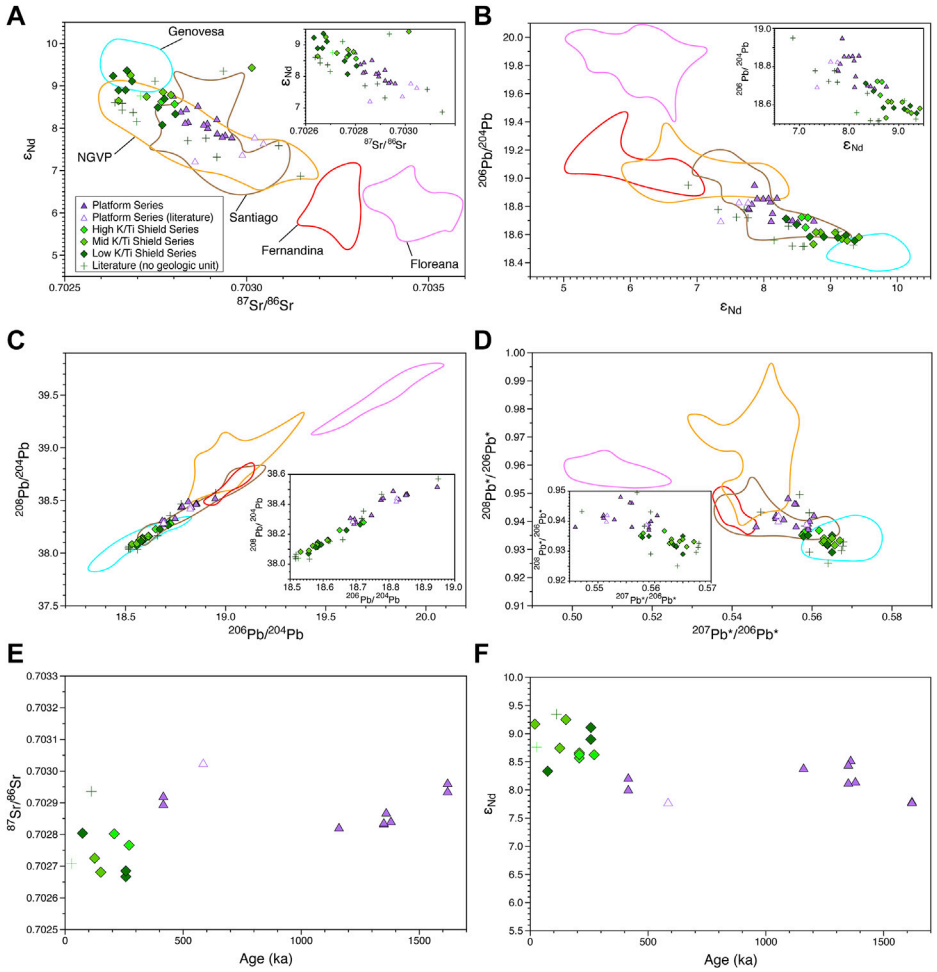


FIGURE 8 | Variations in radiogenic isotope ratios for Santa Cruz lavas. Fields are literature data. Red: Fernandina, blue: Genovesa, brown: Santiago, pink: Floreana, yellow: Northern Galápagos Volcanic Province (Bow and Geist, 1992; White et al., 1993; Harpp et al., 2002; Harpp et al., 2003; Saal et al., 2007; Gibson and Geist, 2010; Gibson et al., 2012; Harpp et al., 2014a; Harpp et al., 2014c). Symbols are larger than 1σ analytical error. **(A)** $^{87}Sr/^{86}Sr$ versus ε_{Nd}; note that two Shield Series samples offset from the main array to higher $^{87}Sr/^{86}Sr$ values are likely contaminated by seawater and their compositions are not considered in further discussion; **(B)** ε_{Nd} versus $^{206}Pb/^{204}Pb$; **(C)** $^{206}Pb/^{204}Pb$ versus $^{208}Pb/^{204}Pb$; **(D)** $^{207}Pb^*/^{206}Pb^*$ versus $^{208}Pb^*/^{206}Pb^*$. Radiogenic lead calculation: $^{208}Pb^*/^{206}Pb^* = [(^{208}Pb/^{204}Pb)_{sample}-(^{208}Pb/^{204}Pb)_{Earth\ Initial}]/[(^{206}Pb/^{204}Pb)_{sample}-(^{206}Pb/^{204}Pb)_{Earth\ Initial}]$, with $(^{208}Pb/^{204}Pb)_{Earth\ Initial} = 29.475$ and $(^{206}Pb/^{204}Pb)_{Earth\ Initial} = 9.307$ based on Canyon Diablo Troilite (Galer and O'Nions, 1985). $^{207}Pb^*/^{206}Pb^* = [(^{207}Pb/^{204}Pb)_{sample}-(^{207}Pb/^{204}Pb)_{Earth\ Initial}]/[(^{206}Pb/^{204}Pb)_{sample}-(^{206}Pb/^{204}Pb)_{Earth\ Initial}]$, with $(^{207}Pb/^{204}Pb)_{Earth\ Initial} = 10.294$ and $(^{206}Pb/^{204}Pb)_{Earth\ Initial} = 9.307$ based on Canyon Diablo Troilite (Galer and O'Nions, 1985). **(E)** $^{87}Sr/^{86}Sr$ variations in Santa Cruz lavas over time (in ka), for all available dates of study samples; **(F)** ε_{Nd} variations in Santa Cruz lavas over time (in ka), for all available dates of study samples. Samples indicated by a cross are literature data from Santa Cruz (White et al., 1993; Kurz and Geist, 1999; Saal et al., 2007); they have not been attributed to either the Platform or Shield Series owing to a lack of GPS coordinates for their origin locations.

lava of Santa Cruz (SC12-020; 1620 ka ± 15 (1σ); Schwartz et al., 2022), was formed when the island was in the current location of Volcán Alcedo, on Isabela Island ~80 km to the west, and most dated Platform Series have ages >1 Ma. We suggest that the Platform Series' greater depth of melt generation, more enriched compositions, and lesser geochemical variation are consistent with its location closer to the hotter plume center.

The low extent of mantle melting suggested by our modeling to generate the Platform Series (1–10%) may be explained by the fact that seismic tomography places the hottest part of the Galápagos plume center to the south and west of Fernandina Island (Hooft et al., 2003; Villagomez et al., 2007; Villagomez et al., 2014). By the time the oldest Platform Series lavas were emplaced, the volcano had moved to the eastern edge of the plume's core and was experiencing a waning magma flux (e.g., Geist et al., 2014a). This is a similar condition to the active Volcán Wolf today, which also taps a depleted source at the northern periphery of the Galapagos plume (Geist et al., 2005).

The younger Shield Series lavas erupted when Santa Cruz was closer to the island's current location, after an apparent hiatus of ~500 ka. Thus, they erupted >150 km from the tomographically identified core of the plume (e.g., Villagómez et al., 2014).

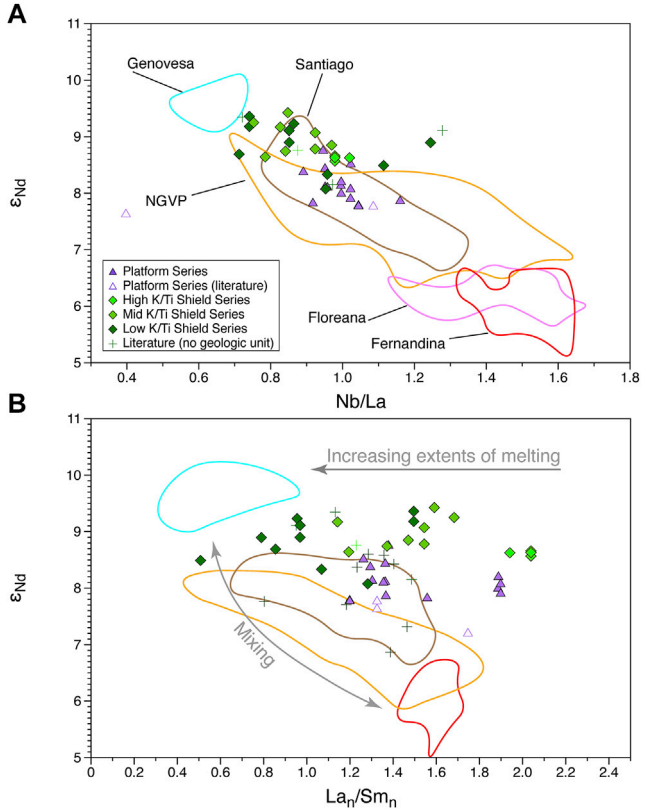


FIGURE 9 | Variations in radiogenic isotope ratios and incompatible trace element ratios for Santa Cruz lavas. Fields are literature data. Red: Fernandina, blue: Genovesa, brown: Santiago, pink: Floreana, yellow: Northern Galápagos Volcanic Province (Bow and Geist, 1992; White et al., 1993; Harpp et al., 2002; Harpp et al., 2003; Saal et al., 2007; Gibson and Geist, 2010; Gibson et al., 2012; Harpp et al., 2014a; Harpp et al., 2014c). Symbols are larger than 1σ analytical error. **(A)** Nb/La versus ε_{Nd}. **(B)** La_n/Sm_n (normalized to primitive mantle; McDonough and Sun, 1995) versus ε_{Nd}. Samples indicated by a cross are literature data from Santa Cruz (White et al., 1993; Kurz and Geist, 1999; Saal et al., 2007); they have not been attributed to either the Platform or Shield Series owing to a lack of GPS coordinates for their origin locations.

Magmatic Processing Prior to Eruption at Santa Cruz

The Platform Series is more evolved and less compositionally variable in its trace element and isotopic variations than the Shield Series (**Figures 2**, **3**, **10**). Furthermore, Platform Series lavas fractionated at shallower depths than the Shield Series, in a regime controlled primarily by plagioclase crystallization, and have, on average, lower phenocryst contents than Shield lavas. The Shield Series lavas experienced deeper fractionation, reflected by stronger clinopyroxene control (**Figure 4**; Geist et al., 1998) and higher average Sm_n/Yb_n values. Taken together, our data indicate that Platform Series magmas were stored in shallower, more mature magmatic bodies that were sufficiently developed to cause partial homogenization of trace element concentrations and isotopic ratios. The Platform Series' greater variability in Mg# relative to western volcanoes such as Fernandina, however, indicates that the Platform Series plumbing system was not able to develop a fully thermochemically buffered system (Geist et al., 2014a; Harpp and Geist, 2018). By contrast, the magmatic reservoirs in which Shield Series melts resided were poorly developed, neither thermochemically buffered nor networked, and likely located at a variety of depths.

Compared to the present-day western shields such as Fernandina, the characteristics of the Platform and Shield Series are those of relatively magma-starved systems, with the Shield Series being supplied by an even lower magma flux than the Platform Series. Similar geochemical systematics related to magma supply are observed at mid-ocean ridges. For example, in high-magma supply areas along the GSC, Colman et al. (2012) observe lower MgO content, lower phenocryst contents, and shallower depths of crystallization, all characteristics of both the Platform and Shield Series, but especially the latter. Colman et al. (2012) argue that low-magma supply ridges have deeper chambers because the magma tends to equilibrate thermally with the mid-to-lower crust, yielding more primitive magmas and higher phenocryst contents. We conclude that magmatic processing conditions at Santa Cruz shifted between the eruption of the Platform Series ~1 Ma and the younger Shield Series. Platform Series lavas were generated by melting a moderately enriched mantle, though more depleted than the current source for Fernandina, to broadly similar extents at, on average, shallower depths than Fernandina (**Figure 10**). Furthermore, western Galápagos shields such as Fernandina and Volcán Sierra Negra exhibit narrow ranges of major and trace element contents, reflecting a thermally buffered magmatic system that efficiently homogenizes melts en route to the surface (Geist et al., 2014a). By contrast, Platform Series lavas have more heterogeneous major element compositions but comparably narrow ranges in trace element ratios, suggesting that the Platform's magmatic plumbing system was sufficiently robust to homogenize melts prior to eruption but inadequate to achieve thermal buffering (Geist et al., 2014a). The younger Shield Series lavas at Santa Cruz were produced from a more depleted mantle source *via* a wide variety of extents and depths of melting similar to those at Santiago (Gibson et al., 2012). Magma supply to the Shield Series, in turn, was considerably lower than that of the Platform Series; Shield Series melts experienced limited crustal processing in small, poorly networked, likely ephemeral magma reservoirs, resulting in more variable and more primitive erupted compositions (e.g., Geist et al., 2014a; Harpp and Geist, 2018).

Magma Supply and Influence of the GSC Across the Archipelago

Construction of Santa Cruz in a Magma-Starved Regime

Geist et al. (2014a) propose a three-stage model for the evolution of the present-day western Galápagos shield volcanoes. The *Juvenile Phase* (e.g., Volcán Cerro Azul, on Isabela; **Figures 1**, **10**) occurs when a volcano is at the leading edge of the hotspot

TABLE 3 | Radiogenic isotope ratios for Santa Cruz lavas.

Sample	Compositional Group	$^{206}Pb/^{204}Pb$	$^{206}Pb/^{204}Pb$ 2s	$^{207}Pb/^{204}Pb$	$^{207}Pb/^{204}Pb$ 2s	$^{208}Pb/^{204}Pb$	$^{208}Pb/^{204}Pb$ 2s	$^{87}Sr/^{86}Sr$	$^{87}Sr/^{86}Sr$ 2s
SC12-008	Platform exposed in fault	18.8542	0.0007	15.5517	0.0007	38.4651	0.002	0.702882	0.000006
SC12-008 re	Platform exposed in fault	18.8522	0.001	15.5492	0.0008	38.4597	0.002		
SC12-009	Platform exposed in fault	18.6941	0.002	15.5406	0.001	38.2675	0.003	0.702798	0.000009
SC12-020	Platform	18.7765	0.0008	15.5542	0.0007	38.4290	0.002	0.702933	0.00001
SC12-020	Platform	18.783	0.001	15.558	0.001	38.440	0.002	0.702959	0.00001
SC12-025	Platform	18.8133	0.0008	15.5604	0.0007	38.4872	0.002	0.702941	0.000008
SC12-059	Platform	18.6910	0.001	15.5409	0.0009	38.2904	0.002	0.702831	0.00001
SC12-059	Platform	18.696	0.0008	15.545	0.0008	38.300	0.002	0.702834	0.00001
SC12-060	Platform	18.699	0.0008	15.543	0.0008	38.282	0.002	0.702819	0.00001
SC12-064	Platform	18.9473	0.0008	15.5590	0.0008	38.5151	0.002	0.702919	0.000007
SC12-065	Platform	18.7469	0.0008	15.5418	0.0007	38.3258	0.002	0.702839	0.00001
SC12-067	Platform	18.683	0.0007	15.548	0.0006	38.306	0.002	0.702866	0.000009
SC12-070	Platform	18.830	0.0009	15.558	0.0007	38.431	0.002	0.702892	0.00001
SC12-572B	Platform exposed in fault	18.8515	0.0008	15.5514	0.0009	38.4635	0.002	0.702893	0.000007
SC12-572B	Platform exposed in fault	18.856	0.0005	15.553	0.0005	38.466	0.001	0.702918	0.00002
SC12-011	Shield Low K/Ti (<0.15)	18.712	0.0009	15.540	0.001	38.265	0.002	0.702804	0.00001
SC12-015	Shield Low K/Ti (<0.15)	18.584	0.001	15.524	0.001	38.116	0.002	0.702667	0.00002
SC12-015	Shield Low K/Ti (<0.15)	18.5780	0.002	15.5201	0.002	38.1127	0.004	0.702685	0.000007
SC12-026	Shield Low K/Ti (<0.15)	18.6711	0.001	15.5303	0.001	38.2267	0.003	0.702756	0.000006
SC12-051	Shield Low K/Ti (<0.15)	18.5559	0.0008	15.5190	0.0008	38.0712	0.002	0.702671	0.00001
SC12-584B	Shield Low K/Ti (<0.15)	18.594	0.001	15.525	0.0009	38.131	0.002	0.702633	0.00001
SCZ15-01	Shield Low K/Ti (<0.15)	18.5839	0.0008	15.5346	0.0007	38.1446	0.002	0.702774	0.000008
SC12-012	Shield Mid K/Ti (0.15-0.24)	18.6148	0.012	15.5322	0.0007	38.1630	0.002	0.702770	0.000008
SC12-012	Shield Mid K/Ti (0.15-0.24)	18.617	0.0009	15.531	0.0007	38.157	0.002	0.702792	0.00001
SC12-012 re	Shield Mid K/Ti (0.15-0.24)	18.6142	0.012	15.5322	0.0008	38.1635	0.002		
SC12-012 re2	Shield Mid K/Ti (0.15-0.24)	18.6129	0.0008	15.5307	0.0008	38.1597	0.002		
SC12-024	Shield Mid K/Ti (0.15-0.24)	18.581	0.0006	15.527	0.0006	38.130	0.002	0.703014	0.00001
SC12-033	Shield Mid K/Ti (0.15-0.24)	18.5690	0.0008	15.5284	0.0007	38.1223	0.002		
SC12-038	Shield Mid K/Ti (0.15-0.24)	18.531	0.0007	15.523	0.0006	38.083	0.002	0.702725	0.00001
SC12-046	Shield Mid K/Ti (0.15-0.24)	18.557	0.0008	15.525	0.0006	38.091	0.002	0.702681	0.00001
SC12-027	Shield High K/Ti (>0.24)	18.7201	0.0008	15.5432	0.0007	38.2853	0.002		
SC12-027	Shield High K/Ti (>0.24)	18.723	0.006	15.543	0.0006	38.280	0.001	0.702802	0.00001
SC12-040	Shield High K/Ti (>0.24)	18.650	0.0007	15.542	0.0006	38.227	0.002	0.702766	0.00001

Sample	Compositional Group	$^{143}Nd/^{144}Nd$	$^{143}Nd/^{144}Nd$ 2s	C_{Nd}	$^{176}Hf/^{177}Hf$	$^{176}Hf/^{177}Hf$ 2s	C_{Hf}
SC12-008	Platform exposed in fault	0.513052	0.000008	8.07	0.283124	0.000005	11.98
SC12-008 re	Platform exposed in fault	0.513043	0.000009	7.90			
SC12-009	Platform exposed in fault	0.513087	0.000006	8.75	0.283133	0.000005	12.32
SC12-020	Platform	0.513037	0.000006	7.78	0.283103	0.000006	11.25
SC12-020	Platform	0.513036	0.000006	7.77			
SC12-025	Platform	0.513039	0.000006	7.82	0.283091	0.000006	10.82
SC12-059	Platform	0.513054	0.000006	8.11	0.283124	0.000006	11.98
SC12-059	Platform	0.513070	0.000005	8.43			
SC12-060	Platform	0.513067	0.000005	8.37			
SC12-064	Platform	0.513041	0.000004	7.86	0.283088	0.000004	10.73
SC12-065	Platform	0.513055	0.000007	8.13	0.283112	0.000007	11.58
SC12-067	Platform	0.513074	0.000005	8.51			
SC12-070	Platform	0.513053	0.000006	8.10			
SC12-572B	Platform exposed in fault	0.513048	0.000008	7.99	0.283112	0.000006	11.56
SC12-572B	Platform exposed in fault	0.513058	0.000006	8.20			
SC12-011	Shield Low K/Ti (<0.15)	0.513065	0.000006	8.33			
SC12-015	Shield Low K/Ti (<0.15)	0.513094	0.000007	8.90			
SC12-015	Shield Low K/Ti (<0.15)	0.513105	0.000006	9.11	0.283142	0.000004	12.63
SC12-026	Shield Low K/Ti (<0.15)	0.513073	0.000006	8.49	0.283127	0.000003	12.10
SC12-051	Shield Low K/Ti (<0.15)	0.513118	0.000006	9.36	0.283146	0.000005	12.76
SC12-051 re	Shield Low K/Ti (<0.15)	0.513109	0.000006	9.18			
SC12-584B	Shield Low K/Ti (<0.15)	0.513111	0.000006	9.23			
SCZ15-01	Shield Low K/Ti (<0.15)	0.513083	0.000006	8.69	0.283134	0.000005	12.34

(Continued on following page)

(Continued on following page)

TABLE 3 | (*Continued*) Radiogenic isotope ratios for Santa Cruz lavas.

Sample	Compositional Group	$^{143}Nd/^{144}Nd$	$^{143}Nd/^{144}Nd$ 2s	C_{Nd}	$^{176}Hf/^{177}Hf$	$^{176}Hf/^{177}Hf$ 2s	C_{Hf}
SC12-012	Shield Mid K/Ti (0.15-0.24)	0.513091	0.000007	8.85	0.283140	0.000003	12.57
SC12-012	Shield Mid K/Ti (0.15-0.24)	0.513088	0.000007	8.78			
SC12-012 re	Shield Mid K/Ti (0.15-0.24)	0.513103	0.000006	9.07			
SC12-024	Shield Mid K/Ti (0.15-0.24)	0.513121	0.000007	9.43			
SC12-033	Shield Mid K/Ti (0.15-0.24)	0.513108	0.000005	9.17	0.283146	0.000005	12.77
SC12-038	Shield Mid K/Ti (0.15-0.24)	0.513086	0.000005	8.74			
SC12-046	Shield Mid K/Ti (0.15-0.24)	0.513112	0.000003	9.25			
SC12-027	Shield High K/Ti (>0.24)	0.513082	0.000005	8.66	0.283131	0.000003	12.22
SC12-027	Shield High K/Ti (>0.24)	0.513077	0.000006	8.57			
SC12-027 re	Shield High K/Ti (>0.24)	0.513081	0.000005	8.63	0.283134	0.000004	12.33
SC12-040	Shield High K/Ti (>0.24)	0.513080	0.000005	8.63			

Analytical details and uncertainties are reported in the Methods section of the text. Italicized samples were analyzed at the Pacific Centre for Isotopic and Geochemical Research at the University of British Columbia; methodological details are available in Harpp and Weis (2020). Several replicate analyses (indicated by "re") are also included.

and the magmatic system is functioning in an unsteady thermal state. When the ~5 km-deep magmatic system is immature and poorly networked, individual batches of magma experience distinct crystallization histories, resulting in moderately heterogeneous geochemical signatures.

Next, the volcano moves into the *Mature Steady-State Phase*. Located directly above the plume stem, magma supply is sufficiently robust to achieve a steady thermal state, as exemplified by Fernandina, Volcán Wolf, and Volcán Sierra Negra (**Figure 10**). Magmas are compositionally monotonous and reside in a 1–3 km-deep sill immediately prior to eruption. The high flux of mantle-derived melts creates a crystal mush that acts as a thermal regulator, yielding a thermochemically buffered system capable of homogenizing most melts passing through it (Stock et al., 2018, 2020). Finally, when a Galápagos volcano is carried downstream from the plume, it reaches the *Dying Phase*. When the melt supply rate decreases, a steady-state magmatic plumbing system can no longer be maintained, and the 1–3 km deep magma reservoir likely freezes. Volcán Alcedo has erupted rhyolites fractionated from such a cooling crystal mush (**Figure 10**; Geist et al., 1995; Geist et al., 2014a).

This evolutionary model, however, only considers the western Galápagos shield volcanoes, and melt systematics of Santa Cruz do not align with any of its proposed phases. While the Platform Series exhibits comparably homogeneous trace element signatures to Fernandina and Volcán Sierra Negra, it lacks the monotonous major element compositions that define the thermochemically buffered Mature Steady-State phase of these younger volcanoes (**Figure 10**; Geist et al., 2014a). Though sampling of Santa Cruz is limited to the uppermost stratigraphic layers, to date no felsic material has been observed on the island, suggesting that it does not emulate Volcán Alcedo's Dying Phase, either (Geist et al., 2014a).

Harpp and Geist (2018) and Cleary et al. (2020) propose an alternative paradigm for the formation of the older, eastern Galápagos volcanoes. They note that the distinct magmatic, compositional, and structural characteristics of the western and central/eastern Galápagos Islands define separate geological provinces. The central and eastern volcanoes, including Santiago, Santa Cruz, Floreana, and San Cristóbal, erupt more primitive, heterogeneous lavas, suggesting that magmas spent shorter times in crustal storage, and their plumbing systems were poorly developed with no thermochemical buffering. The eastern islands lack submarine rift zones, have never hosted summit calderas (Cleary et al., 2020), and are dominated by faults and linear vent systems, characteristics consistent with a magma-starved regime compared to that of the present-day western archipelago. In the eastern Galápagos, regional stresses are the dominant influence on structural and eruptive behavior (Schwartz et al., 2022). This regime contrasts with the western volcanoes, where magmatic pressure is the strongest influence on volcano construction, resulting in large shields with calderas, circumferential and radial faults and fissures, and many submarine rift zones (e.g., Lonsdale, 1989; Chadwick and Howard, 1991; Smith et al., 2002; Bagnardi et al., 2013).

Influence of the Proximal Galápagos Spreading Center on Eastern Volcano Construction

Harpp and Geist (2018) suggest that Santa Cruz and most of the other central and eastern islands are not older, evolved versions of the western shields, but were constructed in a distinct tectonic setting from the younger volcanoes, one strongly influenced by the adjacent GSC. The GSC has been migrating northeast, away from the Galápagos hotspot at 65 km/Ma (Wilson and Hey, 1995; Mittlestaedt et al., 2011). During the past 5 million years, however, the GSC has experienced multiple southward ridge jumps, which occurred at ~4.5 Ma, ~3.5 Ma, between 2.5 and 3.5 Ma, and ~1 Ma, each time resulting in a 20–30 km displacement of a GSC segment toward the archipelago (Mittelstaedt et al., 2012). The last two ridge jumps established the Galápagos Transform Fault (GTF) and a transtensive stress field expressed as oblique faulting near the transform (Taylor et al., 1994).

The regional stress field created by a transform fault along a mid-ocean ridge can have far-reaching effects on the lithosphere (e.g., Gudmundsson, 1995; Ribe, 1996; Ito et al., 2003; Hall and Kincaid, 2004; Georgen, 2014). Mittelstaedt et al. (2012) proposed that the stress field generated by the two most recent GSC jumps may have perturbed the lithosphere within ~150 km sufficiently to promote the formation of the NW/SE-trending seamount chains of the NGVP, between the main archipelago and the GSC (Harpp and Geist, 2002). If the stress field initiated by the

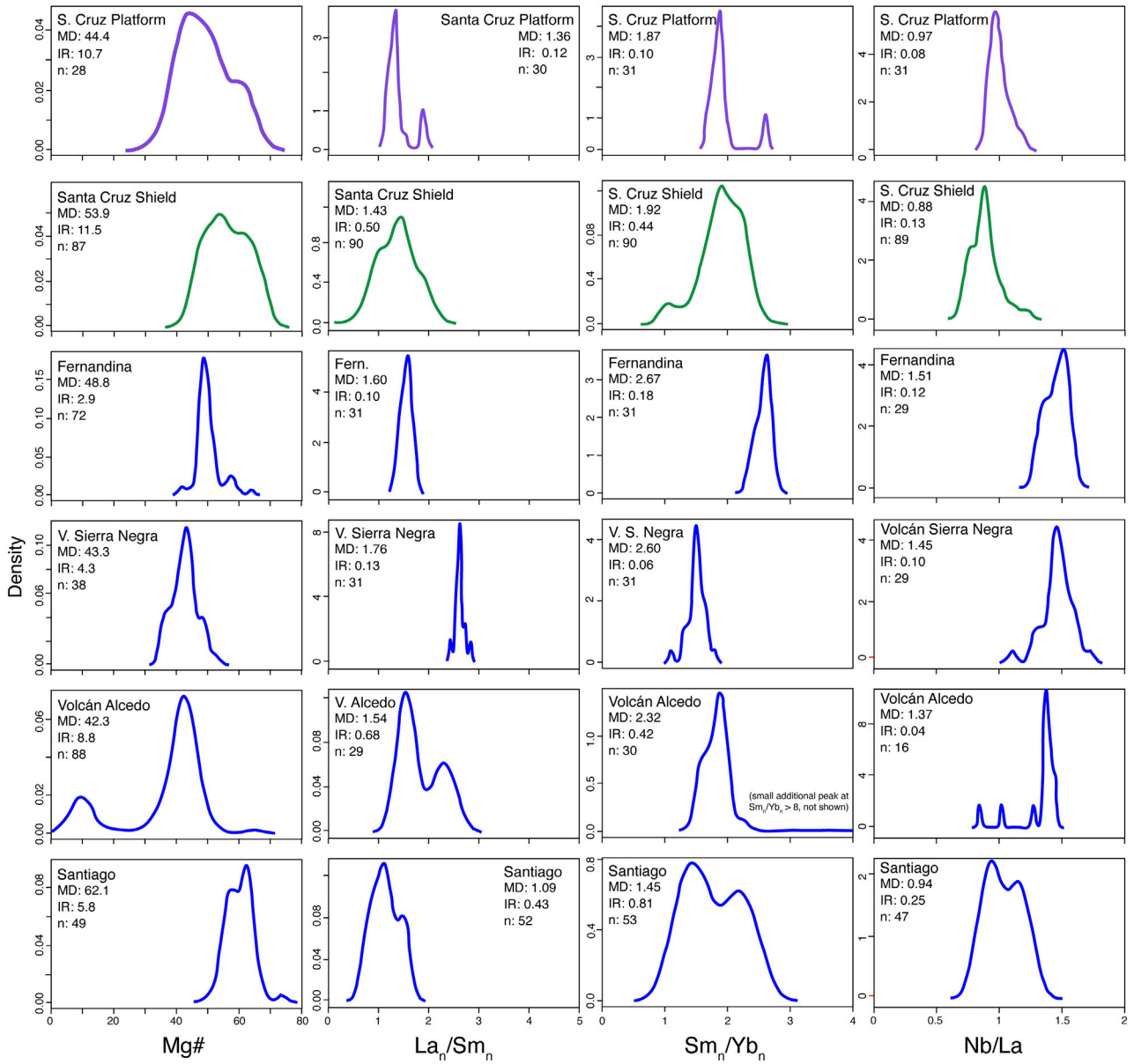


FIGURE 10 | Gaussian kernel distribution statistics for Mg# (proxy for extent of shallow fractionation), La_n/Sm_n (proxy for extent of melting), Sm_n/Yb_n (proxy for depth of melting), and Nb/La (proxy for plume contribution; Kurz and Geist, 1999) for Santa Cruz lavas, shown as Platform and Shield (all sub-groups treated together because they erupted contemporaneously). Also shown for comparison are statistics from Fernandina (White et al., 1993; Kurz and Geist, 1999; Allan and Simkin, 2000), Volcán Sierra Negra (White et al., 1993; Reynolds and Geist, 1995), Volcán Alcedo (Geist et al., 1995), and Santiago (Gibson et al., 2012). MD is the maximum density and IR is the interquartile range, both determined using Wessa (2021). La, Sm, and Yb are normalized to chondrite values (McDonough and Sun, 1995).

GTF is responsible for the Northern Galápagos seamount lineaments, then the present-day central/eastern Galápagos islands forming when the GSC was closer to the plume are likely to have been strongly influenced by the ridge as well. The GTF jumps contemporaneous with Santa Cruz construction, the transtensive kinematics of the GTF (Taylor et al., 1994), and stresses generated by the GSC (e.g., Fujita and Sleep, 1978) may explain the preponderance of linear vent systems and faults across the central and eastern islands, including Santa Cruz. In support of this hypothesis is the fact that Floreana, which would have been the farthest active volcano from the GSC at 1.5 Ma, lacks linear vent structures and faults (Harpp et al., 2014a).

Furthermore, the intensity of the magma flux supplying the central and eastern islands was also likely affected by the proximity of the plume to the GSC. Even though the precise mechanism is debated (e.g., Mittelstaedt et al., 2011; Georgen, 2014; Gibson et al., 2015; Mittal and Richards, 2017; Gleeson and Gibson, 2021), geochemical and morphological behavior clearly

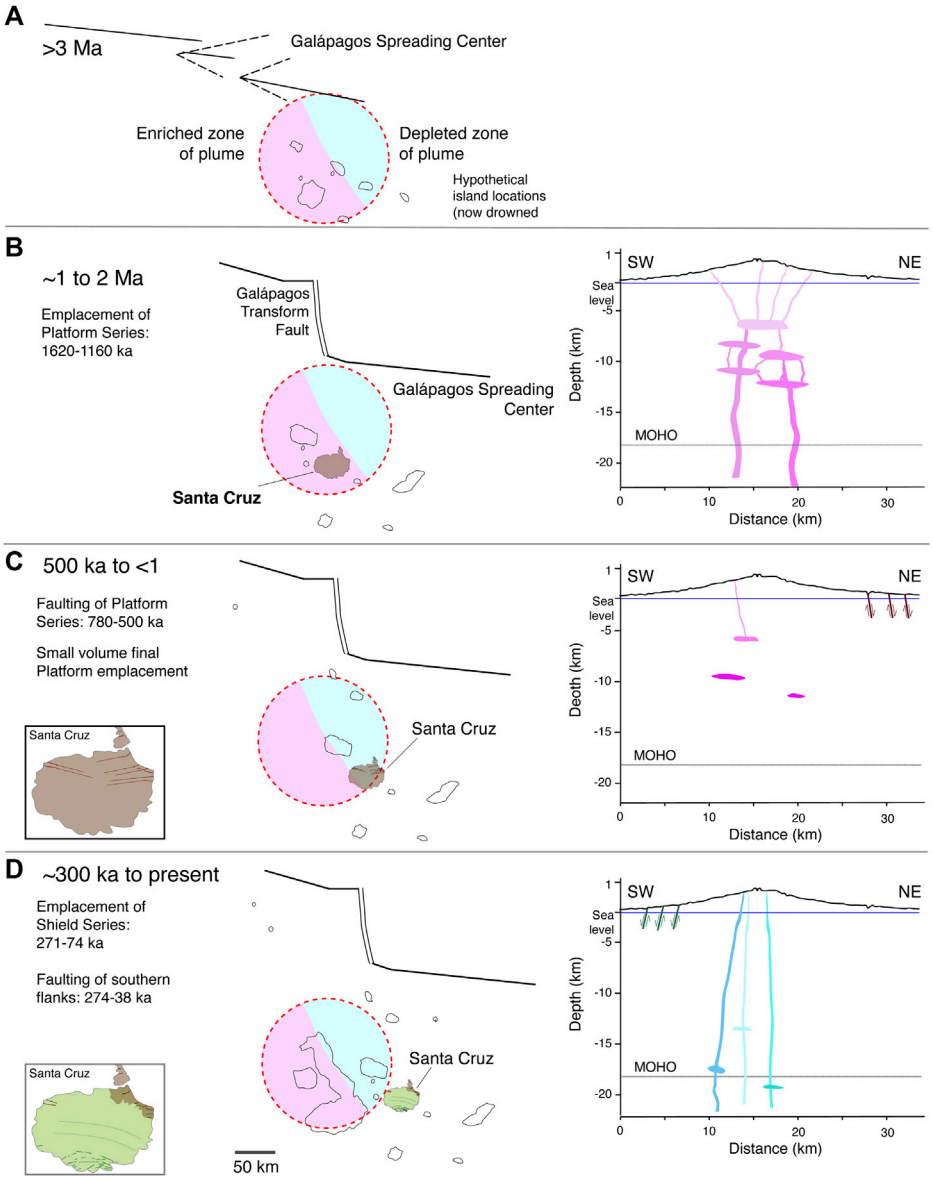


FIGURE 11 | A conceptual timeline of Santa Cruz's volcanic evolution. Left side panels: Map view of archipelago and relationship between plume, islands, and GSC. Right side panels: NE-SW cross-section of Santa Cruz. Note that vertical scales above and below 0 km are different, and that island cross-section has a vertical exaggeration of 4×. Current depth to the MOHO is estimated at ~17 km (Feighner and Richards, 1994). **(A)** LEFT: Prior to ~3 Ma, the GSC was nearly superimposed on the Galápagos plume (Wilson and Hey, 1995). None of the present-day Galápagos Islands date to 3.5 Ma (White et al., 1993), but older islands now submerged downstream to the east existed at the time; their locations are hypothesized here (Christie et al., 1992). The plume's (red dashed circle; limits estimated from Gibson et al., 2012) bilateral compositional asymmetry is indicated with the pink (more enriched, LLSVP-sourced) and blue (more depleted, lower mantle-sourced) zones (Harpp and Weis, 2020). Evolution of the GSC is based on Mittelstaedt et al. (2012). **(B)** LEFT: At ~2 Ma, Santa Cruz begins to form and emerge; between 1629 and 1160 ka, most of the Platform Series lavas sampled in this study are emplaced (brown; Schwartz et al., 2022). The Platform Series is being emplaced as Santa Cruz approaches the compositional boundary of the plume, resulting in geochemical signatures slightly less enriched than present-day Fernandina lavas. According to Mittelstaedt et al. (2012), the Galápagos Transform Fault is formed in the most recent southward jump of the GSC ~1 Ma. RIGHT: The Platform Series lavas constitute the main shield-building phase of Santa Cruz. The proximity of the GSC causes diversion of some plume material toward the ridge, resulting in lower flux to the nascent Santa Cruz volcano than currently supplies Fernandina, sufficient to support formation of a magmatic network capable of partially homogenizing melts prior to eruption, but unable to generate thermochemically buffered conditions. **(C)** LEFT: Between 780 and 500 ka, the Platform Series experiences normal faulting, likely in response to the ~1 Ma southward jump of the GSC. Faults are shown in crimson on the north side of Santa Cruz and Baltra (*see* inset; possible extensions of the faults toward the center of the island are shown as dashes). RIGHT: Normal faulting from Galápagos Transform Fault-related stresses may initiate additional, small volume eruptive activity. **(D) LEFT:** The Shield Series (green) is emplaced between 271 and 74 ka, primarily from aligned vents that cross the volcano's central highlands (green dashed lines). Nearly contemporaneously, normal faulting (dark green lines) occurs along the southern flank of the island (274–38 ka; *see* inset; Schwartz et al., 2022). **RIGHT:** Southern flank of Santa Cruz begins to slump, forming extensional structures. Magma in small, ephemeral, poorly networked reservoirs that are incapable of storing or homogenizing melts is erupted as the Shield Series, with more variable and more primitive compositions compared to the Platform Series. The island has crossed into the plume's eastern compositional zone, causing lavas to have more depleted geochemical signatures (blue colors).

indicates that the GSC currently incorporates material from the Galápagos plume (e.g., Schilling et al., 1982; Ribe, 1996; Canales et al., 1997, 2002; Detrick et al., 2002; Sinton et al., 2003; Behn et al., 2004; Christie et al., 2005; White et al., 2008; Ingle et al., 2010). When the GSC was closer to the plume 1–3 Ma, the ridge probably siphoned even more plume material toward its axis than it does today, diverting it from the nascent volcanoes, and resulting in a constructional regime that was magma-starved compared to today's western Galápagos volcanoes (Harpp and Geist, 2018). At the time of their formation, therefore, Santa Cruz, along with the other central and eastern volcanoes, had a reduced magma supply incapable of establishing thermochemically buffered, crustal-scale mush columns or calderas normally associated with robust magma supplies.

In addition to changes in magma supply related to the migration of the GSC, the constructional and evolutionary trajectories of the eastern volcanoes may also have been controlled by the presence of especially thin lithosphere underlying those structures, owing to their near-ridge location. The lithosphere underlying an ocean island is flexed by the volcanic load, which in turn can have a strong influence on magma ascent pathways during construction (McGovern et al., 2015). On relatively young, thin lithosphere, such as that underlying the western Galápagos (Feighner and Richards, 1994; Gibson and Geist, 2010), the island's load induces compression, which limits and focuses magma ascent, encouraging formation of sill complexes (McGovern et al., 2013; McGovern et al., 2015; LeCorvec and McGovern, 2018). Consistently, the magma reservoirs supporting Fernandina and Volcán Sierra Negra volcanoes are constructed from networks of sills (e.g., Chadwick et al., 2006; Yun et al., 2006; Bagnardi et al., 2013).

The central Galápagos platform has a thinner, weaker lithosphere with an elastic thickness <6 km (Feighner and Richards, 1994; Gibson and Geist, 2010), owing in part to the GTF that displaces the eastern GSC ~100 km closer to the archipelago. When the central volcanoes such as Santa Cruz were forming, from at least 1.6 Ma and up to another million years earlier, the GSC was even closer to the archipelago, and the lithosphere was thinner than it is today. When the lithospheric flexure models of McGovern et al., 2013; Le Corvec and McGovern, 2018; P.J. McGovern, *pers. comm.*, 2021, are extended to near-zero lithospheric thickness, as was probably the case when Santa Cruz was first forming, there is little stress to control the construction process; magma ascent paths are therefore relatively unconstrained, preventing the formation of sill-dominated, centralized magmatic plumbing systems. Instead, magma is free to ascend, resulting in small, dispersed, poorly networked magma storage systems, consistent with the heterogeneous, minimally fractionated lavas erupted across the eastern Galápagos Islands (Harpp and Geist, 2018).

Evolution of Santa Cruz in the Context of the Galápagos Archipelago

To integrate the structural study of Santa Cruz by Schwartz et al. (2022) into our findings for the petrologic evolution of Santa Cruz, we propose the following model (**Figure 11**):

1. Proximity of GSC to plume: Between 3.5 and 2.5 Ma, the GSC experienced a ridge jump of several 10s of kilometers southward toward the plume (Mittelstaedt et al., 2012). Throughout this period, the GSC is considerably closer to the plume than it is currently, diverting plume material toward the ridge (e.g., Ribe, 1996; Ito et al., 2003). Thus, volcanoes forming at the plume center have a reduced magma supply compared to today's western shields (Harpp and Geist, 2018).

2. Emergence of Santa Cruz (1–2 Ma): Geist et al. (2014b) bracket the emergence of Santa Cruz to between 1.1 and 2.3 Ma. Actual emergence must be closer to the old end of this range, because the oldest lavas on Santa Cruz date to ~1.6 Ma (Schwartz et al., 2022).

3. Eruption of the Platform Series: The Platform Series is emplaced primarily between at least ~1620 ± 15 and 1160 ± 35 ka; at the time, the island was ~80 km closer to the plume (51 km/M.y.; Argus et al., 2011). Even though these lavas are the most enriched on Santa Cruz, they are less so than Fernandina (e.g., White et al., 1993; Allan and Simkin, 2000; Harpp and Weis, 2020). Potential explanations for their less-than-pristine enriched plume signatures include either dilution by depleted upper mantle owing to interaction with the then-adjacent GSC or the island's location at the eastern edge of the enriched zone of the plume, where it may have begun transitioning into the more depleted eastern zone (Harpp and Weis, 2020; **Figure 1**). The Platform Series's relatively homogeneous trace element compositions suggest that magma supply was sufficient to homogenize melts to some extent prior to eruption, but inadequate to establish a thermochemically buffered state like Fernandina (Geist et al., 2014a).

4. Platform Series Faulting: According to Schwartz et al. (2022), a series of E/W-trending faults crosscuts the Platform Series <1160 ± 35 ka, possibly between 780 and 500 ka. Given the proximity of the GSC to the archipelago at the time (~65 km closer than the 150–300 km it is today), the Platform Series faulting may reflect regional stresses generated by the most recent southward GSC jump, which displaced the ridge by ~30 km toward the plume and established the regional transtensive stress regime around the now 100 km-long transform fault. The extensional component of the stress field may have generated E-W oriented magmatic intrusions across the near-ridge region (e.g., Mittelstaedt et al., 2012), which may have initiated the Shield Series.

5. Eruption of the Shield Series: The most recent activity on Santa Cruz is the Shield Series, which mostly erupted from 271 ± 17 to 74 ± 38 ka (Bow, 1979; Schwartz, 2014). Regional extension generated by the ~1 Ma GSC ridge jump and Platform Series faulting may have initiated Shield Series activity. The Shield Series lavas are more depleted than the Platform Series, which reflect the island's location farther east, within the less enriched zone of the bilaterally asymmetric plume (Harpp and Weis, 2020). Shield Series melts are highly heterogeneous and more primitive than Platform Series rocks, owing to the ephemeral nature of the small, poorly networked magmatic reservoirs and limited magma supply.

6. Faulting of the Southern Flank's Shield Series: Between 274 ± 18 and 38 ± 8 ka, fault swarms cut Santa Cruz's southern

flanks (**Figure 1**; Schwartz et al. (2022)). Schwartz et al. (2022) propose that these faults are in response to the E/W-oriented intrusions that supplied the Shield Series, although the sequence of events could be reversed (i.e., extensional faulting generates decompression melting; a similar mechanism is modeled for the seamounts and islands in the Northern Galápagos Volcanic Province; *see* Mittelstaedt et al., 2012).

7. Present-day Santa Cruz: Although there has been no documented eruptive activity since 74 ka on Santa Cruz, there has been relatively recent faulting (~38 ka) along the southern flanks. If this phenomenon reflects ongoing structural instability, there is the potential for future tectonic or eruptive events that could pose a risk to the population living along the southern coast of the island in the town of Puerto Ayora.

Mantle Sources at Santa Cruz and Implications for the Galápagos Plume

Harpp and Weis (2020) explained the wide range of geochemical signatures in the Galápagos as the manifestation of a bilaterally asymmetric plume, with the compositional zonation originating at the core-mantle boundary, as originally posited for Hawai'i (Weis et al., 2011). As volcanoes are carried eastward by the Nazca plate, they cross the NW-trending compositional boundary between the western, enriched zone of the plume into the more PREMA-like eastern zone. Consequently, the last material erupted on a Galápagos island will have less enriched signatures than the older material (Harpp et al., 2014b; Harpp and Weis, 2020).

Santa Cruz data are consistent with the bilaterally asymmetric plume model. Harpp and Weis (2020) delineate the boundary between the highly enriched and the less enriched zones immediately west of Santa Cruz. The oldest Platform Series lavas were emplaced when Santa Cruz was located on the eastern edge of the bilateral plume's strongly enriched zone, where the eastern coast of Volcán Alcedo is located today (Harpp and Weis, 2020). The compositions of these 1.6–1.1 Ma lavas, which are not as enriched as material erupted at Fernandina today, may reflect the transition between the western enriched and the eastern, less enriched zone. The more depleted signatures of the younger Shield Series reflect their emplacement location east of the bilateral plume's compositional boundary.

The proximity of the GSC to Santa Cruz >1 Ma when it was first being constructed may also contribute to the Platform Series' being more depleted than Fernandina, *via* two potential mechanisms. In their modeling study of melt transport from plumes to nearby mid-ocean ridges, Gibson and Richards (2018) propose that low-degree, volatile-rich melts formed by initial, deep melting of the plume (>3 GPa; Gleeson and Gibson, 2021) are transported directly to a nearby spreading center *via* channelized flow, reducing contributions from the more enriched, fusible plume to erupted lavas. When the GSC was closer to the Galápagos plume >1 Ma, the intensity of this deep melt transport may have been enhanced, resulting in greater relative depletion of the mantle source responsible for the Platform Series.

A second, well documented mechanism that could explain the depletion of Platform Series lavas relative to Fernandina also reflects the closer proximity of the plume to the GSC >1 Ma. Depleted geochemical signatures at other near-ridge plume systems, including Kerguelen, the Cretaceous Hawaiian plume, and Easter (e.g., Hart et al., 1992; Frey and Weis, 1995; Kingsley and Schilling, 1998; Harrison et al., 2020), have been attributed to dilution of the more enriched plume material by entrainment of depleted upper mantle owing to the proximity of the two magmatic systems. All of the Santa Cruz lavas in this study have MORB-like ΔNb <0 (**Figure 7**; Fitton et al., 1997), suggesting that depleted upper mantle material likely plays an important role in the depleted Santa Cruz lavas (Harpp and Weis, 2020), consistent with their near-ridge origin.

CONCLUSIONS

Like several of its nearest island neighbors and in contrast to the young western Galápagos volcanoes, the geochemistry of Santa Cruz Island is diverse, erupting lavas with variable major and trace element concentrations, in addition to a range of isotopic ratios. The older Platform Series has a more enriched signature than the younger Shield Series, and both are more depleted than younger western Galápagos volcanoes such as Fernandina. Platform Series lavas have relatively invariant trace and isotopic ratios, comparably homogeneous to those at Fernandina, but with heterogeneous, evolved major element compositions. Shield Series lavas are, in turn, significantly more primitive and heterogeneous than those of the Platform Series.

We propose that Santa Cruz has followed a different evolutionary path from the present-day western Galápagos shields, controlled primarily by its proximity to the GSC and its construction in a relatively magma-starved regime (**Figure 11**; Harpp and Geist, 2018). Santa Cruz was formed >1.6 Ma, when the plume was considerably closer to the GSC than it is today. Enhanced plume flow to the ridge may have reduced the magmatic flux available for the construction of Santa Cruz.

Consequently, the Platform Series, the major constructional unit emplaced between ~1620 ± 15 and 1160 ± 35 ka (Schwartz et al., 2022), was established under relatively magma-starved conditions compared to the present-day younger shields. The Platform Series had a sufficiently robust magma supply to develop plumbing systems capable of homogenizing melts to a limited extent, but unable to support development of the caldera-producing, thermochemically buffered systems that exist today in the western archipelago (Geist et al., 2014a; Cleary et al., 2020). The Platform Series is more compositionally depleted than present-day Fernandina lavas because of two factors: *1*) its location at the eastern edge of the plume's enriched zone (Harpp and Weis, 2020); and *2*) dilution of plume material by depleted upper mantle owing to its closer proximity to the GSC at the time of its formation.

The most recent jump of a GSC segment toward the plume ~1 Ma (Mittelstaedt et al., 2012) may have initiated the E-W-trending faults that crosscut the Platform Series <1160 ± 35 ka (Schwartz et al., 2022). After an apparent hiatus in eruptive activity, the Shield Series lavas erupted between 271 ± 17 and 74 ± 38 ka (Schwartz et al., 2022). These lavas are more depleted than the Platform Series, consistent with

migration of the Nazca Plate eastward over the boundary dividing the enriched and depleted zones of the bilaterally asymmetric Galápagos plume (Harpp and Weis, 2020). Owing to their even weaker magma supply farther from the plume center, the more variable, more primitive Shield Series lavas erupted after little to no crustal processing from small, ephemeral, poorly networked reservoirs. Coincident with the emplacement of the Shield Series, the southern flank of Santa Cruz experienced a period of faulting between 274 ± 18 and 38 ± 8 ka (Schwartz et al., 2022). Given that the faulting along the southern flank is extensional, it is possible that tectonic or eruptive activity could occur in the future, putting the population in the town of Puerto Ayora at risk. Much of the distinctive constructional characteristics of Santa Cruz can be attributed to its proximity to the GSC, its limited magma supply owing to diversion of plume material toward the ridge, and the thin, near-zero age lithosphere underlying the volcano.

DATA AVAILABILITY STATEMENT

The original contributions presented in the study are included in the article/**Supplementary Materials**, further inquiries can be directed to the corresponding author.

AUTHOR CONTRIBUTIONS

EW and KH are co-first authors. All authors participated in fieldwork on Santa Cruz Island, primarily EW, DS and RV. All authors participated in trace element analyses of samples. EW performed major element and isotopic ratio analyses, and wrote the original draft of the manuscript as her MSc thesis from the University of Idaho's Department of Geological Sciences.

FUNDING

All research, including analytical fees and the costs of field work, were supported by OCE-0926491 and EAR-1347731 to KH from the National Science Foundation. The University of Idaho provided teaching assistant support for EW during her Master's work. Colgate University provided some of the publication fees.

ACKNOWLEDGMENTS

We are grateful to D. Geist, J. Schleicher, M. Almeida, and Requelme for their assistance in the field. Additional geochemical analyses were performed by J. Mahr, H. Bercovici, and R. Pimentel. We acknowledge the Galápagos National Park Service for granting us permission to collect samples and conduct fieldwork on Santa Cruz Island. N. d'Ozouville and other staff at the Charles Darwin Research Station provided much logistical support, without whom the field seasons could not have been accomplished. Thanks to D. Geist and M. Jackson for constructive reviews during writing of the manuscript, to P.J. McGovern for sharing his expertise and ideas about Galápagos volcanoes and lithospheric thickness, and to M. Gleeson and two additional anonymous reviewers for their insightful comments that helped improve the manuscript. This work was funded by NSF grants EAR-1347731 and OCE-0926491 to KH.

SUPPLEMENTARY MATERIAL

The Supplementary Material for this article can be found online at: https://www.frontiersin.org/articles/10.3389/feart.2022.845544/full#supplementary-material

REFERENCES

Allan, J. F., and Simkin, T. (2000). Fernandina Volcano's Evolved, Well-Mixed Basalts: Mineralogical and Petrological Constraints on the Nature of the Galapagos Plume. *J. Geophys. Res.* 105, 6017–6041. doi:10.1029/1999JB900417

Anderson, M., Wanless, V. D., Schwartz, D. M., McCully, E., Fornari, D. J., Jones, M. R., et al. (2018). Submarine Deep-Water Lava Flows at the Base of the Western Galápagos Platform. *Geochem. Geophys. Geosyst.* 19, 3945–3961. doi:10.1029/2018GC007632

Argus, D. F., Gordon, R. G., and DeMets, C. (2011). Geologically Current Motion of 56 Plates Relative to the No-Net-Rotation Reference Frame. *Geochem. Geophys. Geosyst.* 12, a–n. doi:10.1029/2011GC003751

Bagnardi, M., Amelung, F., and Poland, M. P. (2013). A New Model for the Growth of Basaltic Shields Based on Deformation of Fernandina Volcano, Galápagos Islands. *Earth Planet. Sci. Lett.* 377-378, 358–366. doi:10.1016/j.epsl.2013.07.016

Behn, M. D., Sinton, J. M., and Detrick, R. S. (2004). Effect of the Galápagos Hotspot on Seafloor Volcanism along the Galápagos Spreading Center (90.9-97.6°W). *Earth Planet. Sci. Lett.* 217, 331–347. doi:10.1016/s0012-821x(03)00611-3

Blichert-Toft, J., and White, W. M. (2001). Hf Isotope Geochemistry of the Galápagos Islands. *Geochem. Geophys. Geosyst.* 2, 9. doi:10.1029/2000gc000138

Bow, C. S., and Geist, D. J. (1992). Geology and Petrology of Floreana Island, Galapagos Archipelago, Ecuador. *J. Volcanology Geothermal Res.* 52, 83–105. doi:10.1016/0377-0273(92)90134-y

Bow, C. S. (1979). *The Geology and Petrogenesis of the Lavas of Floreana and Santa Cruz Islands: Galápagos Archipelago. Ph.D. Dissertation*. Eugene, OR: University of Oregon.

Canales, J. P., Dañobeitia, J. J., Detrick, R. S., Hooft, E. E. E., Bartolomé, R., and Naar, D. F. (1997). Variations in Axial Morphology along the Galápagos Spreading center and the Influence of the Galápagos Hotspot. *J. Geophys. Res.* 102, 27341–27354. doi:10.1029/97jb01633

Canales, J. P., Ito, G., Detrick, R. S., and Sinton, J. (2002). Crustal Thickness along the Western Galápagos Spreading Center and the Compensation of the Galápagos Hotspot Swell. *Earth Planet. Sci. Lett.* 203, 311–327. doi:10.1016/s0012-821x(02)00843-9

Chadwick, W. W., and Dieterich, J. H. (1995). Mechanical Modeling of Circumferential and Radial dike Intrusion on Galapagos Volcanoes. *J. Volcanology Geothermal Res.* 66, 37–52. doi:10.1016/0377-0273(94)00060-T

Chadwick, W. W., Geist, D. J., Jónsson, S., Poland, M., Johnson, D. J., and Meertens, C. M. (2006). A Volcano Bursting at the Seams: Inflation, Faulting, and Eruption at Sierra Negra Volcano, Galápagos. *Geol* 34, 1025–1028. doi:10.1130/G22826A.1

Chadwick, W. W., and Howard, K. A. (1991). The Pattern of Circumferential and Radial Eruptive Fissures on the Volcanoes of Fernandina and Isabela Islands, Galapagos. *Bull. Volcanol* 53, 259–275. doi:10.1007/bf00414523

Chen, C. -Y., and Frey, F. A. (1983). Origin of Hawaiian Tholeiite and Alkalic basalt. *Nature* 302, 785–789. doi:10.1038/302785a0

Christie, D. M., Duncan, R. A., McBirney, A. R., Richards, M. A., White, W. M., Harpp, K. S., et al. (1992). Drowned Islands Downstream from the Galapagos Hotspot Imply Extended Speciation Times. *Nature* 355, 246–248. doi:10.1038/355246a0

Christie, D. M., Werner, R., Hauff, F., Hoernle, K., and Hanan, B. B. (2005). Morphological and Geochemical Variations along the Eastern Galápagos Spreading Center. *Geochem. Geophys. Geosyst.* 6, 1. doi:10.1029/2004gc000714

Clague, D. A., and Dalrymple, G. B. (1988). Age and Petrology of Alkalic Postshield and Rejuvenated-Stage Lava from Kauai, Hawaii. *Contr. Mineral. Petrol.* 99, 202–218. doi:10.1007/BF00371461

Clague, D. A., and Dalrymple, G. B. (1987). "The Hawaiian-Emperor Volcanic Chain. Part I. Geologic Evolution," in *Volcanism in Hawaii*. Editors R. W. Decker, T. M. Wright, and P. H. Stauffer (Washington D.C.: US Gov't Printing Office), 5–54.

Cleary, Z., Schwartz, D. M., Mittelstaedt, E., and Harpp, K. (2020). Dynamic Magma Storage at Near-Ridge Hot Spots: Evidence from New Galápagos Gravity Data. *Geochem. Geophys. Geosyst* 21, 3. doi:10.1029/2019gc008722

Colman, A., Sinton, J. M., White, S. M., McClinton, J. T., Bowles, J. A., Rubin, K. H., et al. (2012). Effects of Variable Magma Supply on Mid-ocean ridge Eruptions: Constraints from Mapped Lava Flow fields along the Galápagos Spreading Center. *Geochem. Geophys. Geosyst.* 13, a–n. doi:10.1029/2012GC004163

Detrick, R. S., Sinton, J. M., Ito, G., Canales, J. P., Behn, M., Blacic, T., et al. (2002). Correlated Geophysical, Geochemical, and Volcanological Manifestations of Plume-ridge Interaction along the Galápagos Spreading Center. *Geochem. Geophys. Geosyst.* 3, 10. doi:10.1029/2002gc000350

Eggins, S. M., Woodhead, J. D., Kinsley, L. P. J., Mortimer, G. E., Sylvester, P., McCulloch, M. T., et al. (1997). A Simple Method for the Precise Determination of ≥ 40 Trace Elements in Geological Samples by ICPMS Using Enriched Isotope Internal Standardisation. *Chem. Geology.* 134, 311–326. doi:10.1016/s0009-2541(96)00100-3

Ellam, R. M. (1992). Lithospheric Thickness as a Control on basalt Geochemistry. *Geol* 20, 153–156. doi:10.1130/0091-7613(1992)020<0153:ltaaco>2.3.co;2

Feighner, M. A., and Richards, M. A. (1994). Lithospheric Structure and Compensation Mechanisms of the Galápagos Archipelago. *J. Geophys. Res.* 99, 6711–6729. doi:10.1029/93jb03360

Fitton, J. G., Saunders, A. D., Kempton, P. D., and Hardarson, B. S. (2003). Does Depleted Mantle Form an Intrinsic Part of the Iceland Plume? *Geochem. Geophys. Geosyst.* 4, 3. doi:10.1029/2002gc000424

Fitton, J. G., Saunders, A. D., Norry, M. J., Hardarson, B. S., and Taylor, R. N. (1997). Thermal and Chemical Structure of the Iceland Plume. *Earth Planet. Sci. Lett.* 153, 197–208. doi:10.1016/s0012-821x(97)00170-2

French, S. W., and Romanowicz, B. (2015). Broad Plumes Rooted at the Base of the Earth's Mantle beneath Major Hotspots. *Nature* 525, 95–99. doi:10.1038/nature14876

Frey, F. A., and Weis, D. (1995). Temporal Evolution of the Kerguelen Plume: Geochemical Evidence from 38 to 82 Ma Lavas Forming the Ninetyeast Ridge. *Contrib. Mineral. Petrol.* 121, 12–28. doi:10.1007/s004100050087

Fujita, K., and Sleep, N. H. (1978). Membrane Stresses Near Mid-ocean ridge-transform Intersections. *Tectonophysics* 50, 207–221. doi:10.1016/0040-1951(78)90136-1

Galer, S. J. G., and O'Nions, R. K. (1985). Residence Time of Thorium, Uranium and lead in the Mantle with Implications for Mantle Convection. *Nature* 316, 778–782. doi:10.1038/316778a0

Geist, D., Howard, K. A., and Larson, P. (1995). The Generation of Oceanic Rhyolites by Crystal Fractionation: the Basalt-Rhyolite Association at Volc N Alcedo, Gal Pagos Archipelago. *J. Petrology* 36, 965–982. doi:10.1093/petrology/36.4.965

Geist, D. J., Bergantz, G., and Chadwick, W. W. (2014a). "Galápagos Magma Chambers," in The Galápagos: A Natural Laboratory For the Earth Sciences, *Geophysical Monograph Series V. 204*. Editors K. S. Harpp, E. Mittelstaedt, N. d'Ozouville, and D. W. Graham (Washington, DC: American Geophysical Union), 55–69. doi:10.1002/9781118852538.ch5

Geist, D. J., Fornari, D. J., Kurz, M. D., Harpp, K. S., Adam Soule, S., Perfit, M. R., et al. (2006). Submarine Fernandina: Magmatism at the Leading Edge of the Galápagos Hot Spot. *Geochem. Geophys. Geosyst.* 7, a–n. doi:10.1029/2006GC001290

Geist, D. J., Harpp, K. S., Naumann, T. R., Poland, M., Chadwick, W. W., Hall, M., et al. (2008). The 2005 Eruption of Sierra Negra Volcano, Galápagos, Ecuador. *Bull. Volcanol.* 70, 655–673. doi:10.1007/s00445-007-0160-3

Geist, D. J., McBirney, A. R., and Duncan, R. A. (1986). Geology and Petrogenesis of Lavas from San Cristobal Island, Galapagos Archipelago. *Geol. Soc. America Bull.* 97, 555–566. doi:10.1130/0016-7606(1986)97<555:gapolf>2.0.co;2

Geist, D. J., Naumann, T. R., Standish, J. J., Kurz, M. D., Harpp, K. S., White, W. M., et al. (2005). Wolf Volcano, Galápagos Archipelago: Melting and Magmatic Evolution at the Margins of a Mantle Plume. *J. Petrol.* 46, 2197–2224. doi:10.1093/petrology/egi052

Geist, D. J., Snell, H., Snell, H., Goddard, C., and Kurz, M. D. (2014b). "A Paleogeographic Model of the Galápagos Islands and Biogeographical and Evolutionary Implications," in The Galápagos: A Natural Laboratory For the Earth Sciences, *Geophysical Monograph Series V. 204*. Editors K. S. Harpp, E. Mittelstaedt, N. d'Ozouville, and D. W. Graham (Washington, DC: American Geophysical Union), 145–166. doi:10.1002/9781118852538.ch8

Geist, D. J., White, W. M., and McBirney, A. R. (1988). Plume-asthenosphere Mixing beneath the Galapagos Archipelago. *Nature* 333, 657–660. doi:10.1038/333657a0

Geist, D., Naumann, T., and Larson, P. (1998). Evolution of Galapagos Magmas: Mantle and Crustal Fractionation without Assimilation. *J. Petrology* 39, 953–971. doi:10.1093/petroj/39.5.953

Georgen, J. E. (2014). Interaction of a Mantle Plume and a Segmented Mid-ocean ridge: Results from Numerical Modeling. *Earth Planet. Sci. Lett.* 392, 113–120. doi:10.1016/j.epsl.2014.01.035

Gibson, S. A., Geist, D. G., Day, J. A., and Dale, C. W. (2012). Short Wavelength Heterogeneity in the Galápagos Plume: Evidence from Compositionally Diverse Basalts on Isla Santiago. *Geochem. Geophys. Geosyst.* 13, 9. doi:10.1029/2012GC004244

Gibson, S. A., and Geist, D. (2010). Geochemical and Geophysical Estimates of Lithospheric Thickness Variation beneath Galápagos. *Earth Planet. Sci. Lett.* 300, 275–286. doi:10.1016/j.epsl.2010.10.002

Gibson, S. A., Geist, D. J., and Richards, M. A. (2015). Mantle Plume Capture, Anchoring, and Outflow during Galápagos Plume-ridge Interaction. *Geochem. Geophys. Geosyst.* 16, 5. doi:10.1002/2015gc005723

Gibson, S. A., and Richards, M. A. (2018). Delivery of Deep-Sourced, Volatile-Rich Plume Material to the Global ridge System. *Earth Planet. Sci. Lett.* 499, 205–218. doi:10.1016/j.epsl.2018.07.028

Gleeson, M. L., and Gibson, S. A. (2021). Insights into the Nature of Plume-ridge Interaction and Outflux of H_2O from the Galápagos Spreading Center. *Geochem. Geophys. Geosyst.* 22, 11. doi:10.1029/2020gc009560

Gleeson, M. L. M., Gibson, S. A., and Stock, M. J. (2020). Upper Mantle Mush Zones beneath Low Melt Flux Ocean Island Volcanoes: Insights from Isla Floreana, Galápagos. *J. Petrol.* 61, 1–26. doi:10.1093/petrology/egaa094

Gleeson, M. L., Soderman, C., Matthews, S., Cottaar, S., and Gibson, S. (2021). Geochemical Constraints on the Structure of the Earth's Deep Mantle and the Origin of the LLSVPs. *Geochem. Geophys. Geosyst.* 22, 9. doi:10.1029/2021gc009932

Goss, A. R., Perfit, M. R., Ridley, W. I., Rubin, K. H., Kamenov, G. D., Soule, S. A., et al. (2010). Geochemistry of Lavas from the 2005-2006 Eruption at the East Pacific Rise, 9°46′N-9°56′N: Implications for ridge Crest Plumbing and Decadal Changes in Magma Chamber Compositions. *Geochem. Geophys. Geosyst.* 11, a–n. doi:10.1029/2009GC002977

Graham, D. W., Christie, D. M., Harpp, K. S., and Lupton, J. E. (1993). Mantle Plume Helium in Submarine Basalts from the Galápagos Platform. *Science* 262, 2023–2026. doi:10.1126/science.262.5142.2023

Gudmundsson, A. (1995). Stress fields Associated with Oceanic Transform Faults. *Earth Planet. Sci. Lett.* 136, 603–614. doi:10.1016/0012-821x(95)00164-8

Hall, P. S., and Kincaid, C. (2004). Melting, Dehydration, and the Geochemistry of off-axis Plume-ridge Interaction. *Geochem. Geophys. Geosyst.* 5, 12. doi:10.1029/2003gc000667

Harpp, K., and Geist, D. (2002). Wolf-Darwin Lineament and Plume-ridge Interaction in Northern Galápagos. *Geochem.-Geophys.-Geosyst.* 3, 1–19. doi:10.1029/2002GC000370

Harpp, K. S., Fornari, D. J., Geist, D. J., and Kurz, M. D. (2003). Genovesa Submarine Ridge: A Manifestation of Plume-ridge Interaction in the Northern Galápagos Islands. *Geochem. Geophys. Geosyst.* 4, a–n. doi:10.1029/2003GC000531

Harpp, K. S., Geist, D. J., Koleszar, A. M., Christensen, B., Lyons, J., Sabga, M., et al. (2014a). "The Geology and Geochemistry of Isla Floreana, Galápagos," in The Galápagos: A Natural Laboratory For the Earth Sciences, *Geophysical Monograph Series V. 204.* Editors K. S. Harpp, E. Mittelstaedt, N. d'Ozouville, and D. W. Graham (Washington, DC: American Geophysical Union), 71–117. doi:10.1002/9781118852538.ch6

Harpp, K. S., and Geist, D. J. (2018). The Evolution of Galápagos Volcanoes: An Alternative Perspective. *Front. Earth Sci.* 6, 50. doi:10.3389/feart.2018.00050

Harpp, K. S., Hall, P. S., and Jackson, M. G. (2014b). "Galápagos and Easter," in The Galápagos: A Natural Laboratory For the Earth Sciences, *Geophysical Monograph Series V. 204.* Editors K. S. Harpp, E. Mittelstaedt, N. d'Ozouville, and D. W. Graham (Washington, DC: American Geophysical Union), 27–40. doi:10.1002/9781118852538.ch3

Harpp, K. S., and Weis, D. (2020). Insights into the Origins and Compositions of Mantle Plumes: A Comparison of Galápagos and Hawai'i. *Geochem. Geophys. Geosyst.* 21, 9. doi:10.1029/2019gc008887

Harpp, K. S., and White, W. M. (2001). Tracing a Mantle Plume: Isotopic and Trace Element Variations of Galápagos Seamounts. *Geochem. Geophys. Geosyst.* 2, a–n. doi:10.1029/2000GC000137

Harpp, K. S., Wirth, K. R., and Korich, D. J. (2002). Northern Galápagos Province: Hotspot-Induced, Near-ridge Volcanism at Genovesa Island. *Geol* 30, 399–402. doi:10.1130/0091-7613(2002)030<0399:ngpphi>2.0.co;2

Harpp, K. S., Wirth, K. R., Teasdale, R., Blair, S., Reed, L., Barr, J., et al. (2014c). "Plume-Ridge Interaction in the Galápagos," in The Galápagos: A Natural Laboratory For the Earth Sciences, *Geophysical Monograph Series V. 204.* Editors K. S. Harpp, E. Mittelstaedt, N. d'Ozouville, and D. W. Graham (Washington, DC: American Geophysical Union), 285–334. doi:10.1002/9781118852538.ch15

Harrison, L. N., Weis, D., and Garcia, M. O. (2020). The Multiple Depleted Mantle Components in the Hawaiian-Emperor Chain. *Chem. Geol.* 532. doi:10.1016/j.chemgeo.2019.119324

Hart, S. R., Hauri, E. H., Oschmann, L. A., and Whitehead, J. A. (1992). Mantle Plumes and Entrainment: Isotopic Evidence. *Science* 256, 517–520. doi:10.1126/science.256.5056.517

Herzberg, C., Asimow, P. D., Arndt, N., Niu, Y., Lesher, C. M., Fitton, J. G., et al. (2007). Temperatures in Ambient Mantle and Plumes: Constraints from Basalts, Picrites, and Komatiites. *Geochem. Geophys. Geosyst.* 8, 2. doi:10.1029/2006gc001390

Herzberg, C., and Gazel, E. (2009). Petrological Evidence for Secular Cooling in Mantle Plumes. *Nature* 458, 619–622. doi:10.1038/nature07857

Hirschmann, M. M. (2000). Mantle Solidus: Experimental Constraints and the Effects of Peridotite Composition. *Geochem. Geophys. Geosyst.* 1, 10. doi:10.1029/2000gc000070

Hoernle, K., Werner, R., Phipps Morgan, J., Garbe-Schönberg, D., Bryce, J., and Mrazek, J. (2000). Existence of Complex Spatial Zonation in the Galápagos Plume. *Geology* 28, 435–438. doi:10.1130/0091-7613(2000)028<0435:eocszi>2.3.co;2

Hooft, E. E. E., Toomey, D. R., and Solomon, S. C. (2003). Anomalously Thin Transition Zone beneath the Galápagos Hotspot. *Earth Planet. Sci. Lett.* 216, 55–64. doi:10.1016/S0012-821X(03)00517-X

Ingle, S., Ito, G., Mahoney, J. J., Chazey, W., Sinton, J., Rotella, M., et al. (2010). Mechanisms of Geochemical and Geophysical Variations along the Western Galápagos Spreading Center. *Geochem. Geophys. Geosyst.* 11, a–n. doi:10.1029/2009GC002694

Ito, G., Lin, J., and Gable, C. W. (1997). Interaction of Mantle Plumes and Migrating Mid-ocean Ridges: Implications for the Galápagos Plume-ridge System. *J. Geophys. Res.* 102, 15403–15417. doi:10.1029/97jb01049

Ito, G., Lin, J., and Graham, D. (2003). Observational and Theoretical Studies of the Dynamics of Mantle Plume–Mid-Ocean ridge Interaction. *Rev. Geophys* 41, 4. doi:10.1029/2002rg000117

Ito, G., and Mahoney, J. J. (2005). Flow and Melting of a Heterogeneous Mantle: 1. Method and Importance to the Geochemistry of Ocean Island and Mid-ocean ridge Basalts. *Earth Planet. Sci. Lett.* 230, 29–46. doi:10.1016/j.epsl.2004.10.035

Jackson, M. G., Hart, S. R., Saal, A. E., Shimizu, N., Kurz, M. D., Blusztajn, J. S., et al. (2008). Globally Elevated Titanium, Tantalum, and Niobium (TITAN) in Ocean Island Basalts with high3He/4He. *Geochem. Geophys. Geosyst.* 9, a–n. doi:10.1029/2007GC001876

Johnson, D. M., Hooper, P. R., and Conrey, R. M. (1999). XRF Analysis of Rock and Minerals for Major and Trace Elements on a Single Low Dilution Li-Tetraborate Fused Bead. *Adv. X-ray Anal.* 41, 843–867.

Kingsley, R. H., and Schilling, J.-G. (1998). Plume-ridge Interaction in the Easter-Salas Y Gomez Seamount Chain-Easter Microplate System: Pb Isotope Evidence. *J. Geophys. Res.* 103, 24159–24177. doi:10.1029/98jb01496

Klein, E. M., and Langmuir, C. H. (1987). Global Correlations of Ocean Ridge Basalt Chemistry with Axial Depth and Crustal Thickness. *J. Geophys. Res.* 92, 8089–8115. doi:10.1029/JB092iB08p08089

Kurz, M. D., and Geist, D. (1999). Dynamics of the Galapagos Hotspot from Helium Isotope Geochemistry. *Geochimica et Cosmochimica Acta* 63, 4139–4156. doi:10.1016/s0016-7037(99)00314-2

Kurz, M. D., Rowland, S. K., Curtice, J., Saal, A. E., and Naumann, T. (2014). "Eruption Rates for Fernandina Volcano," in The Galápagos: A Natural Laboratory For the Earth Sciences, *Geophysical Monograph Series V. 204.* Editors K. S. Harpp, E. Mittelstaedt, N. d'Ozouville, and D. W. Graham (Washington, DC: American Geophysical Union), 41–54. doi:10.1002/9781118852538.ch4

Langmuir, C. H., Vocke, R. D., Jr, Hanson, G. N., and Hart, S. R. (1978). A General Mixing Equation with Applications to Icelandic Basalts. *Earth Planet. Sci. Lett.* 37, 380–392. doi:10.1016/0012-821x(78)90053-5

Le Corvec, N., and McGovern, P. J. (2018). The Effect of Ocean Loading on the Growth of Basaltic Ocean Island Volcanoes and Their Magmatic Plumbing System. *Front. Earth Sci.* 6, 119. doi:10.3389/feart.2018.00119

Lonsdale, P. (1989). A Geomorphological Reconnaissance of the Submarine Part of the East Rift Zone of Kilauea Volcano, Hawaii. *Bull. Volcanol.* 51, 123–144. doi:10.1007/bf01081981

Macdonald, G. A., Abbott, A. T., and Peterson, F. L. (1983). *Volcanoes in the Sea: The Geology of Hawaii.* Honolulu, HI: University of Hawaii Press.

MacDonald, G. A., and Katsura, T. (1964). Chemical Composition of Hawaiian Lavas1. *J. Petrology* 5, 82–133. doi:10.1093/petrology/5.1.82

Mahr, J., Harpp, K. S., Kurz, M. D., Geist, D., Bercovici, H., Pimentel, R., et al. (2016). "Rejuvenescent Volcanism on San Cristóbal Island, Galápagos: a Late "Plumer"," in *AGU Fall Meeting Abstracts* (San Francisco, CA).

McDonough, W. F., and Sun, S.-s. (1995). The Composition of the Earth. *Chem. Geology.* 120, 223–253. doi:10.1016/0009-2541(94)00140-4

McGovern, P. J., Grosfils, E. B., Galgana, G. A., Morgan, J. K., Rumpf, M. E., Smith, J. R., et al. (2015). Lithospheric Flexure and Volcano Basal Boundary Conditions: Keys to the Structural Evolution of Large Volcanic Edifices on the Terrestrial Planets. *Geol. Soc. Lond. Spec. Publications* 401, 219–237. doi:10.1144/sp401.7

McGovern, P. J., Rumpf, M. E., and Zimbelman, J. R. (2013). The Influence of Lithospheric Flexure on Magma Ascent at Large Volcanoes on Venus. *J. Geophys. Res. Planets* 118, 2423–2437. doi:10.1002/2013je004455

McKenzie, D., and O'Nions, R. K. (1991). Partial Melt Distributions from Inversion of Rare Earth Element Concentrations. *J. Petrology* 32, 1021–1091. doi:10.1093/petrology/32.5.1021

McLennan, S. M., and Ross Taylor, S. (2012). "Geology, Geochemistry and Natural Abundances," in *Encyclopedia of Inorganic and Bioinorganic Chemistry* (John Wiley & Sons). doi:10.1002/9781119951438.eibc2004

Mittal, T., and Richards, M. A. (2017). Plume-ridge Interaction via Melt Channelization at Galápagos and Other Near-ridge Hotspot Provinces. *Geochem. Geophys. Geosyst.* 18, 4. doi:10.1002/2016gc006454

Mittelstaedt, E., Ito, G., and van Hunen, J. (2011). Repeat ridge Jumps Associated with Plume-ridge Interaction, Melt Transport, and ridge Migration. *J. Geophys. Res.* 116, B01102. doi:10.1029/2010jb007504

Mittelstaedt, E., Soule, S., Harpp, K., Fornari, D., McKee, C., Tivey, M., et al. (2012). Multiple Expressions of Plume-ridge Interaction in the Galápagos: Volcanic Lineaments and ridge Jumps. *Geochem. Geophys. Geosyst.* 13, 5. doi:10.1029/2012gc004093

Morgan, W. J. (1972). Deep Mantle Convection Plumes and Plate Motions. *AAPG Bull.* 56, 203–213. doi:10.1306/819a3e50-16c5-11d7-8645000102c1865d

Naumann, T., Geist, D., and Kurz, M. (2002). Petrology and Geochemistry of Volcan Cerro Azul: Petrologic Diversity Among the Western Galapagos Volcanoes. *J. Petrol.* 43, 859–883. doi:10.1093/petrology/43.5.859

Norrish, K., and Hutton, J. T. (1969). An Accurate X-ray Spectrographic Method for the Analysis of a Wide Range of Geological Samples. *Geochimica et Cosmochimica Acta* 33, 431–453. doi:10.1016/0016-7037(69)90126-4

Reynolds, R. W., and Geist, D. J. (1995). Petrology of Lavas from Sierra Negra Volcano, Isabela Island, Galápagos Archipelago. *J. Geophys. Res.* 100, 24537–24553. doi:10.1029/95JB02809

Ribe, N. M. (1996). The Dynamics of Plume-ridge Interaction: 2. off-ridge Plumes. *J. Geophys. Res.* 101, 16195–16204. doi:10.1029/96jb01187

Saal, A., Kurz, M., Hart, S., Blusztajn, J., Blicherttoft, J., Liang, Y., et al. (2007). The Role of Lithospheric Gabbros on the Composition of Galapagos Lavas. *Earth Planet. Sci. Lett.* 257, 391–406. doi:10.1016/j.epsl.2007.02.040

Schilling, J.-g., Kingsley, R. H., and Devine, J. D. (1982). Galapagos Hot Spot-Spreading Center System: 1. Spatial Petrological and Geochemical Variations (83°W-101°W). *J. Geophys. Res.* 87, 5593–5610. doi:10.1029/jb087ib07p05593

Schwartz, D. M., Harpp, K. S., Kurz, M. D., Wilson, E. L., and VanKirk, R. (2022). Low-Volume Magmatism Linked to Flank Deformation on Isla Santa Cruz, Galápagos Archipelago, using Cosmogenic ^{3}He Exposure and ^{40}Ar/^{39}Ar Dating of Fault Scarps and Lavas. *Bull. Volcanol.* 84, 82. doi:10.1007/s00445-022-01575-3

Schwartz, D. M., Wanless, V. D., Soule, S. A., Schmitz, M. D., and Kurz, M. D. (2020). Monogenetic Near-Island Seamounts in the Galápagos Archipelago. *Geochem. Geophys. Geosyst.* 21. doi:10.1029/2020GC008914

Schwartz, D. (2014). *Volcanic, Structural, and Morphological History of Santa Cruz Island, Galápagos Archipelago*. Moscow, Idaho: University of Idaho. Master's thesis.

Siebert, L., Simkin, T., and Kimberly, P. (2010). *Volcanoes of the World*. Berkeley: University of California Press.

Sinton, C. W., Harpp, K. S., and Christie, D. M. (2014). "A Preliminary Survey of the Northeast Seamounts, Galápagos Platform," in The Galápagos: A Natural Laboratory For the Earth Sciences, *Geophysical Monograph Series V. 204.* Editors K. S. Harpp, E. Mittelstaedt, N. d'Ozouville, and D. W. Graham (Washington, DC: American Geophysical Union), 335–362. doi:10.1002/9781118852538.ch16

Sinton, J., Detrick, R., Canales, J. P., Ito, G., and Behn, M. (2003). Morphology and Segmentation of the Western Galápagos Spreading Center, 90.5-98 W: Plume-ridge Interaction at an Intermediate Spreading ridge. *Geochem. Geophys. Geosyst* 4, 12. doi:10.1029/2003gc000609

Smith, D. K., Kong, L. S. L., Johnson, K. T., and Reynolds, J. R. (2002). "Volcanic Morphology of the Submarine Puna Ridge, Kilauea Volcano," in Hawaiian Volcanoes: Deep Underwater Perspectives, *Geophysical Monograph Series V. 128.* Editors E. Takahashi, P. W. Lipman, M. O. Garcia, J. Naka, and S. Aramaki (Washington, DC: American Geophysical Union), 125–142. doi:10.1029/gm128p0125

Stock, M. J., Geist, D., Neave, D. A., Gleeson, M. L. M., Bernard, B., Howard, K. A., et al. (2020). Cryptic Evolved Melts beneath Monotonous Basaltic Shield Volcanoes in the Galápagos Archipelago. *Nat. Commun.* 11, 3767. doi:10.1038/s41467-020-17590-x

Stock, M. J., Bagnardi, M., Neave, D. A., Maclennan, J., Bernard, B., Buisman, I., et al. (2018). Integrated Petrological and Geophysical Constraints on Magma System Architecture in the Western Galápagos Archipelago: Insights from Wolf Volcano. *Geochem. Geophys. Geosyst.* 19, 12. doi:10.1029/2018gc007936

Taylor, B., Crook, K., and Sinton, J. (1994). Extensional Transform Zones and Oblique Spreading Centers. *J. Geophys. Res.* 99, 19707–19718. doi:10.1029/94jb01662

Villagómez, D. R., Toomey, D. R., Geist, D. J., Hooft, E. E. E., and Solomon, S. C. (2014). Mantle Flow and Multistage Melting beneath the Galápagos Hotspot Revealed by Seismic Imaging. *Nat. Geosci* 7, 151–156. doi:10.1038/ngeo2062

Villagómez, D. R., Toomey, D. R., Hooft, E. E. E., and Solomon, S. C. (2007). Upper Mantle Structure beneath the Galápagos Archipelago from Surface Wave Tomography. *J. Geophys. Res.* 112, B07303. doi:10.1029/2006JB004672

Weis, D., Garcia, M. O., Rhodes, J. M., Jellinek, M., and Scoates, J. S. (2011). Role of the Deep Mantle in Generating the Compositional Asymmetry of the Hawaiian Mantle Plume. *Nat. Geosci* 4, 831–838. doi:10.1038/ngeo1328

Weis, D., Kieffer, B., Maerschalk, C., Barling, J., De Jong, J., Williams, G. A., et al. (2006). High-precision Isotopic Characterization of USGS Reference Materials by TIMS and MC-ICP-MS. *Geochem. Geophys. Geosyst.* 7, 8. doi:10.1029/2006GC001283

Werner, R., Hoernle, K., van den Bogaard, P., Ranero, C., von Huene, R., and Korich, D. (1999). Drowned 14-m.y.-old Galápagos Archipelago off the Coast of Costa Rica: Implications for Tectonic and Evolutionary Models. *Geol* 27, 499–502. doi:10.1130/0091-7613(1999)027<0499:dmyogp>2.3.co;2

Wessa, P. (2021). *Free Statistics Software*. version 1.2.1. Office for Research Development and Education. Available at: https://www.wessa.net.

White, S. M., Meyer, J. D., Haymon, R. M., Macdonald, K. C., Baker, E. T., and Resing, J. A. (2008). High-resolution Surveys along the Hot Spot–Affected Galápagos Spreading Center: 2. Influence of Magma Supply on Volcanic Morphology. *Geochem. Geophys. Geosyst.* 9, 9. doi:10.1029/2008gc002036

White, W. M., and Hofmann, A. W. (1978). Geochemistry of the Galápagos Islands: Implications for Mantle Dynamics and Evolution. *Carnegie Inst. Wash. Yearb.* 77, 596–606.

White, W. M., McBirney, A. R., and Duncan, R. A. (1993). Petrology and Geochemistry of the Galápagos Islands: Portrait of a Pathological Mantle Plume. *J. Geophys. Res.* 98, 19533–19563. doi:10.1029/93jb02018

Wilson, D. S., and Hey, R. N. (1995). History of Rift Propagation and Magnetization Intensity for the Cocos-Nazca Sspreading Center. *J. Geophys. Res.* 100, 10041–10056. doi:10.1029/95jb00762

Wolfe, C. J., Solomon, S. C., Laske, G., Collins, J. A., Detrick, R. S., Orcutt, J. A., et al. (2009). Mantle Shear-Wave Velocity Structure beneath the Hawaiian Hot Spot. *Science* 326, 1388–1390. doi:10.1126/science.1180165

Workman, R. K., and Hart, S. R. (2005). Major and Trace Element Composition of the Depleted MORB Mantle (DMM). *Earth Planet. Sci. Lett.* 231, 53–72. doi:10.1016/j.epsl.2004.12.005

Yun, S., Segall, P., and Zebker, H. (2006). Constraints on Magma Chamber Geometry at Sierra Negra Volcano, Galápagos Islands, Based on InSAR Observations. *J. Volcanology Geothermal Res.* 150, 232–243. doi:10.1016/j.jvolgeores.2005.07.009

Conflict of Interest: The authors declare that the research was conducted in the absence of any commercial or financial relationships that could be construed as a potential conflict of interest.

Publisher's Note: All claims expressed in this article are solely those of the authors and do not necessarily represent those of their affiliated organizations, or those of the publisher, the editors and the reviewers. Any product that may be evaluated in this article, or claim that may be made by its manufacturer, is not guaranteed or endorsed by the publisher.

Copyright © 2022 Wilson, Harpp, Schwartz and Van Kirk. This is an open-access article distributed under the terms of the Creative Commons Attribution License (CC BY). The use, distribution or reproduction in other forums is permitted, provided the original author(s) and the copyright owner(s) are credited and that the original publication in this journal is cited, in accordance with accepted academic practice. No use, distribution or reproduction is permitted which does not comply with these terms.

Advantages of publishing in Frontiers

OPEN ACCESS
Articles are free to read for greatest visibility and readership

FAST PUBLICATION
Around 90 days from submission to decision

HIGH QUALITY PEER-REVIEW
Rigorous, collaborative, and constructive peer-review

TRANSPARENT PEER-REVIEW
Editors and reviewers acknowledged by name on published articles

Frontiers
Avenue du Tribunal-Fédéral 34
1005 Lausanne | Switzerland

Visit us: www.frontiersin.org
Contact us: frontiersin.org/about/contact

REPRODUCIBILITY OF RESEARCH
Support open data and methods to enhance research reproducibility

DIGITAL PUBLISHING
Articles designed for optimal readership across devices

FOLLOW US
@frontiersin

IMPACT METRICS
Advanced article metrics track visibility across digital media

EXTENSIVE PROMOTION
Marketing and promotion of impactful research

LOOP RESEARCH NETWORK
Our network increases your article's readership